

7<sup>th</sup> Workshop on

# The New Boundaries of Structural Concrete 2024

University of Rome Tor Vergata | Rome | September 19-20, 2024



EDITED BY  
SIMONE SPAGNUOLO - LUIGI COPPOLA  
ALBERTO MEDA - ROBERTO REALFONZO

*Proceedings of*

**Seventh Workshop  
New Boundaries of Structural Concrete 2024**

University of Rome Tor Vergata  
19-20 September 2024, Rome, Italy

*Edited by*

**Simone Spagnuolo**

**Luigi Coppola**

**Alberto Meda**

**Roberto Realfonzo**

## **Note by the editors**

This book was carefully produced. However, no liability or responsibility of any kind (including liability for negligence) is accepted by the editors, the authors, the Scientific Committee and the Organizing Committee. Statements, data, illustrations or other issues may be inaccurate or incorrect.

# FOREWORD

The 7th edition of the workshop “The New Boundaries of Structural Concrete” is organized by the American Concrete Institute – Italy Chapter in collaboration with the Department of Civil Engineering and Computer Science Engineering of the University of Rome Tor Vergata, as well as the Tunnelling Engineering Research Centre (TERC). Following the success of previous editions in Salerno (2010), Ancona (2011), Bergamo (2013), Capri (2016), Milan (2019), and Lecce (2022), this year’s workshop takes place in Rome, from September 19th to 20th, 2024.

As with prior editions, the aim of this event is to foster collaboration between the Italian and international scientific communities and to engage leading industrial and professional experts. Together, we will continue the vital dialogue on critical issues facing concrete structures today, while exploring the potential of concrete as a sustainable and resilient building material.

The topics of this year’s workshop reflect the dynamic advancements in the field. Our discussions cover innovative cementitious materials, corrosion, durability and self-healing in reinforced concrete (RC) structures, the behavior of concrete under extreme environmental and accidental conditions (earthquakes, wind, fire, impact, and blast), and the sustainability of green concrete. Additionally, the short- and long-term performance of RC structures, strengthening and repair techniques, bond and connections in prestressed concrete (PC) and hybrid structures, as well as life-cycle assessment (LCA) and structural health monitoring are explored.

The organizing and scientific committees hope that this workshop will provide an inspiring platform for learning, networking, and innovation, extending their best wishes to all participants for a fruitful and engaging experience with the new boundaries of structural concrete.

Rome, September 2024

## **The Editors**

Simone Spagnuolo

Luigi Coppola

Alberto Meda

Roberto Realfonzo





## Scientific Committee

Maria Antonietta Aiello (Italy)  
Maria Cruz Alonso (Spain)  
Carmen Andrade Perdrrix (Spain)  
Luigi Biolzi (Italy)  
Denny Coffetti (Italy)  
Valeria Corinaldesi (Italy)  
Edoardo Cosenza (Italy)  
Romildo Diaz Toledo Filho (Brazil)  
Marco Di Prisco (Italy)  
Rolf Eligehausen (Germany)  
Ciro Faella (Italy)  
Vyatcheslav Falikman (Russia)  
Alessandro Fantilli (Italy)  
Pietro Gambarova (Italy)  
Matteo Gastaldi (Italy)  
Ravindra Gettu (India)  
Ezio Giuriani (Italy)  
Maurizio Guadagnini (UK)  
Eduardus Koenders (Germany)  
Lidia La Mendola (Italy)  
Marianovella Leone (Italy)  
Antonio Liciulli (Italy)  
Gennaro Magliulo (Italy)  
Enzo Martinelli (Italy)  
Stijn Matthys (Belgium)  
Viktor Mechtcherine (Germany)  
Marco Menegotto (Italy)  
Francesco Micelli (Italy)  
Barzin Mobasher (Usa)  
Harald Müller (Germany)  
Antonio Nanni (Usa)  
Emidio Nigro (Italy)  
Maria Rosaria Pecce (Italy)  
Alva Peled (Israel)  
Carlo Pellegrino (Italy)  
Giovanni Plizzari (Italy)  
Andrea Prota (Italy)  
Paolo Riva (Italy)  
Gianpaolo Rosati (Italy)  
Anna Saetta (Italy)  
Marco Savoia (Italy)  
Pedro Serna (Spain)  
Lesley Sneed (USA)  
Timothy Wangler (Switzerland)

## Organizing Committee

Alberto Meda (Chair)  
Zila Rinaldi

Simone Spagnuolo  
Fabio Di Carlo

## ACI Italy Chapter

Mario A. Chiorino (Honorary President)  
Roberto Realfonzo (Past President)

Luigi Coppola (President)  
Liberato Ferrara (Vice-President)



# Table of Contents

Note by the editors .....	II
Foreword .....	III
Scientific Committee .....	V
Organizing Committee .....	V
ACI Italy Chapter .....	V
<b>List of Papers .....</b>	<b>IX</b>
i. Innovative cementitious materials .....	1
ii. Corrosion and self-healing in reinforced concrete (RC) structures .	49
iii. Concrete and reinforced-concrete under extreme environmental conditions (earthquake, wind, temperature) .....	59
iv. Concrete and reinforced concrete in accidental conditions (fire, impact, blast) .....	91
v. Green concrete and sustainability of concrete structures .....	117
vi. Short- and long-term behaviour of RC structures .....	151
vii. Bond and connections in RC, prestressed concretes (PC) and mixed structures .....	161
viii. Bond and connections in RC, prestressed concretes (PC) and mixed structures .....	181
ix. Performance and life-cycle assessment (LCA) of concrete structures .....	215
x. Aging and deterioration of Concrete Structures .....	241
xi. Structural health monitoring .....	259



# List of Papers

## **Innovative cementitious materials**

**1**

- Eco-Friendly Alkali-Activated Mortars for Structural Applications.  
*Francesco Ascione, Francesco Bencardino, Sebastiano Candamano, Fortunato Crea, Pietro Mazzuca, Annalisa Napoli, Luciano Ombres, Roberto Realfonzo.....* 3
- Experimental study of smart cementitious material to monitor deformation and cracking in structures.  
*Marcello Molfetta .....* 11
- Smart cement-based mortars for structural health monitoring applications: a step towards increased scalability.  
*Antonella D'Alessandro, Daniel A. Triana-Camacho, Andrea Meoni, Enrique García-Macías and Filippo Ubertini .....* 19
- Self-cleaning low-carbon mortars based on alkali activated materials: the role of TiO<sub>2</sub> addition.  
*Simone Rapelli, Denny Coffetti, Elena Crotti, Luigi Coppola .....* 27
- Structural Behaviour of HPFRC Walls Subjected to Axial Load and Bending Moment.  
*Alessandro P. Fantilli, Nicholas S. Burello, Bernardino Chiaia, Jorge C. Diaz Garcia, Alfredo A. Flore Gutierrez, Davide Zampini .....* 35
- Electrically conductive mortars based on cement or alkali-activated fly ash: mechanical and electrical characterization.  
*Alessandra Mobili, Gloria Cosoli, Gian Marco Revel and Francesca Tittarelli .....* 41

## **Corrosion and self-healing**

### **in reinforced concrete (RC) structures**

**49**

- Experimental study for the development of constitutive laws of corroded steel rebars.  
*Manuel Bartoli, Paolo Isabella .....* 51

## **Concrete and reinforced-concrete under extreme environmental conditions (earthquake, wind, temperature)**

**59**

- Distributed plasticity models for the seismic response of reinforced concrete shear walls.  
*Chiara Di Salvatore, Gennaro Magliulo, Danilo D'Angela, Claudio Corbo.....* 61

Machine-learning-enhanced variable-angle truss model for shear capacity assessment of reinforced concrete elements.  
*Qingcong Zeng, Dario De Domenico, Giuseppe Quaranta and Giorgio Monti* ..... 69

Seismic Hysteretic Systems for Precast Buildings.  
*Giulio Proietti, Simone Pedullà and Nicola Nisticò* ..... 75

A new numerical model to simulate buckling of steel rebars.  
*Melina Bosco, Andrea Florida, Dario Panarelli, Pier Paolo Rossi, Nino Spinella...* 83

---

**Concrete and reinforced concrete  
in accidental conditions (fire, impact, blast) 91**

---

Thermo-fluid-dynamic simulation of cellulosic fires in precast industrial buildings with vault or shed roof.  
*Bruno Dal Lago, Francesco Rizzo, Paride Tucci* ..... 93

Structural behaviour of reinforced concrete ring tunnels in fire.  
*Bruno Dal Lago, Gaia Casarotto* ..... 99

Structural robustness of reinforced concrete moment resisting frames: deterministic and reliability assessment.  
*Elena Miceli, Diego Gino, Gabriele Neri, Gaetano Alfano, Luca Giordano, Paolo Castaldo* ..... 109

---

**Green concrete and sustainability  
of concrete structures 117**

---

Bond behaviour between steel/FRP bars and sustainable concrete: preliminary study.  
*Maria Antonietta Aiello, Denny Coffetti, Luigi Coppola, Maria Milena Della Vecchia, Marianovella Leone, Annalisa Napoli, Simone Rapelli, Roberto Realfonzo, Vincenzo Romanazzi* ..... 119

Properties of high-performance fiber reinforced concrete containing electric arc furnace slags.  
*Matteo Lamberti, Roberto Rosignoli, Marco Stancari and Fausto Minelli* ..... 127

Evaluation of the of the Italian ready-mix concrete supply chain based on LCA “from cradle to gate”.  
*Denny Coffetti, Elisabetta Palumbo, Simone Rapelli, Elena Crotti, Luigi Coppola..* 135

Assessment of Mid-Span Deflection in Beams Reinforced with Hybrid FRP/Steel Rebars: A Comparative Study. <i>Luciano Ombres, Maria Antonietta Aiello, Pietro Mazzuca, Francesco Campo- longo.....</i>	143
---	-----

---

**Short- and long-term behaviour of RC structures 151**

---

Applicability of an accelerated test for long-term performance estimation of hydrophobic treatment for reinforced concrete structures. <i>Britta M. Schallock, Matteo Gastaldi.....</i>	153
--	-----

**Bond and connections in RC, prestressed concretes (PC) and mixed structures 161**

---

Bond behaviour of FRP bars to concrete: database collection and preliminary analysis. <i>Maria Milena Della Vecchia, Annalisa Napoli, Roberto Realfonzo.....</i>	163
---	-----

Bond of embedded steel reinforcement at high temperature and in fire conditions. <i>Pietro G. Gambarova, Giovanni Metelli, Giovanni Muciaccia, Giovanni Plizzari.....</i>	171
--	-----

**Strengthening and repair of concrete structures 181**

---

Interface bond between SRP system and concrete substrate: modelling. <i>Francesco Ascione, Marco Lamberti, Annalisa Napoli and Roberto Realfonzo.....</i>	183
--	-----

Influence of high temperature exposure on the performances of Textile Reinforced Alkali-Activated Mortar systems. <i>Daniele Berdini, Jacopo Donnini.....</i>	191
--	-----

Strengthening of Varese-type floor. <i>Marco Bosio, Marius Eteme Minkada, Paolo Riva, Andrea Bruggi.....</i>	199
---	-----

The effectiveness of Fiber Reinforced Concrete in shear retrofitting of bridge concrete beams: case study and numerical simulation. <i>A. Greco, S. Pistorio, A. Salvatore, A. Ficociello, A. Basconi, A. Lupoi.....</i>	207
---	-----



## **Performance and life-cycle assessment (LCA) of concrete structures** **215**

---

How Life Cycle Assessment has influenced our mind set in structural designing.  
*Francesco Lomurno, Mauro Eugenio Giuliani*..... 217

Comprehensive environmental comparison of different structural systems for multistorey buildings in Italian and French contexts.  
*Laura Corti, Manuel Manthey, Pierre Navaro-Auburtin, Giovanni Muciaccia* ..... 225

Design and feasibility of sustainable solution for the Genoa sub-port tunnel project.  
*Simone Spagnuolo, Francesca Magnelli, Matteo Pierani, Andrea Magliocchetti, Alberto Meda* ..... 233

## **Aging and deterioration of Concrete Structures** **241**

---

The effect of degradation on the structural response of a reinforced concrete arch bridge.  
*Paolo Andrea Miglietta, Gianni Blasi, Daniele Perrone, Francesco Micelli, Maria Antonietta Aiello* ..... 243

On field evaluation and durability of protective silane based treatments for concrete structures.  
*Denny Coffetti, Simone Rapelli, Andrea Nicoletti, Luigi Coppola* ..... 251

## **Structural health monitoring** **259**

---

Manini Connect: integrated continuous monitoring of precast structures subject to multiple hazards.  
*Manuel Boccolini, Leonardo Casali, Salvatore Romano, Giuseppe Paci, Arianna Peppoloni, Bruno Dal Lago* ..... 261

Reinforced concrete bridge serviceability displacement estimation for DInSAR data interpretation.  
*A. Sandoli, S. Scoccola, C. Rainieri, G. Fabbrocino* ..... 269

Automatic crack pattern detection and assessment of corroded reinforced concrete structures.  
*Stefania Imperatore, Cristina Martellini, Cristina Monteleone, Tiziano Pagliaroli, Fabrizio Patanè, Annalaura Casanova Municchia* ..... 277

Integrated System for monitoring and management of Infrastructures. <i>Antonino Fotia, Raffaele Pucinotti</i> .....	285
Evaluation of Bridge Deflections by means of Clinometers based on Micro-Electro-Mechanical Systems (MEMS). <i>Francesco Filippo Bico, Fabio Di Carlo, Alberto Meda</i> .....	293
Structural Assessment and Maintenance Optimization via Satellite Radar Imagery and Data Integration. <i>Teresa Celozzi, Fabio Di Carlo and Alberto Meda</i> .....	301



# **Innovative cementitious materials**



# Eco-Friendly Alkali-Activated Mortars for Structural Applications

Francesco Ascione<sup>1</sup>, Francesco Bencardino<sup>2</sup>, Sebastiano Candamano<sup>3</sup>, Fortunato Crea<sup>4</sup>, Pietro Mazzuca<sup>5</sup>, Annalisa Napoli<sup>6</sup>, Luciano Ombres<sup>7</sup>, Roberto Realfonzo<sup>8</sup>

<sup>1,6,8</sup> *Department of Civil Engineering, University of Salerno, Fisciano, Salerno, Italy*

<sup>2,5,7</sup> *Department of Civil Engineering, University of Calabria, Rende, Cosenza, Italy*

<sup>3,4</sup> *Department of Mechanical, Energy and Management Engineering, University of Calabria, Rende, Cosenza, Italy*

## Abstract

The development of alternative low-carbon binders with elasto-mechanical properties tuned for repair/retrofitting applications represents a key commercial driver of the sector. Cement-free alkali-activated mortars are a reasonable alternative to the current conglomerates, as they show lower rigidity than Portland cement mortars at equal strength classes and can be produced using industrial by-products. However, their tendency to show high free shrinkage and the risk of efflorescence require an accurate selection of the reactive powders and mix design. The presents work investigates different mix designs for cement-free alkali-activated mortars to be used as matrices in fabric-reinforced composites, maximizing the use of industrial by-products as active powders and cost-effective and environmentally friendly activators. The mortars have been characterized by measuring their capillary water absorption, compressive and flexural strengths, and analyzing them using x-ray diffractometry. It is noteworthy that this experimental study is part of the STRIPES research project, funded by the PRIN-PNRR 2022 call, which aims at developing sustainable mortars for structural repair and retrofitting interventions.

## 1 Introduction

In recent years, the use of Fiber-Reinforced Cementitious Matrix (FRCM) composites has gained significant attention for several civil engineering applications [1], [2]. These systems, composed of high-strength fibers incorporated into an inorganic matrix, exhibit a high strength-to-weight ratio, ease of application, and reduced invasiveness of intervention [3]. Despite the structural benefits offered by FRCM systems, there are significant concerns regarding their environmental impact. Indeed, traditional cement-based matrices, while effective in providing adequate mechanical performance, substantially contribute to carbon emissions and intensive energy consumption. In addition, legitimate sustainability concerns are associated with the use of synthetic fibers, primarily due to their non-biodegradability and contribution to microplastic pollution.

In this context, the need to develop “green” FRCM systems is crucial to promote wider adoption of this composite systems for structural applications. To date, the development of FRCMs with a low environmental impact for structural purposes has shown relatively slow progress, with much of the effort focused on replacing synthetic fibers with natural ones. However, these natural fibers typically exhibit lower mechanical properties compared to conventional synthetic fibers (such as glass, carbon, or aramid), making them less suitable for structural applications. Furthermore, natural fibers of plant origin, such as flax and hemp, are highly hygroscopic, showing a high moisture absorption rate, which leads to durability issues. In this context, a reasonable compromise between environmental sustainability and adequate structural performance can be achieved by combining synthetic or mineral fibers (such as Basalt) with matrices that have reduced or no cement content.

For over seventy years, academic interest has been focused on a broad family of “alkali-activated binders” intended to replace Portland cement in the production of mortars and concretes [4]-[6]. These binders were recently applied on a large scale in Eastern Europe and China [9], [10]. A significant variety of reactive powders-derived from natural resources or industrial by-products-and alkaline activators can be used for the production of these binders.

The nature and quantities of the alkaline activators, as well as the variability in the composition and

reactivity of the raw materials, influence the fresh state properties and the mechanical properties development over time of the mortars and concretes produced with these binders. In general, when the reactive powders are aluminosilicates—such as metakaolin or fly ash—concentrated alkaline solutions and elevated temperatures are required to start the reactions. The material obtained from this process (zeolites known as "geopolymers") are characterized by (i) high initial alkalinity, (ii) the formation of a sodium-based amorphous aluminosilicate hydrate gel (N-A-S-H gel), and (iii) the absence of portlandite as a reaction product [7], [8]. On the other hand, when the reactive powder consists of ground granulated blast-furnace slag (GGBFS), activation occurs at ambient temperature using more diluted solutions, and the main product of the reactions is a calcium aluminosilicate hydrate gel (C-A-S-H gel). Additionally, there are other binders, known as "hybrid or blended alkali-activated binders" composed of a mixture of the two types of reactive powders, with the addition of small quantities of Portland cement to enhance certain physical-mechanical properties in both the fresh and hardened states [9]. Among the activators, sodium carbonate is the most eco-friendly, as it can activate slag by raising the pH to sufficiently high levels. It is an industrial by-product or can be obtained at moderate temperatures from natural raw materials such as trona [10] and is 2-3 times more economical than sodium hydroxide or sodium silicate. However, slag activation with sodium carbonate is characterized by very long setting times and slow development of mechanical properties. To address this issue, a potential solution is to use a mixture of activators containing sodium carbonate and sodium silicate. Regarding the development of FRCM systems using mortars produced with alkali-activated binders, it should be noted that recent studies have shown that systems comprising long steel fibers embedded in geopolymeric mortar exhibit an initial high alkalinity required for geopolymerization, which weakens the matrix-fiber interface [10]. In this context, this paper briefly presents part of the research project funded by the PRIN-PNRR 2022 call, aimed at developing basalt and steel FRCM systems for the strengthening of masonry columns and panels made of both brick and yellow tuff blocks. The innovative aspect of the "STRIPES" Project is the development of "sustainable matrices" whose production drastically reduces CO<sub>2</sub> emissions compared to the commonly used Portland cement mortars [11]. The first stage of the project, conducted by two operational units at the Universities of Calabria and Salerno, concerns the development of a "green" mortar made with alkali-activated binders, and preliminary results are reported here.

## 2 Materials and methods

### 2.1 Mix Design

In a preliminary stage, several "mix designs" were developed to study "green" mortars for use as matrices in FRCM systems. The following raw materials were used for the preparation of the mortars: (i) reactive powders; (ii) alkaline activators; (iii) sand. Fly ash class F and GGBFS were used as reactive powders. The particle size distribution of the fly ash was characterized by a D10 of 0.5 μm, a D50 of 5 μm, and a D90 of 11 μm. The chemical composition, expressed by weight and in terms of oxides, was as follows: SiO<sub>2</sub>=53.5%, Al<sub>2</sub>O<sub>3</sub>=34.3%, CaO=4.4%, Fe<sub>2</sub>O<sub>3</sub>=3.6%. The GGBFS had a particle size distribution with a D10 of 6.76 μm, a D50 of 18.5 μm, and a D90 of 33.17 μm. Its chemical composition, assessed by Energy-dispersive X-ray spectroscopy (EDS), was as follows: CaO=43.04%, SiO<sub>2</sub>=36.13%, Al<sub>2</sub>O<sub>3</sub>=10.19%, MgO=6.72%, SO<sub>3</sub>=1.75%, K<sub>2</sub>O=0.69%. The alkaline activators used were: (i) potassium hydroxide (Titolchimica), with a purity of 85%; (ii) sodium metasilicate powder (Sigma Aldrich), with a purity of 97% and a weight composition of SiO<sub>2</sub> and Na<sub>2</sub>O of 49.6% and 50.4%, respectively; (iii) sodium carbonate mono-hydrate (Carlo Erba) with a purity of 97%. Finally, a commercial dried silica sand, with a particle diameter range of 0.1–1 mm, was used to complete the mixture. The composition of the various mixtures is reported in Table 1. The water/reactive powder and sand/reactive powder ratios were fixed at 0.56 and 2.7, respectively. The developed mortars can be grouped into three subsets. The first subset, which includes mixtures 1, 2, and 3, is characterized by the use of slag as the sole reactive powder, with the activators being adjusted by varying the amounts of sodium carbonate and sodium metasilicate. Specifically, mixture 1 contains the highest amount of sodium carbonate (60g/kg of slag) and the lowest amount of metasilicate (20g). The quantities of the two reagents are inverted in mixture 3, while in mixture 2, equal amounts of the two activators are used (40g/kg).

The second group of mixtures, from 4 to 6, differs from the first subset primarily by reducing the slag content by 20% and replacing it with an equivalent amount of fly ash. The third group (mixtures 7

and 8) differs from the second group by varying the activators: specifically, sodium carbonate is replaced with potassium hydroxide. It is noted that: *a)* mixture 7 contains a lower quantity of activators compared to mixture 8, and *b)* systems 4-8 belong to the hybrid or mixed alkaline activation systems.

Table 1 Composition of mixtures based on 1 kg of reactive powders.

# Mixture	H <sub>2</sub> O	Na <sub>2</sub> CO <sub>3</sub>	Metasilicate	Slag	Fly ash	Sand
	(g)	(g)	(g)	(g)	(g)	(g)
1	560	60.00	20.00	1000	-	2700
2	560	40.00	40.00	1000	-	2700
3	560	20.00	60.00	1000	-	2700
4	560	60.00	20.00	800	200	2700
5	560	40.00	40.00	800	200	2700
6	560	20.00	60.00	800	200	2700
# Mixture	H <sub>2</sub> O	K(OH)	Metasilicate	Slag	Fly ash	Sand
	(g)	(g)	(g)	(g)	(g)	(g)
7	560	22.70	41.00	800	200	2700
8	560	30.00	54.54	800	200	2700

## 2.2 Mortar experimental test

The resulting mortars were then subjected to tests to evaluate their compressive and flexural strength, including their performance over time. Additionally, X-ray diffraction analyses, pull-off bond tests, sulfate attack tests, and capillary water absorption tests were conducted. The experimental campaign started with diffractometric investigations to identify the crystalline phases of the mortar. Subsequently, the experimental study focused on characterizing the mortar in its fresh state. In this context, the consistency of the fresh mortars was evaluated in accordance with EN 13454-2 [12] using a flow table. After the test, the spread was measured along two orthogonal diameters. The average of these two measurements provides the so-called "spread diameter" of the sample, which, expressed in centimeters, determines the "consistency class" of the mortar. The materials were then positioned into prismatic molds with dimensions of 40×40×160 mm<sup>3</sup>. The specimens, demolded after 24/48 hours, were used to conduct compression and flexural tests (Fig. 1) to evaluate their respective mechanical strengths at 2, 7, and 28 days of curing, in accordance with the EN 1015-11 [13]. Additionally, the dynamic elastic moduli were measured using a digital ultrasonic tester at 2, 7, and 28 days of curing. The tester provides the value of the time (in μs) required for the ultrasonic pulse to traverse the specimen. The velocity  $v$  of the pulse is calculated using the following relation:

$$v = \frac{l}{t} \quad (1)$$

where  $l$  is the length of the specimen and  $t$  is the time required for the wave to traverse the specimen. Given the velocity, the dynamic modulus  $E_d$  is provided by:

$$E_d = \frac{v^2 \times \rho \times [(1 + \gamma_d) \times (1 - 2\gamma_d)]}{(1 - \gamma_d)} \quad (2)$$

where  $\rho$  is the specific mass of the cured specimens and  $\gamma_d$  is the Poisson's ratio.

The latter was assumed to be 0.20, taking the average of values ranging from 0.15 to 0.25 reported in the literature for cementitious materials [14]. The capillary absorption tests were conducted in accordance with EN 1015-18 [15]. Samples measuring 40×40×80 mm<sup>3</sup>, obtained from the 40×40×160 mm<sup>3</sup> prisms broken in flexural tests, were first dried in a ventilated oven at a temperature of 50°C until a constant mass was achieved (Fig. 2 left). After being cooled down to 20°C, the samples were immersed



in a thin layer of water to a depth of approximately 5 mm (Fig. 2 right). The capillary water absorption was then measured by assessing the mass increase of each specimen at regular immersion time intervals. The equation used to evaluate the capillary absorption is as follows:

$$A = a_o + S \cdot \sqrt{t} \quad (3)$$

where:  $A$  ( $\text{mg} \times \text{mm}^{-2}$ ) is the water absorbed per unit area;  $S$  ( $\text{mg} \times \text{mm}^{-2} \times \text{h}^{-0.5}$ ) is the sorptivity coefficient of the material;  $t$  (h) is the immersion time;  $a_o$  ( $\text{mg} \times \text{mm}^{-2}$ ) is the water absorbed by the pores instantaneously. Another key aspect that was evaluated is the behavior of the mortar when subjected to sulphate attack. This type of scenario refers to the degradation caused by the interaction between the cementitious paste and sulphate ions from the external environment. The objective of the test is to verify the mechanical performance of the materials after being exposed to a 3% magnesium sulphate heptahydrate solution for 60 days. To assess the progression of mechanical properties, flexural and compressive tests were also conducted at 30 days, at which point the reaction solution was renewed. At the time of the solution change, the mechanical strengths of the samples were recorded. Finally, to further evaluate the suitability of the mortars as matrices for external reinforcements, pull-off bond tests were also conducted. The bond strength is determined by applying a tensile force perpendicular to the mortar bonded to the substrate (either bricks or tuff). At regular intervals of 1 second, a tensile force of 125 N/sec was applied.

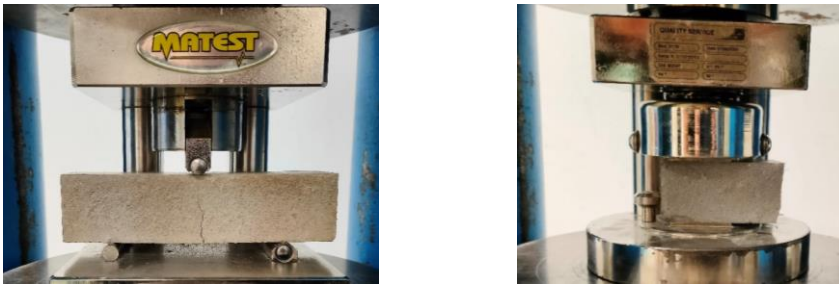


Fig. 1 Mechanical test on the mortar: (left) flexural and (right) compression tests.



Fig. 2 Capillary absorption test: (left) specimens dried in the oven and (right) immersed in the water.

### 2.3 Experimental program on strengthened specimens

The experimental program aimed at developing "green" mortars to be used as matrices for FRCM systems, as an alternative to products made with Portland cement, was briefly described in the previous section and is currently underway. In addition to the ongoing experimental campaign, future tasks will include tensile tests on FRCM specimens made with green mortars and reinforced with steel and/or basalt fibers.

These tensile tests will also be conducted after subjecting the FRCM specimens to: (i) freeze-thaw cycles and (ii) elevated temperatures. Moreover, the bond behavior of the green FRCM will be evaluated through single lap direct shear tests. For this purpose, masonry prisms—some made with bricks, others with tuff blocks—are being constructed (Fig. 3 left). The green FRCM systems, using both steel and basalt fibers, will be then applied to these prisms. Additionally, a subset of these specimens will be "conditioned" before testing to assess the bond properties of the FRCM systems under different environmental conditions. Beyond the bond tests, the experimental program also includes: (i) compression

tests on masonry columns (brick and tuff, Fig. 3 right) confined with green FRCM systems, and (ii) cyclic shear tests on masonry panels reinforced with the same FRCM systems. It is noteworthy that, in addition to the tests on the FRCM systems made with the green mortars developed within the framework of the STRIPES project, similar tests will be conducted on specimens reinforced with commercially available FRCM systems. This comparison will yield valuable insights into the quality of the systems developed during the STRIPES project.



Fig. 3 Preparation of the specimens for the (left) bond and (right) compression tests.

### 3 Experimental results

From the results obtained through the diffractometric analyses (Fig. 4), it is observed that the main crystalline phases are: hydrotalcite (CSD No. 9009272 (COD)); strätlingite (CSD No. 9005059 (COD)); C-A-S-H gel (calcium aluminum silicate hydrate) (PDF 00-034-0002); silica (PDF 00-001-0649); mullite (PDF 00-006-0259); calcite (CSD No. 4502443 (COD)).

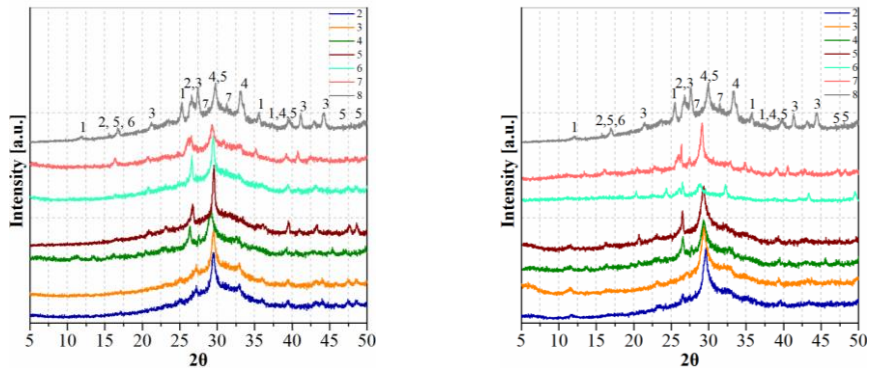


Fig. 4 X-ray diffraction of mortars after (left) 2 days and (right) 28 days of aging: (1) Hydrotalcite; (2) mullite (PDF 00-006-0259); (3) Quartz; (4) C-A-S-H; (5) calcite (CSD n° 4502443(COD), (6) strätlingite and (7) silica (PDF 00-001-0649).

The C-A-S-H gel and hydrotalcite are the products of the reaction between the slag and the alkaline activators, while silica and mullite are impurities present in the reactive powders. At short curing times, calcium carbonate stems from the initial reaction of the  $\text{CO}_2$  from the activator with the  $\text{Ca}^{++}$  ion released from the slag, forming salts such as sodium and calcium carbonates. At longer curing times, calcium carbonate forms as a result of carbonation phenomena in the presence of atmospheric  $\text{CO}_2$ . As can be observed, with the increase in curing time, the peaks related to the reaction products tend to increase in intensity, indicating the presence of a greater quantity of these products in the pastes. Additionally, it is evident that with the increase in sodium metasilicate for each set of mixtures, the peaks become more intense at both 2 and 28 days of curing. This is due to the higher initial basicity produced

in the mixtures by its presence, which accelerates the dissolution and reaction of the slag and fly ash. Considering the fresh properties of the mortar, the results from spreading tests indicate that the addition of fly ash enhances the spread and thus improves the fluidity of the mortars. The average spreading of these mixtures is ~26 cm, which is 1.3 times higher than the spreading observed in the mixtures without fly ash (~20 cm). The rheology of the mortars can then be modified by adding specific thixotropic additives. On the other hand, the mechanical properties of the mortars in their hardened state are presented in Fig. 5, detailing the values of the dynamic elastic moduli, flexural strengths, and compressive strengths at 2, 7, and 28 days of curing. It is worth mentioning that the flexural strength,  $\sigma_f$ , was evaluated using the following equation:

$$\sigma_f = \frac{3}{2} \frac{Fl}{bd^2} \quad (4)$$

where  $F$  is the applied load and  $l$  is specimen's length. In addition,  $b$  and  $d$  are respectively the width and the thickness of the specimen.

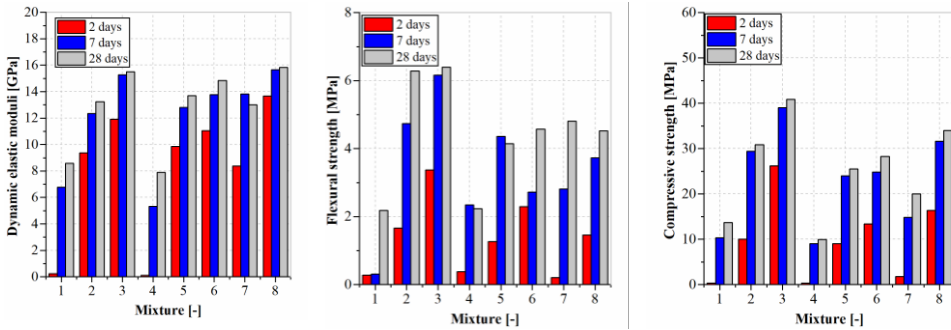


Fig. 5 Results of the mechanical characterization tests performed on the mortar over time.

The values shown in the plot represent the mean values obtained from tests conducted on at least three specimens for each mixture. From the figures, it is evident that, regardless of curing time, the mortars with the poorest mechanical properties are consistently those obtained with the lowest percentage of metasilicate and the highest percentage of sodium carbonate (mixtures 1 and 4). For these mixtures, the performance is particularly poor at two days of curing, and only limited improvements are observed over time. This can be attributed to the lower ability of calcium carbonate to activate the reactive powders in a short period, even in the presence of sodium silicate. During the activation of slag, an initial reaction occurs between the  $\text{CO}_3^{2-}$  from the activator and the  $\text{Ca}^{++}$  ions released by the slag to form salts such as sodium and calcium carbonates. It is worth mentioning that alkalinity increases occur later due to the release of  $\text{OH}^-$  ions, which initiate reactions leading to the formation of the C-A-S-H gel. As expected, in all cases, an increase in curing time results in improvements in mechanical strengths and dynamic moduli. It is interesting to note that in systems with a higher addition of metasilicate, strengths close to those at 28 days of curing are achieved after only one week. Additionally, for the same type and amount of activator, the systems containing fly ash exhibit lower strength values for each curing time. The results obtained can be attributed to the fact that fly ash is primarily composed of aluminosilicates and is low in calcium.

Its activation requires higher alkalinity levels than those required by slag, making it slower to react over time. The compressive and flexural strengths of the investigated mortars were compared with those of commercially available mortars used in FRCM systems. The comparison shows that, except for mortars 1, 4, and 7, all the developed mixtures achieved mechanical strengths at 28 days that are comparable to those of the best commercial mortars, which can exhibit flexural strengths of approximately 4 MPa and compressive strengths of approximately 35 MPa. Concerning the capillary absorption test results, the values of  $a_0$ , the absorption coefficient of the mortar (indicative of the water absorbed by the pores in contact with water), for specimens made using mixtures 2, 3, 5, 6, and 8, were obtained by interpolating the experimental data and are reported, along with the slope values  $S$ , in Table 2. The results obtained show that mortars with the lowest capillary absorption coefficients are those containing a higher amount of sodium metasilicate (mixtures 3, 6, 8).

Table 2 Capillarity absorption test results.

Specimens	2	3	5	6	8
$S[\text{kg}/(\text{m}^2\text{min}^{0.5})]$	0.661	0.337	0.578	0.514	0.442
$a_o[\text{kg}/\text{m}^2]$	0.134	0.992	0.642	1.259	1.053

Another key aspect requiring in-depth analysis is the durability of mortars when subjected to sulphate attack. The results obtained from the tests are reported in Fig. 6.

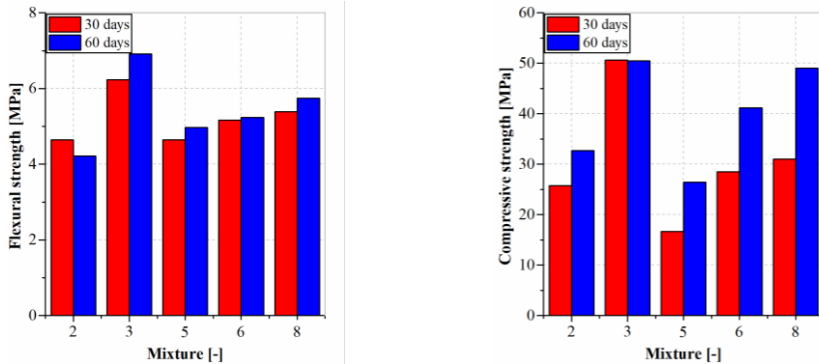


Fig. 6 Results of tests performed on the mortar after being subjected to sulphate attacks.

Overall, sulphate-rich environments induce expansion and degradation in these materials due to the formation of ettringite. This chemical process occurs when sulphate ions react with calcium hydroxide in hydrated cement, forming gypsum and subsequently ettringite, which generates high internal stresses and leads to extensive cracking. The results of this study indicate that at both 30 and 60 days, the samples did not exhibit significant forms of degradation; indeed, there were no notable decreases in either flexural or compressive strength (Fig. 6). However, further investigations are necessary to assess the long-term effects of prolonged exposure to sulphates. Finally, the pull-off bond test is crucial for evaluating the bond strength between mortar and brick in construction applications. This test provides valuable insights into the quality and durability of the bond, ensuring the structural effectiveness of FRCM systems for strengthening masonry structures. Tests performed on mortars applied to both brick and masonry tuff substrates showed a combination of cohesive and adhesive failure modes for all types of mortars, indicating a balanced and well-distributed bond strength and highlighting their potential as effective inorganic matrices in FRCM systems.

#### 4 Conclusions

Within the STRIPES project, the study presented the first results about the development of a sustainable mortar to be used as a matrix in FRCM systems. The following conclusions can be drawn:

- ✓ The presence of fly ash increases the workability of the mortars;
- ✓ Reactive systems with higher sodium carbonate content show low initial reactivity and a moderate performance increase up to 28 days of aging;
- ✓ Increasing the quantity of metasilicate accelerates the performance evolution significantly in both systems with only slag and those with slag and fly ash;
- ✓ Despite being a stronger activator than calcium carbonate, only the addition of appropriate quantities of metasilicate improves mechanical performance at short aging times;
- ✓ As the mechanical strengths of the mortars increase, their sorptivity values decrease;
- ✓ After 30 and 60 days, there were no significant signs of deterioration observed in the samples;
- ✓ The pull-off bond tests conducted to assess mortar adhesion to both brick and tuff masonry substrates revealed cohesive and/or adhesive failure modes across all mortar types;
- ✓ Mixtures 2, 5 and 6 appear to be the most promising for further experimental investigation.

The next steps will involve measuring crucial properties such as drying shrinkage and focusing on controlling fresh state properties. Following the conclusion of the 'green' mortar development stage, the STRIPES project will evaluate its suitability for structural repair and retrofitting interventions.

### Acknowledgements

This research was funded by the European Union – Next Generation EU (STRIPES Project – PRIN PNRR 2022 – CUP H53D23008660001).

### References

- [1] Donnini, J.; Corinaldesi, V.; Nanni, A. 2016. “Mechanical properties of FRCM using carbon fabrics with different coating treatments.” *Compos. Part B Eng* 88:220–228.
- [2] Papanicolaou, C.G.; Triantafillou, T.; Karlos, K.; Papathanasiou, M. 2006. “Textile-reinforced mortar (TRM) versus FRP as strengthening material of URM walls: In-plane cyclic loading.” *Material. Struct.* 40:1081–1097.
- [3] De Santis, S.; De Felice, G. 2015. “Steel reinforced grout systems for the strengthening of masonry structures.” *Compos. Struct.* 134:533–548.
- [4] Purdon, A.O. 1940. “The action of alkalis on blast-furnace slag.” *J. Soc. Chem. Ind.* 59:191–202.
- [5] Pacheco-Torgal, F. 2015. “*Introduction to Handbook of Alkali-activated Cements, Mortars and Concretes*” Woodhead Publishing: Cambridge, UK.
- [6] Provis, J. 2018. “Alkali-activated materials.” *Cem. Concr. Res.* 114:40–48.
- [7] Candamano, S.; De Luca, P.; Frontera, P.; Crea, F. 2017. “Production of Geopolymeric Mortars Containing Forest Biomass Ash as Partial Replacement of Metakaolin.” *Environments* 4:74.
- [8] Candamano, S.; Sgambitterra, E.; Lamuta, C.; Pagnotta, L.; Chakraborty, S.; Crea, F. 2019. “Graphene nanoplatelets in geo-polymeric systems: A new dimension of nanocomposites.” *Mater. Lett.* 236:550–553.
- [9] Bernal, S.A.; Provis, J.; Rose, V.; De Gutiérrez, R.M. 2011. “Evolution of binder structure in sodium silicate-activated slag-metakaolin blends.” *Cem. Concr. Compos.* 33:46–54.
- [10] Carabba, L.; Santandrea, M.; Carloni, C.; Manzi, S.; Bignozzi, M. 2017. “Steel fiber reinforced geopolymer matrix (S-FRGM) composites applied to reinforced concrete structures for strengthening applications: A preliminary study.” *Compos. Part B Eng.* 128:83–90.
- [11] [www.stripesproject.it](http://www.stripesproject.it) (last access: June 2024).
- [12] EN 13454-2. 2019. “Binders for floor screeds based on calcium sulphate - Part 2: Test methods.” European Committee for Standardization: Brussels, Belgium.
- [13] EN 1015-11. 2019 “Methods of Test for Mortar for Masonry-Part 11: Determination of Flexural and Compressive Strength of Hardened Mortar.” European Committee for Standardization: Brussels, BE.
- [14] Neville, A.M., 1995. “*Properties of concrete*”. Long-man London.
- [15] EN 1015-18. 2002. “Methods of test for mortar for masonry - Part 18: Determination of water absorption coefficient due to capillary action of hardened mortar.” European Committee for Standardization: Brussels, Belgium.

# Experimental study of smart cementitious material to monitor deformation and cracking in structures.

**Marcello Molfetta**

Heidelberg Materials Italia Cementi S.p.A,  
Via Lombardia 2/A, Peschiera Borromeo (MI) 20068, Italy  
marcello.molfetta@heidelbergmaterials.com

## Abstract

Concrete is the world's most widely used building material due to its excellent performance, formability, and low cost. To enhance the long-term durability and safety of structures, Heidelberg Materials Italia Cementi S.p.A. has patented an innovative material: Electrical Conductive Graphene Cement Binder (ECGCB). This material, with an electrical resistivity of less than  $0.5 \Omega\text{m}$ , can simultaneously detect deformation and cracking in buildings through its piezoresistive properties.

The results of the experiment on cylindrical and prismatic specimens of two concrete types, after 28 days of curing, confirmed that ECGCB electrical resistivity changes during compression, bending, and loading-unloading cycles. The sensitivity of ECGCB aligned with stress load variations, enabling the detection of deformation and crack formation in concrete structures.

## 1 Introduction

The state of the most of existing concrete structures/bridges, except for some geographical areas and some managing bodies, is not known sufficiently. The structural damage of concrete due to environmental exposition, steel reinforcement corrosion and creep is unavoidable during its service if the structures are not repaired in the right time.

Structural damage monitoring can easily be done either by applying a "Electrical Graphene Conductive Cement Binder" (ECGCB) along the concrete structures surface (thin strip, max 2 cm thickness and 15 cm wide) or by injecting ECGCB into cavities along the new structures.

ECGCB, developed by incorporating graphene-related materials (GRM) into the cement matrix, imparts piezoresistive properties to the compound. Additionally, ECGCB can exhibit thixotropic properties when the water content and specific components are adjusted for the intended application. One of the main challenges is achieving electrical percolation [7] without compromising the compound's mechanical properties. This article highlights the remarkable properties of ECGCB, making it valuable for monitoring structural health.

## 2 ECGCB: GRM in cement matrix

Several studies have used graphene and related materials with various dispersants, which can influence the hydration and the mechanical properties of the cementitious binder. The ECGCB formulation developed and patented by Heidelberg Materials is based on the electrical percolation principle [7], where the composite's conductivity increases significantly when the content of conductive fillers reaches a critical threshold. When ECGCB is mixed with water in a planetary mixer, it forms a mixture that hardens like normal cement mortar (Fig. 1). The fresh and hardened properties are listed in Table



Fig. 1

Table 1. The fresh and hardened properties of ECGCB

<b>Fresh state</b>	Spread diameter	UNI 7044	200 mm
	Fresh density	EN 1015-4	1650 kg/m <sup>3</sup>
<b>Hardened State</b>	Compressive Str. 28 days	EN 196-1	15,3 MPa
	Flexural Strength 28 days	EN 196-1	4,2 MPa
	Resistivity 28 days	Internal Method	< 0,5 $\Omega\text{m}$



### 3 Concrete supports specimens for ECGCB application

To evaluate the piezoresistive performance of the ECGCB product, two types of fiber-reinforced concrete were designed to create specimens (cylinders and prisms) that simulate the stresses on pillars and beams at a laboratory scale. Both types exhibit good ductility and residual strength but differ in compressive and flexural strengths. The first type, C60, has a compressive strength of 60 MPa and a flexural strength of 10 MPa (Fig. 2 a), while the second type, C110, has a compressive strength of 110 MPa and a flexural strength of 14 MPa (Fig. 2 b).

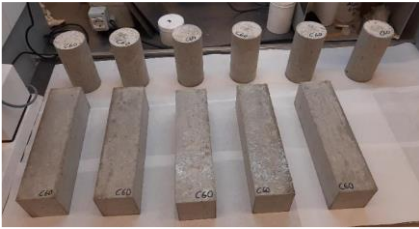


Fig. 2 a



Fig. 2 b

#### 3.1 Preparation of supports for ECGCB application

The sensitivity test of ECGCB to strain deformation was meticulously designed and studied. Specifically, a thin layer of ECGCB was applied to the principal stress zones of a prism (layer dimensions: 30mm x 2.5mm x 370mm) and a cylinder (layer dimensions: 170mm x 2.5mm x 30mm) see respectively Fig. 3 a-b. After curing, these specimens were then subjected to static and cyclic loads to simulate real-world conditions

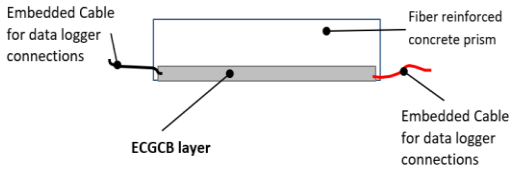


Fig. 3 a

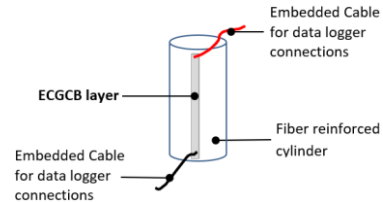


Fig. 3 b

Both C60 and C110 types of fiber reinforced concrete were used to cast support samples, cylinders, and prisms. After 28 days of curing, these samples were prepared (Fig. 4 a-b) for the application of the ECGCB layer (Fig. 4 c-d).



Fig. 4 a



Fig. 4 b



Fig. 4 c



Fig. 4 d

## 4 Self-Sensing Concrete tests

### 4.1 Schemes of Compression and Bending Tests

The piezoresistive properties of ECGCB were tested by placing the ECGCB layer cylinders inside a compression test machine. The ECGCB layer was connected via cables to a data logger to monitor the variation in electrical resistance during both compression and cyclic compression tests. Figure 5 a illustrates the setup and Figure 5 b the compression test equipment.

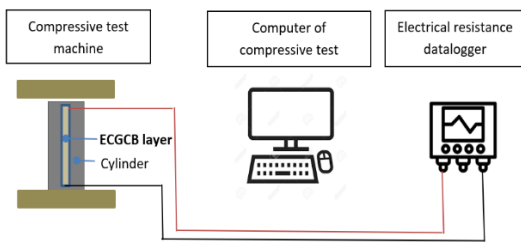


Fig. 5 a

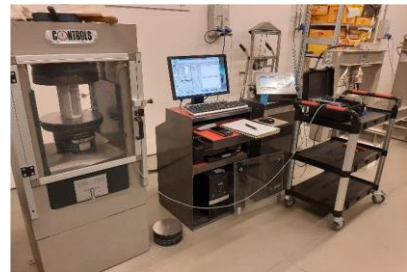


Fig. 5 b

A similar scheme test has been used for bending tests with cycles - loading and unloading before loading until collapse Fig. 6 a - b.

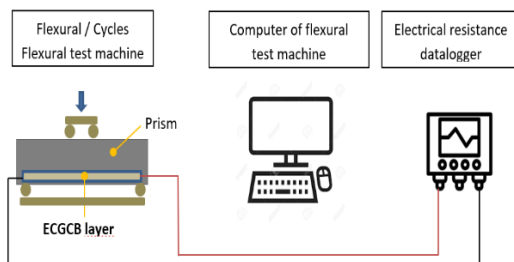


Fig. 6 a



Fig. 6 b



## 4.2 First group of tests response – Cylinders compression

After 28 days of curing, the cylinders with ECGCB layer were tested according to EN 12390-3. The results obtained on both types of cylinders C60-ECGCB and C110-ECGCB are show in Table 2.

Table 2. Cylinders C60-ECGCB and C110-ECGCB compression test values.

Sample code		C60- ECGCB-1	C60- ECGCB-2	C110- ECGCB-1	C110- ECGCB-2
Max Load	[KN]	517	518,5	769,6	753,4
Cylinder Compr. strength $f_c$	[MPa]	65,83	66,02	97,99	95,92
Initial Electrical resistance	[ $\Omega$ ]	108	98,2	627,8	360
Final Electrical resistance	[ $\Omega$ ]	133	141	1136	593

The trend values up to the point of compression collapse, showing stress ( $\sigma$ ) vs electrical resistance ( $\Omega$ ), for the C60-ECGCB and C110-ECGCB cylinders are plotted in Fig. 7 a and Fig. 7 b respectively.

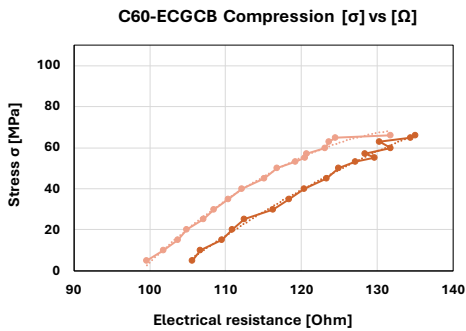


Fig. 7 a

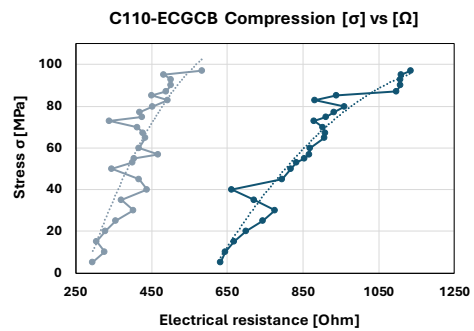


Fig. 7 b

The results of monitored mechanical strength tests underline the follow important points:

- The ECGCB layer applied on both types of concrete support, C60 and C110, is sensitive to strain induced by compressive stress.
- By analyzing the relationship between stress ( $\sigma$ ) and electrical resistance ( $\Omega$ ) for both types of concrete, C60 and C110, the mechanical strength of the supports can be verified by monitoring the variation in electrical resistance ( $\Delta\Omega$ ) of the ECGCB layer. This also allows for the prediction of collapse or the planning of structural repairs when the variation in electrical resistance ( $\Delta\Omega$ ) reaches certain threshold values.

## 4.3 Second group of tests response – Compression cycles tests

The behavior of ECGCB under compression cycle stress was verified. Load and unload cycles were applied to both C60 and C110 cylinders before collapse (Fig. 8 a-b). After curing, cylinders with the ECGCB layer were tested according to UNI 6556. The tests began with three loading and unloading cycles, followed by compression until collapse. The test scheme mirrored the compression test, with parameters set according to UNI 6556 for the secant modulus of elastic compression (see Table 3).

Table 3. Compression cycle stress test values for C60-ECGCB and C110-ECGCB cylinders.

Sample code		C60-ECGCB	C110-ECGCB
Max Load average	[kN]	517	761
Cylinder Compr. strength $f_c$ average	[MPa]	66	96,9
Stress base $\sigma_0$	[MPa]	2	2
Stress $\sigma_1$	[MPa]	10	20
Stress $\sigma_2$	[MPa]	16	26
Stress $\sigma_3$	[MPa]	22	32
Stress $\sigma_c$	[MPa]	Until collapse	Until collapse



Fig. 8 a

Fig. 8 b

The complete cycles (stress ( $\sigma$ ) vs time (s)) of load and unload as well as the stress applied until the cylinders collapse are plotted in graph show in Fig. 9 a-b.

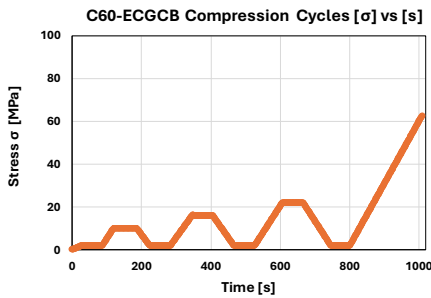


Fig. 9 a

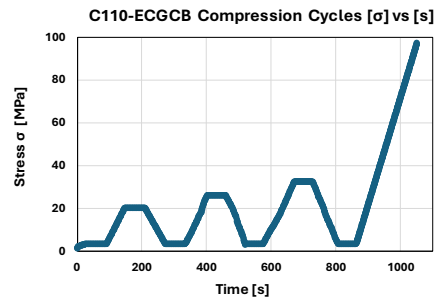


Fig. 9 b

The self sensing tests response of compression cycles, (stress ( $\sigma$ ) vs Electrical resistance ( $\Omega$ )), for both type of cylinders, C60-ECGCB and C110-ECGCB, are shown respectively in Fig. 10 a-b.

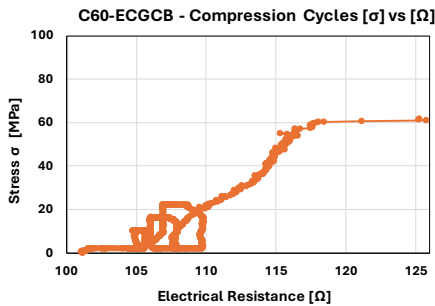


Fig. 10 a

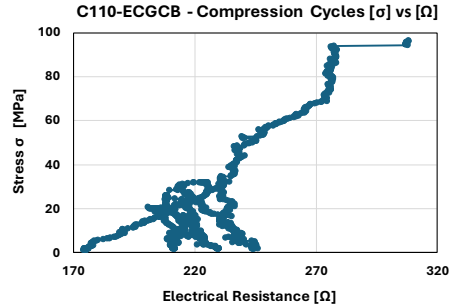


Fig. 10 b

From the tests conducted on compression cycles until final collapse, the following points can be highlighted:

- The ECGCB layer applied to concrete specimens C60 and C110 exhibited a similar trend.
- The ECGCB demonstrated excellent sensitivity with two different types of concrete, each with distinct mechanical strengths and elastic modulus.
- The ECGCB effectively displayed variations in its electrical resistance corresponding to the stresses ( $\sigma$ ) applied during the loading and unloading cycles until the samples collapsed.

#### 4.4 Third group of tests response – Flexural cycles tests

The testing stresses values ( $\sigma$ ) were set in elastic zone of each type of concrete, C60-ECGCB and C110-ECGCB. Refer to Table 4 below for details.

Table 4. Prisms C60-ECGCB and C110-ECGCB flexural cycles stress test values.

Sample code		C60-ECGCB	C110-ECGCB
Max Load average	[KN]	45,24	761
Flexural strength $f_c$ average	[MPa]	13,57	96,9
Stress base $\sigma_0$	[MPa]	0,8	2
Stress $\sigma_1$	[MPa]	4,52	20
Stress $\sigma_2$	[MPa]	4,52	26
Stress $\sigma_3$	[MPa]	4,52	32
Stress $\sigma_c$	[MPa]	Until collapse	Until collapse

Fig. 11 a-b shows the prisms after testing for both type of concrete C60 and C110 treated with ECGCB.



Fig. 11 a



Fig. 11 b

The complete cycles of stress ( $\sigma$ ) vs time (s) for loading and unloading, as well as the stress applied until the prisms collapsed, are plotted in Fig. 12 a-b for both type of concrete support.

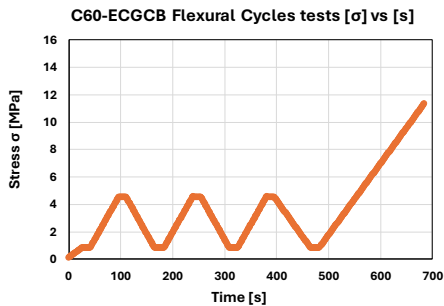


Fig. 12 a

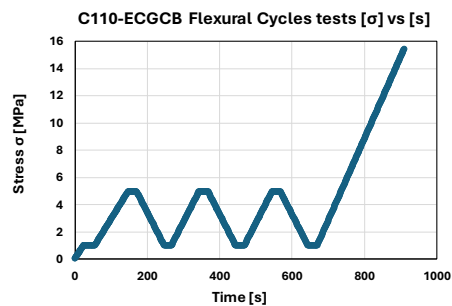


Fig. 12 b

The self sensing flexural cycles tests response, stress ( $\sigma$ ) vs Electrical resistance ( $\Omega$ ), of both prisms C60-ECGCB and C110-ECGCB, are plotted respectively in Fig. 12 a and Fig. 12 b.

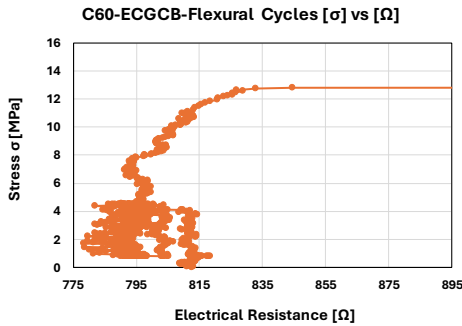


Fig. 12 a

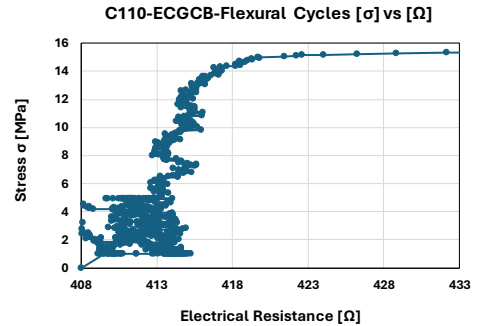


Fig. 12 b

From the tests conducted on flexural cycles leading to final collapse, the following observations can be made:

- The ECGCB layer applied to C60 and C110 prisms demonstrates good sensitivity from elastic stress to plastic deformation.
- The piezoresistive properties of the ECGCB layer are responsive to the stress of load and unload during flexural cycles.
- The ECGCB layer is capable of detecting deformation and crack formation during flexural stress loading up to the point of prism collapse.

## 5 Conclusion

The research on Electrically Conductive Graphene Cement Binder (ECGCB) for self-sensing applications has led to several significant conclusions:

- The ECGCB product exhibits remarkable piezoresistive properties, enabling it to detect both compression and tensile deformation in two types of concrete supports with different elastic modules.
- The tests conducted in this research have demonstrated a strong correlation between the stress ( $\sigma$ ) applied to the concrete supports and the variation in electrical resistance ( $\Omega$ ) of the ECGCB layer. This correlation provides several critical insights:

This would allow to know:

- 1) **Continuous Monitoring:** It allows for real-time monitoring of the mechanical strength of both new and existing structures, helping to prevent sudden collapses due to excessive cracking or deformation caused by overloading or early structural degradation.
- 2) **Enhanced Sustainability:** By facilitating the planning of necessary repairs and maintenance, it increases the sustainability of structures. This proactive approach helps extend the lifespan of structures and avoids the need for demolition and reconstruction, thereby minimizing disruptions and maintaining usability.
- 3) **Comprehensive Health Assessment:** The thin layer of ECGCB applied to the concrete surface of both new and old structures, particularly in stressed areas, provides valuable, continuous information about the overall health of the structure.

## Acknowledgements

The Author wish to thank the Director of Technologies & Quality Department of Heidelberg Materials Italia Cementi S.p.A. ing. G. Bottinelli, Head of Technologies and Technical Support ing. D. Floris, technical staff of concrete laboratory, and prof. L. Placidi of Uninettuno University.

## References

- [1] The Regents of the University of California, Oakland, CA (US). Inventors: Mo Li, Irvine, CA (US); Xiaopeng Li, Irvine, CA (US). Multi-Functional cementitious materials with ultra high damage tolerance and self- sensing ability. Pub. No.: US 2019 / 0202738 A1, Pub. Date: Jul. 4, 2019.
- [2] Pouria Ghods, Gloucester (CA); Mustafa Salehi, Nepean (CA), Sarah De Careful, Ottawa (CA). Embedded wireless monitoring sensors. Pub. No.: US 2017 / 0284996 A1. Pub. Date: Oct. 5, 2017.
- [3] The regents of the University of California Oakland CA (US). Inventors: Kenneth Loh, San Diego, CA (US); Jesus Gonzalez, Bay Point, CA (US). Multifunctional cement voposities with load-bearing, and self-sensing properties. Pub. No.: US 2016 / 0340245 A1. Pub. Date: Nov. 24, 2016.
- [4] D.K. Mishra KMBB College of Engineering and Technology, Daleiput, Odisha, India, J. Yu and C.K.Y. Leung Hong Kong University of Science and Technology, Hong Kong SAR, China. Self-sensing and Self-healing 'Smart' Cement-based Materials-A Review of the State of the Art. Sixth International Conference on Durability of Concrete Structures Paper Number TIM04, 18 - 20 July 2018
- [5] Department of Civil and Environmental Engineering, School of Engineering and Digital Sciences, Nazarbayev University, Nur-Sultan 010000, Kazakhstan; zere. Self-Sensing Cementitious Composites: Reviewand Perspective. *Nanomaterials* 2021, 11, 2355.
- [6] Baoguo Han, Xun Yu, Jinping Ou, Self-sensing concrete in smart structures, Elsevier August 2014.
- [7] Ioanna Papanikolaou, Chrysoula Litina, Amir Zomorodian, Abir Al-Tabbaa, Effect of Natural Graphite Fineness on the Performance and Electrical Conductivity of Cement Paste Mixes for Self-Sensing Structures, *Materials* 21 December 2020.
- [8] Shima TaheriJohn Georgaklis Martin AmsShuying Wu, Smart self-sensing concrete: the use of multiscale carbon fillers, *J MATER SCI* Jan 2022.
- [9] Leonardo Gonçalves Pedroti Luciano de Moura Guimarães Gustavo NalonJosé Carlos Lopes Ribeiro, Residual piezoresistive properties of mortars containing carbon nanomaterials exposed to high temperatures, *CEMENT CONCRETE COMP* May 2021.  
Min Kyoung Kim Le Huy Viet Dong Joo Kim, Electromechanical Response of Smart Ultra-High Performance Concrete under External Loads Corresponding to Different Electrical Measurements. *Sensor-Basel* Feb 2021.
- [10] Mostafa Adresi Jean-Marc Tulliani, Giuseppe Lacidogna, P. Antonaci, A Novel Life Prediction Model Based on Monitoring Electrical Properties of Self-Sensing Cement-Based Materials, DOI:10.3390/app11115080 *Applied Sciences* May 2021.
- [11] José Carlos L Ribeiro, Gustavo Nalon, Leonardo Gonçalves PedrotiDiôgo Silva de Oliveira, Self-Sensing Mortars: Effect of Moisture and Nanocarbon Black Content, *ACI MATER J* Jun 2021.
- [12] Seon Yeol LeeJongwoong Park, Le Huy Viet, Min Kyoung Kim, An Innovative Smart Concrete Anchorage with Self-Stress Sensing Capacity of Prestressing Stress of PS Tendon, *Sensor Basel* Aug. 2021.
- [13] Tae-Uk Kim, Suleman KhanDong-Joo Kim, Le Huy Viet, Development of Low-Cost Wireless Sensing System for Smart Ultra-High Performance Concrete, *Sensor Basel* Sep. 2021.

# Smart cement-based mortars for structural health monitoring applications: a step towards increased scalability

Antonella D'Alessandro<sup>1</sup>, Daniel A. Triana-Camacho<sup>1</sup>, Andrea Meoni<sup>1</sup>, Enrique García-Macías<sup>2</sup> and Filippo Ubertini<sup>1</sup>

<sup>1</sup> *Department of Civil and Environmental Engineering, University of Perugia, Perugia, Italy*

<sup>2</sup> *Department of Structural Mechanics and Hydraulic Engineering, University of Granada, Granada, Spain*

## Abstract

This research investigates the scalability of multifunctional structural mortar with self-sensing properties, specifically focusing on its application in large-scale construction elements. Electrical measurements in alternating current using four electrodes were conducted on medium-sized concrete samples incorporating carbon microfibers. The experimental tests were also further analysed and validated through the generalized effective-medium model of the induced polarization (GEMTIP). The outcomes indicate the potential scalability of the self-diagnosing concrete technology to larger structural elements. However, the research identifies critical considerations concerning the material's sensitivity and emphasizes the need for augmenting the number of electrodes to know how such electrical properties can change in different points of the structure. These challenges are crucial in ensuring the accurate and reliable monitoring of the concrete's health and performance over time. In conclusion, while the results affirm the feasibility of implementing self-diagnosing cementitious materials in real-size structural elements, the study underscores the importance of addressing challenges related to sensitivity and the establishment of a tailored electrical configuration. These findings contribute to advancing the understanding of multifunctional cement-based technologies and their practical implementation in large-scale concrete and masonry construction, paving the way for enhanced structural durability and performance.

## Introduction

The advancements in cement-based composites have been characterized by the addition of new properties for structural health monitoring (SHM) purposes, giving origin to smart cementitious materials [1]. The innovation in these materials is motivated by the need for higher durability and safety of structures, particularly concrete and masonry ones that are prone to cracks in different zones of their structure [2]. Nonetheless, cementitious materials are widely used in construction because of their versatility and ease of use in different applications in building industry [3]. Regarding the cement enhancement, novel high-performance fillers, such as carbon nanotubes (CNTs), allow the development of modified cement-based composites with improved capabilities [4,5]. As a matter of fact, carbon-based materials are commonly utilized to enhance the piezoresistive capabilities of cement-based composites [6], quantified by fractional change in resistance (FCR), which directly depends on strain variations [7]. Furthermore, the concentration of carbon inclusions, such as carbon nanofibers (CNFs) and microfibers (CMFs) can improve the cracking resistance playing a critical role in determining the magnitude of changes in relative resistance and linearity in the gauge factor [8]. For instance, Azhari et al. reported a FCR of approximately 20% under a maximum compressive stress of 9.87 MPa, while fiber reinforcements increase the energy absorption capacity before material failure. Moreover, the fillers can improve the cracking resistance of cement-based materials by effectively bridging cracks [9]. Besides, experimental studies on carbon-doped cementitious mortars show significant improvements in flexural strength, toughness, and electrical conductivity compared to standard cementitious specimens [10]. Consequently, these doped materials exhibit excellent mechanical and electrical properties, with potential applications in enhancing mechanical properties, as well as electrical conductivity, thermal conductivity, and chemical properties and enabling self-sensing for SHM applications [11]. For example, Imanian Ghazanlou et al. [12] conducted a complete study on these topics using rGO@Fe<sub>3</sub>O<sub>4</sub>-cement com-

posites. The research evidenced an incidence in the more compact rGO@Fe<sub>3</sub>O<sub>4</sub>-cement structure, presenting the maximum mechanical strength for the concentrations of rGO at 0.1 wt% and Fe<sub>3</sub>O<sub>4</sub> at 1.0 wt%. Other researchers evaluated the effect of carbon microfibers on the electrical sensitivity and damage detection of the doped cementitious composites [13,14]. Considering the literature exploring, this study focuses on the feasibility of producing carbon microfiber-doped cementitious mortar for new structures or local repairs of existing ones. The manuscript discusses material properties, preparation procedures, and characterization tests, including both electrical and sensing tests. The electromechanical results are presented and discussed, followed by conclusions, evidence, and future directions for the carbon fiber-doped mortar to develop applications for Structural Health Monitoring (SHM) and damage detection. Unlike traditional methods that sense between two points, this work is conducted on a large concrete block with numerous electrodes, producing a network of electrodes. This approach aims to scale this methodology for monitoring a real-size structure.

## 2. Methods

### 2.1. Materials and samples

The base cementitious composite is made of cement 930 g of Portland CEM II/A-LL 42.5R, 4025 g rough aggregates, and 465 g of water. The w/c ratio is 0.5. Carbon microfibers (CMF) are added in the percentage of 0.05% in weight of the binder: they are chopped carbon microfibers, type Sigrafil provided by Sgl Carbon, with a diameter of 7  $\mu\text{m}$  and a length of 6 mm. Although they appear initially joined in small clusters, they can easily separate mechanically. The fibers are dispersed during the mixing of the components until an homogeneous dough is reached. A medium-scale beam-type sample is prepared to assess the strain-sensing ability of the material and explore the behaviour of a configuration of diffuse electrodes. The mold dimensions are  $10 \times 20 \times 10 \text{ cm}^3$ , and the electrodes, copper wires with 0.8 mm of diameter, are placed during the sample production, perpendicular to the maximum dimension, at three height levels, at a mutual distance of 3 cm. Overall, 12 wires are inserted in one sample, passing from one side to the other. Then, the sample is cured in dry laboratory conditions.

### 2.2. Electromechanical behavior

The smart mortar element is tested for resistance and capacitance using a custom-built device called the "smart material electrometer" (SME). This device generates a biphasic square wave signal of  $\pm 10 \text{ V}$  and detects the current response in carbon fiber-doped mortars. This signal can be considered as a direct current signal (DC) because its frequency is 1 Hz. In addition, the device is also capable of generating sinusoidal voltage or alternating current (AC) signals at different frequencies from 1 Hz to 700 kHz. Therefore, the signal shapes are presented in Figure 1 as AC and DC characterization.

Analyzing the data acquired from these electrical techniques requires to develop three Python scripts. The first script allows: i) to search the peaks of a signal; for the AC case, ii) to compute the phase shifting and the impedance magnitude, for the DC case to identify the steady-state current at 80% of the transient current [15], iii) calculate the electrical resistance, and iv) extract the capacitance determined from the area under the current curves. The second script published on the Streamlit [16] fits the impedance data to the proposed cascade Cole-Cole model. Finally, the third script groups the biphasic data and, by using the fractional change in resistance (FCR) and the fractional change in capacitance (FCC), computes the kriging map for seventeen combinations of resistor-capacitor cells. These electromechanical tests involve measuring electrical DC response with three electrodes (see Figure 1) while applying a constant compressive load, of 7.89 kN or 15.68 kN. Besides, the zero-force electrical states are also obtained to determine the fractional changes, above mentioned.

## 3. Results of electrical characterization

To describe the AC electrical properties of smart mortar, a cascaded Cole-Cole model is used, as outlined in Equation (1). Each term in this model is related to the electrical response of three distinct components within the building material [17].

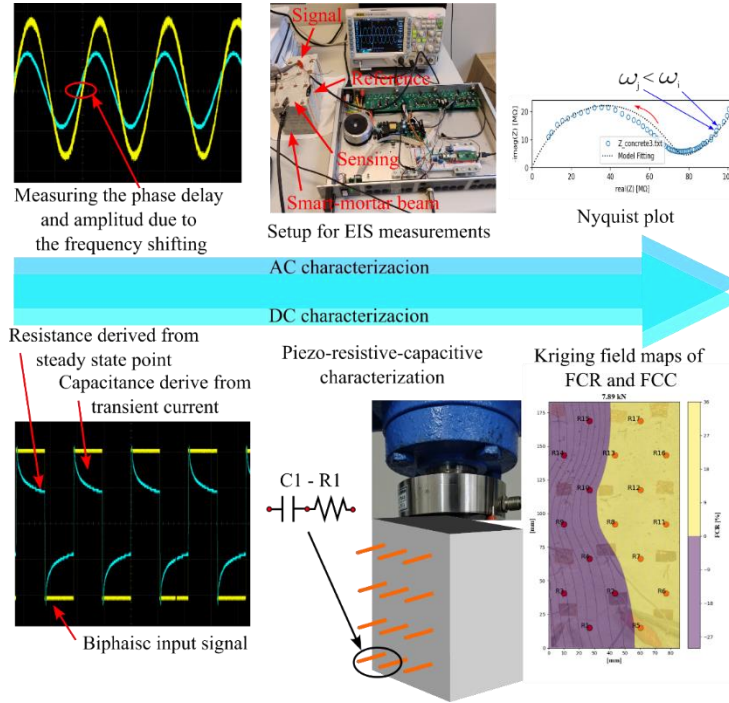


Fig. 1 Scheme of the electrical measurements carried out, processed and visualized

Firstly, the interaction between the electrode and its surrounding bulk is considered, followed by the carbon fibers embedded in the mortar, and finally the pores and rocks that constitute the heterogeneous material. Additionally, the mathematical structure of the cascaded Cole-Cole model and the Generalized Effective Medium Theory of Induced Polarization (GEMTIP) model exhibit an isomorphism, differing only in the interpretation assigned to their parameters [17].

$$Z(\omega) = R_i + \frac{R_1 - R_i}{(j\omega\tau_1)^{1-\alpha_1}} + \frac{R_2}{(j\omega\tau_2)^{1-\alpha_2}} + \frac{R_3}{(j\omega\tau_3)^{1-\alpha_3}} \quad (1)$$

### 3.1. Alternated Current measurements

In this regard, the electrical impedance measurements are fitted to the model presented in Equation (1). The optimization is carried out by combining the basin hopping and least square methods from the Python library `scipy.optimize`. The former is used to enhance the search for initial parameters and bring them closer to the force minimization of the objective function. The latter, also known as the Levenberg-Marquardt algorithm, is implemented to improve the convergence towards the global minimum, considering that this algorithm is more robust when the initial parameters are close to the final solution [18]. Figure 2 shows the Nyquist (a) and Bode (b) plots along with the fitting curve to the experimental data. Furthermore, the Nyquist plot has a similar shape as commonly reported for cement-based composites, that contain carbon-based inclusions [19, 20].

On the other hand, the real part of impedance in the Bode diagrams elucidates a dispersion close to 100 kHz, which has been attributed to small inclusions or grains by GEMTIP [17, 21]. In this case, the contributions to the impedance spectra of the carbon fillers, rocks, and pores are superimposed from 10 kHz up to 1 MHz, while the real part of impedance increases (DC resistance) when frequency tends to zero.



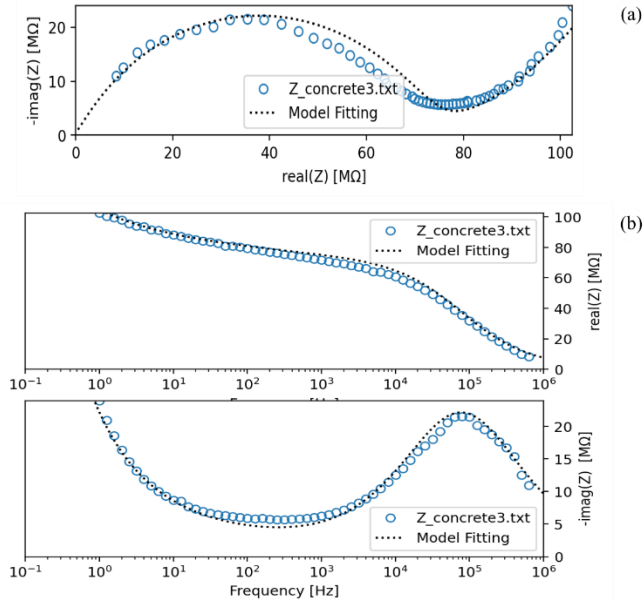


Fig. 2 Nyquist (a) and Bode (b) diagrams of smart mortar beam. The black dot lines depict the model fitting.

As a result,  $R_2$  depicts such DC resistance. That assevation also has a foundation on the highest relaxation time  $\tau_1$  presented in Table 1. This parameter could be considered as directly proportional to the frequency of the dispersion at this range, giving as a result of about 6 mHz, approximable to DC.

Table 1 Parameters optimized from the model presented in Equation 1.

$R_i$ [ $M\Omega$ ]	$R_1 - R_i$ [ $M\Omega$ ]	$\tau_1$ [ $\mu s$ ]	$\alpha_1$	$R_2$ [ $M\Omega$ ]	$\tau_2$ [ $s$ ]	$\alpha_2$	$R_3$ [ $M\Omega$ ]	$\tau_3$ [ $s$ ]	$\alpha_3$
-0.7	70.6	2.0	0.3	102.0	169.7	0.8	115.0	9.9	0.3

### 3.2. Biphasic characterization

The results of the model optimization show that  $\alpha_2$  is close to 1, while  $\alpha_1$  and  $\alpha_3$  are close to 0. Therefore, making these approximations ( $\alpha_1 = \alpha_3 = 0$  and  $\alpha_2 = 1$ ), the component 2 of the impedance has a resistive behavior, while components 1 and 3 have a capacitive behavior. In that sense Equation (1) can be modified in:

$$Z(\omega) = R_i + \frac{R_1 - R_i}{j\omega\tau_1} + R_2 + \frac{R_3}{j\omega\tau_3} \quad (2)$$

.Then, if the frequency  $\omega$  tends to 0, it can be obtained the DC behavior between the net of electrodes which forms conductive and non-conductive paths of smart mortar, as shown in Equation (3). Furthermore, we can consider the following relationship between the resistances ( $R_3 > R_2 > R_1 \gg R_i$ ), which is derived from the values in Table 1:  $R_i$  can vanish when it is added to the other resistances. On the other hand, the relaxation times are depicted as ( $\tau_3 \gg \tau_1$ ): in such a way at low frequency ( $\omega \rightarrow 0$ ) the second term in Equation (2) absorbs the last term, becoming in next expression :

$$Z(\omega \rightarrow 0) = R_2 + \frac{R_1 - R_i}{j\omega\tau_1} \quad (3)$$

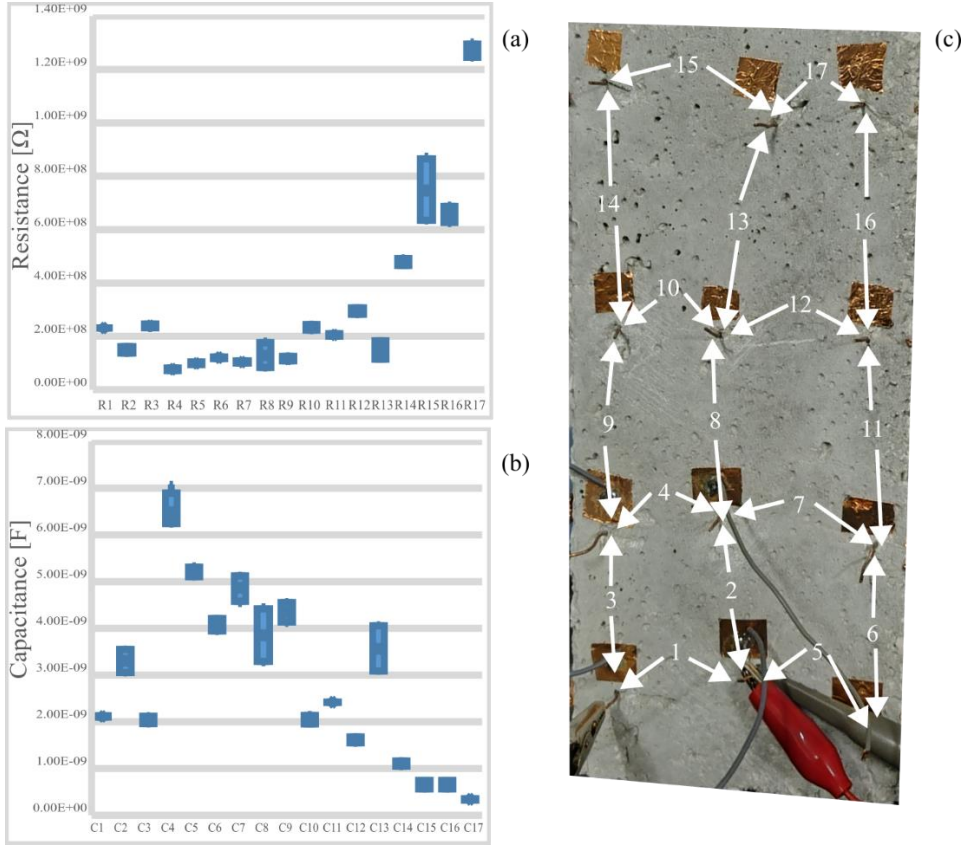


Fig. 3 Resistance (a), and capacitance (b) between adjacent electrodes, aligned in vertical (labelled as 2, 3, 6, 8, 9, 11, 13, 14, and 16) and horizontal (labelled as 1, 4, 5, 7, 10, 12, 15, and 17) directions (c), both obtained from biphasic measurements on the smart-mortar beam without mechanical loading.

Equation (3) elucidates a DC behavior between consecutive vertical or horizontal electrodes as a resistor  $R_2$  in series with a capacitive reactance  $\frac{1}{j\omega C_1}$ , where  $C_1 = \frac{\tau_1}{R_1 - R_i}$ . Indeed, we can simplify a couple of electrodes separated by a portion of smart-mortar as a resistor-capacitor cell. Considering this approach, resistor-capacitor cells can affect the direction of the electrical current, which is described by using two cartesian coordinates (vertical and horizontal), as shown in Figure 3 for biphasic measurements.

In zones where the resistor exhibits minimal deviation in electrical resistance, and consequently a lower magnitude, the capacitor displays greater deviation (noise) and higher capacitance values. For instance, resistors R4 to R10 show minimal noise in the measurements, whereas their corresponding capacitors C4 to C10 exhibit higher noise levels. Conversely, for higher resistance values, the noise increases, as observed with the resistances between the electrodes located at the top of the specimen (R14 to R17). However, in this scenario, the capacitance is low, resulting in reduced noise in these measurements.

Another important result to consider is that the values of resistance and capacitance at different points in the smart-mortar beam are different. However, considering the fractional change of resistance, we will focus only on the relative change of these physical quantities that were obtained using the Kriging Python library and presented as a field contour map in Figure 4. These results point out that the FCR (a, d) has negative and positive values, as well as the FCC (c, e). To make clear this fact, negative and positive values of FCR indicate that electrical resistance decreases or increases, respectively. What is more, the FCC shows a completely opposite behavior of FCR.

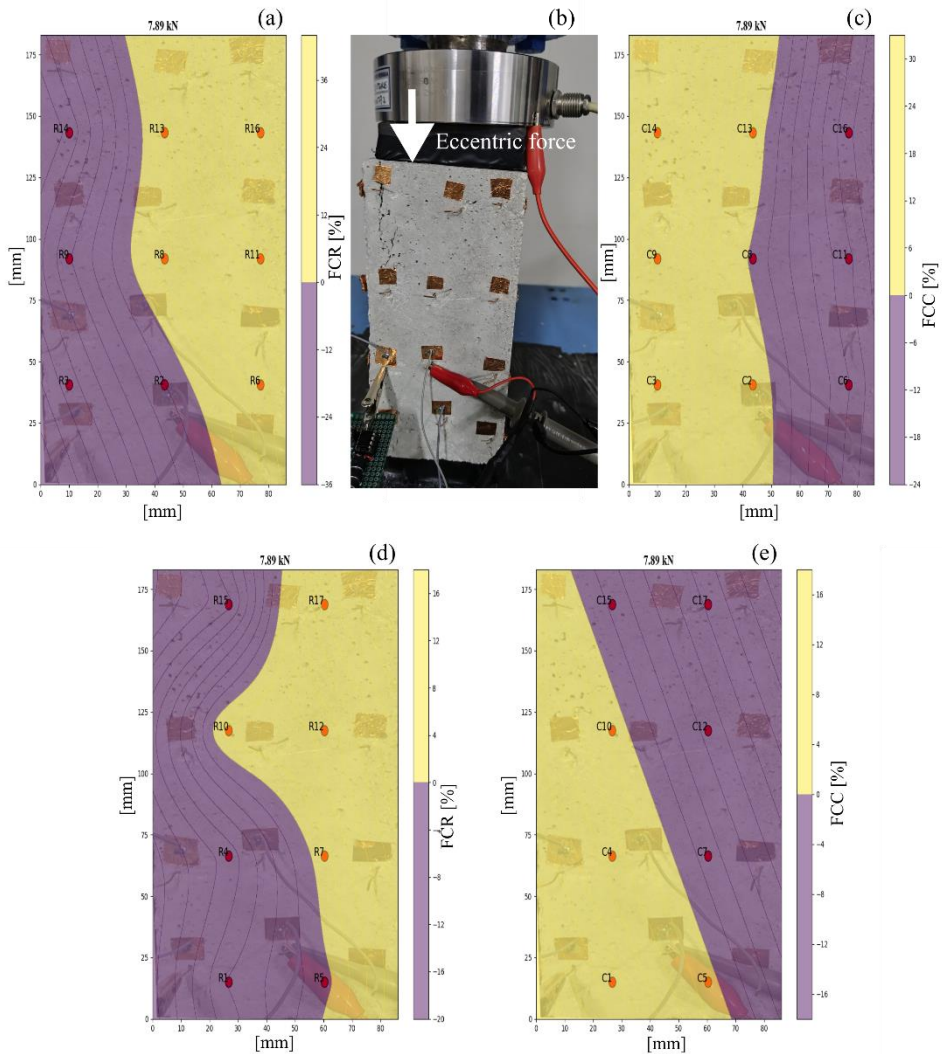


Fig. 4 Kriging field map of the fractional change in resistance (FCR) between adjacent electrodes, aligned in (a) vertical, and (d) horizontal directions. Fractional change in capacitance (FCC) between adjacent electrodes, aligned in (c) vertical and (e) horizontal directions. The piezo-resistive-capacitive measurements were performed on the smart-mortar specimen with twelve electrodes, using a compressive load of (b) 7.89 kN.

This is attributed to a decrease in electrical resistance when fillers' distance decreases due to an increasing compressive stress [22]. Therefore, by this way of presenting the data, it is easy to see the left side of the smart-mortar beam experienced a higher magnitude of applied loading than the right side (bending moment), as described previously in the methods section. After the constant axial load is increased from 7.89 kN up to 15.68 kN, the first crack is generated on the top left side, as shown in Figure 4(b). Then, the compressive load is kept constant for some seconds until the specimen breaks. In that sense, the field contour of electrical resistance and capacitance predicts the biggest gradient of strain is going to appear at the coordinates for R4, R7, R8, R10, and R12, generating the long crack as predicted FCR and FCC field maps, then, the loading was augmented up to 15.68 kN fracturing the beam by the middle.

## Conclusion

This approach demonstrates the electromechanical behavior of a smart-mortar element that can be addressed by modeling a mesh made of 17 single resistor-capacitor cells. The single-cell model in DC was deduced through a model based-on-frequency Cole-Cole. To achieve that, electrical impedance measurements were optimized using least squares in combination with basin hopping algorithms. In addition, the proposed DC model offers more sensitivity due to the opposite behavior of resistor-capacitor cells observed without force electrical measurements. Subsequently, the approach satisfied the superposition principle such as the crack forming is directly depicted with the Kriging field maps of FCR and FCC.

## Acknowledgement

The authors would like to gratefully acknowledge the support of the Italian Ministry of University and Research (MUR) via the FIS2021 Advanced Grant "SMS-SAFEST - Smart Masonry enabling SAFETy-assessing Structures after earthquakes" (FIS00001797).

## References

- [1] Siahkouhi, Mohammad, and Razaqpur, Ghani, and Hoult, N. A., and Baghban, Mohammad H., and Jing, Guoqing 2021. "Utilization of carbon nanotubes (CNTs) in concrete for structural health monitoring (SHM) purposes: A review". *Construction and Building Materials*, 309, 125137.
- [2] Pour-Ghaz, Mohammad, and Weiss, Jasson. 2011. "Detecting the time and location of cracks using electrically conductive surfaces". *Cement and Concrete Composites*, 33(1), 116-123.
- [3] Setareh, Mehdi, & Darvas, Robert. 2017. Concrete structures, *Springer*, Switzerland, 698 pp ISBN-10: 3319241133n, ISBN-13: 978-3319241135
- [4] Ramachandran, Kousalya, and Vijayan, Ponmalar, and Murali, GGunasekaran, and Vatin, Nikolai I. 2022. "A review on principles, theories and materials for self sensing concrete for structural applications". *Materials*, 15(11), 3831.
- [5] Coppola, L., Buoso, A. & Corazza, F. (2011). Electrical Properties of Carbon Nanotubes Cement Composites for Monitoring Stress Conditions in Concrete Structures. *Applied Mechanics and Materials*, 82, 118-123.
- [6] Dong, Wenkui, and Li, Wengui, and Tao, Zhong, and Wang, Kejin. 2019. "Piezoresistive properties of cement-based sensors: Review and perspective" *Construction and Building Materials*, 203, 146-163.
- [7] Dong, Wenkui, and Li, Wengui, and Wang, Kejin, Han, Baoguo, and Sheng, Daichao, and Shah, Surendra P. 2020. "Investigation on physicochemical and piezoresistive properties of smart MWCNT/cementitious composite exposed to elevated temperatures". *Cement and Concrete Composites*, 112, 103675.
- [8] Carísio, Pedro A., and dos Santos Mendonça, Yasmin G., and Teodósio Soares, Carlos F., and Mendoza Reales, Oscar A., and Rego Fairbairn, Eduardo M., and Toledo Filho, Romildo

- D. 2021. "Dispersion of carbon nanotubes with different types of superplasticizer as a dispersing agent for self-sensing cementitious materials". *Applied Sciences*, 11(18), 8452.
- [9] Azhari, Faezeh, & Banthia, Nemkumar. 2012. "Cement-based sensors with carbon fibers and carbon nanotubes for piezoresistive sensing". *Cement and Concrete Composites*, 34(7), 866-873.
- [10] D'Alessandro, Antonella, and Ubertini, Filippo. 2024. "Mechanical and Durability Investigation of Composite Mortar with Carbon Microfibers (CMF)". *Applied Sciences*, 14(7), 2773.
- [11] Birgin, Hasan B., and D'Alessandro, Antonella, and Ubertini, Filippo. 2023. "A new smart sustainable earth-cement composite doped by carbon microfibers with self-sensing properties" *Developments in the Built Environment*, 14, 100168.
- [12] Ghazanlou, Siamak I., Ghazanlou, Siavash I., Ghazanlou, Sroush I., Karimi, Hamid, Azimi, Neda, and Hosseinpour, S. 2023. "Multifunctional performance of core-shell rGO@ Fe<sub>3</sub>O<sub>4</sub> on the mechanical, electrical/thermal, EMI, and microstructure properties of cement-based composites". *Construction and Building Materials*, 394, 132182.
- [13] Chen, M.; Gao, P.; Geng, F.; Zhang, L.; Liu, H. (2017). Mechanical and smart properties of carbon fiber and graphite conductive concrete for internal damage monitoring of structure. *Constr. Build. Mater.* 142, 320–327.
- [14] Galao, O., Baeza, F.J., Zornoza, E. & Garcés, P. 2017. Carbon nanofiber cement sensors to detect strain and damage of concrete specimens under compression. *Nanomaterials*, 7(12), 413
- [15] Downey, Austin, and D'Alessandro, Antonella, and Ubertini, Filippo, and Laflamme, Simon, and Geiger, Randall. 2017. "Biphase DC measurement approach for enhanced measurement stability and multi-channel sampling of self-sensing multi-functional structural materials doped with carbon-based additives" *Smart Materials and Structures*, 26(6), 065008.
- [16] Streamlit website <https://kdsz-impedance.streamlit.app/> retrieved 27-05-2024.
- [17] Triana-Camacho, Daniel A., and Miranda, David A., García-Macías, Enrique, and Mendoza-Reales, Oscar A., and Quintero-Orozco, Jorge H. 2022. "Effective medium electrical response model of carbon nanotubes cement-based composites" *Construction and Building Materials* 344, 128293.
- [18] Moré, Jorge J. 1977. "The Levenberg-Marquardt Algorithm: Implementation and Theory" *Numerical Analysis*, ed. G. A. Watson, Lecture Notes in Mathematics 630, *Springer Verlag*, 105-116.
- [19] Ruan, Yanfeng, and Han, Baoguo, and Wang, Danna, and Zhang, Wei, and Yu, Xun. 2018. "Electrical properties of carbon nanotubes filled cementitious composites" *Materials Research Express*, 5(10), 105704.
- [20] Zhang, Liqing, and Ding, Siqi, and Li, Linwei, and Dong, Sufen, and Wang, Danna, and Yu, Xun, and Han, Baoguo. 2018. "Effect of characteristics of assembly unit of CNT/NCB composite fillers on properties of smart cement-based materials" *Composites Part A: Applied Science and Manufacturing* 109, 303-320.
- [21] Zhdanov, Michael. 2008. "Generalized effective-medium theory of induced polarization" *Geophysics*, 73 (5) F197-F211.
- [22] Ozturk, Murat, and Chung, Deborah D. L. 2021. "Capacitance-based stress self-sensing effectiveness of a model asphalt without functional component" *Construction and Building Materials*, 294, 123591.

# Self-cleaning low-carbon mortars based on alkali-activated materials: the role of TiO<sub>2</sub> addition

Simone Rapelli<sup>1</sup>, Denny Coffetti<sup>1</sup>, Elena Crotti<sup>1</sup>, Luigi Coppola<sup>1</sup>

<sup>1</sup> *Department of Engineering and Applied Sciences,  
University of Bergamo,  
via Marconi, 5 - 24044 Dalmine (BG), Italy*

## Abstract

The purpose of this work is to investigate the influence of the addition of titanium dioxide (TiO<sub>2</sub>) nanoparticles on the rheological, physico-mechanical and photocatalytic properties of alkali-activated slag-based mortars. The self-cleaning capability of TiO<sub>2</sub>-containing composites were evaluated by means of accelerated dye degradation tests and 24-months outdoor exposure tests in comparison with Portland-based mortars. Experimental results show that the variation of the rheological properties of mixtures due to the addition of TiO<sub>2</sub> is negligible while it can be noted a general reduction on the setting times by increasing the amount of the TiO<sub>2</sub> content. The use of TiO<sub>2</sub> seems to have a minor effect on the elasto-mechanical properties of slag-based mortars at early and long ages. Only alkali-activated materials with low alkali content evidence an increase in compressive strength from 9 to 14% with respect to the same mortars manufactured without nanoparticles. The beneficial effect of TiO<sub>2</sub> addition in self-cleaning capability is evident both in cementitious and alkali-activated mortars under accelerated tests. In particular, regardless of UV light exposure time, the color variation increases almost linearly by increasing the nanoparticles content. Finally, the self-cleaning ability has been evaluated by measuring the color variation during the exposure of mortar samples to the industrial environment for 2 years. Results evidenced the efficiency of the TiO<sub>2</sub> on the reduction of the color variation promoted by the polluted environment.

## 1 Introduction

The interest in the photocatalytic properties of cementitious materials has surged over the past few decades, captivating the attention of both academic researchers and construction companies. Beginning with the pioneering work of Fujishima and Honda [1], the potential of nano-TiO<sub>2</sub> to facilitate self-cleaning in materials and mitigate pollutants like volatile organic compounds (VOCs) and nitrogen oxides (NO<sub>x</sub>) under artificial light irradiation (UV light) or natural sunlight has become evident. The photodecomposition process, driven by titanium dioxide's light-absorbing properties, is hailed as one of the most potent forms of photocatalysis currently available. It holds huge promise when integrated with cementitious materials, offering the potential to enhance the performance of buildings and civil structures on a substantial scale.

In recent years, there has been extensive exploration of titanium dioxide's application in construction materials to create "smart" concretes, mortars, plasters, and coatings. In particular, several studies have conducted on the properties of cement-based materials containing TiO<sub>2</sub> nanoparticles, focusing on their mechanical, photocatalytic, and self-cleaning characteristics [2,3]. Furthermore, researchers have examined the durability of these systems through natural exposure tests and accelerated laboratory procedures [4]. In contrast, knowledge about the utilization of TiO<sub>2</sub> in alkali-activated slag-based binders (AAS), a promising environmentally friendly alternative to Portland cement [5,6], remains quite limited. Existing studies have mainly concentrated on the so-called "two-part" AAS systems, and only a handful of papers have explored the influence of TiO<sub>2</sub> on the properties of AAS mixtures [7–9]. These studies have revealed that the addition of TiO<sub>2</sub> enhances the hydration process of slag and results in a denser microstructure, thereby improving the mechanical properties of AAS mixtures by varying degrees, typically between 5% and 15%, depending on the TiO<sub>2</sub> dosage and nanoparticle characteristics [7,10]. Yang et al. [10] and El-Kattan et al. [8] have also investigated the volumetric stability of these systems, noting a reduction in shrinkage due to the formation of novel expansive products such as titanium silicate hydrate (T-S-H) and C<sub>4</sub>TiH<sub>13</sub>. However, Llano-Guerrero et al. [7] observed relatively low photocatalytic activity in TiO<sub>2</sub>-doped AAS pastes compared to metakaolin-based geopolymers when subjected to accelerated tests with rhodamine B.

## 2 Research significance

Given the limited knowledge in this area, this study examines the incorporation of TiO<sub>2</sub> nanoparticles into one-part alkali-activated slag-based mortars to assess their impact on rheological and mechanical properties and self-cleaning capabilities. Additionally, this paper presents the results of a two-year outdoor exposure campaign conducted in an industrial setting in Northern Italy to investigate the natural photoactivity of mortars with varying TiO<sub>2</sub> dosages.

## 3 Materials and methods

### 3.1 Materials

Twelve alkali activated mortars were manufactured with a highly amorphous ground granulated blast furnace slag (GGBFS) with 28-day pozzolanic activity index  $K=0.76$  (according to EN 196-5 [11]), basicity coefficient  $K_b = 1.20$  and quality coefficient  $K_q = 1.77$ . An alkaline powder blend previously developed by the authors (laboratory grade sodium metasilicate pentahydrate, potassium hydroxide and sodium carbonate with relative mass ratio of 7:3:1) was also used as solid activator [12]. Moreover, eight Portland cement-based mortars were manufactured as reference by using a grey Portland cement CEM I 52.5R and a white Portland cement CEM I 52.5R. Five different natural siliceous sands having maximum size of 2.5 mm were combined as fine aggregates. Furthermore, a commercial polycarboxylate-based superplasticizer was used to ensure a plastic consistency of cementitious mortars.

### 3.2 Proportioning, preparation and sample curing

Three different type of one-part AAS mortars were produced by varying the activator/precursor ratio between 8 and 16. In addition, cementitious mortars manufactured with Portland cement (grey or white cement) were used as control mix. In all mixtures, the water-to-binder ratio was set at 0.55 and the sand-to-binder ratio was fixed at 3.0 while different amounts of TiO<sub>2</sub>, i.e., 0%, 1%, 3% and 5% with respect to the binder mass, were used to evaluate the impact of TiO<sub>2</sub> dosage on rheological properties, compressive strength, dynamic elastic modulus and self-cleaning ability (both under natural and accelerated conditions) of AAS materials. The dosages of the TiO<sub>2</sub> in powder form were selected starting from the research by Diamanti et al. [13] on the photocatalytic properties of cementitious mortars containing TiO<sub>2</sub>. The mortars' label indicates the type of binder used for the production (WC: White cement; GC: grey cement; S: Alkali-activated slag) and the number before and after the hyphen indicates the activator-to-slag ratio by mass (only in the alkali-activated slag mortars) and the TiO<sub>2</sub> dosage, respectively.

Superplasticizer (when used) was first mixed with water by means of a high shear mixer for 3 minutes at 250 rpm, then mortars were prepared by blending binders, solid activators (if present), sand, nano-size TiO<sub>2</sub> in powder form and mixing water by using an automatic mortar mixer compliant with EN 196-1 [14]. The fresh mortars were portioned into 4 parts: the first part was used to carry out the fresh state tests, the second to manufacture 40x40x160 mm<sup>3</sup> prisms for the elasto-mechanical tests, the third to produce 80x100x10 mm<sup>3</sup> tiles for the accelerated photocatalytic tests while the last was applied with a thickness of 10 mm on bricks for self-cleaning evaluations under natural conditions. All the samples were finished by using a steel float in order to achieve a smooth surface and they were kept in a climatic chamber (20°C, 95% R.H.) for 24 hours before demolding. After this, the specimens were cured in the same conditions until tests.

### 3.3 Fresh and elasto – mechanical tests

The workability, the specific mass at fresh state and the air content were detected in accordance with EN 1015-3 [15], EN 1015-6 [16] and EN 1015-7 [17], respectively. Moreover, the setting time was determined by using Vicat's apparatus in accordance with EN 196-1 [14]. Compressive strength was determined at 1, 7 and 28 days from casting (EN 1015-11 [18]). Finally, dynamic modulus of elasticity of mixtures was estimated by means of Ultrasonic Digital Indicator Tester at 1, 7 and 28 days in accordance with EN 12504-4 [19].

### 3.4 Accelerated photocatalytic tests

Self-cleaning capability of TiO<sub>2</sub>-containing mortars was determined by monitoring the discoloration of organic dyes (rhodamine B RhB) according to the procedure reported in the Italian standard UNI 11259

[20]. The solutions of organic dyes were prepared by stirring for 5 minutes at 500 rpm 1 g of rhodamine B in 1 liter of distilled water. Subsequently, a hydrophobic product was applied on the 28-days old mortar tiles to delimit an area of 22 cm<sup>2</sup> to be tested. After complete drying of the hydrophobic agent, 0.5 ml of aqueous solution was carefully sprayed onto the test surface and then left to dry in a dark room at 20°C, 60% R.H for 24 hours. Finally, the samples were exposed to a UV-A source with irradiance equal to  $3.75 \pm 0.25$  W/m<sup>2</sup>. The color variation was determined after 4 and 24 hours of exposure to UV light by measuring the a\* coordinate (redness/greenness for RhB) by means of a portable spectrophotometer (PCE-CSM 4, PCE Instruments Italia) working on CIELAB color space. The following equation (Eq.1) was used to evaluate the color variation:

$$a_{\%} = \frac{a_0^* - a_t^*}{a_0^*} \cdot 100 \quad (1)$$

where  $a_0^*$  is the color intensity coordinate of specimens before the exposure to UV irradiation and  $a_t^*$  is the color intensity coordinate of specimens at t hours of irradiation.

### 3.5 Outdoor natural photocatalytic tests

Forty different samples of mortars applied on bricks were exposed to the polluted industrial environment of the Po Valley (Northern Italy) for 2 years. Specimens were put on tilted supports (45° with respect to the ground) on the rooftop of the Engineering Laboratory of the University of Bergamo in order to ensure homogeneous exposure to sunlight without shading and to avoid stagnating rain water on mortar surfaces. One half of mortar samples were positioned facing South while the other half was facing North in order to evaluate the influence of the different exposure on the self-cleaning capability of alkali activated materials. Specimens were monitored over time by measuring the color variation on CIELAB color space  $\Delta E$ , corresponding respectively to the color at the time t and to the initial color at t = 0, by means of the Eq. 2:

$$\Delta E = \sqrt{(L_t^* - L_0^*)^2 + (a_t^* - a_0^*)^2 + (b_t^* - b_0^*)^2} \quad (2)$$

With  $L_t^*$ ,  $a_t^*$  and  $b_t^*$  chromatic coordinates at time t and  $L_0^*$ ,  $a_0^*$  and  $b_0^*$  chromatic coordinates before the exposure to the polluted urban environment. The measurements were done after a rainy day in order to test samples without detached atmospheric soiling that would cause a gray shift of the color and thus unreliable results.

## 4 Results and discussion

### 4.1 Fresh state properties

Figure 1 shows the flowability of fresh mortars as a function of TiO<sub>2</sub> content. Even if other authors evidenced the key modification induced by TiO<sub>2</sub> nanopowders in fresh cementitious mixtures is a decrease in workability, all the samples (both cementitious and alkali activated) show a consistency in the range of 150-200 mm of spreading on the flowing table without significant variations as the TiO<sub>2</sub> nanoparticles dosage increases. This could be explained with the higher average size of TiO<sub>2</sub> nanoparticles with respect to those used by Meng et al. [21] and Suneel et al. [22]. Moreover, as expected, the increase in alkali content leads to an increase in the workability of the mixtures. This behavior is caused by the deflocculating and plasticizing effect promoted by the use of sodium silicate as activator that reduce the yield stress at early ages [23].

The air content and the specific mass at fresh state of mortars containing nano-TiO<sub>2</sub> are similar, regardless of the nanoparticles content. The cementitious mortars are characterized by an entrapped air volume close to 6% while alkali-activated slag-based mixtures are in the range of 3.5-5.2%. Similarly, the variation of specific mass of fresh mortars due to the use of nanoparticles is negligible (lower than 1.5%).

On the contrary, the addition of TiO<sub>2</sub> affects the setting time of fresh mixtures. The initial setting time of cementitious and alkali-activated mortars decreases with the increase of the nanoparticles content up to about 60 minutes while the opening time remains constant by varying the dosage of nano-TiO<sub>2</sub>. Only the alkali-activated S8 evidences a decrease in opening time when nanopowders are added to the mixture. This behavior has already been highlighted by Zhang et al. [24] in cement-based mortars due to a seeding effect promoted by nanoparticles.



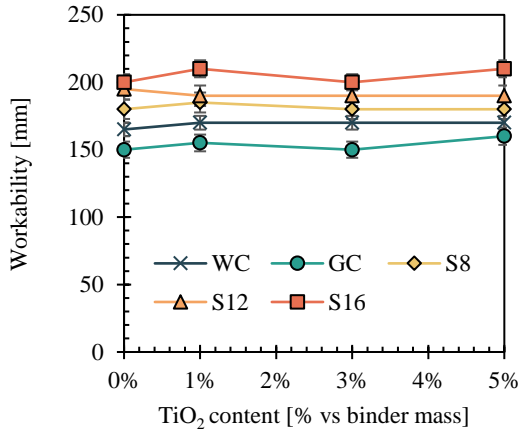


Fig. 1 Workability of mortars as a function of TiO<sub>2</sub> content

## 4.2 Elasto – mechanical properties

Table 1 shows the elasto-mechanical properties of mortars manufactured with different amount of TiO<sub>2</sub>. The 28-day compressive strength of plain WC, GC and S16 are similar and they are in the range of 41-44 MPa while alkali-activated mixtures with lower activators content (S8 and S12) evidence compressive strength after 28 days equals to 22.9 and 36.4 MPa, respectively. On the contrary, at early ages (1 day), the compressive strength of cementitious mixes is higher with respect to that of AAS ones. The dynamic modulus of elasticity (DME) is influenced by both the nature of the binder and the compressive strength of mortars. Notably, cementitious mixtures without nanoparticles exhibits DMEs close to 26-27 GPa at 1 day and 35-36 GPa at 28 days while alkali-activated S16 mortar, even if has a compressive strength similar to that of WC and GC, evidences slightly lower values both at early (24 GPa) and late (31 GPa) ages. Finally, S8 and S12 are characterized by DMEs equal to 26 and 30 GPa, respectively.

Table 1 Elasto – mechanical properties of mortars

	Compressive strength [MPa]			Elastic modulus [GPa]		
	1d	7d	28d	1d	7d	28d
WC-0	18.2	35.1	41.2	25.3	33.3	35.2
WC-1	17.1	36.4	41.6	25.8	34.0	35.3
WC-3	18.7	39.3	45.2	25.7	33.6	35.3
WC-5	19.3	41.3	45.3	25.8	34.0	35.1
GC-0	25.0	42.1	44.8	26.4	35.6	36.5
GC-1	25.7	40.8	45.7	26.2	35.4	36.1
GC-3	26.0	44.0	48.1	26.8	35.4	35.7
GC-5	26.8	44.3	49.5	27.0	36.0	36.1
S8-0	5.1	16.0	22.9	16.8	24.1	25.9
S8-1	5.8	17.9	25.8	18.9	25.8	27.7
S8-3	5.9	18.8	26.0	18.3	26.0	27.6
S8-5	5.6	18.1	25.0	17.6	26.0	28.1
S12-0	10.1	23.8	36.4	23.0	27.8	29.9
S12-1	10.1	24.1	37.1	23.1	27.8	30.2
S12-3	10.0	24.6	36.5	23.1	28.0	30.6
S12-5	10.5	24.9	36.4	23.4	28.1	30.8
S16-0	14.2	31.3	43.4	24.8	28.9	31.3
S16-1	14.0	30.1	44.0	24.6	28.8	31.7
S16-3	15.8	30.4	44.8	24.7	28.9	31.9

S16-5	16.1	31.7	43.7	25.1	28.9	31.6
-------	------	------	------	------	------	------

Furthermore, the results presented show that the addition of TiO<sub>2</sub> nanoparticles seems to have only a marginal effect on the elasto-mechanical properties of mortars at early ages. On the contrary, the 28-day compressive strength of cementitious mixtures linearly increases with the addition of nanoparticles, up to +10% when 5% of TiO<sub>2</sub> nanoparticles with respect to binder mass is used.

This behavior was also highlighted by Shafaei et al. [25] that attributed it to the micro-filling effect of the fine TiO<sub>2</sub> which promotes the formation of denser microstructures, improving the strength of cementitious mixtures, while Chen et al. [26] confirmed that nano-TiO<sub>2</sub> is a non-reactive fine filler without pozzolanic activity, acting as potential nucleation sites for the accumulation of hydration products. On the contrary, alkali activated-based mortars do not evidence significant improvements in 28-day compressive strength when TiO<sub>2</sub> nanoparticles were added to the mixtures, with the exception of the TiO<sub>2</sub>-containing S8 mortar which evidences an increase in strength from 9 to 14% with respect to the S8 mortar manufactured without nano-TiO<sub>2</sub>.

### 4.3 Accelerated photocatalytic tests

Figure 2 reports the color variation a% of mortars sprayed with rhodamine B after 4 and 24 hours of exposure to UV light as a function of TiO<sub>2</sub> nanoparticles content. The cementitious mortars WC and GC manufactured without TiO<sub>2</sub> exhibit a moderate self-cleaning capability as already evidenced by Tyukavkina et al. [27] and Shen et al. [28] with a color variation a% equals to 5% and 16% for WC and 8% and 26% for GC after 4 and 24 hours, respectively. On the contrary, the color variation a% of TiO<sub>2</sub>-free alkali-activated slag-based mortars is less than that shown by cementitious mortars, regardless of the alkali content (S8, S12 or S16) and the exposure time to UV light.

The beneficial effect of TiO<sub>2</sub> addition in self-cleaning capability is evident both in cementitious and alkali-activated mortars. In particular, regardless of UV light exposure time, the color variation a% increases almost linearly by increasing the nanoparticles content, with the exception of the GC mortar which appears to be little affected by the TiO<sub>2</sub> dosage.

In order to evaluate the efficiency of the TiO<sub>2</sub> nanoparticles addition on mortars with different intrinsic ability to degrade organic dyes, the dimensionless efficiency coefficient  $\Gamma$  was calculated as the average slope of the curve a% vs TiO<sub>2</sub> content (with the exception of the GC samples which showed a non-linear trend in Figures 2). Results reported in Table 2 evidence that the alkali content in AAS mortars plays a fundamental role in the efficiency of the TiO<sub>2</sub> nanoparticles to promote the self-cleaning capability, regardless of dyes sprayed on the surface of samples. In fact, when RhB is applied on samples the  $\Gamma_{24h}$  coefficient is 0.0195 for S8, 0.0418 for S12 and 0.0536 for S16 while the cementitious based WC mortar evidenced an efficiency coefficient of 0.0552.

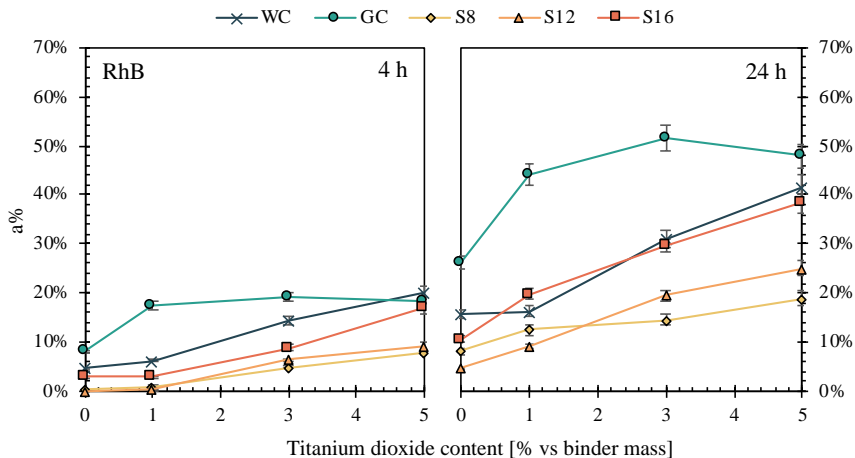


Fig. 2 Colour variation a% after 4 hours (left) and after 24 hours (right) as a function of TiO<sub>2</sub> content (accelerated test)

Table 2 Efficiency coefficient  $\Gamma$  of different mortars after 4 and 24 hours under UV light

Efficiency coefficient $\Gamma$		
	4 hours	24 hours
WC	0.0325	0.0552
S8	0.0156	0.0195
S12	0.0201	0.0418
S16	0.0289	0.0536

#### 4.4 Outdoor natural exposure

The self-cleaning ability, induced by  $\text{TiO}_2$ , has been evaluated by measuring the color variation during the exposure of mortar samples to the polluted industrial environment for 2 years where the rainfall ranging from 0 to 50 mm/hour and global radiation reaches maximum values close to 1000  $\text{W}/\text{m}^2$ . The color variation  $\Delta E$  of samples exposed to the external environment mainly occurred in the first 90 days, beyond which only limited changes were observed to the  $L^*$ ,  $a^*$  and  $b^*$  coordinates, regardless of the  $\text{TiO}_2$  content added to the material.

After 2 years of exposure (Figure 3), it can be seen that the color variation of reference samples (without  $\text{TiO}_2$ ) is strongly influenced by the binder type and, only for AAS systems, alkali content. Regardless of the orientation (North or South), grey cement-based mortars GC show  $\Delta E$  close to 6 while WC and high alkali content AAS (AAS 12 and AAS16) evidence  $\Delta E$  in the range of 7.5-8.5. On the other hand, in the alkali-activated slag-based mortars AAS8 the exposure to polluted environment causes a strong color variation  $\Delta E$  (more than 11) probably due to the high superficial roughness compared to the other mixtures investigated in this research.

The addition of  $\text{TiO}_2$  drastically reduces color variations of all the samples exposed to South of about 40-60% compared to the reference mixtures without  $\text{TiO}_2$ . Moreover, as expected, it can be noted that different exposures modify the efficiency of the  $\text{TiO}_2$  as photocatalyst in mortars due to the lower solar irradiation in the  $45^\circ$ -tilted North-faced surfaces with respect to the South-faced ones. However, the self-cleaning capability is only marginally influenced by the dosage of nanoparticles; in fact, 2-year  $\Delta E$  of samples made with 1, 3 or 5% of  $\text{TiO}_2$  appear very similar with differences not detectable by unexpert human eyes, in general lower than 2. In all this case, the limited color variation of samples containing  $\text{TiO}_2$  is clearly ascribable to the photocatalytic activity of  $\text{TiO}_2$  and not to a different fouling resistance of the surfaces.

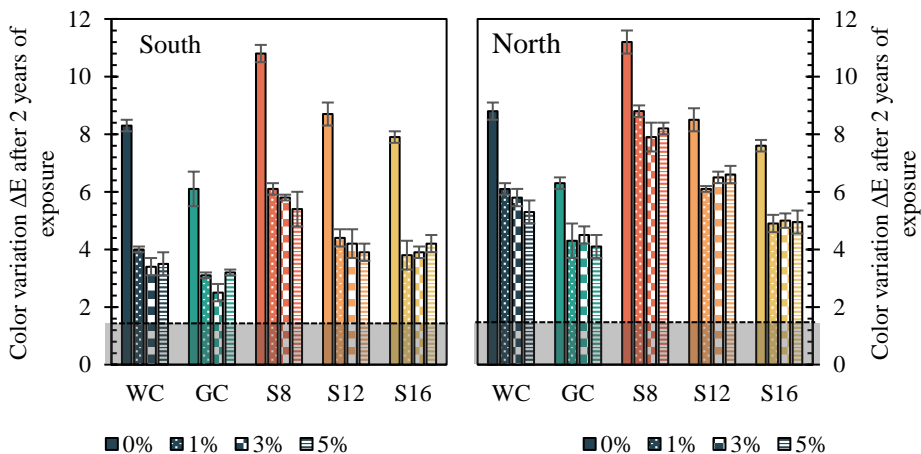


Fig. 3 Colour variation  $\Delta E$  of the specimens South-faced (left) and North-faced (right) after 2 years of natural exposure

## 5 Conclusions

This experimental study was aimed at evaluating the effect of the addition of TiO<sub>2</sub> nanoparticles on the properties of one-part alkali-activated slag-based mortars in comparison with traditional cementitious mixtures. The following conclusions can be drawn:

- The fresh state properties of mortars are not significantly influenced by the addition of TiO<sub>2</sub> nanoparticles. It can be observed only a reduction in the setting times by increasing the TiO<sub>2</sub> dosage;
- The TiO<sub>2</sub>-doped mortars AAS8 and the reference mixtures based on Portland cement show an enhancement in the compressive strength and elastic modulus with the addition of nanoparticles. On the contrary, only negligible improvements can be noticed on AAS mortars with high activator-to-slag ratios;
- The RhB photodegradation shows a pronounced beneficial effect of TiO<sub>2</sub> addition in self-cleaning capability in both cementitious and alkali-activated mortars. However, alkali content in AAS mortars plays a fundamental role in the photocatalytic efficiency of the TiO<sub>2</sub> nanoparticles: the higher the alkali content, the higher the efficiency coefficient  $\Gamma$ ;
- TiO<sub>2</sub> nanoparticles are responsible for a reduction of about 40-60% in color variation after 2 years of exposure in an industrial environment, independently of dosage and binder type.

## References

- [1] A. Fujishima, K. Honda, Electrochemical photolysis of water at a semiconductor electrode, *Nature*. 238 (1972) 37–38. <https://doi.org/10.1038/238037a0>.
- [2] V. Francioso, C. Moro, I. Martinez-Lage, M. Velay-Lizancos, Curing temperature: A key factor that changes the effect of TiO<sub>2</sub> nanoparticles on mechanical properties, calcium hydroxide formation and pore structure of cement mortars, *Cement and Concrete Composites*. 104 (2019) 103374. <https://doi.org/https://doi.org/10.1016/j.cemconcomp.2019.103374>.
- [3] J. Yuenyongsuwan, S. Sinthupinyo, E.A. O’Rear, T. Pongprayoon, Hydration accelerator and photocatalyst of nanotitanium dioxide synthesized via surfactant-assisted method in cement mortar, *Cement and Concrete Composites*. 96 (2019) 182–193. <https://doi.org/https://doi.org/10.1016/j.cemconcomp.2018.11.024>.
- [4] M.V. Diamanti, N. Luongo, S. Massari, S. Lupica Spagnolo, B. Daniotti, M.P. Pedferri, Durability of self-cleaning cement-based materials, *Construction and Building Materials*. 280 (2021) 122442. <https://doi.org/10.1016/j.conbuildmat.2021.122442>.
- [5] D. Coffetti, E. Crotti, G. Gazzaniga, M. Carrara, T. Pastore, L. Coppola, Pathways towards sustainable concrete, *Cement and Concrete Research*. 154 (2022) 106718. <https://doi.org/10.1016/j.cemconres.2022.106718>.
- [6] J.L. Provis, A. Palomo, C. Shi, Advances in understanding alkali-activated materials, *Cement and Concrete Research*. 78 (2015) 110–125. <https://doi.org/10.1016/j.cemconres.2015.04.013>.
- [7] E.A. Llano-Guerrero, L.Y. Gómez-Zamorano, E. Jiménez-Relinque, Effect of the addition of TiO<sub>2</sub> nanoparticles in alkali-activated materials, *Construction and Building Materials*. 245 (2020) 118370. <https://doi.org/10.1016/j.conbuildmat.2020.118370>.
- [8] I.M. El-Kattan, M.S. Saif, M.O.R. El-Hariri, A.H. Elgandy, L. Pérez-Villarejo, D. Eliche-Quesada, Assessing the individual impact of magnesia and titania nano- particles on the performance of alkali-activated slag mortars, *Construction and Building Materials*. 365 (2023) 130103. <https://doi.org/https://doi.org/10.1016/j.conbuildmat.2022.130103>.
- [9] S.-L. Zhang, X.-Q. Qi, S.-Y. Guo, J. Ren, J.-Z. Chen, B. Chi, X.-C. Wang, Effect of a novel hybrid TiO<sub>2</sub>-graphene composite on enhancing mechanical and durability characteristics of alkali-activated slag mortar, *Construction and Building Materials*. 275 (2021) 122154. <https://doi.org/https://doi.org/10.1016/j.conbuildmat.2020.122154>.
- [10] L.Y. Yang, Z.J. Jia, Y.M. Zhang, J.G. Dai, Effects of nano-TiO<sub>2</sub> on strength, shrinkage and

- microstructure of alkali activated slag pastes, *Cement and Concrete Composites*. 57 (2015) 1–7. <https://doi.org/10.1016/j.cemconcomp.2014.11.009>.
- [11] EN 196-5:2011 “Methods of testing cement - Part 5: Pozzolanicity test for pozzolanic cement”.
- [12] L. Coppola, D. Coffetti, E. Crotti, S. Candamano, F. Crea, G. Gazzaniga, T. Pastore, The combined use of admixtures for shrinkage reduction in one-part alkali activated slag-based mortars and pastes, *Construction and Building Materials*. 248 (2020). <https://doi.org/10.1016/j.conbuildmat.2020.118682>.
- [13] M.V. Diamanti, M. Ormellese, M.P. Pedferri, Characterization of photocatalytic and superhydrophilic properties of mortars containing titanium dioxide, *Cement and Concrete Research*. 38 (2008) 1349–1353. <https://doi.org/10.1016/j.cemconres.2008.07.003>.
- [14] EN 196-1:2016 “Methods of testing cement - Part 1: Determination of strength”.
- [15] EN 1015-3:1999 “Methods of test for mortar for masonry - Part 3: Determination of consistence of fresh mortar (by flow table)”.
- [16] EN 1015-6:1998 “Methods of test for mortar for masonry - Part 6: Determination of bulk density of fresh mortar”.
- [17] EN 1015-7:1998 “Methods of test for mortar for masonry - Part 7: Determination of air content of fresh mortar”.
- [18] EN 1015-11:2019 “Methods of test for mortar for masonry - Part 11: Determination of flexural and compressive strength of hardened mortar”.
- [19] EN 12504-4:2021 “Testing concrete in structures - Part 4: Determination of ultrasonic pulse velocity”.
- [20] UNI 11259:2016 “Fotocatalisi - Determinazione dell’attività fotocatalitica di leganti idraulici - Metodo della rodamina”.
- [21] T. Meng, Y. Yu, X. Qian, S. Zhan, K. Qian, Effect of nano-TiO<sub>2</sub> on the mechanical properties of cement mortar, *Construction and Building Materials*. 29 (2012) 241–245. <https://doi.org/10.1016/j.conbuildmat.2011.10.047>.
- [22] M. Suneel, K. Jagadeep, K.K. MahaLakshmi, G. Praveen Babu, G. V Ramarao, An Experimental Study on Workability and Strength Characteristics of M40 Grade Concrete by Partial Replacement of Cement with Nano-TiO<sub>2</sub>, in: B.B. Das, N. Neithalath (Eds.), *Sustainable Construction and Building Materials*, Springer Singapore, Singapore, 2019: pp. 253–263.
- [23] A. Kashani, J.L. Provis, G.G. Qiao, J.S.J. Van Deventer, The interrelationship between surface chemistry and rheology in alkali activated slag paste, *Construction and Building Materials*. 65 (2014) 583–591. <https://doi.org/10.1016/j.conbuildmat.2014.04.127>.
- [24] R. Zhang, X. Cheng, P. Hou, Z. Ye, Influences of nano-TiO<sub>2</sub> on the properties of cement-based materials: Hydration and drying shrinkage, *Construction and Building Materials*. 81 (2015) 35–41. <https://doi.org/10.1016/j.conbuildmat.2015.02.003>.
- [25] D. Shafaei, S. Yang, L. Berlouis, J. Minto, Multiscale pore structure analysis of nano titanium dioxide cement mortar composite, *Materials Today Communications*. 22 (2020) 100779. <https://doi.org/10.1016/j.mtcomm.2019.100779>.
- [26] J. Chen, S.C. Kou, C.S. Poon, Hydration and properties of nano-TiO<sub>2</sub> blended cement composites, *Cement and Concrete Composites*. 34 (2012) 642–649. <https://doi.org/10.1016/j.cemconcomp.2012.02.009>.
- [27] V. V Tyukavkina, E.A. Shchelokova, A. V Tsyryatyeva, A.G. Kasikov, TiO<sub>2</sub>–SiO<sub>2</sub> nanocomposites from technological wastes for self-cleaning cement composition, *Journal of Building Engineering*. 44 (2021) 102648. <https://doi.org/https://doi.org/10.1016/j.jobbe.2021.102648>.
- [28] W. Shen, C. Zhang, Q. Li, W. Zhang, L. Cao, J. Ye, Preparation of titanium dioxide nano particle modified photocatalytic self-cleaning concrete, *Journal of Cleaner Production*. 87 (2015) 762–765. <https://doi.org/https://doi.org/10.1016/j.jclepro.2014.10.014>.

# Structural Behaviour of HPFRC Walls Subjected to Axial Load and Bending Moment

Alessandro P. Fantilli<sup>1</sup>, Nicholas S. Burello<sup>2</sup>, Bernardino Chiaia<sup>1</sup>, Jorge C. Diaz Garcia<sup>2</sup>, Alfredo A. Flore Gutierrez<sup>3</sup>, Davide Zampini<sup>4</sup>

<sup>1</sup> Professor, DISEG, Politecnico di Torino, C.so Duca degli Abruzzi 24, 10129 Torino, Italy

<sup>2</sup> CEMEX Innovation Holding AG Brügg Branch Römerstrasse 13, 2555 Brügg, Switzerland

<sup>3</sup> CEMEX S.A.B de C.V., Av. Constitucion Pte 444, 64000 Monterrey Centro, Mty, Mexico

<sup>4</sup> CEMEX Innovation Holding AG General-Guisan-Strasse 6, 6300 Zug, Switzerland

## Abstract

The compression-bending behaviour of structural elements, made with only High-Performance Fiber-Reinforced Concrete (HPFRC), was experimentally investigated. A total of 15 small-scale walls were subjected to a pre-established axial load, whereas transverse load – applied at the cantilever point, progressively increased, generating the bending moment. The interaction domain was experimentally measured through the tests, and numerically computed in accordance with the Annex L of the new Eurocode 2 (FprEN1992-1-1:2023). In the numerical outcomes, material properties were defined by means of the conventional testing methods (i.e., EN12390-3 and EN14651). As a result, a good agreement between numerical predictions and experimental measurements was obtained.

## 1 Introduction

In several countries, masonry is the most common and affordable building structure. Nevertheless, there are several environmental problems associated with the use of traditional material in conventional masonry structures [1]. On the other hand, in the case of concrete, several strategies can be applied to make the final structure more sustainable. Among them, the use of high-performance concrete, or the application of the so-called performance strategy [2], can be a viable way to reduce the environmental impact of concrete frames [3]. Although the carbon footprint per unit volume is larger, the use of high-performance concrete leads to the reduction of the total volume of concrete, and of the equivalent CO<sub>2</sub> of a as well. Accordingly, an experimental campaign on the use of a specific high performance self-compacting fiber-reinforced concrete [4] in structural walls, hereinafter called HPFRC (High-Performance Fiber-Reinforced Concrete), is presented in the following sections. The goal is to validate the design approach proposed by the new Eurocode 2 [5] in the case of HPFRC bearing walls.

## 2 Experimental campaign

The properties of HPFRC were measured by testing the following samples:

- 3 cubes 150 × 150 × 150 mm<sup>3</sup> (according to EN12390-3)
- 3 beams 150 × 150 × 600 mm<sup>3</sup> (according to EN14651)

A total of 15 walls having size 50 × 250 × 1000 (width, depth, and height, in mm) were tested by applying two loads simultaneously through two MTS hydraulic actuators. The setup of the test is illustrated in Fig.1. A massive concrete foundation was installed to anchor one of the ends of the walls. Namely, the anchorage system consists of a series of embedded threaded rods and a 20 mm thick steel plate (see Fig.1a).

A hydraulic actuator with a capacity of 1000 kN was used to transfer the axial load (i.e., in vertical direction), whereas a second jack (having a nominal capacity of 250 kN) was used to transfer the horizontal force, generating shear and moment along the walls.

For each wall, 4 vertical LVDTs (i.e., 2 on each side) were placed along the longitudinal direction to measure either the shortening or the elongation of the walls. An extensible gauge, having retractable mounts, was used for the vertical displacements. The ends of the mounts were placed at 50 mm from

top and 50 mm from the bottom of the wall. Thus, a total gauge length of 700 mm was adopted for the vertical displacements. In addition, 3 horizontal LVDTs were placed at different heights (at the foundation, at the centre, and at the top of the wall) to measure the transversal displacements. Fig. 1b illustrates the position of all the LVDTs. The vertical LVDTs were also used to centre the vertical load. In fact, in the tests the vertical load is a sort of pre-load, iteratively applied by moving the position of the jack up to reaching an almost uniform shortening at the four LVDTs (V1, V2, V3, and V4 in Fig. 1b). More specifically, to generate the expected behaviour of the wall in flexural-compression, V1-V3 must be in tension and V2-V4 in compression. After setting the vertical jack at the required axial load, it did not vary for the whole duration of the test. Whereas the horizontal jack started acting on the top of the wall under displacement-control at a speed rate of 0.1 mm/min.

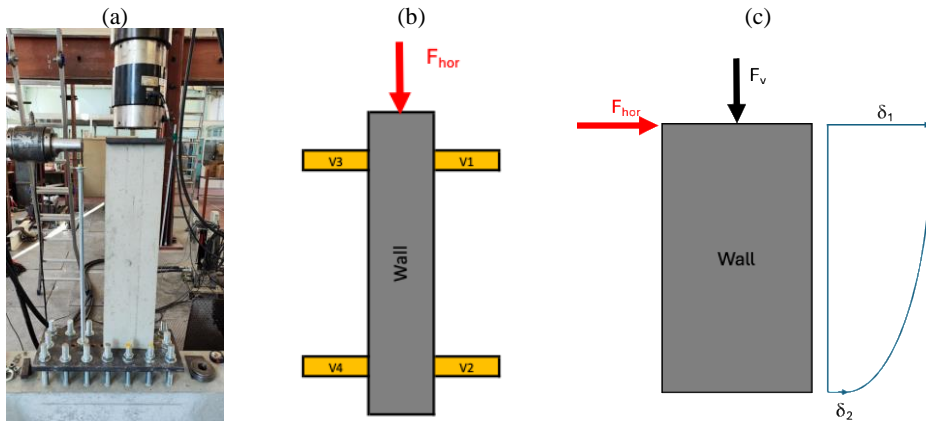


Fig. 1 (a) Setup for biaxial test on concrete walls; (b) nomenclature of vertical LVDTs according to the horizontal force (plan view); and (c) evaluation of the horizontal displacements.

### 3 Test results

In the following sections, the results of the tests are shown in terms of load-deflection curves ( $F_{hor}-\delta$ ), where  $F_{hor}$  is the load measured by the horizontal actuator (the vertical load,  $F_v$ , was constant throughout the test) and the deflection  $\delta$  is the difference between the displacement at the top of the wall ( $\delta_1$  in Fig. 1b) and that measured at the base ( $\delta_2$  in Fig. 1b). The samples are labelled according to the value of the vertical load (e.g., N0#2 is the name of the second sample of the wall the wall with  $F_v = 0$  kN).

#### 3.1 Bending tests without axial loads ( $F_v = 0$ kN)

The first three walls (i.e., N0#1, N0#2, and N0#3) were tested in absence of the axial load (i.e.,  $F_v = 0$ ). In these walls, only the horizontal actuator applied the load, producing shear and bending moment in the cross-sections. As shown in Fig. 2a, the walls failed in correspondence of the end cross-section of the embedded rods, which weakened the concrete cross-section. For this reason, the walls were reinforced with a collar (see Fig. 2b) having a height of 250 mm (namely, the embedded length of the rods with the addition of 50 mm) and a thickness of 50 mm. In this way, the failure occurred in correspondence of a cross-section ( $50 \times 250$  mm<sup>2</sup>) made with HPFRC. Accordingly, two additional tests were carried in the condition of pure bending (N0#4, and N0#5).

Fig. 3 shows the  $F_{hor}-\delta$  diagrams of the five walls, demonstrating the premature failure of the walls without the reinforcing collars. Indeed, in the walls N0#4 and N0#5, the maximum horizontal load is about 50% higher than in the specimens N0#1, N0#2, and N0#3

#### 3.2 Biaxial tests with $F_v = 50$ kN

All the walls tested with  $F_v = 50$  kN were previously reinforced with a collar in the foundation. Two different test setups were conceived for the application of the axial load. More precisely, in two walls (i.e., N50#1 and N50#2) only a roller support device was in direct contact with the stroke of the loading cell (Fig. 4a). To reduce the friction between the actuator and the wall, the device was made by two

horizontal steel plates separated by steel spheres within an hollow lane. Whereas in other two walls (i.e., N50#3 and N50#4) an axial spherical plain bearing, with a capacity of 250kN, was introduced between the actuator and the roller support (see Fig.4b).

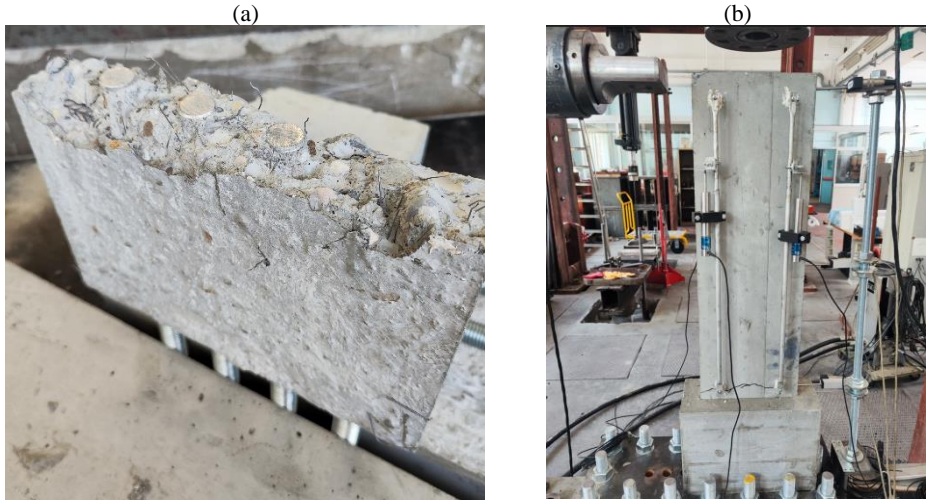


Fig. 2 (a) Failure of the wall subjected to bending and shear; (b) the collars used to reinforce the wall in the foundation.

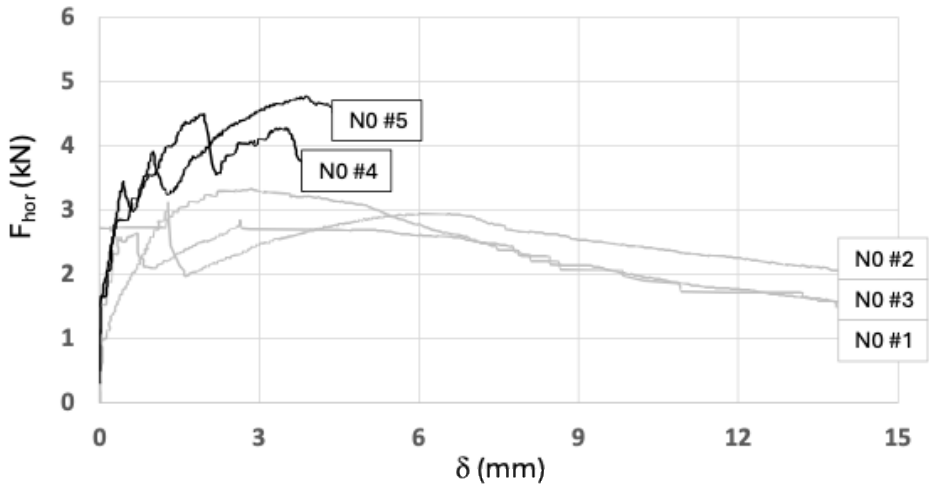


Fig. 3 Load - deflection curves of walls tested in absence of the axial load ( $F_v = 0$ ).

The setup without spherical bearing for the transmission of the axial load did not allow to obtain a pure in-plane bending, whereas the second setup of Fig.4b provided the expected behaviour (i.e., V1-V3 in tension and V2-V4 in compression in Fig.1b). Moreover, the maximum horizontal load in the specimens N50#1 and N50#2 was remarkably higher than that measured in N50#3 and N50#4, as shown in the load deflection diagram of Fig.5.



### 3.3 Biaxial tests with $F_v = 100$ kN and $F_v = 200$ kN

In all the walls subjected to an axial load  $F_v = 100$  kN and  $F_v = 200$  kN, the reinforced collar was present (see Fig.2b), and the test setup was that shown in Fig.4b. In total, five walls were successfully tested in these conditions with  $F_v = 100$  kN (N100#1, N100#2, and N100#3) and two walls with  $F_v = 200$  kN (N200#1 and N200#2). The load-deflection curves of these tests are reported in Fig.6 and Fig.7, respectively.



Fig. 4 Application of axial load: (a) roller support device loaded by the hydraulic jack; (b) axial spherical plain bearing coupled with roller support device.

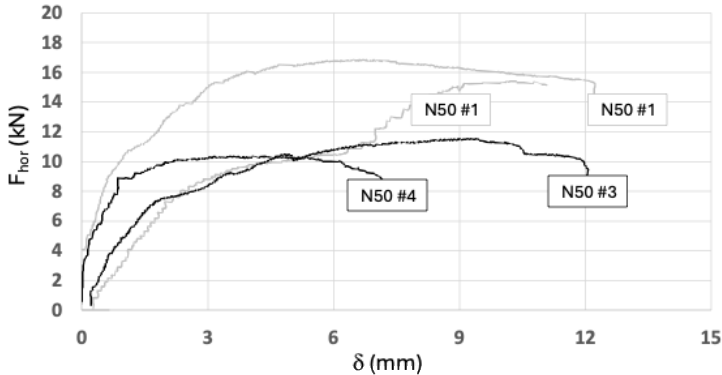


Fig. 5 Load - deflection curves of the walls with  $F_v = 50$  kN.

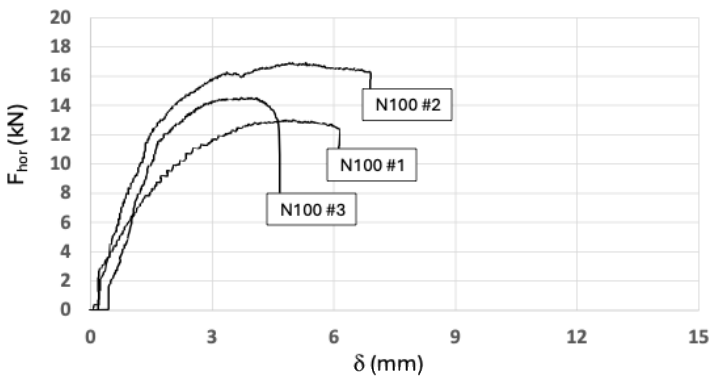


Fig.6 Load - deflection curves of the walls with  $F_v = 100$  kN.

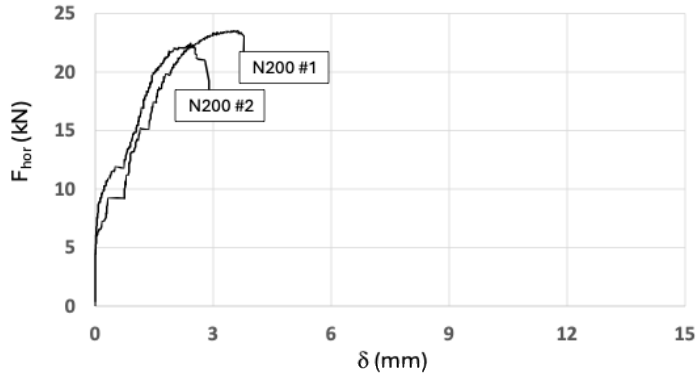


Fig. 7 Load - deflection curves of the walls with  $F_v = 200\text{kN}$ .

#### 4 Experimental data and numerical results

Considering the biaxial loads, the interaction failure domain, bending moment  $M$  vs. normal load  $N$ , is calculated according to Eurocode 2 [5]. The domains are computed by means of a cross-sectional analysis, assuming the nominal sizes of the walls (i.e., width = 50 mm, and depth = 250mm). The experimental data concerning the mechanical characterization of HPFRC samples, cast with the same batches of the walls, are reported in Table 1.

Table 1 Mechanical properties of the HPFRC used to cast the bearing walls

Mechanical property	Average value	Characteristic value
Compressive strength $f_c$ (MPa)	77.18	61.67
Residual flexural strength $f_{R1}$ (MPa)	11.60	7.60
Residual flexural strength $f_{R3}$ (MPa)	12.04	9.30

The compressive strength  $f_c$  of HPFRC was used in the parabola-rectangle stress-strain relationship for structural concrete in compression, with  $\epsilon_{c1} = 0.002$  and  $\epsilon_{cu} = 0.0035$  in accordance with Eurocode 2 [5]. Moreover, for concrete in tension, the residual flexural strengths  $f_{R1}$  and  $f_{R3}$ , and the coefficient  $k_G = 1$  and  $k_0 = 0.5$ , defined the simplified constitutive law in tension (bi-linear shape), as suggested by the Annex L of Eurocode 2.

The resisting interaction domain  $M_R$ - $N_R$  of the wall cross-section was computed twice:

- With the partial safety factor  $\gamma_c = 1.0$  and the average values of both concrete in tension and in compression (see Table 1)
- With the partial safety factor  $\gamma_c = 1.5$  and the characteristic values of materials properties. In particular, the values reported in Table 1 were obtained by adopting a log-normal distribution (5% quantile and 75% confidence level) of the experimental data.

Both the resisting interaction domains are depicted in Fig.8, where also the couples of external action  $M_E$ - $N_E$  obtained from only the significative tests (N0#4, N0#5, N50#3, N50#4, N100#1, N100#2, N100#3, N200#1, and N200#2) are reported. Namely,  $N_E = F_v$ , whereas the corresponding  $M_E$  is the product of the maximum value of  $F_{hor}$  times the height of the wall ( $H = 0.75$  m, which is the distance between the top of the wall and the extrados of the collar).

Comparing the experimental data with the  $M_R$ - $N_R$  curves, it is possible to observe how almost all the  $M_E$ - $N_E$  points are included within the two interaction domains computed in accordance with Eurocode 2 [5]. If the partial safety factors are also applied to the external loads, the interaction domain

computed with  $\gamma_c = 1.5$  and the characteristic values of materials properties represents a safety model for designing HPFRC walls.

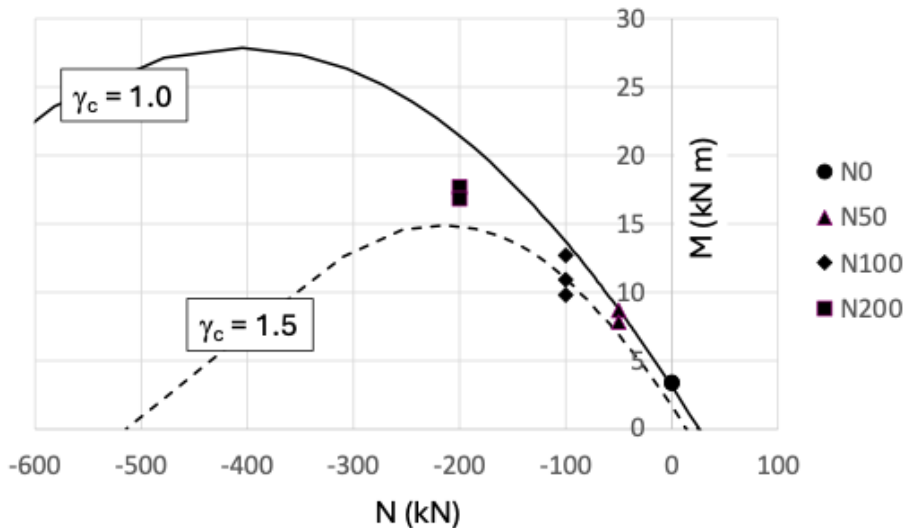


Fig. 8  $M_R$ - $N_R$  domains computed in accordance with EC2 [5] and the  $M_E$ - $N_E$  couples measured in the tests on the walls.

## 5 Conclusions

According to the results of the tests and to the theoretical analyses, the following conclusions can be drawn:

- At material level, the HPFRC [4] can be effectively used as structural materials of bearing walls
- Bearing concrete walls can be correctly designed with the approach proposed in the new Eurocode 2 [5]

## References

- [1] Nayaka, R.R., Alengaram, U.J., Jumaat, M.Z., Fonseca, F.S., 2021. "Structural performance of masonry prisms, wallettes and walls containing." *Construction and Building Materials* 303: 124439
- [2] Habert, G., Roussel, N. 2009. "Study of two concrete mix-design strategies to reach carbon mitigation objectives." *Cement and Concrete Composites* 31(6): 397-402.
- [3] Fantilli, A.P., Mancinelli, O., Chiaia, B. 2019. "The carbon footprint of normal and high-strength concrete used in low-rise and high-rise buildings" *Case Studies in Construction Materials* 11: e00296
- [4] Esser J., Guerini A, Volpatti G, Zampini D. 2015. Advanced fiber reinforced concrete mix designs and admixtures systems, Patent EP3307692 B1 [priority 2015-06-11]. Commercially available as CEMEX® Resilia®.
- [5] EN 1992-1-1:2023 "Eurocode 2: Design of concrete structures. General rules – rules for buildings, bridges and civil engineering structure"

# Electrically conductive mortars based on cement or alkali-activated fly ash: mechanical and electrical characterization

Alessandra Mobili<sup>1</sup>, Gloria Cosoli<sup>2,3</sup>, Gian Marco Revel<sup>3</sup> and Francesca Tittarelli<sup>1,4</sup>

<sup>1</sup>*SIMAU Department,  
INSTM Research Unit,  
Università Politecnica delle Marche,  
via Brecce Bianche 12, 60131, Ancona, Italy*

<sup>2</sup>*Faculty of Engineering,  
Università Telematica eCampus,  
via Isimbardi 10, 22060, Novedrate, Italy*

<sup>3</sup>*DIISM Department,  
Università Politecnica delle Marche,  
via Brecce Bianche 12, 60131, Ancona, Italy*

<sup>4</sup>*Istituto di Scienze dell'Atmosfera e del Clima (CNR-ISAC),  
via Gobetti 101, 40129, Bologna, Italy*

## Abstract

This work presents the study carried out within the SensCrHEAT project (self-SENSing conCretes for HEATING products) funded by the European Union NextGeneration EU within the Proof of Concept (PoC) VALUE program. In this experimentation, mortar compositions have been prepared with two different binders, namely ordinary Portland cement (OPC) and alkali-activated fly ash (AAF). Hence, mortars were loaded with commercial graphene nanoplatelets (GNP) at 0.5% by the total volume and a combination of two recycled materials, i.e., biochar (BCH) and recycled carbon fibres (RCF), in amounts of 0.5% and 0.05% by the total volume, respectively. Mortars have been compared in terms of mechanical and electrical properties according to specific test protocols, test machines and sensors. Results show that the combined addition of the two sustainable materials in both cement-based and alkali-activated fly ash mortars are less impacting on compressive strength and more able to reduce the electrical impedance of the final materials, making them probably better performing in terms of self-sensing/monitoring ability, than the expensive commercial GNP.

## 1 Introduction

Structural health monitoring (SHM) techniques are spreading more and more in different fields, including the construction sector. One of the easiest ways to monitor buildings or infrastructures is the use of electrically conductive materials, which permit to reduce the number of acquiring nodes and use low-cost instrumentation given the better Signal-to-Noise Ratio (SNR) conferred to the element to be monitored [1]. In recent years, several studies have focused on the use of electrically conductive filler and fibres added to cement-based matrices to increase the electrical properties of the hardened material. Generally, carbon-based commercial products are utilised, such as carbon nanotubes (CNT), carbon black (CB), carbon fibres, or graphene. As a matter of fact, Park et al. [2] reported that CNT and carbon fibres added to cement-based matrices reduce significantly the electrical resistivity of the material. Gwon et al. [3] used CB and carbon fibres to decrease electrical resistivity of cement composites and produce self-heating materials. Sevim et al. [4] have found that graphene nanoplatelets (GNP) added to mortars at a concentration of 7.5 wt% by cement provide the lowest bulk resistivity.

Nevertheless, for the benefit of the sustainability of the construction sector and circular economy principles [5], it is necessary to use more environmentally friendly solutions to provide additional properties to building materials such as higher electrical conductivity and, hence, better self-sensing/monitoring properties. One solution could be using recycled carbon-based additions to ordinary Portland cement (OPC)-based materials. For example, Dehghanpour and coworkers [6] showed that recycled nano CB coupled to other types of fillers reduces the electrical resistance of concrete. Faneca et al. [7] found that electrical resistivity of concrete reaches values between 3.0 and 0.6  $\Omega\cdot\text{m}$  for recycled carbon fibres contents ranging from 0.2 to 0.8% in volume. Rhee et al. [8] used rice husk-derived high-surface-area graphene (GRH) to produce electrically conductive cement mortar finding that the resistivity of specimens loaded with 0.8 wt% GRH increased 64% compared to the reference OPC specimen. Recently, the present authors have patented innovative mix-designs for cement-based mortars/concretes with improved electrical properties (“Eco-compatible and self-sensing mortar and concrete compositions for manufacturing reinforced and non-reinforced constructive elements, related construction element and methods for the realization of self-monitorable building structures”, patent n° 10202000022024). In particular, sustainable and recycled materials like char/biochar and recycled carbon fibres have been added in order to reduce the electrical impedance of the material and increase the durability of the final constructive element [9].

Another way to reduce carbon emissions of the construction sector could be the use of more sustainable materials based on environmentally friendly binders produced by alkali-activation. There are several ways to prepare alkali-activated materials, for example by chemically activated industrial aluminosilicate by-products such as ground granulated blast furnace slag (GGBFS) or fly ash (FA). Recently, researchers have tried to reduce electrical resistivity also in alkali-activated materials. For example, Zhang et al. [10] used graphene as an electron acceptor to improve electroconductivity of alkali-activated fly ash (AAF) composites. D’Alessandro and coworkers [11] studied four different inclusions (CNT, carbon nanofibers, CB, and GNP) and found that the specimens with CB and nanofibers were slightly more conductive than the plain ones, while the specimens with GNP exhibited a higher resistance than the plain one-part alkali-activated GGBFS-based mortars.

This paper reports a preliminary study regarding the mechanical and electrical properties of structural mortars (with a compressive strength higher than 25 MPa, according to the EN 1504-3 standard) manufactured with a commercial filler, namely GNP, and a combination of two recycled additions, i.e., biochar (BCH) in form of filler and recycled carbon fibres (RCF) in form of fibres, prepared with two different binders, i.e., OPC and AAF, in order to evaluate if the amount of recycled additions patented by the authors could be suitable for both traditional (e.g., OPC) and innovative (e.g., AAF) electrically conductive binder-based materials.

## 2 Experimental program

### 2.1 Materials

OPC mortar specimens were prepared with a Portland limestone cement CEM II/B-LL 42.5 R supplied by Italcementi Tecnozem® within the group of Heidelberg Materials. AAF mortars were prepared with a class F fly ash (FA) produced by General Admixture S.p.A. and a calcium aluminate cement (CAC) produced by Kerneos Inc. (now part of Imerys Aluminates) as aluminosilicate precursors. FA and CAC have specific surface area between 3000-7500 and 2850-3450  $\text{cm}^2/\text{g}$  and mean particle size around 10-30 and around 10-20  $\mu\text{m}$ , respectively. A blend of sodium silicate solution (SSS) with a water content of 55.5% by mass and a molar ratio  $\text{SiO}_2/\text{Na}_2\text{O}$  of 2.1 kindly offered by Ingessil S.p.A. and potassium hydroxide (KOH) was used as alkaline activator. The activator was prepared 24 hours prior to the test in order to ensure that the solution reached the room temperature. A commercial calcareous sand used commonly for construction products with  $D_{\text{max}}$  lower than 8 mm and water absorption of 5.5% by mass produced by Esinacalce S.r.l. was used as aggregate. Indeed, it is worthy to consider the small specimen sizes (i.e., 4 cm x 4 cm x 16 cm) to choose  $D_{\text{max}}$  as  $\leq 1/4$  of the minimum dimension of structural elements according to the Italian technical standards for buildings. Commercial GNP supplied by Pentachem S.r.l. with a thickness of 6 – 8 nm and a width lower than 5  $\mu\text{m}$  was used as reference carbon-based addition. As sustainable additions, BCH supplied by RES Italia and obtained by the pyrolysis of agricultural wastes at 850 °C was used in form of filler after grinding and sieving at 75  $\mu\text{m}$ , whereas RCF with 6 mm length and 7  $\mu\text{m}$  diameter provided by Procotex Belgium SA were used as fibres.

## 2.2 Methods

### 2.2.1 Mortars preparation

For each different binder (i.e., OPC and AAF), three types of mortars were prepared. With more details, one was manufactured without carbon-based additions as reference (REF). The other two were prepared as follows: one was manufactured with the inclusion of GNP at 0.5% by the total volume and the other one was manufactured with the addition of both BCH and RCF at 0.5% and 0.05% by the total volume, respectively. AAF mortars were prepared at the same aggregate volume of the OPC counterparts. OPC mortars were prepared with a water/binder (w/b) ratio of 0.60, whereas AAF mortars were prepared at a w/b ratio of 0.37. The mix proportions of mortars are given in Table 1.

The casting procedure was done as follows: at first, sand was mixed with solid binder (i.e. OPC in case of cement-based mortars and FA with CAC for AAF mortars), then, BCH or GNP was added in dry form without any previous dispersing methodology, hence RCF were added when needed, and finally water or activator was incorporated gradually until obtaining a homogeneous mixture. Before moulding, the workability of mortars was measured according to the UNI EN 1015-3 and UNI EN 1015-6 standards. After casting, mortars were stored in a climatic chamber set at a temperature (T) of  $20 \pm 1$  °C and a relative humidity (RH) of  $50 \pm 5\%$  until testing. For the first 7 days of curing, mortars were wrapped in plastic sheets in order to keep them moist at RH = 100%; then, they were unwrapped and left inside the chamber at RH of  $50 \pm 5\%$ .

Table 1 Mix proportions (g/L) and flow values (mm) of mortars.

Mortar	OPC	BCH	RCF	GNP	H <sub>2</sub> O	Sand	Precursor		Activator			Flow value
							FA	CAC	SSS	KOH	H <sub>2</sub> O	
OPC_REF	508	-	-	-	305	1407	-	-	-	-	-	160
OPC_GNP	506	-	-	10	303	1400	-	-	-	-	-	153
OPC_BCH+RCF	505	10	1	-	303	1400	-	-	-	-	-	148
AAF_REF	-	-	-	-	-	1407	480	42	156	32	125	162
AAF_GNP	-	-	-	10	-	1400	478	42	155	32	124	145
AAF_BCH+RCF	-	10	1	-	-	1400	477	42	155	32	124	152

### 2.2.2 Mechanical properties

Each mortar composition was tested in terms of compressive strength ( $R_c$ ) after 2, 7, and 28 days of curing. The test was performed on three specimens per composition with 40 mm x 40 mm x 160 mm dimensions according to the UNI EN 1015-11 standard. A hydraulic press (Galdabini S.p.A.) with a maximum load of 400 kN was used. In the following sections, the average value of  $R_c$  is reported for each tested mortar mix.

After 28 days of curing, also the dynamic modulus of elasticity ( $E_d$ ) was measured on the same three prismatic specimens per composition before compression. The test was performed by following the procedure reported in [12].

### 2.2.3 Electrical properties

Electrical tests were performed following the Wenner's method [13]. In details, prismatic specimens with 40 mm x 40 mm x 160 mm dimensions were equipped with embedded stainless-steel rods acting as electrodes. These electrodes had a diameter of 3 mm, a length of 40 mm, and were embedded for half of their length inside the mortar (i.e., 20 mm) with an inter-electrode spacing of 12 mm. After 21, 28, and 35 days of curing three specimens per composition were tested in terms of electrical impedance. In particular, an EVAL-AD5940BIOZ board produced by Analog Devices Inc. was used to carry out electrical impedance measurements according to Electrochemical Impedance Spectroscopy (EIS) method in a galvanostatic configuration. The material was excited with an alternating current (AC) with a frequency of 10 kHz and a signal amplitude of 600 mVpp. To acquire electrical impedance data,

SensorPal software provided by Analog Devices Inc. was used. The software gives the value of the electrical impedance modulus  $|Z|$  in  $\Omega$  and the phase  $\phi$  in degrees for each acquired measurement. Therefore, in order to obtain the real part of the electrical impedance  $Z_{Re}$ , the phase  $\phi$  was converted in rad and the following equation was used:

$$Z_{Re} = |Z| \cdot \cos\phi \quad (1)$$

The  $Z_{Re}$  value was chosen since in case of a pure resistive behaviour (according to the second Ohm's law) it is directly related to electrical resistivity, and it is related to the ionic movement in the material and, therefore, to the durability of the material itself [14].

### 3 Results and discussion

#### 3.1 Workability

All mortars were manufactured in order to reach a plastic workability (Table 1), i.e., slump flow greater than 140 mm measured with a flow table, according to the UNI EN 1015-6 standard. For this reason, AAF mortars were prepared with a water content lower than that of cement-based mortars. Indeed, the presence of FA instead of OPC, due to the spherical particles of FA, increases the workability of mortars [15].

#### 3.2 Mechanical properties

The compressive strength of all manufactured mortars after 2, 7, and 28 days of curing is reported in Fig. 1. As expected, the compressive strength of mortars increases in time and that of AAF mortars is always higher than that of OPC ones. In general, the strength development of OPC mortars is similar between the three different compositions, since after 2 and 7 days of curing the strength gain is approximately 45% and 73%, respectively, of the final compressive strength. The same is found also for AAF mortars since the  $R_c$  value after 2 and 7 days reaches respectively around 60% and 74% of the final strength. Therefore, both mortars based on OPC and AAF register the highest strength gain after the first week of curing, while for longer curing time the compressive strength development is less pronounced.

After 28 days of curing, OPC\_REF mortar reaches 30.3 MPa. When BCH+RCF are added, the compressive strength remains almost unaltered, whereas the mortar containing GNP shows a  $R_c$  value 17% lower than that of the plain mortar. AAF\_REF has a compressive strength equal to 38.7 MPa after 28 days, which is 24% higher than that of OPC\_REF. As for OPC-based mortars, the addition of BCH+RCF does not modify consistently the compressive strength, and the addition of GNP lowers the  $R_c$  value of approximately 10%.

Results obtained in this study confirm what was found by authors in previous works where the combined addition of BCH and RCF does not significantly affect the compressive strength of cement-based concretes after 28 days of curing [9,16]. Conversely, the GNP addition causes a lowering of the mechanical properties of mortars owing to their high specific surface area and hydrophobicity [17], which can create agglomerates difficult to disperse in polar liquids like water. It is interesting to highlight that the effect of GNP and BCH+RCF on mortars is almost the same regardless the type of binder.

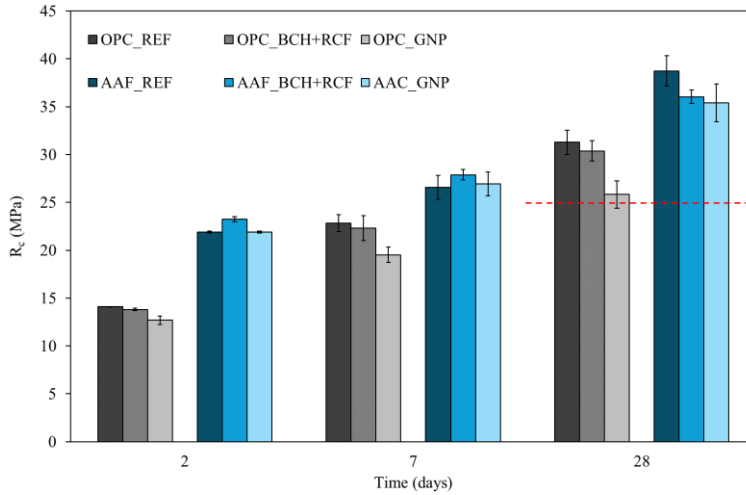


Fig. 1 Mechanical strength of OPC and AAF mortars in time. Results are reported in terms of mean  $\pm$  standard deviation values. Red dashed line shows the lower limit of 25 MPa for structural mortars.

The average dynamic modulus of elasticity of all mortars after 28 days of curing is reported in Fig. 2. The obtained results show that all OPC mortars obtained an  $E_d$  value of 23 GPa. On the contrary, AAF\_REF has a modulus of elasticity of 26 GPa and those containing carbon-based additions of 24 GPa. In general, it can be stated that the dynamic modulus of elasticity does not change consistently between the studied mortars.

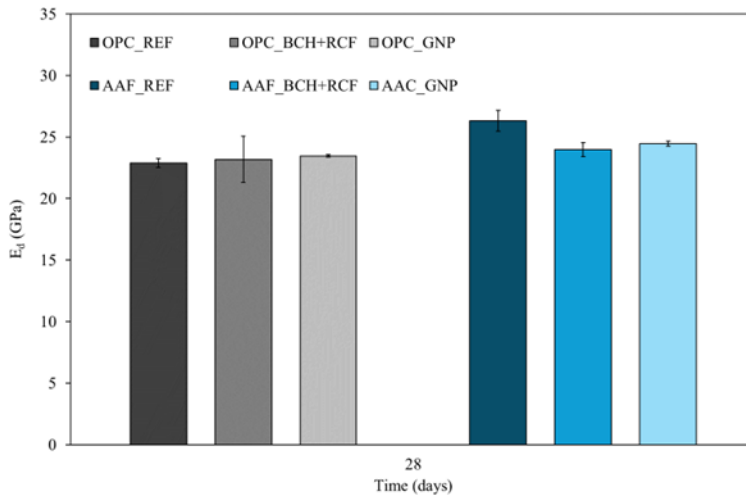


Fig. 2 Dynamic modulus of elasticity of OPC and AAF mortars at 28 days of curing. Results are reported in terms of mean  $\pm$  standard deviation values.

### 3.3 Electrical properties

The electrical impedance of all manufactured mortars after 21, 28, and 35 days of curing is reported in Fig. 3. As for compressive strength, the  $Z_{Re}$  increases in time, since mortars microstructure densifies,



and water evaporates. OPC\_REF obtain the highest impedance values during the whole test duration, with  $Z_{Re}$  equal to 915  $\Omega$  after 35 days of curing. The addition of GNP filler lowers the electrical impedance of OPC mortar of 30% after 35 days of curing, given that it reaches 633  $\Omega$ . Conversely, the inclusion of both BCH and RCF is highly efficient to reduce the electrical impedance of the cement-based material during the entire testing period. Indeed, OPC\_BCH+RCF obtains 139  $\Omega$  at the end of test, which is 85% lower than the reference OPC mortar.

AAF\_REF mortar shows an electrical impedance of 325  $\Omega$  after 35 days of curing, equal to 35% of that of the OPC\_REF one. As for OPC mortars, GNP addition reduces slightly the electrical impedance of mortars during the whole test duration, with a  $Z_{Re}$  value of 204  $\Omega$  at the end of the test, equal to 37% lower than that of the plain mortar AAF\_REF. The highest electrical impedance reduction is found for AAF\_BCH+RCF, which reaches a  $Z_{Re}$  equal to 11  $\Omega$  after 35 days of curing, corresponding to 97% reduction compared to the AAF\_REF mortar.

In general, AAF-based mortars have lower electrical impedance values than their OPC-based counterparts and this occurs either for plain mortars or mortars loaded with carbon-based additions like GNP and BCH with RCF. The higher electrical conductivity of alkali-activated materials has already been reported by Rovnanik and coworkers [18] who studied slag-based matrices. As for slag aluminosilicate, the fly ash used in this work contains iron microparticles that do not take part in the activation of fly ash itself. Moreover, the solution present in the pores is composed by very soluble and mobile hydrated  $Na^+$  and  $K^+$  ions, which contribute to the high electrical conductivity of these types of materials.

It can be stated that GNP is able to slightly decrease the electrical impedance of both OPC- and AAF-based mortars. The lowering of electrical impedance is related to the high electrical conductivity of graphene and this was found also by Qureshi et al. [19] for OPC-based pastes and by Zhang et al. [10] for AAF materials. However, the highest reduction is given by the combined addition of filler and fibres like BCH and RCF. This finding was already reported by the present authors [9] in cement-based concretes, but, in our knowledge, it has never been reported for alkali-activated matrices.

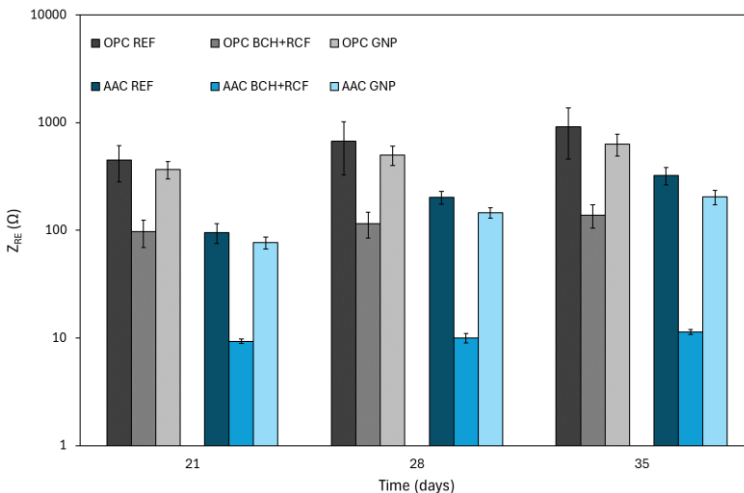


Fig. 3 Electrical impedance of OPC and AAF mortars in time. Results are reported in terms of mean  $\pm$  standard deviation values.

#### 4 Conclusions

The present paper presents a preliminary study on the use of different carbon-based additions on structural mortars ( $R_c \geq 25$  MPa after 28 days of curing, according to the EN 1504-3 standard) to decrease their electrical impedance for the benefits of Structural Health Monitoring (SHM) techniques. Ordinary Portland cement and alkali-activated fly ash have been chosen as binders. Three types of carbon-based

additions have been selected, i.e., graphene nanoplatelets (GNP) and a combination of biochar (BCH) and recycled carbon fibres (RCF). The obtained results are listed hereafter:

- It is possible to manufacture mortars with and without carbonaceous additions belonging to structural classes and with a plastic workability if water content is opportunely dosed.
- The addition of GNP decreases by 17% and by 10% the compressive strength of OPC and AAF mortars, respectively, after 28 days of curing.
- The combined addition of BCH and RCF does not negatively influences the compressive strength of mortars, regardless the adopted binder.
- GNP decreases by 30% and 37% the electrical impedance of OPC and AAF mortars, respectively, whereas the combination of BCH and RCF reduces by 85% and even by 97% the  $Z_{Re}$  value of OPC and AAF mortars, respectively.

It has been demonstrated that the combined addition of two sustainable materials like biochar and recycled carbon fibres on both cement-based and alkali-activated fly ash mortars is more able to effectively reduce the electrical impedance of the final materials, making them probably better performing in terms of self-sensing/monitoring ability, than the expensive GNP.

In the future, authors plan to investigate the self-sensing properties of the studied mortars by carrying out compressive loading cycles. Such study will be aimed at evaluating if mortars with the lowest electrical impedance would be also those showing the best piezoresistive behaviour, in terms of fractional change in resistance (FCR), Gauge Factor (GF), and Strain Sensitivity (SS). Moreover, also the self-heating properties of the studied compositions will be investigated in order to evaluate their possible application for indoor floor heating screeds or for outdoor de-icing pavements and hence to produce multifunctional construction materials.

## Acknowledgements

This research activity was carried out within the SensCrHEAT project (self-SENSing conCretes for HEATing products) funded by the European Union NextGeneration EU within the Proof of Concept (PoC) VALUE program.

Authors wish to thank Procotex Belgium SA for the recycled carbon fibers, RES Italia for biochar, General Admixture S.p.A. for the fly ash, and Ingessil S.p.A. for the sodium silicate solution kindly offered for this work.

## References

- [1] N. Giulietti, P. Chiariotti, G. Cosoli, G. Giacometti, L. Violini, A. Mobili, G. Pandarese, F. Tittarelli, G.M. Revel, Continuous monitoring of the health status of cement-based structures: electrical impedance measurements and remote monitoring solutions, *Acta Imeko*. 10 (2021) 132–139.
- [2] H.M. Park, G.M. Kim, S.Y. Lee, H. Jeon, S.Y. Kim, M. Kim, J.W. Kim, Y.C. Jung, B.J. Yang, B.J. Yang, Electrical resistivity reduction with pitch-based carbon fiber into multi-walled carbon nanotube (MWCNT)-embedded cement composites, *Constr. Build. Mater.* 165 (2018) 484–493. doi:10.1016/j.conbuildmat.2017.12.205.
- [3] S. Gwon, H. Kim, M. Shin, Self-heating characteristics of electrically conductive cement composites with carbon black and carbon fiber, *Cem. Concr. Compos.* 137 (2023) 104942. doi:10.1016/J.CEMCONCOMP.2023.104942.
- [4] O. Sevim, Z. Jiang, O.E. Ozbulut, Effects of graphene nanoplatelets type on self-sensing properties of cement mortar composites, *Constr. Build. Mater.* 359 (2022) 129488. doi:10.1016/j.conbuildmat.2022.129488.
- [5] G.M. Revel, E.M. Rodriguez Sierra, C. Partsch, M.-P. Arnaud-Guiraudet, T. Biel, M. Boutouil, G. Gluth, A. Javadin, H. Madsen, T. Mueller, A. Paraboschi, I. Rafois, P. R  ther, N. Saeidi, N. Stefan, A. Zarli, D. Zangani, White Paper on Sustainable Material-based Solutions For Energy Efficient Buildings, 2023.
- [6] H. Dehghanpour, K. Yilmaz, M. Ipek, Evaluation of recycled nano carbon black and waste erosion wires in electrically conductive concretes, *Constr. Build. Mater.* 221 (2019) 109–121. doi:10.1016/j.conbuildmat.2019.06.025.
- [7] G. Faneca, I. Segura, J.M. Torrents, A. Aguado, Development of conductive cementitious materials using recycled carbon fibres, *Cem. Concr. Compos.* 92 (2018) 135–144.

- doi:10.1016/j.cemconcomp.2018.06.009.
- [8] I. Rhee, J.S. Lee, Y.A. Kim, J.H. Kim, J.H. Kim, Electrically conductive cement mortar: Incorporating rice husk-derived high-surface-area graphene, *Constr. Build. Mater.* 125 (2016) 632–642. doi:10.1016/j.conbuildmat.2016.08.089.
- [9] A. Mobili, G. Cosoli, N. Giuliotti, P. Chiariotti, T. Bellezze, G. Pandarese, G.M. Revel, F. Tittarelli, Biochar and recycled carbon fibres as additions for low-resistive cement-based composites exposed to accelerated degradation, *Constr. Build. Mater.* 376 (2023) 131051. doi:10.1016/j.conbuildmat.2023.131051.
- [10] Y.J. Zhang, P.Y. He, Y.X. Zhang, H. Chen, A novel electroconductive graphene/fly ash-based geopolymer composite and its photocatalytic performance, *Chem. Eng. J.* 334 (2018) 2459–2466. doi:10.1016/j.cej.2017.11.171.
- [11] A. D’Alessandro, D. Coffetti, E. Crotti, L. Coppola, A. Meoni, F. Ubertini, Self-Sensing Properties of Green Alkali-Activated Binders with Carbon-Based Nano-inclusions, *Sustainability*. 12 (2020) 9916. doi:10.3390/su12239916.
- [12] A. Mobili, C. Giosuè, M. Bitetti, F. Tittarelli, Cement mortars and geopolymers with the same strength class, *Proc. Inst. Civ. Eng. Constr. Mater.* 169 (2015) 3–12. doi:10.1680/coma.14.00063.
- [13] F. Wenner, A method for measuring Earth resistivity, *J. Washingt. Acad. Sci.* 5 (1915) 561–563. doi:10.6028/bulletin.282.
- [14] C.G. Berrocal, K. Hornbostel, M.R. Geiker, I. Löfgren, K. Lundgren, D.G. Bekas, Electrical resistivity measurements in steel fibre reinforced cementitious materials, *Cem. Concr. Compos.* 89 (2018) 216–229. doi:10.1016/j.cemconcomp.2018.03.015.
- [15] X. Li, X. Ma, S. Zhang, E. Zheng, Mechanical Properties and Microstructure of Class C Fly Ash-Based Geopolymer Paste and Mortar, *Materials (Basel)*. 6 (2013) 1485–1495. doi:10.3390/ma6041485.
- [16] S. Gupta, H.W. Kua, C.Y. Low, Use of biochar as carbon sequestering additive in cement mortar, *Cem. Concr. Compos.* 87 (2018) 110–129. doi:10.1016/j.cemconcomp.2017.12.009.
- [17] S.G. Prolongo, R. Moriche, A. Jiménez-Suárez, M. Sánchez, A. Ureña, Advantages and disadvantages of the addition of graphene nanoplatelets to epoxy resins, *Eur. Polym. J.* 61 (2014) 206–214. doi:10.1016/j.eurpolymj.2014.09.022.
- [18] P. Rovnaník, I. Kusák, P. Bayer, P. Schmid, L. Fiala, Comparison of electrical and self-sensing properties of Portland cement and alkali-activated slag mortars, *Cem. Concr. Res.* 118 (2019) 84–91. doi:10.1016/j.cemconres.2019.02.009.
- [19] T.S. Qureshi, D.K. Panesar, Nano reinforced cement paste composite with functionalized graphene and pristine graphene nanoplatelets, *Compos. Part B.* 197 (2020) 108063. doi:10.1016/j.compositesb.2020.108063.

# **Corrosion and self-healing in reinforced concrete (RC) structures**



# Experimental study for the development of constitutive laws of corroded steel rebars

Manuel Bartoli, Paolo Isabella

*University of Rome Tor Vergata, Department of Civil Engineering and Computer Science Engineering  
Via del Politecnico 1, Rome (00133), Italy*

## Abstract

The deterioration of reinforced concrete structures due to natural corrosion significantly reduces their strength, safety, and service life. Accurate assessment of this degradation is essential for analytical or numerical modelling. Corrosion influences the mechanical behaviour of steel rebars by decreasing their strength and deformation capacity and altering the rebar-concrete interaction. This study presents experimental results on artificially corroded steel rebars, focusing on the effects of corrosion on mechanical properties such as nominal yielding, ultimate strength, and ultimate strain. Particular attention is given to the corrosion morphology, whether distributed or localised (pitting). The results show that a simple measurement of mass loss is not sufficient to fully characterize the mechanical behaviour of corroded elements. Even small mass loss can lead to significant strength and deformation reductions if there is significant cross-section area loss due to pitting. This study also includes a literature review to provide a database aimed at developing degradation laws that take into account both mechanical and morphological characteristics.

## 1 INTRODUCTION

Evaluation the structural integrity of reinforced concrete structures beyond their original design life presents a contemporary challenge. One of the main cause of deterioration in such structures is the corrosion of reinforcing steel bars, which induce a significant risk of structural failure. Corrosion occurs through two main mechanisms: carbonation, involving the diffusion of carbon dioxide (CO<sub>2</sub>) in the presence of oxygen, and chloride attack in presence of water. Accurate assessment of degradation phenomena is essential for analytical or numerical modeling. Numerous studies have investigated how corrosion affects the mechanical behavior of reinforcing steel. Research has focused on bars extracted from existing structures [1], as well as on corrosion phenomena replicated in laboratory settings using various artificial methods such as electrolytic corrosion [2], acid bath [3], and salt spray fog [4]. Corrosion alters the tensile properties of steel bars by reducing their cross-sectional area and thus the capacity of the element. The morphology of corrosion can lead to two types of cross-sectional reduction in bars: uniform distribution along the bar or localized in different spots [5]. The localised effects can significantly reduce load capacity even with low mass loss values. Studying the degradation in mechanical properties such as yielding strength, ultimate strength, and ultimate strain in relation to mass loss through equations that link these reductions can be complex and may not lead to a specific formulation for each parameter This paper presents the results of experimental work on artificially corroded specimens. The experimental data on mechanical parameters are collected into a database along with available from existing literature.

## 2 MATERIAL AND EXPERIMENTAL CAMPAIGN

The experimental campaign in this research project investigated the corrosion process of rebars with nominal diameters of 10, 14, and 16 mm. Three types of samples were used: 3 corroded bare bars (Fig. 1a), 33 single bars embedded in concrete elements (Fig. 1b, 1c), and 5 uncorroded bars as reference samples.



Fig.1 Specimens: a) bare bar, b) prismatic element, c) tie beam element.

The specimens were immersed in a saline solution (3% NaCl) and subjected to accelerated electrolytic corrosion. The current direction was set so that the corroded bar acted as the anode (positive pole) and an uncorroded bare bar of the same diameter acted as the cathode (negative pole), as shown in Figure 2a and with the result of the corrosion process is shown in Figure 2b. The process was set up with different current density, from 200 to 800  $\mu\text{A}/\text{cm}^2$ , to achieve varying values of mass loss, from 5% to 25%.

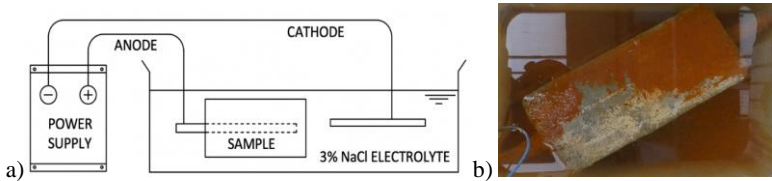


Fig. 2 a) scheme artificial corrosion process, b) artificial corrosion result.

Corrosion duration time was determined according to modified Faraday's law (Eq. 1):

$$time [sec] = \alpha \cdot \frac{M_{loss} \cdot n_{specimen} \cdot C_{Faraday}}{I_{corr} \cdot M_{specimen}} \quad (1)$$

where  $M_{loss}$  is the theoretical mass loss after the corrosion process,  $n_{specimen}$  is the steel valence, equal to 2,  $C_{Faraday}$  is the Faraday constant, equal to 96485 g/mol,  $M_{specimen}$  is the molar mass of the steel reinforcement,  $I_{corr}$  is the values of current intensity express in Ampere and  $\alpha$  is a constant accounting for the possibility that the corrosive process does not start immediately (equal to 1 for bare bars, greater than 1 for embedded specimens).

After the corrosion process, the bars were extracted (Fig. 3a), cleaned according to [6] (Fig. 3b) and weighed. The mass loss was determined from the weight of the uncorroded bar ( $m_0$ ) and the corroded bar ( $m_c$ ) according to the following formula:

$$M_{loss} [\%] = \frac{m_0 - m_c}{m_0} \cdot 100 \quad (2)$$

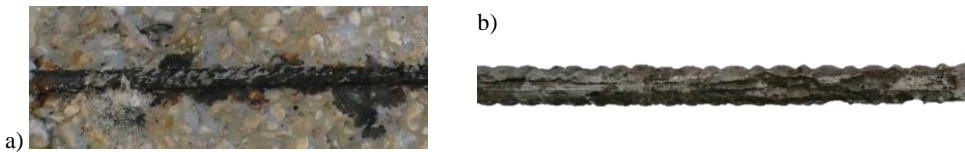


Fig.3 a) corroded bar embedded in concrete, b) cleaned corroded bar.

To investigate the effects of corrosion on reinforced steel bars, various reinforced concrete elements and bare bars were prepared and artificially corroded. The corroded bars were then subjected to monotonic tensile tests to determine their mechanical properties, including yielding strength, ultimate strength, and ultimate strain. The results were compared with results from uncorroded bars. The data collected was combined with data from other experimental studies available in the literature, creating a large database to analyse how the corrosion process alters the morphology of the bars and its effect on their mechanical behaviour.

All bars, both corroded and uncorroded, were subjected to monotonic tensile tests up to failure using a tensile testing machine with a maximum load of 600 kN. Each bar was equipped with a Penny&Giles model SLS130 displacement transducer to measure axial deformation. Tests were performed at a displacement rate speed of 20 mm/min.

### 3 RESULTS

Forty-one tensile tests were carried out: 5 uncorroded bars and 36 corroded bars, the results in terms of stress-strain are shown in Figure 4a.

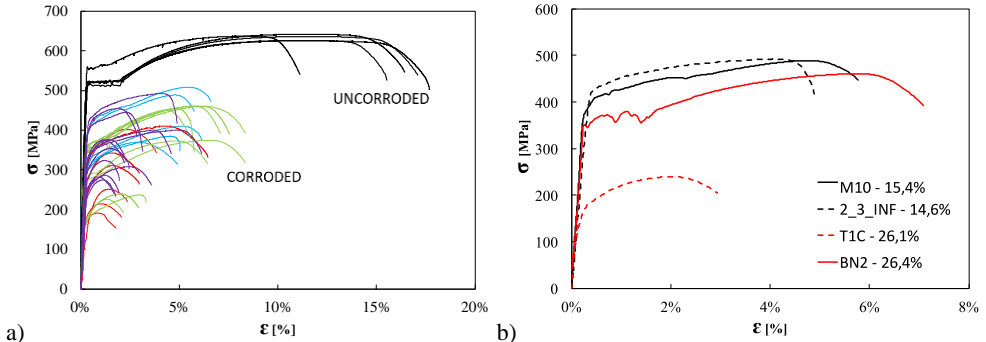


Fig.4 a) stress-strain curves, b) comparison of corroded curves.

In Table 1 results are collected concerning yielding and ultimate strength, denoted as  $\sigma_{y,corr}$ , and  $\sigma_{u,corr}$ , respectively. Stress values were calculated for each corroded bar based on the nominal diameter. Experimental results indicate that yielding point, ultimate strength, and ductility decrease due to corrosion for all diameters. For the corroded tests, an apparent Young's Modulus ( $E_c$ ) was obtained, corresponding to the initial elastic-linear portion of the stress-strain curves. This value appear lower than the Young's Modulus for steel of 210 GPa. This reduction does not indicate a real loss of stiffness but is a consequence of calculating stress as a function of the nominal section instead of the actual corroded section (Fig. 5a). A detailed explanation of the methodology used to determine the mechanical parameters is provided in Figure 5b. For both corroded and uncorroded curves, the values of ultimate strength ( $\sigma_{u,corr}$ ) and ultimate strain ( $\epsilon_{u,corr}$ ) correspond to the points of maximum stress value.

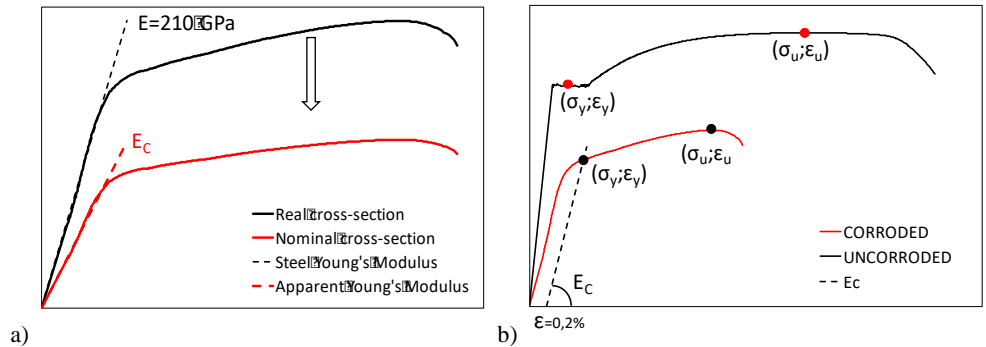


Fig.5 a) Real curve and reduction effect for nominal cross-section b) yielding and ultimate evaluating point.

The yielding stress ( $\sigma_{y,corr}$ ) and yielding strain ( $\epsilon_{y,corr}$ ) are determined by assuming a residual strain in the unloading path of 0.2%. For the yielding point of uncorroded curves, the translation procedure was performed using  $E=210$  GPa, while for corroded curves, the apparent value of  $E_c$  was used. The experimental results obtained are presented in the following Table 1.



Table 1 Results for corroded and uncorroded bars.

ID	$\emptyset_{nom}$	Gauge	$J_{corr}$	Sample	$M_{loss}$	$\sigma_{u,corr}$	$\sigma_{y,corr}$	$\epsilon_{u,corr}$	$\epsilon_{y,corr}$
[-]	[mm]	[mm]	[ $\mu A/cm^2$ ]	[-]	[%]	[MPa]	[MPa]	[%]	[%]
C-UC	16	200	-	-	0	626.2	579.6	11.25	0.25
C0	16	200	800	Embedded	24.2	410.9	326.9	4.26	0.42
C1	16	200	500	Embedded	18.4	310.9	243.9	1.60	0.37
C2	16	200	250	Embedded	28.7	251.1	218.1	1.38	0.69
C3	16	200	250	Embedded	18.4	191.1	164.4	0.83	0.27
C4	16	200	500	Embedded	26.3	214.4	181.4	1.01	0.31
C5	16	200	250	Embedded	17.8	402.4	319.0	2.29	0.42
C6	16	200	500	Embedded	18.2	343.2	281.3	1.53	0.41
M13-UC	16	200	-	-	0	626.2	521.2	10.68	0.25
M7	16	250	300	Embedded	21.4	410.1	323.9	5.07	0.46
M8	16	200	800	Embedded	13.8	508.8	438.9	5.43	1.07
M9	16	200	800	Embedded	25.2	369.7	306.5	2.85	0.40
M10	16	250	150	Embedded	15.5	489.1	406.9	4.71	0.45
M11	16	260	150	Embedded	28.9	385.2	301.6	4.53	0.39
T-UC	14	200	-	-	0	636.4	513.4	11.07	0.24
T1A	14	200	-	-	0	642.1	518.2	10.93	0.25
TEC	14	250	500	Embedded	35.3	226.0	175.5	1.31	0.36
T1B	14	260	150	Embedded	13.1	455.4	362.4	4.80	0.38
T1C	14	280	150	Embedded	26.1	239.5	186.8	1.97	0.42
T1D	14	270	150	Embedded	15.5	459.7	349.9	6.00	0.40
T2A	14	310	250	Embedded	40.2	237.0	174.4	2.96	0.30
T3A	14	200	500	Embedded	17.8	373.3	288.8	4.71	0.44
T3B	14	200	500	Embedded	22.5	374.5	277.5	6.33	0.46
BN1	14	264	500	Bare	23.3	450.6	345.6	4.26	0.40
BN2	14	295	150	Bare	26.4	460.9	361.0	5.63	0.45
BN3	14	250	250	Bare	24.3	461.4	344.5	6.03	0.40
UC_SUP	10	202	-	-	0	637.0	554.8	7.69	0.26
1_1_INF	10	200	600	Embedded	21.4	353.6	306.0	1.40	0.43
1_1_SUP	10	200	600	Embedded	17.8	445.6	406.5	2.32	0.48
1_3_INF	10	200	600	Embedded	24.0	329.8	306.3	1.04	0.47
1_3_SUP	10	200	600	Embedded	23.1	400.2	343.1	4.74	0.48
1_4_INF	10	200	600	Embedded	32.5	308.1	262.3	2.52	0.52
1_4_SUP	10	200	600	Embedded	29.5	286.1	262.8	1.19	0.52
2_1_INF	10	200	600	Embedded	23.6	274.9	247.5	1.06	0.48
2_2_SUP	10	200	600	Embedded	17.6	375.1	340.5	1.10	0.45
2_3_INF	10	200	600	Embedded	14.6	492.7	433.0	4.01	0.56
2_3_SUP	10	200	600	Embedded	22.5	400.2	346.3	3.61	0.58
2_4_INF	10	200	600	Embedded	24.1	323.4	287.0	1.13	0.44
3_1_SUP	10	200	600	Embedded	21.7	376.9	335.1	1.34	0.47
3_2_INF	10	200	600	Embedded	16.6	455.4	418.6	1.83	0.52
3_3_INF	10	200	600	Embedded	28.7	282.5	259.6	0.81	0.41

Referring to Table 1 and Figure 4b, two different curves with similar mass loss values, M10-15.5% and 2\_3\_INF-14.6%, show comparable mechanical behaviours in terms of strength and deformation. However, comparing other curves with similar mass loss values, BN2-26.4% and T1C-26.1%, shows a significant reduction in strength and deformation, with yield and ultimate strength decreasing by approximately 48% and ultimate strain by about 65%. During artificial corrosion, bare bars typically exhibit a uniform corrosion profile, whereas embedded elements experience a more complex process. The

variation in mechanical behaviour is attributed to the different corrosion phenomena experienced by the bars. The corrosion process in steel bars shows two different degradation morphologies: uniform (Fig. 6a) and localised also called pitting (Fig. 6b).



Fig.6 Corrosion morphology: a) uniform “BN2”, b) localised “C3”.

Concrete plays a crucial role in the artificial corrosion process. The void ratio, determined by the water-cement ratio during mix design, increases permeability and facilitates the connection between the anode and cathode via the saline solution in which the specimen is immersed. Larger voids can lead to localized corrosion phenomena, causing concentrated mass loss in specific sections, critical points during tensile testing. Additionally, corrosion products such as rust occupy a greater volume than the original material thus inducing tensile stresses in the concrete, leading to cracking and further corrosion of the bar (Fig. 7).



Fig.7 Crack along the specimen.

#### 4 LITERATURE AND DEGRADATION LAWS

In order to obtain a wide set of results, additional studies were analyzed to examine the impact of corrosion on the mechanical properties of steel rebars. A database of 867 tensile test results was created. This database includes a wide range of mass loss (0–80%), different nominal diameters (9–29 mm), various corrosion methodologies (artificial or natural), different current densities (10–2000  $\mu\text{A}/\text{cm}^2$ ), types of specimens (bare bars, embedded bars, bars extracted from existing structures), and various types of steel. A summary of the details from the articles used is presented in Table 2.

Table 2 Database reference summary.

Reference	$\emptyset_{nom}$	Corrosion Method	$M_{loss}$	Tests
[-]	[mm]	[-]	[%]	[-]
Almusallam (2001)	6-12	2000 $\mu\text{A}/\text{cm}^2$	0.9-80	43
Apostolopoulos et al. (2006)	8	salt spray fog	0.6-31.5	7
Apostolopoulos and Papadopoulos (2007)	10	salt spray fog	1.6-8.5	7
Apostolopoulos et al. (2013)	8	salt spray fog	1.3-53.2	18
Apostolopoulos and Matikis (2016)	10	salt spray fog	0.8-9.2	15
Cobo et al. (2011)	16-20	10 $\mu\text{A}/\text{cm}^2$	4.0-14.6	78
Fernandez et al. (2015)	10-12	–	8.4-21.5	37
Fernandez-et-al (2019)	16	natural	1.3-19.2	61
Hawileh et al. (2011)	10	Acid Bath	9.5-19.6	4
Imperatore et al. (2017)	8-12-16-20	100 $\mu\text{A}/\text{cm}^2$	4.4-53.2	63
Lu et al. (2016)	16	drying-wetting	1.9-5.8	26
Meda et al. (2014)	16	–	11.9-23.4	23
Matthews, B. J. (2023)	25	200-300-1500 $\mu\text{A}/\text{cm}^2$	2.6-24.3	157
Ou et al. (2016)	13-16-19-29	natural-600 $\mu\text{A}/\text{cm}_2$	4.2-50.7	36
Papadopoulos et al. (2007)	12	2000 $\mu\text{A}/\text{cm}^2$	1.4-8.9	11
Tariq and Bhargava (2021)	8-10-12-16-20	–	1.9-44.5	125
Vanama and Ramakrishnan (2020)	12.7-16	natural-4412 $\mu\text{A}/\text{cm}^2$	4.0-79.6	50
Zhang et al. (2012)	6.5-12	natural-100 $\mu\text{A}/\text{cm}^2$	0.05-0.4	65
This Paper	10-14-16	150-250-500-600-800 $\mu\text{A}/\text{cm}^2$	13.1-40.2	41

The mechanical parameters obtained from the corroded curves were normalized to the corresponding values of uncorroded bars. The experimental data and literature together form a data set of parameters grouped to study corrosion degradation through normalized indexes of yield strength  $\sigma_{y,ad}$  (Eq. 3), ultimate strength  $\sigma_{u,ad}$  (Eq. 4), ultimate strain  $\varepsilon_{u,ad}$  (Eq. 5), and apparent Young's Modulus  $E_{c,ad}$  (Eq. 6). The decrease in mechanical parameters with increasing mass loss (Fig. 8) was compared to the degradation law equation proposed by [2], calibrated for a mass loss range up to 40%.

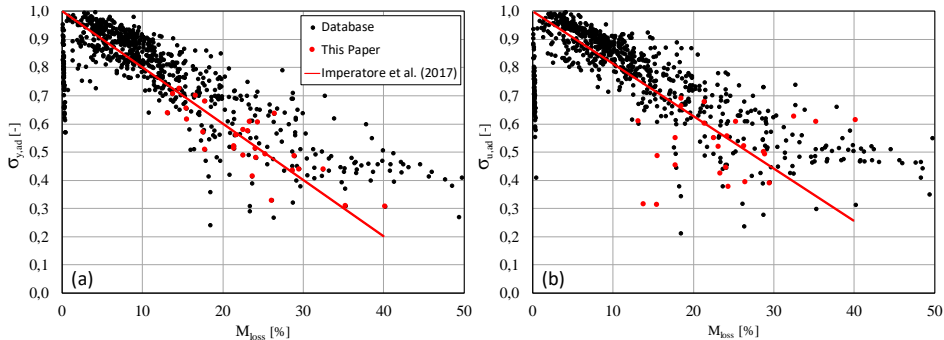
$$\sigma_{y,ad} [-] = \frac{\sigma_{y,corr}}{\sigma_{y,uncorr}} \quad (3)$$

$$\sigma_{u,ad} [-] = \frac{\sigma_{u,corr}}{\sigma_{u,uncorr}} \quad (4)$$

$$\varepsilon_{u,ad} [-] = \frac{\varepsilon_{u,corr}}{\varepsilon_{u,uncorr}} \quad (5)$$

$$E_{c,ad} [-] = \frac{E_c}{E} \quad (6)$$

Higher mass loss values indicate an advanced stage of structural deterioration and significantly impairs the structural rehabilitation in term of load-bearing capacity of the structure. The experimental results from this study, in Figure 8, show a slight deviation from the degradation laws for yielding strength. Also for ultimate strain there is a high degree of scatter with a significantly different trend.



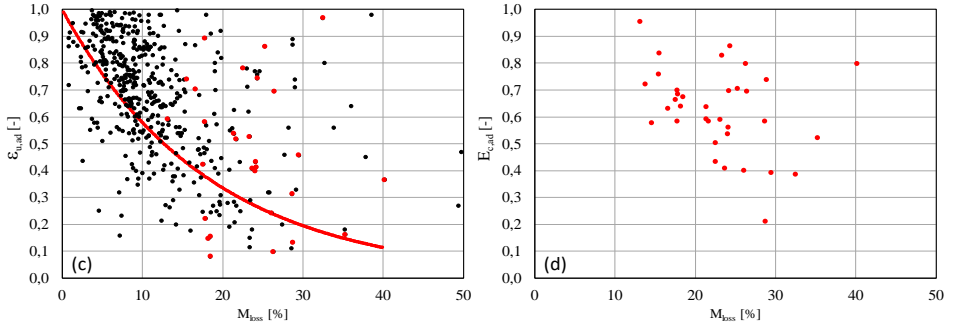


Fig.8 Normalised indexes: a) yield strength, b) ultimate strength, c) ultimate strain, d) apparent Young's Modulus.

These differences highlight the limitations of using mass loss alone as a parameter for decay indices, as it does not account for corrosion profiles resulting from pitting. To better understand the apparent Young's Modulus ( $E_c$ ), more data are needed to refine its characterization. This parameter is crucial in defining a constitutive law, especially in a bilinear model, where using a single yielding strength value could lead to errors in evaluating yielding strain if assumed in relation to a Young's Modulus of 210 GPa. Further insights into pitting phenomena can be gained by introducing a pitting factor  $\alpha_{pit}$ , as defined by [7], where  $\phi_0$  represents the nominal diameter,  $\phi_t$  the equivalent diameter associated with a mass loss value, and  $P_x$  is the maximum pit depth.

$$\alpha_{pit} [-] = \frac{\phi_0 - \phi_t}{P_x} \quad (7)$$

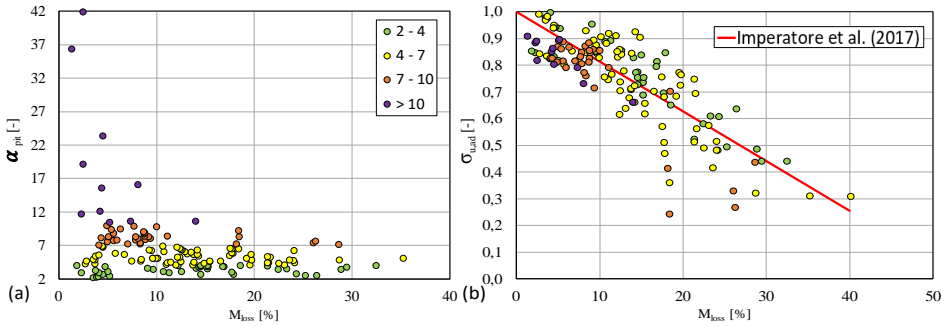


Fig.9 a) pitting factor compared with mass loss, b) detail of tensile tests with a pitting factor value

For  $\alpha_{pit}=2$  no pitting at all occurs. A threshold value for  $\alpha_{pit}$  can distinguish between uniform and pitting corrosion phenomena. The high values over 10 shown in Figure 9a are consistent with the degradation law observed for ultimate strength in Figure 9b, similarly for yielding. However, the data analyzed in this study are not sufficient to propose a definitive assessment. Extensive experimentation is necessary to establish a clear relationship among pitting, mass loss, and mechanical parameters.

## 5 CONCLUSIONS

The issue of steel rebar corrosion is investigated through artificial corrosion tests on various types of specimens, together with tensile tests on both corroded and uncorroded bars. Additionally, relevant literature detailing similar experimental campaigns are analysed. The set of results, in terms of mechanical parameters normalized such as yielding strength, ultimate strength, and ultimate strain, are analyzed to investigate their decrease with increasing mass loss. Further attention is given to the pitting phenomenon to introduce an additional representative index of the mechanical parameter reduction. Based on the results is observed how the corrosion process alters the morphology of the bar, resulting in uniform

or localised corrosion profiles that influence the mechanical response. To qualitatively investigate pitting phenomena and corrosion morphology is essential develop decay laws capable to account both the mass loss and the morphology.

## References

- [1] Fernandez, I., & Berrocal, C. G. 2019. "Mechanical properties of 30 year-old naturally corroded steel reinforcing bars." *International Journal of Concrete Structures and Materials*, 13(1), 9.
- [2] Imperatore, S., Rinaldi, Z., & Drago, C. 2017. "Degradation relationships for the mechanical properties of corroded steel rebars." *Construction and Building Materials*, 148, 219-230.
- [3] Hawileh, R. A., Abdalla, J. A., Al Tamimi, A., Abdelrahman, K., & Oudah, F. 2011. "Behavior of corroded steel reinforcing bars under monotonic and cyclic loadings." *Mechanics of Advanced Materials and Structures*, 18(3), 218-224.
- [4] Apostolopoulos, C. A., Demis, S., & Papadakis, V. G. 2013. "Chloride-induced corrosion of steel reinforcement–Mechanical performance and pit depth analysis." *Construction and Building Materials*, 38, 139-146.
- [5] Lu, C., Yuan, S., Cheng, P., & Liu, R. 2016. "Mechanical properties of corroded steel bars in pre-cracked concrete suffering from chloride attack." *Construction and Building Materials*, 123, 649-660.
- [6] ASTM G1-90. Practise for preparing, cleaning and evaluating corrosion test specimens. ASTM International, West Conshohocken, Pa, 2002.
- [7] Fagerlund, G. (Ed.), & et al. 2001. *CONTECVET: A validated Users Manual for assessing the residual service life of concrete structures*. (Report TVBM (Intern 7000-rapport); Vol. 7161). Division of Building Materials, LTH, Lund University.
- [8] Almusallam, A. A. 2001. "Effect of degree of corrosion on the properties of reinforcing steel bars." *Construction and building materials*, 15(8), 361-368.
- [9] Apostolopoulos, C. A., Papadopoulos, M. P., & Pantelakis, S. G. 2006. "Tensile behavior of corroded reinforcing steel bars BSt 500s." *Construction and building Materials*, 20(9), 782-789.
- [10] Apostolopoulos, A., & Matikas, T. E. 2016. "Corrosion of bare and embedded in concrete steel bar-impact on mechanical behavior." *International Journal of Structural Integrity*, 7(2).
- [11] Apostolopoulos, C. A., & Papadopoulos, M. P. 2007. "Tensile and low cycle fatigue behavior of corroded reinforcing steel bars S400." *Construction and Building Materials*, 21(4), 855-864.
- [12] Cobo Escamilla, A., Moreno Fernandez, M. E., & Canovas, F. M. 2011. "Variación de las características mecánicas de armaduras de alta ductilidad B500SD en función de su grado de corrosión/Mechanical properties variation of B500SD high ductility reinforcement regarding its corrosion degree." *Materiales de construcción*, 61(304), 517-532.
- [13] Fernandez, I., Bairán, J. M., & Marí, A. R. 2015. "Corrosion effects on the mechanical properties of reinforcing steel bars. Fatigue and  $\sigma$ - $\epsilon$  behavior." *Construction and Building Materials*, 101, 772-783.
- [14] Meda, A., Mostosi, S., Rinaldi, Z., & Riva, P. 2014. "Experimental evaluation of the corrosion influence on the cyclic behaviour of RC columns." *Engineering Structures*, 76, 112-123.
- [15] Matthews, B. J. 2023. "Deteriorated capacity assessment of aging bridge structures in seismic areas complimented by artificial intelligence modeling". *PhD thesis, University of Canterbury*.
- [16] Ou, Y. C., Susanto, Y. T. T., & Roh, H. 2016. "Tensile behavior of naturally and artificially corroded steel bars." *Construction and Building Materials*, 103, 93-104.
- [17] Papadopoulos, M. P., Apostolopoulos, C. A., Alexopoulos, N. D., & Pantelakis, S. G. 2007. "Effect of salt spray corrosion exposure on the mechanical performance of different technical class reinforcing steel bars." *Materials & design*, 28(8), 2318-2328.
- [18] Tariq, F., & Bhargava, P. 2021. "Stress–strain curves and mechanical properties of corrosion damaged super ductile reinforcing steel." *In Structures* (Vol. 33, pp. 1532-1543). Elsevier.
- [19] Vanama, R. K., & Ramakrishnan, B. 2020. "Improved degradation relations for the tensile properties of naturally and artificially corroded steel rebars." *Construction and Building Materials*, 249, 118706.
- [20] Zhang, W., Song, X., Gu, X., & Li, S. 2012. "Tensile and fatigue behavior of corroded rebars." *Construction and Building Materials*, 34, 409-417.

**Concrete and reinforced-concrete under  
extreme environmental conditions  
(earthquake, wind, temperature)**



# Distributed plasticity models for the seismic response of reinforced concrete shear walls

Chiara Di Salvatore<sup>1</sup>, Gennaro Magliulo<sup>1,2</sup>, Danilo D'Angela<sup>1</sup>, Claudio Corbo<sup>1</sup>

<sup>1</sup>*Dept of Structures for Engineering and Architecture,  
University of Naples Federico II,  
via Claudio, 21, Naples (80125), Italy*

<sup>2</sup>*Construction Technology Institute URT Naples,  
National Research Council of Italy,  
via Claudio, 21, Naples (80125), Italy*

## Abstract

The paper tackles the nonlinear modeling of seismic resistant reinforced-concrete walls. Two different models are built in OpenSees, both taking into account the mechanical nonlinearity distributed along the wall element. The former, referred to as MVLEM (Multiple Vertical Line Element Model), is a two-dimensional model able to reproduce both the flexural and the shear behavior of the wall, although assumed as uncoupled. The wall is simulated by means of two horizontal rigid beams, connected by several vertical uniaxial springs with proper stiffness, absorbing the bending moment of the wall. Moreover, a uniaxial horizontal spring is located along the height of the element in order to provide the shear deformability. The latter model is a fiber model, with a force-based formulation. The element is discretized in several control cross sections, each of which is further divided in fibers, according to the structural materials and accounting for their nonlinearity. This approach is not able to reproduce the shear deformability of the wall. The effectiveness of the investigated modeling approaches is assessed by means of an application to a case-study structure, consisting in a five story RC frame. Nonlinear time histories analyses, considering properly scaled real floor motions, are performed on both the models. The structural response of both the models is assessed and compared; advantages and shortcomings deriving by the use of each implemented models are reported and commented, providing useful insights for the modeling of RC walls.

## 1 Introduction

Reinforced concrete walls represent an efficient solution in seismic zones, especially for tall buildings. A reliable numerical model is necessary to catch the actual hysteretic and nonlinear behavior of such elements under horizontal forces. Two different approaches are possible: micro-modeling and macro-modeling. The former is surely the most effective in reproducing the nonlinear local behavior of the wall, but the complexity in the modelling implementation and output data interpretation, together with the excessive time required by the analyses, make this approach very difficult to apply. On the other hand, macro-models are quite spread nowadays. Several research studies have been focused on the development, calibration and validation of new and ever more sophisticated macro-models, capable to reproduce the axial and bending response and/or the shear response, assumed coupled or uncoupled (e.g., [1-8]).

The aim of this preliminary work is the comparison of two nonlinear models for RC walls, available in literature and already implemented in the OpenSees software [9]: the Multiple Vertical Line Element Model (MVLEM) and the Force-Based fiber Element Model (FBEM), both considering a distributed plasticity along the wall. A five-story RC frame is considered as case study and nonlinear dynamic time-history analyses are performed on both the developed nonlinear models. The comparison shows the effectiveness of both the models in reproducing the proper behavior of the structure, providing very similar results in terms of wall base shear, top displacement and floor accelerations. A slight difference is detected, probably due to the different implementation of the concrete material nonlinear behavior,



leading to a little higher dissipation of seismic energy, i.e., a more damped response, in the case of the MVLEM.

## 2 Nonlinear modelling

The case-study structure consists in a 5-story bi-dimensional RC frame (Figure 1), designed according to the current European seismic codes [10] so as to satisfy the requirements of medium ductility class and design capacity, for the Italian site Castelnuovo di Conza ( $a_{g,475y} = 0.26 g$ ). C28/35 concrete and B450C reinforcing steel are used as construction materials. Shear wall cross sections in both critical (0-3.4 m) and non-critical (3.4-15.6 m) zone are illustrated in Figure 2.

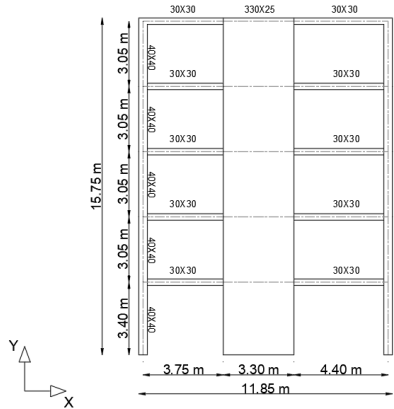


Fig. 1 Case-study structure layout.

Nonlinear models are developed in OpenSees [9], using a mixed approach for plasticity: monodimensional structural members (i.e., beams and columns) follow a lumped plasticity model, with nonlinear rotational springs at both the ends of the elastic elements, whilst the bidimensional element, that is the shear wall, is characterized by a distributed plasticity. Plastic hinges in beams and columns are defined by a moment-chord rotation backbone, according to the Haselton et al. [11] model. Hysteretic behavior is assigned following the Ibarra et al. [12] formulations. Concerning the shear wall, two different models are implemented and compared: Multiple Vertical Line Element Model (MVLEM) and Force-Based fiber Element Model (FBEM). In the following, both the models are illustrated in detail providing the parameters needed for their implementation.

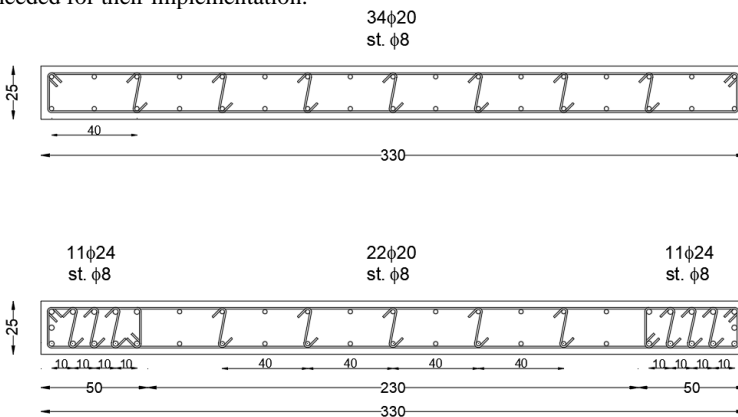


Fig. 2 Cross-section of the RC wall in non-critical zone (up) and critical zone (down) [measures in cm].

## 2.1 Multiple Vertical Line Element

The Multiple Vertical Line Element [1-4], for the sake of brevity MVLEM hereinafter, is a bidimensional model for shear resistant walls, characterized by six degrees of freedom. It is constituted by several vertical springs, simulating the axial-flexural behavior of the wall. Such springs are connected by two infinitely rigid beams, at the top and the bottom of the element. In the mid-span of these beams, the degrees of freedom are lumped, three for each beam (i.e., translations along the horizontal and the vertical axis plus a rotation in the plane of the element). The model also accounts for the shear response of the wall through a horizontal spring located in the central line of the MVLEM at a distance of  $ch$  from the bottom, where  $h$  is the height of the element and  $c$  is a constant set equal to 0.4, as suggested by Vulcano et al. [1] based on the experimental validation of the model. However, since the shear behavior is uncoupled from the axial-flexural response, the MVLEM is actually suited for RC walls with a predominantly flexural behavior.

OpenSees [9] allows the implementation of a Multiple Vertical Line Element Model through a specifically included element command “element MVLEM”. The wall horizontal cross-section is discretized in several macro-fibers, each of which characterized by a thickness, a width, a reinforcement ratio and a proper nonlinear behavior for concrete and steel materials. Moreover, it is recommended to divide the whole vertical element in several shorter MVLEM elements, stacked one on the top of the other, in order to ease convergence.

In the considered case-study, twentyeight MVLEM elements are defined in series along the height of the wall; in order to accurately capture the nonlinear behavior of the wall, their distribution is not uniform along the height, but a higher number of elements is provided where the plastic hinge is expected to form, that is at the base of the element. The cross section of each element is divided in twentythree macro-fibers, 0.25 m thick with variable width; in particular, in the outer regions, that is the confined zones, the width is set equal to 0.1 m, whilst in the internal region, that is the unconfined region, the width doubles (0.2 m). Concrete CM and Steel MPF are the suggested uniaxial materials capable to properly describe the inelastic response of the shear wall; however, it is demonstrated that a negligible differences in the response can be obtained if Steel O2 uniaxial material is implemented in the place of the Steel MPF [16]. In the present case-study, Steel O2 is used in order to allow a better comparability with the Force-Based Element Model. The confinement effect for concrete is taken into account defining two different Concrete CM uniaxial materials: the former for the central zone considered not confined and the latter for the boundary regions, considered confined. Mean values of the mechanical characteristics are used for all the materials, evaluated according to the Italian and the European codes [13,14,15]. The shear response of the wall, that is the uniaxial material defining the behavior of the horizontal spring at a distance  $ch$  from the base, is assumed as indefinitely elastic, since it is expected that brittle shear failure is prevented, due to the design compliant to ductility and capacity design requirements. The elastic stiffness assigned to the horizontal spring is equal to the elastic shear stiffness of the wall.

## 2.2 Force-Based fiber Element

FBEM belongs to the distributed plasticity models framework, allowing the spread of plasticity along the whole element [17-19]. The nonlinear flexural behavior of the element is obtained integrating the nonlinear fiber-discretized cross-sections response, defined for specific control points, along the whole element. The FBEM formulation takes advantage by load shape functions for axial load and bending moment, ensuring the equilibrium satisfaction at each integration step.

Such elements can be reproduced in the software OpenSees through a specific command “element forceBeamColumn”. The required parameters are the number of integration points (control points), the identification tag of the previously defined fiber-discretized cross section, and the integration type. Indeed, users can define the number of control points, but their location is not known; integration algorithms help to define the position of some of the integration points, enabling a better control on the results (e.g., Gauss-Lobatto algorithm defines two integration points at the ends of the element). Accuracy of the results varies depending on the number of control points and the number of sub-elements in which the whole member is divided.

In the case-study structure, one FBE per floor is implemented, for a total of five FBEs working in series. Gauss-Labatto integration algorithm is chosen with three control points for each element. The number of control sections is defined after a sensitivity analysis, verifying that an increase in this number does not produce a significant difference in the outcomes. Wall cross section is discretized in fibers

considering the unconfined concrete for the web zone and the boundary zones' cover, the confined concrete for the boundary zones' core and the steel. As in [8], Concrete 04 and Steel 02 uniaxial materials are implemented, using the same mean properties of the MVLEM case.

### 3 Seismic inputs

Nonlinear dynamic analyses are performed considering both the implemented models and outcomes are compared. Three monodirectional seismic inputs are applied at the bases of the models, referred to as rec1, rec2 and rec3. They are derived from Center for Engineering Strong Motion Data (CESMD) [18], taking into account real ground motions recorded at the foundations of 5-story RC buildings in the USA. In order to ensure the analysis inputs compatibility with a reference level of seismic intensity, the corresponding spectra in terms of pseudo-accelerations are scaled so as to have the pseudo-acceleration corresponding to the fundamental period of the models  $S_a(T_1)$  equal to the one given by the Italian code seismic spectrum corresponding to a return period,  $T_R$ , equal to 50 years for the same fundamental structural period. The choice of a low seismic intensity, corresponding to a damage limit state for the Italian code [13], is due to the nature of this work, which is a pilot study, with the main aim of checking the feasibility and the effectiveness of the modeling approaches, together with the reliability of the provided results and eventual numerical convergence issues in the elastic field. Fundamental periods  $T_1$  are quite similar, confirming the accuracy of the nonlinear modeling, being equal to 0.64 s and 0.61 s for the MVLEM and FBE case, respectively. The slightly higher period recorded for the MVLEM case is attributable to the shear deformability, which is not reproduced in the FBEM. The obtained scale factors are 0.67/0.66 for rec1, 1.38/1.34 for rec2, and 0.90/0.84 for rec3, for MVLEM/FBE model. Fig. 3 shows the scaled time history for the three ground motion considered.

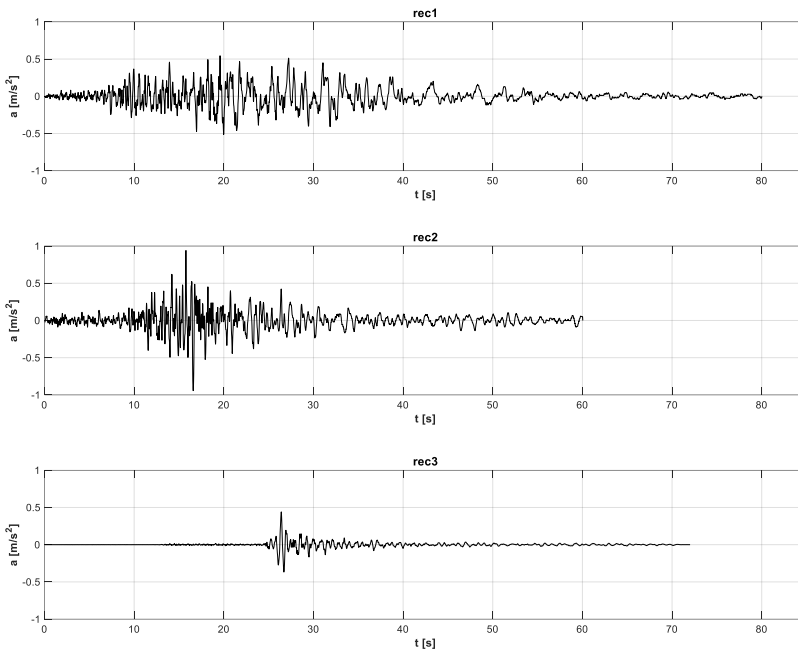


Fig. 3 Ground acceleration time history for rec1 (up), rec2 (middle) and rec3 (down).

### 4 Outcomes

Nonlinear dynamic analyses are performed through OpenSees [9] applying to both the models the selected and scaled accelerograms. A 5% Rayleigh damping is set, proportional to both mass and initial stiffness matrix. Fig. 4 and Fig. 5 present the comparison between the MVLEM and the FBEM, for the three seismic inputs, in terms of base reaction and top displacement of the wall, respectively. A good accordance between the two models is detected, confirming the effectiveness and the validity of both

the implemented models. Going into detail, it can be noted that up to the first significant peak the response in term of both forces and displacements is practically coincident; after the peak, the MVLEM shows lower base reaction and lower top displacement, even if the difference is very low. This could be ascribable to the different uniaxial material implemented for the concrete. Indeed, Concrete CM material (used for the MVLEM) experiences more and wider hysteretic cycles with respect to Concrete 04 material (used for FBE), due to the inherent dissipation properties. This allows the MVLEM to dispel more input energy coming from the ground motions, mitigating the effect of the earthquake. However, it has to be noted that, given the low seismic intensity applied ( $T_R=50$  years), the amount of dissipated energy is very small. Also, steel material always shows a linear elastic response in both the modelling approaches.

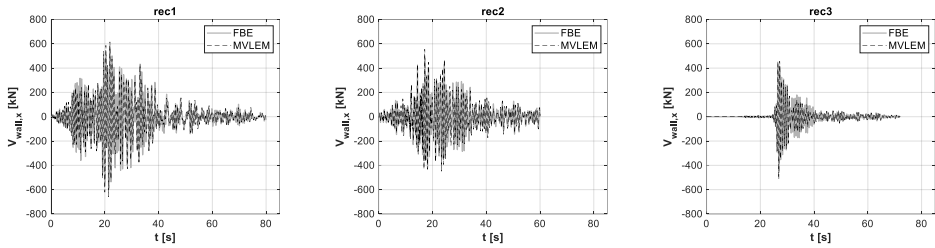


Fig. 4 Wall base reaction for rec1 (left), rec2 (middle) and rec3 (right).

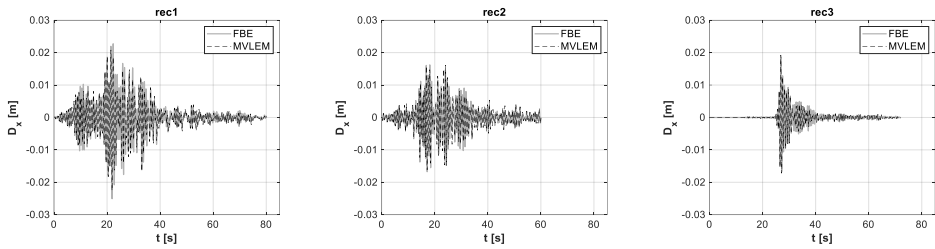


Fig. 5 Wall top displacement for rec1 (left), rec2 (middle) and rec3 (right).

Floor accelerations are recorded for each floor and both the models (Fig. 6). As expected, an increase in the acceleration amplitude from the first floor up to the fifth floor can be detected. Once again, the MVLEM and FBEM provide very similar results; in general, with MVLEM model, lower accelerations are recorded, especially at the higher floors, due to the fact that the concrete material to a higher plastic excursion.

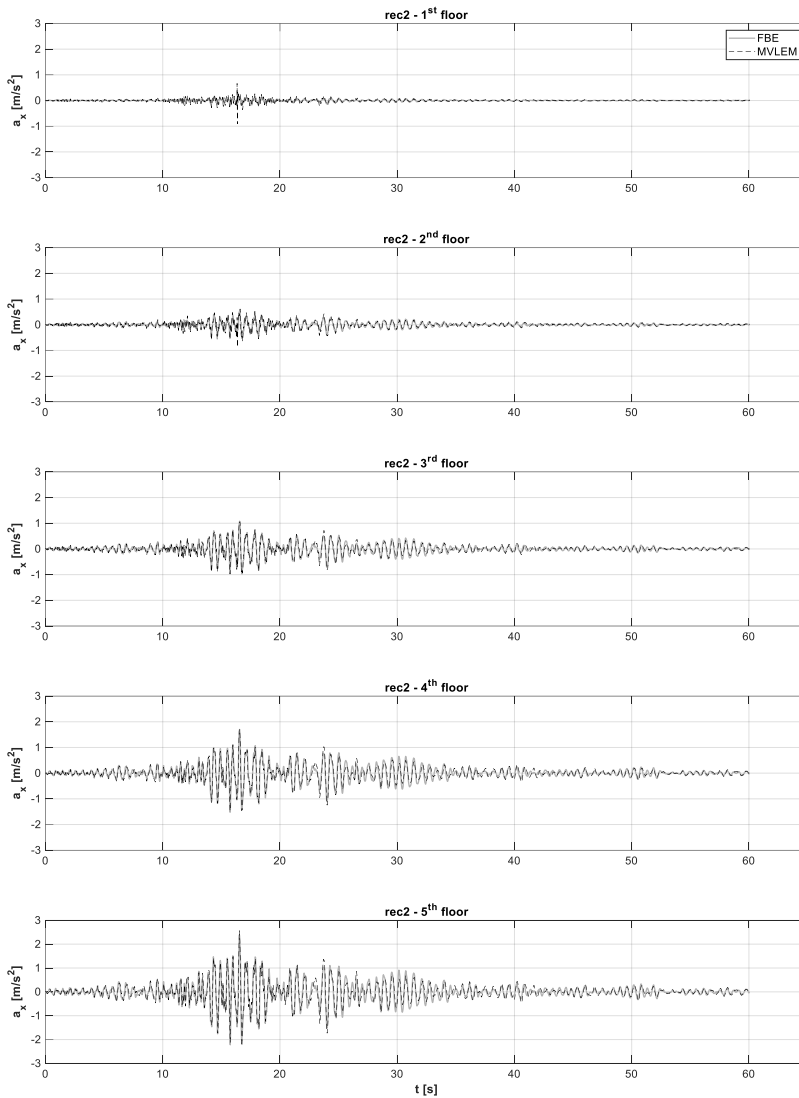


Fig. 6 Floor accelerations for rec2 : comparison between MVLEM and FBEM.

## 5 Conclusions

In the present work, the effectiveness of different nonlinear modelling approaches for reinforced concrete (RC) shear walls is investigated. In particular, two distributed plasticity models are considered: the Multiple Vertical Line Element Model (MVLEM) and the Force-Based Element Model (FBEM). A five-story RC planar frame is considered as case-study structure, provided with a RC wall in the middle span; it is designed according to the modern European seismic codes, and modelled through the OpenSees software. Dynamic analyses are performed applying to both the models three real ground motions, scaled so as to match the pseudo-acceleration corresponding to the fundamental period of the structure according to the Italian code for  $T_R = 50$  years. Outcomes show that:

- the MVLEM is able to reproduce the flexural response of the wall together with its shear behavior, although uncoupled. FBEM is able to only reproduce the flexural response of the wall. For this reason, MVLEM provides a slightly higher period of vibration, for the same structure. However, the shear deformability seems not to affect the results of dynamic analyses;

- outcomes from MVLEM and FBEM in terms of wall base shear, top displacement and floor accelerations are in good agreement. This proves the effectiveness and the reliability of both the implemented modelling approaches;
- the use of different materials for concrete leads to a slightly different cyclic response of the wall in the implemented models. Indeed, Concrete CM used for the MVLEM shows a little higher dissipation of energy for all the applied ground motions with respect to Concrete 04 used for the FBEM. However, given the low intensity of the applied earthquakes, a comprehensive assessment of the nonlinear behavior provided by the investigated modelling approaches is not possible.

The study is a preliminary evaluation framed in a wider scientific work, which aims at the identification of the best approach for the modeling of RC shear resistant walls. Indeed, further efforts should be done to generalize the results presented in this work considering other case-study structures and higher seismic intensities. Moreover, coupling between the flexural and the shear response of the wall should be implemented.

### Acknowledgements

The study was funded by (1) PRIN PNRR “Rock-Resilience” 2022 Rocking-based strategies for resilience of reinforced concrete structures: conception, structural design, nonstructural components, efficiency and sustainability – scientific coordinator Prof. Gennaro Magliulo and by (2) PRIN 2020 project “ENRICH project: ENhancing the Resilience of Italian healthCare and Hospital facilities” – scientific coordinator Prof. Gennaro Magliulo.

### References

- [1] Vulcano, Alfonso, Vitelmo V. Bertero, and Vincenzo Colotti. 1988. “Analytical modeling of RC structural walls”. Paper presented at the 9th world conference on earthquake engineering, Tokyo, Kyoto, Japan, August 2-9.
- [2] Fischinger, Matej, Tatjana Isakovic and Peter Kante. 2004. “Implementation of a macro model to predict seismic response of RC structural walls”. *Computers and Concrete*, 1.2: 211-226, doi:10.12989/cac.2004.1.2.211.
- [3] Orakcal, Kutay, John W. Wallace, and Joel P. Conte. 2004. “Flexural Modeling of Reinforced Concrete Walls - Model Attributes”. *ACI Structural Journal*, 101(5).
- [4] Orakcal, Kutay, and John W. Wallace. 2006. “Flexural modeling of reinforced concrete walls - experimental verification”. *ACI Materials Journal*, 103(2), 196.
- [5] Pugh Joshua S., Laura N. Lowes, and Dawn E. Lehman. 2015. “Nonlinear line-element modeling of flexural reinforced concrete walls”. *Engineering Structure*, 104, doi:10.1016/j.engstruct.2015.08.037
- [6] Kolozvari, Kristijan, Kutay Orakcal, and John W. Wallace. 2015. “Shear-flexure interaction modeling for reinforced concrete structural walls and columns under reversed cyclic loading”. *PEER Report*, 12. Pacific Earthquake Engineering Research Center, University of California, Berkeley, CA, USA.
- [7] Pozo, Juan D., Matias A. Hube, and Yahya C. Kurama. 2020. “Quantitative assessment of nonlinear macro-models for global behavior and design of planar RC walls. ” *Engineering Structures*, 224, 111190.
- [8] Di Domenico, Mariano, Marco Gaetani D’Aragona, Maria Polese, Gennaro Magliulo, Andrea Prota, Gerardo M. Verderame, and Koichi Kajiwara. 2023. “Nonlinear modeling of the ten-story RC building at E-Defense (2015): assessment with different modeling assumptions”. *Bulletin of Earthquake Engineering*, 21(15), 6585-6622, doi:10.1007/s10518-023-01627-9.
- [9] OpenSees. 2020. Open system for earthquake engineering simulation OpenSees framework. Pacific Earthquake Engineering Research Center, University of California, Berkeley.
- [10] CEN. 2005. Eurocode 8 - Design of structures for earthquake resistance - EN 1998-1: General rules, seismic actions and rules for buildings. Brussels, Belgium.
- [11] Haselton, Curt B., Abbie B. Liel, Sarah Taylor-Lange, and Gregory G. Deierlein (2008) “Beam-column element model calibrated for predicting flexural response leading to global collapse of

- RC frame buildings", *PEER Report*, 2007/03, Pacific Earthquake Engineering Research Center, University of California, Berkeley, CA, USA.
- [12] Ibarra, Luis F., Ricardo A. Medina, and Helmut Krawinkler. 2005. "Hysteretic models that incorporate strength and stiffness deterioration." *Earthquake engineering & structural dynamics* 34.12, 1489-1511. Doi: 10.1002/eqe.495.
- [13] MIT. 2018. Decreto Ministeriale 17/01/2018. Norme tecniche per le costruzioni (in Italian), Gazzetta Ufficiale, 42
- [14] CEN. 2005. Eurocode 8: Design of structures for earthquake resistance - EN 1998-3: Assessment and retrofitting of buildings, Brussels, Belgium.
- [15] CEN. 2005. Eurocode 8: Design of structures for earthquake resistance - EN 1998-2: Bridges, Brussels, Belgium.
- [16] OpenSees Wiki. Available at [https://opensees.berkeley.edu/wiki/index.php/Main\\_Page](https://opensees.berkeley.edu/wiki/index.php/Main_Page).
- [17] Neuenhofer, Ansgar, and Filip C. Filippou. 1988. "Geometrically nonlinear flexibility-based frame finite element." *Journal of Structural Engineering*, 124.6, 704-711. [https://doi.org/10.1061/\(ASCE\)0733-9445\(1998\)124:6\(704\)](https://doi.org/10.1061/(ASCE)0733-9445(1998)124:6(704)).
- [18] Taucer, Fabio, Enrico Spacone, and Filip C. Filippou. 1991. "A fiber beam-column element for seismic response analysis of reinforced concrete structures." Vol. 91. Berkeley, CA, USA: Earthquake Engineering Research Center, College of Engineering, University of California.
- [19] Neuenhofer, Ansgar, and Filip C. Filippou. 1997. "Evaluation of nonlinear frame finite-element models." *Journal of structural Engineering*, 123.7, 958-966. [https://doi.org/10.1061/\(ASCE\)0733-9445\(1997\)123:7\(958\)](https://doi.org/10.1061/(ASCE)0733-9445(1997)123:7(958))
- [20] Center for Engineering Strong Motion Data database. Available at <https://www.strongmotion-center.org/>

# Machine-learning-enhanced variable-angle truss model for shear capacity assessment of reinforced concrete elements

Qingcong Zeng<sup>1</sup>, Dario De Domenico<sup>2</sup>, Giuseppe Quaranta<sup>3</sup> and Giorgio Monti<sup>4</sup>

<sup>1</sup>College of Civil Engineering and Architecture,  
Zhejiang University,  
866 Yuhangtang Road, Hangzhou 310058, China

<sup>2</sup>Department of Engineering,  
University of Messina,  
Contrada Di Dio, 98166 Sant'Agata, Messina, Italy

<sup>3</sup>Department of Structural and Geotechnical Engineering,  
Sapienza University of Rome,  
Via Eudossiana 18, 00184 Rome, Italy

<sup>4</sup>Department of Structural and Geotechnical Engineering,  
Sapienza University of Rome,  
Via Gramsci 53, 00197 Rome, Italy

## Abstract

Shear failure of reinforced concrete (RC) elements are typically more brittle and sudden than flexural failure. Consequently, it is of utmost importance to estimate properly the shear capacity of RC members when assessing and retrofitting existing structures as well as in the design of new constructions under later loads, for instance due to earthquakes. Historically, the development of shear capacity equations for RC beams and columns has originated from the conceptualization of a resisting mechanism. Recently, the use of data-driven approaches based on standard regression techniques has evolved by exploiting machine learning techniques. In contrast, this research advances a hybrid approach to formulate a shear capacity equation for RC beams and columns with rectangular/square cross-sections. This approach enhances a mechanics-based, code-conforming formulation through the integration of a machine-learning-aided approach. Specifically, the Genetic Programming technique is employed to enrich the shear capacity equation based on a variable-angle truss resisting mechanism. This integration results in the formulation of novel expressions for the two key coefficients governing the concrete contribution. The performance of the newly derived equation is assessed for beams and columns with both solid and hollow cross-sections under uniaxial shear. Some future research lines are drawn concerning ongoing experimental and theoretical efforts to extend the proposed model to biaxial shear. Hence, this research establishes a unified shear capacity equation for RC beams and columns. Additionally, it demonstrates the advantages of merging mechanics-based and data-driven methods. This integration proves beneficial in developing capacity equations, as it preserves the physical meaning as well as the general validity of the resisting mechanism while enhancing the accuracy through a machine learning technique.

## 1 Introduction

The accurate estimation of the shear capacity of reinforced concrete (RC) elements is a critical topic that has engaged researchers for the past four decades [1]. Many RC buildings from the 1970s have insufficient transverse reinforcement, often falling below the minimum amounts required by current design codes. As a result, these structures may be susceptible to brittle shear failure. To properly evaluate the vulnerability of the buildings and to optimize retrofitting interventions, it is thus essential to develop reliable, unbiased, and precise numerical models for predicting the actual shear strength of RC elements with stirrups. The development of shear capacity equations for RC beams and columns has



been grounded in the conceptualization of suitable resistance mechanisms. Although several mechanical models have been proposed so far for uniaxial shear loading conditions, they have proven to be overly conservative and exhibit significant variability [2]. As far as biaxial shear is concerned, only a few mechanical models are available while the assumption of an empirical quadratic interaction domain is mostly used within some current codes and guidelines. Since this domain leverages on the prediction of uniaxial shear capacities in the two principal directions, it may lead to significant scattering [3]. Such variability is typically addressed by assuming large numerical values for the safety factors. This, in turn, hinders the optimum design of new buildings and the sustainable retrofitting of existing structures. Furthermore, the inconsistency among existing proposals for shear assessment of RC elements should not be overlooked. In fact, the available proposals often employ incompatible capacity equations for beams and columns, as well as for uniaxial and biaxial shear loading conditions. This inconsistency contrasts with the fact that, if the shear-resisting mechanism is properly identified, it should be universally applicable, given that its variables are redefined for the specific RC member considered.

To enhance the predictive accuracy of shear capacity equations, data-driven approaches based on the machine learning techniques have been explored recently [4][5]. While these models exhibit high accuracy within the specific contexts for which their coefficients are calibrated, they lack interpretability and generalizability to other cases, such as varying loading conditions or different cross-sectional shapes. Therefore, rather than developing new uniaxial or biaxial shear capacity equations solely based on data-driven methods [6][7], the strategy considered in this work explores a rational use of artificial intelligence tools to generalize and enhance one of the most widely adopted mechanical models for predicting the shear capacity of RC elements with stirrups, namely the variable-angle truss model.

The present contribution then aims to highlight the key steps undertaken in the general scope of this research toward the goal of establishing a unified shear-resisting mechanism for accurately estimating the uniaxial and biaxial shear capacity of RC beams and columns with rectangular/square cross-section. Accordingly, the remaining parts of the manuscript are organized as follows. Initially, the original variable-angle truss model for uniaxial shear loading is briefly revisited in Section 2. Next, its machine-learning-based generalization and improvement is illustrated in Section 3. Current efforts to extend the variable-angle truss model to biaxial shear loading are outlined in Section 4.

## 2 The original variable-angle truss model for uniaxial shear

According to the original variable-angle truss model, the shear capacity  $V$  for slender RC members with stirrups depends on two contributions, namely the maximum force attained by the stirrups  $V_s$  and the maximum force corresponding to concrete strut crushing  $V_c$  as follows:

$$V = \min\{V_s, V_c\}, \quad (1)$$

$$V_s = A_{sw} \frac{z \cot \theta}{s} f_{yw}, \quad (2)$$

$$V_c = \alpha_c b_w z \cos \theta v f_c \sin \theta, \quad (3)$$

where  $A_{sw}$  is the cross-sectional area of the transverse reinforcement,  $s$  is the spacing of the stirrups,  $z$  is the inner lever arm (with  $z = 0.9d$ ,  $d$  being the effective depth of the cross section),  $f_{yw}$  is the yield strength of the shear reinforcement,  $\theta$  is the angle between the concrete compression struts and the longitudinal axis of the RC member,  $b_w$  is the (minimum) width of the concrete cross section and  $f_c$  is the concrete (cylinder) compressive strength.

The first generation of Eurocode 2 [8] as well as the current Italian building code [9] are based on Eqs. (1-3). In particular, the strength reduction factor for concrete cracked in shear  $v$  and the coefficient taking account of the state of stress in the compressed chord  $\alpha_c$  in Eq. (3) can be evaluated as follows [8]:

$$v = 0.6 \left( 1 - \frac{f_c}{250} \right) \quad \text{with } f_c \text{ in [MPa]}, \quad (4)$$

$$\alpha_c = \begin{cases} 1 + \frac{\sigma_c}{f_c}, & \text{if } 0 \leq \frac{\sigma_c}{f_c} \leq 0.25 \\ 1.25, & \text{if } 0.25 < \frac{\sigma_c}{f_c} \leq 0.50 \\ 2.50 \left( 1 - \frac{\sigma_c}{f_c} \right), & \text{if } 0.50 < \frac{\sigma_c}{f_c} \leq 1.00 \end{cases} \quad (5)$$

### 3 Improving the variable-angle truss model for uniaxial shear

Quaranta et al. [10] proposed a new capacity equation to predict the uniaxial shear capacity of RC beams and columns that still exploits the resisting mechanism based on variable-angle truss model given by Eqs. (1-3), while new formulations are provided for the involved parameters  $\nu$  and  $\alpha_c$ . Hence, two new corrective coefficients  $\eta$  and  $\eta_c$  governing the concrete contribution have been proposed to replace  $\nu$  and  $\alpha_c$  given by Eq. (4) and Eq. (5), respectively.

To elaborate new formulations for such coefficients, an experimental database of RC beams and columns with solid rectangular/square cross-section failing in shear under uniaxial monotonic and cyclic loading conditions, respectively, has been prepared. Afterwards, the optimal values of  $\eta$  and  $\eta_c$  are obtained by solving the following constrained optimization problems sequentially:

$$\min_{\eta} \frac{|V_{num}(\eta|\eta_c = 1) - V_{exp}|}{V_{exp}} \quad \text{s. t.} \begin{cases} \eta_{min} \leq \eta \leq \eta_{max} \\ \theta_{min} \leq \theta \leq \theta_{max} \end{cases} \quad (6)$$

$$\min_{\eta_c} \frac{|V_{num}(\eta_c|\eta = f(\boldsymbol{\theta})) - V_{exp}|}{V_{exp}} \quad \text{s. t.} \begin{cases} \eta_{c,min} \leq \eta_c \leq \eta_{c,max} \\ \theta_{min} \leq \theta \leq \theta_{max} \end{cases} \quad (7)$$

First, the problem in Eq. (6) is solved for RC beams under monotonic loading: herein,  $V_{num}$  is the numerical prediction of the uniaxial shear capacity based on Eqs. (1-3) under the assumption  $\eta_c = 1$  so to exclude the effect of the axial compressive stress, whereas  $V_{exp}$  is the related experimental value. The coefficient  $\eta$  is constrained to vary within an admissible interval whose lower and upper bound are  $\eta_{min}$  and  $\eta_{max}$ , respectively. The strut inclination angle  $\theta$  is also bounded by a minimum and maximum value equal to  $\theta_{min}$  and  $\theta_{max}$ , respectively. Once the optimal values of  $\eta$ , namely  $\eta_{opt}$ , are calculated by solving Eq. (6) for each sample of the database collecting the experimental uniaxial shear capacity of the RC beams under monotonic loading, a genetic programming algorithm [5] is employed to derive an analytical expression depending on some relevant variables  $\boldsymbol{\theta}$ , thereby obtaining a new symbolic formulation  $\eta = f(\boldsymbol{\theta})$  that matches as best as possible the numerical optimal values  $\eta_{opt}$ . Next, Eq. (7) is solved for RC columns under uniaxial cyclic loading: herein,  $V_{num}$  is the numerical prediction of the shear capacity based on Eqs. (1-3) given the new formulation of the strength reduction factor for concrete cracked in shear  $\eta = f(\boldsymbol{\theta})$ , whereas  $V_{exp}$  is the related experimental value. So doing, optimal values of  $\eta_c$ , namely  $\eta_{c,opt}$ , are carried out within an admissible interval whose lower and upper bound are  $\eta_{c,min}$  and  $\eta_{c,max}$ , respectively. Finally, genetic programming is applied once again considering all  $\eta_{c,opt}$  values to define an analytical expression depending on some relevant variables  $\boldsymbol{\varphi}$ , namely  $\eta_c = g(\boldsymbol{\varphi})$ , able to fit the identified optimal values  $\eta_{c,opt}$  in the best possible manner.

The new expressions proposed by Quaranta et al. [10] for  $\eta$  and  $\eta_c$  to replace  $\nu$  and  $\alpha_c$  are the following:

$$\eta = 0.12 + \frac{3.86 + 3.94(b_w/d)}{8.21 - 0.08(b_w/d) - 0.08f_c + f_c(b_w/d)} \quad \text{with } f_c \text{ in [MPa]}, \quad (8)$$

$$\eta_c = 0.37 + \frac{0.30 + 0.75(\sigma_c/f_c) - 1.39(a/d)\omega_{sw}}{(a/d)} \left( 3.79 + 57.52 \frac{\sigma_c/f_c}{\mu^2} \right). \quad (9)$$

Equation (9) is valid for columns under cyclic loading, whereas  $\eta_c = 1$  must be assumed for beams under monotonic loading. The parameter  $\mu$  in Eq. (9) is the displacement ductility demand and accounts for the degradation of the shear capacity due to cyclic loading [11]. Additionally, the following constraints apply to Eqs. (8-9):  $0.1 \leq \eta \leq 1.0$ ,  $1/3 \leq \eta_c \leq 2.6$ . As far as the strut inclination angle is concerned,  $\theta_{max} = 45^\circ$  is assumed in agreement with the first generation of Eurocode 2 [8], since this upper bound is motivated by mechanical considerations and supported by experimental evidence [11]. As pointed out by Biskinis et al. [11],  $\theta_{min}$  can be lower than the value of  $21.8^\circ$  recommended in the first generation of Eurocode 2 [8]. In this regard, it is worth highlighting that the wider range of variation of  $\eta$  and  $\eta_c$  compared to that of  $\nu$  and  $\alpha_c$  implies a wider class of plastically admissible stress fields. Taking also into account other truss models [12], the lower bound for  $\theta$  is thus set to  $\theta_{min} = 11.31^\circ$ . This means that  $1 \leq \cot \theta \leq 5$  is assumed when Eqs. (8-9) are implemented in Eqs. (1-3) in place of  $\nu$  and  $\alpha_c$ , respectively.

The accuracy of Eqs. (8-9) for RC columns and beams under uniaxial shear load has been demonstrated by comparison with experimental results available from the literature. This comparative assessment has been performed for beams and columns with solid cross-section [10] as well as for columns

with hollow cross-section [13] (in this case, the thickness of the hollow cross section plays the role of the minimum width of the solid cross-section). The results presented in Figures 1-3 demonstrate that the proposed machine-learning-calibrated coefficients enhance both the mean value and the coefficient of variation of the ratio between experimental data and numerical estimates.

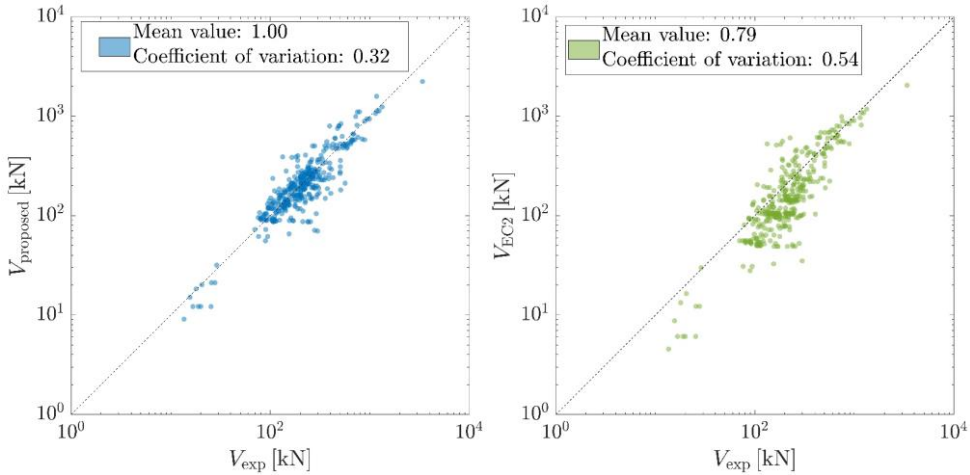


Fig. 1 Comparison between experimental values and numerical predictions of the shear capacity for RC beams with solid cross-section under uniaxial monotonic shear load: results obtained by means of the proposed improvement of the variable-angle truss model (left) and the original formulation in the first generation of Eurocode 2 (right).

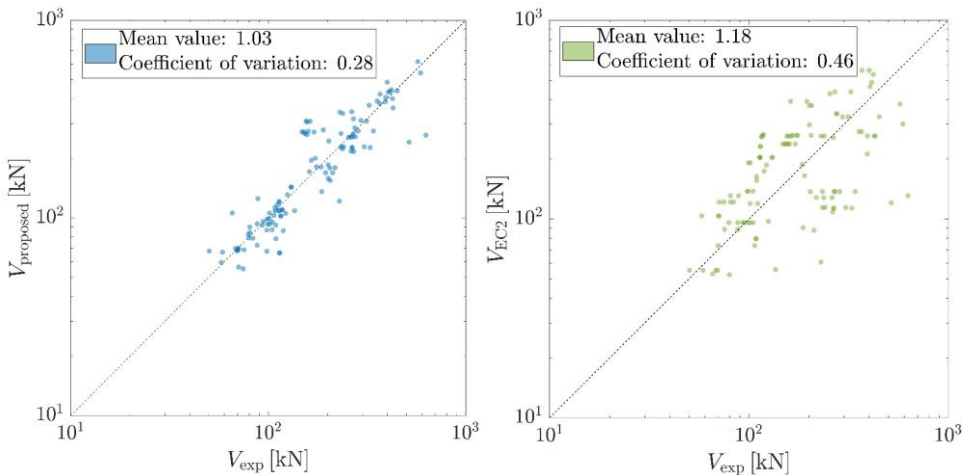


Fig. 2 Comparison between experimental values and numerical predictions of the shear capacity for RC columns with solid cross-section under uniaxial cyclic shear load: results obtained by means of the proposed improvement of the variable-angle truss model (left) and the original formulation in the first generation of Eurocode 2 (right).

#### 4 Extending the variable-angle truss model to biaxial shear

The proposed variable-angle truss mechanism for uniaxial shear is then extended to biaxial shear load. In this regard, it is pointed out that the standard variable-angle plane truss mechanism under uniaxial loading assumes that the width of the cross-section of the diagonal concrete struts is parallel to the neutral axis and perpendicular to the loading direction. The extension of the variable-angle truss mechanism to biaxial shear loads originates from the same assumption. Indeed, section cuts of RC columns

subjected to biaxial shear show that the main cracks are generally parallel to the neutral axis and perpendicular to the loading direction [14][15][16].

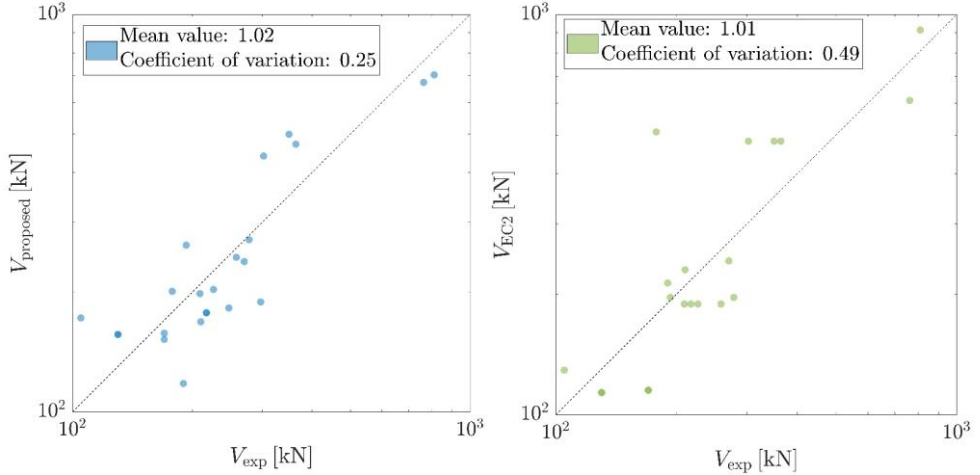


Fig. 3 Comparison between experimental values and numerical predictions of the shear capacity for RC columns with hollow cross-section under uniaxial cyclic shear load: results obtained by means of the proposed improvement of the variable-angle truss model (left) and the original formulation in the first generation of Eurocode 2 (right).

An analytical capacity equation is now being developed and an experimental campaign is also being completed for its validation, see Fig. 4. This consists of six full-scale cantilever RC columns designed to exhibit a hybrid flexural-shear failure, four of which with a rectangular cross-section and two with a square cross-section. The dimensions are 300 mm  $\times$  500 mm and 400 mm  $\times$  400 mm for the columns with rectangular and square cross-section, respectively, whereas the height is 1,400 mm. The loading angle (with respect to the strong axis) is equal to 0°, 30°, 60° and 90° for the rectangular columns, and 0° and 45° for the square columns. The transverse reinforcement is provided by stirrups with a diameter of 8 mm and constant spacing equal to 100 mm. A constant axial load ratio equal to 0.15 is considered.



Fig. 4 Preparation of the specimens for biaxial tests.

## Conclusions

This study has illustrated the Authors' ongoing efforts in advancing a unified approach for assessing the shear capacity of RC members. In this perspective, an overview of the original variable-angle truss model for uniaxial shear has been initially provided. Then, new machine-learning-enhanced formulations for the two coefficients governing concrete contribution have been considered. Building on the accuracy achieved in predicting uniaxial shear capacity, the variable-angle truss model is currently being expanded to accommodate biaxial loading conditions. Concurrently, laboratory biaxial shear tests are underway to validate its effectiveness. Ultimately, the approach being pursued rests on the integra-

tion of mechanics-based and data-driven methods to formulate a unique framework for the shear capacity assessment of RC elements, in such a way to maintain the physical meaning while significantly improving accuracy and robustness through machine learning.

## Acknowledgements

Giuseppe Quaranta acknowledges the support received through the project “Artificial Intelligence for Sustainable seismic risk reduction of Structures (AI-SUST)” (project code: 2022LEFKHS) funded by European Union – NextGeneration EU through the PRIN 2022 program of the Italian Ministry of University and Research (MUR) (D. D. n. 104, 02-02-2022). This work reflects only the Author’s views and opinions whereas the MUR cannot be considered responsible for them.

## References

- [1] ASCE-ACI Committee 445 on Shear and Torsion. 1998. “Recent approaches to shear design of structural concrete.” *Journal of structural engineering* 124(12):1375–1417.
- [2] Cladera, A., and Mari, A. R. 2007. “Shear strength in the new Eurocode 2. A step forward?” *Structural concrete* 8(2):57–66.
- [3] Massone, L. M. and Correa, A. 2020. “Behavior of reinforced concrete columns under biaxial shear forces based on ACI 318.” *Engineering Structures* 219:110731.
- [4] Azadi Kakavand, M. R., Sezen, H., and Taciroglu, E. 2021. “Data-driven models for predicting the shear strength of rectangular and circular reinforced concrete columns.” *Journal of Structural Engineering* 147(1):04020301.
- [5] Quaranta, G., Lacarbonara, W., and Masri, S. F. 2020. “A review on computational intelligence for identification of nonlinear dynamical systems.” *Nonlinear Dynamics* 99(2):1709–1761.
- [6] Fiore, A., Quaranta, G., Marano, G. C., and Monti, G. 2016. “Evolutionary polynomial regression-based statistical determination of the shear capacity equation for reinforced concrete beams without stirrups.” *Journal of Computing in Civil Engineering* 30(1):04014111.
- [7] Pang, Y., Azim, I., Rauf, M., Iqbal, M.F., Ge, X., Ashraf, M., Tariq, M.A.U.R. and Ng, A.W. 2022. “Prediction of bidirectional shear strength of rectangular RC columns subjected to multidirectional earthquake actions for collapse prevention.” *Sustainability* 14(11):6801.
- [8] European Committee for Standardization. 2004. *Eurocode 2: Design of concrete structures – Part 1-1: General rules and rules for buildings*.
- [9] Italian Ministry of Infrastructure and Transport, 2018. *Decreto 17 gennaio 2018: Aggiornamento delle norme tecniche per le costruzioni*.
- [10] Quaranta, G., De Domenico, D., and Monti, G. 2022. “Machine-learning-aided improvement of mechanics-based code-conforming shear capacity equation for RC elements with stirrups.” *Engineering Structures* 267:114665.
- [11] Biskinis, D. E., Roupakias, G. K., and Fardis, M. N. 2004. “Degradation of shear strength of reinforced concrete members with inelastic cyclic displacements.” *ACI Structural Journal* 101(6):773–83.
- [12] De Domenico, D. and Ricciardi, G. 2019. “Shear strength of RC beams with stirrups using an improved Eurocode 2 truss model with two variable-inclination compression struts.” *Engineering Structures* 198:109359.
- [13] De Domenico, D., Quaranta, G., Zeng, Q. and Monti, G. 2023. “Shear capacity of RC elements with transverse reinforcement through a variable-angle truss model with machine-learning-calibrated coefficients.” In: *Artificial Intelligence and Machine Learning Techniques for Civil Engineering*, IGI Global, 163–180.
- [14] Rodrigues, H., Varum, H., Arêde, A. and Costa, A. G. 2013. “Behaviour of reinforced concrete column under biaxial cyclic loading – state of the art.” *International Journal of Advanced Structural Engineering* 5:1–12.
- [15] Hua, J., Gu, X., Eberhard, M. O., and Wouagabe, J. 2022. “Influence of lateral loading direction on seismic behavior of shear-critical reinforced concrete intermediate short columns.” *Engineering Structures*, 252, 113573.
- [16] Yoshimura, M. and Tsumura, K. 2000. “Shear-failing reinforced concrete columns subjected to multi-axial loading.” *Proceedings of the 12th World Conference on Earthquake Engineering*, Auckland, New Zealand.

# Seismic Hysteretic Systems for Precast Buildings

Giulio Proietti<sup>1</sup>, Simone Pedullà<sup>1</sup> and Nicola Nisticò<sup>1</sup>

<sup>1</sup>*Department of Structural and Geotechnical Engineering,  
Sapienza Università di Roma,  
Via Eudossiana 18, 00184 Roma, Italy*

## Abstract

The objective of this work is to explore innovative approaches to structural prefabrication, with a focus on enhancing seismic performance through the implementation of seismic hysteretic systems. Specifically, the study aims to develop precast reinforced concrete structures using a frame-like typology that addresses the challenge of mitigating seismic forces acting on prestressed beams. The design incorporates non-monolithic beam-to-column and column-to-column connections, integrated with hysteretic U-shaped dissipative devices, which are discussed and validated through numerical and experimental tests.

## 1 Introduction

The seismic event [1] that occurred in Emilia Romagna (2012) highlighted the urgent need to improve the seismic capacity of prefabricated constructions made with reinforced concrete elements. The observed damages [2] were attributable to inadequate connections between: 1) beams and columns; 2) columns and foundations; 3) infill walls and adjacent structures as well as to the inadequacy of columns, panels, infill walls and shelves.

Most of the damaged constructions concerned industrial activities and consequently, the interruption of production services caused: 1) job losses [3]; 2) damages amounting to approximately 5 billion euros [3],[4], encompassing both the costs of restoring constructions and systems, as well as the loss of sales. Following the Emilia Romagna events, retrofitting strategies were proposed [5],[6], including hysteretic devices [7].

The use of precast concrete elements became prominent [8], beginning in the 1960s with flooring systems and expanding in the 1980s to include moment-resisting frames and walls, which were regarded as enhancements for seismic performance. A systematic review of seismic-resistant precast concrete buildings is reported in [9]. Priestley (1996), while introducing the Precast Seismic Structural Systems (PRESSS) as part of a United States-Japan Program [10], outlined the scope of three planned phases. These phases covered the following topics: 1) connections [11], with a focus on a) classification and modeling (Phase I) and b) ductile connections (Phase II); 2) testing (Phase III) of two five-story precast office buildings, each incorporating frames and shear walls aligned along two orthogonal directions [12]-[14]. Different projects [15] were scheduled and concluded to support Eurocode 8 [16] principles and design rules. Among them, PRECAST, SAFECAST and SAFECLADDING can be mentioned. The PRECAST EC8 project, concluded in 2007, aimed at calibrating the Eurocode design rules. The Italo-Slovenian Group's activities [17] concerned pseudodynamic and cyclic tests on two single-story full-scale prototypes [18]. The SAFECAST project [19] concerned, among other activities, the investigation, supported by experimental activities, of the seismic performance of four classes of connections: floor-to-floor, floor-to-beam, beam-to-column and column-to-foundation. The activities of Work Package WP6, "Derivation of design rules," served to support the guidelines for connections [20] included in ISO 20987 [21]. The SAFECLADDING project [22],[23] investigated the seismic performance of cladding wall panels of precast buildings with the support of experimental studies [24],[25]. The obtained results supported the drafting of ISO 22502 [26]. International Codes and Recommendations are spread across different countries [27] and the FIB documents [28]-[30] can be mentioned among others. Traditional and innovative solutions can be adopted, noting that the overarching goal of minimizing damage and promoting sustainability will continue to guide future implementations. This will necessitate the development of increasingly effective anti-seismic devices, which will include materials with controllable friction, viscous fluids within special mechanisms, viscoelastic polymers and metals with highly dissipative hysteresis characteristics. The origins of structural control concepts can be traced back to the works of Skinner et al. [31], Housner et al. [32], Soong and Spencer [33] and Martinez-Rueda [34]. The pioneering testing of hysteretic dampers began in 1970 at the Physics and Engineering

Laboratory in Gracefield, Lower Hutt, New Zealand. Subsequent research efforts have further expanded the field of seismic protection: Roorda [35] conducted tests involving the use of tendons as active bracing systems on small-scale structural models. Kelly and Skinner [36] explored and tested different types of energy absorbers, including a) U-shaped devices that relied on the bending of flat steel strips and b) torsional and flexural predominant devices. C-shaped devices were developed and tested by Ciampi and co-workers at the University of Rome “La Sapienza” [37],[38]. Dolce et al. [39] designed and tested a system of radially arranged U-shaped steel elements. Dolce and co-workers [40] also designed and tested a cover plate for friction joints, intended to induce plasticization in a steel shear-predominant device.

Building upon these pioneering studies and applications [41], various typologies have been proposed in the past. As far as hysteretic systems are concerned, SOMMA, an Italian company, has conceived and tested (both numerically and experimentally) a steel displacement-dependent device with high versatility for use in a wide range of scenarios. Although its application is well established, ongoing developments are still necessary. To this end, a collaboration has been initiated [42] to support a PhD study on the subject. The presented work can thus be considered the starting point of a synergistic contribution between industry and academia to conceive and develop systems to be implemented in existing and new precast industrial and residential buildings.

## 2 Precast building conception

The conception of multi-story constructions, in accordance with the Italian Code [43] can be based on standard typologies, including, among others, frame and shear wall systems, as well as specific solutions such as: 1) panel and monolithic cellular structures and 2) structures with columns fixed at the base and floors hinged to them. It is important to note that other types of structures may also be adopted, provided that the general safety requirements are justified.

The role of connections is fundamental: beams are typically placed on pads which, depending on their deformability, may require dowel systems designed with non-adherent dowels in combination with other systems to prevent local hammering. In non-monolithic structures, connections do not affect the dissipative capacities of the structure when located far from the dissipative zones. Alternatively, they need to be over-dimensioned to avoid hindering the plasticization of the dissipative zones or must be equipped with qualified mechanical devices to ensure adequate characteristics in terms of ductility and energy dissipation.

Shear wall systems are often employed in areas where lift and stair cores are located, allowing columns to be primarily designed for gravity loads. In such cases, column-beam connections must transfer both vertical and horizontal loads induced by seismic actions. However, these systems are often characterized by irregular floor plans, leading to high drift demands on the column systems. Emerging solutions [44]-[46] involve cores designed as independent non-structural systems, incorporating non-monolithic connections combined with anti-seismic devices, which may include various types as referenced in [7], [46]-[50]. These devices can be implemented, as shown in Figure 1 and Figure 2, to connect parts of columns, beam-to-column and beam-to-beam using appropriately designed systems, assisted by post-tensioned systems similar to those pioneeringly proposed within the framework of the aforementioned PRESSS program. The selection of the systems to be adopted is currently under study and preliminary results will be presented in the next sections, referring to a seven-story precast reinforced concrete building (Figure 3) with prestressed beams supporting prestressed floor panels. The ongoing program includes, as final results, the performance evaluation of four solutions: wall system, cantilever column, monolithic frame system and non-monolithic connections with and without dissipative devices.

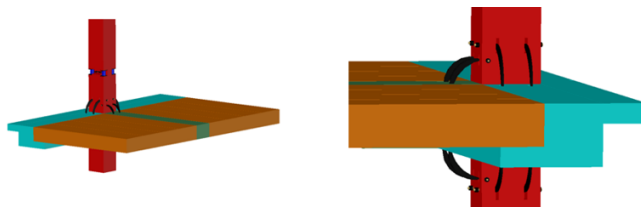


Fig. 1 Non-monolithic column-to-column connection and beam-to-column solution.

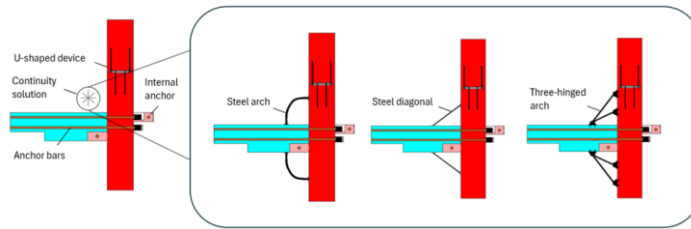


Fig. 2 Non-monolithic column-to-beam connections using: (i) steel arch; (ii) steel diagonal; (iii) three-hinged arch. Connections can be integrated with post-tensioning tendons or anchor bars passing through the beams.

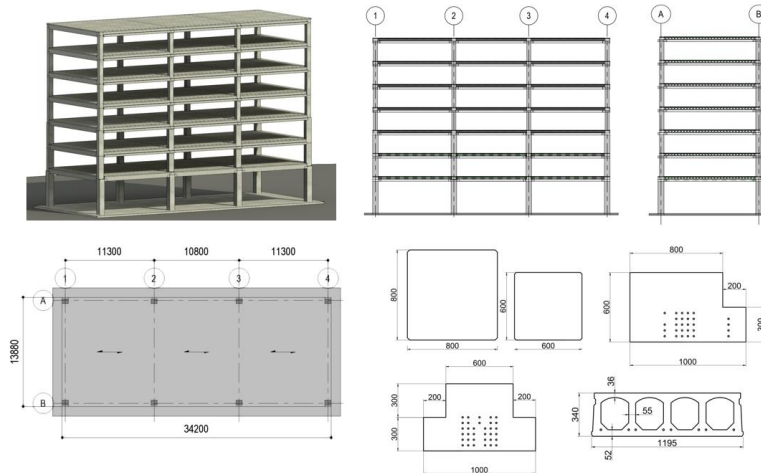


Fig. 3 Multi-story building: general view; longitudinal and transversal section; plan; column, beam and slab panel section.

### 3 Dissipative device selection

The investigated device can be categorized among the various proposed hysteretic systems [41] shown in Figure 4, where it is identified as the Steel Hysteretic Multiple-Arch Device (SH-MAD).

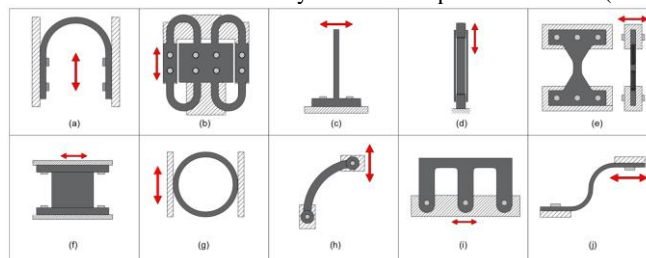


Fig. 4 Steel hysteretic device families; (a) Arch; (b) Multiple-Arch; (c) Cantilever; (d) Buckling-Restrained; (e) ADAS; (f) Shear Panel; (g) Pipe; (h) C-Shaped; (i) E-Shaped; (j) S-Shaped.

The SH-MAD (Figure 5) consists of four appropriately shaped elements interconnected through a central plate and two pairs of external plates [51]. The system is defined here as the combination of the device and additional connecting elements that integrate the device into part of the construction. It is worth noting that the interconnecting elements are, when integrated in a bracing system, friction-bolted to the central and lateral plates. To further reduce load eccentricity, depending on the number of devices, the interconnecting elements can have different sandwich configurations consisting of: 1) two pairs of



interconnecting elements with an internal device; 2) two external devices with one pair of internal interconnection systems. The push-pull actions imposed on the central and lateral plates result in relative displacements. The device can serve, when combined with elastomeric supports, the column-to-column connection (Figure 6) and a new configuration proposed here (Figure 7) for the beam-to-column connection.

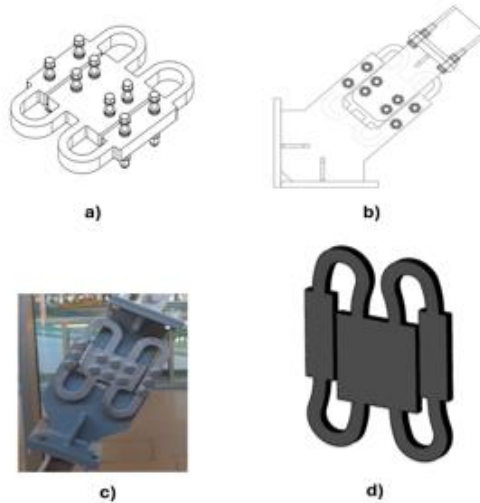


Fig. 5 U-shaped device: (a) representation of device and (b) bracing system; (c) real system application; (d) deformed configuration.



Fig. 6 U-shaped device for column-to-column connection. The system consists of two external steel plates and elastomeric supports coupled with the device. The device is anchored to the upper column through its external flanges and to the bottom column via the central plate.

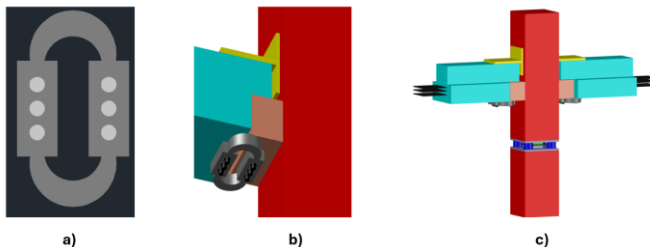


Fig. 7 Modified U-shaped device: (a) illustration of the proposed device; (b) beam-to-column system implemented with the modified U-shaped device, where hysteretic energy dissipation is generated by the relative displacement between the corbel and the beam; (c) proposed connections for column-to-column, beam-to-column and beam-to-beam using the U-shaped device, modified U-shaped device and post-tensioning tendons.

#### 4 Proposed devices: preliminary results

Experimental tests are usually performed according to UNI-EN standards [52]: 1) a displacement-controlled procedure is used to define quasi-static cyclic loading consisting of three different displacement levels (25%, 50% and 100% of the design displacement) with a fixed frequency of 0.05 Hz; 2) five triangular waveform cycles are conducted for the first two displacement levels, while ten cycles are performed for the final design displacement. Currently, numerical tests are conducted using 3D Finite Element Models implemented in ABAQUS®. Nonlinear material models are adopted, using a plastic J2 model [53]. Examples of the FEM models are shown in Figure 8a, along with the displacement in Figure 8b and Von-Mises stress levels in Figure 8c. Additionally, the numerical backbone force-displacement curve is compared (Figure 9, in black line) with experimental results (dotted grey line).

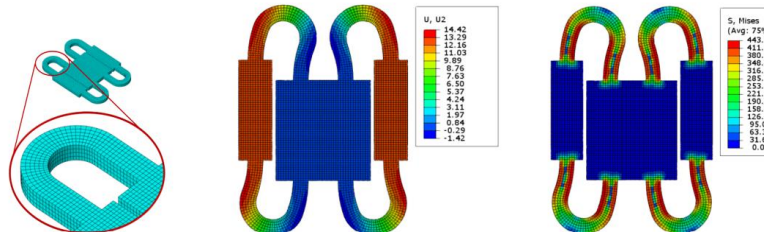


Fig. 8 U-shaped device finite element modelling: a). FEM mesh; b) typical deformation (mm) due to the displacements applied on the lateral plates; c). Von Mises stresses (MPa) due to the displacement load. Adopted properties: Elastic Young's Modulus = 210 GPa, Poisson's Ratio = 0.3, Initial Yielding Stress = 390 MPa,  $Q_{\infty}$  = 160 MPa or Final Saturation Stress = 450 MPa, Hardening Parameter  $b = 5$ .

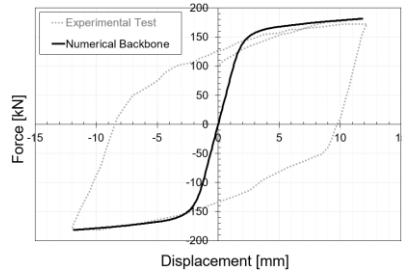


Fig. 9 U-shaped device: numerical modeling backbone curve vs experimental result.

Developments in structural optimization strategies are currently underway to enhance hysteretic energy dissipation and optimize the system by varying the shape of the device (Figure 10). However, the efforts required to implement these new shapes may outweigh the benefits gained in terms of increased hysteretic energy dissipation compared to traditional device shapes.

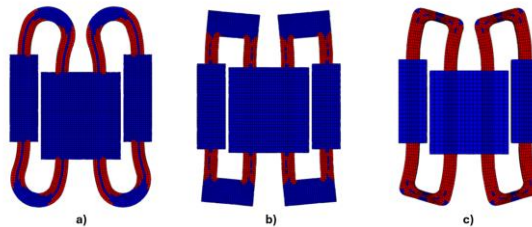


Fig. 10 Device plasticity exploitation: a) classical U-shaped; b) frame device; c) modified U-shaped.

## 5 Conclusions and future proposals

A literature overview of the current state-of-the-art in innovative approaches to structural prefabrication, with a focus on enhancing seismic performance, is presented, later proposing a precast building concept that includes alternative solutions for beam-to-column and column-to-column connections equipped with easily replaceable hysteretic dissipative devices to increase seismic performance. The mechanical behavior of the proposed U-shaped device can be predicted through numerical FEM analyses validated based on performed experimental tests. Further investigations are needed, including the evaluation of cyclic numerical capacity curves to assess the real device hysteretic energy dissipation and consequently support the development of alternative device shapes that maximize hysteretic energy dissipation without altering production costs. Future developments shall include the seismic performance evaluation of the proposed precast building solution compared to different structures designed with other static schemes, such as wall systems, cantilever columns, monolithic frame systems and non-monolithic connections without dissipative devices. The solutions will be supported by a parametric investigation that will hopefully allow for the definition of principles and design rules.

## Acknowledgements

The Lazio Region of Italy and SOMMA Engineering Company are thanked for funding the Doctoral Scholarship, under which part of this work was developed.

## References

- [1] Dolce, Mauro and Di Bucci, Daniela. 2014. "National Civil Protection Organization and technical activities in the 2012 Emilia earthquakes (Italy)." *Bull Earthquake Eng* 12(5): 2231:53.
- [2] ReLuis. 2012. *Linee di indirizzo per interventi locali e globali su edifici industriali monopiano non progettati con criteri antisismici*. Gruppo di Lavoro Agibilità Sismica dei Capannoni Industriali. [http://www.reluis.it/images/stories/Linee\\_di\\_indirizzo\\_GDL\\_Capannoni.pdf](http://www.reluis.it/images/stories/Linee_di_indirizzo_GDL_Capannoni.pdf).
- [3] Magliulo, Gennaro, Ercolino, Mariann, Petrone, Crescenzo, Coppola, Orsola and Manfredi, Gaetano. 2014. "The Emilia earthquake: seismic performance of precast reinforced concrete buildings." *Earthquake Spectra* 30(2):891–912.
- [4] Liberatore, Laura, Sorrentino, Luigi, Liberatore, Domenico and Decanini, Luis D. 2013. "Failure of industrial structures induced by the Emilia (Italy) 2012 earthquakes." *Engineering Failure Analysis* 34:629–47.
- [5] Bournas, Dionysios A., Negro, Paolo and Taucer, Fabio F. 2014. "Performance of industrial buildings during the Emilia earthquakes in northern Italy and recommendations for their strengthening." *Bull Earthquake Eng*.12: 2383–404.
- [6] Minghini, Fabio and Tullini, Nerio. 2021. "Seismic Retrofitting Solutions for Precast RC Industrial Buildings Struck by the 2012 Earthquakes in Northern Italy." *Front. Built Environ.* 7:631315.
- [7] Di Salvatore, Chiara, Magliulo, Gennaro and Caterino, Nicola. 2024. "Innovative hysteretic device for seismic retrofit of single-story RC precast buildings." *Engineering Structures* 313:118621.
- [8] Bull, Des K. 1999. *Guidelines for the use of structural precast concrete in buildings*. Centre for Advanced Engineering, University of Canterbury.
- [9] Guaygua, Byron, Sanchez-Garrido, Antonio J. and Yepes, Victor. 2023. "A systematic review of seismic-resistant precast concrete buildings." *Structures* 58:1-24.
- [10] Priestley, Nigel M.J. 1991. "Overview of PRESSS Research Program." *PCI Journal* 36(4):50–57.
- [11] Priestley, Nigel M.J. 1999. "The PRESSS Program - Current Status and Proposed Plans for Phase III." *PCI Journal* 41(2):22–40.
- [12] Dow Nakaki, Suzanne, Stanton, John F. and Sritharan, Sri S. 1999. "An Overview of the PRESSS Five-Story Precast Test Building." *PCI Journal* 44(2):26–39.
- [13] Sritharan, Sri S., Igarashi, Alkira, Priestley, Nigel M.J. and Seible, Frieder. 1999. "Test Design of the PRESSS Five-Story Precast Concrete Building." Paper presented at 68th Annual Convention, Structural Engineers Association of California, Santa Barbara, CA, September 30–October 3.

- [14] Priestley, Nigel M.J., Sritharan, Sri S., Conley, James R. and Pampanin, Stefano. 1999. "Preliminary results and conclusions from the PRESS five-storey precast concrete test building." *PCI Journal* 44(6):42–67.
- [15] Toniolo, Giandomenico. 2012. SAFECAST project: "European research on seismic behaviour of the connections of precast structures." Paper presented at the 15th World Conference of Earthquake Engineering, Lisbon, Portugal, September 24–28.
- [16] CEN, 2004. *Eurocode 8: Design of structures for earthquake resistance – Part 1: General rules, seismic action and rules for buildings*. EN 1998-1.
- [17] Negro, Paolo, Mola, Elena, Ferrara, Liberato, Zhao, Bin, Magonette, Georges and Molina, Javier F. 2007. *PRECAST STRUCTURES EC8: seismic behaviour of precast concrete structures with respect to EC8*. Contract N. G6RD-CT – 2002-00857. Final report of the experimental activity of the Italo-Slovenian Group:1-190.
- [18] Ferrara, Liberato, Mola, Elena and Negro, Paolo. 2006. "Pseudodynamic and Cyclic Testing of full-scale prototypes of R/C Precast single story industrial buildings." Paper presented at First European Conference on Earthquake Engineering and Seismology, Geneva, Switzerland, September 3–8.
- [19] ASSOBTETON, 2012. *SAFECAST: Performance of innovative mechanical connections in precast buildings structures under seismic conditions*. Grant agreement ID: 218417. Final Report.
- [20] Negro, Paolo and Toniolo, Giandomenico. 2012. *Design Guidelines for Connections of Precast Structures under the Seismic Action*. EC-JRC-IPSC: European Union, 2012.
- [21] ISO 20987. 2019. *Simplified design for mechanical connections between precast concrete structural elements in buildings*. International Organization for Standardization. Geneva, Switzerland.
- [22] Bureau International du Béton Manufacture, 2015. *SAFECLADDING: Improved Fastening System of Cladding Wall Panels of Precast Building in Seismic Zone*. Grant agreement ID: 314122. Final Report.
- [23] Colombo, Antonella, Negro, Paolo and Toniolo, Giandomenico. 2014. "The Influence of Claddings on the Seismic Response of Precast Structure: the SAFECLADDING project." Paper presented at the second European Conference on Earthquake Engineering and Seismology, Istanbul, Turkey, August 25–29.
- [24] Negro, Paolo and Lamperti Tornaghi, Marco. 2017. "Seismic response of precast structures with vertical cladding panels: the SAFECLADDING experimental campaign." *Engineering Structures* 132:205–28.
- [25] Lamperti Tornaghi, Marco, Scalbi, Agnese and Negro, Paolo. 2022. "Precast RC buildings: What is wrong with horizontal cladding panels?". *Engineering Structures* 266:114456.
- [26] ISO 22502. 2020. *Simplified design of connections of concrete claddings to concrete structures*. International Organization for Standardization. Geneva, Switzerland.
- [27] Kurama, Yahya C., Sritharan, Sri S., Fleischman, Robert B., Restrepo, Jose I., Henry, Richard S., Cleland, Ned M., Ghosh, S.K. and Bonelli, Patricio. 2018. "Seismic-Resistant Precast Concrete Structures: State of the Art." *Journal of Structural Engineering* 144(4):1–18.
- [28] Park, Robert. 2003. "The fib state-of-the-art report on the seismic design of precast concrete building structures." Paper presented at the seventh Pacific Conference on Earthquake Engineering, Christchurch, New Zealand, February 13–15.
- [29] FIB (2003). *Seismic design of precast concrete building structures State-of-art report*. Fédération Internationale du Béton. fib bulletin 27: Task Group 7.3.
- [30] FIB (2008). *Structural connections for precast concrete buildings*. Fédération Internationale du Béton. fib bulletin 43: Task Group 7.3.
- [31] Skinner, Ivan R., Tyler, R.G., Heine, A.J. and Robinson, William H. 1980. "Hysteretic dampers for the protection of structures from earthquakes." *Bull NZ Soc EQE* 13(1):22–36.
- [32] Housner, George W., Masri, Sami F. and Soong, Tsu Teh. 1994. "Activities in structural control in the USA. Earthquake Engineering." Paper presented at the Tenth World Conference, Madrid, Spain, July 19–24.
- [33] Soong, Tsu Teh and Spencer, Billie F. 2002. "Supplemental energy dissipation: state-of-the-art and state-of-the-practice." *Eng Struct* 24:243–59.
- [34] Martínez-Rueda, Juan Enrique. 2002. "On the Evolutin of Energy Dissipation Devices for Seismic Design". *Earthquake Spectra* 18 (2):309–46.

- [35] Roorda, John. 1980. *Experiments in feedback control of structures. Structural control*. H.H.E. Leipholz, North Holland, Amsterdam.
- [36] Kelly, James M., Skinner, Ivan R., Heine, Arnold J. 1972. "Mechanisms of energy absorption in special devices for use in earthquake resistant structural control structures." *Bulletin of the New Zealand Society for Earthquake Engineering* 5(3):63–88.
- [37] Ciampi, Vincenzo and Marioni, Agostino. 1991. "New Types of Energy Dissipating Devices for Seismic Protection of Bridges". Paper presented at the Third World Congress on Joint Sealing and Bearing Systems for Concrete Structures, Toronto, Canada, October 27–31.
- [38] Ciampi, Vincenzo. 1995. "Research and development of passive energy dissipation techniques for civil buildings in Italy." Paper presented at the International Post-SMiRT Conference Seminar on Seismic Isolation, Passive Energy Dissipation and Active Control of Vibrations of Structures, Santiago, Chile, August 21–23.
- [39] Dolce, Mauro, Filardi, B., Marnetto, Roberto and Nigro, Domenico. 1996. "Experimental tests and applications of a new biaxial elastoplastic device for the passive control of structures." Paper presented at the Fourth world congress on joint sealants and bearing systems for concrete structures, Sacramento, California, September 29–October 3.
- [40] Dolce, Mauro and Marnetto, Roberto. 2000. "Coprigiunti dissipative di controventi in acciaio per l'adeguamento sismico di edifici in c.a." *Costruzioni metalliche* 0010–9673.
- [41] Javanmardi, Ahad, Ibrahim, Zainah, Ghaedi, Khaled, Ghadim, Hamed Benisi and Hanif, Muhammad Usman. 2019. "State-of-the-Art Review of Metallic Dampers: Testing, Development and implementation." *Archives of Computational Methods in Engineering* 25: 455–78.
- [42] Nisticò, Nicola. 2022. "Concezione, ingegnerizzazione e sperimentazione di dispositivi di protezione sismica finalizzati al miglioramento delle capacità prestazionali di edifici prefabbricati o parzialmente prefabbricati." Studi cofinanziati dalla Regione Lazio (Italia) e Somma-International, nell'ambito dell'avviso pubblico. Intervento per il rafforzamento della ricerca e innovazione nel Lazio - incentivi per i dottorati di innovazione per le imprese e per le PA." (Vincitore: Giulio Proietti).
- [43] Ministero delle Infrastrutture e dei Trasporti. 2018. "Aggiornamento delle Norme Tecniche per le Costruzioni". Decreto 17 gennaio, 2018.
- [44] Comodini, Fabrizio and Mezzi, Marco. 2012. "Ricerca di Sistema di protezione appropriati per schemi prefabbricati ricorrenti." *Esempi di Architettura*. ISSN 2035-7982.
- [45] Dal Lago, Bruno, Negro, Paolo and Dal Lago, Alberto. 2018. "Seismic design and performance of dry-assembled precast structures with adaptable joints." *Soil Dynamics and Earthquake Engineering* 106:182–195
- [46] Casali, Leonardo, Dal Lago, Bruno, Fulco, Alessandro and Mezzi, Marco. 2023. "Environmental impact reduction of precast multi-storey buildings by crescent-moon seismic dampers hidden in beam-column joints." Paper presented at the 8th International Symposium on Life-Cycle Civil Engineering, Milan, Italy, 2nd-6th July, 2523–2530.
- [47] Morgen, Brian G. and Kurama, Yahya C. 2004. "A friction damper for post-tensioned precast concrete beam-to-column joints." Paper presented at the 13th World Conference on EQE. Vancouver, Canada.
- [48] Marinini, Luca, Spatti, Pietro, Riva, Paolo, Nascimbene, Roberto, Izzo, Livio, Spadavecchia, Alessandro and Maffioletti, Marcello. 2012. "Sviluppo di una connessione dissipativa per strutture prefabbricate." Lavoro presentato al 17° convegno C.T.E., Roma, Italia.
- [49] Belleri, Andrea, Torquati, Mauro and Riva, Paolo. 2014. "Seismic performance of ductile connections between precast beams and roof elements." *Magazine of Concrete Research*.
- [50] Rodrigues, Hugo, Batalha, Nadia, Furtado, Andre, Arede, Antonio, Sousa, Romain and Varum, Humberto. 2024. "Retrofitting solution for beam-to-column connections of precast reinforced concrete industrial buildings." *Engineering Structures* 302: 117424.
- [51] Proietti, Giulio, Castino, Chiara, Cicalese, Anna Maria and Nisticò Nicola. 2024. A Passive Control System Based on Double U-Shaped Metal Elements: Case Applications, Design, and Developments. Paper presented at 9th International Conference "Civil Engineering – Science and Practice" – Kolašin, Montenegro, March 5-9.
- [52] CEN/TC 340: *Anti-seismic devices*. European Standard UNI-EN 15129:2009.
- [53] Borja, Ronaldo I. 2013. *J2 Plasticity. Plasticity: Modeling & Computation*, Springer.

# A new numerical model to simulate buckling of steel rebars

Melina Bosco, Andrea Florida, Dario Panarelli, Pier Paolo Rossi, Nino Spinel-la

*Department of Civil Engineering and Architecture,  
University of Catania,  
via S. Sofia 64, 95125 Catania (Italy)*

## Abstract

This paper presents a new uniaxial material model of reinforcing steel bars with the aim of achieving a more accurate evaluation of the response of rebars including the effects of lateral buckling. The proposed model is calibrated on the results of numerical analyses conducted on refined models of steel rebars characterised by low-to-high slenderness ratios. The proposed model incorporates the possibility to simulate the behaviour of bare and embedded rebars. The response is path-dependent and described by means of smooth curves so as to guarantee numerical stability in nonlinear finite element simulations. The accuracy of the model has been validated by comparison with the response of laboratory tests performed by other researchers on steel rebars.

## 1 Introduction

Most of the buckling models available in the literature do not simulate the phenomenon of the lateral buckling of rebars directly, but incorporate the effects of the lateral deflection empirically in the uniaxial material model, namely in the average stress - average strain uniaxial response. The uniaxial response of such models is calibrated by means of laboratory tests [1-6] or numerical analyses [7-8] of bare rebars. Since the late 20<sup>th</sup> century, several research studies have been carried out to calibrate the compression backbone curve of deformed or smooth rebars subjected to lateral instability [1, 4-6, 9-11]. In most of these studies, the numerical models were obtained by modifications of the uniaxial material models suggested by other researchers for steel, e.g. Menegotto and Pinto [12], Chang and Mander [13] or Restrepo-Posada et al. [2]. These modified models were calibrated to replicate the compression backbone curve of rebars characterised by slenderness ratios in the range from low-to-medium values (i.e. up to 15) [1, 9-11, 14], but they were not able to simulate the transition branches from compression to tension with adequate accuracy. Only recently, some enhanced models have proved to replicate the above transition response accurately, but still in the range of low-to-medium values of the slenderness ratio [8, 15]. The relevance of the response of rebars with high slenderness ratio (i.e. up to 40) has been underlined by other researchers [4, 5] as such values of the slenderness ratio have been reported to be common in columns of existing buildings. Referring to such latter values of the slenderness ratio, the above researchers [4,5] have also outlined the difficulties in simulating by numerical models the above highly nonlinear transition branches [4]. The calculation of the actual buckling length of the longitudinal rebars has been deeply investigated in some recent research studies [16] to consider that longitudinal rebars may buckle over a length that is longer than the spacing between two subsequent stirrups. Nonetheless, these studies do not consider the restrain effects due to the concrete cover, even though laboratory tests have shown that the response of the bare rebars is different from that of the rebars embedded in RC members.

In this paper, a new uniaxial material model for steel rebars is presented and calibrated by means of the results of numerical analyses on a refined numerical model, later referred to as the reference rebar model. The proposed model has been implemented in the software OpenSees and calibrated to replicate the cyclic response of steel rebars with different mechanical properties and slenderness ratios in the range from 1 to 30. The proposed model has been validated by comparison with responses of steel rebars tested in laboratory by other researchers and with results of numerical analyses carried out on

the reference model subjected to loading protocols different from those considered in the phase of calibration. Smooth curves are used to characterise the path-dependent uniaxial response, ensuring numerical stability in nonlinear finite element simulations.

## 2 The model of the reference rebar

Data for calibration of the uniaxial material model are obtained from a parametric analysis carried out on a refined model of a bare rebar built by means of the OpenSees computer program. The rebar is discretized into twenty forceBeamColumn elements with three Gauss–Lobatto integration points per element. The cross-section is circular and discretized into ten concentric rings and thirty-six radial sectors.

The mesh size has been selected by means of a preliminary sensitivity analysis so as to obtain an objective response. The uniaxial response of steel is simulated by means of the uniaxial material model Steel02, based on the formulation proposed by Menegotto and Pinto [12]. This latter model has been preferred to the more accurate ReinforcingSteel model, proposed by Kunnath et al. [14] and based on the formulation by Chang and Mander [13], because of its greater numerical stability. The initial geometric imperfection is assumed to be null at the ends of the rebar model and varying linearly within the length of the rebar up to the middle cross-section of the rebar. The geometric imperfection at this latter cross-section ( $i_{ini}$ ) is equal to 1/1000 of the length of the rebar. To reproduce the boundary conditions of laboratory tests, all the degrees of freedom of the end nodes have been fixed with the only exception of the longitudinal degree of freedom at one end of the rebar. This latter degree of freedom has been released to allow the application of the axial displacement loading protocols. The corotational coordinate transformation has been used to account for large displacements. Convergence of the numerical solution has been checked in terms of norm of the displacement increment with a tolerance of 10E-8 over a maximum of 100 iterations. Namely, four algorithms (i.e., Newton–Raphson, ModifiedNewton, KrylovNewton and SecantNewton) have been used in sequence to reach convergence at the single step of the axial displacement history. If convergence has not been achieved with this strategy, the displacement step is divided into smaller steps with a length up to one-fifth of the initial step length.

The numerical reference model is validated by comparison with the responses of 21 specimens tested in laboratory by other researchers. Of these specimens, 9 were tested by Monti and Nuti [1] and are characterised by slenderness ratios between 5 and 11, whereas 12 were tested by Prota et al. [4, 5] and are characterised by slenderness ratios between 5 and 20. As shown in Figure 1, the numerical reference model is able to capture the behaviour of rebars characterised by different slenderness ratios and mechanical properties of steel.

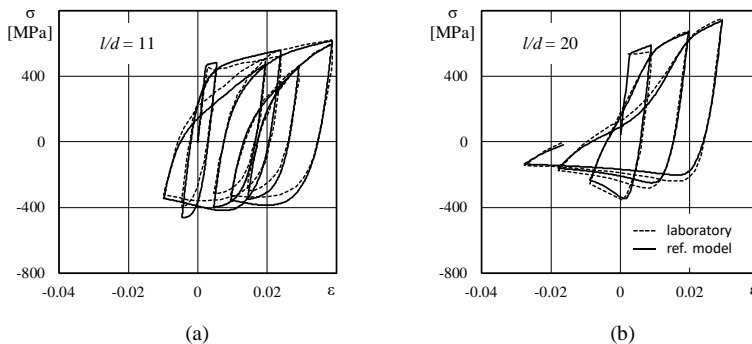


Fig. 1. Comparison between results of laboratory tests and numerical results of the reference numerical model: (a) specimen C1 [1] and (b) specimen R14 [4]

## 3 Response of the reference rebar model

The reference rebar model has been used to simulate rebars characterised by different geometric and mechanical properties. The length  $l$  of the rebar is equal to 24 cm, whereas the diameter  $d$  of the cross-section is calculated so as to obtain ten different slenderness ratios in the range from 1 to 30. The mechanical properties assumed for the reference rebar model are those of rebars used in the past by

other researchers for laboratory tests on RC columns or those of rebars used in Italy in the late 20<sup>th</sup> century. In particular, the yield strength of steel  $f_y$  is in the range from 300 to 600 MPa and the post-yielding modulus  $E_h$  is in the range from 0.002 to 0.008 times  $E_s$  where  $E_s$  is the initial elastic modulus of steel.

The reference model has then been subjected to monotonic and cyclic displacement histories. These latter histories are symmetric or non-symmetric and built to comprehend the behaviour of rebars subjected to cycles of increasing strain amplitudes or local load reversals.

To identify common trends and rules in the responses of the reference rebar model, the axial force of the rebar has been first averaged over the cross-sectional area, the relative axial displacement between the ends of the model has been averaged over the length of the model and the tangent modulus to the average stress strain curve has been calculated as the ratio of the increment of the average stress to the increment of the average strain. Then, the average stress has been normalized to the yield strength of steel  $f_y$ , the average strain has been normalized to the yield strain of steel  $\varepsilon_y$  and the tangent modulus has been normalized to the elastic modulus of steel  $E_s$ . In the following sections of the paper, normalised stress, strain and tangent modulus of the model responses are intended as specified above and indicated as  $\hat{\sigma}$ ,  $\hat{\varepsilon}$  and  $\hat{E}$ , respectively.

The inelastic response of the reference rebar model has been investigated to find trends with specific regard to three normalized parameters, later named fundamental parameters. These parameters are the slenderness ratio  $l/d$ , the normalized strain amplitude  $\Delta\hat{\varepsilon}_{\text{tot}} = (\varepsilon_{\text{max}} - \varepsilon_{\text{min}}) / \varepsilon_y$ , defined as the ratio of the amplitude of the largest strain cycle to the yield strain of steel (Fig. 2) and the asymmetry factor  $\Delta\hat{\varepsilon}_{\text{sh}} = (\varepsilon_{\text{max}} + \varepsilon_{\text{min}}) / (\varepsilon_{\text{max}} - \varepsilon_{\text{min}})$ , defined as the ratio of the difference between the maximum and minimum strains corresponding to the largest strain cycle to the strain amplitude of the largest strain cycle. The latter fundamental parameter varies in the range from  $-1$  to  $1$  as it is normalised to the strain amplitude of the largest strain cycle. In particular,  $\Delta\hat{\varepsilon}_{\text{sh}}$  is equal to  $-1$  if the strain cycles are characterized by only negative strain values,  $\Delta\hat{\varepsilon}_{\text{sh}}$  is equal to  $1$  if the strain cycles are characterized by only positive strain values and  $\Delta\hat{\varepsilon}_{\text{sh}}$  is equal to  $0$  if the strain cycles are symmetric.

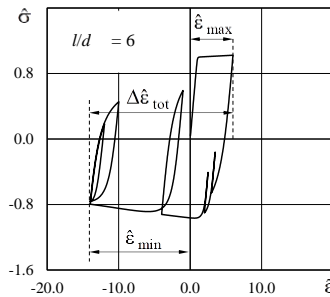


Fig. 2. Fundamental response parameters of the reference rebar model

As expected, the response of the reference rebar model characterised by slenderness ratio equal to 1 does not exhibit any effect from the lateral deflection. Regardless of the value of the asymmetry factor, the response of such a model is equal to the material response. With the increase of the slenderness ratio in the range from 1 to 8, the response of the model shows distinct trends depending on the value of the asymmetry factor of the strain history.

For a slenderness ratio roughly equal to 5, the monotonic response corresponding to an asymmetry factor equal to  $-1$  (Fig. 3a) shows a post-elastic branch that remains almost linear if the ratio of the ultimate to yield strength  $f_u/f_y$  is higher than 1.35 and highlights a slight nonlinear trend with downward concavity for lower values of the above ratio. The response corresponding to cyclic strain protocols shows a higher reduction of strength compared with that resulting from monotonic strain protocols. The transition curves from compression to tension are characterised by a single curvature when developing after the achievement of small to medium values of the normalised strain amplitude and are characterised by two changes in the curvature sign after the achievement of high values of the normalised strain amplitude.



For slenderness ratios from 5 to 8, the monotonic response corresponding to an asymmetry factor equal to  $-1$  usually shows a negative slope of the post-elastic branch. The normalised stress may be as low as about 40% at a strain of 50 times the yield strain. The tangent modulus at the unloading point from the tension backbone curve is equal to the initial elastic modulus, whereas that at the unloading point from the compression backbone curve shows a gradual decrease with the increase of the normalised strain amplitude. This reduction is more pronounced in case of negative asymmetry factors of the strain history. After strain cycles with medium-to-large normalised strain amplitudes, the transition curves from compression to tension highlight two points of contraflexure.

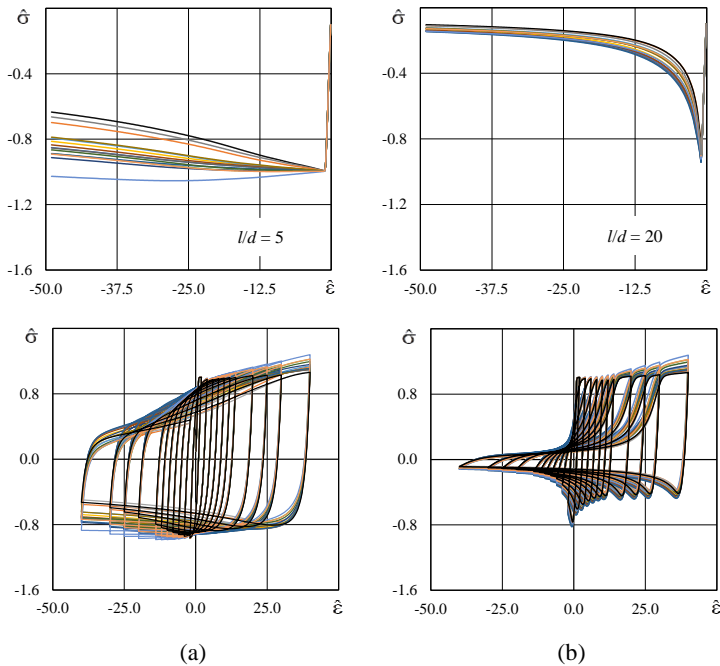


Fig. 3. Response of the reference rebar model: (a)  $l/d = 5$ , (b)  $l/d = 20$

For slenderness factors higher than 8 (Fig. 3b), the monotonic normalised responses of models characterised by different mechanical properties of steel tend to gather along common curves. In particular, the scattering of the normalised responses decreases with the increase of the slenderness ratio. The compression response is characterized by a markedly nonlinear behaviour with a rapid loss of strength, even for low values of the normalised strain amplitude. Again, the tangent modulus at the unloading point from the tension backbone curve is not affected by the lateral buckling and can be assumed equal to the elastic modulus. The tangent modulus at the unloading point from the compression backbone curve, instead, strongly decreases with the increase of the normalised strain amplitude. This leads to a slow recovery of strength, which results in reloading curves characterized by a markedly nonlinear behaviour and two points of contraflexure.

#### 4 The proposed uniaxial material model

Numerical procedures built in Matlab and Microsoft Excel software have been used to identify points of the normalized responses of the reference rebar model corresponding to maximum and minimum strains, loading and unloading points, counterflexure points in transition curves from compression and peak points in transition curves from tension. Strain, stress and tangent modulus of the above points have been fitted by means of linear or nonlinear relations to minimise relative and global errors with regard to all the investigated values of the slenderness ratio. These relations are expressed as a function of the fundamental parameters defined in the previous section.

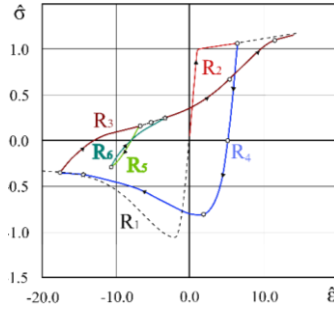


Fig. 4. Rules of the proposed uniaxial material model

Based on the above study, a rule-based uniaxial material model has been formulated and implemented in OpenSees as SteelRebar. The stress-strain response of steel is described by means of six rules, later indicated with the letter “R” and with subscripts from 1 to 6 (Fig. 4). The curves described by the rules are distinguished into backbone curves, transition curves and connection curves. Backbone curves are curves corresponding to monotonically increasing negative and positive strains (rules R<sub>1</sub> and R<sub>2</sub>). Transition curves are loading curves from the points with minimum and maximum strains to the tension and compression curves respectively (rules R<sub>3</sub> and R<sub>4</sub>). Connection curves are curves from a transition curve (or other connection curve) to a backbone curve (rules R<sub>5</sub> and R<sub>6</sub>). The curves described by the rules connect basic points that are later referred to as characteristic points of the response. These points include points corresponding to maximum and minimum strains, loading and unloading points, contraflexure points in transition curves from compression, peak points in transition from tension but also points of connection between curves corresponding to different rules. The characteristic points connected by each rule are reported in Table 1.

Table 1. Rules and characteristic points

Rule	Description	Characteristic points	Notes
R <sub>1</sub>	Compression backbone curve	P <sub>10</sub> - P <sub>11</sub> - P <sub>12</sub> - P <sub>13</sub>	
R <sub>2</sub>	Tension backbone curve	P <sub>max</sub>	
R <sub>3</sub>	Transition curve from compression backbone	P <sub>30</sub> - P <sub>31</sub> - P <sub>32</sub> - P <sub>33</sub>	P <sub>30</sub> ≡ P <sub>min</sub>
R <sub>4</sub>	Transition curve from tension backbone	P <sub>40</sub> - P <sub>41</sub> - P <sub>42</sub> - P <sub>43</sub> - P <sub>44</sub>	P <sub>40</sub> ≡ P <sub>max</sub>
R <sub>5</sub>	Connection curve from tension to compression	P <sub>unl</sub> - P <sub>t</sub>	
R <sub>6</sub>	Connection curve from compression to tension	P <sub>unl</sub> - P <sub>t</sub>	

The parts of the normalised responses between two consecutive characteristic points, later referred to as characteristic curves, are described by means of linear or nonlinear relations. In particular, general relations have been formulated to describe the characteristic curves with either null, simple or double curvature (Fig. 5). The selection of the type of curve (with null, simple or double curvature) depends on the values of the normalised strain, stress and tangent at the starting and ending points of the characteristic curve. The normalised coordinates of the starting and ending points are later indicated as  $(\hat{\epsilon}_{in}, \hat{\sigma}_{in})$  and  $(\hat{\epsilon}_{end}, \hat{\sigma}_{end})$  whereas the normalised tangent moduli are  $\hat{E}_{in}$  and  $\hat{E}_{end}$ . The normalised strain, stress and tangent modulus at the initial and ending points are also required to describe the entire characteristic curve. The relations that describe the characteristic curves are class C1, i.e. they are differentiable and their derivative is a continuous function. This ensures computational efficiency and avoids problems of convergence during the calculation of the response.

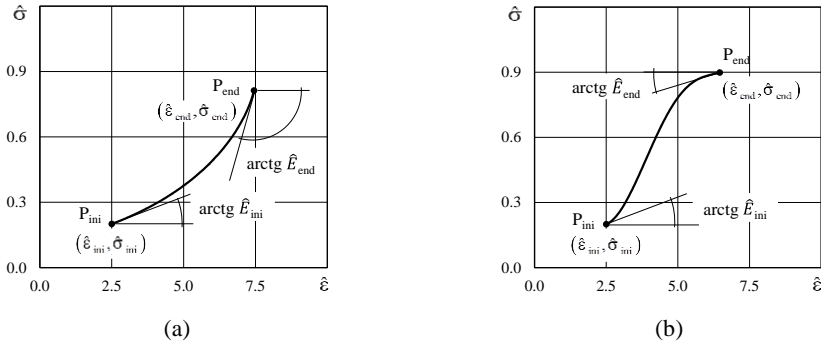


Fig. 5. Basic curves with (a) simple and (b) double curvature

#### 4.1 Compression backbone curve

The compression backbone curve is described by means of four points, named  $P_{10}$ ,  $P_{11}$ ,  $P_{12}$  and  $P_{13}$ . For values of the slenderness ratio higher or equal to 5, the initial values of stress and strain of these points are calculated based on the proposal by Akkaya et al. [9]; for slenderness ratios lower than 5, the stress and strain of the same points are determined by linear interpolation between the values corresponding to slenderness ratios equal to 1 and 5. The compression backbone curve corresponding to a slenderness ratio equal to one is assumed to be coincident with the response of steel, which is given by the Menegotto-Pinto uniaxial material model [12]. The initial values of strain of points from  $P_{10}$  to  $P_{13}$  are later indicated as from  $\hat{\varepsilon}_{10}^*$  to  $\hat{\varepsilon}_{13}^*$ .

The above points of the compression backbone curve are then shifted towards the positive part of the strain axis as a function of the maximum plastic positive strain  $\hat{\varepsilon}_{pl,max}$ . Based on the results of the numerical analyses on the reference rebar model, the strain of points from  $P_{10}$  to  $P_{13}$  of the shifted compression backbone curve is calculated by means of the following relations:

$$\hat{\varepsilon}_{10} = \hat{\varepsilon}_{10}^* + \hat{\varepsilon}_{pl,max} \cdot \min \left[ 0.04 \hat{\varepsilon}_{pl,max}^2, 1 \right] \quad (1)$$

$$\hat{\varepsilon}_{1k} = \hat{\varepsilon}_{1k}^* + 0.5 \cdot \hat{\varepsilon}_{pl,max} \cdot \min \left[ 0.04 \hat{\varepsilon}_{pl,max}^2, 1 \right] \quad \text{for } k=1 \text{ to } 3 \quad (2)$$

To compute the tangent modulus at points  $P_{10}$ ,  $P_{11}$ ,  $P_{12}$  and  $P_{13}$ , these points are first connected by segments which define the multilinear skeleton of the compression backbone curve. Then, the tangent moduli  $E_{1i}$  at points  $P_{1i}$  are assumed equal to the mean values of the secant moduli of the segments of the multilinear skeleton that are adjacent to the point under examination. Once the normalised stress, strain and tangent modulus at points  $P_{1i}$  have been determined, the compression backbone curve is obtained by means of the abovementioned relations with either null, simple or double curvature. The residual normalised stress of the rebar model is always assumed not lower than 0.1.

## 5 Validation of the proposed uniaxial material model

To validate the proposed uniaxial material model, the response of the specimens tested in laboratory by Monti and Nuti [1] and Prota et al. [4, 5] has been compared with the response of the numerical model built by means of the proposed uniaxial material model.

The response of the rebar is obtained by means of a single truss element. The cross-section of the element is circular with an area equal to the equivalent cross-sectional area of the test specimen. The restrains are such as to reproduce the conditions of the test setup. In particular, the transverse displacements and the rotations of the ends of the numerical model are fixed; the longitudinal displacement is fixed at the one end of the model and free at the other end so as to apply the displacement protocol of the laboratory tests.

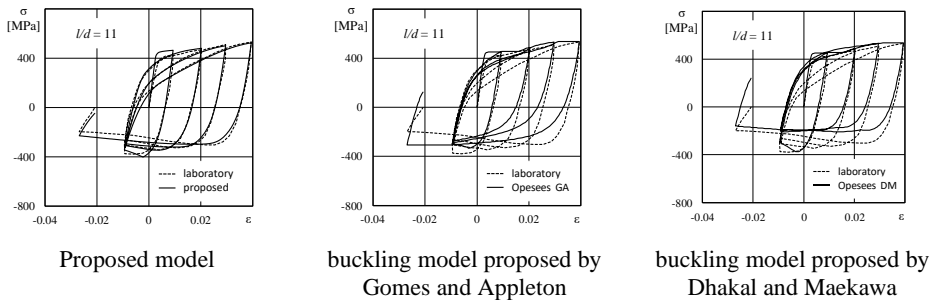


Fig. 6. Comparison between results of laboratory tests carried out by Prota et al. [4, 5] and numerical analyses: specimen R24

To evaluate the effectiveness of the proposed numerical model, the results of the proposed uniaxial material model have been compared with the laboratory results and with the response of the material model named ReinforcingSteel in Opensees. In this latter case, the theory proposed by either Dhakal and Maekawa [10] or Gomes and Appleton [11] has been considered to simulate the lateral buckling effects in the numerical model. As suggested in the online manual of OpenSees the optional parameter  $\alpha$  required for the buckling model proposed by Dhakal and Maekawa is assumed equal to unity, whereas the parameters  $\beta$ ,  $r$  and  $\gamma$  required for the model proposed by Gomes and Appleton are assumed equal to 1.0, 0.4 and 0.5, respectively.

Figure 6 shows some exemplary comparisons between results of numerical models and laboratory tests. The results of the proposed uniaxial material model are in good accord with the experimental data in terms of both compression peaks and transition from the compression backbone curve. A similar satisfactory conclusion cannot be formulated with reference to the uniaxial material model ReinforcingSteel, as the buckling model proposed by Dhakal and Maekawa, and particularly that formulated by Gomes and Appleton, are less accurate in the simulation of the response in compression of the laboratory specimens characterised by moderate-to-high slenderness ratios. Additionally, the transition curves of the model ReinforcingSteel overestimate stress and tangent modulus of rebars with moderate-to-high slenderness ratios.

## 6 Conclusion

The paper proposes a new uniaxial material model to simulate the response of steel bars in reinforced concrete members. The proposed material model incorporates the effects of lateral buckling of rebars into an average strain-average stress uniaxial model. The response is path-dependent and described by means of smooth curves so as to guarantee numerical stability in nonlinear finite element simulations. The model is calibrated against results of refined rebar models characterised by different mechanical properties of steel and slenderness ratios up to 30. The model has been implemented in the OpenSees computer program and validated by comparison with the response of laboratory specimens characterized by different slenderness factors and mechanical properties. To value the accuracy of the proposed model, the response of these laboratory specimens has also been evaluated by means of other uniaxial steel models present in OpenSees.

The numerical analyses performed with the proposed material model have led to the following conclusions:

- the results of the proposed uniaxial material model are in satisfactory accord with the laboratory test results in terms of both compression peaks and transition from the compression backbone curve. This finding is independent of the value of the slenderness ratio in the range of values considered in this paper (i.e. up to 30);
- the results of the uniaxial material model ReinforcingSteel with the buckling model proposed by Dhakal and Maekawa, and particularly with the buckling model formulated by Gomes and Appleton, are less accurate than those obtained by means of the proposed model. This is particularly true

in the simulation of the response in compression and in the transition curves from compression to tension of the laboratory specimens characterised by moderate-to-high slenderness ratios.

## Acknowledgements

The authors thank the ReLUI Consortium as the studies presented here have been carried out as part of the activities envisaged by the Agreement between the High Council of Public Works (CSLLPP) and the ReLUI Consortium implementing Ministerial Decree 578/2020 and Ministerial Decree 240/2022. The contents of this paper represent the authors' ideas and do not necessarily correspond to the official opinion and policies of CSLLPP.

## References

- [1] Monti, G. and Nuti, C. „Nonlinear Cyclic Behavior of Reinforcing Bars Including Buckling“, *Journal of Structural Engineering*, 118(12): 3268–3284, 1992, doi: 10.1061/(ASCE)0733-9445(1992)118:12(3268)
- [2] Restrepo-Posada, J. I., Dodd, L. L., Park, R. and Cooke, N. „Variables Affecting Cyclic Behavior of Reinforcing Steel“, *Journal of Structural Engineering*, 120 (11): 3178–3196, 1994, doi: 10.1061/(ASCE)0733-9445(1994)120:11(3178)
- [3] Rodriguez, M.E., Botero, J.C. and Villa, J. “Cyclic stress-strain behavior of reinforcing steel including effect of buckling“. *Journal of Structural Engineering*, 125(6): 605-612, 1999
- [4] Prota, A., De Cicco, F. and Cosenza, E. “Cyclic behavior of smooth steel reinforcing bars: Experimental analysis and modeling issues“, *Journal of Earthquake Engineering*, 13(4): 500–519, 2009, doi: 10.1080/13632460902837686
- [5] Cosenza, E. and Prota, A. “Experimental behaviour and numerical modelling of smooth steel bars under compression“, *Journal of Earthquake Engineering*, 10(3): 313–329, 2006, doi: 10.1080/13632460609350599
- [6] Yang, H., Wu, Y., Mo, P. and Chen, J. “Improved nonlinear cyclic stress-strain model for reinforcing bars including buckling effect and experimental verification“, *International Journal of Structural Stability and Dynamics*, 16(1): paper 1640005, 2016
- [7] Mau, S. T. and El-Mabsout, M. “Inelastic Buckling of Reinforcing Bars“, *Journal of Engineering Mechanics*, 115 (1): 1–17, 1989, doi: 10.1061/(ASCE)0733-9399(1989)115:1(1)
- [8] Korentz, J. “The Effect of Yield Strength on Inelastic Buckling of Reinforcing Bars“, *Mechanics and Mechanical Engineering*, 14(2): 247-255, 2010
- [9] Akkaya, Y., Guner, S. and Vecchio, F. J. “Constitutive model for inelastic buckling behavior of reinforcing bars“, *ACI Structural Journal*, 116(2): 195–204, 2019, doi: 10.14359/51711143
- [10] Dhakal, R. P. and Maekawa, K. Modeling for Postyield Buckling of Reinforcement, *Journal of Structural Engineering*, 128 (9): 1139–1147, 2002, doi: 10.1061/(ASCE)0733-9445(2002)128:9(1139)
- [11] Gomes, A. and Appleton, J. “Nonlinear cyclic stress-strain relationship of reinforcing bars including buckling“, *Engineering Structures*, 19(10): 822-826, 1997
- [12] Menegotto, M. and Pinto, P. E. “Method of Analysis for Cyclically Loaded R. C. Plane Frames Including Changes in Geometry and Non-Elastic Behavior of Elements under Combined Normal Force and Bending“, Proc. IABSE Symp. Resist. Ultim. Deform. Struct. Acted by Well Defin. Loads: 15–22, 1973
- [13] Chang, G. A. and Mander, J. B. “Seismic energy based fatigue damage analysis of bridge columns: part 1 - evaluation of seismic capacity“, Natl. Cent. Earthq. Eng. Res.: 230, 1994, doi: Technical Report NCEER-94-0006
- [14] Kunnath, S. K., Heo, Y. and Mohle, J. F. “Nonlinear uniaxial material model for reinforcing steel bars“, *Journal of Structural Engineering*, 135(4): 335–343, 2009. [https://doi.org/10.1061/\(asce\)0733-9445\(2009\)135:4\(335\)](https://doi.org/10.1061/(asce)0733-9445(2009)135:4(335))
- [15] McKee, C., Sideris, P. and Hubler, M. “A micromechanical constitutive model for rebar buckling“, *Journal of Structural Engineering*, 149(8): paper 04023105, 2023
- [16] Dhakal, R. P. and Maekawa, K. “Reinforcement stability and fracture of cover concrete in reinforced concrete members“, *Journal of Structural Engineering*, 128(10): 1253–1262, 2002, doi: 10.1061/(ASCE)0733-9445(2002)128:10(1253)

**Concrete and reinforced concrete in  
accidental conditions  
(fire, impact, blast)**



# Thermo-fluid-dynamic simulation of cellulosic fires in precast industrial buildings with vault or shed roof

Bruno Dal Lago<sup>1</sup>, Francesco Rizzo<sup>1</sup>, Paride Tucci<sup>2</sup>

<sup>1</sup>*Department of Theoretical and Applied Sciences,  
Università degli Studi dell'Insubria,  
via Dunant 3, Varese (21100), Italy*

<sup>2</sup>*Professional Fire Safety Engineer,  
Varese (21100), Italy*

## Abstract

Precast concrete industrial buildings are typically characterised by high fire risk due to production or storage of materials/products having high combustion potential, in function of the specific activities carried out in the facility. Due to the large dimensions of these buildings, the accuracy of common simplified and less advanced methods for the determination of the fire-induced demand both in terms of structural performance and safety of occupants and firefighters result far from accurate. Most large industrial buildings rely on many translucent surfaces installed on the roof to let zenithal natural light enter the building, typically made with polycarbonate. Due to the low melting temperature of polycarbonate, these openings can efficiently act as evacuators of smoke and heat, despite they are currently neglected by most practitioners, leading to the installation of mechanical evacuators. This paper presents the results of thermo-fluid-dynamic analyses carried out on archetypal precast industrial buildings with typical arrangement of either vault or shed roof, with the aim to characterise the development of fire within these large compartments and the effectiveness of the natural smoke/heat evacuation provided by melted windows.

## 1 Introduction

Industrial buildings are often more prone to fire exposure with respect to other facilities, mainly since many industrial activities involve production or storage of combustible materials. The design methods currently available in the technical literature consist mainly in simplified approaches assuming nominal fire curves or parametric curves [1], both neglecting the nature of the combustible and the combustion process, and the latter only accounting in a simplified manner for the geometry and physical properties of the compartment structure. More advanced methods include zone models, which may include refined properties of the combustion process. Nevertheless, these methods fail in accurately simulate fire in large compartments, mainly due to the assumption of constant thermo-physical properties in the whole compartment (or zone).

Computational Fluid Dynamic (CFD) analysis can be used as a sophisticated tool for the simulation of fires in such confined environments [2]. Despite the wide skills and multidisciplinary knowledge required by the user, as well as the high computational cost of such analyses, they can be used to accurately simulate realistic fire events with several aims, including: (I) to characterise the fire development; (II) to obtain the temperature time history of the air surrounding compartment and structural elements; (III) to check the evacuation process of occupants and/or the safe operation of firefighters. This further allows to carry out thermal mapping [3] and to predict the resistance of compartment and structural elements [4,5].

This paper presents the results of CFD analyses carried out on archetypal precast industrial buildings provided with either vaulted or shed roofs. The main objective of this research is to analyse the efficiency of the translucent polycarbonate windows installed in the roof as passive evacuators of smoke and heat. Moreover, the simulations allow to derive realistic temperature time histories near the main structural elements, and to derive comments about their difference with respect to the nominal standard ISO834 fire curve [1].



## 2 Case study buildings

The case study buildings are archetypal examples of precast concrete industrial buildings representative of the current production of such structures. These buildings are made with cantilever columns, pre-stressed beams and wing-shaped roof elements [6,7], respectively 12 m, 18 m, and 24 m long. The distance between adjacent roof elements is covered by reinforced concrete vaults (Fig. 1a) or reinforced concrete inclined shed elements supported by a metallic strut (Fig. 1b). To be noted that two lines of vaults are placed at the ends of the shed roof as a standard practice. A total floor area of  $(2 \times 19 + 2) \text{ m} \times (24 + 2) \text{ m} = 988 \text{ m}^2$  is considered in the two models. The clear height from the concrete pavement to the beam intrados is equal to 12 m. Precast concrete panels external to the columns clad the building perimeter. One opening of dimensions 5 m x 3 m is inserted at the middle of each side of the building.

To be noted that the building structures receive light from zenithal windows located in the top of the vault elements or in the shed elements, only. These windows are covered with translucent polycarbonate. Vault windows have individual dimensions of 1.1 m x 0.6 m, for a total of 10.56 m<sup>2</sup> per each vault line. Shed windows are continuous with a total net translucent surface of 21.70 m<sup>2</sup> per each shed line.

The shape of the elements was imported into the graphical interface Pyrosim [8] from an interchange .ifc extension file of a Building Information Modelling (BIM) source.

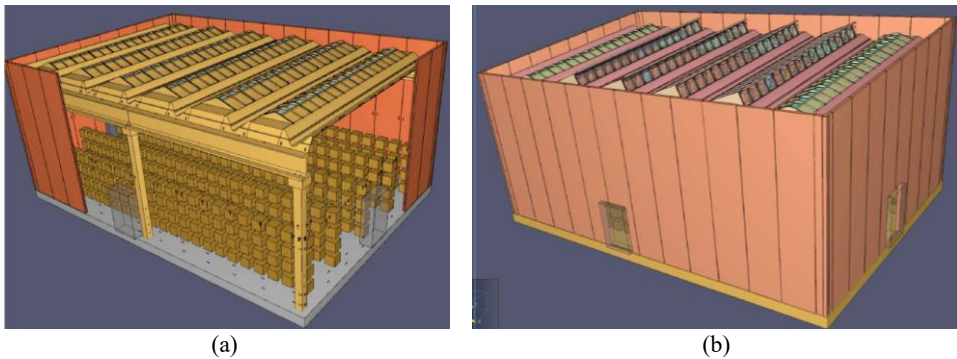


Fig. 1 Case study archetypal precast industrial structures with: (a) vaulted roof; (b) shed roof.

## 3 Numerical models

The thermo-physical properties of concrete structural elements, metallic struts (for shed roof only) and translucent surfaces were attributed to the model. Moreover, all polycarbonate windows were provided with a logic command so that they disappear at the attainment of 150 °C, simulating melting of the polycarbonate. Side openings are assumed constantly open throughout the analysis.

A regular distribution of cellulosic combustible was implemented in the form of cubic boxes of 1 m<sup>3</sup>, distributed simulating an accumulation of piled material beside distributive corridors. The boxes are placed at a relative distance of 0.4 m in vertical and in the horizontal direction parallel to the corridors.

To each side of the boxes, the curve of Heat Release Rate Per Unit Area (HRRPUA) of Fig. 2b was attributed, based on the modification of the experimental HRR curve described in the SPFE handbook [9] found after burning a wood crib with side equal to 1.22 m and height of 1 m below a calorimeter. In particular, the original curve (Fig. 2a) was modified initially adjusting the recorded value over time up to the assumed complete combustion of the crib. This was done with a linear softening branch by imposing to the curve a total fire load of 2521 MJ, based on the evaluation of its integral function. The curve was also adjusted based on the different sides of the model cube with respect to the original test parallelepiped, as well as with respect to the total number of cubes placed over the environment, assuming a specific fire load distribution of about 1600 MJ/m<sup>2</sup>. To be noted that, following Eurocode 2 [1] approach, this would correspond to a characteristic fire performance of 120 min.

One box placed at the bottom level in the centre of the building plan was assumed as fire starter (burner). The fire propagation was left natural, with an ignition temperature of the wood of 245 °C.

Concerning the combustion parameters, a simple chemistry reaction relative to red oak wood was selected, as well as a CO yield parameter of 0.004 and a soot yield of 0.015.

Thermocouple and radiative flux measuring devices were placed along all structural elements, in several points within the environment, and over the polycarbonate surfaces, as previously explained.

The dimension of the mesh in the Fire Dynamics Simulator (FDS) software [10] was selected on the basis of the  $D^*$  criterion [11], resulting in two zones: the bottom zone of the building was meshed with elements with side of 50 cm. The upper zone, where the area of interest as well as of complex geometry for the simulation is located, was meshed with elements having side of 25 cm.

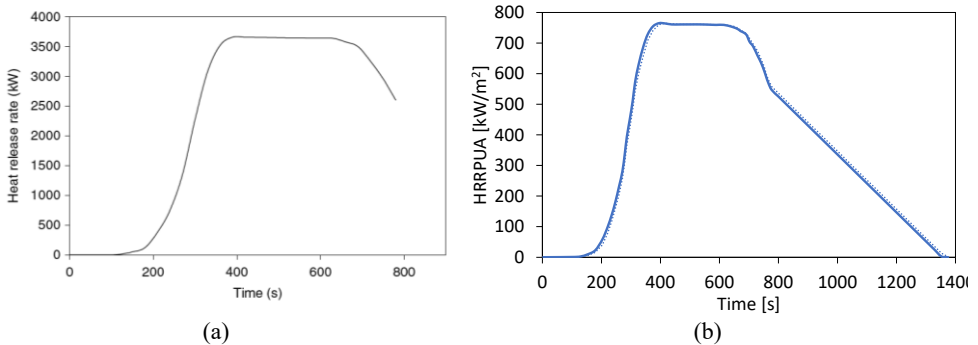


Fig. 2 Wood crib combustible modelling: (a) experimental HRR [9]; (b) HRRPUA attributed to block sides.

#### 4 Results

Computing the analyses required around 2 weeks per analysis on a multi-processor employing 24 cores in parallel. The parallel computing was carried out by attributing a portion of the total mesh to each core processor. A series of preliminary calibration/verification analyses required about another month, which brought to the main result of including the four base openings, which were initially imposed as only one, due to their high influence over the results. A single opening resulted in a fire severely controlled by oxygen supply, thus more conservative with respect to the ones obtained in the final analyses, which according to the authors simulate a more severe though more realistic fire scenario.

Fig. 3 shows the resulting HRR curves. Very high peak HRR was obtained, associated with specific values of about  $950 \text{ kW/m}^2$  and  $1100 \text{ kW/m}^2$ , respectively for vault and shed roof.

The fire progressively propagated from the starter box following the upward curve of the HRR diagrams, attaining a flashover condition after around 2200 s from the ignition for the model with vault roof (Fig. 4a) and soon later for the model with shed roof (Fig. 4b).

The temperature distribution shown in Fig. 5 for an instant of generalised fire shows that, even after flashover occurred, there is a relevant gradient of temperature in the environment. Moreover, a lower temperature in the centre of the building is due to the propagation of fire: the central combustible boxes burnt first, and when flashover occurred, they have a low residual fire load. This effect is typical of propagating (or travelling) fires [12].

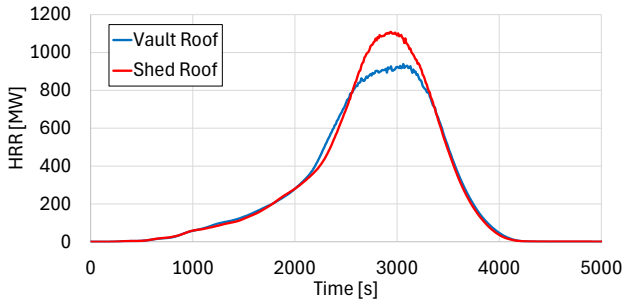


Fig. 3 HRR curves.

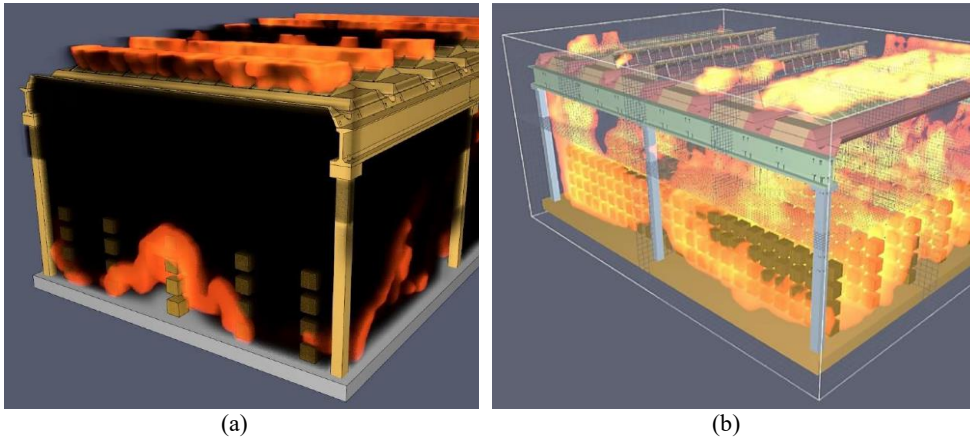


Fig. 4 Flashover phase: (a) vaulted roof (view with smoke); (b) shed roof (view without smoke).

Fig. 5 also clarifies how the smoke/heat evacuation flow differs between the different roof configurations: vaults convey smoke/heat at their top, leading to a vertical dispersion in the outer environment; shed elements create an inclined flow. It is interesting to observe that the smoke/heat flow of the shed elements brings hot gases over the extrados of the reinforced concrete shed elements.

The gas temperature time history near the structural elements is shown in Fig. 6. It is relevant to note that relatively high peak values of temperature were obtained around the main structural elements, in the range of  $900\text{ }^{\circ}\text{C}$  –  $1100\text{ }^{\circ}\text{C}$ . This finding is in line with ISO834 curve, which for 120 min of exposition gives a temperature of  $1045\text{ }^{\circ}\text{C}$ . Nevertheless, the time span of the generalised strong fire is much more limited, shorter than 20 min. This is deemed to be very positive for the behaviour of reinforced concrete structures, which thanks to their low thermal diffusivity are sensible not only to the peak temperature, but especially to the duration of the strong fire.

A different outcome comes from the behaviour of the inclined metallic struts supporting shed elements. As shown in Fig. 6d, their peak temperature is higher, up to  $1250\text{ }^{\circ}\text{C}$ , due to their presence within the main evacuation flow of smoke/heat. Since steel structures are typically more sensible to peak temperature, rather than to the duration of the strong fire, this result highlights their vulnerability.

The efficiency of smoke/heat evacuation passively provided by polycarbonate glazing is shown in Table 1 with reference to typical parameters relevant for the safe evacuation of occupants in terms of time from ignition to measure a temperature higher than  $60\text{ }^{\circ}\text{C}$  and time for smoke accumulation at a height of 2 m above the pavement. The results clearly indicate that shed roof arrangement allows a larger evacuation time, mainly due to the practically double area of melting glazing. Nevertheless, the time allowed even by vault roof configuration allows more time room than what typically needed to evacuate single-storey industrial buildings. To be noted that smoke accumulation is the critical parameter for both roof configurations, despite the temperature parameter allows very slightly larger time room.

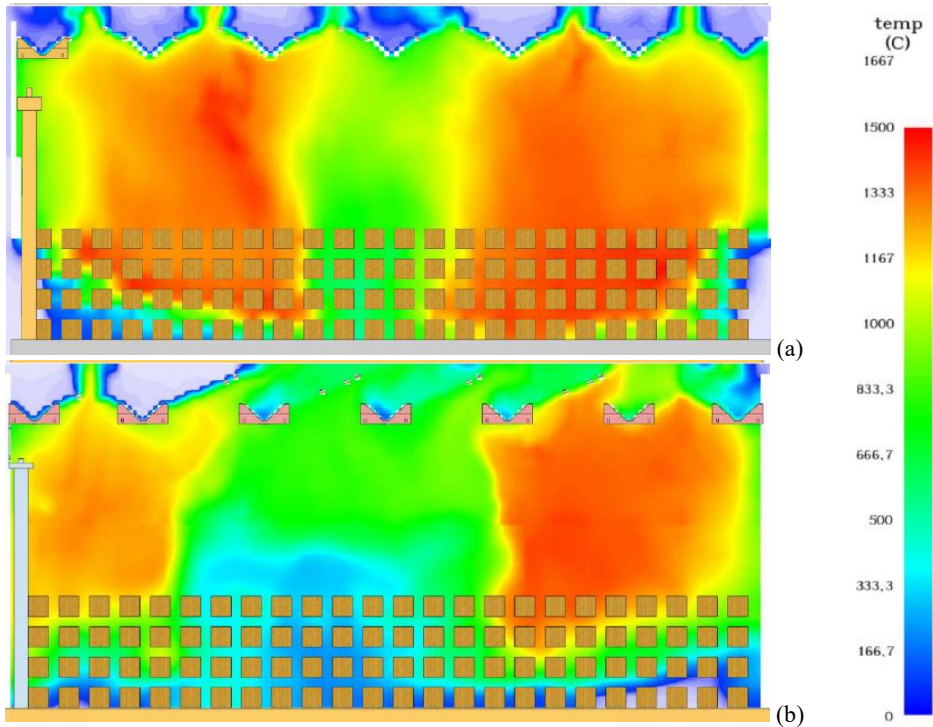


Fig. 5 Temperature over central slice parallel to beams at flashover: (a) vaulted roof; (b) shed roof.

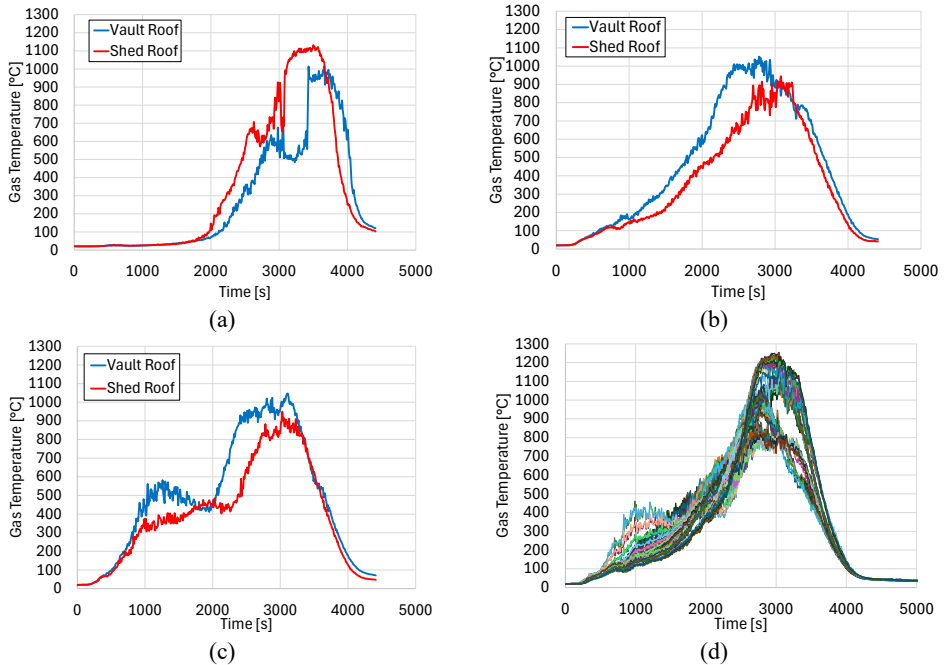


Fig. 6 Temperature distribution over main roof elements: (a) one lateral column top; (b) one beam midspan; (c) the central roof element at midspan; (d) all metallic shed struts.

Table 1 Results of parameters relevant for evacuation.

	Vault Roof	Shed Roof
Time to attain 60°C on ambient thermocouple at 2 m	470-800 s 8-13 min	1600-1950 s 26-32 min
Time for smoke to accumulate down to ~2 m	440-500 s 7-8 min	1325-1500 s 22-25 min

## 5 Conclusions

The CFD analyses allowed to characterise the fire in peculiarly large industrial compartments, identifying large peak temperatures, in line with the equivalent requirement of the nominal standard fire curve, although with much limited duration of the strong fire time span. The efficiency of the passive polycarbonate windows was better with the shed configuration, although in both roof arrangement enough to allow for safe evacuation of occupants. Next research steps will concern differences in building height, fire load, and combustible nature.

## References

- [1] CEN-EN 1991-1-2. 2002. Eurocode 1: Actions on Structures, Part 1-2: General Actions – Actions on Structures Exposed to Fire. European Committee for Standardization, Brussels, Belgium.
- [2] Dal Lago, B., Nicora, A., Tucci, P., and Panico, A. 2023. “Precast concrete industrial portal frames subjected to simulated fire.” *fib Symposium 2023*, Ilki, A., Çavunt, D., Çavunt, Y.S. (eds) Building for the Future: Durable, Sustainable, Resilient. *fib Symposium 2023*, Istanbul, Turkey, 5th-7th June. Lecture Notes in Civil Engineering, 350:13-23. doi: 10.1007/978-3-031-32511-3\_2.
- [3] Bolina, F.L., Dal Lago, B., and Martínez, E.D.R. 2024. “The effect of experimental thermal-physical parameters on the temperature field of UHPC structures in case of fire.” *Construction and Building Materials* 411:134254. doi: 10.1016/j.conbuildmat.2023.134254.
- [4] Dal Lago, B., and Tucci, P. 2023. “Causes of local collapse of a precast concrete industrial roof after a fire event.” *Computers & Concrete* 31(5):371-384. doi: 10.12989/cac.2023.31.5.371.
- [5] Dal Lago, B., and Lo Monte, F. 2023. “Structural performance of a large-span bi-directional partially precast waffle slab system under fire exposure”, Proceedings of *IFireSS2023*, Rio de Janeiro, Brazil, 21st-23rd June, 411-420.
- [6] Dal Lago, B. 2017. “Experimental and numerical assessment of the service behaviour of an innovative long-span precast roof element.” *International Journal of Concrete Structures and Materials* 11(2):261-273. doi:10.1007/s40069-017-0187-6.
- [7] Bosio, M., Di Salvatore, C., Bellotti, D., Capacci, L., Belleri, A., Piccolo, V., Cavalieri, F., Dal Lago, B., Riva, P., Magliulo, G., Nascimbene, R., and Biondini, F. 2023. “Modelling and seismic response analysis of non-residential single-storey existing precast buildings in Italy.” *Journal of Earthquake Engineering* 27(4):1047-1068. doi: 10.1080/13632469.2022.2033364.
- [8] Thunderhead Engineering. 2010 PyroSim: a model construction tool for fire dynamics simulator (FDS). PyroSim User Manual, Rel. 2010.2, Manhattan, USA.
- [9] SFPE Handbook of Fire Protection Engineering, Third Edition. 3rd ed. National Fire Protection Association; Society of Fire Protection Engineers, 2002.
- [10] McGrattan K, McDermott R, Hostikka S, Floyd J, Vanella M, Weinschenk C, and Overholt K. 2017. Fire Dynamics Simulator. NIST Special Publication 1019, 6th Edition.
- [11] USNRC and EPRI. 2007. Verification and Validation of Selected Fire Models for Nuclear Power Plant Applications, Volume 1: Main Report, U.S. Nuclear Regulatory Commission, Office of Nuclear Regulatory Research (RES), Rockville, MD, and Electric Power Research Institute (EPRI), Palo Alto, CA, NUREG- 1824 and EPRI 10 11999.
- [12] Dai, X., Alam, N., Liu, C., Nadjai, A., Rush, D., and Welch, S. 2024. “‘Scaling-up’ fire spread on wood cribs to predict a large-scale travelling fire test using CFD.” *Advances in Engineering Software* 189:103589. doi: 10.1016/j.advengsoft.2023.103589.



# Structural behaviour of reinforced concrete ring tunnels in fire

Bruno Dal Lago and Gaia Casarotto

*Department of Theoretical and Applied Sciences,  
Università degli Studi dell'Insubria,  
via Dunant 3, 21100 Varese, Italy*

## Abstract

The wide use of boring machines for the excavation and casting of galleries brought to the diffusion of reinforced concrete tunnels characterised by axial-symmetric ring cross-sections. Fire is among the most dangerous endogenous threats to the safety of tunnels, due to the high temperature that typically can develop because of the combustion of the diesel oil and gasoline used for the propulsion of trucks and cars, and to the confined geometry of the system. The present paper provides an analytical solution for the structural problem of reinforced concrete ring tunnels, typically resulting from excavation and concreting with boring machines, subjected to fire. Thanks to the axial-symmetry of the case, it can be solved considering a 1D mathematical setting of a sector of the ring. After non-linear transient thermal analysis carried out considering the nominal hydrocarbon temperature-time curve, the thermo-mechanical structural analysis is carried out by plotting the evolution of the moment-curvature diagrams over exposure time through the imposition of sectional equilibrium on the basis of the advanced constitutive laws of steel and concrete provided by Eurocode 2. The structural behaviour of the tunnel is then investigated by parametric analysis considering different concrete thickness, steel reinforcement area, and stiffness of the surrounding ground. The analytical methodology employed in this paper can be rather easily implemented and can be used to drive preliminary design conception and to check advanced solutions from finite element codes.

## 1 Introduction

European tunnels have experienced several accidents involving trucks transporting highly combustible goods, including their fuel and that of the other vehicles involved, such as the Monte Bianco (1999) and Fréjus (2005) accidents (Fig. 1). The structural performance of the tunnels was good enough to avoid tunnel collapse, which would have turned the accidents into tragedies of huge proportions. Nevertheless, concern had arisen about the post-fire performance of the reinforced concrete tunnels, which appeared heavily damaged by localised fire in the inner portion of the gallery, often with phenomena of concrete spalling.



Fig. 1 Pictures after fires developed in the tunnels of: (a) Monte Bianco (1999), and (b) Fréjus (2005).

The structural assessment and design of reinforced concrete tunnels is nowadays typically carried out by means of advanced software programs, able to simultaneously consider the non-linear behaviour of the gallery, the progressive damage induced by the exposure of concrete and steel to high temperatures, and the effect of indirect actions displaying thanks to the geometry of the tunnel and the stiffness of the outer soil [1-4].

This paper explores an alternative methodology for the fast assessment of the structural performance of tunnel linings in fire, based on the solution of equilibrium equations at the level of the tunnel cross-section [5,6]. This formulation is consistent with axial-symmetric cross-sections and loads, for example rings built by boring machines, which nowadays consists in a very diffused construction technique.

The results that can be easily obtained by the proposed analytical formulation can be used also for the assessment of tunnels with non-perfect-axial-symmetric cross-sections, and/or for tunnels where their stress history is necessary to define a non-axial-symmetric initial load condition as well as in case of asymmetric exposure to the temperature of the cross-section [4,7]. In such cases, however, it is strongly suggested to employ the results of the analytical formulation just for a check of the soundness and trend of the results from a finite element refined model.

In the next chapters, the formulation of the proposed analytical method is provided, and the application to a selected case study is shown, followed by a parametric analysis encompassing the thickness of the concrete ring, the reinforcement, and the stiffness of the outer soil.

## 2 Formulation

In case of axisymmetry for geometry, reinforcement and loads, which can be at least simplistically attributed to most reinforced concrete ring cross-sections resulting from TBM bored tunnels, the solution for both the thermal and the mechanical analyses can be set in the form of a monodimensional (1D) problem. This affirmation can be analysed with respect to the peculiar case of ring tunnels.

Fire-induced temperature gradients originated within the tunnel impose to the reinforced concrete cross-section a complex non-linear distribution of thermal strain, which results in a mean curvature, a mean elongation, and a compensating distribution of self-equilibrated longitudinal stress along the thickness of the ring.

As shown in Fig. 2, the thermally-induced curvature would make the tunnel ring bend. Thanks to the axisymmetry of this case, however, bending and distortion induced by uniform curvature are restrained by geometry, and thus indirect bending moments inducing tension on the outer circumferential fibre and compression in the inner display as a compensation of the restrained bending and displacement of the ring.

The effect of the mean thermal elongation highly depends upon the compressibility of the surrounding soil: assuming a very soft soil typical of superficial tunnels would simply lead to the enlargement of the ring diameters, whilst assuming a very stiff soil typical of rocks would hamper the ring extension, thus originating a confinement compressive axial load.

Since both bending moments, axial loads, and compensative self-equilibrated stress distributions are assumed to be constant for the whole ring, a unitary sector of the ring can be analysed and solved, and the results can be extended to the full ring.

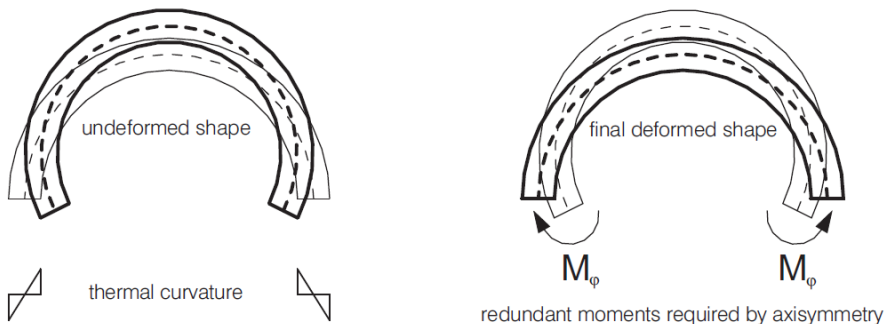


Fig. 2 Genesis of indirect bending actions on a tunnel ring induced by restrained curvature by geometry (courtesy of Prof. P. Bamonte).

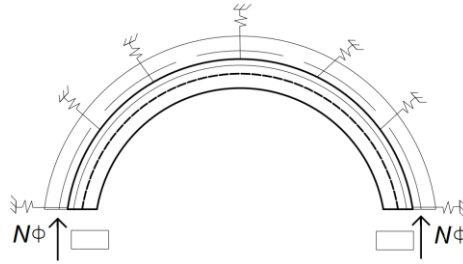


Fig. 3 Genesis of indirect axial compressive actions on a tunnel ring induced by soil confinement.

The unitary sector can hence be solved concerning both thermal and mechanical responses. Moreover, in simple combination of uniaxial bending and compression, the mechanical response will be determined by two equilibrium equations, following Eqs. 1 (translation) and 2 (rotation), accounting for the proper thermally-induced strain.

$$N(\varepsilon_{ctop}, \chi) = \int_0^H \sigma_c \left( \varepsilon(y, \varepsilon_{ctop}, \chi) - \varepsilon_{c\theta}(\Delta\theta_n(y)), \Delta\theta_n(y) \right) b(y) dy + \sum_{i=0}^{n_s} \sigma_s \left( \varepsilon(y_i, \varepsilon_{ctop}, \chi) - \varepsilon_{s\theta}(\Delta\theta(y_i)), \Delta\theta(y_i) \right) A(y_i) \quad (1)$$

$$M(\varepsilon_{ctop}, \chi) = \int_0^H \sigma_c \left( \varepsilon(y, \varepsilon_{ctop}, \chi) - \varepsilon_{c\theta}(\Delta\theta_n(y)), \Delta\theta_n(y) \right) b(y)(y - y_g) dy + \sum_{i=0}^{n_s} \sigma_s \left( \varepsilon(y_i, \varepsilon_{ctop}, \chi) - \varepsilon_{s\theta}(\Delta\theta(y_i)), \Delta\theta(y_i) \right) A(y_i)(y_i - y_g) \quad (2)$$

Where  $N$  is the external axial load;  $M$  is the external bending moment;  $\varepsilon$  is the total longitudinal strain as a function of  $y$ ;  $\varepsilon_{ctop}$  is the longitudinal strain of the top concrete chord;  $\chi$  is the sectional curvature;  $\sigma_c$  is the concrete longitudinal stress;  $\sigma_s$  is the steel longitudinal stress;  $\Delta\theta$  is the temperature gradient;  $n_s$  is the number of steel rebar levels;  $H$  is the total depth of the concrete cross-section;  $y$  is the coordinate through the thickness of the element starting from the external side;  $\varepsilon_{c\theta}$  is the thermal strain of concrete as defined by EC2 law;  $\varepsilon_{s\theta}$  is the thermal strain of steel as defined by EC2 law;  $b$  is the chord width of the concrete cross-section;  $y_g$  is the centre of gravity of the idealised cross-section;  $A$  is the area of the steel rebars for a specific level.

In order to evaluate the mean elongation of the cross-section, a weighed strain was considered as per Eq. 3.

$$\varepsilon_{mean} = \frac{\int_0^{H_{tot}} \varepsilon_{cT}(\Delta T(y)) * b(y) dy}{\int_0^{H_{tot}} b(y) dy} \quad (3)$$

### 3 Case study

A benchmark case study was selected with the aim to characterise the behaviour of a realistic ring tunnel in fire. For this purpose, the typical cross-section of a tunnel currently under construction in Italy was selected. It represents an example of a rather large ring tunnel, both concerning diameter (14 m internal) and thickness (1.2 m). The tunnel ring is reinforced with two uniformly-distributed annular layers of  $\Phi 24$  rebars placed at 200 mm of spacing with 5 cm of gross cover (to the rebar axis) from both internal and external edges. Concrete class is C28/35, and reinforcement steel grade is B450C. To be noted that the tunnel is not provided with fire protectives, as typical. Polypropylene microfibres are



assumed to be included in the concrete mix in order to reduce the probability of thermal spalling [8,9].

In order to extend the results to general cases, a parametric analysis was conducted concerning lower thickness (1 – 0.8 – 0.6 m) and, for the case of minimum thickness, lower reinforcement ( $\Phi 20$  –  $\Phi 16$  –  $\Phi 12$  with same spacing and cover).

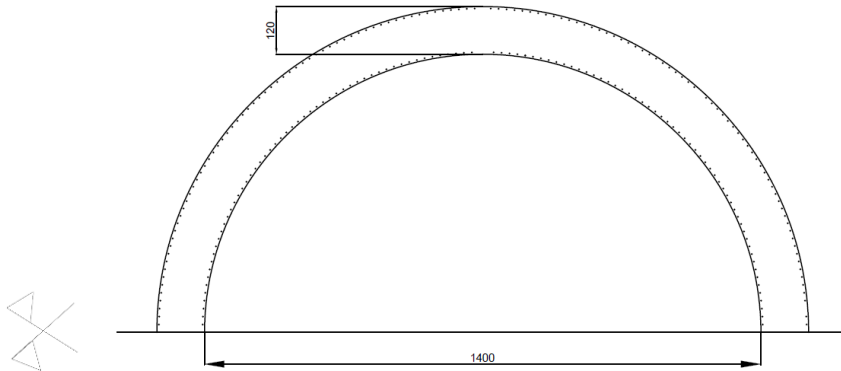


Fig. 4 Case study benchmark ring tunnel cross-section.

#### 4 Thermal analysis

Based on the thermal properties of concrete as provided in EN1992-1-2:2004 (Eurocode 2 part 1-2) [10], the thermal fields shown in Fig. 5 are calculated assuming different time exposures to the nominal hydrocarbon curve following EN1991:2004 (Eurocode 1) [11]. A preliminary analysis clearly showed that, considering the thickness of the case study ring tunnel of 1.2 m, the thermal modelling of the soil behind the tunnel would not be required, since the thermal wave would only affect a limited portion of the tunnel ring thickness, as confirmed by the results shown in Fig. 5.

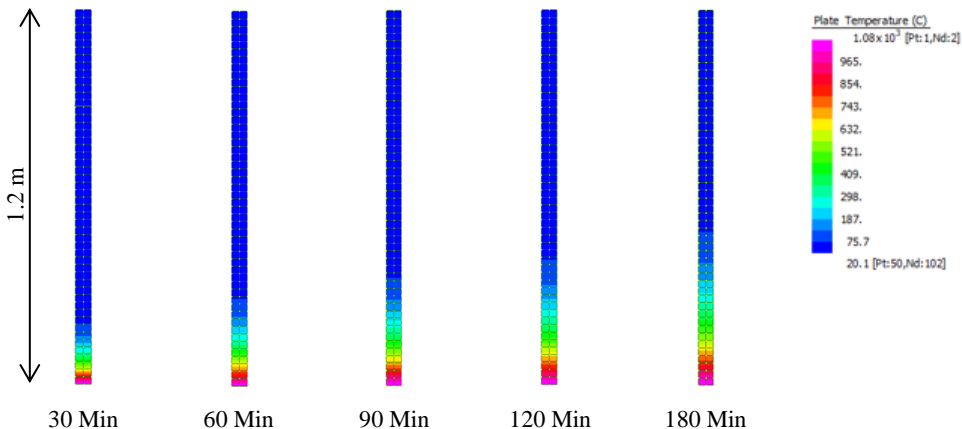


Fig. 5 Thermal field along the thickness of the tunnel ring for different time exposures to the nominal hydrocarbon fire curve.

## 5 Mechanical analysis

Based on the mechanical stress-strain non-linear properties of concrete and mild steel as provided in EN1992-1-2:2004 (Eurocode 2 part 1-2), non-linear moment-curvature diagrams can be obtained by solving the equilibrium system shown in Eq. 1 and Eq. 2 with reference to translation and rotation, respectively.

Non-linear moment-curvature diagrams are shown in Fig. 6 with reference to a ring sector section and to an equivalent rectangular cross-section having the mean width of the ring sector, when subjected to an exposure to the nominal hydrocarbon curve of 120 minutes and assuming an ideally deformable soil. Bending of the cross-section with tension applied to the inner circumferential chord of the tunnel is depicted in the first (positive) quadrant. Thus, bending with tension applied to the outer circumferential chord of the tunnel is depicted in the third (negative) quadrant. Despite the symmetry of reinforcement, the behaviour is strongly asymmetric: in positive bending the thermal damage to the rebars induced by heat lowers the resistance and amplifies the deformability of the cross-section, while negative bending is characterised by a much stronger cracking moment associated with the attainment of the tensile strength of the outer undamaged concrete chord, and plasticisation of the outer rebar layer occurs rather soon after cracking, with a ductile trend. Note that in the diagram the point of origin of the curvature does not coincide with the point of zero bending moment. This is due to the indirect effect of the restrained thermal curvature, which induces a negative moment. This condition of null curvature corresponds to the expected performance point.

$$N(\varepsilon_{ctop}, \chi) = \int_0^H \sigma_c(\varepsilon(y, \varepsilon_{ctop}, \chi) - \varepsilon_{c\theta}(\Delta\theta(y)), \Delta\theta(y)) b(y) dy + \sum_{j=0}^{n_s} \sigma_s(\varepsilon(y_{sj}, \varepsilon_{ctop}, \chi) - \varepsilon_{s\theta}(\Delta\theta_{sj}), \Delta\theta_{sj}) A_{sj} \quad (1)$$

$$M(\varepsilon_{ctop}, \chi) = \int_0^H \sigma_c(\varepsilon(y, \varepsilon_{ctop}, \chi) - \varepsilon_{c\theta}(\Delta\theta(y)), \Delta\theta(y)) b(y) (y - y_g) dy + \sum_{j=0}^{n_s} \sigma_s(\varepsilon(y_{sj}, \varepsilon_{ctop}, \chi) - \varepsilon_{s\theta}(\Delta\theta_{sj}), \Delta\theta_{sj}) A_{sj} (y_{sj} - y_g) \quad (2)$$

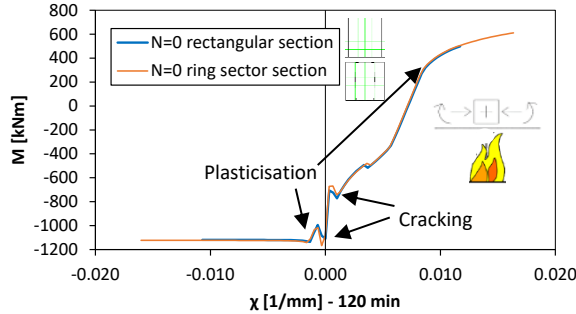


Fig. 6 Moment-curvature non-linear diagrams for benchmark rectangular and ring sector cross sections.

The maximum axial load that the ring tunnel cross-section can be subjected to can be evaluated on the basis of the fully hampered ring elongation by imposing the general mean elongation as per Eq. 3 null. Based on the equivalent rectangular cross-section, Eq. 3 simplifies by assuming the variable chord width  $b(y)$  constant as  $b$ , taking these terms out of the integrals and simplifying the denominator in  $H_{tot}$ .

$$\varepsilon_{mean} = \frac{\int_0^{H_{tot}} \varepsilon_{cT}(\Delta T_m(y)) * b(y) dy}{\int_0^{H_{tot}} b(y) dy} \quad (3)$$

The structural performance of the benchmark ring tunnel is well represented by the nonlinear moment-curvature and stress diagram in Fig. 7 and Fig.8, respectively.

From the moment-curvature diagrams, it can be clearly seen that the positive moment curves (tensioned reinforcement exposed to fire) are subjected to relevant decay along with the exposure to the fire, due to the decay of the rebar steel properties. For higher exposures, the curves also tend to become more deformable. Contrarily, in condition of negative moment, the decay of the concrete mechanical properties of the inner ring chords appears to only marginally influence the moment-curvature diagrams, both in terms of resistance and of trend. For all the curves, axial loading appears being beneficial, since also in its maximum value  $N_{max}$  associated to fully constrained ring (stiff rocky surrounding soil) both cracking and resisting moment appear larger than in the case with null axial load (soft landfill surrounding soil).

Analysing the stress tendency, it can be observed that the thermal loading induces a stress wave close to the exposed surface, which tends to displace through the ring thickness with time. The wave presents an irregularity in correspondence of the position of the inner reinforcement. The inner exposed chord results subjected to low axial stress, since its mechanical properties result very rapidly damaged by the exposure to the high temperatures. The peak compressive stress is slightly lower than 12 MPa, compatible with the concrete resistance. It can be clearly seen from the diagrams that the thermal stress wave is compensated by the tensile stress active in the outer larger portion of the ring. Considering this, the effect of a compressive axial force, for instance induced by indirect action, results highly beneficial since it subtracts the concrete of this area from being tensioned, leaving practically identical the compressive stress wave. In case the ring elongation is fully hampered, the concrete not interested by the stress wave results unstressed, i.e. the compressive wave is exactly equilibrated by the indirect axial action.

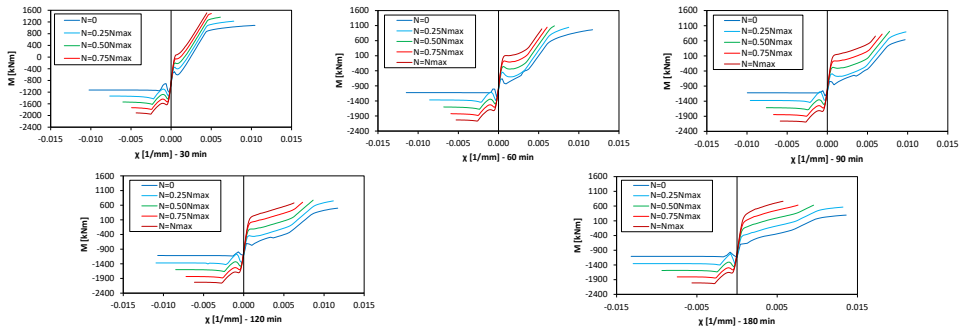


Fig. 7 Moment-curvature non-linear diagrams for the benchmark (1.2 m thick) cross section following different exposure time and axial load.

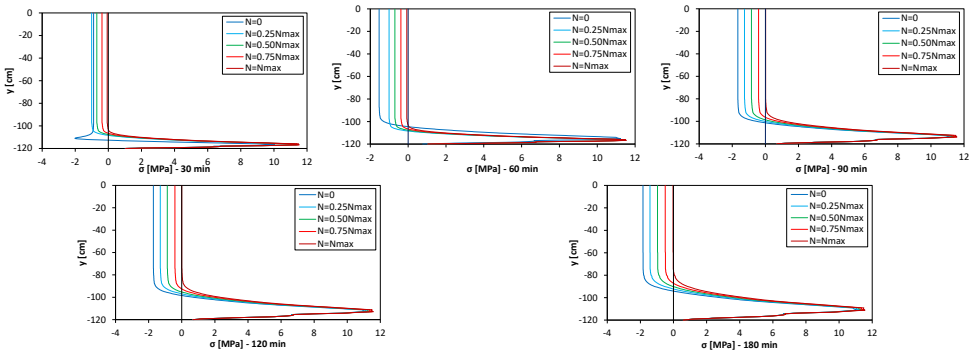


Fig. 8 Stress distribution along the ring thickness for the benchmark (1.2 m thick) cross section following different exposure time and axial load.

## 6 Effect of thickness reduction

The effect of a reduction of the lining thickness can be observed in the moment-curvature and stress diagrams reported in Fig. 9. In terms of bending moment-curvature performance, it can be clearly observed how the curves tend towards a less resisting and more deformable structural behaviour.

In terms of stress, the behaviour of the ring tunnels with thickness of 100 cm and 80 cm is very similar to the benchmark case. The case with thickness of 60 cm presents a peculiarity: for low exposure time, in the case of null axial load cracking occurs behind the compressive stress wave; moreover, cracking occurs for all axial load cases when analysing the response under exposure times of 120 and 180 minutes. In these conditions, where concrete fails in tension and the cross-section cracks, the tensile load resultant is provided by the tensioned rebars located near the outer chord of the tunnel ring. However, cracking has a beneficial effect, reducing the amplitude of the compressive stress wave: by reducing its bending stiffness, the tunnel ring subtracts itself from the indirect bending load.

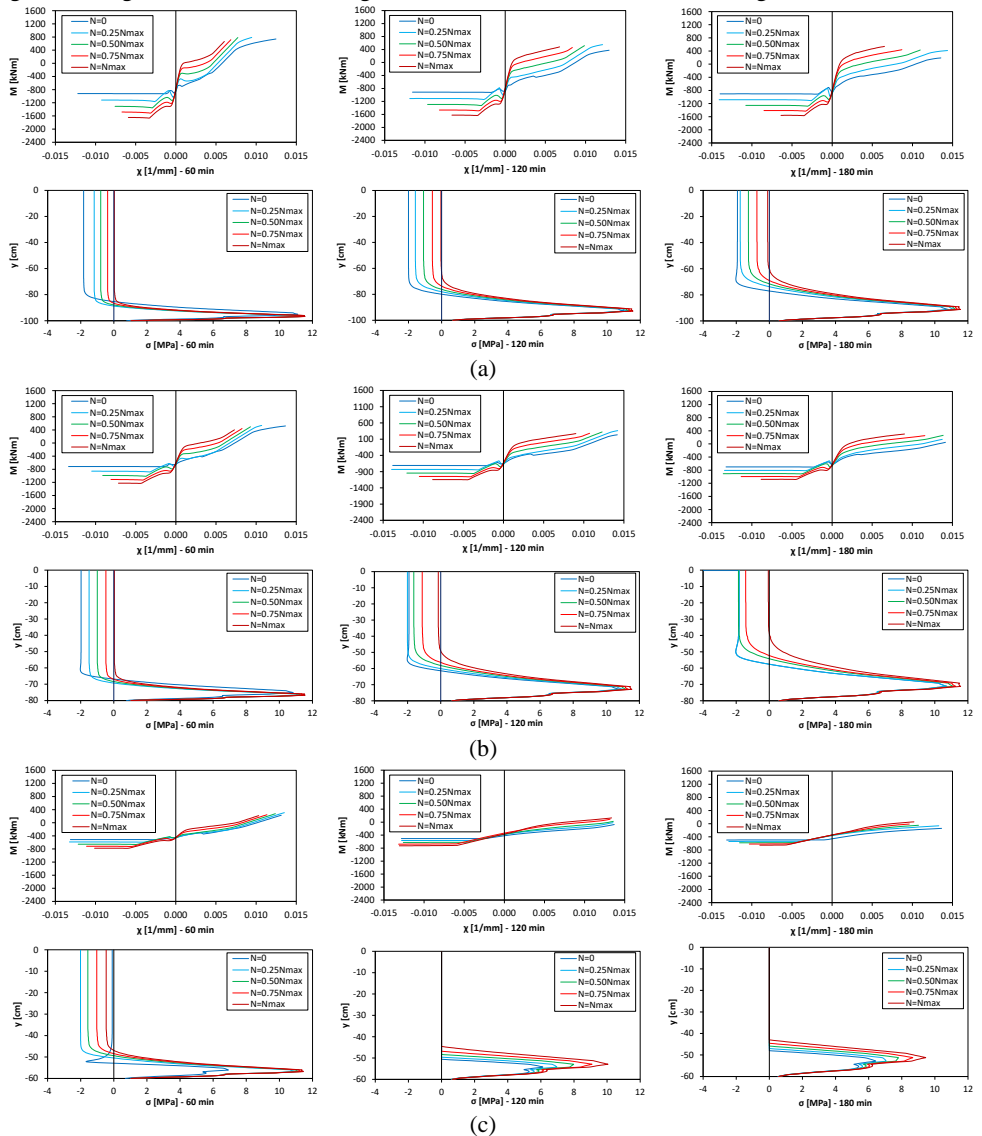


Fig. 9 Moment-curvature and stress non-linear diagrams following different exposure time and axial load for the cross sections with depth of: (a) 100 cm; (b) 80 cm; (c) 60 cm.

## 7 Effect of reinforcement

The effect of reinforcement ratio was parametrically investigated by investigating by adopting different bar diameters instead of different bar spacings. Only the cross-section with lower thickness of 60 cm was studied, since negligible effects are to be expected if analysing larger thicknesses, due to the hampered cracking of the outer concrete chords and the subsequent low contribution of reinforcement.

The results shown in Fig. 10 show the strong dependency of the negative moment resistance upon the rebar diameter. In particular, for all the diameters lower than  $\Phi 24$  (benchmark), for an exposure of 60 minutes the cracking moment results larger than the plateau branch associated with plasticisation of the rebars. Moreover, the performance point (zero curvature) results very close to the full plasticisation condition. This condition is deemed not to be critical, since indeed the demand is an indirect load which acts mainly in terms of imposed strain, rather than load. This is also observed in terms of reduction of the compressive stress wave amplitude, which lowers when cracking occurs. Thus, the ductility ensured by steel rebars results the main instrument to ensure a robust performance in fire. This lesson is deemed to be dealt within the potential application of fragile reinforcement, such as mineral composites [12,13].

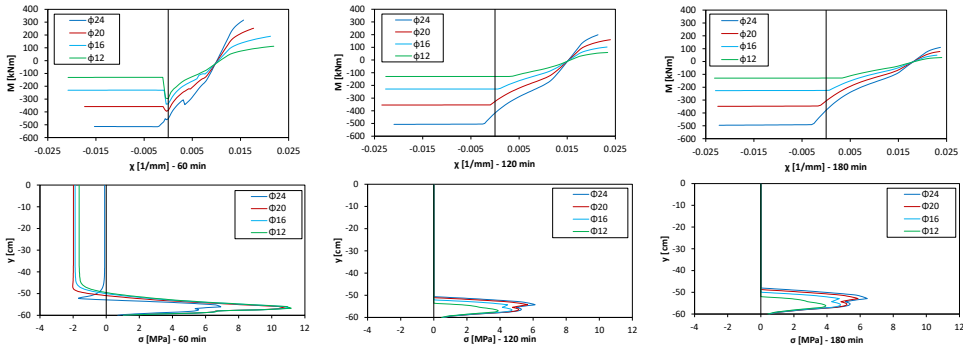


Fig. 10 Moment-curvature and stress non-linear diagrams following different rebar diameter and exposure time for the cross sections with depth 60 cm under null axial load.

## 8 Effect of indirect actions and soil-induced confinement

The effect of indirect actions and ground confinement was already taken into account implicitly in the previous sections by considering the structural behaviour of the ring tunnel as a function of a fraction of the maximum axial load, obtained in the condition of hampered ring expansion. This chapter is aimed at providing a direct correlation between the considered fraction of axial indirect action and the deformability of the surrounding soil. The solution of the problem is based on 3 parameters: (i) the increased outer diameter  $\Delta\varphi$  of the ring tunnel induced by expansion; (ii) the indirect axial load  $N$ ; (iii) the soil Winkler coefficient  $K_w$ .

In particular, the axial load can be written both as a function of the diameter elongation and of the axial stiffness of the ring  $EA$  as a function of the temperature  $\theta$  following equilibrium as per Eq. 4.

$$N = K_w * \Delta\varphi = N_{max} - EA_{\theta} * \frac{\Delta\varphi}{\varphi_{in}} \quad (4)$$

Rearranging the terms, the unknown Winkler coefficient can be obtained as a function of the imposed axial load following Eq. 5.

$$K_w = \frac{N}{N_{max} - N} * \frac{EA_{\theta}}{\varphi_{IN}} = \frac{1}{\frac{N_{max}}{N} - 1} * \frac{EA_{\theta}}{\varphi_{IN}} \quad (5)$$

where the axial stiffness of the ring section can be written including the effect of the thermally-induced damage as per Eq. 6.

$$EA_{\theta} = \int_0^{H_{tot}} Ec(\theta) * b(y)dy + \sum_{i=0}^{ns} Es(\theta) * Asi \quad (6)$$

The resulting equivalent Winkler coefficients are shown in Fig. 11 as a function of the thickness of the ring tunnel and of the fraction of maximum axial load.

Red curves are associated with high values of Winkler coefficient, typical of rocky soil, while light blue curves are associated with deformable soil, compatible with compact gravel soil. Green curves lie in between. It can also be observed that the curves associated with low Winkler coefficient are almost flat, meaning that there is negligible dependency upon the fire exposure time. On the contrary, red curves show a non-negligible variability which suggests that the soil stiffness influences the behaviour of the ring tunnel in fire non-linearly along with the fire exposure time.

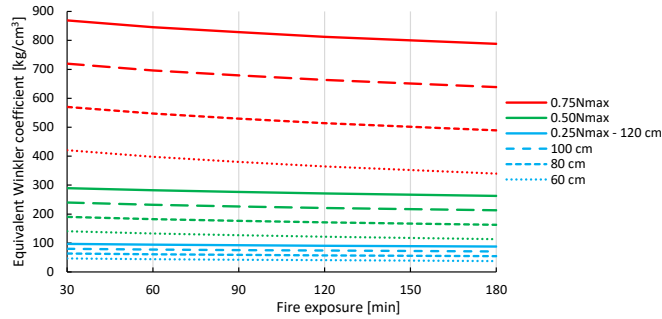


Fig. 11 Equivalent Winkler coefficient following different ring thickness and percentage of maximum axial load.

## 9 Conclusions

Thanks to its low thermal diffusivity, concrete delays heat transfer at high temperature even after several dozens of minutes of exposure to the considered hydrocarbon nominal fire curve, making unnecessary the thermal modelling of the outer soil even for the considered case of maximum exposure (180 min) associated with lower thickness (60 cm).

The fire induces indirect actions in terms of both bending moments, due to the axisymmetry of the problem, which stress in tension the outer concrete portion of the ring protected from the temperature rise, and axial compression stresses in function of the deformability of the surrounding soil.

The effect of fire over the reinforced concrete ring displays as a compressive stress wave which progressively spreads across the ring thickness, with peak values comprised within 6 and 12 MPa. Near the exposed surface, the stress wave tends to zero because of the mechanical degradation of the concrete exposed to very high temperatures.

In all the analysed cases with thickness larger than 60 cm, cracking did not occur in the outer portion of the ring. Moreover, for those cases characterised by lower thickness of 60 cm associated with scarce soil stiffness, where cracking was attained, the resistance of the tunnel resulted robustly ensured by the ductile deformation of the steel rebars, able to fully withstand the plastic strain induced by self-equilibrated thermal stress.

## Acknowledgements

Prof. Patrick Bamonte from Politecnico di Milano is kindly acknowledged for his suggestions concerning the formulation of the effect of deformable soil.

## References

- [1] ANAS. 2006. Linee guida per la progettazione della sicurezza nelle gallerie stradali.
- [2] Carvel R., and Beard, A.N. 2005. The handbook of Tunnel Fire Safety.
- [3] Maraveas C., and Vrakas A.A. 2014. "Design of concrete tunnel linings for fire safety." *Structural Engineering International* 24(3):319–329.
- [4] Stucchi R., and Amberg F. 2020. "A practical approach for Tunnel Fire Verification." *Structural Engineering International* 30(4):515–529.
- [5] Lo Monte F., and Bamonte P. 2022. "Simplified Approach for the Evaluation of the Bearing Capacity of Deep R/C Tunnels Exposed to Fire." Paper included in the proceedings of the 12th International Conference on Structures in Fire – SiF2022 and presented in Hong Kong, November 30 – December 2.
- [6] Lo Monte, F., and Bamonte P. 2023. Fire performance of r/c and frc tunnels exposed to fire: Comparison between linear and non linear analyses via a simplified 1D approach." Paper included in the proceedings of the International Fire Safety Symposium – IFireSS2023, and presented in Rio de Janeiro, Brazil, June 21–23.
- [7] Lo Monte F., Bamonte P., and Beltrami, C. 2023. "Study on the effects of cooling phase and construction technology on the fire performance of RC tunnels." *Tunnelling and Underground Space Technology* 132:104838.
- [6] Lo Monte F., Felicetti R., Meda A., and Bortolussi A. 2019. *Explosive spalling in reinforced concrete tunnels exposed to fire: Experimental assessment and numerical modelling*. In: "Tunnels and Underground Cities. Engineering and Innovation Meet Archaeology, Architecture and Art." CRC Press:9780429424441.
- [8] Maluk C., Tignard J., Ridout A., Clarke T., and Winterberg R. 2021. "Experimental study on the fire behaviour of fibre reinforced concrete used in tunnel applications." *Fire Safety Journal* 120:103173.
- [9] Lo Monte F., Felicetti R., Meda A., and Bortolussi A. 2019. "Assessment of concrete sensitivity to fire spalling: A multi-scale experimental approach." *Construction and Building Materials* 212:476–485.
- [10] EN 1992-1-2:2004. Eurocode 2 - Design of concrete structures - Part 1-2: General rules – Structural fire design. European Committee for Standardization (CEN), Brussels (Belgium).
- [11] EN 1991-1-2:2002. Eurocode 1 – Actions on structures - Part 1-2: Actions on structures exposed to fire. European Committee for Standardization (CEN), Brussels (Belgium).
- [12] Spagnuolo S., Meda A., Rinaldi Z., and Nanni, A. 2017. "Precast concrete tunnel segments with GFRP reinforcement." *Journal of Composites for Construction* 21(5):04017020.
- [13] Spagnuolo S., and Meda, A. 2024. "Precast CSA-based concrete tunnel lining segments reinforced with GFRP bars: Challenges and opportunities." *Construction and Building Materials* 425:136007.

# Structural robustness of reinforced concrete moment resisting frames: deterministic and reliability assessment

**Elena Miceli<sup>1</sup>, Diego Gino<sup>1</sup>, Gabriele Neri<sup>1</sup>, Gaetano Alfano<sup>1</sup>, Luca Giordano<sup>1</sup> and Paolo Castaldo<sup>1</sup>**

<sup>1</sup> Dipartimento di Ingegneria Strutturale, Edile e Geotecnica (DISEG),  
Politecnico di Torino,  
Corso Duca degli Abruzzi 24, 10129 Turin, Italy

## Abstract

This work describes the robustness evaluation of a 2D reinforced concrete moment resisting frame designed in a highly seismic area. In detail, the loss of the central column at the ground-storey level is assumed to trigger the progressive collapse of the frame. At first, a deterministic analysis is elaborated by modelling the frame in the finite element software (FEM) ATENA 2D and performing non-linear pushdown analyses. These analyses consist in applying an increasing vertical displacement in the point of column removal and registering the corresponding reaction. By means of the derived displacement-reaction curves, the capacity of the structure against the removal of the supporting column is studied. Then, a full probabilistic approach is adopted, by sampling 100 different realizations from both material and load properties to evaluate the reliability of the frame. By performing static equivalent non-linear analyses (i.e., amplifying the gravity loads according to properly calibrated dynamic amplification factors) the probability of failure in different cross-sections of the structure is computed. The results demonstrate the lacking safety level associated to the frame under a progressive collapse scenario.

## 1 Introduction

Dramatic events like the terrorist attack of 2001, which caused the total collapse of the Twin Towers and resulted in thousands of fatalities, represented a shock for the entire community. In recent decades, such catastrophic events impacting strategic structures have prompted architecture, engineering and construction experts to focus increasingly on structural robustness. European codes [1]-[5] have incorporated specific sections addressing structural robustness with guidelines and general requirements. International guidelines [6]-[9] have further explored the concept of extreme actions and their consequences on structures, making it clear that risk analysis should be part of strategies for preventing collapses from low-probability high-consequence (LPHC) events, aiming to find socially acceptable and technically feasible solutions [10]-[13].

Quantitative risk analysis in probabilistic terms can reliably assess the safety level associated with LPHC events by incorporating uncertainties in engineering issues [14]-[17]. For instance, [18] details a sensitivity analysis to compute the bearing capacity of various reinforced concrete (RC) structural members when a central supporting element is removed. Fragility analyses in [19] compute the exceedance probability of different damage states for low-rise RC buildings in a column loss scenario. Global variance-based sensitivity analysis is used in [20] to identify major sources of uncertainty in the response of RC structures to sudden column loss. A reliability-based index of structural collapse for 2D linear elastic truss systems is computed in [21], using random sampling of loads and strengths. The reliability of RC frames under different column-loss scenarios is investigated in [22] identifying side column-loss scenarios as the worst case if infill walls are not considered.

This study evaluates the structural reliability of 2D RC MR frames, focusing on the accidental loss of the central supporting column. Initially, a deterministic approach is adopted to assess the frame's bearing capacity. The frame is modeled in nonlinear finite element (NLFE) software, using mean values of mechanical properties, and a displacement-controlled pushdown analysis is conducted by removing the supporting column and applying an increasing vertical displacement.

Following this, a full probabilistic approach is applied, sampling 100 realizations for various basic random variables related to both material properties and external loads, accounting for their statistical



correlations. Preliminary simulations are finalized to compute Dynamic Amplification Factors (DAFs) which are then used in probabilistic equivalent static NLFE analyses to simulate the column removal and to amplify loads on adjacent spans due to dynamic effects. The output of these analyses were strains at sections close to beam-column nodes, distinguishing between confined concrete and reinforcement. Convolution integrals between these strains and ultimate strain distributions are used to determine failure probabilities concerning the ultimate limit state (ULS). Results highlight the need for improved design strategies to enhance the robustness and reliability of structures against such critical scenarios.

## 2 Case study and finite element modelling

The basis of this work is the design of a 2D multi-story RC MR frame that is regular in elevation and symmetrical. This structure consists of four floors and a roof, each with an inter-story height of 3 meters, and four spans, each having 5 meters in length. The width of the spans in transverse direction is also 5 meters, as shown in Figure 1 (left). Located in L'Aquila, Italy, the structure is designed to meet a high ductility class according to [3]-[4]. The materials specified are B450C steel for the reinforcing bars and C25/30 concrete with a clear concrete cover of 3.5 cm for all structural elements [3]-[4].

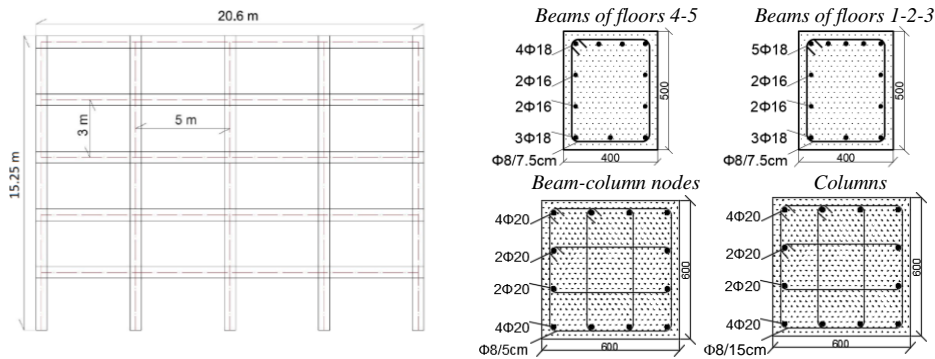


Fig. 1 Characteristics of the frame under investigation: front view (left), reinforcement detailing of the structural elements in the most stressed sections (right).

To define the geometry and reinforcement, both static and modal analyses were conducted, adhering to ultimate limit states (ULSs), serviceability limit states (SLSs), and the capacity design principles for seismic verifications in all structural elements. Figure 2 (right) shows the reinforcement details:  $\phi 18$  longitudinal bars and  $\phi 8$  stirrups for all structural components. All the beams have cross-sections measuring  $40 \times 50 \text{ cm}^2$ . The transverse reinforcement in the beams includes 2-leg  $\phi 8$  stirrups, spaced at 10 cm in the dissipative zones and at 15 cm in the central zones of the spans, for all floors, with the dissipative zones extending 100 cm from the beam-column nodes. Columns have cross-sections measuring  $60 \times 60 \text{ cm}^2$ . The longitudinal reinforcement consists of  $12 \phi 20$  bars, symmetrically arranged in both directions, and the shear reinforcement is composed of 4-leg  $\phi 8$  stirrups, spaced at 10 cm throughout the column length, except at the beam-column joints where the spacing is reduced to 5 cm.

The FE models of the three frames were developed using the FEM software ATENA 2D [23], employing four-node quadrilateral iso-parametric plane stress finite elements based on linear polynomial interpolation. The element sizes ranged from 0.05 to 0.1 meters, determined through an iterative process for numerical accuracy. The nonlinear system of equations was solved using the standard Newton-Raphson iterative procedure, assuming a linear approximation, with a maximum of 2000 iterations.

For the behavior of concrete in compression, the pre-peak stress behavior is based on the formula from CEB-FIP Model Code 90 [24], while the post-peak response is modeled with a linearly descending branch, incorporating local strain softening. The characteristics of the response in compression in terms of elastic modulus, the peak stress and strain as well as the ultimate strain were assumed including the confinement effects according to the Saatcioglu and Razvi model [25]. The reduction in compressive strength due to cracking is taken as 0.4, consistent with [26]. The compressive behavior of concrete is depicted in Figure 2 (left), using the mean values of the mechanical properties. The tensile behavior of

the concrete has been modeled using a local strain tension softening approach. This involves a linear post-peak branch extending to zero strength at a strain equal to  $2f_{ct}/E_c$ , where  $f_{ct}$  is the tensile strength of concrete and  $E_c$  is the secant elastic modulus. Additionally, the cracking process has been modeled using the “Smearred cracking” approach with a fixed crack direction model [27].

For the reinforcement steel, a bi-linear constitutive law has been applied for both tension and compression, incorporating a hardening law. The reinforcement was modeled using discrete bar elements, assuming a perfect bond with the surrounding concrete. Figure 2 (right) illustrates the compressive and tensile behavior of steel, based on the mean values of the mechanical properties.

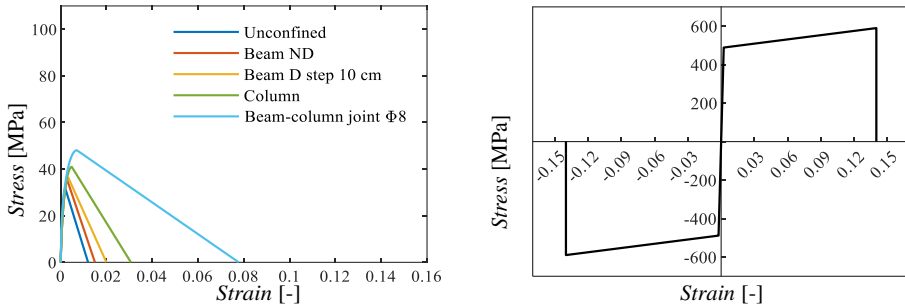


Fig. 2 Constitutive models assuming mean values of the mechanical properties for: concrete in compression (left), reinforcement steel both in compression and in tension (right).

### 3 Deterministic assessment

A displacement-controlled pushdown analysis has been performed in order to compute the response of the structure against the central supporting column removal. Mean values of the mechanical properties are adopted in this stage. In detail, an increasing vertical displacement is applied where the column is removed and the corresponding reaction given by the structure is registered, allowing to define the capacity curve (i.e., displacement-reaction curve).

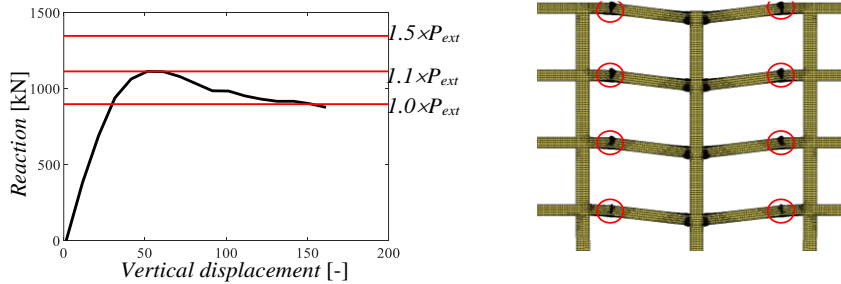


Fig. 3 Results of the pushdown analysis: capacity curve and comparison with the gravity loads (left), deformed shapes and crack formation before failure (right).

Figure 3 (left) shows the results in terms of capacity curve, demonstrating how the structure fails without showing any catenary behavior (i.e., the resistance is not recovered after the softening stage). In addition, by considering the resultant of the gravity loads  $P_{ext}$ , obtained considering the accidental combination of the gravitational loads according to [2], it is possible to observe that for a dynamic amplification of the external loads larger than 1.1, the structure is not able to sustain the phenomena of progressive collapse. Furthermore, Figure 3 (right) shows that concentrated curvatures are localized in critical areas of the beams where there is the transition between dissipative and non dissipative zone, where also the longitudinal reinforcement in the upper chord changes. This result suggests that the

longitudinal reinforcement should be placed continuously over the beam-column nodes, as widely recognized in many standards [6]-[9], but guaranteeing a continuity over at least 1/3 of the length of the beam, as underlined in [28].

## 4 Probabilistic assessment

To assess the structural robustness of the frame, a full probabilistic approach is adopted by following the next steps:

- sampling the random properties of both materials and loads;
- conducting displacement-controlled pushdown NLFE simulations on the structure in order to define the probabilistic capacity curves (i.e., displacement-reaction curves);
- using the energy equivalence approach, as proposed by Izzuddin [29], compute the dynamic displacement and the corresponding dynamic gravitational load  $P_d$  that causes that displacement;
- evaluating the dynamic amplification factors (DAFs) as the ratios between the dynamic and static gravitational loads  $P_{ext}$ ;
- performing equivalent static non-linear analysis to simulate the removal of the base column and amplify the loads of the adjacent spans on each floor using the energy-based DAFs, while maintaining non-amplified gravity loads on the other spans
- analyzing the aleatory results in terms of strains for different materials to assess the structural reliability at the ULS.

### 4.1.1 Sampling of the basic random variables

A full-probabilistic approach was considered by sampling both materials and loads as basic random variables, using the Latin Hypercube Sampling (LHS) technique [30] and including the following statistical characteristics:

- permanent structural load:  $G_1 \sim \text{Normal} (16 \text{ kN/m} ; 0.05)$ ;
- permanent non-structural load  $G_2 \sim \text{Normal} (13 \text{ kN/m} ; 0.05)$ ;
- floor variable loads:  $Q_f \sim \text{Gumbel} (7.3 \text{ kN/m} ; 0.20)$ ;
- roofing variable loads:  $Q_r \sim \text{Gumbel} (1.8 \text{ kN/m} ; 0.20)$ ;
- and snow load:  $Q_s \sim \text{Gumbel} (4.7 \text{ kN/m} ; 0.20)$ ;
- concrete compressive strength:  $f_c \sim \text{Lognormal} (31.9 \text{ MPa} ; 0.15)$ ;
- reinforced concrete specific weight:  $\rho \sim \text{Normal} (25 \text{ KN/m}^3 ; 0.05)$ ;
- reinforcing steel elastic modulus:  $E_s \sim \text{Lognormal} (210000 \text{ MPa} ; 0.03)$ ;
- reinforcing steel yielding strength:  $f_y \sim \text{Lognormal} (488.6 \text{ MPa} ; 0.05)$ ;
- reinforcing steel ultimate strength:  $f_u \sim \text{Lognormal} (589.8 \text{ MPa} ; 0.05)$ ;
- reinforcing steel ultimate strain:  $\varepsilon_{su} \sim \text{Lognormal} (0.14 ; 0.09)$ ;

where the symbol  $\sim$  indicates “distributed as”, the first number in the parenthesis indicates the mean value and the second one denotes the coefficient of variation of the basic random variable. In detail, 100 realizations were sampled for each basic variable. In addition, the following correlation coefficients between reinforcement parameters are considered:

- 0.85 between  $f_y$  and  $f_u$ ;
- -0.5 between  $f_y$  and  $\varepsilon_{su}$  ;
- -0.55 between  $f_u$  and  $\varepsilon_{su}$ .

## 4.2 Probabilistic pushdown analysis and DAFs

This section focuses on computing the DAFs necessary for probabilistic equivalent static NLFE analyses to address the dynamic nature of a column removal scenario. The DAFs are calculated using the energy equivalence method by [29]. According to this method, the maximum dynamic displacement occurs when the external work (work done by gravity loads) equals the internal energy (energy absorbed by the structure). Subsequently, the DAF is computed as the ratio between the dynamic load  $P_d$  and

static load  $P_{ext}$ . Specifically,  $P_d$  is evaluated at the maximum dynamic displacement, whereas  $P_{ext}$  represents the static gravity load concentrated at the top of the removed column, evaluated according to the accidental combination of gravity loads (i.e., permanent and variable loads), as defined in the previous section adopting the mean values.

To evaluate the dynamic response  $P_d$ , static displacement-controlled pushdown NLFAs were performed following the previously described procedure. Specifically, one set composed of 100 random NLFE models was defined, varying material properties while keeping geometry and constraints consistent. This process generated aleatory force-displacement curves (Figure 4), referred to as aleatory pushdown or capacity curves. The results in Figure 4 confirm that the structure does not show any catenary behavior even for the most ductile mechanisms. In addition, there is a large variability of the ultimate response of the structure due to both the uncertainty in the concrete and steel mechanical characteristics.

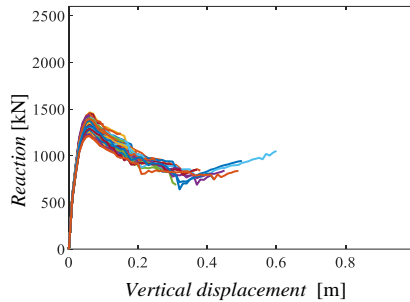


Fig. 4 Probabilistic capacity curves.

By applying the energetic equivalence approach, the DAFs were determined for only about 25% of the cases, as only those combinations of load and material properties allowed achieving a performance point (i.e., equality between internal energy and external work). The mean value of the DAFs where a performance point was reached is equal to 1.16. The number of collapse cases are taken into account in the computation of the failure probability in the following section.

In Table 1, the statistical properties of the dynamic load and external load are shown.

Table 1 Maximum, minimum and mean values of the external and dynamic load.

$P_o$ [kN]			$P_d$ [kN]		
Max	Min	Mean	Max	Min	Mean
1228	1009	1127	1433*	1168*	1267*

\*Evaluated only for the cases where the performance point was obtained between the internal and external energies.

### 4.3 Probabilistic equivalent static analysis and probability of failure

This section focuses on the equivalent static NLFE analyses to simulate the progressive collapse and compute the corresponding failure probability. For the cases where the energetic equilibrium was obtained, the simulations consisted in applying gravity loads, removing the central supporting column, and amplifying the gravity loads on the spans of the five floors adjacent to the central column based on the previously computed DAFs. The load amplification was limited to these spans because the damping properties of the structural RC elements prevented other spans from being affected. In cases without DAFs, simulations were run until collapse occurred, as predicted by the energetic approach, by slightly amplifying the loads in the spans adjacent to the removed column.

Next, the principal total strains at significant points of the RC frames were extracted for each set of simulations. Specifically, in the cross-sections of both beams and columns near each beam-column joint, various points were considered, distinguishing between points in the confined concrete core and those related to reinforcement, including ordinary reinforcement and stirrups.

The failure probability was then determined for each material in each cross-section, calculated as the probability of the demand exceeding the capacity concerning the ULS. Specifically, the failure probability was computed by performing a convolution integral between the Probability Density Function (PDF) of the demand, derived from the 100 aleatory principal total strains, and the Cumulative Density Function (CDF) of the capacity, obtained from the sampled ultimate strain thresholds. All ultimate strains were associated with lognormal distributions according to statistical inference analysis with a 5% significance level. The failure probability in the central spans also accounted for the collapse cases applying the total probability theorem.

In figure 5 the sections where failure may occur and the probability of their failure are shown. The largest failure probabilities were generally observed at the concrete level. In detail, the maximum failure probability is equal to 0.82 and it is reached in the beams of the first floor adjacent to the removed column, but also the beams of the upper floors are subjected to values much larger than  $10^{-1}$ . In addition, the lateral spans are characterised by failure probabilities between  $10^{-2}$  and  $10^{-1}$ , indicating a damage spread from the area directly affected by the collapse and the one indirectly affected. As already anticipated within the deterministic analysis, this result indicates that the structure designed according to actual code rules is not able to sustain the accidental removal of the supporting column. In fact, the largest failure probability corresponds to a safety level in terms of reliability coefficient much lower than 1.

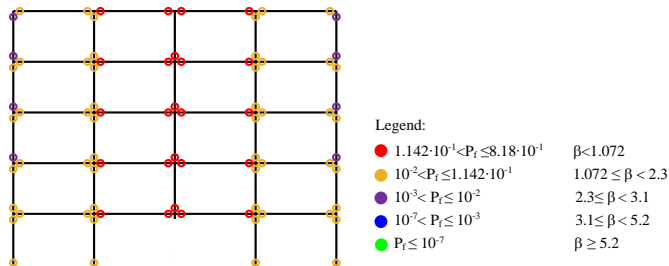


Fig. 5 Maximum probability of failure between concrete and steel reinforcement.

## 5 Conclusions

This study evaluates the structural reliability of planar seismically designed frames, particularly focusing on the accidental loss of the central supporting column. At first, a deterministic approach is adopted to evaluate the bearing capacity of the frame. In detail, the frame is modelled in a nonlinear finite element software, considering mean values of mechanical properties and carrying out a displacement-controlled pushdown analysis, by removing the supporting column and applying an increasing vertical displacement. Results in terms of displacement-reaction demonstrated that, for a dynamic amplification of the external gravity loads larger than 1.10, the structure is not able to sustain the accidental removal of the supporting column. Then, a full probabilistic approach is applied, sampling 100 realizations for various basic random variables related to both material properties and external loads, accounting for their statistical correlations. Preliminary analyses are carried out to compute the dynamic amplification factors (DAFs) for all the realizations, demonstrating that the structure failed to find an energetic equivalence at the performance point for the majority of cases. These DAFs were used to conduct probabilistic equivalent static nonlinear finite element analyses to simulate the column removal and amplifying loads on adjacent spans due to the dynamic effects. Subsequently, these analyses evaluated strains at beam-column joints, distinguishing between confined concrete and reinforcement. Convolution integrals between these strains and ultimate strain distributions were used to determine failure probabilities with respect to the ULS. The maximum failure probability, equal to 0.82, was reached in the beams of the first floor adjacent to the removed column. Additionally, the beams of the upper floors exhibited failure probabilities significantly larger than 0.1. The lateral spans also showed failure probabilities ranging between 0.01 and 0.1, indicating that damage spread from the area directly affected by the collapse to areas indirectly affected. This result confirms again that the structure designed according to current code rules is not capable of sustaining the accidental removal of the supporting column. In fact, **safety levels in terms of the reliability coefficient are much lower than 1. This underscores the need for**

improved design strategies to enhance the robustness and reliability of structures against such critical scenarios.

## Acknowledgements

This work was carried out within the RETURN Extended Partnership and received funding from the European Union Next-GenerationEU (National Recovery and Resilience Plan—NRRP, Mission 4, Component 2, Investment 1.3—D.D. 1243 2/8/2022, PE0000005).

## References

- [1] European Committee for Standardization. 1990. *Eurocode - Basis of structural and geotechnical design*.
- [2] European Committee for Standardization. 1991. *Eurocode 1 - Actions on structures - Part 1-7: General actions - Accidental actions*.
- [3] Ministry of Infrastructure. 2018. *Technical Standards of Construction NTC2018, DM 17.01.18*.
- [4] Ministry of Infrastructure. 2019. *Istruzioni per l'applicazione dell'«Aggiornamento delle "Norme tecniche per le costruzioni"» di cui al decreto ministeriale 17 gennaio 2018*.
- [5] International Federation for Structural Concrete Federation (*fib*). 2010. *Model Code for Concrete Structures*.
- [6] General Services Administration (GSA). 2003. *Progressive collapse analysis and design guidelines*. Washington, DC: Office of Chief Architects.
- [7] Department of Communities and Local Government. 2010. *The building regulations 2010 - structure: approved document A*. UK: HM Government.
- [8] Consiglio Nazionale delle Ricerche (CNR). 2018. *Istruzioni per la valutazione della robustezza delle costruzioni*.
- [9] American Society of Civil Engineers (ASCE). 2016. *Standard 7-02, Minimum Design Loads for Buildings and Other Structures*. Reston, VA.
- [10] Ellingwood, Bruce R. 2006. "Mitigating risk from abnormal loads and progressive collapse." *Journal of Performance of Constructed Facilities* 20(4):315–323.
- [11] Troisi, Roberta, Annamaria Nese, Rocío Blanco-Gregory and Monica Anna Giovannello. 2023. "The Effects of Corruption and Innovation on Sustainability: A Firm-Level Analysis". *Sustainability (Switzerland)* 15(3):1848.
- [12] Troisi, Roberta and Gaetano Alfano. 2023. "Is "justice hurried actually justice buried"? An organisational perspective of the Italian criminal justice". *International Journal of Public Sector Management* 36(1):94–109.
- [13] Troisi, Roberta, Stefania De Simone, Massimo Franco. 2023. "Illegal firm behaviour and environmental hazard: The case of waste disposal". *European Management Review*.
- [14] Joint committee on Structural Safety (JCSS). 2000. *Probabilistic Model Code, Part 1 – Basis of design*
- [15] Bertagnoli, Gabriele, Mario Ferrara, Elena Miceli, Paolo Castaldo and Luca Giordano. 2024. "Safety assessment of an existing bridge deck subject to different damage scenarios through the global safety format ECOV". *Engineering Structures* 306:117859.
- [16] Ferrara, Mario, Diego Gino, Elena Miceli, Luca Giordano, Marzia Malavisi and Gabriele Bertagnoli. 2024. "Safety assessment of existing prestressed reinforced concrete bridge decks through different approaches". *Structural concrete: journal of the fib*.
- [17] Gino, Diego, Elena Miceli, Paolo Castaldo, Antonino Recupero, and Giuseppe Mancini. 2024. "Strain-Based Method for Assessment of Global Resistance Safety Factors for NLNAs of Reinforced Concrete Structures". *Engineering structures* 304.
- [18] Botte, Wouter, Didier Droogné, and Robby Caspeele. 2021. "Reliability-Based Resistance of RC Element Subjected to Membrane Action and Their Sensitivity to Uncertainties". *Engineering structures* 238: 112259.
- [19] Brunesi, Emanuele, Roberto Nascimbene, Fulvio Parisi, and Nicola Augenti. 2015. "Progressive Collapse Fragility of Reinforced Concrete Framed Structures through Incremental Dynamic Analysis". *Engineering structures* 104:65–79.

- [20] Xu, Guoqing and Bruce R. Ellingwood. 2011. “Probabilistic Robustness Assessment of Pre-Northridge Steel Moment Resisting Frames”. *Journal of Structural Engineering* 137(9):925-934.
- [21] Arshian, Amir Hossein, Guido Morgenthal, and Shanmugam Narayanan. 2016. “Influence of Modelling Strategies on Uncertainty Propagation in the Alternate Path Mechanism of Reinforced Concrete Framed Structures”. *Engineering structures* 110: 36–47.
- [22] Zhang, Qiang, Yan-Gang Zhao, Kristijan Kolozvari, and Lei Xu. 2022. “Reliability Analysis of Reinforced Concrete Structure against Progressive Collapse”. *Reliability engineering & system safety* 228:108831.
- [23] Cervenka Consulting s.r.o.. 2014. *ATENA 2D v5*, Prague, Czech Republic.
- [24] Committee Euro-International du Beton (CEB-FIP).1990. *Model Code 1990. Bulletin d'information No. 195*.
- [25] Saatcioglu, Murat and Salim R. Razvi. 1993. “Strength and ductility of confined concrete”, *Journal of Structural Engineering* 119(10):3109-3110.
- [26] Dyngeland. 1989. *Behavior of Reinforced Concrete Panels, Dissertation*. Trondheim University, Norway.
- [27] Darwin, David, and D.A.W. Pecknold. 1974. “Inelastic Model for Cyclic Biaxial Loading of Reinforced Concrete”. *Civil Engineering Studies*.
- [28] Miceli, Elena, and Paolo Castaldo. 2023. “Robustness Improvements for 2D Reinforced Concrete Moment Resisting Frames: Parametric Study by Means of NLFE Analyses.” *Structural concrete* (2023). <https://doi.org/10.1002/suco.202300443>.
- [29] Izzuddin, Bassam, A.G. Vlassis, A.Y. Elghazouli, and D.A. Nethercot. 2008. “Progressive Collapse of Multi-Storey Buildings Due to Sudden Column Loss — Part I: Simplified Assessment Framework”. *Engineering structures* 30(5):1308–1318.
- [30] Ronald L. Iman. 2008. Latin Hypercube Sampling, *Encyclopedia of Quantitative Risk Analysis and Assessment*.

# **Green concrete and sustainability of concrete structures**





# Bond behaviour between steel/FRP bars and sustainable concrete: preliminary study

Maria Antonietta Aiello<sup>1</sup>, Denny Coffetti<sup>2</sup>, Luigi Coppola<sup>2</sup>, Maria Milena Della Vecchia<sup>3</sup>, Marianovella Leone<sup>1</sup>, Annalisa Napoli<sup>3</sup>, Simone Rapelli<sup>2</sup>, Roberto Realfonzo<sup>3</sup> and Vincenzo Romanazzi<sup>1</sup>

<sup>1</sup>*Department of Engineering for Innovation, University of Salento, Piazza Tancredi 7, 73100 Lecce, Italy*

<sup>2</sup>*Department of Engineering and Applied Sciences, University of Bergamo, via Salvecchio 19, 24129 Bergamo, Italy*

<sup>3</sup>*Department of Civil Engineering, University of Salerno, via Giovanni Paolo II 132, 84084 Fisciano (Sa), Italy*

## Abstract

The present study deals with the development and characterization of an innovative shrinkage-compensating high-workability alkali-activated slag-based eco-concrete for the repair and strengthening of reinforced concrete (RC) members. Specifically, it considers applications such as the section enlargement of beams and columns (concrete jacketing). Following the characterization of the developed mixture at both fresh and hardened state, the paper focuses on the bond behaviour between the new concrete and metallic and non-metallic (fiber reinforced polymer – FRP) bars. The goals are: a) to identify the main parameters influencing the stress transfer mechanisms at the interface and, b) to evaluate the bond-slip constitutive relationship by varying the steel bar diameter, the bonded length and, in the case of FRP bars, the surface treatment. To this end, a comprehensive experimental program was organized, including more than 100 pull-out tests performed on various types of bars bonded to the new concrete, and the preliminary results are presented here. The bond performance is also examined through a comparison with results from similar tests using ordinary Portland cement concrete blocks with equivalent compressive strength and workability class to the innovative green concrete.

## 1 Introduction

Although Portland cement-based concrete is the most widely used construction material globally, its production is highly impactful due to the significant carbon footprint from the energy-intensive kilns required to burn raw materials. Additionally, it necessitates the consumption of vast natural resources. Replacing Portland cement with ground granulated blast furnace slag (GGBFS) offers a promising, more sustainable alternative. With a similar composition to Portland cement and good availability, blast furnace slag - a by-product of the cast-iron production process - serves as an effective binder and addresses disposal concerns. Utilizing slag in concrete can thus reduce the CO<sub>2</sub> emissions, decrease energy and raw material consumption and promote the reuse of waste materials.

Regarding internal reinforcement for reinforced concrete (RC) structures, steel is traditionally used due to its excellent mechanical properties, including high tensile strength, elastic modulus, and ductility. However, steel is prone to corrosion, an electrochemical process involving electron flow on the reinforcement surface. Fiber reinforced polymer (FRP) bars provide a solution to steel corrosion in RC structures. Being electrochemically inert, FRP bars do not participate in the reactions that cause rust. Additionally, their low weight, high tensile strength, wear resistance, enhanced fatigue life, and low thermal expansion make FRP materials valuable for internal reinforcement in RC structures and for upgrading existing structures.

The study presented in this paper contributes to exploring alternative solutions to the use of RC materials, aiming to address the sustainability of concrete and the durability of reinforcing bars. To this purpose, an innovative shrinkage-compensating high-workability alkali activated slag-based eco (“green”) concrete to use for structural purposes was developed and mechanically characterized. Then, the interface performance between the green concrete and non-metallic (FRP) bars was examined by means of pull-out tests. The first results presented in this paper are part of a research program involving teams from three universities: the University of Bergamo (UniBg), primarily focused in developing and

characterizing green concrete, the University of Salento (UniSal) and University of Salerno (UniSa), both mainly investigating the bond mechanism between FRP bars and green concrete. The paper reports the outcomes of the initial direct pull-out tests conducted.

## 2 Development and characterization of sustainable concrete

The initial phase of this experimental research was dedicated to the development and characterization of an innovative alkali-activated slag-based concrete for the repair and reinforcement of reinforced concrete (RC) structures characterized by low-shrinkage and high-workability. The binder, which excludes Portland cement, was formulated using a blend of commercial ground granulated blast furnace slag and silica fume, activated by a solid precursor consisting of sodium metasilicate, potassium hydroxide, and sodium silicate [1], [2]. Natural siliceous sands and gravels, with a maximum size of 12 mm, were combined according to a modified Bo-lomey granulometric curve. Given the high susceptibility of alkali-activated materials to cracking [3], [4], 12 mm polypropylene fibers (with a shape index of approximately 400) were incorporated to mitigate plastic shrinkage cracking. Additionally, a CaO-based expansive agent and an ethylene glycol-based shrinkage reducing admixture (SRA) were included to achieve shrinkage compensation [5]. Viscosity modifiers, specifically methylcellulose and modified starch, were used to ensure appropriate rheology of the fresh concrete, while a commercial superplasticizer containing modified acrylic polymers was selected to enhance workability and regulate the setting time of the eco-concrete. The water-to-binders ratio was maintained at 0.44 (see Table 1).

Table 1 Composition of green concrete.

Components		Dosage [kg/m <sup>3</sup> ]
Precursors	Ground granulated blast furnace slag	450
	Silica Fume	60
Activators	Sodium metasilicate	71.6
	Potassium hydroxide	30.7
	Sodium Carbonate	10.2
Aggregates	Sand	995
	Gravel	405
Admixtures	Methylcellulose	0.56
	Modified starch	0.19
	SRA	6.75
	Expansive agent	13.5
	Superplasticizer	4.5
Polypropylene fibers		1
Tap water		198

To effectively compare the interface behaviour of green concrete (namely GC) and traditional concrete (i.e., ordinary Portland cement-based concrete, namely OC) with reinforcements [6], the reference concrete was designed using the same aggregates as the alkali-activated concrete, achieving similar workability (> 650 mm in the flow table test) and a 28-day compressive strength (> 45 MPa). The reference material was a flowable, Portland-based, shrinkage-compensating concrete, incorporating 400 kg/m<sup>3</sup> of a commercial premixed binder that also contained superplasticizers, expansive agents, and shrinkage reducing admixture in powder form. The water content was adjusted to achieve a water-to-binder ratio of 0.46. Various sample types were produced and cured in a climatic chamber at 20°C and 95% relative humidity. These included 100 mm cubes for evaluating compressive strength at different ages and 150 mm cubes with embedded steel or fiber-reinforced polymer (FRP) bars to characterize bond behaviour.

### 3 Pull-out tests

#### 3.1 Experimental program

The experimental program, planned to investigate the bond between the ordinary/green concrete and the steel/FRP bars, includes a total of 140 pull-out tests, to be performed both at UniSal and UniSa labs. The following study parameters are considered in the test matrix (see Table 2):

- the concrete type: ordinary Portland cement-based concrete (OC) and green concrete (GC)
- the type of bars: deformed steel (S) and glass FRP (G);
- the type of composite bars: G1 and G2 bars, supplied by Owens Corning Pinkbar® [7] and by Schöck Combar® [8], respectively;
- the nominal bar diameter ( $\emptyset$ ): 8 and 12 mm;
- the bonded length of bar ( $L_b$ ) within the concrete block:  $L_b = 2.5\emptyset$  or  $5\emptyset$ .

Table 2 Test matrix.

Concrete	Bar	Nominal bar diameter, $\emptyset$ (mm)	Bond length, $\emptyset$	# of planned tests		# of tests in the paper		
				UniSal	UniSa	UniSal	UniSa	
Green (GC)	Steel (S)	12	2.5 $\emptyset$	5	5	-	-	
			5 $\emptyset$	5	5	2	3	
		8	5 $\emptyset$	2	3	-	-	
	FRP (G1)	12	2.5 $\emptyset$	3	5	-	-	
			5 $\emptyset$	3	5	-	-	
		8	5 $\emptyset$	5	5	-	-	
	FRP (G2)	12	2.5 $\emptyset$	3	-	-	-	
			5 $\emptyset$	3	3	-	-	
		8	5 $\emptyset$	-	5	-	-	
	Ordinary (OC)	Steel (S)	12	2.5 $\emptyset$	5	5	-	-
				5 $\emptyset$	5	5	2	5
			8	5 $\emptyset$	2	3	-	-
FRP (G1)		12	2.5 $\emptyset$	5	5	-	-	
			5 $\emptyset$	5	5	2	5	
		8	5 $\emptyset$	5	5	-	-	
FRP (G2)		12	2.5 $\emptyset$	5	-	-	-	
			5 $\emptyset$	5	3	5	3	
		8	5 $\emptyset$	2	5	-	-	

Concerning the FRP bars, those denominated G1 were characterized by a fiber mass content equal to 70% and by the following mechanical properties [7]: tensile strength = 900 MPa; ultimate strain = 2%; modulus of elasticity = 46.88 GPa. The G2 bars, instead, were made of 87% of EC-R glass fibers (diameter of 20 $\mu$ m) and 13% of Vinyl ester resin. Values of both tensile strength and elastic modulus provided by the manufacturer [8] are respectively equal to 1000 MPa and 60 GPa, respectively.

To simulate the typical bond behaviour between concrete and deformed steel bars, both the GFRP bars chosen for the experimental testing were characterized by a ribbed surface (Fig. 1a and 1b show their surface configurations). The spacing and dimensions of ribs were accurately measured before testing: in particular, the width and the thickness of ribs on G1 bars surface – 6 mm spaced – were 5 and

0.25 mm; the corresponding dimensions for G2 bars – having ribs spacing equal to 3.5 mm - were 5 and 0.75 mm.

The counterpart deformed steel bars were of the B450C type, as conventionally used in Italy to date.

Finally, regarding the bond length, it has to be underlined that both the considered lengths are consistent with the assumption of the uniform bond model adopted in estimating the bond stress values.

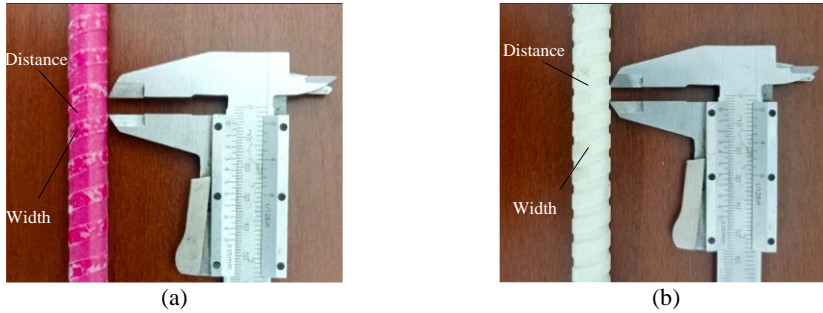


Fig. 1 Detail of bar surface: G1 bar (a); G2 bar (b).

### 3.2 Test set-up

All tests have been conducted under displacement-control at a rate of 0.2 mm/min.

The test setup, shown in Fig. 2a, was basically the same for both laboratories at UniSa (Fig. 2b) and UniSal (Fig. 2c); it was designed drawing inspiration from the RILEM Recommendations [9].

The concrete samples were cubes with 150 mm side and were always cast orthogonally to the bar. Each bar was centrally embedded within the sample so that the concrete cover was greater than  $4.5\phi$ . As shown in Fig. 2a, the bonded length was in the lowest part of the cube because, during the test, the compression stresses from the steel plate exert a confinement action on the concrete, enhancing the bond mechanism and potentially affecting the test results. Thus, the chosen condition is as unfavorable as possible for the bond, to obtain more reliable results. The unbonded zone was obtained by applying a plastic tube over the specific length of the bars (Fig. 2d).

Some Linear Displacement Transducers (LDTs) were used to measure slips between bars and concrete at the loaded and unloaded ends (see Fig. 2a, 2b and 2c). Additionally, a strain gauge was glued directly onto each bar to monitor its deformation throughout the testing phase.

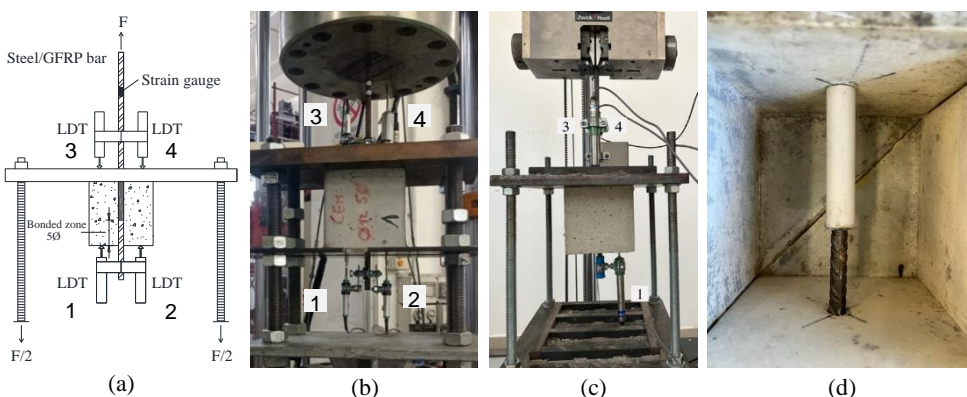


Fig. 2 Schematic of the pull-out test set-up (a); set-up at UniSa Lab (b) and UniSal lab (c); specimen before casting (d).

#### 4 First experimental results

The main experimental data of the 27 tests already performed will be summarized below (see the last two columns of Table 2). All these pull-out tests concern Ø12 bars bonded to the concrete for a length equal to 5Ø. In particular, 22 samples were made of ordinary Portland cement-based concrete, of which 7 reinforced with steel bars, 7 with G1 bars and 8 with G2 ones. Only the remaining 5 specimens were produced with green concrete (and reinforced with steel bars).

Table 3 Main data and results

Lab	ID Specimen	Age of test [days]	R <sub>cm</sub> [MPa]	F <sub>max</sub> [kN]	F <sub>max,av</sub> [kN]	τ <sub>max</sub> [MPa]	τ <sub>max,av</sub> [MPa]	S <sub>max</sub> [mm]	S <sub>max,av</sub> [mm]
UniSa	GC1_S_1	28	43.7	32.4	29.99	14.3	13.3	0.54	0.52 (5.06%)
	GC1_S_2	28	43.7	27.6	(11.46%)	12.2		0.50	
	GC1_S_3	50	48.2	34.8	-	15.4	-	0.80	-
UniSal	GC1_S_1	130	50.0	38.6	40.6	17.1	17.9	0.55	0.51 (12.6%)
	GC1_S_2	130	50.0	42.5	(6.80%)	18.8		0.46	
UniSa	OC1_S_1	50	47.1	26.2	30.55 (15.44%)	11.6	13.5	0.96	0.70 (42.82%)
	OC1_S_2	50	47.1	30.0		13.2		0.79	
	OC1_S_3	50	47.1	35.5		15.7		0.37	
	OC6_S_4	28	50.9	42.0	43.43	18.6	19.2	0.88	1.03 (20.60%)
	OC6_S_5	28	50.9	44.9	(4.72%)	19.8		1.18	
UniSal	OC1_S_1	135	50.6	38.5	41.0	17.0	18.1	1.00	0.91 (14.0%)
	OC1_S_2	135	50.6	43.5	(8.62%)	19.2		0.82	
UniSa	OC2_G1_1	50	52.0	35.0	36.11 (4.35%)	14.6	15.1	2.43	2.34 (5.75%)
	OC2_G1_2	50	52.0	20.5 <sup>1</sup>		8.5 <sup>1</sup>		1.46 <sup>1</sup>	
	OC2_G1_3	50	52.0	37.2		15.6		2.24	
	OC4_G1_4	32	52.4	33.0	33.43	13.7	14.0	1.63	1.70 (5.82%)
	OC4_G1_5	32	52.4	33.9	(1.93%)	14.2		1.77	
Unisal	OC2_G1_1	132	51.4	44.9	43.3	18.8	18.1	2.58	2.56 (1.38%)
	OC2_G1_2	132	51.4	41.6	(5.40%)	17.4		2.53	
Unisa	OC3_G2_1	50	51.0	30.3	29.8 (3.58%)	13.4	13.2	0.4	0.35 (13.6%)
	OC3_G2_2	50	51.0	28.5		12.6		0.02 <sup>1</sup>	
	OC3_G2_3	50	51.0	30.5		13.5		0.3	
Unisal	OC5_G2_1	100	46.3	29.7	33.2 (9.8%)	13.1	14.7	0.3	0.39 (29%)
	OC5_G2_2	100	46.3	32.8		14.5		0.5	
	OC5_G2_3	100	46.3	30.3		13.4		0.3	
	OC5_G2_3	100	46.3	36.7		16.2		0.4	
	OC5_G2_3	100	46.3	36.2		16.0		0.5	

*In the round brackets the coefficients of variation are reported*

<sup>1</sup> Not considered in the calculation of the mean values

The main data and results of the tests are shown in Table 3. The table reports:

- the university lab in which the test was performed;
- the label identifying each test (“sample ID”);
- the age of concrete specimen at the test day;
- the mean value,  $R_{cm}$ , of the cubic compressive strength measured at the test day (values in italics have been estimated);
- the maximum value,  $F_{max}$ , of the extracting force experienced by each specimen during the test and the corresponding mean value,  $F_{max,av}$ , calculated for each set of identical specimens;
- the bond strength,  $\tau_{max}$ , estimated by assuming a uniform distribution of the bond stresses at the bar-concrete interface:

$$\tau_{max} = \frac{F_{max}}{\pi \cdot \phi \cdot L_b} \quad (1)$$

- the mean values of  $\tau_{max}$  calculated for each set of identical specimens;
- the slip at the free end,  $s_{f,max}$ , corresponding to the  $\tau_{max}$ ;
- the mean values of  $s_{f,max}$  calculated for each set of identical samples.

The test ID in Table 3 provides the following information: a) the number following “OC” provides information about the concrete casting to which the specimen belongs (GC or OC, from OC1 to OC6), b) the reinforcing bar material (S, G1 or G2). About the concrete casting, it is highlighted that the 5 specimens made of GC and tested so far were cast all together, while the 22 OC cubes were cast in six different casting times, indicated in Table 3 with labels going from OC1 to OC6.

It is noteworthy that two values of concrete compressive strength marked with an asterisk were not obtained from lab compressive tests but were estimated according to the formula reported in EC2 [10].

Concerning the slip data, instead, it is noted that values of the free-end slip of the bar reported in Table 3 represent the average of the measures directly provided by the LDT 1 and LDT 2 illustrated in Fig. 2b for UniSa and the slip recorded by LDT1 in Fig. 2c for UniSal. Conversely, the values of the slip at the loaded end of the bar, omitted in Table 3 for brevity, can be derived from the average of the measures provided by LDT 3 and LDT 4 in Fig. 1a, 1b and 1c for both laboratories. These measurements must be pre-adjusted to account for the elastic elongation of the bar between the top side of the concrete cube and the anchor system of the LDTs.

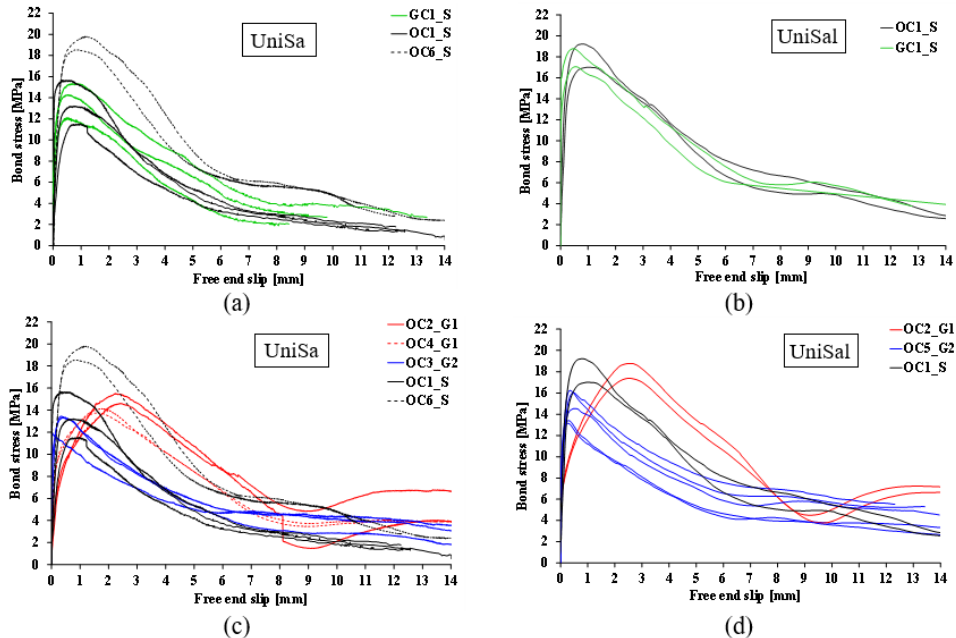


Fig. 3 Bond stress versus free-end slip curves: comparison between GC and OC (a,b), and between steel and GFRP bars (c,d).

In both labs all the specimens failed by pull-out without any damage on the concrete cover.

Fig. 3 shows some comparisons in terms of bond stress-free end slip ( $\tau - s$ ) curves. Specifically, the graphs in Fig. 3a,c refers to tests performed at UniSa lab, while Fig. 3b,d to tests at UniSal lab.

By observing data in Table 3 and  $\tau$ - $s$  curves in Fig. 3 some considerations can be made. First of all, from the graphs in Fig. 3a and Fig. 3b it is noted that the curves relative to both types of concrete follow the theoretical definitions given by Model Code 2010 [11]. These curves are characterized by an initial ascending branch in which the first part is governed by the chemical adhesion, while for the remaining one the mechanical interlocking governs the bond behaviour. In particular, the slips are almost zero in the first branch of the graphs, where the transfer mechanism is given by the chemical adhesion between the concrete matrix and the bar. The next stage up to the bond stress peak is governed by the mechanical interlocking. Once the bond strength is reached, the stress decay is observed until a horizontal residual plateau. In this case, the curves of OC1 and GC1 are almost overlapped showing that the bond between alkali-activated concrete mixes and steel bars seems to be similar to that characterizing the ordinary Portland cement-based concrete. As expected, the bond mechanism's dependence on concrete compressive strength is evident: the higher the  $R_{cm}$ , the higher the peak bond stress (see Fig. 3a).

In Fig. 3c and Fig. 3d the results obtained with OC mixes and steel bars are compared with those obtained with GFRP bars.

The bond stress – slip curve shape suggests the different bond mechanism developed by the three different bars. In fact, while the constitutive law observed for the G2 bar is quite comparable to the steel one, the same cannot be said for G1 bars. G2 bars exhibited a stiffer curve and lower free-end slip values, with respect to G1 bar. This consideration is also confirmed by observing the specimens after the pull-out tests, as shown in Fig. 4. In particular, Fig. 4 (b) highlights that the bond mechanism in G2 bars is mainly ruled by the contribution of mechanical interlocking, not so dissimilar to steel bars behaviour. Conversely, Fig. 4 (a) shows a different behaviour for the G1 bars, being the ribs on their surface unable to hold concrete. In fact, G1 bars ribs appear distinctly damaged and smoothed after the test, proving that the major contribution to bond in this kind of bar is due to friction, leading to a less stiff  $\tau$ - $s$  curve and lower slip values. This evidence proves the deep influence of the surface treatment of the bar on bond mechanism. In this regard, Metelli and Pizzari observed that the bond stiffness of this branch is directly linked with the ribs geometry [12].

A further difference between the two kinds of bar is given by the final frictional branch of the  $\tau$ - $s$  curve. While G2 bars exhibit a constant decrease in bond stress, in G1 bars a moderately sudden increase of bond stress has been observed. Once again, this aspect may be related to the different behaviour of ribs on the surface of the bars which affects the different bond mechanism. In the case of G1 bar, the slight increase in the bond stress after the peak stage is probably related to the engagement of a new-undamaged-rib. Conversely, in the case of G2 bar where the bond mechanism is ruled by mechanical interlocking, a different condition occurs, i.e., a “cylindrical element” composed of the bar coupled to the concrete among ribs advances inside the concrete during the test.



Fig. 4 Photos of G1 (a) and G2 (b) after the test.

## 5 Conclusions

This paper presented the first results from a wider experimental program carried out by a research



team involving three different universities (UniBg, UniSa and UniSal). With the aim of contributing to overcome both the sustainability problems from building industry and durability issues of reinforced concrete structures, eco-sustainable blast furnace alkali-activated slag, in place of traditional Portland cement, and GFRP bars have been investigated. In particular, in order to explore the suitability of the developed sustainable concrete for structural use, the bond performance to traditional (steel) reinforcing deformed bars or glass (G)-FRP bars the results of the first 27 performed pull-out tests were analysed.

The main considerations are reported in the following:

- quite negligible differences were noted in bond mechanism developed by ordinary and eco-sustainable concrete with steel bars, in terms of both bond strength values and constitutive laws;
- steel and GFRP bars embedded into ordinary concrete behaved differently. The first ones exhibited slightly higher bond strength and stiffer behaviour than those made of GFRP;
- as expected, the bar surface treatment has an influence of the bond behaviour. Indeed, the first tests showed that the G-FRP bars characterized by closely spaced thicker ribs (G2 bars) showed lower slips than the counterparts with widely spaced thinner ribs (G1 bars). A better contribution to bond from mechanical interlocking was developed in G2 bars which led to a stiffer  $\tau$ -s curve.

## Acknowledgements

The research was carried out with the financial support from ReLUIS (Network of the Italian University Laboratories for Seismic Engineering—Italian Department of Civil Protection) - Executive Project 2022–24—WP14.

The authors thank Owens Corning (Toledo, Ohio, USA) and Schöck Italia GmbH S.r.l. (Bolzano, Italy) for providing the GFRP bars used in the experimental investigation.

## References

- [1] Coffetti, Denny, Candamano, Sebastiano, Crea, Fortunato and Coppola, Luigi. 2023. “On the role of alkali content on one-part alkali activated slag pastes produced with ribblend solid activators.” *Construction and Building Materials* 409:133868. doi: 10.1016/j.conbuildmat.2023.133868
- [2] Komkova, Anastasija and Habert Guillaume. 2023. “Environmental impact assessment of alkali-activated materials: Examining impacts of variability in constituent production processes and transformation.” *Construction and Building Materials* 363(2023):129032. doi: 10.1016/j.conbuildmat.2022.129032
- [3] Ye, Hailong and Radlinska, Aleksandra. 2016. “Shrinkage mechanisms of alkali-activated slag.” *Cement and Concrete Research* 88:126-135. doi: 10.1016/j.cemconres.2016.07.001
- [4] Zhang, Wenyan, Xue, Mengfen, Lin, Huaxia, Duan, Xiaohang, Jin, Yuzhong and Su, Faqiang. 2023. “Effect of polyether shrinkage reducing admixture on the drying shrinkage properties of alkali-activated slag.” *Cement and Concrete Composites* 136:104865. doi: 10.1016/j.cemcomp.2022.104865.
- [5] Coppola, Luigi, Coffetti, Denny, Crotti, Elena, Candamano, Sebastiano, Crea, Fortunato, Gazzaniga, Gabriele and Pastore, Tommaso. 2020. “The combined use of admixtures for shrinkage reduction in one-part alkali activated slag-based mortars and pastes.” *Constr Build Mater* 248 (2020). doi: 10.1016/j.conbuildmat.2020.118682.
- [6] Yan, Fei, Lin, Zhibin and Yang, Mijia. 2016. “Bond mechanism and bond strength of GFRP bars to concrete: A review.” *Comp. part B: Eng.* 98:56-69. doi: 10.1016/j.compositesb.2016.04.06.
- [7] Owens Corning website. Accessed 10 December 2023. <https://www.owenscorning.com/en-us/composites/product/flatworkfiberglassrebar>.
- [8] Schöck website. Accessed 10 December 2023. <https://www.schoeck.com/en/combar>
- [9] RILEM TC, RC 6 Bond test for reinforcement steel. 2. Pull-out test. 1983.
- [10] EN 1992-2 2005. Eurocode 2: Design of concrete structures.
- [11] CEB-FIP, Fib Model Code for Concrete Structures. 2010. doi: 10.1007/s13398-014-0173-7.2.
- [12] Metelli, Giovanni and Plizzari, Giovanni A.. 2014. “Influence of the relative rib area on bond behaviour.” *Magazine of Concrete Research*. 66:277–294. doi: 10.1680/mac.13.00198.

# Properties of high performance fiber reinforced concrete containing electric arc furnace slags

Matteo Lamberti<sup>1</sup>, Roberto Rosignoli<sup>2</sup>, Marco Stancari<sup>2</sup> and Fausto Minelli<sup>1</sup>

<sup>1</sup> *Department of Civil, Environmental, Architectural Engineering and Mathematics, Università degli studi di Brescia, Via Branze 43, Brescia (25123), Italy*

<sup>2</sup> *Technical Management, Research and Development, Azichem Srl, Via Giovanni Gentile 16A, Goito (46044), Italy*

## Abstract

Alternative materials from industrial waste, used to minimize the consumption of natural raw materials, have long been investigated to make concrete with an eco-sustainable profile. In this study eco-high performance fiber reinforced concretes (HPFRC), manufactured with the use of large amounts of electric arc furnace slags (EAFS) generated by steel industry, have been investigated. Statistical data (2021) shows Italy as the second largest steel producer in Europe. In this contest Brescia district, in Lombardy region, contributes around 30-35% of national steel production. Most of these Brescia district plants are based on electric arc furnaces (EAF), and the annual volume of EAFS in this district can be estimated at 825 thousand tonnes. Based on these eco-sustainability objectives, the research has been carried out to investigate the feasibility of partially replacing natural aggregates (NA) with steel slag (SS), thus also promoting the circular economy with the aim of mitigating the environmental impact of the HPFRC. This paper presents ongoing research carried out by the University of Brescia and a Lombardy-based company (Azichem Srl) specialised in building products, in which the impact of replacing 40% of NA with EAFS on two different formulations HPFRC is evaluated. Preliminary results suggest that the introduction of dimensionally calibrated EAFS, as a partial substitute of NA, does not decrease the mechanical performance of HPFRC. In addition, the introduction of EAFS, with calibrated grain sizes that integrate the particle sizes of NA, produce significant effects on increasing elastic modulus, density, and abrasion resistance, in agreement with other results in the literature. Further investigations in term of durability are being carried out, to verify the impact of EAFS into HPFRC exposed under severe environmental conditions.

## 1 Introduction

The focus on sustainability in industrial production and the construction sector has intensified in recent years. At the same time, over the past two decades, global steel production has more than doubled, rising from 905 million tons in 2002 to 1885 million tons in 2022, with a peak of 1962 million tons in 2021 [1]; as a result, the generation of steel slag (SS) from steel mills has significantly increased as well. As an indication of the amount of SS produced annually on the Italian territory, it is worth to look at the data (refer to 2021) reported in [2]: considering a slag rate of about 100-150 kg per ton of steel produced, for Basic Oxygen Furnace (BOF) and Electric Arc Furnace (EAF) plants, the SS production can be estimated between 0.4÷0.6 and 2.1÷3.1 million tons, respectively, thus a total range between 2.5 and 3.7 million tons per year. On the other hand, the construction sector is a major player in terms of pollution and especially consumption of raw materials [3]. In this context, the use of SS to replace a fraction of natural aggregates (NA) offers advantages both in reducing the consumption of new resources and in improving the management of waste products from metallurgical processes by limiting their disposal in landfills [4]. The interest on the sustainability theme is also significant worldwide from a regulatory prospective [5]. Indeed, in recent years, an increasing number of countries around the world have introduced regulations that require waste materials to be reused for recycling rather than disposed of in landfills. Over 150 world leaders signed the 2030 Agenda for Sustainable Development [6] in 2015, aiming to achieve ambitious sustainability goals by 2030. Considering the significant impact of the construction sector, which generates 35% of all waste in Europe [7], the European Commission has adopted several measures, among which it is worth mentioning the European Union Action Plan for the

Circular Economy (COM2015) [8] and the most recent strategy update (COM2020) [9]. This growing interest has led to numerous studies in the literature on the use of SS as aggregates in concrete [10]-[21]. However, most of these studies focus on the replacement of coarse aggregates, while other works focus more on the characterization of the slag itself, which is a crucial aspect since the properties of SS can vary significantly depending on the production process from which it is derived. As mentioned previously, SS can be obtained from two different main steel production processes: the BOF plant process, which uses about 25-35% of scrap, or the EAF plant process, which uses almost 100% of scrap [13]. In the latter case, there are two subcategories of slag (EAFS), depending on the type of steel produced: EAFS-S, which is generated from stainless steel production, and EAFS-C, which results from carbon steel production. One of the main problems of SS is their dimensional stability, as highlighted in several publications [12],[14],[15]. Among these SS types, EAFS-C stands out as the most dimensionally stable due to its lower concentrations of free calcium and magnesium oxides than those found in BOF slag (BOFS). In addition, several strategies to mitigate these expansive trends are provided in the literature. This topic has been extensively investigated by colleagues at the University of Brescia in a comprehensive study that analysed the properties of concretes using EAFS-C as a natural coarse aggregate replacement [16]. The research presented in this paper, carried out by a different research group, shifts the focus to finer grain sizes of EAFS-C and high-performance fiber-reinforced concrete (HPFRC), with totally different mechanical properties and final commercial utilization. Aware that different chemical and physical characteristics of the slags can influence the behaviour of cementitious compounds, an extensive literature review was carried out, in which studies were filtered on the basis of particle size and chemical composition of the slag examined for results comparison. In [17],[18] results obtained with aggregates with chemical compositions similar to those of the EAFS used in this work are presented. EAFS grain sizes is another important aspect considered, cause HPFRC have an aggregates size up to 3 mm or even finer [22], considerably different from the coarse EAFS grain sizes, most frequently examined in the literature. From extensive literature review, as presented in [13], the different behaviors exhibited by several slag types are highlighted, considering their chemical and physical properties: in general, most mixtures incorporating SS showed a decrease in workability and this aspect may tend to worsen as a result of steel fibers addition in the mixture [23]; for this reason, additives are provided in most cases to improve the workability of the mix. In addition, to improve several product characteristics, such as workability, mechanical and chemical resistance, a considerable amount of Silica Fume is often added. As stated in [24], the incorporation of Silica Fume into concrete results in significant improvements in both the tensile and compressive strengths of the concrete. On the other hand, from the literature survey [13], an increase in performance in terms of compressive strength, splitting strength, and flexural strength was recognized in most analyzed cases. Furthermore, about 82% of the studies reported an improvement in elastic modulus and even 100% agreed on the increase in matrix abrasion resistance, as also stated by [25]. However, examination of other parameters produced contradictory results, probably due to the different types of SS; for example, about 50% of the studies reported decreased performance in water absorption, permeability, and porosity compared with mixtures where only NA were used. Improvements in mechanical properties are attributed to the advantages that slag offers as an aggregate, including better adhesion to the matrix, its intrinsic strength, and enhanced Interfacial Transition Zone (ITZ) quality [18]. Researches intended to investigate the microscopic behavior of the matrix have shown that there is generally better adhesion between the cement matrix and the aggregate due to the greater angularity of SS compared to NA; furthermore, it is also accepted that the morphology and quality of the ITZ play a significant role on the porosity and thus durability of mortars and concretes [18]. As previously mentioned, the ongoing research presented in this paper focuses on EAFS-C, regarding the current application of this type of SS in the construction industry: a considerable amount is used in road construction due to its high resistance to polishing and abrasion [13]; moreover, the feasibility of producing Portland cement by incorporating a percentage of EAFS into the clinker has been studied [15]. Concretes with SS as aggregate typically have an increase in self-weight, since slag has a density of about 3000-4000 kg/m<sup>3</sup> and an interesting application for these heavy-concretes is in situations requiring counterweights [26]; heavy-concretes containing EAFS also have excellent radiation shielding properties [27], as they possess high attenuation of gamma radiation [28], similar and even higher than concrete made with barite aggregates. It is worth noting that some researchers have also explored the high-temperature behavior of concretes containing EAFS, but the results were not entirely positive [29]. Finally, it is important to note that concretes with EAFS are already accepted and used in practice applications, as shown, for example, by their use in foundations

and basement walls in Kubik's laboratory, as mentioned by [14]. Few studies have been performed on fiber-reinforced concretes (FRC) containing SS [5],[14],[30],[31],[32],[33] with encouraging results. However, these studies have focused on coarse aggregate sizes and lower strengths, very different from those obtained with HPFRC. The latter field seems to be little investigated [5]. The present work aims to fill this gap in the literature, focusing on HPFRCs containing EAFS.

## 2 Materials and methods

Two products with very similar compositions were examined in this study: the chemical composition of the EAFS aggregate use is shown in Table 1 (aggregates size 0-4 mm). Both were studied in their standard versions, consisting entirely of NA (NA1 and NA2), and in another version in which 40% of the NA were replaced with EAFS (EAF1 and EAF2), as shown in Table 2; the Coefficient of Variation (CV) are provided in round brackets, in order to provide information about the experimental scatter. The two products mainly differ in fiber content: the NA1-EAF1 formulation has a volumetric content of 13 mm fibers of about 1.27%, while in the NA2-EAF2 formulation a hybrid steel fibre cocktail is utilized with 0.51% is 13 mm fibers and 0.76% of 6 mm long fibers: the brass-coated steel fibers used have an aspect ratio of 65 for those 13 mm in length and 25 for those 6 mm in length, both with tensile strengths exceeding 2400 MPa. Both mixes also contain a small amount of polypropylene (PP) fibers that can help release steam overpressures generated in case of a fire. Above 200°C, PP melts, leaving a micro-channel through which steam can travel. The EAFS were tested by the manufacturer for compliance with European standards that specify the properties of aggregates and filler aggregates obtained by processing natural, manufactured, or recycled materials for use in concrete (EN 12620:2008) and in mortar (EN 13139:2002). The first part of the research was spent to evaluate workability and strength evolution of HPFRC using different percentage of EAFS replacing NA. Physical mechanical tests, replacing up to 40% NA with EAFS, demonstrated excellent compatibility in terms of workability and development of mechanical strength, while with 50% of substitution a slight loss of fluidity occurred. After defining the percentage of substitution of NA with 40% of EAFS, the study proceeded to test 40x40x160 mm beams under bending and compression (EN 1015-11). Moreover, Three Point Bending Tests were conducted on 150x150x600 mm notched beams (EN 14651); in addition to the standard characterization tests for FRC, the elastic modulus was also measured, revealing a percentage increase in EAF specimens as expected. Tests were also performed at long curing times on all the formulations investigated. Finally, compression and flexural tests were performed on long-term cured (i.e., more than 17 weeks after casting) NA2 and EAF2 40x40x160 mm members following freeze-thaw cycles and on some these specimens that were exposed to chloride ( $\text{NaCl} = 50 \text{ gr/l}$ ) and sulfate ( $\text{MgSO}_4 = 50\text{g/l}$ ) baths during the thaw phase. Tests on the NA2 and EAF2 formulations took place 146 days after casting: the first 28 days of curing followed the standard procedure, i.e., the samples were kept in a climatic chamber at 20°C with relative humidity constantly above 95%. For the next 7 days, all specimens were moved to a cold room at -30°C and after this week the specimens were moved back to the climate chamber for 21 days. From this time, the specimens alternated between the cold room and the climatic chamber with immersion in a chloride-rich solution, sulfate solution or cured in standard conditions. The samples were subjected to 14 temperature shocks of 50°C, spent a total of 63 days in the climate chamber (with two groups also exposed to aggressive conditions) and 50 days in cold storage. Other specimens, on the other hand, spent the entire maturation in the climate chamber under standard conditions and were tested 121 days after casting. Before being subjected to compression and flexural tests, the samples were stored at room temperature in a protected environment for 7 days. This test has no standards behind it and was developed by the authors; however, it is worth noting that the current procedure for obtaining Italian technical validation certificates (as required by the guidelines issued by the Italian Superior Council of Public Works) requires less severe tests, with 14 days of temperature variations (from -20°C to +20°C) and 4-hour freeze-thaw cycles, without any immersion in aggressive waters. As shown below, these tests provided very promising results, especially in the development of compressive strength and specific gravity; HPFRC often show high compactness and reduced porosity, giving them high performance in terms of durability. In addition, research has also been conducted in the past on very similar formulations in which the effects of healing on freeze-thaw damaged UHPFRC and autogenous self-healing on high temperature exposed UHPFRC were investigated [34],[35].

It is important to note that the results presented in this work concern ongoing research, and more time and tests will be needed to obtain more reliable results. This will allow for an in-depth characterization

of these materials, estimating the impact of replacing NA with EAFS on physical and mechanical properties, both in the short and long term, even in highly exposed environments.

Table 1 Chemical composition of EAFS (%).

Ca	Fe	Si	Al	Mn	Mg	Others
~30	30÷40	10÷15	5÷10	2÷5	2÷5	<2

Table 2 Mix composition dosage (kg/m<sup>3</sup>).

Costituent	NA1*	EAF1	NA2*	EAF2
Cement (CEM I + CEM II)	700	700	710	710
w/c	0.3	0.3	0.3	0.3
NA 0-2 mm (Siliceous sand)	1220	820	1225	820
EAFS 0-4 mm	-	570	-	575
Microsilica and reactive filler	120	140	110	130
Polypropylene fibers (lf = 6 mm)	0.6	0.6	0.3	0.3
Steel fibers (lf = 13 mm)	100	100	40	40
Steel fibers (lf = 6 mm)	-	-	60	60
Superplasticizer	25	30	25	30

\*NA1 and NA2 formulations correspond to the products Rinfor Grout Col<sup>®</sup> and Grout 2 SFR<sup>®</sup>, respectively.

### 3 Experimental results and critical discussion

Tests on 40x40x160 mm specimens (EN 196-1) provided consistent and promising results. Mean data for all products are presented in Table 3, showing that replacing 40% of NA with EAF does not appear to have a negative impact on the tested properties. On the other hand, tests on 150x150x600 mm notched specimens, according to EN 14651, revealed less clear and homogeneous results: as shown in Figure 1, in the left-hand graph for the NA1 and EAF1 formulations, the mean curve representing the specimens with EAFS (continuous red line) significantly outperforms the specimens containing only NA (dashed black line); on the contrary, in the right-hand graph, the behavior of the two formulations (NA2 in dashed black line and EAF2 in continuous red line) is the opposite. These tests are characterized by inherent variability and high sensitivity and they showed in one case a significantly higher mean value for the formulation incorporating EAF, while for the other formulation more satisfactory values were achieved with the mixture including 100% of NA. The results are presented in Table 3, the CV are provided in round brackets; these contradictory results further highlight the importance of more investigations that will be conducted in the coming months so as to increase the number of the testing samples. The results present in Table 4 (the CV are provided in round brackets) show that the incorporation of recycled aggregates in both formulations resulted in an increase of about 5% in density and 13% in elastic modulus (\*\*note that the elastic modulus for the NA2 formulation is based on data provided by the product data sheet). Compressive and flexural strengths seem to remain almost constant when comparing formulations consisting of just NA with their corresponding formulations incorporating EAFS. However, it is worth noting that the characterization of these parameters will need to be refined by expanding the specimen population. Regarding specimens of NA2 and EAF2 mixtures exposed to freeze-thaw cycles and severe environmental conditions, data were compared with those obtained from specimens cured under standard conditions at 28 days as well as those subjected to long-term curing (121 days), as shown in Figure 2. In terms of density, it was noted that it was steadily higher for specimens containing EAFS, as expected. The absence of decreases compared to specimens cured under standard conditions, as well as the lack of differences between specimens subjected to different curing conditions, can be attributed to the high compactness and low porosity of these products. These characteristics are crucial, especially since these products are designed and often used to strengthen

deteriorated structural elements, and the need for these interventions often arises from the location of these structures in severe environmental conditions. No significant performance differences were recorded between the formulations with NA and those with EAFs; additionally, no damage such as erosion, scaling, or cracking was observed on the specimens surfaces.

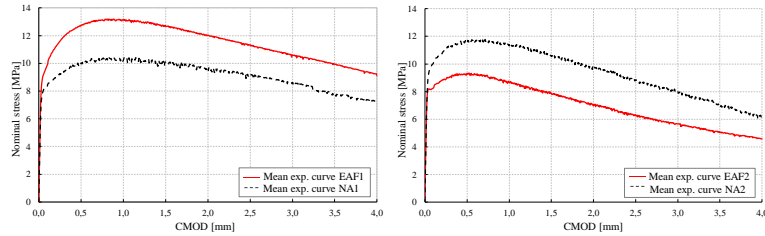


Fig. 1 Nominal stress vs. CMOD mean e curve for NA1-EAF1 (left) and NA2-EAF2 (right).

Table 3 Lists limit of proportionality  $f_{Lm}$  and residual flexure strengths  $f_{R1}$ ,  $f_{R2}$ ,  $f_{R3}$ ,  $f_{R4}$ .

Mix	$f_{Lm}$ [MPa]	$f_{R,1m}$ [MPa]	$f_{R,2m}$ [MPa]	$f_{R,3m}$ [MPa]	$f_{R,4m}$ [MPa]	Class
NA1	8.0 (2.0%)	9.8 (8.3%)	9.8 (6.5%)	9.1 (5.5%)	7.8 (1.7%)	8c
EAF1	9.0 (2.7%)	12.6 (1.8%)	12.6 (1.0%)	11.2 (1.5%)	9.9 (1.9%)	12b
NA2	9.0 (8.7%)	10.3 (20.8)	9.2 (26.8%)	7.7 (30.1%)	6.2 (32.1%)	10b
EAF2	8.2 (7.6%)	9.4 (9.0%)	7.8 (8.7%)	6.3 (6.7%)	5.1 (8.8%)	8a

Table 4 Mean hardened HPFRC properties - Tests on 40x40x160 mm specimens (UNI EN 196-1).

Properties	NA1	EAF1	NA2	EAF2
Density ( $\text{kg/m}^3$ )	2437 (1.0%)	2597 (0.5%)	2492 (0.8%)	2594 (0.4%)
Compressive strength (MPa)	121.5 (5.9%)	121.6 (3.5%)	125.7 (1.9%)	115.1 (5.9%)
Flexural Strength (MPa)	21.6 (29.1%)	22.3 (14.1%)	17.1 (7.5%)	19.3 (6.9%)
Elastic Modulus (GPa)	36.3 (4.2%)	40.9 (2.2%)	37.3**	41.9 (3.4%)

Prolonged immersion in NaCl and MgSO<sub>4</sub> saturated water, combined with freeze-thaw cycles, was an effective way to verify the negligible permeability of these products. Regarding the behavior under compression and flexure, a decrease of about 40% in flexural strength was observed in both the specimens with NA and EAFs, while the decrease in compressive strength is much more contained (see Figure 2). Despite a significant drop in flexural strength, which still remains within acceptable limits considering the severe curing conditions of the specimens, the comparison between the strengths of NA2 and EAF2 specimens reveals that the introduction of SS slightly worsens the performance only in the case of freeze-thaw cycles combined with chloride baths (-6%), while it slightly improves in the other two conditions (+12% in both cases). In general, as observed for density, these two properties also do not seem to be significantly affected by the presence of SS. Regarding the compressive strength, the reduction is less evident compared to the values at 121 days for specimens cured under standard conditions (-7%). Note that due to an issue with the machine used for the compression test, it was not possible to obtain the 121-day value for EAF2 and for this reason the 121-day value for EAF1 was reported in the graph, considering that NA1 and NA2 showed very similar strengths at 121 days and have very similar compositions ( $NA1_{121\text{days}} = 135.5 \text{ MPa}$ ,  $NA2_{121\text{days}} = 138.0 \text{ MPa}$ ). The tests on the 40x40x160 specimens confirmed the increase in specific weight, but a slight increase in compressive strength could have also been expected; however, compressive strength seems to remain unchanged or show only slight variations, with no clear improvement linked to the presence of SS. On the other hand, almost all cases recorded greater flexural strength, as observed through tests on the 40x40x160 specimens. As mentioned above, these outcomes will need to be verified and further investigated by increasing the number of tests in the next steps of the research. In addition to performing further tests for

materials characterization, future research developments involve running full-scale experimental tests to evaluate the performance of these products when used to strengthen structural elements.

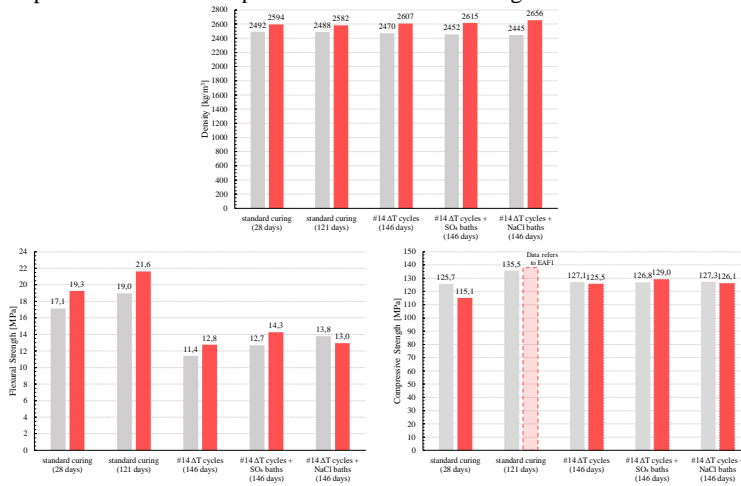


Fig. 2 Results of NA2 (gray) and EAF2 (red) specimens after curing under standard conditions at 28 days and 121 days, and following freeze-thaw cycles and exposure to NaCl and MgSO<sub>4</sub>.

Although the research is still in its early stages, a positive trend has emerged, as preliminary results suggest that the introduction of dimensionally calibrated EAFS as a partial substitute for NA does not reduce the mechanical performance of HPFRC. These findings highlight the potential for developing eco-HPFRC that meets performance requirements while improving the sustainability of the strengthening process for existing structures, for which these products are intended. The latter aspect, along with the development of more environmentally sustainable materials, is becoming increasingly important, as both topics will become progressively more crucial over the years. Additionally, this research opens up a new application field for steel mill slag of these grain sizes, whose production is continuously increasing, with most of the slag currently being disposed of in landfills.

#### 4 Conclusions

In this ongoing research the impact of replacing 40% of NA with EAFS on two different formulations HPFRC is evaluated. The following main conclusions can be drawn:

- Physical and mechanical tests were carried out, revealing excellent compatibility concerning workability and mechanical strength development.
- Tests conducted on 40x40x160 mm specimens, subjected to standard curing conditions for 28 days, showed consistent and promising results. The preliminary outcomes suggest that the introduction of dimensionally calibrated EAFS, as partial substitute of NA (40%), does not decrease the mechanical performance of HPFRC.
- Specimens exposed to freeze-thaw cycles and severe conditions didn't show significant performance differences between the formulations with NA and those with EAFS; additionally, no damage such as erosion, scaling, or cracking was observed on the specimens surfaces. Prolonged immersion in NaCl and MgSO<sub>4</sub> saturated water, combined with freeze-thaw cycles, was an effective way to verify the negligible permeability of these products. In terms of strength, both types of specimens experienced a 40% decrease in flexural strength, while the decrease in compressive strength was much smaller (7%).
- Tests on 150x150x600 mm notched specimens, according to EN 14651, revealed less clear and homogeneous results, highlighting the importance of more investigations.
- Although research is still in its early stages, a positive trend has emerged, suggesting the potential for the development of eco-HPFRCs that fulfill performance requirements while simultaneously enhancing the sustainability of the strengthening process for existing structures, for which these products are mainly intended.

#### Acknowledgements

The authors want to express their gratitude to the Arvedi Group, particularly to Roberto Muselli.

They also extend their thanks to the staff of the Laboratory for Testing Materials "Pietro Pisa" at the University of Brescia, with special emphasis on Mr. Luca Martinelli.

## References

- [1] World Steel Association, "2023 World Steel." Accessed 14 May 2024. <https://worldsteel.org/data/world-steel-in-figures-2023/>
- [2] A. Piemonti, A. Conforti, L. Cominoli, A. Luciano, G. Plizzari, and S. Sorlini, "Exploring the Potential for Steel Slags Valorisation in an Industrial Symbiosis Perspective at Meso-scale Level," *Waste and Biomass Valorization*, vol. 14, no. 10, pp. 3355–3375, 2023, doi: 10.1007/s12649-022-01940-5.
- [3] J. Tomaszewska, "Polish transition towards circular economy: Materials management and implications for the construction sector," *Materials (Basel)*, vol. 13, no. 22, pp. 1–17, 2020, doi: 10.3390/ma13225228.
- [4] A. Piemonti, A. Conforti, L. Cominoli, S. Sorlini, A. Luciano, and G. Plizzari, "Use of iron and steel slags in concrete: State of the art and future perspectives," *Sustain.*, vol. 13, no. 2, pp. 1–27, 2021, doi: 10.3390/su13020556.
- [5] A. Aghajanian, A. Cimentada, K. Behfarnia, A. S. Brand, and C. Thomas, "Microstructural analysis of siderurgical aggregate concrete reinforced with fibers," *J. Build. Eng.*, vol. 64, no. November 2022, p. 105543, 2023, doi: 10.1016/j.jobe.2022.105543.
- [6] G. A. United Nations, "Transforming our world: the 2030 Agenda for Sustainable Development." Accessed 14 May 2024. <https://sdgs.un.org/2030agenda>
- [7] G. Foster, F. Flachenecker, and D. Tonini, "Science of the Total Environment Environmental and socio-economic effects of construction and demolition waste recycling in the European Union," vol. 908, no. October 2023, 2024, doi: 10.1016/j.scitotenv.2023.168295.
- [8] European Commission, "Closing the loop - An EU action plan for the Circular Economy." Accessed 14 May 2024. <https://environment.ec.europa.eu/topics/circular-economy/first-circular-economy-action-plan>
- [9] European Commission, "A new Circular Economy Action Plan For a cleaner and more competitive Europe." Accessed 14 May 2024. <https://environment.ec.europa.eu/strategy/circular-economy-action-plan>
- [10] J. M. Manso, J. A. Polanco, M. Losañez, and J. J. González, "Durability of concrete made with EAF slag as aggregate," *Cem. Concr. Compos.*, vol. 28, no. 6, pp. 528–534, 2006, doi: 10.1016/j.cemconcomp.2006.02.008.
- [11] A. Santamaría, J. M. Romera, I. Marcos, V. Revilla-Cuesta, and V. Ortega-López, "Shear strength assessment of reinforced concrete components containing EAF steel slag aggregates," *J. Build. Eng.*, vol. 46, no. November 2021, 2022, doi: 10.1016/j.jobe.2021.103730.
- [12] C. Pellegrino, V. Gaddo, "Mechanical and durability characteristics of concrete containing EAF slag as aggregate," *Cem. Concr. Compos.*, vol. 31, no. 9, pp. 663–671, 2009, doi: 10.1016/j.cemconcomp.2009.05.006.
- [13] A. M. Rashad, "Behavior of steel slag aggregate in mortar and concrete - A comprehensive overview," *J. Build. Eng.*, vol. 53, no. January, p. 104536, 2022, doi: 10.1016/j.jobe.2022.104536.
- [14] J. A. Fuente-Alonso, V. Ortega-López, M. Skaf, Á. Aragón, and J. T. San-José, "Performance of fiber-reinforced EAF slag concrete for use in pavements," *Constr. Build. Mater.*, vol. 149, pp. 629–638, 2017, doi: 10.1016/j.conbuildmat.2017.05.174.
- [15] A. M. Rashad, "A synopsis manual about recycling steel slag as a cementitious material," *J. Mater. Res. Technol.*, vol. 8, no. 5, pp. 4940–4955, 2019, doi: 10.1016/j.jmrt.2019.06.038.
- [16] A. Piemonti, "Electric Arc Furnace slag (EAF):use in concrete for structural applications," PhD diss., University of Brescia.
- [17] M. Van Tran, C. Van Nguyen, T. Nawa, and B. Stitmannathum, "Properties of High Strength Concrete Using Steel Slag Coarse Aggregate," *ASEAN Eng. J.*, vol. 4, no. 2, pp. 22–32, 2014, doi: 10.11113/aej.v4.15448.
- [18] I. Arribas, A. Santamaría, E. Ruiz, V. Ortega-López, and J. M. Manso, "Electric arc furnace slag and its use in hydraulic concrete," *Constr. Build. Mater.*, vol. 90, pp. 68–79, 2015, doi: 10.1016/j.conbuildmat.2015.05.003.
- [19] E. Anastasiou, K. Georgiadis Filikas, and M. Stefanidou, "Utilization of fine recycled



- aggregates in concrete with fly ash and steel slag,” *Constr. Build. Mater.*, vol. 50, pp. 154–161, 2014, doi: 10.1016/j.conbuildmat.2013.09.037.
- [20] D. Trento, V. Ortega-Lopez, M. A. Zanini, and F. Faleschini, “Stress-strain behavior of electric arc furnace slag concrete under uniaxial compression: Short- and long-term evaluation,” *Constr. Build. Mater.*, vol. 422, no. February, p. 135837, 2024, doi: 10.1016/j.conbuildmat.2024.135837.
- [21] F. Faleschini, M. A. Fernández-ruíz, M. Angelo, K. Brunelli, C. Pellegrino, and E. Hernández-montes, “High performance concrete with electric arc furnace slag as aggregate : Mechanical and durability properties,” *Constr. Build. Mater.*, vol. 101, pp. 113–121, 2015, doi: 10.1016/j.conbuildmat.2015.10.022.
- [22] E. Brühwiler, “UHPFRC technology to enhance the performance of existing concrete bridges,” *Struct. Infrastruct. Eng.*, vol. 16, no. 1, pp. 94–105, 2020, doi: 10.1080/15732479.2019.1605395.
- [23] R. F. Zollo, “Fiber-reinforced concrete: An overview after 30 years of development,” *Cem. Concr. Compos.*, vol. 19, no. 2, pp. 107–122, 1997, doi: 10.1016/s0958-9465(96)00046-7.
- [24] S. Bhanja and B. Sengupta, “Influence of silica fume on the tensile strength of concrete,” *Cem. Concr. Res.*, vol. 35, no. 4, pp. 743–747, 2005, doi: 10.1016/j.cemconres.2004.05.024.
- [25] A. Chatzopoulos, K. K. Sideris, and C. Tassos, “Production of concretes using slag aggregates: Contribution of increasing the durability and sustainability of constructions,” *Case Stud. Constr. Mater.*, vol. 15, no. October, p. e00711, 2021, doi: 10.1016/j.cscm.2021.e00711.
- [26] A. Kukreti, P. Kundra, L. Kathait, N. Garg, and S. Kumar, “A Review on Properties of Heavy Weight Concrete,” *IOP Conf. Ser. Earth Environ. Sci.*, vol. 1086, no. 1, 2022, doi: 10.1088/1755-1315/1086/1/012049.
- [27] A. L. Beaucour, P. Pliya, F. Faleschini, R. Njinwoua, C. Pellegrino, and A. Noumowé, “Influence of elevated temperature on properties of radiation shielding concrete with electric arc furnace slag as coarse aggregate,” *Constr. Build. Mater.*, vol. 256, p. 119385, 2020, doi: 10.1016/j.conbuildmat.2020.119385.
- [28] B. Pomaro, F. Gramegna, R. Cherubini, V. De Nadal, V. Salomoni, and F. Faleschini, “Gamma-ray shielding properties of heavyweight concrete with Electric Arc Furnace slag as aggregate: An experimental and numerical study,” *Constr. Build. Mater.*, vol. 200, pp. 188–197, 2019, doi: 10.1016/j.conbuildmat.2018.12.098.
- [29] I. Netinger, D. Varevac, D. Bjegović, and D. Morić, “Effect of high temperature on properties of steel slag aggregate concrete,” *Fire Saf. J.*, vol. 59, pp. 1–7, 2013, doi: 10.1016/j.firesaf.2013.03.008.
- [30] V. Ortega-López, J. A. Fuente-Alonso, A. Santamaría, J. T. San-José, and Á. Aragón, “Durability studies on fiber-reinforced EAF slag concrete for pavements,” *Constr. Build. Mater.*, vol. 163, pp. 471–481, 2018, doi: 10.1016/j.conbuildmat.2017.12.121.
- [31] M. Papachristoforou, E. K. Anastasiou, and I. Papayianni, “Durability of steel fiber reinforced concrete with coarse steel slag aggregates including performance at elevated temperatures,” *Constr. Build. Mater.*, vol. 262, p. 120569, 2020, doi: 10.1016/j.conbuildmat.2020.120569.
- [32] V. Ortega-López, A. García-Llona, V. Revilla-Cuesta, A. Santamaría, and J. T. San-José, “Fiber-reinforcement and its effects on the mechanical properties of high-workability concretes manufactured with slag as aggregate and binder,” *J. Build. Eng.*, vol. 43, 2021, doi: 10.1016/j.jobe.2021.102548.
- [33] A. Abushanab, W. Alnahhal, M. G. Sohail, N. Alnuaimi, R. Kahraman, and N. Altayeh, “Mechanical and durability properties of ultra-high performance steel FRC made with discarded materials,” *J. Build. Eng.*, vol. 44, no. August, 2021, doi: 10.1016/j.jobe.2021.103264.
- [34] N. P. Kannikachalam, E. C. Asensio, E. M. G. Brac, R. Rosignoli, N. De Belie, and L. Ferrara, “an Experimental Methodology To Assess Effects of Healing on Freeze-Thaw Damaged Ultra High-Performance Concrete,” *fib Symp.*, pp. 280–287, 2022.
- [35] N. P. Kannikachalam, A. M. E. M. Alhadad, F. Lo Monte, E. Maria, G. Brac, R. Rosignoli, N. De Belie and L. Ferrara, “Effect of autogenous self-healing on high temperature exposed Ultra High-Performance Concrete,” *Int. Fire Saf. Symp.*, no. June, pp. 667–676, 2023.

# Evaluation of the Italian ready-mix concrete supply chain based on LCA “from cradle to gate”

Denny Coffetti<sup>1</sup>, Elisabetta Palumbo<sup>1</sup>, Simone Rapelli<sup>1</sup>, Elena Crotti<sup>2</sup>, Luigi Coppola<sup>1</sup>

<sup>1</sup> *Department of Engineering and Applied Sciences,  
University of Bergamo,  
via Marconi, 5 - 24044 Dalmine (BG), Italy*

<sup>2</sup> *Engineer, PhD, and independent professional expert in the field of concrete technology*

## Abstract

Concrete is the most extensively used construction material globally, with an annual production ranging from 9 to 13 billion cubic meters. This material significantly impacts the environment, accounting for about 9% of anthropogenic CO<sub>2</sub> emissions and consuming large amounts of energy and raw materials. In Italy, the ready-mix concrete industry is crucial, producing 33.1 million cubic meters in 2022 and employing over 11,500 people. Despite efforts to reduce environmental impact by incorporating recycled aggregates, Italian regulations limit their use to 30% for the most commonly produced strength classes, namely C25/30 and C30/37. This paper presents a segment of a more extensive research project aimed at enhancing the sustainability of the concrete industry, with only a portion presented here due to space limitations. In particular, following ISO 14040 and 14044 standards, it deals with a Life Cycle Assessment (LCA) “from cradle to gate” in accordance with EN 15804:2019 of the Italian concrete supply chain, focusing on C25/30 XC1-XC2 S4 concrete with various aggregates (natural, industrial, and demolition-derived).

Results corroborate that cement production is the primary contributor to environmental impact of concrete, accounting for 75% of the total impact, while aggregate production and transportation contribute 6.6% and 9%, respectively. The partial substitution (15%) of natural aggregates with recycled ones results in negligible environmental benefits due to the relatively minor role of aggregates in the overall environmental footprint and to regulatory constraints. This emphasizes the importance of targeting cement production in decarbonization efforts.

## 1 Introduction

Concrete, with an annual global production of approximately 9-13 billion cubic meters, is the most widely used construction material in the world. It is made by mixing raw materials that have a significant environmental impact [1,2], both in terms of CO<sub>2</sub> emissions, estimated to be around 9% of anthropogenic carbon dioxide emissions [3,4], and in terms of energy and natural raw material consumption.

In Italy, the ready-mix concrete sector, involving over 11,500 employees across approximately 850 manufacturing companies, generated a turnover of around 2.9 billion euros in 2021, according to ISTAT and ATECAP data. This makes it one of the main sectors in the national construction industry in terms of economic impact and employment. Indeed, Italian concrete production in 2022 reached 33.1 million cubic meters, with significant variability in both environmental exposure class and compressive strength class [5]. Specifically, more than half of the concrete produced in Italian batching plants falls under the exposure classes XC1-XC2, intended for structural elements in dry internal environments (XC1) or those in permanent contact with water or completely buried (XC2). Another significant portion (13.1%) is in the exposure classes XC3-XC4, meant for external structures protected from rain (XC3) or those exposed to rain and/or alternating dry and wet conditions (XC4). Additionally, less than 10% of the produced concrete is designated for structural elements in contact with chlorides (4.2%) from both de-icing salts (XD) and marine sources (XS), concrete intended for structures exposed to chemically aggressive waters or soils (XA, 3.1%), and concrete for structures in severe climates subject to freeze-thaw cycles (XF, 0.9%). The remaining 19.5% of the produced concrete either has no specified exposure class or belongs to class X0 (non-reinforced structures with negligible risk of degradation).

Regarding the division of concrete based on compressive strength class, the Federbeton report [5] shows that about three-quarters of the produced concrete (73.4%) falls within the strength classes C25/30 and C30/37. Only 7.4% of the production reaches or exceeds class C35/45, while 14.8% does not exceed class C20/25, and 3.9% of the concrete does not have a declared strength class.

To reduce the environmental impact of concrete, Italy has introduced the possibility of partially replacing natural aggregates with recycled ones from industrial processes or the demolition of reinforced concrete buildings. This encourages the use of waste material that would otherwise be destined for landfill. However, data from the "L'Italia del Riciclo 2023" report shows that, despite Italy's construction and demolition (C&D) waste recovery rate being consistently above the legal limit of 70%, about one twentieth of this waste is used in concrete production [6]. These data are also consistent with the latest Federbeton Sustainability Report [7], which in 2022 estimated a replacement rate of natural aggregates with industrial or recycled ones at 0.44%.

This paper summarizes the LCA study of the concrete supply chain and recycled aggregates from demolition, developed in accordance with the Arcadia project methodology for supply chain studies [8]. This study was conducted in accordance with ISO 14040 and 14044 standards and resulted in the development of an ILCD format dataset in the Italian LCA Database (<https://www.arcadia.enea.it/la-banca-dati.html>).

## 2 Aim and boundaries of the study

To well represent the Italian market, this study involved the development of 32 datasets necessary to cover more than 96% of Italian production of performance-specified ready-mix concrete. Specifically, based on compressive strength class, workability class, and environmental exposure class of the elements they are intended for, the 32 datasets were classified into 8 groups. Within these groups, the mixes were further specialized according to the type of aggregate used:

- R: rounded natural aggregates of alluvial origin;
- C: natural aggregates obtained by crushing rocks;
- I: mixed aggregate consisting partly of natural crushed aggregate and partly (15% by mass) of recycled aggregate from industrial processes;
- C&D: mixed aggregate consisting partly of natural crushed aggregate and partly (15% by mass) of recycled aggregate from the demolition of concrete structures.

The function of the system is the production of performance-specified ready-mix concrete, manufactured with raw materials compliant with current regulations, for civil and industrial structures. The composition and properties ensure adequate durability of the material to resist environmental aggressions affecting the steel reinforcements or the concrete itself, in compliance with UNI 11104:2016, UNI EN 1992-1-1:2015, and UNI EN 206:2021 standards.

The functional unit was defined as "1 m<sup>3</sup> of concrete suitable for the construction of internal or underground elements (exposure class XC1-XC2, strength class C25/30)". The scope of this study covers the steps of raw material acquisition (A1), transportation (A2), and processing and manufacturing of concrete composites (A3), in alignment with the organization of EN 15804:2019 which is commonly called "cradle to the gate" (Figure 1). In particular, the research includes:

- the extraction and production phases of both natural (e.g., sand and gravel) and artificial (e.g., cement, superplasticizer, recycled aggregates) raw materials;
- transportation to the manufacturing plant and processing at the concrete plant;
- transformation at the concrete plant, including the initial storage of raw materials, subsequent dosing, and finally mixing. The material obtained at the end of this process is the ready-mix concrete.

The study excluded phases related to washing the mixer trucks and the movements of batching plant personnel.

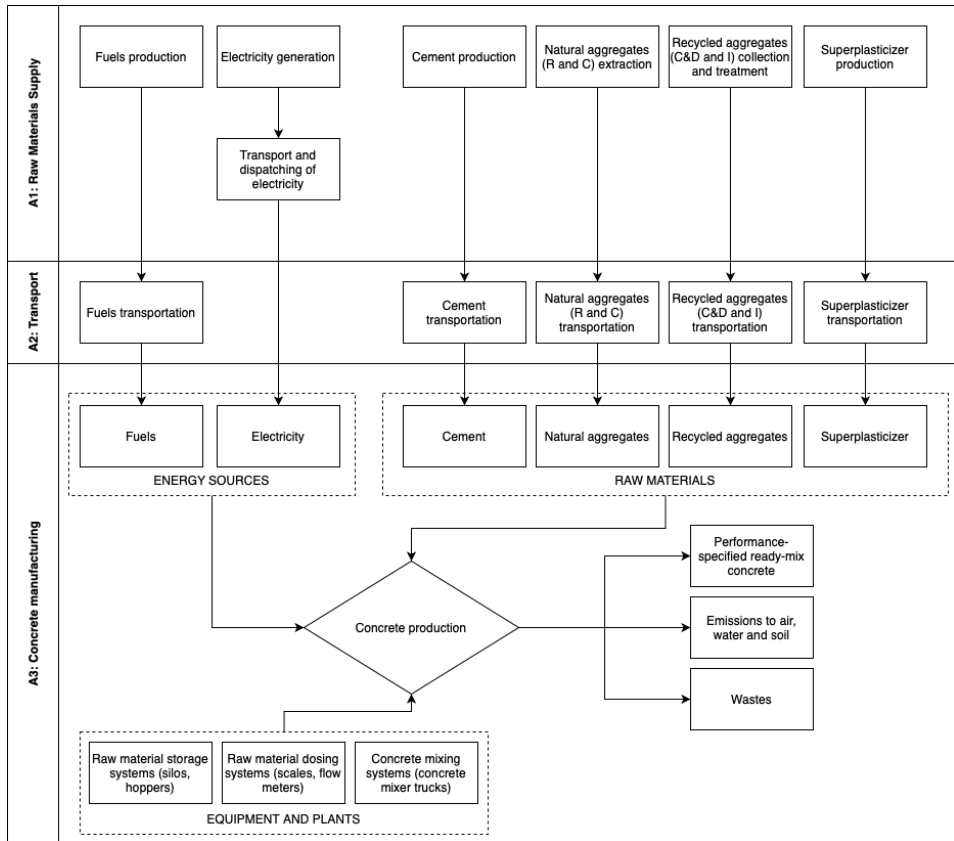


Fig. 1 - System Boundaries

### 3 Life Cycle Inventory

The inventory data collection was conducted starting from primary data collected by Federbeton, both in the form of industry reports [5,7] and sector-specific Environmental Product Declarations (EPDs). The other data was gathered from scientific literature and databases, particularly Ecoinvent 3.8. Based on these and the consolidated extensive knowledge of the research group, a Life Cycle Inventory (LCI) was defined for the production of 1 m<sup>3</sup> of concrete produced in Italy, considering compositions and their respective mixtures representing (over 96% of Italian production) the current national market. Among these, approximately 73% [5] is represented by the production of concrete with compressive strength classes ranging from C25/30 to C30/37. Therefore, this paper will focus on the analysis of four different C25/30 concrete, with slump class S4, composed of limestone Portland cement CEM II/A-LL 42.5R, water, superplasticizer, and four different aggregates (R, C, C&D and I, respectively) (Figure 2), used for the construction of internal or underground elements (exposure class XC1-XC2).

In particular, the modeling of C25/30 XC1-XC2 S4 concretes was developed based under the following hypothesis:

- Quantities and classification of raw materials composing the concrete mix refer to average values assumed in the analyzed EPDs of Italian concretes;

- The specific type of cement, along with the other five introduced in the research, were modeled based on the average cement developed by the parallel study of the ENEA research group within the ARCADIA project and subsequently compared with findings from the analysis of over 100 EPDs of Italian cements;

- Supply distances for aggregates, admixtures, and cements were taken from average values reported in the Federbeton Sustainability Report [7]. Specifically, aggregates transport averages 37 km, admixtures 178 km, and cement 98 km;

- Transport to the end user or construction site is excluded from the investigation.

The composition of the concretes is reported in Table 1. The variation in superplasticizer content arises from the differing physical properties of the aggregates, requiring varying admixture dosages to achieve a consistent workability class.

Table 1 Composition of concretes used in the LCA.

Dosage [kg/m <sup>3</sup> ]	R	C	I	C&D
CEM II/A-LL 42.5R	300	300	300	300
Rounded natural aggregates	1890			
Crushed natural aggregates		1890	1600	1600
Recycled industrial aggregates			290	
Recycled C&D aggregates				290
Water	180	180	180	180
Superplasticizer	1,8	2,4	2,4	2,4

#### 4 Life Cycle Impact

In accordance with ISO 14040, the study examined 16 impact categories, which are presented in this paper as characterized, normalized, and weighted values using the EF 3.0 assessment method with the software SimaPro 9.3.0.3. Specifically, Table A.1 (in Appendix) displays the characterization results for the life cycle of 1 m<sup>3</sup> of C25/30 XC1-XC2-S4 concrete production with rounded natural aggregates (R), also indicating the contributions from the individual analyzed phases (A1-A2 and A3) and their respective subcategories.

Subsequently, the interpretation of the normalized results (Fig. 2) reveals that over 90% of the total impact is determined by the following ten categories (% of total normalization results): freshwater ecotoxicity (24.8%), climate change (19.0%), fossil resource use (13.6%), photochemical ozone formation (7.8%), particulate matter (6.2%), marine eutrophication (5.5%), human toxicity, non-cancer (4.9%), terrestrial eutrophication (4.6%), freshwater eutrophication (2.8%) and use of mineral and metal resources (2.6%). The remaining impact categories, which are less significant compared to the others, have been grouped under the heading “other impact categories” and include: Acidification, Human toxicity - cancer, Ionising radiation, Water use, Land use, Ozone depletion.

Normalization further indicates that the cement production phase dominates the total impact (75%), followed by the more modest contributions from aggregate transportation and production (approximately 9% and 7%, respectively), and finally by the minimal contributions from the concrete processing phase (4%) and cement transportation (3%) (Fig. 4).

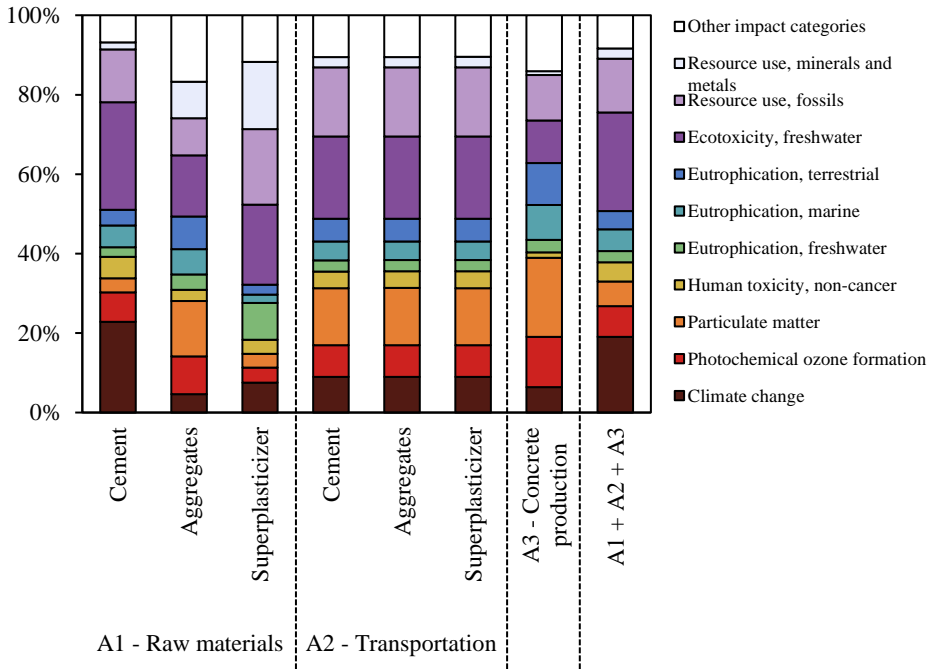


Fig. 2 Normalized impact values related to the production of 1 m<sup>3</sup> of C25/30 XC1-XC2-S4 concrete with rounded natural aggregates (R): detail of the impact categories.

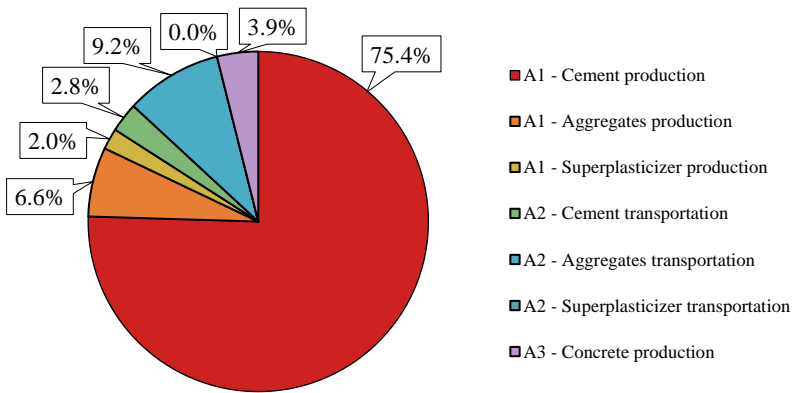


Fig. 3 Normalized impact values related to the production of 1 m<sup>3</sup> of C25/30 XC1-XC2-S4 concrete with rounded natural aggregates (R) divided in raw material procurement (A1), transportation to the concrete plant (A2), and production (A3).

From the analysis of the weighted data across the four different scenarios (concretes manufactured with four different aggregates) presented in Figure 4, it is evident that the partial replacement of natural aggregate with recycled aggregate does not result in substantial changes in the primary environmental impact parameters. This is mainly due to the limited contribution of aggregate production to the overall environmental impact of concrete, which is approximately 6.6%. Combined with current Italian regulatory restrictions that do not permit a substitution rate higher than 30% for C25/30 and C30/37 concretes, this significantly limits the potential environmental benefits of using recycled aggregates.

This finding also highlights the central role of the cement. It is crucial to focus on binder production when defining decarbonization strategies and environmental impact mitigation measures to achieve tangible benefits for enhancing the sustainability of concrete.

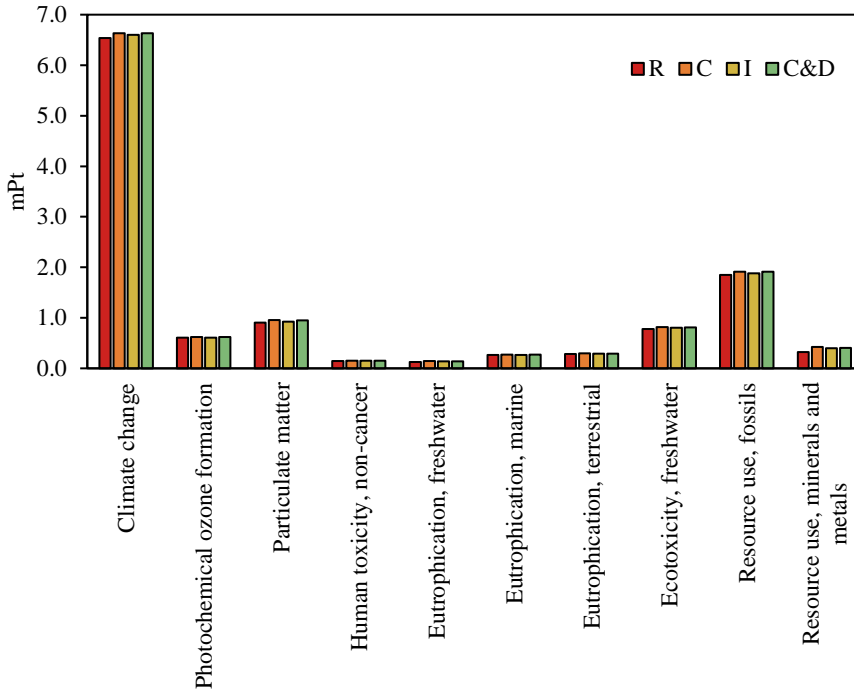


Fig. 4 Weighted impact values related to the production of 1 m<sup>3</sup> of C25/30 XC1-XC2-S4 concrete with different aggregate type.

## 5 Conclusions

This study provides a LCA “from cradle to gate” of the concrete supply chain, specifically focusing on the environmental impacts of using different types of aggregates, including natural and recycled materials. The findings are based on 32 datasets representing over 96% of the Italian ready-mix concrete production, categorized by compressive strength class, workability class, and environmental exposure class. Sixteen impact categories in the manufacturing stage (A1-A3) were included to analyze each concrete mixture, and only those contributing to 90% of the total impact were taken into account. Due to page limitations, only a subset of the extensive work conducted can be presented here, specifically related to a C25/30 XC1-XC2-S4 concrete with rounded natural aggregates of alluvial origin (R), natural aggregates obtained by crushing rocks (C), mixed aggregate consisting partly of natural crushed aggregate and partly (15% by mass) of recycled aggregate from industrial processes (I) or mixed aggregate consisting partly of natural crushed aggregate and partly (15% by mass) of recycled aggregate from the demolition of concrete structures (C&D).

Taking into account the results, the following conclusions can be drawn:

- The cement production phase is the dominant contributor to the overall environmental impact, accounting for approximately 75% of the total impact. This underscores the importance of focusing on decarbonization strategies and environmental impact mitigation measures in cement production to achieve significant sustainability improvements in the concrete industry;

- The production of aggregates marginally contributes to the total environmental impact of concrete, representing about 6.6%. Consequently, the partial replacement of natural aggregates with recycled aggregates does not result in substantial changes in the primary environmental impact parameters;
- Current Italian regulations restrict the substitution rate of natural aggregates with recycled aggregates to 30% for the most commonly produced strength classes, namely C25/30 and C30/37. This limitation significantly limits the potential environmental benefits that could be derived from the use of recycled aggregates in concrete production.

## References

- [1] A. Sivakrishna, A. Adesina, P.O. Awoyera, K. Rajesh Kumar, Green concrete: A review of recent developments, *Mater. Today Proc.* 27 (2020) 54–58. <https://doi.org/https://doi.org/10.1016/j.matpr.2019.08.202>.
- [2] D. Coffetti, E. Crotti, G. Gazzaniga, M. Carrara, T. Pastore, L. Coppola, Pathways towards sustainable concrete, *Cem. Concr. Res.* 154 (2022) 106718. <https://doi.org/10.1016/j.cemconres.2022.106718>.
- [3] S.A. Miller, V.M. John, S.A. Pacca, A. Horvath, Carbon dioxide reduction potential in the global cement industry by 2050, *Cem. Concr. Res.* 114 (2018) 115–124. <https://doi.org/10.1016/j.cemconres.2017.08.026>.
- [4] P.J.M. Monteiro, S.A. Miller, A. Horvath, Towards sustainable concrete, *Nat. Mater.* 16 (2017) 698–699. <https://doi.org/10.1038/nmat4930>.
- [5] Federbeton, Rapporto di filiera 2022, 2023.
- [6] UNICIRCULAR Fondazione per lo sviluppo sostenibile – FISEUNICIRCULAR Unione Imprese Economia, L'Italia del riciclo 2023, 2023.
- [7] Federbeton, Rapporto di sostenibilità 2022, 2023.
- [8] L. Coppola, E. Palumbo, D. Coffetti, C. Panozzo, S. Rapelli, M. Cellulare, C. Rinaldi, Studio LCA della filiera del calcestruzzo e degli aggregati riciclati, 2023.



## Appendix

Table A.1 Characterized impact values related to the production of 1 m<sup>3</sup> of C25/30 XC1-XC2-S4 concrete with rounded natural aggregates (R): impact during raw material procurement (A1), transportation to the concrete plant (A2), and production (A3).

Impact category	A1			A2			A3
	Cement	Aggregates	Superpl.	Cement	Aggregates	Superpl.	
Climate change [kgCO <sub>2</sub> eq]	2,28E+02	4,01E+00	2,02E+00	3,38E+00	1,10E+01	2,91E-02	3,29E+00
Ozone depletion [kgCFC1 <sub>1eq</sub> ]	1,57E-05	6,78E-07	3,18E-07	8,06E-07	2,62E-06	6,94E-09	6,27E-07
Ionising radiation [kBq U235 <sub>eq</sub> ]	6,00E+00	1,26E+00	1,89E-01	2,66E-01	8,65E-01	2,29E-03	3,03E-01
Photochemical ozone formation [kg NMVOC <sub>eq</sub> ]	3,71E-01	4,14E-02	5,16E-03	1,51E-02	4,92E-02	1,30E-04	3,28E-02
Particulate matter [disease inc.]	2,61E-06	8,93E-07	6,82E-08	3,97E-07	1,29E-06	3,42E-09	7,55E-07
Human toxicity, non-cancer [CTUh]	1,53E-06	7,00E-08	2,72E-08	4,50E-08	1,46E-07	3,87E-10	2,07E-08
Human toxicity, cancer [CTUh]	2,22E-08	5,45E-09	1,67E-09	1,14E-09	3,70E-09	9,79E-12	1,10E-09
Acidification [mol H <sup>+</sup> <sub>eq</sub> ]	2,23E-01	3,69E-02	7,98E-03	1,41E-02	4,58E-02	1,21E-04	2,78E-02
Eutrophication, freshwater [kg P <sub>eq</sub> ]	4,88E-03	6,64E-04	4,97E-04	2,10E-04	6,83E-04	1,81E-06	3,20E-04
Eutrophication, marine [kg N <sub>eq</sub> ]	1,32E-01	1,35E-02	1,38E-03	4,30E-03	1,40E-02	3,70E-05	1,09E-02
Eutrophication, terrestrial [mol N <sub>eq</sub> ]	8,53E-01	1,56E-01	1,44E-02	4,70E-02	1,53E-01	4,05E-04	1,19E-01
Ecotoxicity, freshwater [CTUe]	1,43E+03	7,05E+01	2,87E+01	4,11E+01	1,34E+02	3,54E-01	2,93E+01
Land use [Pt]	1,77E+02	1,24E+02	5,63E+00	6,02E+01	1,96E+02	5,19E-01	9,23E+00
Water use [m <sup>3</sup> depriv.]	1,39E+01	4,04E+00	1,03E+00	1,81E-01	5,89E-01	1,56E-03	2,72E+00
Resource use, fossils [MJ]	1,06E+03	6,60E+01	4,12E+01	5,26E+01	1,71E+02	4,53E-01	4,74E+01
Resource use, minerals and metals [kg Sb <sub>eq</sub> ]	1,35E-04	6,25E-05	3,59E-05	7,74E-06	2,52E-05	6,67E-08	3,93E-06

# Assessment of Mid-Span Deflection in Beams Reinforced with Hybrid FRP/Steel Rebars: A Comparative Study

Luciano Ombres<sup>1</sup>, Maria Antonietta Aiello<sup>2</sup>, Pietro Mazzuca<sup>1</sup>, Francesco Campolongo<sup>3</sup>

<sup>1</sup>*Department of Civil Engineering, University of Calabria, 87036 Arcavacata di Rende, Cosenza, Italy.*

<sup>2</sup>*Department of Innovation Engineering, University of Salento, via Monteroni, 73100 Lecce, Italy.*

<sup>3</sup>*Department of Earth and Geoenvironmental Sciences, University of Bari, 70125 Bari, Italy.*

## Abstract

Fiber-reinforced polymer (FRP) rebars have emerged as a promising alternative to steel reinforcement due to their high tensile strength, lightweight nature, and good corrosion resistance. However, concrete members reinforced with FRP (FRP-RC) often exhibit drawbacks such as larger deflections and wider cracks compared to steel-reinforced concrete (steel-RC) members with equivalent reinforcement areas. This is primarily due to the lower elastic modulus of FRP rebars. To address these challenges, hybrid systems combining steel and FRP components have gained attention as a viable solution. These hybrid systems combine the higher stiffness and ductility of steel with the corrosion resistance and lightweight properties of FRP. In this context, this study provides an overview of the serviceability limit state behavior of concrete beams reinforced with both steel and FRP bars, with a focus on a key design parameter, namely the mid-span deflection. Furthermore, the study compares analytical expressions derived from national and international guidelines with experimental data available in the literature to evaluate their accuracy and applicability. The results obtained indicate that current formulations often do not accurately predict the behavior of beams reinforced with both FRP and steel bars under service conditions. Therefore, there is a clear need for additional research efforts, encompassing both experimental investigations and theoretical developments, to enhance our understanding in this area.

## 1 Introduction

Corrosion of steel reinforcement is the main cause of degradation for concrete structural elements. Ineffective cover and the exposure to aggressive environmental conditions enhance this phenomenon, causing an important reduction of the rebars and, consequently, a progressive decay of structural element mechanical properties.

FRP (Fiber Reinforced Polymers) rebars represent an alternative solution to traditional steel rebars to improve the durability of concrete structures. Composite rebars offer several advantages, including high strength, light weight, excellent corrosion resistance, non-magnetic properties, and low thermal conductivity. These benefits make FRP rebars an attractive alternative to traditional steel reinforcements in various applications, particularly where durability and resistance to environmental factors are critical.

Despite these advantages, there are certain drawbacks that need to be carefully considered in structural design. One significant issue is that FRP rebars exhibit an elastic-linear behavior, thus they do not yield before failure, leading to a brittle collapse. This lack of ductility is a concern mostly when the structural capacity under seismic actions is required. Additionally, FRP rebars have a significantly lower modulus of elasticity compared to steel rebars. This lower stiffness results in larger deflections, which can compromise the serviceability of the structure. Larger deflections can lead to issues such as increased crack widths, which not only affect the aesthetic appearance but also potentially compromise the durability and long-term performance of the structure. It is also worth mentioning that wider cracks can allow the penetration of harmful substances like water and chemicals, leading to further deterioration of the concrete and the reinforcement over time. The high deformability of structural elements may also compromise the integrity of non-structural elements, and the possibility of accomplishing specific performances from a functionality point of view.

Therefore, while FRP rebars offer distinct advantages in terms of corrosion resistance and weight, their application must be carefully evaluated to mitigate issues related to brittle failure modes, excessive deflections, and crack width. In this context, the combined use of FRPs and steel reinforcement, forming

a hybrid system, offers an optimal solution to address the ductility and serviceability challenges associated with FRP rebar-reinforced elements. In addition, by placing the composite rebars in the outer layer and the steel bars in the inner layer of the tensile zone, the overall durability of the reinforced structural element can be significantly improved. Therefore, this hybrid approach takes advantage of the high strength, low weight, and corrosion resistance of FRP while also benefits from the ductile behavior and the higher stiffness of steel, providing better crack control, reducing excessive deflections, and increasing resistance to environmental degradation.

Over the past two decades, several authors studied the flexural behavior of beams reinforced with a hybrid FRP/steel system [1-4].

Aiello and Ombres [1] conducted an experimental campaign on beams reinforced with Aramid-FRP and steel reinforcements placed on the same or different levels within the tension zone. The authors conducted four-point bending tests on six beams, each measuring 3000 mm in length with a rectangular cross section of 150 mm in width and 200 mm in height. The experimental results demonstrated that the thickness of the cover significantly influences the structural response of the beams. Considering two beams with identical amount of steel and FRP reinforcements, the first beam (A1) has steel rebars with a cover thickness twice than that of the FRP bars, while the second beam (C1) has both types of reinforcement placed at the same level. Under service conditions the A1 beam exhibited higher stiffness compared to the C1 beam. The configuration of the reinforcement also influences the crack width; in fact, the one-layer reinforced beams showed crack widths higher than those of the double-layer hybrid reinforced ones.

Qu et al [2] investigated both experimentally and analytically the structural behavior of six beams reinforced with a combination of steel and glass fiber-reinforced polymer (GFRP) bars. Four-point bending tests were carried out on the beams with a span of 1800 mm and a rectangular cross section of 180mm in width and 250 mm in height. The authors observed that the flexural capacity improves as a function of the effective reinforcement ratio, while the axial stiffness of reinforcement had a negligible influence.

El Refai et al [3] evaluated the structural performance of six concrete beams reinforced with a combination of steel and GFRP rebars. All beams tested (with 4000 mm length and a rectangular cross section of 230 mm in width and 300 mm in height) were reinforced with hybrid (GFRP and steel) rebars arranged in one layer in the tensile region. The authors evaluated the influence of the effective reinforcement ratio and the axial stiffness ratio (ratio of the axial stiffness of the steel bars to that of the GFRP rebars) on the flexural capacity of the tested beams. The experimental findings showed that the influence of the reinforcement ratio is significantly higher than that of the stiffness ratio, confirming the results obtained by Qu et al [2].

The results reported above highlight the significant advantages associated with the use of hybrid FRP/steel systems compared to the solely FRP, especially concerning serviceability conditions. For design purposes, evaluating serviceability limit state in terms of deformability plays a crucial role. Despite its importance, current regulations do not provide specific relationships for the deflections evaluation of beams reinforced with hybrid systems. Some formulations proposed by various authors rely on limited experimental data and are therefore not widely applicable. In this context, this paper aims to assess the accuracy of existing design models assessed for FRP reinforced concrete beams (ACI 440.1R-06 [5], ACI 440.1R-15 [6], and CSA-S806-12 [7]) when applied to hybrid reinforced beams. Additionally, the experimental data are compared with those obtained using the design model proposed in CNR-DT 203–2006 [8]. To this scope, a database comprising seven beams tested by various authors was used.

## 2 Design models for the deflection computation

This section presents the analytical procedures reported in the literature for beams reinforced with FRP rebars, adapted to hybrid FRP/steel systems by the authors. Specifically, the relationships reported in the following were adapted from American models, Canadian standard, Italian regulation, as well as models proposed by various authors. The deflection evaluation is referred to four-point bending beams coherently with the structural scheme utilized in the experimental campaigns.

### 2.1 ACI codes

For the four-point bending beam, before cracking, the mid-span deflection is calculated as follows:

$$\Delta m = \frac{P_a a}{48 E_c I_g} (3l^2 - 4a^2) \quad (1)$$

where  $P_a$  is the applied load;  $a$  is the shear span;  $E_c$  is the modulus of elasticity of concrete;  $l$  is the beam length  $I_g$  is the gross moment of inertia which can be calculated using Eq. (2)

$$I_g = \frac{b h^3}{12} \quad (2)$$

where  $b$  and  $h$  are the width and height of section. To account for the variation in beam stiffness as the applied load increases, the ACI [5]-[6] codes introduce the effective moment of inertia after cracking ( $I_e$ ) in the Eq. (1):

$$\Delta m = \frac{P_a a}{48 E_c I_e} (3l^2 - 4a^2) \quad (3)$$

The term  $I_e$  varies between different ACI codes. For purely FRP-reinforced beams, the ACI 440.1R-06 [5] recommends the use of Eq. (4) to estimate the effective moment of inertia:

$$I_e = I_{cr} + (\beta_d I_g - I_{cr}) \left( \frac{M_{cr}}{M_a} \right)^3 \leq I_g \quad (4)$$

where  $I_{cr}$  represents the cracked moment of inertia;  $\beta_d$  is a coefficient for reducing the tension stiffening contribution,  $M_a$  is the applied moment and  $M_{cr}$  represent the cracking moment which can be derived from the Eq. (5):

$$M_{cr} = \frac{0.62 \lambda \sqrt{f'_c} I_g}{y_t} \quad (5)$$

where  $f'_c$  is the concrete compressive strength;  $\lambda=1$  is the modification factor reflecting the reduced mechanical properties of a normal density concrete, and  $y_t$  is the distance from the centroidal axis of the gross section. Furthermore, the coefficient  $\beta_d$ , introduced to consider the reduced tension stiffening in FRP-reinforced members, is calculated as follows:

$$\beta_d = \frac{1}{5} \left( \frac{\rho_f}{\rho_{fb}} \right) \leq 1,0 \quad (6)$$

in which the FRP-bars reinforcement ratio ( $\rho_f$ ) and the balanced reinforcement ratio ( $\rho_{fb}$ ) are obtained from Eq. (7) and (8) respectively:

$$\rho_f = \frac{A_f}{b d} \quad (7)$$

$$\rho_{fb} = 0.85 \beta_1 \frac{f'_c}{f_{fu}} \frac{E_f \varepsilon_{cu}}{E_f \varepsilon_{cu} + f_{fu}} \quad (8)$$

where  $A_f$  is the area of FRP reinforcement;  $\varepsilon_{cu}$  is the maximum concrete compressive strain;  $E_f$  represent the modulus of elasticity of FRP bars, and  $f_{fu}$  is their tensile strength. In the Eq. (4),  $I_{cr}$  indicates the cracked moment of inertia obtained from elastic cracked-section analysis, as reported in Eq. (9) for hybrid reinforcement:

$$I_{cr} = \frac{1}{3} b (k d)^3 + (n_f A_f + n_s A_s) d^2 (1 - k)^2 \quad (9)$$

$$k = \sqrt{(n_f \rho_f + n_s \rho_s)^2 + 2 (n_f \rho_f + n_s \rho_s)} - (n_f \rho_f + n_s \rho_s) \quad (10)$$

$$n_s = \frac{E_s}{E_c}; \quad n_f = \frac{E_f}{E_c} \quad (11)$$

where,  $k$  is the ratio between the depth of the neutral axis and that of the FRP reinforcement,  $\rho_s$  is the steel reinforcement ratio,  $n_s$  and  $n_f$  are the ratio between the modulus of elasticity of FRP and steel rebars and the modulus of elasticity of concrete, respectively. The ACI 440.1R-15 [6] suggests a revised relationship for the determination of  $I_e$  (Eq. (12)), introducing an additional factor to account for the variation in stiffness along the length of the member ( $\gamma$ ) which is reported in Eq.(13).

$$I_e = \frac{I_{cr}}{1 - \gamma \left( 1 - \frac{I_{cr}}{I_g} \right) \left( \frac{M_{cr}}{M_a} \right)^2} \leq I_g \quad (12)$$

$$\gamma = 1.72 - 0.72 \left( \frac{M_{cr}}{M_a} \right) \quad (13)$$

Applying the ACI 440.1R-15 [6] code (and its previous versions) Ruan et al. [4] observed that the analytical results do not effectively approximate the experimental findings under the serviceability limit state. Therefore, the authors introduced a corrective coefficient ( $\kappa=0.64$ ), proposing the following equation in order to calculate the effective moment of inertia:

$$I_e = \kappa \frac{I_{cr}}{1 - \gamma \left(1 - \frac{I_{cr}}{I_g}\right) \left(\frac{M_{cr}}{M_a}\right)^2} \leq I_g \quad (14)$$

The latest version of ACI 440-22 [9] code proposed further modifications primarily aimed at reducing the cracking moment of inertia, as reported in the following:

$$I_e = \frac{I_{cr}}{1 - \gamma \left(1 - \frac{I_{cr}}{I_g}\right) \left(\frac{0.8 M_{cr}}{M_a}\right)^2} \leq I_g \quad (15)$$

$$\gamma = 1.72 - 0.72 \left(\frac{0.8 M_{cr}}{M_a}\right) \quad (16)$$

## 2.2 CSA code

In order to determine the deflection in the beams tested under four-point loadings, the CSA-S806-12 [7] proposes the following equation:

$$\Delta m = \frac{P_a l^3}{48 E_c I_{cr}} \left[ 3 \left(\frac{a}{l}\right) - 4 \left(\frac{a}{l}\right)^3 - 8 \left(1 - \frac{I_{cr}}{I_g}\right) \left(\frac{L_g}{l}\right)^3 \right] \quad (17)$$

$$L_g = a \frac{M_{cr}}{M_a} \quad (18)$$

where  $L_g$  represents the distance from the support to the point where  $M=M_{cr}$ .

## 2.3 CNR code

For calculating deflections in FRP-reinforced members, the CNR-DT 203 – 2006 [8] suggests a simplified model based on Eurocode 2 (EC2) [10] provisions for referred steel reinforced concrete members. The accuracy of Equation (19) has been validated through numerous experimental tests conducted on FRP-reinforced beams.

$$f = f_1 \beta_1 \beta_2 \left(\frac{M_{cr}}{M_{max}}\right)^m + f_2 \left[1 - \beta_1 \beta_2 \left(\frac{M_{cr}}{M_{max}}\right)^m\right] \quad (19)$$

In the above relationship,  $f_1$  and  $f_2$  are the deflections determined for the uncracked and cracked stage, respectively;  $\beta_1=0.5$  is a non-dimensional coefficient accounting for bond properties of FRP bars;  $\beta_2$  (1.0 for short time loading; 0.5 for long time or cyclic loading) is a non-dimensional coefficient accounting for the duration of loading;  $M_{max}$  is the applied maximum moment, and  $M_{cr}$  is the cracking moment calculated at the same cross section of  $M_{max}$ ;  $m$  is a coefficient assumed equal to 2. The deflection ( $f$ ) is determined using Eq. (20) as follows:

$$f_1 = \frac{P_a a}{48 E_c I_1} (3l^2 - 4a^2) \quad (20)$$

$$I_1 = \frac{b h^3}{12} + b h (0.5 h - x_c)^2 + n_s A'_s (x_c - \delta)^2 + n_s A_s (d - x_c)^2 + n_f A_f (d - x_c)^2 \quad (21)$$

where  $A'_s$  and  $A_s$  are the area of compressive and tensile steel reinforcement respectively,  $I_1$  represent the un-cracked section moment of inertia. The depth of the neutral axis ( $x_c$ ) is considered equal to  $h/2$ . In the second stage, when the section is cracked, the deflection is calculated using the following equations:

$$f_2 = \frac{P_a a}{48 E_c I_2} (3l^2 - 4a^2) \quad (22)$$

$$I_2 = \frac{b x_c^3}{3} + n_s A'_s (x_c - \delta)^2 + n_s A_s (d - x_c)^2 + n_f A_f (d - x_c)^2 \quad (23)$$

$I_2$  is the cracked section moment of inertia.

### 3 Theoretical results and analysis

The theoretical models reported in section 2 were used to evaluate the deflection of tested specimens available in the literature. The geometric and mechanical data needed for the calculation are listed in Table 1.

Table 1 Mechanical and geometric data of considered specimens.

Reference	Specimen	$l$ [mm]	$b$ [mm]	$h$ [mm]	$f'_c$ [MPa]	$A_f$ [mm <sup>2</sup> ]	$A_s$ [mm <sup>2</sup> ]	$M_{u,ACI}$ [kNm]	$M_{u,EC2}$ [kNm]
Ombres&Aiello [1]	C1	2700.00	150.00	200.00	45.70	88.31	100.48	22.67	21.50
Qu et al [2]	B3	1800.00	180.00	250.00	28.14	253.23	226.08	40.44	40.46
	B5				29.20	141.69	401.92	39.39	38.87
	B7				34.60	141.69	113.04	24.99	30.59
El Refai et al [3]	2G12-2S10	3700.00	230.00	300.00	40.00	226.19	157.08	58.43	66.31
	2G12-2S12					226.19	226.19	55.72	70.60
	2G16-2S12					402.12	226.19	70.92	83.83

The reported  $M_{u,ACI}$  and  $M_{u,EC2}$  represent the theoretical ultimate moments calculated following the ACI [6] and Eurocode [10] guidelines respectively.

Fig. 1-3 compare theoretical moment-deflection curves with experimental results. Additionally, to evaluate deflections at the serviceability limit state, curves obtained up to 40% of the ultimate moment are also reported.

As illustrated in Fig. 4 left, the applied models are unable to effectively approximate the experimental deflections. Moreover, the theoretical results mostly underestimate the experimental values, with differences exceeding 15%. When observing the results obtained at 40% of the ultimate moment, indicative of the serviceability limit state (Fig. 5right), only the model proposed by Ruan et al. [4] seems to provide predictive values closer to those observed experimentally, highlighting the effective improvement suggested by the authors. On the other hand, all theoretical models derived from the codes [5]-[6]-[7]-[8] continue to underestimate the experimental results.

It is important to note that these observations are based on a limited number of beams and therefore require a broader database for validation of available models or possible proposal of revised design relationships.

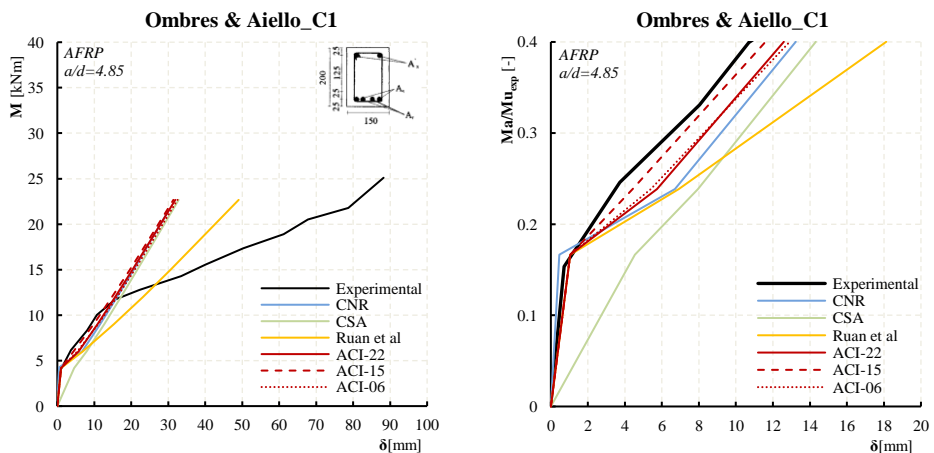


Fig. 1 Comparisons of mid-span deflection between theoretical and experimental results [1].

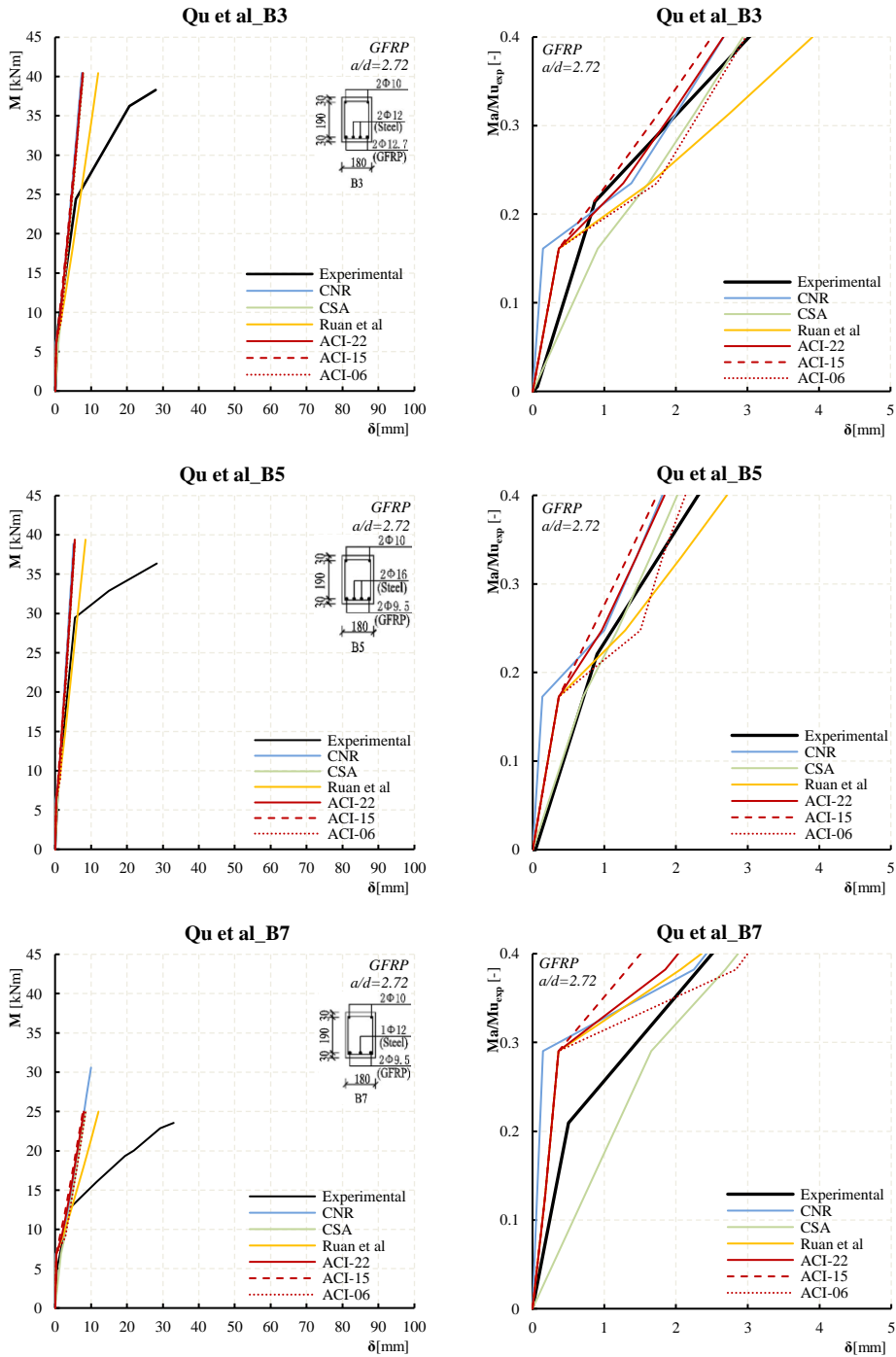


Fig. 2 Comparisons of mid-span deflection between theoretical and experimental results [2].

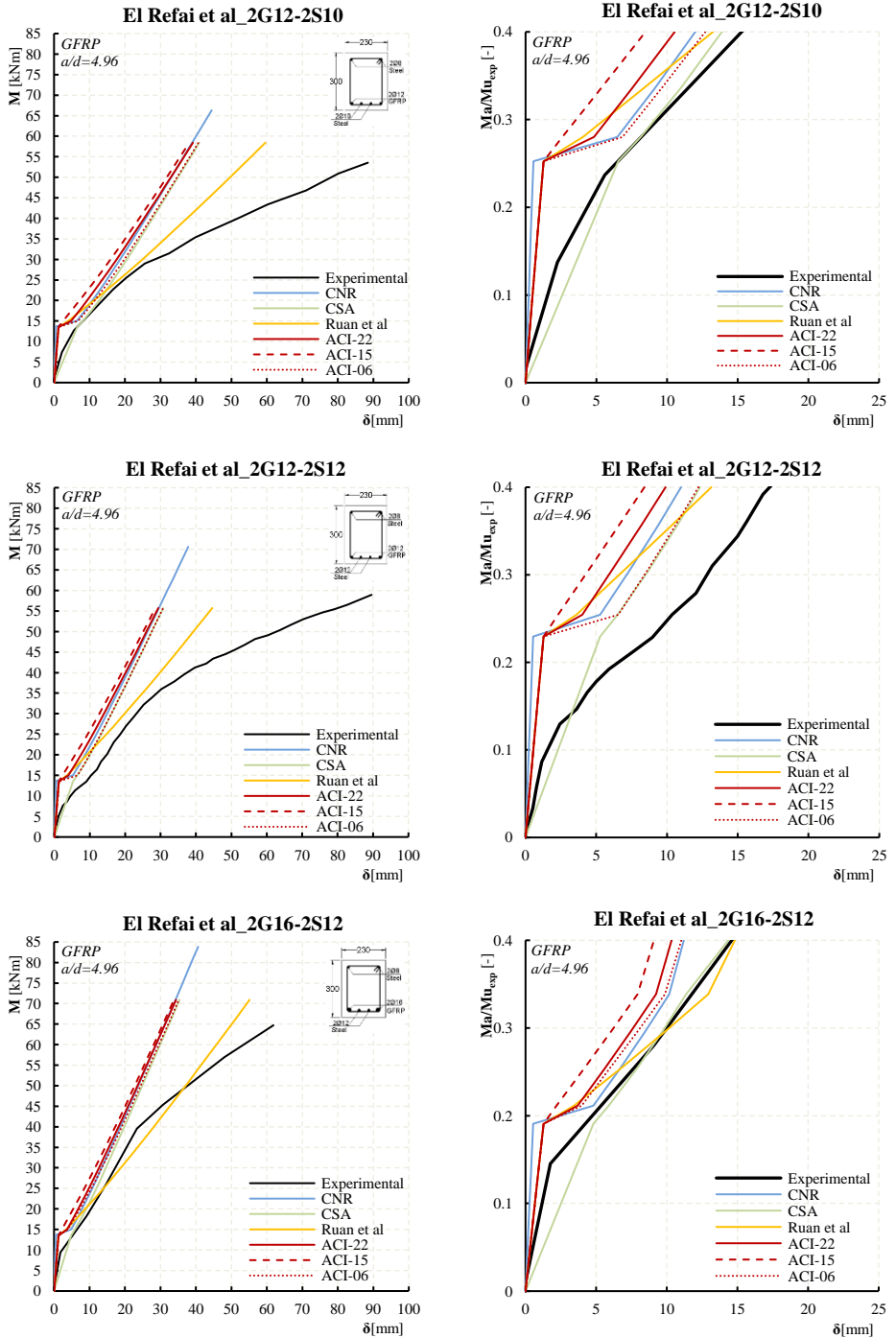


Fig. 3 Comparisons of mid-span deflection between theoretical and experimental results [3].



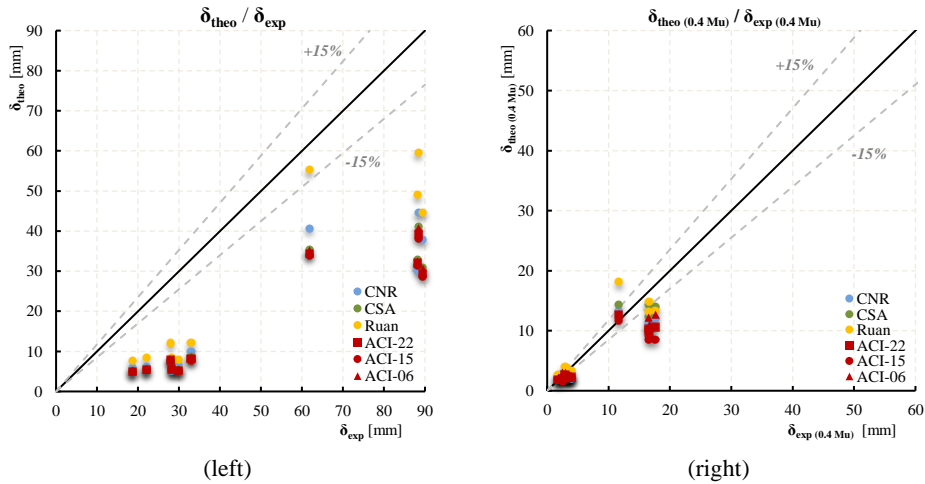


Fig. 4 Overview of the (a) experimental vs theoretical comparison (at ultimate moment); b) experimental vs theoretical comparison (at 40% of ultimate moment).

## 4 Conclusions

In conclusion, the study highlights the challenges and advantages associated with using hybrid FRP/steel systems in reinforced concrete beams. The comparison between some available experimental results and relationships based on ACI, CSA, and CNR provisions reveal discrepancies, indicating a need for further calibration and refinement to accurately predict deflection for hybrid reinforced beams.

Future research should focus on expanding experimental datasets to enhance the reliability and applicability of existing design guidelines for hybrid FRP/steel structures. Furthermore, there is a clear need for conducting comprehensive parametric analyses to identify the factors that significantly influence the behavior of beams reinforced with hybrid FRP/steel systems, such as cover thickness, distribution, and ratio between FRP and steel reinforcement. Investigating these variables is crucial for enhancing the reliability of existing guidelines and optimizing the design of structures reinforced with hybrid systems.

## References

- [1] Aiello, M. A., & Ombres, L. (2002). Structural performances of concrete beams with hybrid (fiber-reinforced polymer-steel) reinforcements. *Journal of Composites for Construction*, 6(2), 133-140.
- [2] Qu, W., Zhang, X., & Huang, H. (2009). Flexural behavior of concrete beams reinforced with hybrid (GFRP and steel) bars. *Journal of Composites for construction*, 13(5), 350-359.
- [3] El Refai, A., Abed, F., & Al-Rahmani, A. (2015). Structural performance and serviceability of concrete beams reinforced with hybrid (GFRP and steel) bars. *Construction and Building Materials*, 96, 518-529.
- [4] Ruan, X., Lu, C., Xu, K., Xuan, G., & Ni, M. (2020). Flexural behavior and serviceability of concrete beams hybrid-reinforced with GFRP bars and steel bars. *Composite structures*, 235, 111772.
- [5] American Concrete Institute (ACI) Committee 440, Guide for the design and construction of structural concrete reinforced with FRP bars, ACI 440.1R-06, American Concrete Institute, Farmington Hills, MI, USA, 2006.
- [6] ACI Committee 440. Guide for the design and structural of concrete reinforce with Fiber-reinforced polymer (FRP) bars (ACI 440.1R-15). American Concrete Institute, Farmington Hills, MI, USA, 2015.
- [7] Canadian Standards Association (CSA), Design and construction of building components with fiber-reinforced polymers, CSA-S806-12, Mississauga, ON, Canada, 2012.
- [8] CNR-DT 203 – 2006, National Research Council of Italy, guide for the design and construction of concrete structures reinforced with fiber-reinforced polymer bars. Advisory Committee on Technical Recommendations for Construction, Roma, 2006.
- [9] ACI Committee 440. Guide for the design and structural of concrete reinforce with Fiber-reinforced polymer (FRP) bars (ACI 440-22). American Concrete Institute, Farmington Hills, MI, USA, 2022.
- [10] EN 1996-2:2005, Eurocode 2, Design of concrete structures. European Committee for Standardisation CEN, Brussels, 2006.

# **Short- and long-term behaviour of RC structures**



# Applicability of an accelerated test for long-term performance estimation of hydrophobic treatment for reinforced concrete structures

Britta M. Schallock<sup>1</sup>, Matteo Gastaldi<sup>2</sup>

<sup>1</sup> *Department of Chemistry, Materials and Chemical Engineering “Giulio Natta”  
Politecnico di Milano  
Via Luigi Mancinelli, Milano (20131), Italy  
[britta.schallock@polimi.it](mailto:britta.schallock@polimi.it)*

<sup>2</sup> *Department of Chemistry, Materials and Chemical Engineering “Giulio Natta”  
Politecnico di Milano  
Via Luigi Mancinelli, Milano (20131), Italy  
[matteo.gastaldi@polimi.it](mailto:matteo.gastaldi@polimi.it)*

## Abstract

Rebar corrosion in reinforced concrete structures does not only lead to high maintenance and repair costs but also causes problems related to user's safety.

Preventative methods may prolongate the structural service life by limiting corrosion initiation and/or propagation. One among those are the so-called hydrophobic pore lining treatments which are limiting the penetration of water and can promote the dry condition into the concrete. However, only little information is available regarding the long-term performance of this products. The lack in knowledge does not only regard the influence of the coating on different durability relevant parameters (water penetrability, breathability, ...) but also the possible degradation of the latter.

A prediction of the long-term behaviour of a coated structure is thus difficult and even more, time consuming. This paper is discussing the applicability of an accelerated test procedure carried out in order to evaluate the long-term behaviour of a coated structure.

Reinforced concrete samples were prepared and subjected to accelerated carbonation. One carbonated sample was coated by a hydrophobic pore lining treatment and the other one was left uncoated. The samples were then initially submitted to atmospheric conditions of Milano (2 years) and subsequently moved to an accelerated chamber applying a 48 hours cycle that simulates a harsh atmospheric exposure (rain, wind, IR and UV- radiation). By comparison of the results of the coated and uncoated sample obtained during atmospheric and accelerated exposure, the effectiveness of the accelerated test procedure for the evaluation of the long-term performance of the coated reinforced concrete structures was analysed.

## 1 State of Art

In alkaline concrete, steel rebars form a passive layer at their surfaces which generally leads to corrosion rates of steel that are rather negligible. However, in chlorides-contaminated concrete (when a certain chlorides threshold is reached) or in carbonated concrete (reaction of alkaline constituents in the concrete pore solution with CO<sub>2</sub> from the atmosphere leading to drop in pH of concrete) embedded steel is depassivated. Once this occurs corrosion may propagate in presence of water and oxygen. Formation of expansive corrosion products then leads to cracking and spalling as well as loss of adhesion between steel and concrete and reduction of reinforcement cross section. All these phenomena might compromise the structural safety [1].

Aiming to extend the service life of reinforced concrete structures a possible preventative method is the application of so-called surface coatings. One type of surface coating is the hydrophobic impregnation of concrete which increases the contact angle between water and pore walls and thus causes a decrease in molecular attraction between water and concrete. This leads to a reduction of concrete penetrability to water (and possible aggressive species dissolved in it) [2].

Several researches confirmed a beneficial effect of hydrophobic surface treatments. For example, the sorptivity, and in consequence also the conductivity of hydrophobic- coated concrete, was found to be significantly reduced in respect to non- coated concrete [2], [3].

However, the long-term behaviour of hydrophobic coated structures is not well known. It is assumed that exposure to UV light or alkaline solutions might cause deterioration of this type of coating. The long-term performance is thus expected to be strongly related to the product penetration depth since UV light may not affect higher concrete depth [4], [5].

A laboratory test carried out in the Netherlands found a continuing reduction of water absorption into samples exposed to atmospheric conditions for a total duration of 5 years [3].

A study regarding existing structures in the UK coated in different time periods (up to 20 years) implied a time dependant reduction of the performance of hydrophobic treatments [4].

Thus, long-term behaviour is, in literature, generally determined by means of long-term atmospheric exposure which is rather time consuming and not easy to apply to new products; moreover, the comparability of tests carried out in different climates is rather poor. This study is discussing the possibility to evaluate the long-term behaviour of hydrophobic treatments by means of an accelerated procedure.

## 2 Experimental procedure

Two reinforced concrete samples with 400 kg/m<sup>3</sup> of cement (type CEM II/ A-L 42,5R) were prepared in laboratory. The mix design is reported in Table 1. The maximum diameter of used aggregates was 9.5 mm.

Table 1 Mix design of concrete.

Cement (kg/m <sup>3</sup> )	Water (l/m <sup>3</sup> )	Aggregates (kg/m <sup>3</sup> )	w/c
400	260	1606	0.65

The sample geometry was prismatic (side length: 150x120x50mm) (Figure 1). In both samples, at a concrete cover of 10 mm, two rebars of type B450C ( $\varnothing=10$  mm), were embedded. Before casting the rebars surfaces were sandblasted and subsequently cleaned by alcohol. Electrical connections were realized at one end of each rebar respectively and both ends were then covered by non-conductive material (exposed length limited to 80 mm in this way). Additionally, a reference electrode consisting of activated titanium was placed alongside each rebar. Two stainless steel wires ( $\varnothing=2$  mm; exposed length 60 mm) were placed between the two rebars for each sample in order to allow measurements of corrosion rate and electrical resistivity. After casting the samples were cured for 7 days (at RH>95% and 20°C) and afterwards submitted to accelerated carbonation until full carbonation of the sample was obtained (147 days).

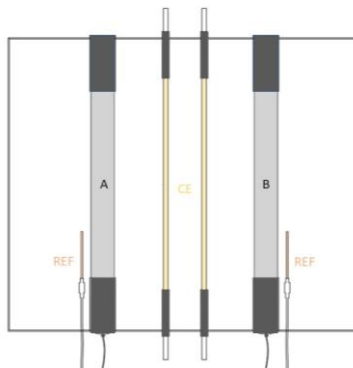


Fig. 1 Sample geometry.

On one out of the two samples the hydrophobic treatment was then applied. Therefore, the top and bottom surfaces were roughened by abrasive paper, cleaned and the hydrophobic treatment (commercial product, silane based) was applied (4g of gel/ 100 cm<sup>2</sup>). The respective faces of the other sample were kept uncoated. All the lateral faces of the samples were coated by epoxy resin. Both samples were then exposed to atmospheric conditions of Milano for a total period of around 2 years. Afterwards they were moved to a special chamber (Fig. 2 *left*) applying accelerated cycles consisting of wetting (water spraying), drying (ventilation), IR and UV (280-400 nm) radiation. For the determination of the program the standard ASTM G154-16 [6] was taken into consideration. The program of the applied cycle, that lasts 48 hours, was: 2 hours wetting, 4 hours drying, 30 hours and 12 hours of exposure to IR and UV radiation respectively (Figure 2 *right*). The total exposure period to the accelerated cycles was around 400 days. On a weekly basis, during both exposures (natural and accelerated), concrete electrical resistivity, corrosion rate (LPR- technique) and potential of reinforcement (vs. embedded activated titanium electrode and external calomel reference electrode, SCE) were measured.

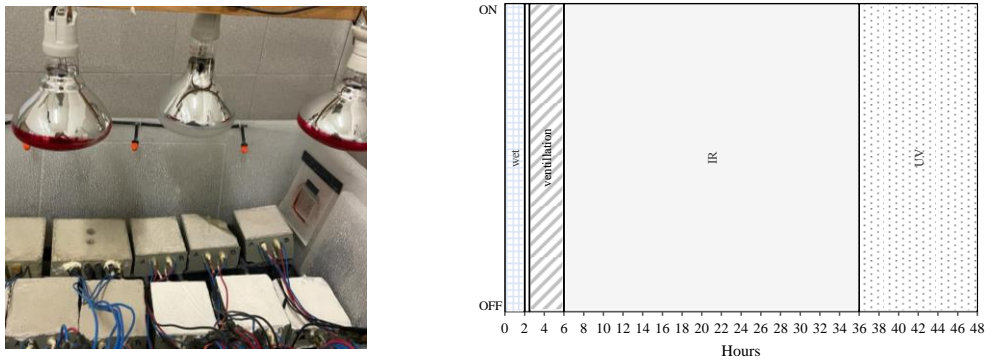


Fig. 2 *left*: Chamber used for cycles; *right*: Cycles.

### 3 Results and Discussion

#### 3.1 Atmospheric exposure

Figure 3 shows the results for electrical resistivity measurement as well as the precipitations (light blue) and minimum and maximum temperature [7] recorded during the 2 years of exposure to Milano atmosphere of the samples.

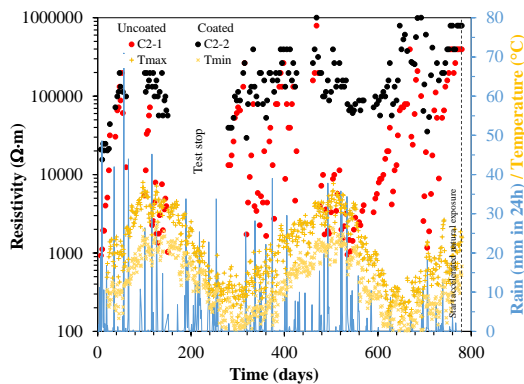


Fig. 3 Concrete electrical resistivities, precipitations (cumulated mm of rain in 24 hours) and temperature (minimum and maximum values) recorded during exposure to Milano atmosphere.

It was noted, that the resistivities recorded in the uncoated samples (red symbols) over time showed a strong dependence on the precipitations, thus in periods with stronger precipitations the resistivities dropped to values of around  $1'000 \Omega \cdot m$  while in drier periods the resistivities reached values up to around  $100'000 \Omega \cdot m$ . In the coated sample (black symbols) all resistivities, independently from the precipitations ranged around  $100'000 \Omega \cdot m$  and higher during all the exposure period. Thus, the treatment seems to efficiently avoid penetration of water into concrete.

The found result was underlined also by the measurements of potential and corrosion rate carried out in the same period. The results obtained for the coated and uncoated sample are shown in Figure 4.

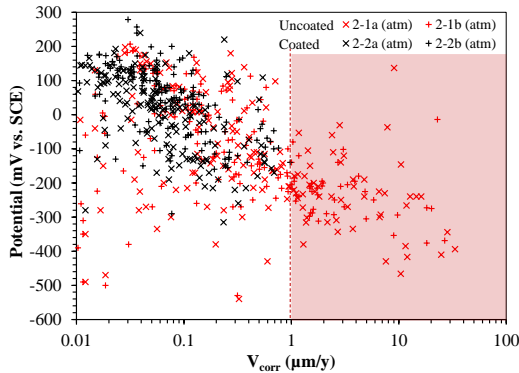


Fig. 4 Corrosion rates and potentials for coated and uncoated samples exposed to the Milano atmosphere.

It may be noted, that, also the corrosion rate and potential (vs. SCE reference electrode) measured for the rebars present in the uncoated sample (red symbols) showed strong fluctuations. Corrosion potential reached minimum values of  $-540 \text{ mV vs. SCE}$  and maximum values of around  $+200 \text{ mV vs. SCE}$ . In the same period corrosion rates ranged from around  $30 \mu\text{m/y}$  to  $0.01 \mu\text{m/y}$ . The rebars present in the sample treated with the hydrophobic coating showed lower periodical fluctuations, with corrosion potential ranging between  $+280$  and  $-300 \text{ mV vs. SCE}$  and corrosion rates remained during all exposure period at values  $< 1 \mu\text{m/year}$ . Considering corrosion rates higher than  $1 \text{ mA/m}^2$  as non-negligible values (red area of the graph) it may be noted, that only black symbols are present out of this zone and thus, that only the rebars present in the coated sample exhibited no propagation of corrosion. The rebars in the uncoated samples instead, periodically (during the wet periods) showed high corrosion rates.

Thus, it may be stated that, the hydrophobic coating efficiently reduced the penetration of water into the sample during wet periods, thus propagation of corrosion in this sample was negligible due to the lack of electrolyte. In contrast, in the uncoated sample the wet periods led to a strong reduction in resistivity allowing the propagation of corrosion (drop in potential and rise in corrosion rate).

### 3.2 Accelerated exposure

After 2 years of atmospheric exposure the samples were moved in the chamber that apply the accelerated cycles (Fig. 2). Figure 5 shows the monitoring of temperature and concrete electrical resistivity during 300 hours of exposure of the samples to the cycles.

As to be noted in Figure 5 the temperature ranges from  $15^\circ\text{C}$  during the wet period to around  $40^\circ\text{C}$  during the IR cycles; this is also the maximum temperature detected during the atmospheric exposure (Figure 3). The resistivity measured in the uncoated sample was influenced by the applied cycle, it thus dropped to values around  $2'000 \Omega \cdot m$  during the wet cycle and subsequently rose during ventilation, UV and IR cycles to values around  $6'000 \Omega \cdot m$ .

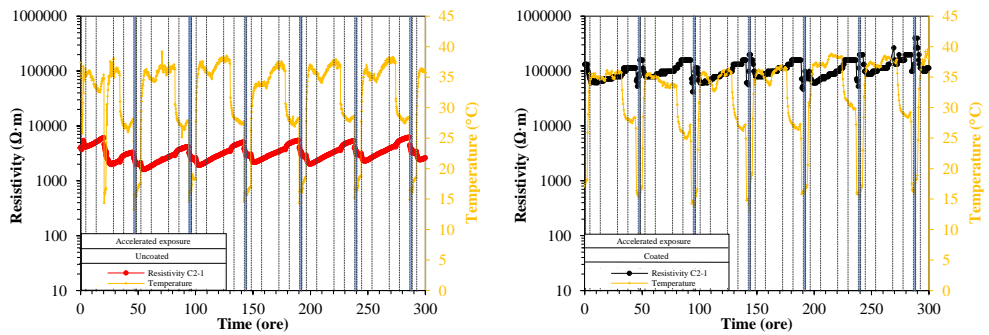


Fig. 5 *left*: Resistivity of uncoated sample during accelerated cycles; *right*: Resistivity of coated sample during accelerated cycles.

In the case of the coated specimen the fluctuation of resistivity during the cycle resulted lower and between  $40 \cdot 1000 - 200 \cdot 1000 \Omega \cdot m$ . A small drop in resistivity during the wetting cycle has been observed which, however, was rather related to the reduction in temperature than the wetting of the concrete.

Figure 6 shows the results of the manual measurements of corrosion rate and potential carried out during the exposure of the samples to the accelerated cycles.

It may be noted, that in the case of the uncoated sample measurements give strong indications for the propagation of corrosion. The corrosion rate for both rebars embedded in this sample are considered to be in a non-negligible corrosion condition during almost all the period of exposure to the accelerated cycles ( $> 1 \mu m/y$ ) reaching values even higher than  $10 \mu m/y$ . For the rebars in the coated sample instead, rather positive potentials and negligible corrosion rates, always  $< 1 \mu m/y$  were determined.

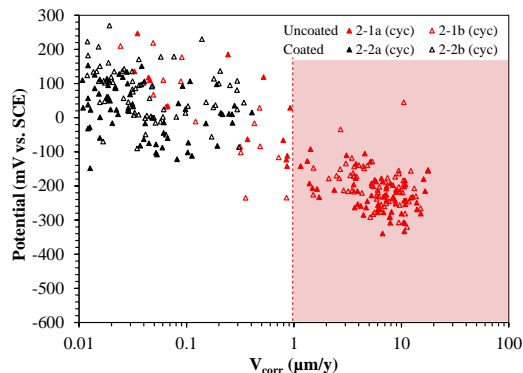


Fig. 6 Corrosion rates and potentials for coated and uncoated samples exposed to the accelerated cycles.

### 3.3 Natural / accelerated exposure comparison

Comparing Figure 4 and Figure 6 it was noted how, in the case of the uncoated specimens the exposure to the cycles led to more severe conditions. The measurements carried out during the exposure to accelerated cycles (red symbols) predominantly fall in the area highlighted in red. Considering the coated sample (black symbols) it may be noted that all measurements are located in the white area of both Figures corresponding to negligible corrosion risk. This behaviour was also underlined by the comparison of the average corrosion conditions for the rebars in the coated and uncoated samples in the two exposures reported in Figure 7.

In the case of the uncoated specimen the corrosion rate rose from values between  $1-2 \mu m/y$  to  $5.4-6 \mu m/y$  passing from the atmospheric to the accelerated exposure.



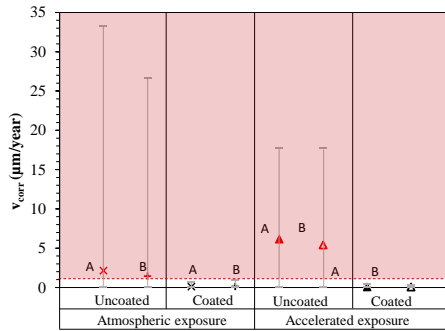


Fig 7. Average corrosion rates, and range of variation of the results, in different exposures.

In the case of the coated specimen the change in exposure did not influence the average corrosion rate. For both rebars it remained at values  $<<1 \mu\text{m}/\text{y}$  independently from the exposure. This allows the conclusion that the coating efficiently prevented propagation of corrosion even when the samples were exposed to the more severe conditions of the accelerated cycles. Furthermore, a degradation of the coating due to UV light or temperature was not noted after more than one year of exposure to the cycles and 2 years of exposure to Milano atmosphere.

In the case of the uncoated samples it was also noted how the fluctuation in results was strongly reduced passing from the atmospheric exposure to the accelerated one. Considering the difference between maximum/minimum and mean value it may be noted how the mean value in the atmospheric exposure is located in the bottom of the range of variation of the results, thus only few corrosion rates, during very rainy periods, resulted very high while the mean value during the two years of exposure resulted much lower. In the case of the accelerated exposure the mean value resulted closer to the middle of the range of variation of the results, stating that the fluctuation was reduced by this exposure and the fluctuations were stabilised by the more controlled exposure conditions. For the coated sample in both exposures the deviation of results was found to be very low which confirms that the condition of the rebars remained unchanged independently from the exposure as well as from the applied cycles.

Thus, the accelerated cycles showed to reproduce the worst conditions (of humidity and temperature) detected in atmospheric exposure condition and can provide useful data for the evaluation of the effectiveness of the coating over time.

#### 4 Conclusions

The comparison of the results of tests carried out in non-accelerated and accelerated conditions, showed, how the accelerated cycles led to an increase in the propagation of corrosion (lower potentials, increase in corrosion rate) in the uncoated samples, thus the accelerated test method proved to lead to a more severe exposure than the non-accelerated exposure, due to the more controlled exposure conditions, mainly related to the wet period. Instead, in the case of the coated samples no propagation of corrosion was found. This allowed to assess that, since degradation of the coating has not occurred even after 400 days of exposure to elevated hours of UV light, high temperatures and strong rainfalls, it may be assumed that, also in atmospheric conditions, this would not occur for many years. In order to find a correlation able to predict the real service life of the coating itself and a coated structure more data would be needed.

#### References

- [1] Bertolini L., Elsener B., Pedersen P., Redaelli E., Polder R.B. 2014. Corrosion of steel in concrete: Prevention, Diagnosis, Repair. Weinheim: John Wiley & Sons.
- [2] Sohawon H., Beushausen H. "The effect of hydrophobic (silane) treatment on concrete durability characteristics." Paper presented at the ICCRRR 2018, Cape Town, South Africa, November 19-21.
- [3] Polder R.B., Borsje H., De Vries J. 2001. "Corrosion Protection of Reinforcement by Hydrophobic treatment of Concrete." *HERON* 46:227-238.

- [4] Christodoulou C., Goodier C.I., Austin S.A., Webb J., Glass G.K. 2013. "Long-term performance of surface impregnation of reinforced concrete structures with silane." *Construction and Building Materials* 48:708-716.
- [5] De Vries J., Polder R.B. 1997. "Hydrophobic treatment of concrete." *Construction and Building Materials* 11:259-265.
- [6] ASTM STP Society for Testing and Materials. 1993. ASTM G154-16 "Standard Practice for Operating Fluorescent Ultraviolet (UV) Lamp Apparatus for Exposure of Nonmetallic Materials".
- [7] ARPA Lombardia "Sistema Nazionale per la Protezione dell'Ambiente." Accessed April 24. <https://www.arpalombardia.it/dati-e-indicatori/meteo-e-clima/>



**Bond and connections in RC,  
prestressed concretes (PC)  
and mixed structures**



# Bond behaviour of FRP bars to concrete: database collection and preliminary analysis

Maria Milena Della Vecchia<sup>1</sup>, Annalisa Napoli<sup>1</sup>, Roberto Realfonzo<sup>1</sup>

<sup>1</sup>*Department of Civil Engineering, University of Salerno, Via Giovanni Paolo II 132, 84084 Fisciano (SA), Italy*

## Abstract

The paper presents a preliminary analytical study on the bond behavior between concrete and internal reinforcement. To this purpose, a wide experimental database, which includes more than 1000 tests devoted to investigating bond mechanism on steel and FRP bars embedded into concrete blocks, was compiled from the literature. Further 40 tests have been performed by the authors.

Concerning the concrete, several collected tests were performed on specimens made of ordinary Portland cement-based (OC) concrete, others on sustainable cement-less concrete (“green concrete”) blocks, such as those made with alkali-activated blast furnace slag (cast-iron production waste).

Regarding the reinforcement, to take care of the durability of reinforced concrete structures, many pull-out or beam-tests included in the abovementioned database were performed using fiber reinforced polymer (FRP) bars in place of the traditional steel ones.

Several types of FRP bars were considered in the database, made of glass, carbon, basalt or aramid fibers, manufactured in different diameters and surface treatments.

The collected database was a useful tool to organize the current knowledge on the topic in a systematic framework and examine the main parameters affecting the interface bond between concrete and reinforcement, such as the bond length, the bar surface finish and its diameter, the position of the bar in the concrete block (eccentric or centred), the concrete strength, etc.

Concerning the use of FRP bars, it is worth highlighting that the results of this study will also be useful for the updating of the Italian Guidelines CNR-DT 203/2006 which are currently under revision.

## 1 Introduction

Pollution is doubtless one of the main concerns of this century, a challenge that even construction industry must face, due to the huge environmental impact of the production of both steel and ordinary concrete (OC). Concerning steel industry, it is the world’s biggest energy-consuming manufacturing industry, responsible for about the 25-30% of overall energy use in the manufacturing industry [1]. Quite the same can be said for Portland cement production, which is the nowadays worldwide most used binder [2]. Production of Portland cement is an energy-intensive process and needs about 1.5 tons of raw materials per each ton of clinker produced [2].

Therefore, among the various ways in which a more sustainable construction industry can be achieved, there is the employment of new materials and products. For example, alternative concrete (AC) made without Portland cement have been developed and studied: an example is the substitution of traditional Portland cement as a binder with ground granulated blast furnace slag, a by-product of cast-iron production, suitable to replace, partially or totally, Portland cement due to its similar composition [3].

On the other hand, significant improvements of sustainability of the reinforced concrete (RC) structures can also be achieved by substituting steel bars with the Fiber Reinforced Polymer (FRP) ones, thus increasing the durability of RC members. In fact, despite the ductile behaviour, high tensile strength and elastic modulus, steel is prone to corrosion, which can be highly injurious. Hence, steel bars show lacking resistance whenever they are exposed to harsh operative environmental conditions, such as the presence of seawater, freeze-thaw cycles or de-icing salt. This is the case, for example, of bridge decks, tunnels, foundations, and so on [4]. In this perspective, FRP bars can be useful to avoid bars corrosion and, consequently, to increase the durability and decrease maintenance costs of RC constructions. Nevertheless, a part the larger purchase costs, if compared with deformed steel bars, FRP ones show lower values of the elastic modulus (mainly in case of glass fiber polymers) and, almost always, worse bond performances, both factors that can strongly influence the behaviour of RC members both at serviceability and ultimate limit states.

After all, it is well known that bond between concrete and bars is a relevant mechanism able to deeply influence the structural behaviour of reinforced concrete (RC) elements. This is the reason why, during time, bond between concrete and (plain/deformed) steel bars has been vastly investigated.

The aim of this paper is to present the state-of-the-art concerning those topics, with particular attention to the bond mechanism developed in unconventional kinds of reinforced concrete. Particular attention will be paid to the different parameters able to influence adherence between concrete and internal reinforcement. For this reason, an experimental database has been built, collecting the results obtained by performing 1049 tests (taken from a total of 21 papers: [5]-[24]) on samples made in several ways and with heterogenous materials. The said database also includes the first stages of a wider experimental program carried out at University of Salerno, where, to date, a total of 40 pull-out tests has been performed on specimens made with both ordinary and sustainable concrete and reinforced with steel or FRP bars.

## 2 Experimental database

The complete experimental database includes data in terms of bond strength, slip values and failure mode, with particular attention to those parameters mostly able to influence bond. They are: bar type (steel/ FRP bar), concrete type (Ordinary Portland cement-based Concrete/Alternative Concrete), concrete strength, bar diameter, bond length, bar position (concentric/eccentric), surface treatment of the bar and internal/external confinement.

The 1049 tests (Fig. 1a) have been divided into 356 homogenous datasets (Fig. 1b), according to the procedure recommended by Eurocode 0, Appendix D [25]. Each dataset includes the results in terms of mean values obtained by tests performed on identical samples.

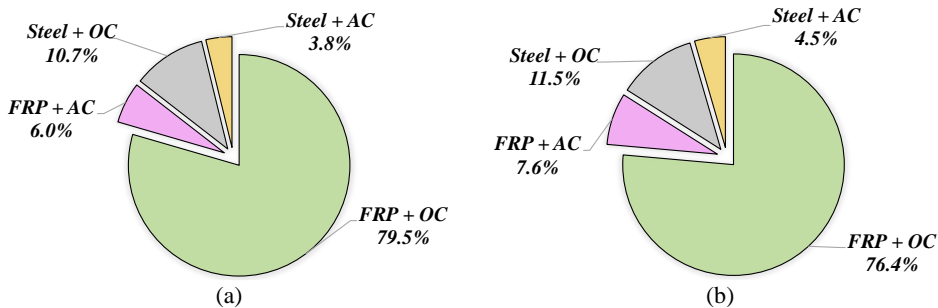


Fig. 1 Distribution of tests (a) and datasets (b), divided in function of the materials specimens were made of.

As a reinforcement, instead, both steel and FRP bars are used. Their distribution is shown in Fig. 2 left and right. The most used FRP bars are those made of glass fibers (GFRP), since they guarantee a noteworthy performance/cost ratio with respect other kinds of fibers (i.e. Carbon fibers). Despite that, Carbon (CFRP), Aramid (AFRP) and Basalt (BFRP) are proposed too.

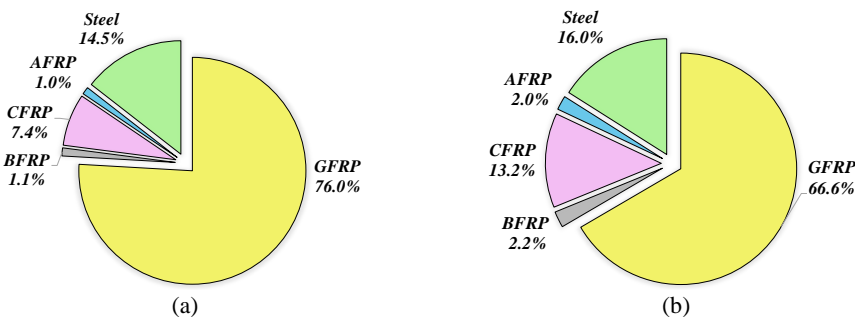


Fig. 2 Distribution of tests (a) and homogeneous datasets (b) in function of the material bars were made of.

### 3 Bond mechanism in FRP reinforced concrete

The first studies about the use of FRP bars in RC structures date back to the early 1990. Cosenza et al. [26] have presented one of the first reports about the state-of-the-art of bond mechanism in FRP bars. The database collected by the authors was subsequently included in Fib Bulletin n. 10 [27], a document aimed to investigating bond mechanism in RC, in which a focus about FRP bars is also offered.

After that, FRP bars use has received renewed attention due to some tragic events linked to the lacking durability of steel in bad environmental conditions (i.e. “Polcevera bridge”, Genova, 2018). This led many scholars to conduct new studies, focusing their attention on the many parameters able to influence bond mechanism. The aim of the papers summarized in next is to quantify the influence of these variables in FRP reinforced concrete.

Aiello et al. [5] have analyzed bond performances of several kinds of FRP bars. Made of carbon, glass and aramid fibers. The surface treatment types were sanded (fine and course), ribbed and spiral wound with carbon fibers. The authors have observed that both bond mechanism and strength were deeply influenced by the surface treatment. In particular, in the case of ribbed and spiral wound AFRP, CFRP and GRFP bars, the contribution of mechanical interlocking was very effective, allowing to achieve high peak bond stress, 3-4 times that of sanded bars. Quite the same can be said for slip values, which resulted much lower in ribbed bars. For sanded bars the bond mechanism was completely different from that of ribbed bars, since in the first case bond resistance was due to chemical adhesion and friction. A sudden drop of bond strength occurred when chemical adhesion failed.

Achillides et al. [6], performed similar research, studying the behavior of GFRP, CFRP, AFRP and hybrid bars, characterized by rough surface. This kind of surface have been obtained by the addition of a peel-ply on the surface of the bar during its production process, which have been then removed after curing process of resin. The authors did not find significant differences between the bond strength developed by GFRP and CFRP bars, while aramid and hybrid bars (carbon and glass together) showed slightly lower bond strength. They observed that the principal bond mechanism was due to chemical adhesion, being the contribution of deformations on the surface of the bars quite irrelevant.

El-Nemr et al. [7] have studied the performances of bond mechanism in FRP reinforced concrete by carrying out eighty-seven pull-out tests on specimens produced with normal- and high-strength concrete and reinforced with GFRP and CFRP bars. The surface treatments of the bars were several: sand-coated, ribbed and sand-coating + helically wrapped. Tests results showed that bond strength of FRP reinforced bars was 60% of that attributable to steel bars. The authors underline that, among the investigated parameters, bar diameter, surface configuration and concrete strength were the ones mostly able to affect bond behaviour. In particular, results showed that the higher is concrete strength, the higher bond stiffness and peak load. Concerning the type of fiber, the authors observed an increase of bond strength whenever the elastic modulus of the bar increases. This phenomenon has been recognizable mostly in sand-coated bars. Finally, as also [8], [9], [10] show, it has been confirmed that bond resistance decreases whenever the bar diameter increases.

### 4 Influence of concrete strength

The influence of the resistance of the concrete is strictly linked to the surface treatment of the bar. In general, it has been proved that higher compressive concrete strength results in higher bond resistance [7], [8], but this influence may vary if bond mechanism is mostly frictional or driven by mechanical interlocking. For example, in the case of sand coated bars, concrete strength plays a minor role, due to the peeling off of the coating. Conversely, in ribbed bars this aspect is more relevant because ribs get smoothed or damaged by concrete during laboratory tests. Concerning the importance of this parameter, it has been demonstrated [27] that bond resistance depends on the square root of concrete cylindrical compressive strength in bars able to develop mechanical interlocking. The same could not be true for bars developing frictional mechanism, since they do not involve concrete strength due to the detachment of the external coating [26].

Doostmohamadi et al. [11] have chosen three types of concrete, normal-weight concrete, light-weight concrete and light-weight fiber-reinforced concrete, in order to try to better understand the differences in bond performances in concretes characterized by different compressive strength. As expected, it has been proved that a way to enhance the bond resistance is that to improve the resistance of concrete. However, the results show that increase of compressive strength in normal-weight concrete



causes relatively higher bond strength in comparison with light-weight concrete. Moreover, adding macro-fibers to the light-weight concrete has upgraded its weak adherence mechanism.

## 5 Influence of bond length

Among the parameters able to influence bond behaviour, the embedded length has been often mentioned in different studies. The general results obtained by many scholars show that the bigger is bond length, the higher the peak load exhibited and the lower the bond strength [12], [13]. Saleh et al. [10], have performed numerous pull-out tests on samples made of high-strength-concrete and GFRP bars with the purpose to examine the effects of diameters, embedment length and surface configuration of the reinforcing bars. The authors observed that the bond strength of both GFRP bar types increased with reducing the embedment length. In general, this decrease was reduced in the case of high-strength concrete.

## 6 Influence of internal/external confinement and bar positioning

Another parameter that influences bond behaviour is confinement. Gao et al. [9] presented the results of a series of pull-out tests performed on GFRP reinforced samples, among which some were internally confined with stirrups (diameter and interspace equal, respectively, to 8 mm and 40 mm). The analysis of tests results has proved that the presence of stirrups has been able to change mode of failure of the specimen, since samples confined with stirrups showed pull-out mode of failure and higher bond strength.

The bar positioning is also a parameter examined in scientific literature, since pull-out tests on samples reinforced with both concentric and eccentric bars have been carried out [13]. Fakhruddin et al. [14] have studied both the importance of the bar positioning in the sample and of external confinement. The authors investigated the bond stress behaviour between GFRP bars and concrete by carrying out pull-out tests on samples with three different configurations: samples with a concentric GFRP bar (hence with concrete cover), samples reinforced with eccentric GFRP bar (no concrete cover) and samples externally confined with a complete wrapping of GFRP sheet. Particular attention must be paid to the third group of specimens which have been realized with an eccentric bar positioned on the edge of the cube and then wrapped with a E-GFRP sheet. This study has proved that providing an external confinement can enhance the bond resistance, since specimens externally reinforced showed an initial stiffness higher than the identical specimen produced without the external GFRP sheet. It has also been proved the deep influence of the bar positioning, so that the authors have observed a relevant reduction in bond strength and stiffness, as well as change in failure mode. The concentric bars demonstrated ductile behaviour and failed due to pull-out. The same was not valid for eccentric bars, which showed brittle failure and a sudden drop of bond strength due to the crashing of concrete, hence no residual bond resistance was available. The tests performed on externally confined specimens exhibited lower slips and higher stiffness, but quite similar bond strength with respect to specimens reinforced with an eccentric bar.

## 7 A focus on the surface treatment of FRP bars

A vast variety of FRP bars is nowadays available also due to the different surface treatments currently studied. The ultimate goal is that to try to emulate the well appreciated bond performance of ribbed steel bars. Therefore, ribbed FRP bars have been also developed, which surface is covered by ribs similar to the steel ones. However, also other kinds of surfaces have been studied, like the sanded and the helically wrapped ones. The following studies have demonstrated that this parameter is the one which can particularly influence slip values.

Baena et al. [8] have confirmed that the same bar with different surface treatments developed highly different bond mechanism, leading to multiple possibilities of failure modes. They have tested GFRP and CFRP bars, characterized by sand coated, sand coated + spiral wound, helically wrapped or ribbed surface. It has been observed that sand coated bars failed mainly due to the peeling off of the external coating, while the other kinds of bar failed due to pull-out. However, the results obtained by tests performed on helically wrapped bars showed higher values of slip than those relative to sand coated bars. Moreover, the higher was the compressive strength of concrete, the higher the dependance of bond strength on surface treatment, since the ribs turn more damaged.

Gao et al. [9] carried out pull-out tests on helically wrapped, helically wrapped + sand coated and ribbed GFRP. The first two failed due to detachment of the fibers spiral, while the shearing off of the sand grains has been observed in sand coated bars. On the other hand, failure in ribbed bars occurred due to the shearing off of the ribs. It has been seen that in the case of helically wrapped bars the main contribution is given by friction, while mechanical interlocking is the most significant one in ribbed bars. The highest bond resistance has been experienced in the latter case.

Quite the same evidence has been found in the first stages of the experimental campaign currently going on at University of Salerno where, to date, 40 pull-out tests have been performed. The samples have been reinforced with steel or GFRP bars, provided by two different manufacturers: Schöck Combar and Owen Corning Pinkbar. Both presented a typical ribbed surface, but ribs had different geometry and sizes. It has been seen that this difference affected  $\tau$ -slip curve, resulting in the observation of different initial stiffness and, consequently, slip values. Even though the bond strength exhibited by the two different GFRP bars was barely dissimilar, the same can not be said for the slip values, which resulted higher in Owens Corning Pinkbar. The reason appeared evident by checking the bar after the test. It has been clearly observed a more efficient mechanical interlocking developed in Schöck Combar, in which the ribs were able to hold concrete more than those in Owens Corning Pinkbar. Thus, the behaviour exhibited by Schöck Combar looked like similar to the steel one, while the greater contribution to bond in Pinkbars was due to friction.

All the data corresponding to each dataset included in the database are represented in the graphs reported in Fig. 3, that are suitable to better understand the aforementioned results.

It appears quite evident that the high variability of available bars turns to a high dispersion of  $\tau$ - $s$  trends. Nevertheless, even though the average values of bond strength appear quite uniform, the same can not be said for slip values.

Furthermore, the values of bond strength have been divided by the square root of concrete cylindrical compressive strength, in order to obtain comparable values. As already mentioned, this dependence has been fully proved for ribbed bars, but it is an approximation for the other kinds of bars, which develop mostly frictional bond mechanisms.

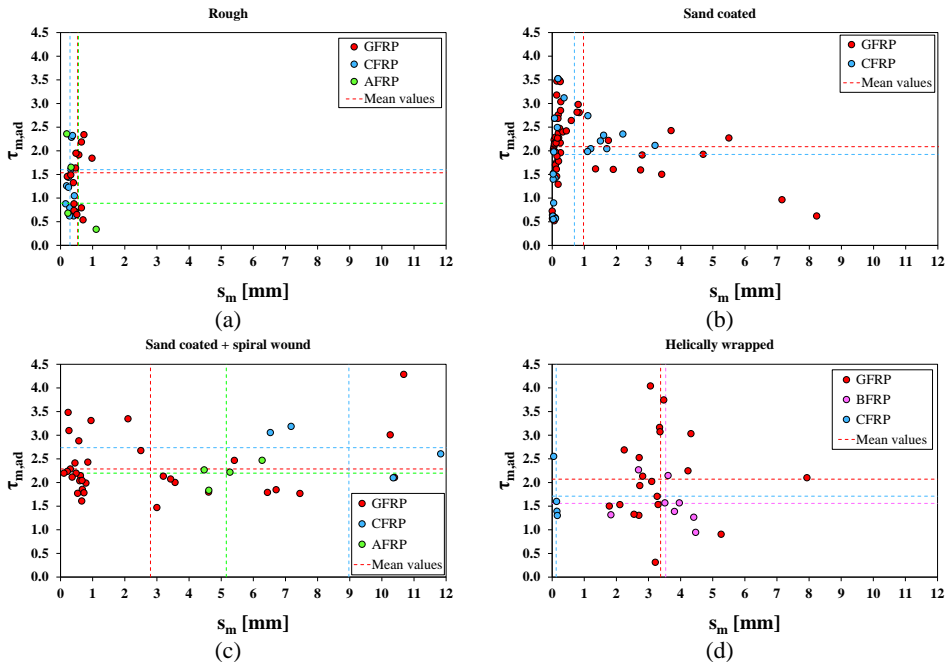


Fig. 3 Values of normalized bond strength and slip per each dataset for rough (a), sand coated (b), sand coated + spiral wound (c), helically wrapped (d) and ribbed (e) bars.

A further interesting comparison can be made between FRP ribbed bars and steel bars (Fig. 4). Despite the high values exhibited by some GFRP bars, the average values of slip are quite similar,

proving that also FRP bars in a few circumstances can develop an appreciable bond mechanism. However, as expected, the higher peak values of bond stress are experienced by steel bars.

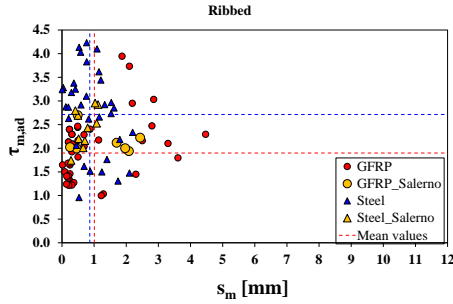


Fig. 4 Comparison between ribbed FRP bars and steel bars.

All the data reported in Fig. 3 and Fig. 4 per each dataset are summarized in Table 1. It is noteworthy that the kind of fiber mostly investigated is the glass one. Furthermore, it is highlighted that the most relevant variability can be found in slip values (see coefficient of variations in brackets), while average values of bond strength appear more comparable one to each other than the said slip values.

Table 1 Results collected in the experimental database in terms of average values of maximum bond stress and corresponding slip values per each type of bar and surface treatment.

Bar type	# of tests	Surface treatment	# of tests	$\tau_{m,ad}$ [-]	$s_m$ [mm]
GFRP	796	Rough	172	1.54 (39.84%)	0.53 (35.50%)
		Sand coated	222	2.09 (40.17%)	0.98 (184.30%)
		Sand coated + spiral wound	83	2.29 (26.26%)	2.80 (116.49%)
		Helically wrapped	62	2.07 (43.92%)	3.38 (39.59%)
		Ribbed	248	1.90 (36.27%)	1.01 (109.21%)
		Plain	9	0.88 (3.33%)	-
CFRP	78	Rough	24	1.60 (39.68%)	0.29 (28.75%)
		Sand coated	38	1.92 (44.58%)	0.69 (132.27%)
		Sand coated + spiral wound	6	2.74 (18.00%)	8.97 (28.25%)
		Helically wrapped	10	1.71 (33.57%)	0.12 (41.48%)
AFRP	11	Rough	3	0.89 (76.45%)	0.56 (86.55%)
		Sand coated + spiral wound	8	2.20 (12.05%)	5.16 (15.94%)
BFRP	12	Helically wrapped	12	1.56 (28.69%)	3.54 (25.12%)
Steel	152	Ribbed	129	2.71 (30.54%)	0.87 (63.29%)
		Plain	23	0.21 (2.62%)	12.90 (0.96%)

## Conclusions

The paper is aimed to present an experimental database including tests performed on various kinds of specimens, produced with both conventional and unconventional materials. The purpose is to present the improvements obtained in the field of reinforced concrete structures, devoted to try to give a solution to some of the problems related to its use. The most important ones are durability of RC structures and sustainability of building industry. In this perspective Fiber Reinforced Polymer bars have been herein presented.

The attention of the authors has been focused on bond behaviour developed by those kinds of bars, in order to better understand how it is influenced by the typical parameters affecting adherence at reinforcing bar-concrete interface. It has been demonstrated that bond mechanism deeply modifies if steel bars are replaced by FRP ones. The parameters affecting adherence have been taken into account, paying particular attention to the outer treatment of the bar. Indeed, it has been seen that, in function of the surface configuration of the bar, bond can be mainly ruled by friction (rough, sand coated or helically wrapped bars) or mechanical interlocking (ribbed bars). This aspect affects also bond strength and slips values, so that even though the great heterogeneity, the general trend sees higher bond resistance and lower slip values in ribbed bars.

Furthermore, it has been seen that bond strength decreases whenever bar diameter and bond length increase or when the FRP bar is positioned eccentrically with respect to the center of the specimen.

Finally, both internal and external confinement is able to enhance bond resistance.

## References

- [1] Olmez, Gulnur Maden, Dilek, Filiz B., Karanfil, Tanju and Yetis, Ulku. 2015. "The environmental impacts of iron and steel industry: a life cycle assessment study." *Journal of Cleaner Production* 130:195-201. Accessed July 12, 2024. doi: 10.1016/j.jclepro.2015.09.139.
- [2] Coppola, Luigi, Coffetti, Denny and Crotti, Elena. 2018. "Pre-packed alkali activated cement-free mortars for repair of existing masonry buildings and concrete structures." *Construction and Building Materials* 173:111-117. Accessed July 12, 2024. doi: 10.1016/j.conbuildmat.2018.04.034.
- [3] Puertas, Francisca, Gonzalez-Fontboa, Belen, González-Taboada, Iris, Alonso, M. M., Torres-Carrasco, M., Rojo-López, Gemma and Martínez-Abella, F.. 2018. "Alkali-activated slag concrete: Fresh and hardened behaviour." *Cement and Concrete Composites* 85:22-31. Accessed May 30, 2024. doi: 10.1016/j.cemconcomp.2017.10.003
- [4] Chaallal, Omar and Benmokrane, Brahim. 1993. "Pullout and bond of glass-fibre rods embedded in concrete and cement grout." *Materials and Structures* 26:167-175.
- [5] Aiello, Maria Antonietta, Leone, Marianovella and Pecce, Maria Rosaria. 2007. "Bond Performances of FRP Rebars – Reinforced Concrete." *Journal of Materials in Civil Engineering* 19(3):205-213. Accessed September 25, 2023. doi: 10.1061/(ASCE)0899-1561(2007)19:3(205).
- [6] Achillides, Zenon, and Pilakoutas Kypros. 2004. "Bond behavior of Fiber Reinforced Polymer Bars under Pullout Conditions." *Journal of composites for construction* 8(2):173-181. Accessed September 26, 2023. doi: 10.1061/(ASCE)1090-0268(2004)8:2(173).
- [7] El-Nemr, Amr, Ahmed, Ehab A., Barris, Cristina, Joykland, Panuwat, Hussain, Qudeer and Benmokrane, Brahim. 2023. "Bond performance of fiber reinforced polymer bars in normal- and high-strength concrete." *Construction and Building Materials* 393 (2023) 131957. Accessed September 25, 2023. doi: 10.1016/j.conbuildmat.2023.131957.
- [8] Baena, Marta, Torres, Lluís, Turon, Albert and Barris, Cristina. 2009. "Experimental study of bond behaviour between concrete and FRP bars using a pull-out test." *Composites: Part B Engineering* 40(2009):784–797. Accessed May 29, 2024. doi: 10.1016/j.compositesb.2009.07.003.
- [9] Gao, Kui, Li, Zhao, Zhang, Jiarui, Tu, Jianwei, Li, Xiping. 2019. "Experimental Research on Bond Behavior between GFRP Bars and Stirrups-Confined Concrete." *Applied Science* 9(7):1340. Accessed September 17, 2023. doi: 10.3390/app9071340.
- [10] Saleh, Najia, Ashour, Ashraf and Sheehan, Therese. 2019. "Bond behavior between glass fibre reinforced polymer bars and high-strength concrete." *Structures* 22:139-153. Accessed September 17, 2023. doi: 10.1016/j.istruc.2019.08.003.

- [11] Doostmohamadi, Alireza, Vatani Oskouei, Asghar and Kheyroddin, Ali. 2021. "An Experimental Study on Effect of Concrete Type on Bond Strength of GFRP Bars." *Journal of Rehabilitation in Civil Engineering* 9-1 (2021):52-70. Accessed September 17, 2023. doi: 10.22075/JRCE.2020.19922.1392.
- [12] Maranan, Gingham, Manalo, Allan, Karunasena, Karu and Benmokrane, Brahim. 2015. "Bond Stress-Slip Behavior: Case of GFRP Bars in Geopolymer Concrete." *Journal of Materials in Civil Engineering* 27(1):04014116. Accessed September 22, 2023. doi: 10.1061/(ASCE)MT.1943-5533.0001046.
- [13] Islam, Sirajul, Afefy, Hamdy M., Sennah, Khaled and Azimi, Hossein. 2015. "Bond Characteristics of straight- and headed- end, ribbed surface, GFRP bars embedded in high-strength concrete." *Construction and Building Materials* 83:283-295. Accessed November 24, 2023. doi: 10.1016/j.conbuildmat.2015.03.025.
- [14] Fakhruddin, Kusnadi, Djamaluddin, Rudy, Irmawaty, Rita, Hamzah, Suharman and Ngeljaratan, Luna. 2023. "Effect of Bonding Area on Bond Stress Bahvior of GFRP Bars in Concrete." *Civil Engineering Journal*. Accessed September 17, 2023. doi: 10.28991/CEJ-SP2023-09-010.
- [15] Romanazzi, Vincenzo, Leone, Marianovella, Aiello, Maria Antonietta and Pecce, Maria Rosaria. 2022. "Bond behavior of geopolymer concrete with steel and GFRP bars." *Composite Structures* 300 (2022) 116150. Accessed September 25, 2023. doi: 10.1016/j.compstruct.2022.116150.
- [16] Parvizi, Mehran, Noël, Martin, Vasquez, Jeison, Rios, Alejandros and Gonzáles, Marcelo. 2020. "Assessing the bond strength of Glass Fiber Reinforced Polymer (GFRP) bars in Portland Cement Concrete fabricated with seawater through pullout tests." *Construction and Building Materials* 263 (2020) 120952. Accessed September 22, 2023. doi: 10.1016/j.conbuildmat.2020.120952.
- [17] Sun, Wen, Zheng, Yu, Zhou, Linzhu, Song, Jiapeng and Bai, Yun. 2020. "A study of the Bond Behavior of FRP Bars in MPC Seawater Concrete." *Advances in Structural Engineering* 24(6):1110-1123. Accessed September 17, 2023. doi: 10.1177/1369433220956816
- [18] Caro, Manjola, Jemaa, Yaser, Dirar, Samir and Quinn, Andrew. 2017. "Bond performance of deep embedment FRP bars epoxy-bonded into concrete." *Engineering Structures* 147(2017):448-457. Accessed October 1, 2023. doi: 10.1016/j.engstruct.2017.05.069.
- [19] Di, Bo, Wang, Jingkai, Li, Haotian, Zheng, Jinhang, Zheng, Yu and Song, Gangbing. 2019. "Investigation of Bonding Behavior of FRP and Steel Bars in Self-Compacting Concrete Structures Using Acoustic Emission Method." *Sensors* 19:159-173. Accessed September 25, 2023. doi: doi:10.3390/s19010159.
- [20] Ifrahim, Muhammad Saad, Sangi, Abdul Jabbar, Hamza and Syed Muhammad. 2022. "Experimental Study on Bond Strength of Locally Manufactured GFRP Bar." *Engineering Proceeding*. Accessed September 17, 2023. doi: 10.3390/engproc2022022004
- [21] Larralde, Jesus and Silva-Rodriguez, R.. 1993. "Bond and Slip of FRP Rebars in Concrete." *Journal of Materials in Civil Engineering* 5(1):30-40. Accessed February 9, 2024. doi: 10.1061/(ASCE)0899-1561(1993)5:1(30).
- [22] Patil, Sagar B., Maniunatha, G.S.. 2019. "Experimental Study on Bond Strength of GFRP Bars." Paper presented at the Sixth international conference on recent advances in composite materials, ICRAACM-2019, Varanasi, India, February 25-28.
- [23] Rossetti, Vito Alunno. 1995. "Local bond stress-slip relationships of glass fibre reinforced plastic bars embedded in concrete." *Materials and Structures* 28:340-344. Accessed February 9, 2024. doi: 10.1007/BF02473149.
- [24] Pecce, Maria Rosaria, Manfredi, Gaetano, Realfonzo, Roberto and Cosenza, Edoardo. 2001. "Experimental and Analytical Evaluation of bond properties of GFRP bars." *Journal of materials in Civil Engineering* 13(4):282-290. Accessed September 15, 2023. doi: 10.1061/(ASCE)0899-1561(2001)13:4(282)
- [25] EN 1990. Eurocode 0. "Basis of structural design."
- [26] Cosenza, Edoardo, Manfredi, Gaetano and Realfonzo, Roberto. 1997. "Behaviour and Modeling of bond of FRP rebars to concrete." *Journal of materials in Civil Engineering* 1(2):40-51. Accessed September 15, 2023. doi: 10.1061/(ASCE)1090-0268(1997)1:2(40)
- [27] CEB-FIP. 2000. "Fib Bulletin n. 10: Bonf of reinforcement in concrete." Accessed October 20, 2023. doi: 10.35789/fib.BULL.0010

# Bond of embedded steel reinforcement at high temperature and in fire conditions

Pietro G. Gambarova<sup>1</sup>, Giovanni Metelli<sup>2</sup>, Giovanni Muciaccia<sup>1</sup>  
and Giovanni Plizzari<sup>2</sup>

<sup>1</sup>*Dept. of Civil and Environmental Engineering,  
Politecnico di Milano,  
Piazza Leonardo da Vinci 32, 20133 Milan, Italy*

<sup>2</sup>*Dept. of Civil and Environmental Engineering, Architecture and Mathematics,  
University of Brescia,  
Via Branze 43, 25123 Brescia, Italy*

## Abstract

Bond behavior in reinforced-concrete, pre-stressed pre-tensioned members and composite structures relies on the interaction along the mutual interfaces of anchored bars and lapped splices. At high temperature - and specifically in fire conditions - the mechanical degradation of the concrete and of the reinforcement impairs bond at the local level with structural effects on anchored bars and laps. In new construction, the design at high temperature and in fire has to be mostly focused on the anchorage/lap length, while in existing construction bond degradation under fire load has to be checked against a reduced allowable stress in the bar. Model Code 2020 – more than the previous Model Code 2010 and much more than other design codes - takes care of the complex behavior of bond in such extreme conditions, in different ways concerning the local bond-stress slip law (that tends to flatten off at high temperature with a strength and stiffness loss) and the redistribution of the bond stresses along the bars (leading to more uniform stress profiles). Many are the parameters involved, that are related to bond conditions, confinement, bar geometry (*plain* or *deformed/ribbed* bars) and bar position inside the structural members. With respect to MC 2010, MC 2020 is definitely more focused on the structural behavior of bonded reinforcement, with some advanced issues either extensively covered - like heat-controlled vs. load-controlled bond failures and bond stiffness – or just mentioned as they are still open to investigation – like the effect of the heating-loading sequence. Face to the many above-mentioned issues, this paper is meant to provide an overview of the background document on bond of embedded steel reinforcement, to facilitate designers and codemakers in optimizing the design of the reinforcement.

## 1 Introduction

Fire has always been considered as an exceptional and dangerous load condition, to be avoided, confined and extinguished firstly to guarantee human safety and goods preservation, and secondly to prevent partial or even full structural collapses. With reference to fire-related collapses, the main resistant mechanisms have been systematically studied in the past (flexure, tension, compression, shear and torsion) in fire conditions, while bond – albeit fundamental for the very existence of reinforced-concrete structures – has been given less attention, all the more because “experience has yet very rarely produced evidence of failures (in fire) by debonding in reinforced structures”, as observed in MC2010, Section 7.5.1.2.2 “Concrete and steel in fire”. In this same section, however, it is noted that “the problem is more critical in prestressed pretensioned members”.

In fact, between MC1990 and MC2010 [1] a lot of work has been done on bond at high temperature and in fire, but mostly with the focus on bond behavior as such, by testing specimens made of different cementitious materials, failing by bar pull-out or cover splitting (*fib* Bulletin No. 10, 2000 [2]; see Bamonte et al., 2024 [3] for the references). In the last 10-15 years, however, more attention has been devoted to the structural behavior of anchored

bars and lapped splices, and to their effects on the structural behavior (concerning beams, girders, columns, walls and slabs in fire conditions).

The previous situation stands out clearly in MC2010, where fire is treated in two short sections, 6.1.7.4 “Fire” and 7.5.1.2.2 “Concrete and steel (in fire)”. In the former section, bond degradation in fire is declared to be similar to that of concrete in tension. Concrete thermal spalling is mentioned as well, as it reduces the cover of the reinforcement. Reference is also made to plain round bars, whose residual bond strength after heating to 300 and 500° may be a mere 50% and 10% of the initial bond strength in ambient conditions. In Section 7.5.1.2.2, thermal spalling is introduced as a phenomenon favored by high moisture contents, high compressive stresses, high thermal gradients, low porosity and geometry (for instance, at the corners). Hence, spalling may become critical in high-strength concretes, because of their closed and dispersed porosity (see also *Bond of Reinforcement in Concrete*, 2000 [2] and *Bond in Concrete* 2012, 2012 [4a]).

The limited attention devoted to fire and to its structural effects in MC2010 is counterbalanced by the much more extensive coverage in the proposed MC2020 [5], as anticipated in several papers published in the proceedings of *Bond in Concrete 2022* (2022 [4b]). With reference to both design needs (*new construction*) and in-situ assessment (*existing construction*), such topics as bond-slip law, anchored bars, lapped splices (beams and columns), pull-out and splitting failures, bond shear modulus in the loading and unloading phases, and required bonded length in fire are treated, taking into consideration bond conditions, concrete strength in compression, bar diameter, concrete cover, spacing between the anchored or spliced bars, stirrup density and position of the anchored or spliced bars.

Some issues are still open to investigation and need appropriate provisions in the codes, like – among others – concrete thermal spalling (Lo Monte and Gambarova, 2014 [6]), the heating-loading process (either simultaneous or sequential, (Muciaccia and Consiglio, 2021 [7]), and – last but not least – test procedures which require realistic test specimens able to include pull-out and splitting failures, as well as the effect of transverse reinforcement (Metelli et al., 2023 [8]; Tonidis et al., 2021 [10]), see Fig. 1.

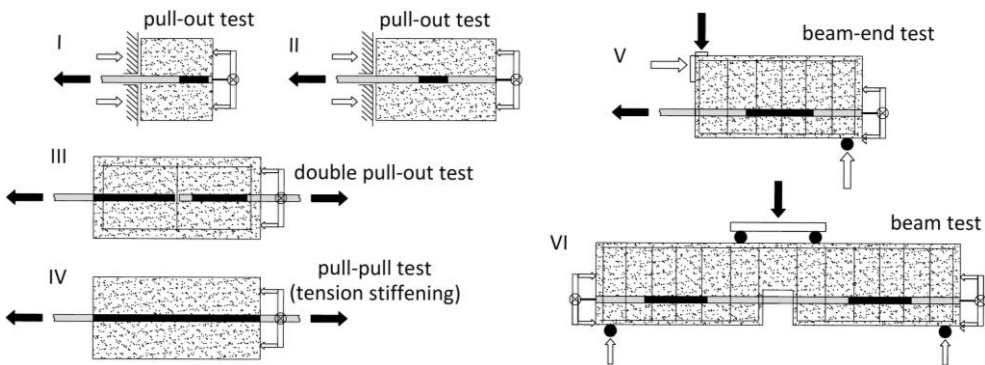


Fig. 1 Various types of tests on bond aimed at investigating bond constitutive behavior (I, II and III), tension stiffening (IV), and bond interaction with section geometry and transverse reinforcement (V and VI).

To end these preliminary considerations on bond at high temperature, one should remember that the design of anchored and lapped bars in fire is based on the criterion of the maximum bond effectiveness, in order to have bar yielding and failure preceding bond failure. During a prolonged and severe fire, however, the opposite may become true since bond strength is basically related to concrete strength in compression and tension, that are more affected by the temperature than steel strength.

The likelihood of a bond-controlled failure may even increase after cooling down to ambient temperature, because bond is further weakened by the damage accumulated in the concrete embedment under decreasing temperatures.

In this paper, after recalling the heat-induced degradation of concrete, steel reinforcement and bonded interfaces, some issues – mostly concerning anchored bars - will be treated, such as: design approach for bond degradation at high temperature and in fire; local bond-slip law under elevated temperature (bond capacity and bond shear modulus in *quasi-steady thermal conditions*); and local bond-slip law under fire (*highly-unsteady conditions*).

## 2 Heat-induced degradation of materials and interfaces

### 2.1 Concrete degradation

All cementitious composites undergo a similar degradation at high temperatures, because of many chemo-physical phenomena activated in the cement paste and in the aggregates at different temperatures. Six are the main reasons of concrete degradation: (a) water evaporation (100-200°C); (b) water expulsion from the siliceous aggregates (> 300°C); (c) dissociation of calcium hydroxide (450-500°C); (d) endothermic reversible transformation from the trigonal to the hexagonal crystalline system in the quartz contained in the sand and siliceous aggregates (550-600°C); (e) decomposition of calcium-silica hydrates – C-S-H (close to 80% of cement paste by mass) at 600-700°C; and (f) calcination, i.e., dissociation of calcium carbonate into calcium oxide and carbon dioxide (> 700°C).

Moisture and porosity may also trigger thermal spalling between 200 and 400°C, with the expulsion of concrete shards and the exposure of the reinforcement to the flames. Thermal spalling is also favored by both the thermal stresses and the load-induced stresses.

### 2.2 Reinforcement degradation

Commonly-used hot-rolled bars (made of carbon steel, either spring-tempered or self-tempered) exhibit a sizable mechanical degradation at high temperature (typically, the normalized residual strength is close to 25% at 700-750°C, but most of the mechanical loss is recovered after cooling down to room temperature (for  $T_{\max} < 700-750^\circ\text{C}$ ). On the contrary, high-strength cold-drawn bars and strands have a definitely higher thermal sensitivity (typically, the normalized residual strength at 700-750°C is from 5 to 10%, while the post-cooling recovery is a mere 30-35%. In all cases, steel ductility markedly increases to the detriment of bar-concrete bond.

### 2.3 Bond degradation

Bond heat-triggered degradation (Fig. 2) is mainly related to the degradation of the concrete layer in contact with the reinforcement, where not the bulk concrete but a cement mortar consisting in fine aggregate, water, binder and ultrafines (often in the form of powders) prevails in dictating bond properties, even at high temperature; in the latter condition, the decomposition of portlandite (CH) and calcium-silica hydrates (C-S-H) plays a substantial role.

Adding ultrafines to the mix (like silica fume and calcareous powders) improves bond properties by increasing the homogeneity of the cementitious binder, through the reduction or elimination of *weak* and *spiky* crystals (made of *portlandite* and *ettringite*).

Contrary to plain bars (not considered here), in deformed and ribbed bars both friction and micro-roughness at bar-concrete interface play a minor role compared to the macro-roughness resulting from the pattern of the deformations impressed on the bars. In RC members these deformations come in the form of either lugs or small niches, while in PC members the deformed shape is provided by the helicoidal wires of the strands.

In all cases, as soon as the mortar-like concrete adhering to the bars starts cracking, diagonal micro-struts form from the surface of the bar or strand, and their outwardly-pushing action generates hoop tensile stresses and radial/splitting microcracks in the embedment. In normal environmental conditions, the micro-struts make bond behavior similar to that of



concrete in compression. The same occurs at high temperature and in fire, below 400°C (Fig. 4), while in the range 400-550°C bond strength decreases sharply due to concrete disruption.

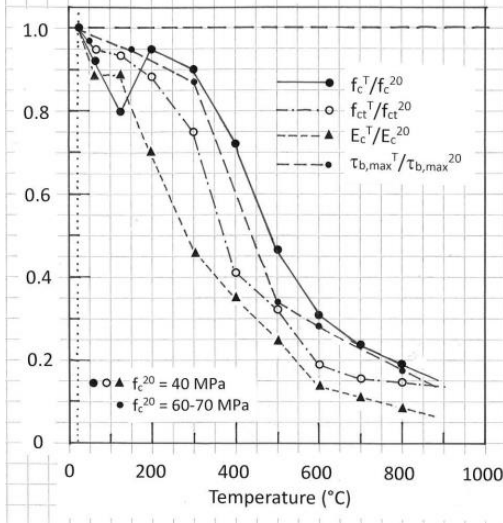


Fig. 2 Typical normalized diagrams of concrete properties vs. temperature, from tests on uniformly-heated specimens: tension and compression from Takeuchi et al. (SMiRT 12, Paper H04/4, 1993, calcareous aggregate); and bond from Lublóy and Hlavička (2017, quartzitic aggregate [9]).

Above 550-600°C bond behavior tends to become similar to that of concrete in tension or remains halfway between the two behaviors in tension and compression (Fig. 2). It should be noted that at any temperature bond fails in accordance with either the pull-out mode or the splitting mode. Only in the pull-out mode bond can be fully exploited (unless the bar yields first), while in the splitting mode concrete-cover cracking markedly reduces bond capacity, unless a passive confinement is provided (by adding stirrups).

Bond behavior can be represented in different ways (Figs. 3a,b), generally via bond stress-bar slip curves (Fig. 3a), at room temperature ( $T = T_{env}$ ), at high temperature ( $T = T^*$ ) or after cooling down to room temperature, by adopting an uncoupled procedure (UCP, Fig. 3a, heating followed by loading or heating+cooling followed by loading) or a coupled procedure (CPL, Fig. 3b, heating+loading). For the same value of  $T^*$ , more damage is produced by the second procedure, but above 500°C the results are very close (Fig. 3c).

### 3 Effect of high temperature on anchorages

Concrete degradation at high temperature has direct consequences on anchored bars mostly because of concrete degradation, while steel degradation plays a definitely-smaller role. In fact, in most cases, even after a severe fire the mechanical properties of the steel are fully or mostly recovered, while the mechanical post-cooling properties of the concrete are even worse than those at high temperature and much worse than the initial properties (prior to the fire). Studies are still in progress to investigate to what extent bond strength and stiffness are affected by such entities, as: cementitious matrix (for instance in self-compacting concrete), confinement (Fig. 4), fibers (amount, type - polymeric, metallic, hybrid - and aspect ratio, Fig. 5), aggregates (natural, artificial, light, heavy, recycled), additives and admixtures, heating and cooling procedures, curing, thermal history, stress state, confinement, bar position and diameter, anchorage length (*bonded length*, generally  $> 10\varnothing$  in actual anchorages) and net cover-to-bar diameter ratio ( $c/\varnothing =$  normalized net cover). Note that in ordinary conditions the value 3 for  $c/\varnothing$  is often considered the threshold between pull-out and splitting failures, see Schenkel's Report No.237 (ETH, Zurich, Birkhäuser, CH, 1998).

The decreasing tensile strength of the concrete with the temperature makes anchored bars - generally fairly close to the exposed surface - more likely to fail by cover splitting than by bar pull-out, since radial cracking in the concrete cover is facilitated, all the more because

along an exposed side the cover protecting the reinforcement is subjected to the highest temperatures and thermal gradients. Transverse reinforcement (mostly stirrups), however, is very effective in limiting the opening and width of the radial cracks through the cover.

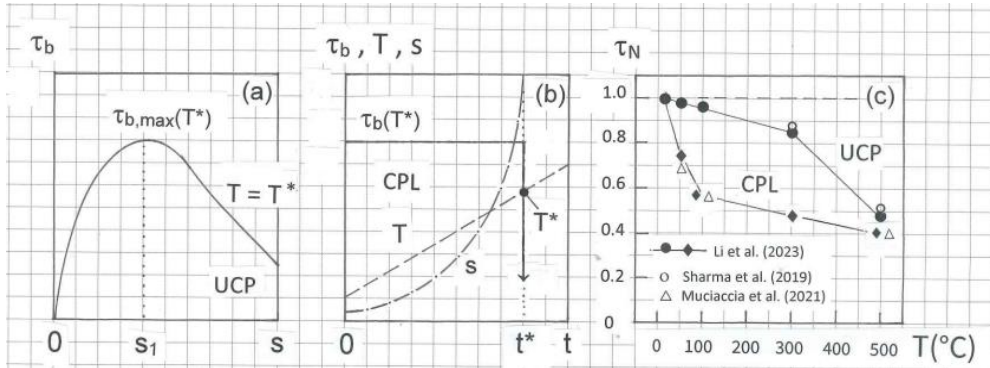


Fig. 3 Uncoupled – UCP (a) vs. coupled – CPL (b) heating (+cooling) and loading procedures; and bond capacity vs. temperature in both cases (c).

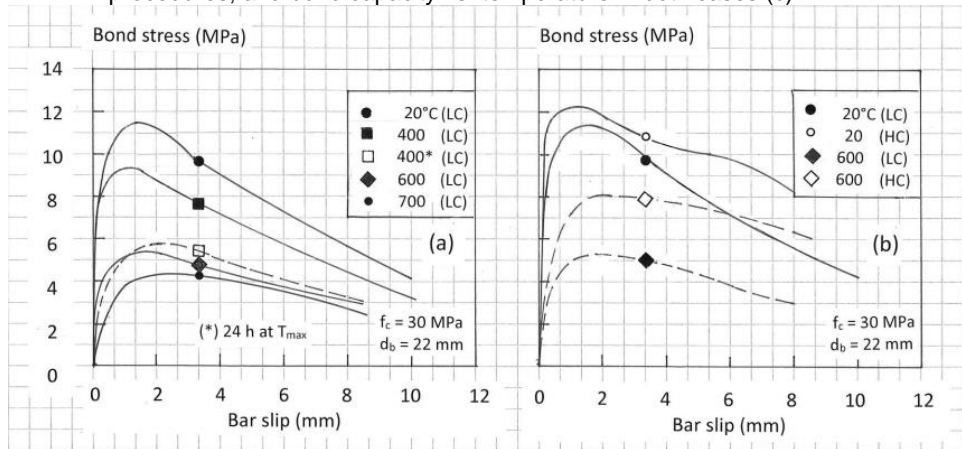


Fig. 4 Residual bond stress-bar slip curves from pull-out tests on anchored bars (rest at  $T_{max} = 2h$  but 24h at 400°C): (a) temperature and (b) confinement effects;  $f_c = 30$  MPa;  $\varnothing = 22$  mm;  $l_b/\varnothing = 9$ ; LC = low confinement ( $p_{st} = 0.8\%$ ) and HC = high confinement ( $p_{st} = 1.6\%$ );  $p_{st}$  = stirrup ratio; adapted from Ghajari and Yousefpoor (2023, see Bamonte et al., 2024 [3]); pull-out or mixed failure mode.

#### 4 Bond degradation in the design of anchored bars

Bond degradation at high temperature is treated in the proposals for MC2020 in two different ways, depending on whether the design of new construction or the safety of existing construction is at issue.

In the former case, bond degradation in fire conditions is introduced by multiplying the design anchorage or lap length  $l_{b,20}$  (valid in ambient conditions) by an amplification factor  $\lambda_{fi}$  ( $= 1.0-1.5$ ), to calculate the anchorage  $l_{b,fi}$  required at high temperature:

$$l_{b,fi} = \lambda_{fi} \cdot l_{b,20} \quad (1a)$$

In the latter case, bond degradation in fire conditions is introduced by limiting the stress in the reinforcement ( $f_{fire}$ ) to a fraction of the allowable design stress  $f_{std}$  ( $\leq f_{yd}$ ) valid in ambient conditions; to this end,  $f_{std}$  is divided by the same coefficient  $\lambda_{fi}$  introduced in Eq. 1a:

$$f_{fire} = f_{std} / \lambda_{fi} \quad (1b)$$

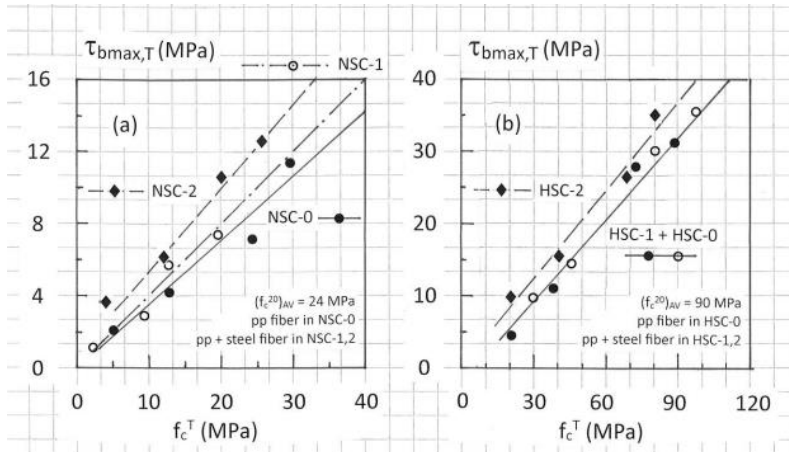


Fig. 5 Bond strength vs. compressive strength at ambient/high temperature: (a) normal-strength, and (b) high-strength concrete ( $\varnothing = 12$  mm,  $l_b/\varnothing = 5$ , adapted from Varona et al., 2018, see Bamonte et al., 2024 [3]); pp/st = polymeric/steel fibers;  $v_{pp} = 0.15\%$  (NSC) and  $0.25\%$  (HSC);  $v_{st} = 0.25\%$ ; steel-fiber aspect ratio: 47 (NSC-1 and HSC-1), and 86 (NSC-2 and HSC-2); fiber content by volume; pull-out failure.

The factor  $\lambda_{fi}$  takes care of the following issues:

- In fire situations, the loads to be introduced are smaller than those to be introduced at the ultimate limit state – ULS; hence, in a fire situation a reduction factor  $\eta_{fi}$  ( $= 0.5-0.75$ , right-hand-side of Fig. 6) is applied to the loads acting at the ULS.
- In fire situations, the partial safety factors for the materials (concrete and steel) should be smaller than those introduced in ambient conditions (generally,  $\gamma_{m,fi} = 1.0$  compared to  $\gamma_m = 1.5$  for the concrete at the ULS); hence,  $\gamma_{m,fi}/\gamma_m = 0.67$ .
- In the case of standard fire (ISO 834), bond capacity is smaller than in ordinary conditions, depending on the fire duration; a reduction factor  $\beta_{fi}$  (Fig. 7a) is introduced; note that bond degradation under the standard fire (that is a *transient situation*) is generally less severe than bond degradation at any given high temperature (that is a *quasi-static situation*, reduction factor  $\xi_{fi}$ , Fig. 7a). The factors  $\beta_{fi}$  and  $\xi_{fi}$  are plotted as a function of the temperature in Fig. 7b, together with some experimental results.

## 5 Local bond-slip behavior under elevated temperature (quasi static conditions)

The cloud of the bond-strength values coming from numerous experimental campaigns is comprised between two top curves (continuous and dash-dotted curves in Fig. 7b) and one bottom straight line (dash line). The two top curves are a sort of upper bound representing the normalized bond strength under the standard fire -  $\tau_{bmax,SF}$  (i.e., in highly-variable transient conditions) and the bottom straight line is a conservative lower-bound value representing the normalized bond strength  $\tau_{bmax,T}$  in quasi-static conditions (MC2010/2020). The equations of the two top curves are reported in the *fib* background document on bond (MC 2020 [5]) in a normalized form, through  $\beta_{fi}$  and  $\xi_{fi}$ , while the bottom straight line has the following mathematical expression:

$$\tau_{bmax,T} = \tau_{bmax,20} \cdot [1 - (T^* - 0.02)/0.72] \quad (2)$$

where  $T^* = T/1000$ ;  $T = 20-740^\circ\text{C}$  = temperature along the axis of the reinforcing bar; and  $\tau_{bmax,20}$  is the bond strength in ambient conditions ( $20^\circ\text{C}$ ). As for  $\tau_{bmax,20}$ , it is either the pull-out strength (PO) or splitting strength (SP), whichever is smaller; the expressions for the calculation of  $\tau_{bmax,20}$  are:

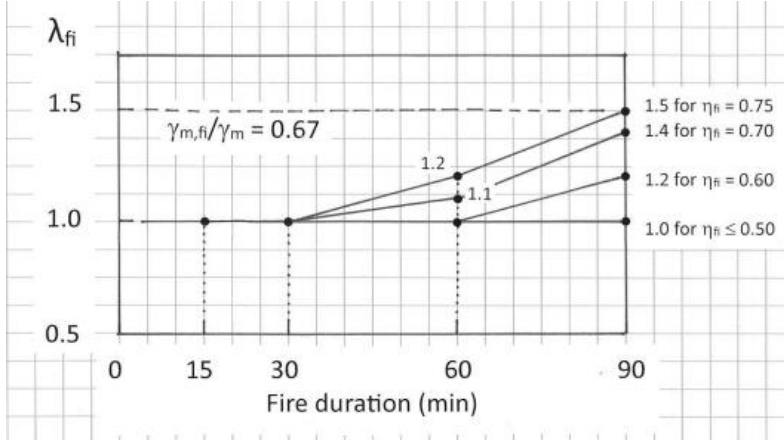


Fig. 6 Bonded length in fire: amplification factor  $\lambda_{fi}$  as a function of the fire duration, for various values of the load factor  $\eta_{fi}$  (share of the loads applied in fire conditions with respect to the loads applied at the ULS).

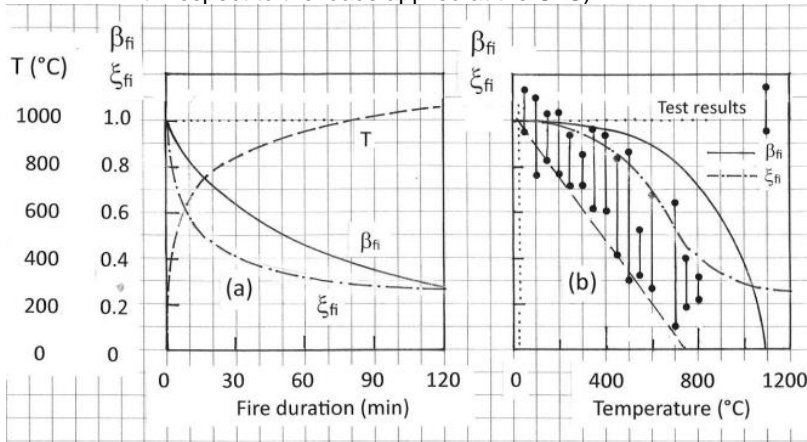


Fig. 7 Normalized bond strength and temperature under the Standard Fire ISO 834): (a) as a function of the fire duration; and (b) as a function of the temperature; the dash straight line in (b) is a conservative lower limit for  $\tau_{bmax,T}/\tau_{bmax,20}$  (MC2010/2020).

- PO (good bond conditions):  $\tau_{bmax,20} = \tau_{bmax} = 2.5 \cdot f_c^{1/2}$  (3a)
- SP – split1 (good bond conditions; no stirrups):  $\tau_{bmax,20} = \tau_{bu,split1} = 3.1 \cdot f_c^{1/4}$  (3b)
- SP – split2 (good bond conditions; with stirrups):  $\tau_{bmax,20} = \tau_{bu,split2} = 3.6 \cdot f_c^{1/4}$  (3c)

Note that the previous expressions are valid as long as the reinforcement is below the yield threshold ( $\varepsilon_s \leq \varepsilon_{s,y}$ ).

The general shape of the bond-slip curves at high temperature in the pull-out mode is the same as that in ambient conditions (Fig. 8a, qualitative dash curve, MC2010/2020), and can

be approximated by means of a multilinear curve, with an initial nonlinear branch followed by a first plateau, a linearly-descending branch and a residual plateau, as shown by the continuous curve in Fig. 8a, where the parameters that define the four branches are indicated as well. These parameters ( $\tau_{bmax,T}$ ;  $S_{1,T}$ ;  $S_{2,T}$ ;  $S_{3,T}$ ;  $\tau_{bf,T}$ ) are a function of the temperature. The equation of the initial nonlinear branch is:

$$\tau_{bT} = \tau_{bmax,T} \cdot (S/S_{1,T})^\alpha \text{ for } S = 0-S_{1,T} \quad (\alpha = 0.4) \quad (4)$$

In the splitting mode with/without passive confinement, simpler curves describe bond behavior at high temperature, similarly to ambient temperature.

A physical explanation of the four branches of the multilinear design curve concerning *bond failure in the pull-out mode* can be found in Auer and Stempniewski, and Muttoni and Fernandez-Ruiz, both in the proceedings of BiC 2012 (2012) [4a].

In both MC2010 and in the proposal for MC2020  $s_{1,T}$ ,  $s_{2,T}$  and  $s_{3,T}$  are given different values depending on whether bond failure is by pull-out or by splitting, and in case of splitting  $s_{3,T}$  takes care – with different values – of the confinement offered by the stirrups.

The residual strength  $\tau_{bf,T}$  – represented by the second plateau in Fig. 8a – is a sizable fraction of bond strength in the cases of pull-out failure and confined splitting failure, while  $\tau_{bf,T}$  is zero in the case of unconfined splitting failure. The expressions for  $\tau_{bf,T}$  are:

$\tau_{bf,T} = 0.40 \tau_{bmax,T}$  in the case of pull-out failure

$\tau_{bf,T} = 0.40 \tau_{bu,split2,T}$  in the case of splitting failure in confined conditions

$\tau_{bf,T} = 0$  in the case of splitting failure in unconfined conditions

Beside bond strength, bond shear modulus  $k$  (MPa/mm) plays a substantial role in many problems, namely whenever concrete and reinforcement deformations come into play and structural stiffness is a major issue. For instance, in service conditions after crack stabilization or after an accident with the formation of a well-defined crack pattern, bond shear modulus controls tension stiffening in longitudinal bars. In anchored bars bond shear modulus controls the stress and strain distributions in the bars and in the embedment prior to the formation of more or less distributed cracks.

In numerical analysis, knowing bond shear modulus is necessary to formulate refined models for RC structures, where zero-thickness bond elements are often introduced at bar-concrete interface via longitudinal springs, whose stiffness stands for bond shear modulus.

Like all other concrete properties, bond shear modulus is affected by high temperatures and fire (see refs. in Bamonte et al., 2024 [3]).

With reference to bond pull-out failure, in Fig. 8b, bond shear modulus can be introduced in different ways such as the secant stiffness to the peak stress  $k$  (a commonly- adopted criterion) or to other well-defined points like  $k_1$ , the quasi-tangent stiffness ( $s < 0.05-1$  mm) or the slope of the unloading branch  $S_s$ .

## 6 Local bond-slip behavior under fire (highly-unsteady thermal conditions)

In fire conditions, for any given fire duration, at high temperature or after cooling down to ambient temperature, bond capacity is reduced compared to ambient conditions, because of the temperature-induced damage and thermal gradients in the concrete surrounding the anchored bar, accompanied by cover splitting, thermal spalling of the concrete (in certain circumstances) and the further damage accumulated during the cooling phase.

Since concrete mechanical properties in tension are more heat-sensitive than those in compression, bond failure in fire conditions tends to occur in a mixed pull-out/splitting mode or by cover splitting, mitigated by the confining action exerted by either the supports (*active confinement*) or the transverse reinforcement (links, stirrups, spirals, *passive confinement*). Bond strength loss is accompanied by an increase in ductility (i.e., in bar slip).

In fire conditions, the bond capacity ( $\tau_{bmax,fi} = \tau_{bu,fi}$ ) and the bar displacements ( $S_{i,fi}$ ) of the points defining the bond-slip curve are a function of the same quantities in ambient conditions ( $\tau_{bmax,20} = \tau_{bu,0}$ , and  $S_{i,20}$ , respectively, Eqs. 6 and 7, Fig. 10):

$$\tau_{bu,fi} = \xi_{fi} \tau_{bu,0} ; S_{i,fi} = \xi_{s,fi} S_{i,20} \quad (i = 1,2,3) \quad (6,7)$$

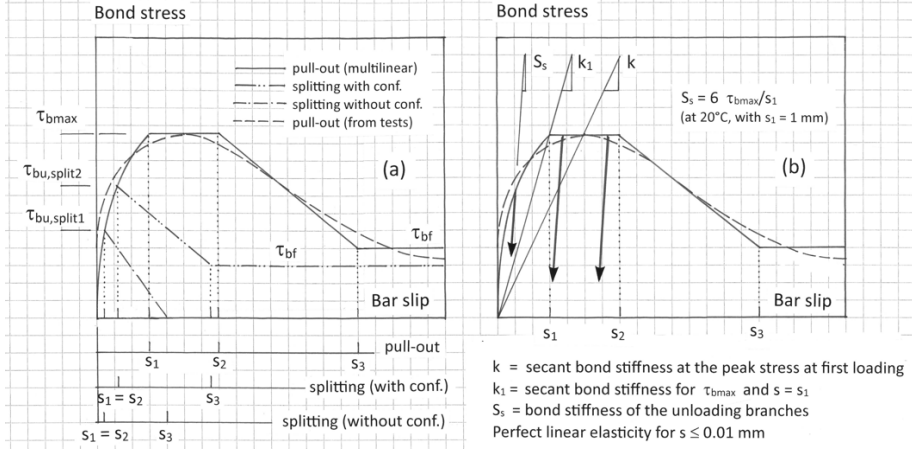


Fig. 8 Qualitative bond stress-bar slip curve from the tests (dash curve) and multilinear design curve (continuous curve) from MC10/20: (a) relevant parameters; and (b) secant bond shear moduli for loading and unloading; the superscript T is omitted.

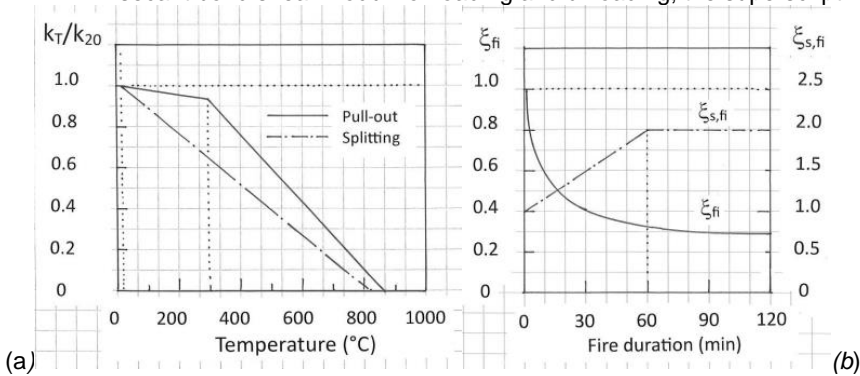


Fig. 9 Secant bond shear modulus (at the max. bond stress) for bond pull-out and splitting failures (a); and reduction factor  $\xi_{fi}$  for bond capacity - and amplification factor  $\xi_{s,fi}$  for the slip values characterizing the bond-slip curve - (b).

In Eq. 6 the reduction factor  $\xi_{fi}$  takes care of fire duration (standard fire) with increasing temperatures (Figs. 9a,b), and  $\tau_{bu,0}$  takes care of actual bond conditions, concrete strength, bar diameter, concrete cover (in two directions), confinement efficiency and density of the transverse reinforcement;  $\tau_{bu,0}$  is provided by Eq. 8, where the failure mode in fire conditions is assumed to be by *splitting*, as in actual RC structures the net bar cover is generally close to  $1.5\varnothing$ , well below the value  $3\varnothing$  often proposed as the threshold between splitting and pullout failures (Schenkel's Report No.237, 1998, ETH, Zurich, Birkhäuser, CH):

$$\tau_{bu,0} = 6.5 \eta_2 (f_{cm}/f_{cm0})^{0.25} (\varnothing_0/\varnothing)^{0.2} [(C_{min}/\varnothing)^{0.25} (C_{max}/C_{min})^{0.1} + k_m K_{tr}] \quad (8)$$

where:  $\eta_2$  = coefficient for bond conditions (= 0.7-1.0);  $f_{cm0}$  = 25 MPa;  $\varnothing_0$  = 25 mm;  $C_{max}$  and  $C_{min}$  = concrete covers;  $k_m$  = efficiency coefficient of the confinement (= 0-12); and  $K_{tr}$  = density coefficient of the transverse reinforcement ( $\leq 0.05$ ).

## 7 Concluding remarks

The numerous studies on concrete at high temperature and in fire carried out in the last twenty years explain the much greater coverage of bond in such extreme conditions provided by Model Code 2020. In fact, the tenet *first bar yielding then bond collapse* may fail (a) at high temperature, due to the loss of concrete strength; and (b) after cooling down to room temperature, due to the further weakening of bond caused by the damage accumulated in the concrete under decreasing temperatures.

Within such a complex framework, the new proposals make it possible to design – or to check – anchored bars and splices with a greater safety level, even if many issues are still open to investigation, like: (a) concrete thermal spalling, which may even directly expose anchored and lapped bars to the flames; (b) thermal inertia of solid/thick members, which may delay the attainment of the maximum temperature in the reinforcement after the fire has peaked; (c) indirect actions that are typical of R/C statically-redundant structures and may markedly increase the pull-out forces acting on anchored or lapped bars in the regions not directly exposed to the fire; (d) the heating-loading process, since simultaneously-applied heating and loading may worsen bond behavior with respect to a sequential process; and – last but not least – (e) test procedures based on more realistic specimens able to include pull-out and splitting failures, as well as the effect of transverse reinforcement and temperature.

## Acknowledgements

This paper – focused on anchorages - is derived from the background document that *fib* Task Group 2.5 “Bond of embedded steel reinforcement: anchorages and splices” (Convenors Giovanni Plizzari and Giovanni Metelli) is preparing to elucidate the provisions of Model Code for Concrete Structures 2020.

## References

- [1] *fib* MC 2010 (2010). *Model Code 2010 for Concrete Structures*. Ed. by *fib* – Fédération Internationale du Béton, publ. by Wiley VCH, 434 p.
- [2] *fib*/CEB-FIP. 2000. Bond of Reinforcement in Concrete. *State-of-Art Report. Bulletin No.10. fib Task Group 4.5 “Bond Models”*, convenor Ralejs Tepfers, 427 p.
- [3] Bamonte P., Gambarova P.G. and Lo Monte F. 2024. “Bond shear modulus in reinforced concrete at high temperature: A design-oriented approach”. *Structural Concrete*, DOI: 10.1002/suco.202300160, 16 p.
- [4] BiC 2012/BiC 2022. 2012/2022. Bond in Concrete: Bond, Anchorage, Detailing. *Proc. 4<sup>th</sup> and 5<sup>th</sup> Int. Symposia*, Brescia (Italy) and Stuttgart (Germany), 1103 and 1073 p.
- [5] *fib* MC 2020 (in progress). *Model Code 2020 for Concrete Structures*. To be edited by *fib* – Fédération Internationale du Béton.
- [6] Lo Monte F. and Gambarova P.G. 2014. “Corner Spalling and Tension Stiffening in Heat-Damaged R/C Members: a Preliminary Investigation”. *Materials and Structures*, V. 48, No. 11, 3657-3673.
- [7] Muciaccia G. and Consiglio A.N. 2021. “Local bond properties of reinforcement in concrete subjected to elevated temperatures: Effects of clear cover, bonded length and heating and loading procedures”. *Engineering Structures*, V. 230, 111594, 9 p.
- [8] Metelli G., Cairns J. and Plizzari G. 2023. “A new *fib* Model Code proposal for a beam-end type bond test”. *Structural Concrete*, V. 24, No. 4, 4446-4463.
- [9] Lublőy Ě. and Hlavička V. 2017. “Bond after Fire”. *Construction and Building Materials*, No. 2, V. 132, 210-218.
- [10] Tonidis M., Bošnjak J. and Sharma A. 2021. “Post-fire performance of RC beams with critical lap splices”. *Journal of Building Engineering*, V. 44, 102637, 15 p.

# **Strengthening and repair of concrete structures**





# Interface bond between SRP system and concrete substrate: modelling

Francesco Ascione<sup>1</sup>, Marco Lamberti<sup>2</sup>, Annalisa Napoli<sup>1</sup> and Roberto Realfonzo<sup>1</sup>

<sup>1</sup>*Department of Civil Engineering,  
University of Salerno,  
Via Giovanni Paolo II 132, 84084 Fisciano (SA), Italy*

<sup>2</sup>*ENEA,  
Brasimone Research Centre,  
Località Brasimone, 40032 Camugnano (BO), Italy*

## Abstract

Steel Reinforced Polymers (SRPs) represent an innovative class of composite materials used for externally strengthening and repairing reinforced concrete (RC) and masonry structures. These composites consist of High Tensile Strength Steel (HTSS) micro wires twisted into small diameter cords or strands, embedded in an epoxy matrix. The SRP-concrete interface bond is a critical aspect that requires further research, as it often causes premature failure in the strengthening system. This paper contributes to this topic by presenting a theoretical study on the bond behavior between the SRP system and the concrete substrate, following extensive experimental investigations conducted at the University of Salerno. Specifically, an analytical procedure—recently proposed by the authors—is applied for the indirect identification, or back analysis, of the local bond-slip model, which aims to capture the interfacial behavior of SRP bonded to concrete. The analysis incorporates results from direct single-lap shear tests on SRP-concrete joints available to the authors. Key parameters in the analytical bond-slip law are calibrated by fitting the analytical model to the experimental load-slip data.

## 1 Introduction

Steel Reinforced Polymer (SRP) represents a new generation of composite materials designed for the external strengthening and repair of reinforced concrete (RC) and masonry structures. These composites consist of High Tensile Strength Steel (HTSS) micro wires twisted into small diameter cords or strands and embedded in an epoxy matrix. Depending on the cord spacing, various textile densities are available: low (L, 0.157 cords/mm), low-medium (LM, 0.314 cords/mm), medium (M, 0.472 cords/mm), and high (H, 0.709 cords/mm).

The SRP-concrete interface bond is a critical issue since it often leads to premature failure of the strengthening system [1,2]. To address this, a comprehensive experimental study was conducted at the University of Salerno in Italy, involving 130 direct single-lap shear (DSLSS) tests on SRP-concrete joints with different concrete surface finishes: sandblasted (SB), bush hammered (BH), and grinded (GR). The findings from these tests, documented in previous studies [3], have been utilized to develop a simplified analytical procedure to simulate DSLSS tests. This procedure, detailed in [4], uses closed-form solutions to predict the debonding process. It involves an appropriate local shear stress-slip ( $\tau$ - $s$ ) law, from which specific expressions for the interface shear stress distribution, axial stress profile, and concrete-SRP relative displacement (slip) function can be derived. This method allows for analytical estimation of the effective bonded length of the SRP and the maximum axial stress (or peak force) in the SRP before debonding.

To apply and validate the proposed analytical procedure, the relevant local bond-slip laws were directly calibrated using DSLSS test data for the three concrete surface finishes (GR, BH, and SB) [3],[5]. The sets of parameters defining these laws were determined by minimizing the difference between theoretical and experimental shear stress ( $\tau$ ) at specific slip ( $s$ ) values. The experimental ( $\tau$ - $s$ ) values were obtained from strain measurements provided by strain gauges bonded to the SRP strip, following the procedures outlined in previous research [5].

This paper presents an alternative application of the proposed model through the indirect identification of the relevant parameters of the local bond-slip interface law, known as "back-analysis." This method involves identifying the interface law that produces a global load-slip (F-s) response that best matches the corresponding experimental curve. This procedure, similar to that used by Pecce et al. for the bond between FRP reinforcement and concrete [6], is fully described in this paper. It is applied to determine a ( $\tau$ -s) law suitable for concrete substrates subjected to the three surface treatments studied in the experimental program (GR, BH, and SB). The resulting bond-stress models are compared to each other. The results show good agreement between experimental and numerical data in terms of F-s or axial-stress ( $\tau$ -s) curves, particularly when using the interface models calibrated through back analysis.

## 2 THE BOND-SLIP MODELLING

In a recent study, Ascione et al. [4] presented a mechanical model to capture the SRP-concrete debonding, which is governed by the following:

$$E_f t_f \frac{d^2 s(x)}{dx^2} = \tau[s(x)] \quad (1)$$

where  $s(x)$  is the slip at distance  $x$  along the SRP strip (see Fig. 1),  $\tau$  is the interfacial shear stress corresponding to  $s(x)$ ,  $E_f$  and  $t_f$  are the elastic modulus and thickness of the SRP strip, respectively. By integrating Equation (1) and adopting an appropriate constitutive law  $\tau(s)$ , it is possible to evaluate the unknown function  $s(x)$ , which describes the variation of slip along the interface.

A closed form solution of Equation (1) could be obtained only if:

- an expression for  $\tau(s)$  is adopted that could be integrated in closed form;
- the SRP which is subjected to a tensile force  $F$ , is perfectly bonded to the concrete substrate (i.e., when the development length  $l_d$ , is shorter than, or equal to the bonded length,  $l_b$ , that means delamination is prevented).

If the last condition is satisfied, the  $x$ -axis origin must be located at distance  $l_d$  from the system loaded end (see Fig. 1) because from the origin to the strip unloaded or free end the slip would be zero. Once  $s(x)$  has been determined, the  $\sigma(x)$  and  $\tau(s)$  distribution along the strip can be determined as follows:

$$\sigma(x) = E_f \varepsilon_f(x) \cong E_f \frac{ds(x)}{dx} \quad (2a)$$

$$\tau(x) = E_f t_f \frac{d^2 s(x)}{dx^2} \cong t_f \frac{d\sigma}{dx} \quad (2b)$$

where the concrete tensile strain is neglected.

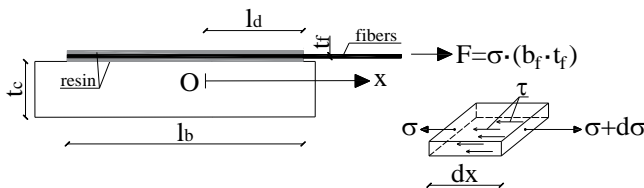


Fig. 1 Modelling of DSLS test.

For further details of the analytical procedure, reference can be made to [4], where the solution to equation (1) is given for three bond-slip laws, each defined by a certain number of characterising parameters. Another application of the proposed modelling is the indirect identification of the relevant parameters of the local interfacial bond-slip law through the so-called "back-analysis", which makes use of experimentally obtained load-slip curves (F-s) or, alternatively, normal stress-slip curves ( $\tau$ -s), where  $\sigma$  is the applied axial stress in the SRP strip. Therefore, based on the experimental curves obtained from the DSLS tests, parameter identification can be achieved by minimising the scatter between the experimental and theoretical results by adjusting the relevant parameters in the bond-slip law. Details of the latter analysis are presented below, in the context of identifying the bond-slip laws applicable

to each of the SRP-concrete interfaces, where the concrete bonded surface has a GR, BH or SB finish, irrespective of the concrete strength  $f_{cm}$ .

## 2.1 Back analysis procedure

The application of the proposed analytical procedure is demonstrated here by utilizing it on two of the three  $\tau$ - $s$  laws discussed in the previous study. These constitutive laws are depicted in Figure 2. In this figure,  $\tau_m$  and  $s_m$  denote the maximum bond stress and the corresponding slip, respectively, while  $s_u$  represents the ultimate slip, which occurs when  $\tau$  reaches zero on the descending portion of the curve.

The 4-parameter ( $\tau_m, s_m, s_u, \alpha$ ) law shown in Figure 2a, labeled *Type A*, was introduced in [8]. It features a non-linear ascending branch and a linear descending, or softening, branch. The simplified law in Figure 2b, labeled *Type B*, is a 3-parameter ( $\tau_m, s_m, s_u$ ) model commonly used in the literature for bond modeling.

Applying the procedure requires the analytical derivation of the axial stress-slip law  $\sigma(s)$ , as detailed below. To avoid dependence of the interfacial law on the substrate's concrete strength, the peak shear stress  $\tau_m$  can be replaced by  $\bar{\tau}_m = \tau_m / \sqrt{f_{cm}}$ , a common practice in modeling concrete bond to reinforcement [9].

Once the relevant  $\tau$ - $s$  law in Figure 2 (*Type A* or *Type B*) is selected, the procedure begins with selecting the appropriate parameters: four for *Type A*  $\{\bar{\tau}_m; s_m; s_u, \alpha\}^I$  and three for *Type B*  $\{\bar{\tau}_m; s_m; s_u\}^I$ . For each experimental slip value  $s_i$  measured at the loaded end of the strip during the  $i$ -th loading step—provided that  $s_i$  is less than the ultimate value  $s_u$ —the corresponding theoretical value of the shear stress  $\tau^{th}(s = s_i)$  is calculated using the relevant expression in Figure 2, depending on whether  $s_i \leq s_m$  or  $s_m < s_i \leq s_u$ .

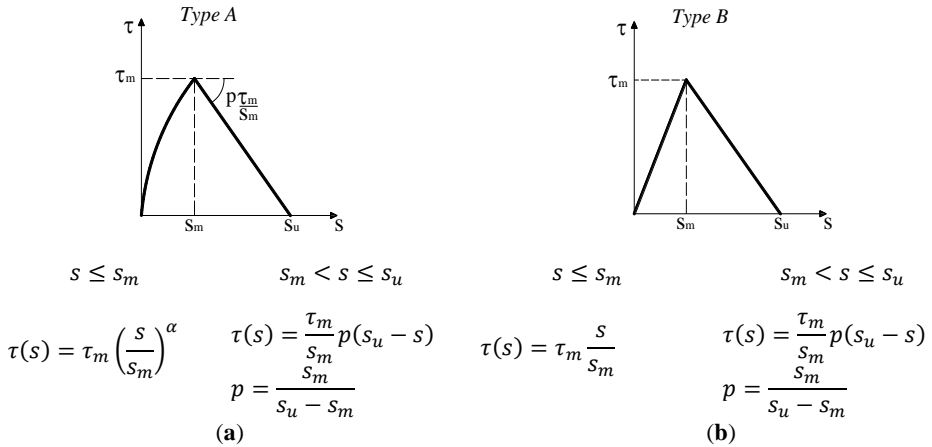


Fig. 2 Considered bond-slip laws: (a) Type A; (b) Type B.

Hence, the function  $\sigma^{th}(s)$  can be derived using Equation 3, which represents an energy-based formulation [6,8] between the area underneath the ( $\tau$ - $s$ ) curve (namely,  $A_\tau$ , which has to be specified for *Type A* and *Type B* laws) and the area underneath the ( $\sigma$ - $\varepsilon$ ) curve (namely,  $A_\sigma$ ) - assumed linear elastic - multiplied by the thickness of the SRP strip  $t_f$ , i.e.:

$$A_\tau(s) = t_f A_\sigma(\sigma) \quad (3)$$

where  $A_\sigma(\sigma)$  is given by:

$$A_\sigma(s) = \frac{1}{2} \frac{\sigma^2}{E_f} \quad (4)$$

whereas the relevant  $A_\tau(s)$  is given by one of the following expressions, depending on the value of  $s$  and the type of model:

$$\begin{array}{l} \text{Type A} \\ \text{model} \end{array} \quad \begin{array}{l} s \leq s_m \\ s_m < s \leq s_u \end{array} \quad \begin{array}{l} A_\tau(s) = \frac{\tau_m}{\alpha + 1} \left(\frac{s}{s_m}\right)^\alpha s \\ A_\tau(s) = \tau_m \left\{ \frac{s_m}{\alpha + 1} + \left[ \frac{p}{s_m} (s_u - s) + 1 \right] \frac{(s - s_m)}{2} \right\} \end{array} \quad \begin{array}{l} (5a) \\ (5b) \end{array}$$

$$\begin{array}{l} \text{Type B} \\ \text{model} \end{array} \quad \begin{array}{l} s \leq s_m \\ s_m < s \leq s_u \end{array} \quad \begin{array}{l} A_\tau(s) = \frac{1}{2} \frac{\tau_m}{s_m} s^2 \\ A_\tau(s) = \frac{\tau_m}{2} \left\{ s_m + (s - s_m) \left[ 1 + \frac{p}{s_m} (s_u - s) \right] \right\} \end{array} \quad \begin{array}{l} (6a) \\ (6b) \end{array}$$

By inserting Equations 4 and 5, or 4 and 6, for  $A_\sigma(\sigma)$  and  $A_\tau(s)$ , respectively in Equation (3), the function  $\sigma(s)$  for the two examined cases can be defined as follows:

$$\begin{array}{l} \text{Type A} \\ \text{model} \end{array} \quad \begin{array}{l} s \leq s_m \\ s_m < s \leq s_u \end{array} \quad \begin{array}{l} \sigma^{th}(s) = \sqrt{2 \frac{E_f}{t_f} \frac{\tau_m}{s_m} \frac{\tau_m}{\alpha} s^{\alpha+1}} \\ \sigma^{th}(s) = \sqrt{2 \frac{E_f}{t_f} \tau_m \left\{ \frac{s_m}{\alpha + 1} + \left[ \frac{p}{s_m} (s_u - s) + 1 \right] \frac{(s - s_m)}{2} \right\}} \end{array} \quad \begin{array}{l} (7a) \\ (7b) \end{array}$$

$$\begin{array}{l} \text{Type B} \\ \text{model} \end{array} \quad \begin{array}{l} s \leq s_m \\ s_m < s \leq s_u \end{array} \quad \begin{array}{l} \sigma^{th}(s) = \sqrt{\frac{E_f \tau_m}{t_f s_m} s} \\ \sigma^{th}(s) = \sqrt{\frac{E_f}{t_f} \tau_m \left\{ s_m + (s - s_m) \left[ 1 + \frac{p}{s_m} (s_u - s) \right] \right\}} \end{array} \quad \begin{array}{l} (8a) \\ (8b) \end{array}$$

Therefore, by setting  $s = s_i$  in Equation (7) or (8), the current value of the error between the theoretical,  $\sigma(s_i)^{th}$ , and the experimental,  $\sigma(s_i)^{exp}$ , values of the axial stress can be estimated as:

$$E_i = \frac{\sigma(s_i)^{exp} - \sigma(s_i)^{th}}{\sigma(s_i)^{exp}} \quad (9)$$

Finally, the optimal set of values for the parameters  $\{\bar{\tau}_m; s_m; s_u; \alpha\}$  or  $\{\bar{\tau}_m; s_m; s_u\}$  can be obtained by minimizing the Mean Absolute Percentage Error (MAPE), as:

$$MAPE = \frac{\sum_{n=1, N_{test}} \sum_{i=1, K} |E_i| \cdot 100}{N_{meas}} \quad (10)$$

where  $K$  represents the number of experimental  $s_i$  values considered for each test,  $N_{test}$  is the number of tests included in the error minimization process, and  $N_{meas}$  is the total number of experimental points or measurements considered.

It is worth mentioning that in this procedure the error  $E_i$  for  $s_i$  values greater than the  $s_u$  of the current set of parameters is assumed to be zero.

### 3 Application of the best-analysis to the experimental database

The back analysis was applied to several DSLS tests included in the experimental database published in [3], where the three different concrete surface finishes (SB, BH, GR) were analyzed separately. For each surface finish, the tests were considered together in order to find a unique local bond stress-slip law suitable for any concrete strength and any strip density (L, LM, M and H).

The DSLS tests with the GR surface considered in the current analysis include 39 out of 48 tests, characterized by  $f_{cm}$  values ranging from 13 to 45 MPa and a strip width  $b_f = 100$  mm. For the BH

finish, 24 out of 34 tests were considered, all referred to as "soft bush-hammering" in [3], with  $f_{cm}$  values between 13 and 26 MPa and  $b_f = 100$  mm. Finally, for the SB finish, 21 out of 29 DSLS tests were considered, with  $f_{cm} = 13$  MPa,  $b_f = 100$  mm, and a sandblasted surface [3].

Table 1 provides, for the three concrete finishes, the values of the relevant parameters ( $\bar{\tau}_m$ ;  $s_m$ ;  $s_u$ ,  $\alpha$ ), obtained by the proposed procedure or indirect method (IM), for the normalized bilinear and nonlinear shear stress-slip laws. The following additional information is reported in Table 1:

- $\bar{\Gamma}_F$ , which is the normalized fracture energy, defined by the area underneath the normalized ( $\tau$ - $s$ ) law up to  $s = s_u$ ;
- #data, which is the per cent ratio between the number of experimental points effectively counted in the error minimization process (i.e.,  $N_{meas}$  in Equation 10) and the total number of points available on the experimental ( $\sigma$ - $s$ ) curves (namely,  $N_{meas}^{total}$ ) counted on all the  $N_{test}$ . Specifically,  $N_{meas}^{total}$  is obtained by summing up, for each DSLS test, the measured ( $\sigma$ - $s$ ) values up to  $s = 1$  mm, i.e., the minimization process for all the experimental curves was applied up to 1.0 mm slip.
- MAPE, which is the resulting error calculated according to Equation (10) by considering the found values for the mentioned sets of parameters.

Table 1 Back analysis: values of the calibrated bond slip model's parameters.

Model	Surface	$\bar{\tau}_m$ $\sqrt{MPa}$	$s_m$ mm	$s_u$ mm	$\alpha$ -	$\bar{\Gamma}_F^*$ $\sqrt{MPa} mm$	#data (%)	MAPE (%)
Type A (non linear)	GR	0.164	0.247	0.839	0.25	0.081	95.78	24.09
	BH	0.186	0.248	0.850	0.25	0.093	96.63	23.88
	SB	0.172	0.250	0.850	0.25	0.086	86.04	24.51
Type B (linear)	GR	0.211	0.179	0.850	-	0.090	96.18	22.58
	BH	0.274	0.192	0.668	-	0.091	87.40	23.46
	SB	0.285	0.250	0.850	-	0.121	86.55	18.68

$$* \bar{\Gamma}_F = \Gamma_F / \sqrt{f_{cm}}$$

In Figure 3, the nonlinear and bilinear ( $\tau$ - $s$ ) laws obtained through back analysis for the three concrete surface finishes are plotted. Regardless of the calibration method and  $\tau$ - $s$  model (*Type A* or *Type B*), the calculated fracture energy is generally the highest for the SB surface, followed by the BH and GR surfaces, respectively, confirming the experimental best bonding performance of the SB surface specimens [3].

In terms of both the calibrated values for the relevant parameters and the calculated fracture energy, the differences observed between *Type A* and *Type B* models are not significant for any surface finish.

Compared to *Type B*, *Type A* always gives higher slip values at peak stress, with the exception of the SB surface where the calibrated  $s_m$  value is the same for both model types.

Regardless of the type of concrete surface finish, the MAPE values range between 19 and 25%, calculated on the basis of the experimental data containing up to 97% of the test results for the BH surface.

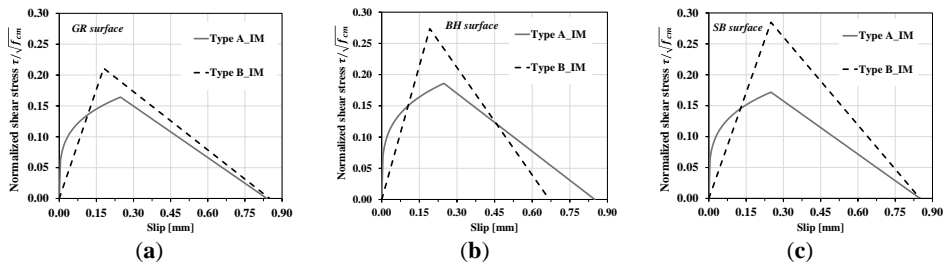
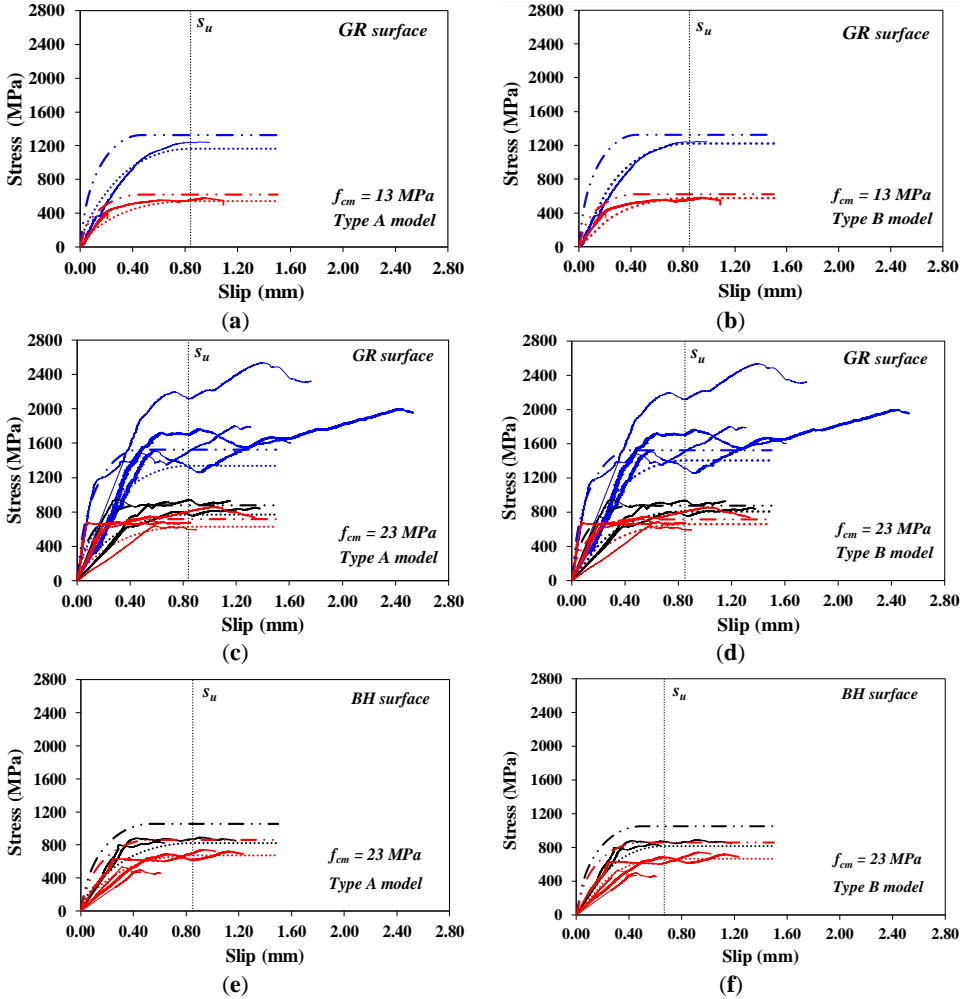


Fig. 3 Bond-slip considered in the back analysis: (a) Type A; (b) Type B.

### 4 Axial stress-slip curves: experimental-numerical comparison

Figures 4-5 illustrate some experimental and theoretical  $\sigma$ - $s$  curves for DSLS tests on specimens having the same concrete strength. The different colours used in the plots pertain to the variation of the SRP density, viz. low (L, blue curves), low-medium (LM, green curves), medium (M, black curves) and high (H, red curves). The plots in Figures 4a-d pertain to specimens with GR surface and  $f_{cm}$  values equal to 13 and 23 MPa; the plots in Figures 4e,f refer to specimens with BH surface and  $f_{cm}$  value equal to 23 MPa, whereas those in Figure 5 to specimens with  $f_{cm} = 13$  MPa and SB surface.



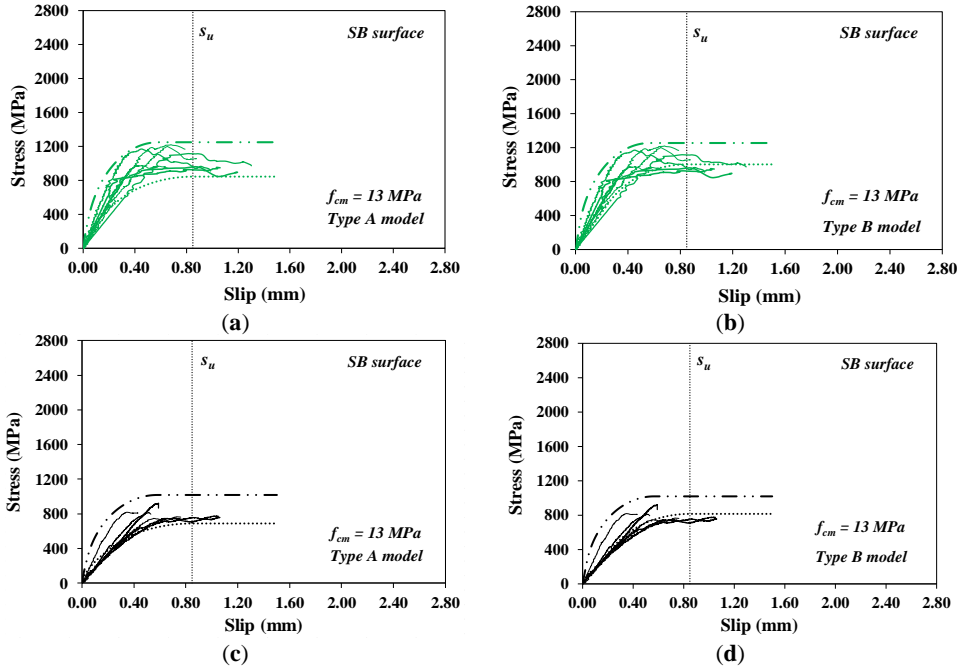
Legend:  
 — Exp. Curve – L density      ..... Indirect method (IM) – L density      — · — Direct method (DM) – L density  
 — Exp. Curve – M density      ..... Indirect method (IM) – M density      — · — Direct method (DM) – M density  
 — Exp. Curve – H density      ..... Indirect method (IM) – H density      — · — Direct method (DM) – H density

Fig. 4 Axial stress-slip curves for GR and BH surface: comparison between IM and DM for different  $f_{cm}$  values: (a,b)  $f_{cm} = 13$  MPa; (c,d,e,f)  $f_{cm} = 23$  MPa.

For each density, the experimental curves are compared with curves obtained by two numerical simulations, one making use of the  $(\tau$ - $s$ ) law calibrated through the direct method (DM, dash dot line curve) and the other one employing the interface law obtained from the back analysis (dotted line

curve). It is highlighted that the law calibrated through the direct method was derived by considering the experimental ( $\tau$ - $s$ ) values obtained from strain measurements provided by strain gauges bonded to the SRP strip, following the procedures outlined in previous research [5].

The plots on the left side (Fig. 4a,c,e and Fig. 5a,c) show the comparison obtained by using the ( $\tau$ - $s$ ) law *Type A* while those on the right side (Fig. 4b,d,f and Fig. 5b,d) refer to the ones by applying law *Type B*. Both numerical simulations are obtained by assuming increasing values of the slip up to a 1.5 mm and calculating the corresponding stress value through Equation (5) or (6).



Legend:

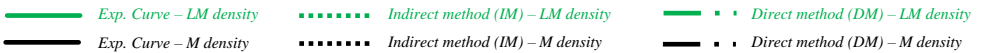


Fig. 5 Axial stress-slip curves for SB surface: comparison between IM and DM for the same  $f_{cm}$  value and different steel cord densities: (a,b) LM density; (c,d) M density.

The experimental to theoretical/numerical comparisons in Figures 4-5 allow one to make the following main observations:

- irrespective of the concrete surface finish, in general good agreement is observed, mainly in terms of stiffness in the pre-peak stage when using the ( $\tau$ - $s$ ) laws calibrated via indirect method. The ( $\tau$ - $s$ ) laws obtained by direct method yield higher values of the debonding stress (the fracture energy  $\Gamma_F$  being higher) which, in some cases, leads to even better agreement between the experimental and corresponding numerical responses;
- the models *Type A* and *Type B* calibrated based on either indirect or direct method do not play a key role in the simulation of the experimental curves since the numerical responses given by the two are negligibly different. However, even if the simplified bilinear ( $\tau$ - $s$ ) law can be successfully implemented in bond modeling problems for simulating the overall behavior of DSLS tests, the issue of the correct estimate of the SRP development length remains. Indeed, models *Type A* and *Type B*, yield basically identical  $\sigma$ - $s$  curves, but the differences in the prediction of the development length can be sometimes significant.

## 5 Conclusions



In this paper, an analytical procedure has been applied to indirectly identify the local bond-slip model that captures the interfacial behavior of SRP bonded to concrete. The analysis utilized results from 85 single shear tests conducted at the University of Salerno on SRP-concrete joints. These tests were organized into three sets based on the concrete surface finish: grinded (GR), bush hammered (BH), and sandblasted (SB). The concrete compressive strength  $f_{cm}$  varied within the range of 13-26 MPa or 40-45 MPa, except for the SB group where  $f_{cm}$  was 13 MPa for all specimens.

For the three concrete types, the key parameters in the analytical bond-slip law for each concrete strength were calibrated by fitting the analytical model to the experimental load-slip data. The study specifically examined two bond-slip laws: a non-linear model (*Type A*) and a bilinear model (*Type B*).

The following main conclusions were drawn:

- irrespective of the ( $\tau$ - $s$ ) model, the calculated fracture energy is highest in the case of the SB surface, followed by the BH and GR surfaces, respectively, confirming the best experimental bond performance of the SB surface specimens;
- in terms of both the calibrated values for the relevant parameters and the calculated fracture energy, considering any of the surface finishes, only small differences are observed between the *Type A* and *Type B* models.

The experimental and theoretical/numerical comparisons in terms of axial stress-slip showed that, regardless of the concrete surface finish and the ( $\tau$ - $s$ ) model (*Type A* or *Type B*), a good agreement is generally observed, mainly in terms of stiffness in the pre-peak stage, when using the ( $\tau$ - $s$ ) laws calibrated by the indirect method. However, even if the simplified bilinear ( $\tau$ - $s$ ) law can be successfully implemented in bond modelling problems to simulate the overall behaviour of DSLS tests, the problem of correctly estimating the SRP development length remains. Therefore, further research is needed to better validate the study performed using a larger database of DSLS tests.

## Acknowledgements

The financial support by ReLUIIS (Network of the Italian University Laboratories for Seismic Engineering - Italian Department of Civil Protection) is acknowledged (Executive Project 2022-24-WP14).

## References

1. De Santis S., de Felice G., Napoli A. and Realfonzo R. 2016. "Strengthening of structures with steel reinforced polymers: a state-of-the-art review." *Compos. B. Eng.* 104: 87–110. doi: 10.1016/j.compositesb.2016.08.025.
2. Krzywoń R 2020. "Steel-Reinforced Polymers and Steel-Reinforced Composite Mortars for Structural Applications—An Overview." *J. Compos. Sci.* 4(3), 142. doi: 10.3390/jcs4030142.
3. Ascione F., Napoli A. and Realfonzo R. 2020. Experimental and analytical investigation on the bond of SRP systems to concrete. *Compos. Struct.* 242, 112090. doi: 10.1016/j.compstruct.2020.112090.
4. Ascione F., Napoli A. and Realfonzo R. 2021. "Interface bond between FRP systems and substrate: Analytical modeling." *Compos. Struct.* 257, 112942. doi: 10.1016/j.compstruct.2020.112942.
5. Ascione F., Lamberti M., Napoli A., Razaqpur A.G. and Realfonzo R. 2019. "Modeling SRP-concrete interfacial bond behavior and strength." *Eng. Struct.* 187: 220-230. doi: 10.1016/j.engstruct.2019.02.050.
6. Pecce M., Manfredi G., Realfonzo R. and Cosenza E. 2001. "Experimental and analytical evaluation of bond properties of GFRP bars." *J Mater Civil Eng.* 13(4): 282-290. doi: 10.1061/(ASCE)0899-1561(2001)13:4(282).
7. Cosenza E., Manfredi G., Realfonzo R. Behaviour and Modeling of bond FRP rebars to concrete. *J. Compos. for Constr.* 1997, 1(2), 40-51. doi:10.1061/(ASCE)1090-0268(1997)1:2(40)
8. Lu X.Z., Teng J.G., Ye L.P., Jiang J.J. Bond-slip models for FRP sheets/plates bonded to concrete. *Eng. Struct.* 2005, 27(6), 920-937. Doi: 10.1016/j.engstruct.2005.01.014
9. Yuan H., Wu Z.S., Yao J. Full-range behavior of FRP-to-concrete bonded joints. *Eng Struct* 2004; 26, 553–65. doi: 10.1016/j.compositesb.2018.11.030
10. Ascione F., Lamberti M., Napoli A., Realfonzo R. Indirect Identification of the Bond-Slip Model at SRP-Concrete Interface. In: Proc. of ICC 2022, Napoli, Italy, October 12-15, 2022.

# Influence of high temperature exposure on the performances of Textile Reinforced Alkali-Activated Mortar systems

Daniele Berdini<sup>1</sup>, Jacopo Donnini<sup>2</sup>

<sup>1</sup> Department of Science and Engineering of Matter, Environmental and Urban Planning, Marche Polytechnic University, Via Breccie Bianche 12, Ancona, 60131, Italy, [d.berdini@pm.univpm.it](mailto:d.berdini@pm.univpm.it)

<sup>2</sup> Department of Science and Engineering of Matter, Environmental and Urban Planning, Marche Polytechnic University, Via Breccie Bianche 12, Ancona, 60131, Italy, [jacopo.donnini@staff.univpm.it](mailto:jacopo.donnini@staff.univpm.it)

## Abstract

In recent years, the use of TRM (Textile Reinforced Mortar) composite systems, based on lime or cementitious mortars, to strengthen masonry or concrete structures, has garnered engineering interest due to their great mechanical properties, high durability and ease of application. However, the use of traditional mortars involves significant energy consumption and CO<sub>2</sub> emissions, pushing the exploration of new solutions with a lower environmental footprint such as AAM (Alkali-Activated Mortar). Furthermore, the use of AAM could be beneficial when TRM systems are exposed to high temperatures. Nevertheless, this aspect is still widely debated and needs to be thoroughly investigated.

This study aims to investigate and compare the performances of TRM systems made with different mortars (lime, cement-based or AAM), reinforced with basalt fabric, after high temperature exposure. Both the single components (fibers and mortars) and the TRM composite system were subjected to different temperature regimes, up to 600 °C. Results indicate that exposure to 200 °C has a limited impact on the performances of fibers and mortars, with even improvements in the case of AAMs. TRMs made with metakaolin-based AAM exhibit a great resistance to high temperatures, at least up to 400 °C. All other TRM systems show a tensile strength reduction as the temperature increases, up to -82 % when exposed to 600 °C.

## 1 Introduction

Textile Reinforced Mortar (TRM) has recently emerged as a promising alternative to traditional reinforcement systems for concrete and masonry structures, offering several advantages such as lightness, ease of application, cost effectiveness and safety for operators [1,2]. TRMs are usually made of fabrics made of carbon, glass, basalt or PBO fibers, embedded within a lime or cement-based mortar. Recently, alternative matrices, such as alkali-activated mortars (AAMs), have gained interest from the scientific community thanks to their lower carbon footprint compared to traditional mortars [3]. Furthermore, in some cases AAMs showed better durability [4] and greater resistance to high temperatures [5–7]. These characteristics make the use of AAM for TRM systems very interesting [8]. However, the possibility of using these matrices for TRM applications has still been little investigated. Furthermore, the TRM mechanical behavior when exposed to high temperatures, especially when made with AAM, has still been little addressed.

Estevan et al. [9] evaluated the mechanical behavior of different lime-based TRM systems, showing that their capacity is seriously compromised at temperatures greater than 400 °C. Kapsalis et al. [10] investigated the tensile performances of alkali-activated TRM systems after exposure to temperatures up to 600 °C, showing a degradation of mechanical properties for temperatures ranging from 200 °C to 450 °C. When 600 °C is reached the TRM coupons showed severe degradation and zero residual capacity due to heavy damage of the carbon textile. Arce et al. [11] tested AAM TRM systems up to 550 °C to evaluate the in-plane shear capacity of reinforced masonry, showing that exposure up to 550 °C for 2 hours did not affect the mechanical performances.

The goal of this study is to evaluate the feasibility of using AAM, based on fly ash (FA) or metakaolin (MK), for TRM applications. The experimental results are then compared to those obtained from two TRM commercial systems, based on lime and cement-based matrices. Furthermore, residual mechanical properties of both the matrices and TRM systems after exposure to temperatures up to 600 °C are evaluated.

## 2 Materials and methods

### 2.1 Mortars and reinforcement

Two different aluminosilicate sources, class F fly ash (FA) and metakaolin (MK), were used to manufacture the alkali-activated mortars. FA had a specific surface area (SSA) of 5000 cm<sup>2</sup>/g and mean particle size of 20 µm, whereas MK had a SSA of 140000 cm<sup>2</sup>/g and mean particle size of 3 µm. A calcareous sand with maximum diameter of 3 mm and water absorption capacity of 3.4 % by mass was used. A blend of sodium silicate (SS) with a molar ratio of 2:1 and 50 wt% solution of potassium hydroxide (KOH) was used to activate the mortars. The mix proportions of AAMs, named FAK and MKK, are provided in Table 1.

Table 1 Mix proportions of alkali-activated mortars.

Materials	Sand [g/l]	FA [g/l]	MK [g/l]	SS [g/l]	KOH [g/l]	Water [g/l]
FAK	1350	460	-	150	60	110
MKK	1350	-	500	300	80	280

Two commercial mortars have been also investigated, the first one is a lime-based mortar with strength class R1 (according to UNI EN 1504-3:2006) and the second one is a cement-based mortar, strength class R4.

The reinforcement used for this study is a basalt bidirectional fabric, with a mesh size of 20x20 mm<sup>2</sup>, pre-impregnated with a polyester-based coating. Geometric and mechanical properties of the fabric are reported in Table 2.

Table 2 Properties of basalt reinforcement fabric (from manufacturer).

Properties [unit]	Net weight [g/m <sup>2</sup> ]	Total weight [g/m <sup>2</sup> ]	Basalt density [g/cm <sup>3</sup> ]	Average thickness [mm]	Cross sectional area of a single yarn [mm <sup>2</sup> ]	Resistant section [mm <sup>2</sup> /m]	Warp tensile strenght [kN/m]
Fabric	365	420	2.70	1.15	1.33	66.67	132

### 2.2 Specimens' preparation

Mechanical properties of mortars were evaluated on 40x40x160 mm<sup>3</sup> specimens, according to UNI EN 1015-11:2019. TRM tensile properties were evaluated on prismatic coupons with dimensions of 190x40x10 mm<sup>3</sup>, reinforced with basalt fabric having two yarns in the longitudinal direction. Before testing, Glass Fiber Reinforced Polymer (GFRP) tabs were applied at the ends of TRM coupons (see Fig. 1) to avoid slipping of the grips. TRM coupons were tested in tension with a clamped system using a Zwick/Roell Z050 machine under displacement control, with a crosshead speed of 1.5 mm/min (Fig. 2). Digital Image Correlation (DIC) was used to measure axial strain and to monitor the formation of cracks during the test. A total of 32 mortar prisms and 48 TRM coupons were tested, respectively 2 mortar prisms and 3 TRM coupons for each temperature exposure. All specimens were cured at laboratory conditions (20 ± 2 °C, RH = 65 ± 5 %) for 90 days before starting the temperature conditioning.

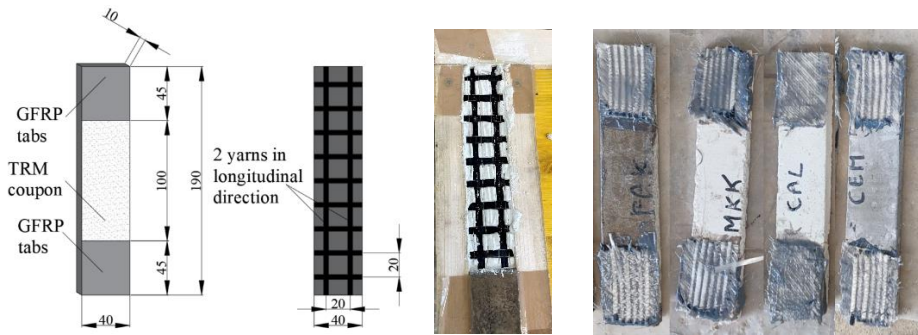


Fig. 1 Geometric properties of TRM coupon (190x40x10 mm<sup>3</sup>) and details of the manufacturing process.

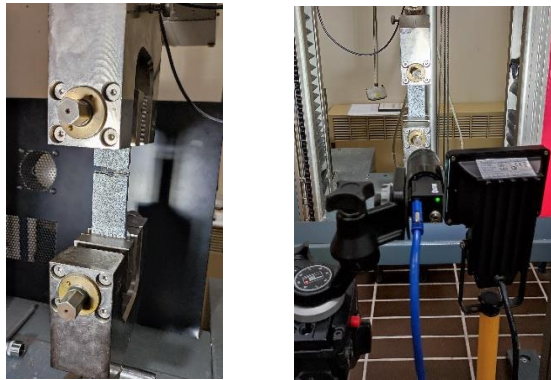


Fig. 2 Details of tensile test on TRM coupons (left) and DIC setup (right).

### 2.3 Exposure to high temperatures

After 90 days of curing at laboratory conditions, both the mortar prisms and TRM coupons were exposed to temperatures of 200 °C, 400 °C and 600 °C. The specimens were placed in a laboratory electric muffle furnace, heated by 10 °C/min and maintained at the test temperature for 2 h. Then, heating was stopped, and the furnace allowed to cool back spontaneously to room temperature. K-type thermocouples were used to monitor the temperature of the air inside the oven, at the core of the mortar prisms, and at the interface between fabric and mortar in TRM specimens (Fig. 3).



Fig. 3 Mortar prisms and TRM coupons with K-type thermocouples (left). Arrangement of specimens within the furnace (right).

### 3 Experimental results and discussion

#### 3.1 Temperature profiles

Fig. 4 shows the temperature profiles obtained for both mortar prisms and TRM coupons exposed to different temperatures. “T\_load” is the thermal load applied to the specimens, while “AIR” is the temperature measured by thermocouples within the furnace. The core temperature of mortar prisms exposed to 400 °C and 600 °C slightly exceeded the target temperatures, probably due to temperature fluctuations within the furnace, while the specimens exposed to 200 °C always maintained core temperatures below the target. In particular, MKK and LIME mortar prisms exposed to 200 °C reached core temperatures of 112 °C and 126 °C, respectively. TRM coupons exposed to 200 °C reached temperatures comprised between 139 °C and 150 °C at the fabric-to-mortar interface. It can be observed that MKK specimens always reached lower temperatures than other specimens, probably due to their greater porosity and lower thermal conductivity.

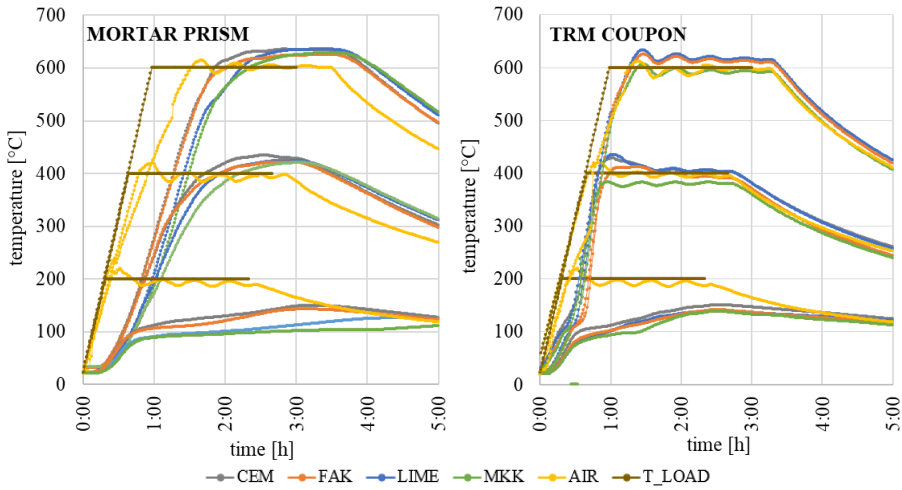


Fig. 4 Temperature development at the core of mortar prisms (left) and at the fabric-to-mortar interface in TRM coupons (right).

Visual inspection of mortar prisms and TRM coupons after high temperature exposures are reported in Figs. 5 and 6. A gradual color alteration can be observed for all specimens. A slight decoloration was observed for FAK specimens, while MKK and LIME specimens turned from white to grey by increasing the exposure temperature. Furthermore, some cracks formed on specimens exposed to 600 °C (highlighted in white in Fig. 5). In the case of TRM coupons, some cracks formed already starting from 200 °C, except for CEM coupons (see Fig. 6). This is probably due to the greater slenderness of the coupons compared to the mortar prisms. Furthermore, the cracking of FAK and MKK could also be partly due to the hygroscopic shrinkage of the matrices, amplified by the exposure to high temperatures.



Fig. 5 Mortar prisms after exposure to high temperatures (cracks highlighted in white).

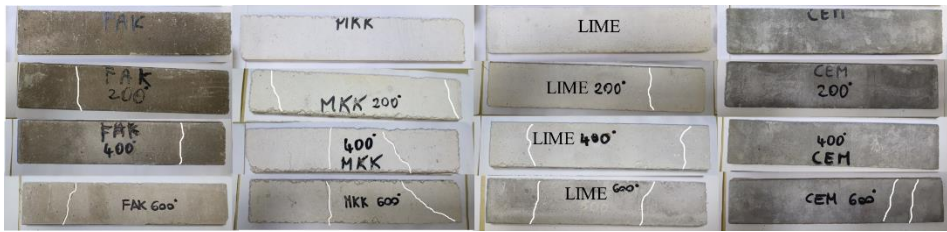


Fig. 6 TRM coupons after exposure to high temperatures (cracks highlighted in white).

### 3.2 Mechanical properties of mortars

Compressive ( $\sigma_{c,max}$ ) and flexural strength ( $\sigma_{f,max}$ ) of all mortars, after high temperature exposure, are reported in Table 4, while normalized values with respect to the ambient temperature (20 °C) are reported in Fig. 7. A gradual reduction of mechanical properties is observed for LIME and CEM matrices by increasing the exposure temperature. On the other hand, it is interesting to observe an increase of mechanical properties in the case of AAMs after exposure to 200 °C. This is probably due to the geopolymerization process, which benefits from the high temperature exposure (between 112 °C and 142 °C at the core of mortar prisms) even after 90 days of curing. The compressive strength increases by 14 % and 28 % in the case of MKK and FAK matrices, respectively. However, it can be observed that the flexural strength of FAK specimens at 200 °C is significantly reduced. This could be due to the formation of microcracks inside the matrix, which led to the reduction of the flexural strength. Further investigations are necessary to understand this phenomenon, however, a possible confirmation could derive from the elastic modulus of the FAK matrices (not reported here for brevity) which is reduced when the matrix is exposed to 200 °C. When exposed to 400 °C, only the metakaolin-based matrix (MKK) maintains the compressive strength almost unchanged, while both compressive and flexural strengths of all the other mortars are reduced. When exposed to 600 °C, FAK, LIME and CEM matrices showed a reduction in compressive strength of between 55 and 77 %, while the MKK matrix showed a reduction of only 9 %, compared to room temperature.

Table 4 Mechanical properties of mortars after exposure to different temperatures.

Temperature [°C]	FAK		MKK		LIME		CEM	
	$\sigma_{c,max}$ [MPa]	$\sigma_{f,max}$ [MPa]	$\sigma_{c,max}$ [MPa]	$\sigma_{f,max}$ [MPa]	$\sigma_{c,max}$ [MPa]	$\sigma_{f,max}$ [MPa]	$\sigma_{c,max}$ [MPa]	$\sigma_{f,max}$ [MPa]
20	52.64	11.51	8.60	1.78	12.15	3.82	56.64	10.51
200	67.55	7.28	9.82	2.42	10.91	4.20	42.29	9.83
400	29.92	2.99	8.35	1.15	8.17	2.93	31.20	4.46
600	23.37	2.14	7.78	0.93	2.72	0.30	19.47	2.57



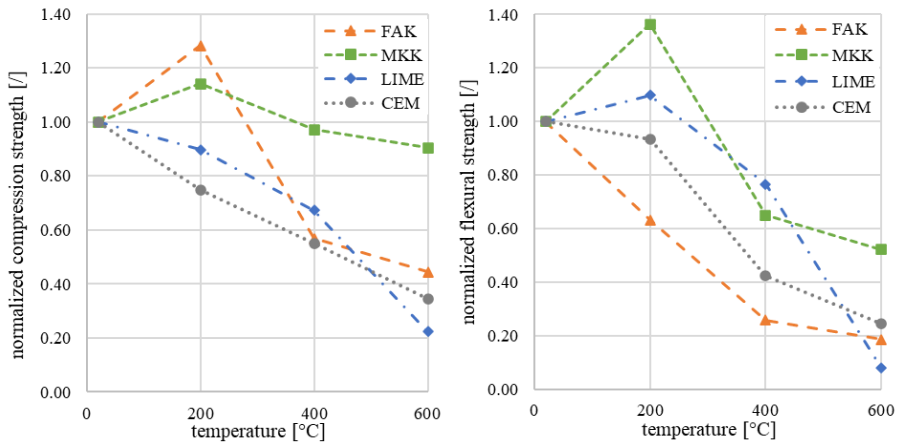


Fig. 7 Normalized compressive (left) and flexural (right) strengths of mortars after temperature exposure.

### 3.3 Tensile properties of TRM coupons

Tensile stress ( $\sigma_{t,max}$ ) was calculated by dividing the maximum tensile load by the cross-sectional area of the two basalt yarns, while the post-cracking modulus ( $E_2$ ) was graphically evaluated on the cracked phase of the stress-strain curves. Results of tensile tests are reported in Table 5. The failure mode observed for all the specimens was due to slippage of the basalt fabric within the matrix, after the formation of multiples cracks. In general, tensile strength of TRM coupons decreases as the exposure temperature increases, except for TRM systems based on MKK mortar, which exhibit a significant enhancement in tensile strength after exposure to 200 °C (equal to +30 %). When the temperature reaches 400 °C, a reduction in tensile strength is observed for all specimens. This reduction is probably due, in addition to the deterioration of the performance of the matrix, to the degradation of the polymeric coating that surrounds the basalt fibres. CEM and FAK specimens showed a similar trend at various exposure temperatures. Tensile strength decreases by 10 and 19 % at 200 °C, 27 and 33 % at 400 °C, 77 and 78 % at 600 °C, respectively. LIME specimens show a continuous reduction in tensile strength, with very low values (less than 100 MPa) already starting from 400 °C and with a reduction of 82 % at 600 °C. Similar considerations can be made for the post-cracking elastic modulus, which is reduced for all specimens by increasing the exposure temperature, except for MKK and LIME exposed to 200 °C. When exposed to 600 °C (and 400 °C for LIME) the strength and stiffness of TRM composites is strongly compromised, and it is no longer possible to evaluate the elastic modulus.

Table 5 Tensile strength and post-cracking modulus of TRM coupons after temperature exposure.

Temperature [°C]	FAK		MKK		LIME		CEM	
	$\sigma_{t,max}$ [MPa]	$E_2$ [GPa]	$\sigma_{t,max}$ [MPa]	$E_2$ [GPa]	$\sigma_{t,max}$ [MPa]	$E_2$ [GPa]	$\sigma_{t,max}$ [MPa]	$E_2$ [GPa]
20	399.77	30.79	370.68	20.91	420.45	41.20	604.10	49.29
200	323.57	26.68	480.84	21.05	401.32	42.39	544.83	37.20
400	293.84	14.87	212.02	6.54	97.70	-	405.48	34.88
600	93.35	-	117.22	-	73.55	-	135.58	-

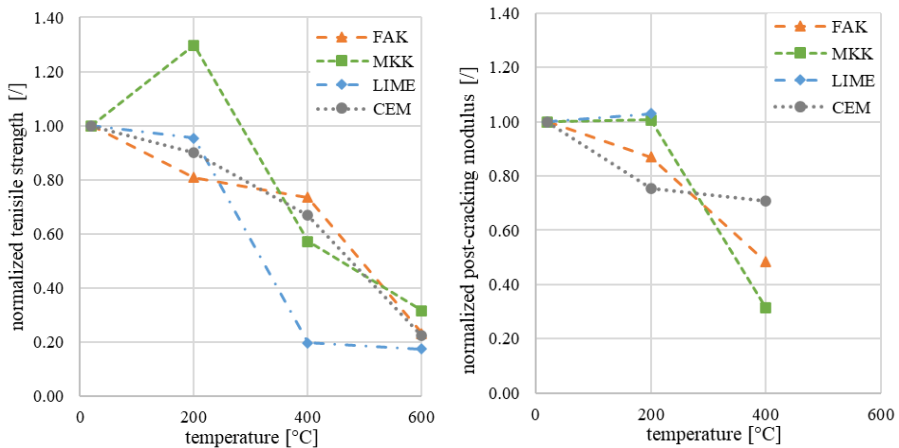


Fig. 8 Normalized tensile strength (left) and post-cracking elastic modulus (right) of temperature exposed TRM coupons.

#### 4 Conclusions

This study investigates the residual mechanical performances of basalt TRM specimens manufactured with alkali-activated or traditional mortars after exposure to high temperatures, up to 600 °C. Experimental results show that alkali-activated mortars based on metakaolin (MKK) are the most promising in terms of resistance to high temperatures. The residual compressive strength of MKK mortars is kept almost unchanged up to an exposure temperature of 400 °C, with a reduction of about 9 % when exposed to 600 °C.

Concerning the TRM coupons, the tensile strength is slightly reduced when exposed to 200 °C, except for the MKK specimens which even show an increase. A significant reduction in tensile strength and stiffness is observed for all TRM coupons when the exposure temperature exceeds 400 °C. This is probably due to the cracking of the matrix, in addition to the degradation of the polymeric coating, which therefore causes a reduction in adhesion at the fibre-matrix interface. When the temperature reaches 600 °C, even the basalt fibers are irreparably damaged, thus causing the total loss of strength of the TRM composite.

#### Acknowledgements

Biemme Srl is gratefully acknowledged for providing the basalt textiles. The technicians Orlando Favoni and Giampaolo Giuliani are thanked for their invaluable support during the experimental campaign.

#### References

- [1] Raouf SM, Bourmas DA. TRM versus FRP in flexural strengthening of RC beams : Behaviour at high temperatures. *Constr Build Mater* 2017;154:424–37. <https://doi.org/10.1016/j.conbuildmat.2017.07.195>.
- [2] Donnini J, Maracchini G, Lenci S, Corinaldesi V, Quagliarini E. TRM reinforced tuff and fired clay brick masonry: Experimental and analytical investigation on their in-plane and out-of-plane behavior. *Constr Build Mater* 2021;272. <https://doi.org/10.1016/j.conbuildmat.2020.121643>.
- [3] McLellan BC, Williams RP, Lay J, Van Riessen A, Corder GD. Costs and carbon emissions for geopolymer pastes in comparison to ordinary portland cement. *J Clean Prod* 2011;19:1080–90. <https://doi.org/10.1016/J.JCLEPRO.2011.02.010>.



- [4] Wang A, Zheng Y, Zhang Z, Liu K, Li Y, Shi L, et al. The Durability of Alkali-Activated Materials in Comparison with Ordinary Portland Cements and Concretes: A Review. *Engineering* 2020;6:695–706. <https://doi.org/10.1016/j.eng.2019.08.019>.
- [5] Yao X, Zhang Z, Zhu H, Chen Y. Geopolymerization process of alkali-metakaolinite characterized by isothermal calorimetry. *Thermochim Acta* 2009;493:49–54. <https://doi.org/10.1016/j.tca.2009.04.002>.
- [6] Ascensão G, Faleschini F, Marchi M, Segata M, Van De Sande J, Rahier H, et al. High-Temperature Behavior of CaO-FeOx-Al<sub>2</sub>O<sub>3</sub>-SiO<sub>2</sub>-Rich Alkali Activated Materials. *Applied Sciences (Switzerland)* 2022;12. <https://doi.org/10.3390/app12052572>.
- [7] He R, Dai N, Wang Z. Thermal and Mechanical Properties of Geopolymers Exposed to High Temperature: A Literature Review. *Advances in Civil Engineering* 2020;2020. <https://doi.org/10.1155/2020/7532703>.
- [8] Donnini J, Mobili A, Maracchini G, Chiappini G, Tittarelli F, Corinaldesi V. A multi-performance comparison between lime, cementitious and alkali-activated TRM systems: Mechanical, environmental and energy perspectives. *Constr Build Mater* 2024;440. <https://doi.org/10.1016/j.conbuildmat.2024.137396>.
- [9] Estevan L, Varona FB, Baeza FJ, Torres B, Bru D. Textile Reinforced Mortars (TRM) tensile behavior after high temperature exposure. *Constr Build Mater* 2022;328. <https://doi.org/10.1016/j.conbuildmat.2022.127116>.
- [10] Kapsalis P, Papanicolaou C, Triantafillou T. Residual performance of alkali-activated TRM after exposure to high temperatures. *Cice2023, 11th International Conference on FRP composites in civil engineering, 2023*.
- [11] Arce A, Kapsalis P, Papanicolaou C, Triantafillou T. Textile-Reinforced Alkali-Activated Mortar for In-Plane Shear Capacity Improvement of Masonry Before and After High Temperature Exposure. *RILEM Bookseries*, vol. 46, Springer Science and Business Media B.V.; 2024, p. 849–57. [https://doi.org/10.1007/978-3-031-39450-8\\_69](https://doi.org/10.1007/978-3-031-39450-8_69).

# Strengthening of Varese-type floor

Marco Bosio<sup>1</sup>, Marius Eteme Minkada<sup>1</sup>, Paolo Riva<sup>1</sup> and Andrea Bruggi<sup>2</sup>

<sup>1</sup>*Department of Engineering and Applied Sciences,  
University of Bergamo  
Via Guglielmo Marconi, Dalmine (24044), Italy*

<sup>2</sup>*Laterlite S.p.A.,  
Via Correggio, Milano (20149), Italy*

## Abstract

The construction needs of the mid-20th century led to the development of construction techniques that were both fast and simple to meet the high demand generated by the massive post-war reconstruction. To facilitate and speed up construction, new hybrid technologies between traditional systems and precast were developed, including the emergence of semi-prefabricated floor systems such as SAP or 'Varese' floors. This technology not only accelerates construction but also simplifies it from a construction perspective. With these prefabricated elements, it is no longer necessary to support the entire floor, but it is sufficient to support the beams in the early stages of construction. The versatility and ease of execution of this construction method have led to its widespread use, to the extent that many old buildings are constructed using these floor systems. Unfortunately, the knowledge of that time was limited, resulting in many of these buildings having structural deficiencies both in seismic and static terms. It should be noted, however, that due to economic and sustainability reasons, the demolition and reconstruction of these buildings may not be feasible, especially considering how, due to urban development, these buildings, which were once located in peripheral areas, are now fully integrated into the city centre, significantly increasing their value. The proposed paper aims to investigate reinforcement techniques for Varese-type floors, based on the use of a superimposed collaborating cementitious material layer, through a series of experimental tests.

## 1 Introduction

In addition to providing structural support, floors are elements that divide spaces vertically; they also play an important role in ensuring the comfort and energy performance of buildings. The evolution of architecture over the centuries has given rise to a considerable variety of floor-types, ranging from traditional wooden floors to modern precast reinforced concrete floors. Among the existing floor systems, there are Varese-type floors. These are a type of reinforced concrete floor made of prefabricated reinforced concrete joists, with double-layer terracotta blocks in between, forming an air chamber. This solution was introduced as a hybrid (semi-prefabricated) technology allowing for reduced construction times on-site. To date, Varese-type floors present in existing buildings may require retrofitting interventions for a series of reasons related to aging, changes in use and/or construction defects.

In this work, a strengthening technique using a collaborating topping was analyzed. This technique was developed for the reinforcement of wooden floors, where a thin layer of ordinary [1], [2] or high strength [3] concrete could be used due to the requirement for lightness. The typical dimensions used for the additional layer represent a possibility for the designer to choose the most appropriate type of product for different applications encountered. Furthermore, it is well known that the effectiveness of the intervention to stiffen and strengthen floors with a thin concrete topping entirely depends on the efficiency of the collaboration between the existing and the new concrete layer. In recent years, several types of connections between the aforementioned layers have been studied [1], [4]. In the study herein presented, two distinct types of products were analyzed for the creation of a collaborating concrete slab: "LECACLS 1400" [5] and "MICROCALCESTRUZZO CENTROSTORICO" [6]. "LECACLS 1400" is a lightweight, pre-mixed structural cementitious product, whereas "MICROCALCESTRUZZO CENTROSTORICO" is a high-performance (HPC), self-flowing, fiber-reinforced concrete (FRC). In

both cases, the new slab is made to collaborate with the existing one through the application of a two-component epoxy adhesive known as “CONNETTORE CHIMICOSTORICO” [7].

The purpose of the research was to investigate reinforcement techniques for Varese-type floors, based on the use of an additional collaborating material layer. Specimen fabrication and subsequent experimental testing were conducted at the Laboratory of the University of Bergamo.

## 2 Specimen and test methodology

### 2.1 Description of the specimens

Three Varese-type floors were made (Table 1), each using three Varese joists, with terracotta blocks (approximately 80 cm long) placed between them at both the top and bottom. To complete the floor, a 2.5 cm-thick layer of concrete slab was cast to simulate typical historical flooring systems. Any additional layer was made after the 28-day curing period of the concrete.

Table 1 Compression test results of the specimens.

ID of the floor	Strengthening product	Thickness of the collaborating slab
S1	-	-
S2	LECACLS 1400	50 mm
S3	MICROCALCESTRUZZO CENTROSTORICO	30 mm

The preparation of the specimens was made possible thanks to the availability of unused Varese joists found in a company warehouse. It is worth noting that these joists were stored in the warehouse without protection from weather conditions, resulting in their precarious state with biological material present on the surfaces. However, from a structural point of view, there was no specific cracking pattern except for the breakage of the concrete cover in some point near the supports, indicating significant corrosion of the reinforcement bars. The precise demolition of the joists after the tests allowed to reconstruct the geometry and the amount of reinforcement in the section (Fig. 1). In particular, the beam had uniform reinforcement consisting of 1 $\Phi$ 8 (top) and 2  $\Phi$ 8 (bottom).

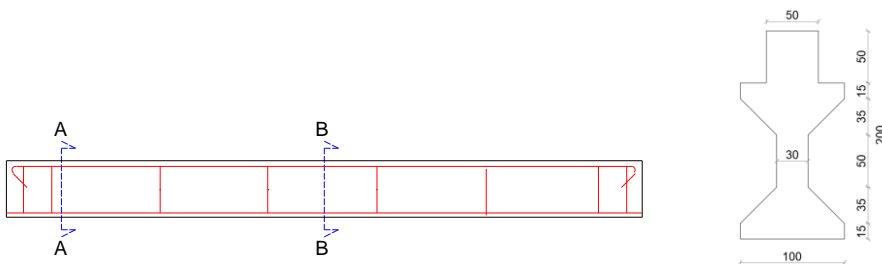


Fig. 1 Longitudinal and transverse section of the floor joist.

### 2.2 Test methodology and setup

In order to assess the flexural capacity of the prototypes, a three-point bending test setup (Fig. 2) was prepared. The support points, made of 6 discontinuous steel cylinders, were positioned approximately 12.5 cm from the ends of the floors. The load (at the mid-span of the floor) is applied by an electromechanical jack with a 500mm stroke and a force capacity of 1000 kN. A load cell and a (rigid) beam are

mounted under the jack to distribute the test load. The latter is applied via a steel cylinder positioned between the redistribution frame and the specimen.

The test instrumentation (Fig. 3) focuses on determining the deflection of the slab as a function of the load. Deflection is measured using three position transducers placed as close as possible to the mid-span of the slab. For tests on strengthened slabs, an additional pair of transducers is placed near the bonding surface between the existing and new layers to measure any detachment between the two surfaces. It's worth noting that all measurements are taken with respect to an external reference point resting on the Laboratory floor.



Fig. 2 Setup used for floor bending tests.

As for the testing procedure, the slabs were subjected to cyclic loads following the protocol described below. The test steps consist of a series of triplets with incremental displacements of 1 mm up to 10 mm (with 1 mm increments), followed by increments of 2 mm until a load loss greater than 20% of the maximum load reached is recorded. In particular, the loading phase is performed in displacement control using the transducer at the mid-span of the central joist as the control instrument, while the unloading phase is also conducted under displacement control but stopping when the load read by the load cell is zero.

### 3 Tests on basic materials

This section is dedicated to the tests performed on the materials used in the construction of the prototypes (specimens). For each floor, two 15 cm side cubic specimens were made for both the concrete and the reinforcing materials to verify their performance. The results of the specimen compression tests are summarized in Table 2.

Table 2 Compression test results of the specimens.

Material	Floor ID	Average density [kg/m <sup>3</sup> ]	Compressive strength [MPa]	
			Sample 1	Sample 2
Basic concrete	F1	2097.19	24.53	24.20
Basic concrete	F2	2163.26	25.23	25.86
Basic concrete	F3	2158.23	25.50	27.02
LECACLS 1400	F2	1540.86	31.46	29.01
MICROCLCESTRUZZO CENTROSTORICO	F3	2170.51	85.21	83.99

In addition, tensile tests were performed on reinforcing bars extracted from the Varese beams. In fact, at the end of the bending tests, two 600 mm long reinforcing bar specimens were extracted from the joists and tensile tests were performed. In accordance with the yield stress values (553.74 MPa and 511.74 MPa) and the ultimate stress values (625.20 MPa and 630.57 MPa) obtained, it was possible to conclude that the steel present was similar to B450C; which was therefore used in the subsequent estimation of the yield moment of the beam section; well aware that this underestimates the yield moment of the section.

## 4 Tests Results

This section will present the results of the bending tests on the floors. For each prototype, a graph with two vertical axes will be shown containing the values of force and moment reached at the mid-span, as a function of the deflection for the three joists of the floor. Subsequently, the residual displacement values at the end of the three cycles or the single cycle (last monotonic ramp) will be shown.

### 4.1 Non-reinforced floor

Fig. 3 and Fig. 4 show the results of the test on the unreinforced floor. It can be observed that the curves for joist 3 are much more compact than those for joist 2, which are in turn more compact than those for joist 1 (Fig. 4). Furthermore, for the first few cycles the curves are very close together and have a linear trend, while in the last cycles there different cycles are well spaced. This is the evidence that the collapse of the slab occurred in a non-uniform manner, with Joist 1 collapsing earlier than the others.

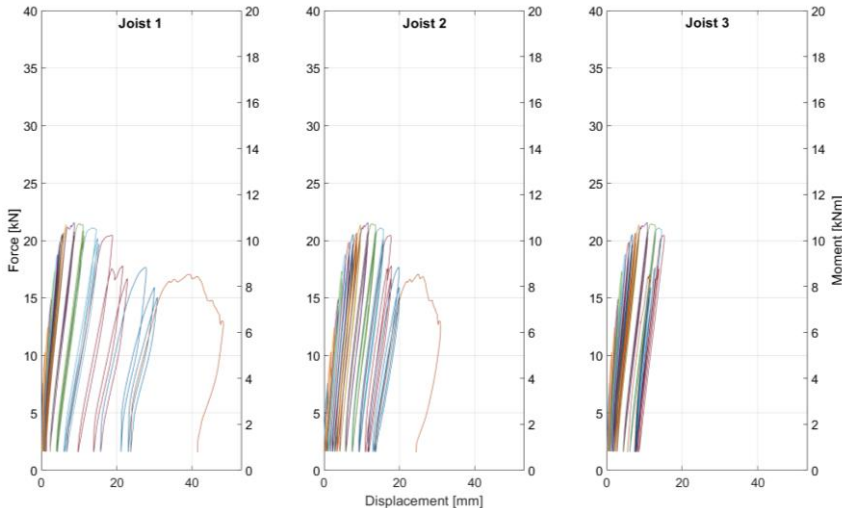


Fig. 3 Load/moment-displacement curve for the joists of the F1 floor.

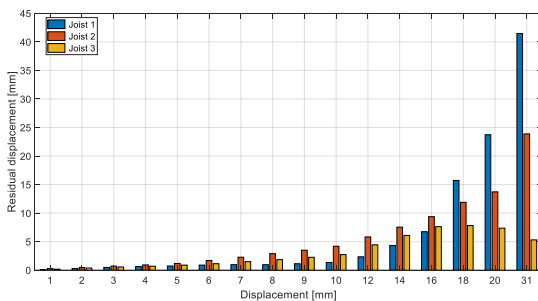


Fig. 4 Residual displacement (left) and evidence of slab shear failure mechanism (right) for the F1 floor.

The previous result can also be observed in more detail in the graph shown in Fig. 4 (left) where, a linear growth of the residual displacement can be observed up to the 10 mm cycle, followed by an exponential growth up to the 20 mm cycle at which point the first beam collapses in shear (Fig. 4 - right).

#### 4.2 Floor strengthened with LECACLS 1400

Fig. 5 shows the load-moment-deflection curve for the three joists. It is evident that in this case, the collapse occurred following significant plasticization of the elements. Indeed, a portion of the graph can be identified in which the curves shift to the right while maintaining an almost constant stiffness. Furthermore, the collapse mode particularly affected joists 1 and 2; as they present the last cycles much wider than joist 3 for which the displacement remains fixed at the values reached in the previous cycles. This is due to the sudden, brittle, failure of joists 1 and 2, which led to concentrating all the deformations at those specific points without allowing the load to be distributed.

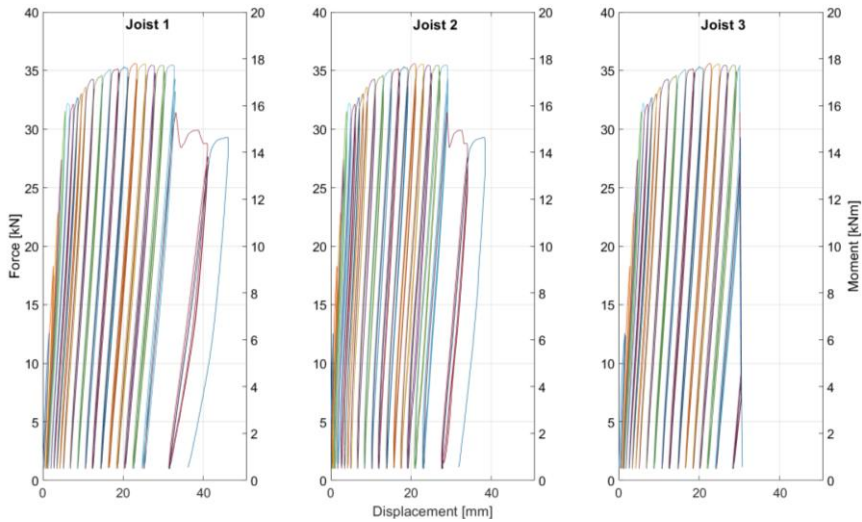


Fig. 5 Load/moment-displacement curve for the joist of the F2 floor.

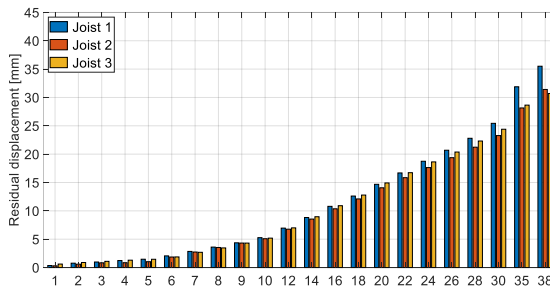


Fig. 6 Residual displacement (left) and post test condition of the F2 floor.

For this test, the maximum load (106.77 kN) was reached at the cycles characterized by a 30 mm displacement; followed by a sudden loss of strength (greater than 20% compared to the maximum load) at the second cycle; characterized by a 35 mm displacement.

The residual displacement (Fig. 6), increase almost uniformly in joists 2 and 3, while in joist 1 there is a more marked increase following the 30mm displacement cycle, which led to flexural failure. Regarding the detachment between the substrate in “LECACLS 1400” and the existing concrete slab, there are no significant detachments between the two layers.

### 4.3 Floor strengthened with MICROCALCESTRUZZO CENTROSTORICO

With regards to the S3 floor, strengthened with “MICROCALCESTRUZZO CENTROSTORICO”, it is important to present the condition of the specimen before the test. In fact, compared to the other prototypes, this slab exhibited a significant deformation generated by the differential shrinkage between the reinforcing product and the existing substrate. There is a significant loss of surface flatness with a rise of the four corners of the slab of about 20 mm, leading to an evident cracking pattern on the reinforcing substrate and the breakage of some tiles, due to the excessive tensile stress (Fig. 7, right) of the slab itself.



Fig. 7 Condition of the S3 floor before testing: cracking pattern of the slab (left) and tensile failure of the clay tiles.

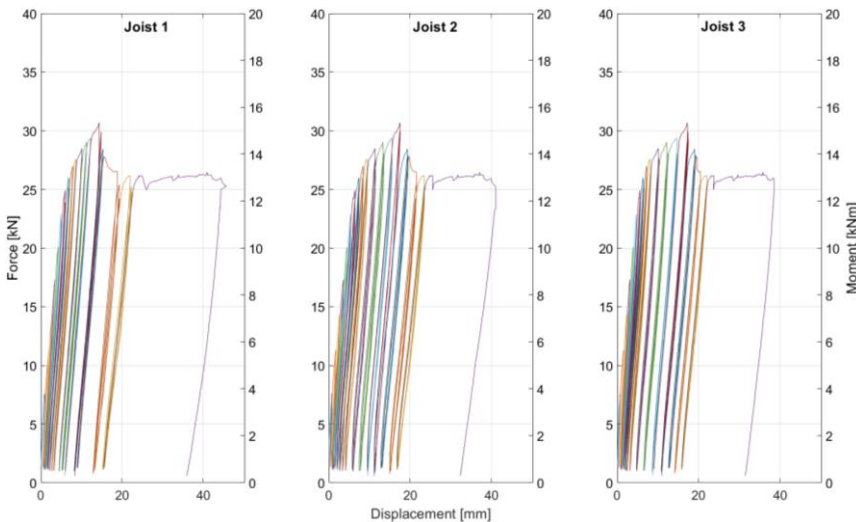


Fig. 8 Load/moment-displacement curve for the joist of the F3 floor.

The load-moment-displacement curves for the three joists are shown in Fig. 8. The similarity in the deformation values recorded in the three joist is characteristic of good specimen homogeneity as well as good distribution of the test load. The collapse of the floor occurs after the cycle characterized by a displacement of 18 mm with a maximum applied load of 91.04 kN (45.51 kNm) with a progressive loss of the maximum load reached. The good redistribution of loads can also be observed from the residual displacement in Fig. 9, which shows that the three joists have very similar values for all test cycles. Considering that the resisting moment of the section is estimated at around 10.4 kNm, it can be stated that the failure occurred through a flexural mechanism due to yielding of the reinforcement bars.



Regarding the detachment between the substrate in “MICROCALCESTRUZZO CENTROSTORICO” and the existing concrete slab, also in this case there are no significant detachments between the two layers.

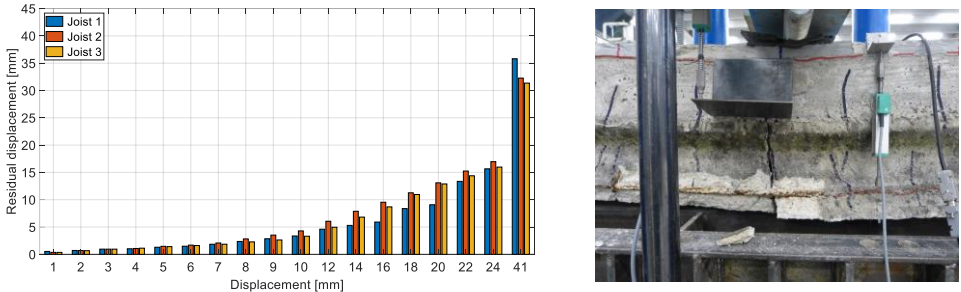


Fig. 9 Residual displacement (left) and post test condition of the F3 floor.

#### 4.4 Discussion of the results

In this section, a comparison is proposed between the results obtained and presented in the previous sections. Fig. 10 compares the bending moment-deflection curves of the three tested slabs. Three figures are shown, with the results of the edge joists at the top and bottom, and the results of the central joist in the center. For the purpose of a uniform comparison of the floors (with different section heights), the bending moment has been presented dimensionlessly relative to the yield moment of the joist. The latter has been approximately estimated using the analytical formulation presented in equation (1), where  $A_s$  and  $f_y$  represent the area of the reinforcement and the yield stress of the steel, respectively, while  $d$  is the effective height of the section. The effective height has been taken as 180 mm, 210 mm, and 230 mm for floors F1, F2, and F3, respectively, while the yield stress has been assumed to be 450 MPa.

$$M_{Rd} = A_s \cdot f_y \cdot d \tag{1}$$

The effectiveness of the collaborating slab reinforcement intervention is observed in both cases; albeit to a lesser extent in the case of F3 floor, i.e., the use of “MICROCALCESTRUZZO CENTROSTORICO”.

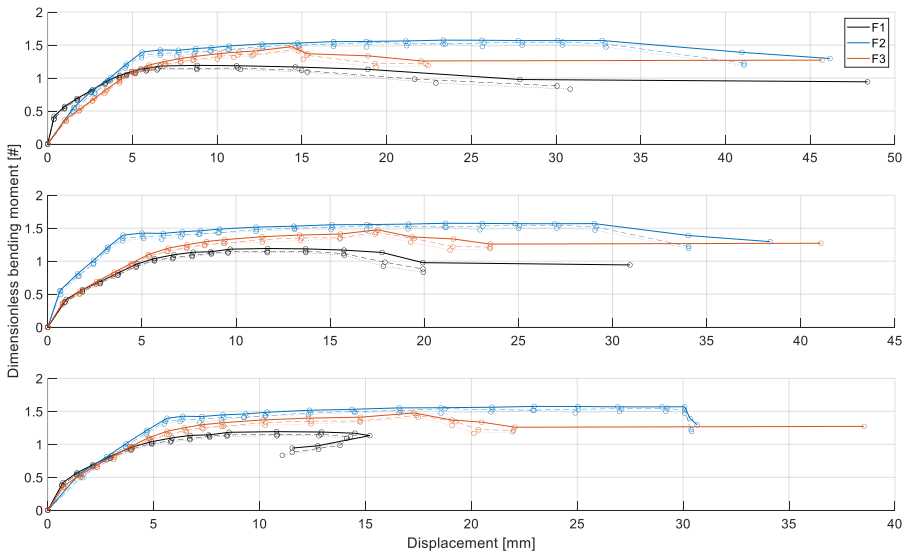


Fig. 10 Summary of test results. Note: the circles correspond to the points of maximum adimensional moment in the test cycles.



## 5 Conclusion

In this paper, part of the results of the experimental campaign to evaluate the effectiveness of strengthening interventions on Varese-type floors using a collaborating concrete slab were presented. The experimental campaign involved four-point bending tests on Varese-type floors of different lengths (2m, 2.25m, 4m, and 4.25m) and two commercial cementitious products. At the conclusion of the experimental tests, the University of Bergamo issued an extensive report containing the results of all the tests performed. In this work, only the results of the three-point tests on 2.25m-long slabs are presented.

Based on the results obtained, it can be stated that the strengthening intervention with a thin collaborating concrete slab can increase the performance of the existing Varese-type floors. However, it is noted that in some cases, the collapse occurred due to shear of the joists after yielding of the reinforcement bars; therefore, the collapse mechanism of the Varese-type floors can be assumed to be mixed (shear-flexure). This highlights how the shear verification of Varese slabs is essential in the design phase of retrofitting interventions.

## Acknowledgements

The results presented in this article are extracted from an experimental testing campaign financed by Laterlite S.p.A. in 2023.

## References

- [1] Piazza, M., Turrini, G., 1983. *Una tecnica di recupero statico die solai in legno*. Recuperare, 5,6,7, Milano.
- [2] Giuriani, E., 2002. *Solai in legno rinforzati con lastra collaborante: criteri di dimensionamento*. L'Edilizia Speciale Legno Strutturale, n°4.
- [3] Meda, A., Riva, P., 2003. *Wooden Floors Strengthened with High Performance Concrete Subjected to In-Planem Cyclic Actions*. Intern. Journal for Restoration of buildings and Monuments, Vol. 9, n°6, 619-638.
- [4] Ronca, P., Gelfi, P., Giuriani, E., 1991. *The behaviour of a wood-concrete composite beam under cyclic and long term loads*. Proc., Structural Repair and Maintenance of Historical Buildings II: 2nd International Conference (Stremah 91), I. Brebbia, C. A., Seville, Spain, Vol. 1, 263-275.
- [5] Laterlite. 2022. *LECALs 1400: Calcestruzzo leggero Strutturale Premiscelato per Getti di Rinforzo e Solette Collaboranti-Rck 25 MPa*
- [6] Laterlite. 2023. *Microcalcestruzzo Centrostorico: Microcalcestruzzo Fibrorinforzato (FRC) ad Elevate Prestazioni (HPC) e Fluidità per il Rinforzo Strutturale a Basso Spessore die Solai*.
- [7] Laterlite. 2022. *Connettore Centrostorico Chimico: Adesivo epossidico Bicomponente per il Consolidamento e il Rinforzo Statico die Solai in Calcestruzzo, in Leterocemento e a Travetti Armati tipo SAP*.

# The effectiveness of Fiber Reinforced Concrete in shear retrofitting of bridge concrete beams: case study and numerical simulation

A. Greco<sup>1</sup>, S. Pistorio<sup>1</sup>, A. Salvatore<sup>1</sup>, A. Ficociello<sup>2</sup>, A. Basconi<sup>1</sup>, A. Lupoi<sup>2</sup>

<sup>1</sup>TECNESPERI BRIDGE DESIGNERS Via Emanuele Orlando, 75, Roma (00185), Italy ales-sandro.greco@tecnesperi.it; andrea.salvatore@tecnesperi.it; alessandro.basconi@tecnesperi.it; silvia.pistorio@tecnesperi.it

<sup>2</sup>SPERI SPA Lungotevere delle Navi, 19, Roma (00196), Italy aficociello@sperispa.com

<sup>3</sup>SAPIENZA UNIVERSITÀ DI ROMA Piazzale Aldo Moro, 5, Roma (00185), Italy alessio.lupoi@uniroma1.it

## Abstract

*Fiber-Reinforced concrete (FRC)* is a composite material characterized by a cement matrix and discrete discontinuous fibers: the fibers can be made of steel, polymeric material, glass, carbon, or natural material. Unlike ordinary concrete, the presence of fibers ensures a high residual tensile strength (named *toughness*) after cracking of the cement matrix, giving ductility to the material. Due to these rheological properties, *FRC* with steel or polymer fibers is frequently used for construction of industrial flooring and tunnel linings. Although the design guidelines currently effective are mainly focused on new structural *FRC* elements, the characteristics of the *FRC* allow its application also in retrofitting of existing structures, in particular concrete bridge beams. This article illustrates an application of *FRC* for the shear retrofit of a bridge beam through web thickening. Specifically, the capacity of the reinforced beam is estimated with a capacity model in which the failure behavior involves two Morsch truss models in parallel, whose mutual exchange of forces is allowed by the sliding resistance at the interface between materials. In order to validate the proposed formulation, numerical simulations are carried out and the results show a good agreement with analytical predictions.

## 1 Introduction

Fiber Reinforced Concrete (FRC) consists of a matrix (cement, water, aggregates, additives) and randomly oriented fibers (steel, carbon or glass) mixed within it. The fiber content significantly enhances the tensile strength of FRC. Due to its high strength and durability, FRC is increasingly used in retrofitting existing reinforced concrete structures to address aging issues, extend service life, and resolve strength or structural problems. FRC is also valid for in situ applications as it requires minimal manual labour and is particularly effective in retrofitting bridge decks [1], [2] to improve shear performance without adding dead load, especially in structures lacking shear reinforcement [3]. Several studies on the shear behaviour of FRC beams rely on regression analysis [4]. Tests on composite beams [5] have shown that adding a layer of FRC delays the formation of inclined shear cracks in the concrete section. Despite the increasing use of FRC, current design codes lack equations for calculating shear strength in FRC-retrofitted beams. For instance, design guidelines for UHPFRC are available in countries like Canada, Germany, Switzerland, Spain, Australia, and Japan. However, each set of guidelines provides different approaches to the design process and imposes different requirements for material characterization [6]. Therefore, there is a need to develop an analytical model to predict the shear strength of composite beams, aiming to establish a simple and validated procedure for design codes. This work compares the outcomes of the nonlinear finite element analysis with those derived from an analytical formulation based only on the design characteristics, easily available from the technical data sheet provided by the producer. This method estimates the shear strength of a beam reinforced with FRC in a straightforward and conservative manner.

## 2 Theoretical formulations

The capacity model developed to estimate the shear resistance of the FRC retrofitted beams considers two Morsch truss models arranged in parallel. In particular, the two Morsch trusses are the existing beam and the FRC layers. The shear capacity of the existing beam ( $V_{rd,B}$ ) is evaluated according to the

standard formulation of Mörsch truss with variable inclination [7] expressed in (1) and (2), while the shear capacity of the FRC layers ( $V_{rd,F}$ ) is computed through a derivation of the same formulation. Specifically, the resistant contributions of the internal truss within the FRC jacket are calculated using equations (3) and (4).

$$V_{rsd,B} = z \frac{A_{sw}}{s} f_{yd} (\cot g \alpha_b + \cot g \theta_B) s e n \alpha_b \quad (1)$$

$$V_{rcd,B} = z b_w \alpha_c v f_{cd} (\cot g \alpha_b + \cot g \theta_B) / (1 + \cot g^2 \theta_B) \quad (2)$$

$$V_{rsd,F} = z_F b_{w,F} f_{tud,F} (\cot g \theta_F) \quad (3)$$

$$V_{rcd,F} = z_F b_{w,F} \alpha_c v f_{cd,F} (\cot g \theta_F) / (1 + \cot g^2 \theta_F) \quad (4)$$

Where:

- $z$  is the lever arm of the internal forces equal to  $0.9d$ ;
- $\alpha_b$  is the angle between the tie and the beam axis;
- $\theta_B$  is the angle between the strut and the beam axis;
- $b_{w,F}$  is the thickness of the FRC jacket, which is 5 cm per side;
- $f_{tud,F}$  is the design tensile strength of the FRC, assumed to be equal to the residual value of the cracks at  $w = w_u$  at the Ultimate Limit State (as specified by the product used);
- $f_{cd,F}$  is the design compressive strength of the FRC;
- $z_F$  is the lever arm of the internal forces within the FRC jacket at failure;
- $\theta_F$  is the angle of the compression strut in the FRC truss.

The aim of the calculation is to determine the optimal value of  $\theta_{B,ott}$  and  $\theta_{F,ott}$  that maximizes the shear resistance of each truss  $V_{rd,B}$  and  $V_{rd,F}$ , while being compatible with the tensile capacity of the lower tie of the beam and of the FRC trusses (respectively  $T_{rd,B}$   $T_{rd,F}$ ), such condition is expressed in the (5).

$$\theta_{i,ott} = \{ V_{rd,i} \max \wedge (T_{ed,i} = \frac{V_{rd,i}}{2} (\cot g \theta_i) < T_{rd,i}) \} \quad (5)$$

The check  $T_{ed,B} < T_{rd,B}$  for beam truss is conducted by calculating the tensile strength of the tension tie considering the longitudinal reinforcement according to (6). For the FRC truss, the check  $T_{ed,F} < T_{rd,F}$  is executed by calculating the tensile strength of the tension tie considering only the tensioned area as the resistance area, given in (7), where  $h_F$  is the height of FRC layers and  $y_{NA}$  is the neutral axis depth.

$$T_{rd,B} = A_{sw} f_{yd} \quad (6)$$

$$T_{rd,F} = (h_F - y_{NA}) b_{w,F} f_{tud,F} \quad (7)$$

The shear resistance value is given by the sum of the minimum values obtained from the strut and tie formulation for beam and the FRC reinforce, (8). The unknown quantities, in order to calculate the shear capacity of the FRC truss, are: the constitutive model to determine the design compressive and tensile strength of the FRC; the lever arm of the internal forces, the neutral axis depth at failure within the FRC and the angle of the struts in both beam and FRC trusses.

$$V_{rd} = V_{rd,B} + V_{rd,F} = \min(V_{rsd,B}, V_{rcd,B}) + \min(V_{rsd,F}, V_{rcd,F}) \quad (8)$$

The tensile stress-strain response of FRC is initially dominated by the cementitious matrix until cracking occurs. Post-cracking, fibers control the process, increasing shear capacity and providing significant post-peak resistance and ductility. The fibers spanning the cracks engage and carry the load, resulting in either strain-softening or strain-hardening behaviour, depending on the fiber dosage [3]. The constitutive model is rigid-plastic in tensile behaviour and parabola-rectangle in compressive behaviour, according to the guidelines for FRC LG2022 [8] and as shown in Figure 1. The technical specifications are illustrated in the next section.

The failure strain in the tensioned fiber (bottom flange) is assumed to find the internal force lever arm and the depth of the neutral axis at failure. In fact, given that the compressive strength of the FRC is much greater than its tensile strength, the neutral axis at failure is not placed at midpoint but shifted upward, leading to a tension-side failure. Assuming a linear distribution of compressive stresses, the equations for the neutral axis  $y_{NA}$  and the lever arm of internal forces  $z_F$  can be expressed in closed

form as given respectively in (9) and (10). The dimensionless ratios  $\hat{y}_{NA} = \frac{y_{NA}}{h_F}$  and  $\hat{z}_F = \frac{z_F}{h_F}$  do not depend on geometric quantities, meaning they remain constant regardless of changes in  $h_F$  of  $b_{w,F}$  but depend exclusively on the constitutive characteristics of the FRC: tensile strength  $f_{td}$ , tensile failure strain  $\varepsilon_{ut}$  and initial elastic modulus  $E_{f0}$ . Specifically, the latter is calculated by deriving the constitutive equation of the FRC under compression (parabola-rectangle model) and is given by (11).

$$y_{NA} = \frac{-2h_f f_{td} + \sqrt{4h_f^2 f_{td}^2 - 4 \left( \frac{\varepsilon_{ut} E_{f0}}{2} - f_{td} \right) (f_{td} h_f^2)}}{2 \left( \frac{\varepsilon_{ut} E_{f0}}{2} - f_{td} \right)} \quad (9)$$

$$z_f = \frac{(h_f - y_{NA})}{2} + \frac{2}{3} y_{NA} \quad (10)$$

$$E_{f0} = \frac{2f_{cd}}{\varepsilon_{c2}} \quad (11)$$

The last variable is the angle of the compression strut in the FRC  $\theta_F$ . Assuming that the capacity of the strut is greater than that of the ties  $V_{r_{cd,F}} > V_{r_{sd,F}}$ , the failure of the FRC truss occurs upon reaching  $V_{r_{sd,F}}$ . Therefore, the angle that optimizes the contribution of the FRC is the smaller angle such that  $T_{ed,F} = T_{rd,F}$ . The derivation of  $\theta_F$  is given in the (12)s.

$$T_{ed,F} = V_{r_{sd,F}} \frac{\cot g(\theta_F)}{2} = z_F b_{w,F} f_{tud,F} \frac{\cot g \theta_F^2}{2} \quad (12a)$$

$$T_{rd,F} = (h_F - y_{NA}) b_{w,F} f_{tud,F} \quad (12b)$$

$$\cot g \theta_F = \sqrt{\frac{2(h_F - y_{NA})}{z_f}} \quad (12)$$

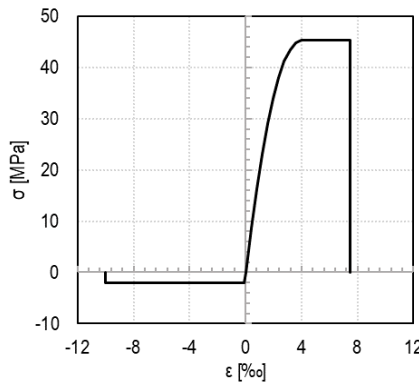


Fig. 1 Simplified stress-strain constitutive laws behaviour.

### 3 Case of study

The reinforcement of the bridge deck beams with FRC layers is designed for the static and seismic upgrade project for an Italian highway bridge. This project is chosen as a case study to apply the proposed formulations and to define the input parameters for the finite element model. The beam is made by prestressed concrete with transverse reinforcement, stirrups ( $2\phi 10@150\text{mm}$ ). The shear FRC reinforcement is applied in the part of the beams between the bearing and the first transverse element, to cover the shear span, by thickening the web on both sides with a layer of 5 cm of FRC. The input material properties of the existing beam and of FRC are summarized in Table 1 and Table 2. The geometrical properties are illustrated in Figure 2. The operational methodologies of retrofitting involve the removal of approximately 2 cm of concrete on each side, followed by cleaning of the reinforcement and sandblasting to cut any friable or loose parts, ensuring that the concrete surface is perfectly clean, solid, and highly rough. Additional transverse reinforcement bars are placed and anchored into the

upper and lower bulbs of the beam to ensure perfect adhesion of the FRC layer. These bars were not considered in the resistance calculations. Such process justifies the assumption of perfect bond in the analysis.

Table 1  $f'_c$  = normal concrete cylinder strength;  $E_c$  = Young’s modulus of normal concrete;  $f'_{ct}$  = normal concrete tensile strength;  $f_y$  = yield strength of transversal bars;  $E_s$  = Young’s modulus of steel;  $A_s$  = area of stirrups;  $s$  = step of the stirrups;  $f_{yp}$  = yield strength of tendons;  $f_{up}$  = ultimate strength of tendons;  $\phi$  = diameter of tendons.

Concrete			Reinforcement								
			Stirrups				Tendons				
$f'_c$ [MPa]	$E_c$ [MPa]	$f'_{ct}$ [MPa]	$f_y$ [MPa]	$E_s$ [MPa]	$A_s$ [mm <sup>2</sup> ]	$s$ [mm]	$f_{yp}$ [MPa]	$f_{up}$ [MPa]	$E_s$ [MPa]	No. of bars #	$\phi$ [mm]
23.29	$3 \times 10^4$	1.65	410	$2 \times 10^5$	157	150	1237.5	1650	$2 \times 10^5$	6x42	7

Table 2  $l_f$  = fiber length;  $d_f$  = fiber diameter;  $F_u$  = fiber ultimate tensile strength;  $V_f$  = fiber volume ratio;  $T_{FRC}$  = thickness of FRC layers;  $f_{c,F}$  = compressive strength of the FRC;  $f_{tu,F}$  = tensile strength of the FRC;  $E_{c,F}$  = Young’s modulus of the FRC;  $\epsilon_{cu}$  = compressive failure strain;  $\epsilon_{ut}$  = tensile failure strain.

Fibers					FRC				
Fibre Type	$l_f$ [mm]	$d_f$ [mm]	$F_u$ [Mpa]	$T_{FRC}$ [mm]	$f_{c,F}$ [MPa]	$f_{tu,F}$ [MPa]	$E_{c,F}$ [MPa]	$\epsilon_{cu}$ [%]	$\epsilon_{ut}$ [%]
End-Hooked	30	0.28	3070	50	45.33	2.09	22900	7.47	10

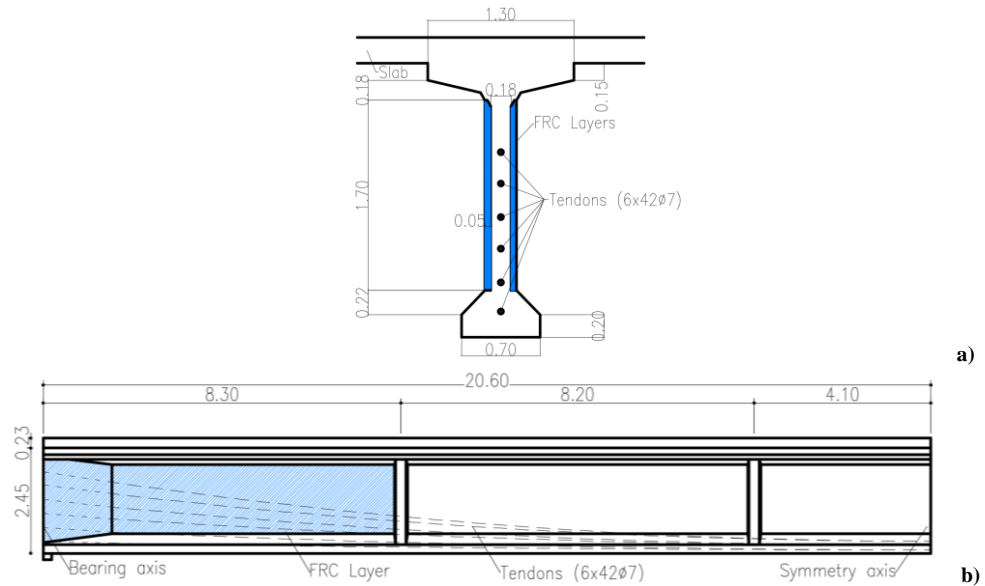


Fig. 2 Geometry and reinforcement details of the prestressed beam, with layer of FRC: cross section a) and longitudinal view b).

#### 4 Finite element analysis

This section details the nonlinear finite element analysis (FEM) of the selected case study conducted using the program VecTor2 [9]. The finite element model's predictions are compared with formulation results to validate the procedure. VecTor2, based on the Modified Compression Field Theory (MCFT), is used for analyzing two-dimensional structures and predicting load-deflection responses, crack patterns, and failure modes of reinforced concrete elements under in-plane shear and axial stresses. The

program ensures equilibrium, compatibility, and constitutive stress-strain relationships for nonlinear solutions [10]. The concrete's pre-peak and post-peak responses were modeled using the Hognestad (parabola) Model and the Modified Pank-Kent Model, respectively. Other material behavior models were set to VecTor2's default options. The Simplified Diverse Embedment Model (SDEM)-Monotonic [11] was used for the FRC model. The beam is modelled with triangular elements for the concrete and truss bar elements for the longitudinal tendons. Two reinforced concrete material types are used. One type stands for the plain concrete cover. The other type models the web, flanges and slab regions of the beam with one smeared reinforcement component, which represents the stirrup reinforcement. Also, the fiber reinforcement was modelled as smeared reinforcement embedded in the concrete. The ductile steel reinforcement material types are defined according to the reinforcement ratio. Each longitudinal reinforcing tendons were entered as a separate reinforcement path with its corresponding material type. Only half of the beam needs to be modeled, as both the beam and loading conditions are symmetrical about the midspan. Nodes at the midspan of the beam are restrained from displacements in the longitudinal direction. The nodes at the support are restrained from displacements in the transverse direction. The load is transferred to the top surface of the element by a plate (same material and dimensions as used for the supports) perfectly connected to the concrete elements, to avoid unrealistic punching failure and numerical instability problems due to the load concentration. Two load case analysis was defined: (1) dead load, and (2) point load. The beam was loaded under a four-point bending configuration. The point load is applied as a monotonically increasing displacement up to failure to capture the post-peak behavior of the beam. The Vector2 model is validated by simple calculations for deflection under self-weight. Since only half of the beam is modelled and given the restrained condition, the maximum deflection due to self-weight of the concrete only, can be calculated using the formula  $\delta = \frac{5qL^4}{384EI}$ , where  $q$  is the uniformly distributed load due to self-weight given by the product of the cross sectional area of the concrete  $A_c = 1.93 \text{ m}^2$  and the specific weight of the concrete  $\gamma_c = 22 \text{ kN/m}^3$ , which gives  $q = 42.5 \text{ kN/m}$ . With span  $L = 20.6 \text{ m}$ ,  $E = 30000 \text{ MPa}$  and  $I = 1.56 \text{ m}^4$  the deflection at midspan is  $\delta = 0.034 \text{ m}$ . From the Vector2 model we have deflection due to self-weight at midspan  $\delta = 0.037 \text{ m}$ . A parametric study was conducted to investigate the shear peak capacity as function of the shear span 'a' to effective depth 'd' ratio 'a/d'. As concerned the analysis, the a/d ratio was selected to induce a shear failure mode.

## 5 Results and discussion

The load displacement curves (Figure 3) and the crack pattern (Figure 4) of the design state beam are compared to those of the state of art beam for a selected range of a/d ratio. The a/d ratio is crucial for the resulting load transfer actions. A large a/d ratio results in greater moments due to the increased lever arm, leading to a reduction in capacity. Additionally, the flexural crack pattern, depending on the failure mechanism, is also affected by the a/d ratio [12]. In fact, the shear failure mechanisms fall into three approximate bands of a/d ratios, according to [13]: Type I: failure of the beam mechanism, when  $4 < a/d < 5$ ; Type II: Failure of the arch action, when  $2.5 < a/d < 4$ ; Type III: failure by crushing or splitting of the concrete, when a/d is smaller than 2.5.

Although the aforementioned mechanisms are assumed for a beam without web reinforcement, the latter are valid also for a shear reinforced beam, where the presence of stirrups enhances the strength of the shear mechanisms [13]. The numerical analysis shows that, for a/d = 0.9 and 1.8, the state of art beam fails in a brittle way by splitting of the concrete due to the opening of a diagonal crack that connects directly the loading point and the support. As soon as the a/d ratio increases the crack pattern changes and the failure mode becomes more ductile. For higher ratio, the beam developed firstly an inclined cracks then it develops into a diagonal crack which connects the closest support with an almost horizontal branch and the failure occurs. Yielding of the stirrups occurs for a/d = 3.6 in failure type II. Yielding of the tendons occurs for a/d = 4.4 in failure type I.

The shear failure mechanisms in the design state beam remain conceptually the same. The shear capacity is larger in the band of type II failure mechanism as there are no additional flexural cracks between the critical crack and the support disturbing the load transfer. The beam fails after yielding of the tendons, whereas stirrups do not yield in the portion where the FRC layer is applied. As well as for type III mechanism: the shear-critical crack formed too, but the presence of the FRC layers is able to provide sufficient capacity to postpone the crushing of the concrete and therefore the failure. The truss

mechanism of the stirrups governs the failure for the design state beam for  $4 < a/d < 5$  (type I failure range), however the shear capacity is improved by the engagement of the additional FRC truss. The predictions of the FEM analysis are compared to the shear strength evaluated according to two design code, such as Eurocode 2, (EC02) [14], fib Model Code 2020, LoA III (fib2020) [15], as well as the proposed FRC capacity model.

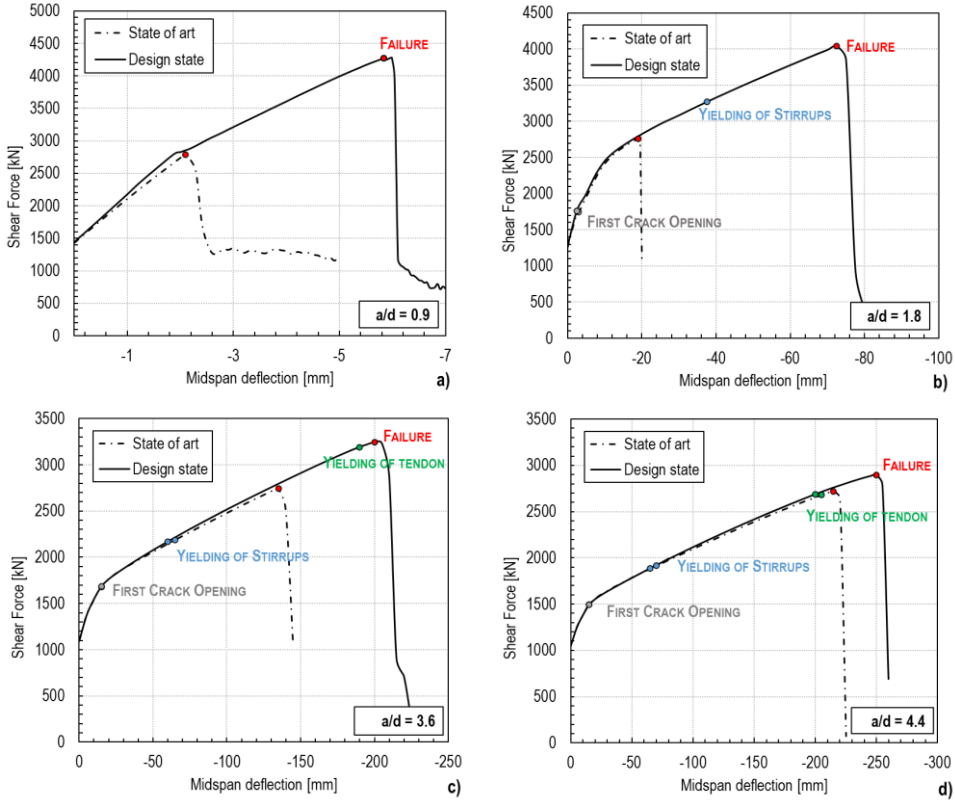


Fig. 3 Load deflection response for a)  $a/d=0.9$ ; b)  $a/d = 1.8$ ; c)  $a/d = 3.6$ ; d)  $a/d = 4.4$ .

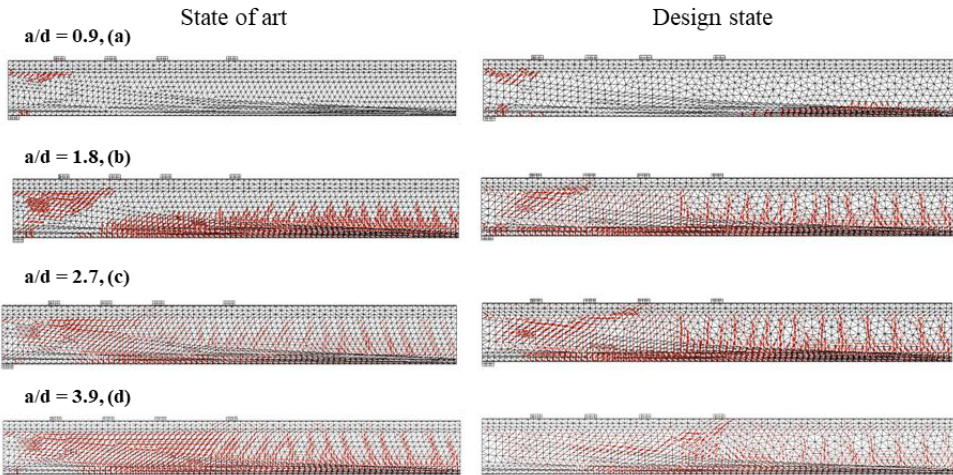


Fig. 4 Schematic crack patterns after failure: a)  $a/d=0.9$ , b)  $a/d=1.8$ , c)  $a/d=3.6$ , d)  $a/d=4.4$ .

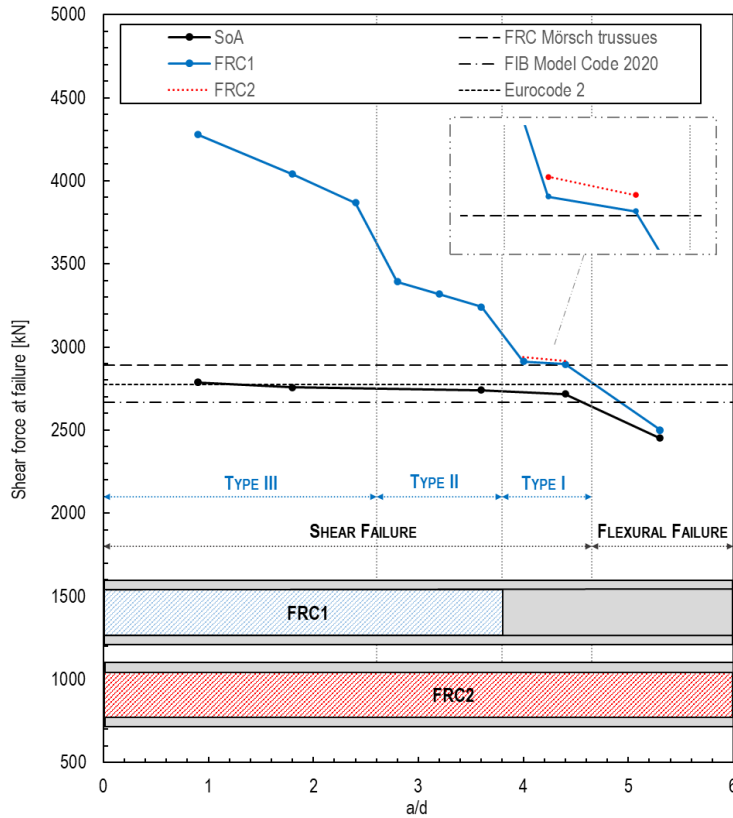


Fig. 5 Comparison of shear strength across shear span-to-depth ratio ( $a/d$ ) from FEM analysis, Eurocode 2, fib Model Code 2020, and proposed FRC capacity model prediction, for retrofitted and conventional beams. Mechanisms include Type I (Morsch truss failure), Type II (compression arch failure), and Type III (concrete strut failure via crushing or splitting). FRC layer 1 covers the shear span up to truss mechanism activation, while FRC layer 2 covers the entire beam length.

## 6 Conclusions

The main goal of these work was to study the effectiveness of beam retrofitting with Fibre Reinforced Concrete (FRC) layer on shear strengths, crack control, and ductility. Additionally, this research proposes a simple analytical formulation to predict the shear strength of beams strengthened with FRC. The finite element analysis validates the theoretical formulations both for the design state and for the actual state of art. The retrofit of the beam with FRC delays the collapse and allows a diffused cracking without significant shear cracks. Moreover, both strength and displacement levels improve. It is shown that the formulation based on the two Morsch trusses in parallel capture adequately the behaviour of the beam for aspect ratio values ( $a/d$ ) where the truss mechanism governs the failure mode, even though the FRC retrofitted beam is able to enhance capacity thanks to the arch mechanism and to the concrete struts mechanisms. In addition, it is demonstrated that retrofitting the beam with an FRC layer covering only the shear span is sufficient to achieve a significant increase in capacity. Future developments may involve an exhaustive model for bonding mechanism and bond properties at the interface of reinforcement material and concrete substrate, which is, according to many authors [17], the most principal issue when considering durability and a key factor in the success of repair and rehabilitation works.

## Acknowledgements



Authors would like to gratefully acknowledge Speri S.p.A. and TecneSperi Bridge Designers S.r.l. for providing the opportunity to work on this research topic. The support and collaboration of the entire team was essential to the success of this project.

## References

- [1] Brühwiler, E., and Denarié, E., 2008. “*Rehabilitation of concrete structures using ultra-high performance fibre reinforced concrete*”, (No. CONF), University of Kassel.
- [2] Brühwiler, E., Bastien-Masse, M., Mühlberg, H., Houriet, B., Fleury, B., Cuennet, S., & Maurer, M., 2015. September. “*Strengthening the Chillon viaducts deck slabs with reinforced UHPFRC*”, in IABSE Symposium Report (Vol. 105, No. 24, pp. 1-8). International Association for Bridge and Structural Engineering.
- [3] Naaman, A. E., “*High Performance Fiber Reinforced Cement Composites: Classification Applications*” in CBM-CI International Workshop, Karachi, Pakistan, 2008.
- [4] Iavarone, F., 2021. “*Shear strengthening of RC elements with Ultra High-Performance Fibre Reinforced Concrete*,” PhD diss., Università degli studi di Brescia, Italia.
- [5] Noshirvani, T., and Brühwiler, E., 2013. “*Analytical model for predicting response and flexure-shear resistance of composite beams combining reinforced ultrahigh performance fiber-reinforced concrete and reinforced concrete*”, Journal of Structural Engineering, 140(6), 04014012.
- [6] Larsen, I. L., and Thorstensen, R., T., 2020. “*The influence of steel fibres on compressive and tensile strength of ultra-high-performance concrete: A review*,” Construction and Building Materials, Volume 256.
- [7] Morsch, E., 1908. “*Der Eisenbeton. Seine Theorie und Anwendung*“, Wittwer, Stuttgart.
- [8] Linee Guida FRC - CNR-DT 204/2006, “*Guide for the Design and Construction of Fiber-Reinforced Concrete Structures*”, Roma, 2022.
- [9] Vecchio, F. J., “*VecTor2 Nonlinear Finite Element Analysis*”, 1990.
- [10] Wong, P.S., & Vecchio, F.J., 2002. “*VecTor2 and FormWorks User’s Manual*”, Technical Report, Department of Civil Engineering, University of Toronto.
- [11] Lee, S. C., Cho, J. Y., & Vecchio, F. J., 2012. “*Simplified Diverse Embedment Model for Steel Fiber Reinforced Concrete in Tension*,” ACI Material Journal.
- [12] Herbrand, M., “*Shear strength models for reinforced and prestressed concrete members*”, Thesis, IMB Lehr Stuhl und Institut für Massivbau, 2017.
- [13] Park, R., Paulay, T., “*Reinforced Concrete Structures*”, Department of Civil Engineering, University of Canterbury, Christchurch, New Zealand, 1974.
- [14] EN 1992-1-1: Eurocode 2. 2005. “*Design of concrete structures. Part 1–1: General rules and rules for buildings*”.
- [15] Fédération Internationale Du Béton (fib). 2023. “*fib Model Code for Concrete Structures (2020)*”, International Federation for Structural Concrete, Lausanne, Switzerland, 2023.
- [16] Vass. G., 2018. “*Finite Element Modelling of Different Strengthening Strategies for Reinforced Concrete Deep Beams*,” PhD diss., Université de Liège, Liège, Belgique.
- [17] Naaman, A. E., Paramasivam P., Balazs G.L., Eibl J., Erdelyi L., Hassoun N.M., et al. “*Reinforced and prestressed concrete using HPRCC matrices. Highperformance fiber reinforced cementitious composites*”, RILEM Proc 1996; [291–348].

# **Performance and life-cycle assessment (LCA) of concrete structures**



# How Life Cycle Assessment has influenced our mind-set in structural designing

Francesco Lomurno<sup>1</sup>, Mauro Eugenio Giuliani<sup>2</sup>

<sup>1</sup>Designer <sup>2</sup>Director

Redesco Progetti - Via V.Gioberti, 5, Milan (20123), Italy

## Abstract

This article aims to share our experience in applying Life Cycle Assessment (LCA) to the structures we design and how the sensitive awareness derived from it has influenced our approach to projects.

**Redesco (Research-Design-Consulting)** is an important Italian structural engineering company, characterized by a holistic vision but driven by the pursuit of the best structural shape for elegance, economy, and ecology. In recent years, we have introduced the LCA approach as an analytical tool for measuring environmental impact for some new projects and for retrospective analysis of past accomplishments.

Engineers need numbers to measure the world and bring as much order as possible to complex systems. Through LCA, organization and scientific rigor are introduced into the environmental aspects of structural design, which is no longer guided merely qualitatively and by intuition. Doing reference to numerical indices, graphs, and phase studies has allowed us to better understand the impact of our design choices. In concrete terms, it has improved the design paradigm and our awareness of what we do.

We want to share the results of our studies and our changed perspective. We found ourselves wondering: what are the key factors in reducing the environmental impact of structures and foundations? do tall buildings have a greater impact than common building types? what is the role of the designer in CO<sub>2</sub> savings? what are the fundamental parameters for a faster and more certain decarbonization of structures?. Furthermore: what should we ask to lawmakers? It is necessary to rethink the performance requirements for structures, rationalize codes and prescriptive regulations. As designers, we should seek a better balance between construction speed, labor utilization, and material consumption that employing resources in practical R&D for real-scale projects.

In this article, we present our reflections born from our design experience, our questions, and some answers.

## 1 Reflections on the present approach to design

The act of construction has always entailed a delicate balance between various aspects: functionality of the structure, material consumption, labor utilization, construction time, aesthetic effects, and so forth. Throughout different eras, depending on the specific project, this equilibrium has leaned towards one aspect or another due to varying customs and economic circumstances.

Consider the course observed in recent generations of designers. In the post-war period, typically, the construction industry was focused on minimizing material consumption, often at the expense of a significant use of labor. Conversely, during periods of economic recovery, when material resources were more available, key priorities shifted towards speed and replicability in construction processes.

Since the 1990s, however, industry factors such as: mechanization, rise of economies of scale, and increasing labor costs have driven designers towards an approach preferring constructive simplicity. Over this period and subsequent decades, particularly pronounced was the imbalance between labor and material costs, tilting in favor of the latter, thus somewhat relegating material efficiency in design paradigms. This long-term conditioning has exerted a significant influence on engineers, construction firms, and legislators alike, a legacy still evident today.

Yet, in the face of evolving market dynamics and increasingly ecological imperatives, this approach is no longer acceptable. In recent years, the landscape has shifted significantly: in the years

2021/2022, we witnessed a remarkable surge in construction material costs [1]. This phenomenon coincided with the post-covid era, marked by a resurgence in construction activities driven by governmental promotions and an upsurge in demand, alongside rising raw material costs, inflation, and international political instability. Moreover, from an environmental point of view, the calls from national and international organizations for urgent action are becoming more insistent. The sector now demands a concerted effort to limit environmental impact and, with other industries as well, struggles to limit the global temperature increase to 2°C above pre-industrial levels [2].



Fig. 1 e 2 Construction site machinery in the assembly of a building using simple schemes of precast reinforced concrete elements, 2012; Labor force in the construction of the Palazzetto dello Sport in Rome designed by P.L. Nervi, 1956.

Therefore, a return to fundamental principles in project approach becomes indispensable to tackle the environmental and economic challenges of our time. Especially in an industry characterized by a limited propensity for innovation and change, it is crucial that this transformation process starts from the initiative of designers, who bear primary responsibility for the initial setting of the works.

A holistic conception of construction, which also encompasses environmental aspects, still represents something onerous from various perspectives and is not always achievable by private and public investors. On the side of contractors and design firms, there is often observed a conservative mindset that is not very open to investments in R&D on the subject. The sector needs to be sensitized through a campaign that should start from inside, through the sharing of ideas and know-how. Engineering firms should not limit themselves to activities aimed solely at profit but are called to a broader professional role as promoters of change and carriers of value.

Redesco is actively engaged in research and awareness-raising regarding structural design and its environmental impact, continually developing better competence and awareness on the subject. A recent internal study [3] demonstrates the worsening, from an environmental perspective, of design solutions, through a practical case.

**CASI STUDIO:**

	anno	interasse colonne ed altezza			campi int.	volum. cls.	A		B	
		L <sub>1</sub> (m)	L <sub>2</sub> (m)	H <sub>TOT</sub> (m)			N° <sub>cl</sub>	V (m <sup>3</sup> )	p=g <sub>1</sub> +q	h <sub>c,eq</sub> (m)
4 Messaggerie Italiane (MI)	1980	9.97	8.80	0.60	9	18.35	7.00	<b>0.209</b>	2932	
3 Edificio CCI (Venaria, TO)	1980	10.30	8.27	0.75	9	17.84	10.00	<b>0.209</b>	3631	
2 Edificio Ricordi (MI)	1982	8.00	5.00	0.48	6	5.66	10.00	<b>0.141</b>	1655	
1 Laboratori Poli (Rozzano MI)	1986	8.40	7.20	0.60	9	8.93	12.00	<b>0.148</b>	2643	0.304
----- piastre piene / alleggerite spessori 30 / 35 cm -----										
5 Variante proposta UNIMI	2022	8.40	8.40	0.40	4	10.55	8.00	<b>0.150</b>	2267	0.279

Anni '90  
Oggi

Anno del progetto

Spessore equivalente

Fig. 3 Except from the internal research report "Studies on concrete slabs" by Redesco Progetti.

Various solutions for a very common building typology such as reinforced concrete slabs in projects from different eras have been analyzed. Projects executed from the 1970s to the present day were examined, elaborating on some indices such as:  $h_{c,eq} = \frac{v}{A}$ , for equivalent thickness,

$$P_f = q_{Ed} \cdot l^2, \text{ for flexural performance index, and correlating them with each other.}$$

It has emerged that for comparable performances, the average concrete consumption in these building typologies has increased from 20 cm equivalent before 1990 to as much as 30 cm, despite the general improvement in material quality. This increase is attributed to criteria and standards defined by contractors and legislation.

Through this comparison and other similar studies, we have understood how the design of structures has deviated from the fundamental principles upon which modern discipline should be based, as taught by eminent figures such as Nervi [4]. There has been a leaving from the correct principles that nature itself applies in structural forms with minimal use of material resources and energy. This, along with numerous other factors of pollution from human activity, has led to worsening environmental and climatic conditions, a circumstance that we must strive to slow down.

Recent international [5] research has shown how impactful the activity of structural engineers is. It appears that, in practical terms, applying a 20% reduction in the embodied carbon of structures designed by a single engineer in a year could result in a reduction of 200 tons of CO<sub>2</sub>, considering an average design activity for 5000 m<sup>2</sup> of construction annually.



Fig. 4 A comparison between the annual CO<sub>2</sub> saved through some virtuous behavioral practices and that saved by implementing a 20% reduction in the structures designed by a single engineer would be illuminating.

This scenario is realistic, considering that the same source [5] highlights the results of a study indicating that, upon examining a certain sample of structures designed in recent years, 50% of them would be oversized compared to the mechanical performance required.

## 2 Autogenous approach to estimating the environmental impact of structures

The growing awareness taken from design practice and research on environmental issues has incited the idea of conducting a detailed analysis on pollutants emitted during the construction of a structure. This has led to the formulation of crucial questions such as: what are the major polluting factors and how can they be reduced? Given the same technology, which building typology is the most polluting?

A journey began several years ago thanks to the initiative of Engineer Gian Carlo Giuliani, who initiated an initial approach to calculating the CO<sub>2</sub> emissions generated in the construction of a structure, developing a dedicated spreadsheet and establishing an initial database.

5.5.2 Produzione delle armature				
L'emissione di CO <sub>2</sub> ed il consumo dell'uso di fonti energetiche non rinnovabili necessari per la produzione delle armature: sono desunti da tabelle Arcelor-Mittal riportate nella tabella seguente:				
Armature	$f_{yk}$ (N/mm <sup>2</sup> )	$\gamma$ (kg/m <sup>3</sup> )	CO <sub>2eq</sub> (kg/t)	energia (kWh/t)
barre	450	7850	1230	14237
reti	450	7850	1620	20440
reciclo (kg/t)				
				0
Nei conteggi sono già considerati i benefici derivanti dal riciclo perché la produzione avviene con 840 kg/t di rottame.				
Valori estesi a tutti i materiali metallici sono riportati dalla versione BETA di EC3.				
5.6 Parametri di emissione relativi ai mezzi di trasporto e sollevamento				
5.6.1 Emissioni per motori endotermici				
Si richiamano i dati consolidati per i motori diesel:				
motori diesel	consumo gasolio 1 (kg/90Wh)	densità (kg/m <sup>3</sup> )	consumo gasolio 2 (kg/90Wh)	emissione base CO <sub>2</sub> (kg/t)
	0,28	0,85	0,306	2,6
				0,795
consumi riferiti alla potenza utile sviluppata, tenendo conto del rendimento termico				
			rendimento meccanico: $\xi_m =$	0,70
Allo stato attuale non sono presenti mezzi usuali di trasporto ad azionamento elettrico.				
All'emissione di CO <sub>2</sub> sono associati altri composti inquinanti come SO <sub>2</sub> , NO <sub>x</sub> etc ma non considerati nello studio perché hanno incidenza ridotta.				
5.6.2 Emissioni per motori elettrici				
motori elettrici	potenza nominale (kW)	rendimento (%)	potenza effettiva (kW)	emissioni (CO <sub>2</sub> ) (kg/kWh)
	1.000	0,8	0.800	0,290

armature	CO <sub>2</sub> (kg/t)	NOTE
produzione	1347,00	
trasporto	12,00	con autocarro
assemblaggio	10,00	valore stimato
sollevamento	0,10	
	<b>Σ CO<sub>2</sub> (kg/t)</b>	<b>W<sub>g</sub> (t/m<sup>3</sup>)</b>
	<b>1369,10</b>	<b>0,08</b>
		<b>CO<sub>2</sub> (kg/m<sup>3</sup>)</b>
		<b>110,0</b>

calcestruzzo preconfezionato	f <sub>ck</sub> (N/mm <sup>2</sup> )	Holcim - clis preconfezionato	E(CO <sub>2</sub> ) (kg/m <sup>3</sup> )
35			445
autobetoniera	capacità M (m <sup>3</sup> )	potenza P <sub>g</sub> (kW)	emissioni kg(CO <sub>2</sub> )
10	600		170
pompa autocarata	N° stazionamenti	potenza P <sub>g</sub> (kW)	emissioni kg(CO <sub>2</sub> )
5	450		120
pompa	potenza P <sub>g</sub> (kW)	emissioni kg(CO <sub>2</sub> )	E(CO <sub>2</sub> ) (kg/m <sup>3</sup> )
50	29,82		0,60
casasforme [1]			E(CO <sub>2</sub> ) (kg/m <sup>3</sup> )
[1] armo e disarmo			0,06
			<b>ΣE(CO<sub>2eq</sub>) (kg/m<sup>3</sup>)</b>
			<b>466</b>

Fig. 5 Extract from one of the first reports on the calculation of CO<sub>2</sub> emissions.

This initiative has opened an extremely broad and challenging field of inquiry due to the limited availability of reliable scientific data and the lack of dialogue in the Italian academic and professional world.

Then as today, there is a pressing need for greater collective effort on the issue, both in Italy and abroad, involving universities, industry, and professionals. Standardized methodologies, a shared taxonomy, and a comprehensive database are required for this field, which is destined to become a technically and professionally significant branch.

These critical issues and gaps have been partially addressed in recent years by the commendable initiatives of prestigious institutes and associations in Northern Europe and America, some of which are mentioned below. Through their work and collaboration, we have progressively arrived at an initial formulation of an approach to the topic with solid technical bases. Drawing partially from what has already been done in other industrial sectors, the methodology of Life Cycle Assessment has been adapted to the construction industry. Significant contributions have come from countries such as the United Kingdom, Denmark, and Finland, while Italian contributions have been scarce up to now.

### 3 Rise of life cycle assessment in the construction industry

The Life Cycle Assessment (LCA), developed as a tool to assess the environmental impact of industrial products, has gained international recognition as a method for sustainability assessment. In recent times, it has been embraced in the construction sector, where we hope it will become a standard tool. It can be briefly defined as a methodology for analytically calculating the various pollutant factors related to construction processes. The computation is carried out systematically and rigorously, referring to the schematization of the various life stages of the materials comprising the building: from raw material extraction, to installation, to end-of-life disposal.

Shared knowledge and standardized schematizations enable professionals and builders to speak a common language, which is crucial in the context of a growing new discipline. Some guidelines and successful models are already in common use, such as the Environmental Product Declaration (EPD) certification for materials. Despite the absence of mandatory regulations in Italy, it has been widely embraced by producers and software companies alike.

From the earliest studies initiated years ago, it has been clear that in a construction project, considering all aspects: finishes, facades, MEPs, etc., the structures and foundations play a predominant role in terms of pollution during the initial phases of a building's lifecycle.

The present publication aims to highlight the state of the art in the discipline, underscore some foundational references, and encourage a push within the Italian landscape to promote the development of a national approach to LCA.

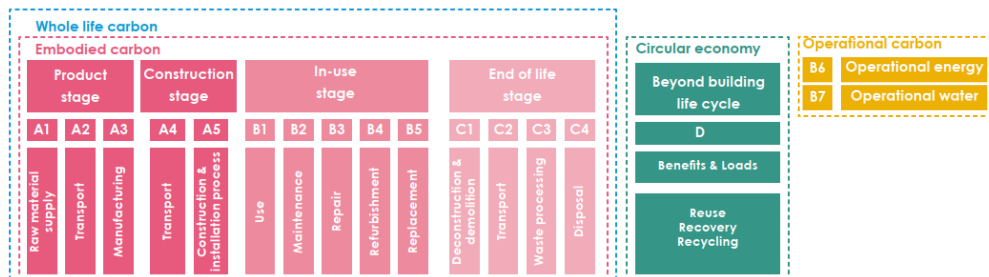


Fig. 6 A foundational outline of a building's life for the application of the LCA approach.

#### 3.1 Literature references

In the field of applying LCA to the construction sector, we have identified some fundamental sources that can serve as references. Among these, several publications and guidelines from prestigious international authors and institutes stand out, including:

- "Embodied Carbon Primer," 2020, by the London Energy Transformation Initiative (LETI);
- "Whole life carbon assessment for the built environment," 2017, by the Royal Institution of Chartered Surveyors (RICS);
- "Model for Life Cycle Assessment of buildings," 2018, by the Joint Research Centre (JRC).

These resources provide practical insights into integrating LCA into building sustainability assessment. In Italy, there is still a lack of significant initiatives by private entities, professional associations, or regulatory bodies to promote the adoption and development of LCA in the construction sector. This disparity highlights the need for greater commitment and coordination within the Italian context to address environmental challenges and promote sustainability. Important references can also be found in standardization norms, such as:

- ISO 14040 and 14044:2006, guidelines for conducting LCA;
- ISO 21930:2017, principles and requirements for assessing impact of construction materials.

Regarding the adoptable assessment scales, there doesn't appear to be a universally recognized classification yet, although one of the initial attempts was the Sustainable Construction and Renovation Scale (SCORS) [5] developed by RICS. However, there is currently no universally recognized reference in this area, both nationally in Italy and internationally.

#### 4 Life cycle assessment in Redesco's application

Drawing from the aforementioned references, we have initiated the initial applications of LCA on projects in the development phase, and subsequently applied them ex-post to projects already completed. The objective was to cultivate greater awareness in design choices and commence the establishment of an initial database of information available to our designers.

The environmental impact of a construction is attributed to the complexity of the pollutants involved; however, concerning the structures of civil buildings in urbanized areas, it has emerged that the most significant indicator is undoubtedly the Global Warming Potential (GWP) [6]. This index particularly illustrates a pronounced peak for phases A1-A3 of the building's life cycle, accompanied by a notable value for phases A4-A5. Pollutant components in phases B generally have a negligible value compared to the total, while studying phases C and D proves more challenging. The treatment of these latter stages is almost never exhaustive due to the lack of strategies on decommissioning, not predetermined by the clients, and essentially due to a regulatory void on the subject.

##### 4.1 Examples of LCA application

One of the early opportunities to engage with LCA was during the development of the project known as "Westgate" by MIND [7] in Milan, where we inherited an initial environmental assessment from the preliminary phase for comparison. The project comprises two buildings constructed with glulam timber and reinforced concrete. There are two main features: the use of timber for the frame and floors, and the disassembly capability due to the dry connections of its components.



Fig. 7 Some features of the buildings and the value of the structures in terms of GWP per square meter of gross floor area, during an intermediate design phase.

The GWP indices presented in the previous image have taken into account the overall impact of carbon sequestration intrinsic to the wooden components. Another noteworthy project, both for its significance and the considerable effort involved, is the headquarters of Banca Pictet in Geneva. The



building features a concrete structure that has been particularly optimized, composed as much as possible of prefabricated elements.

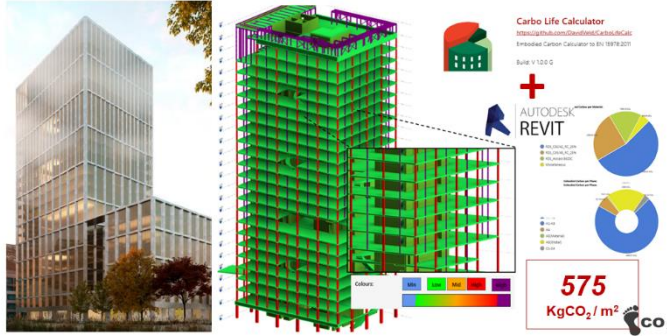


Fig. 8 Extract from the report on the LCA of the Banque Pictet building, executive design phase

The building complex features a 24-story tower with imposing, deep foundations composed of 70-meter-deep concrete "piles" due to the poor mechanical properties of the soil. Despite being mitigated by the optimization of other design aspects, this unfavorable factor resulted in a particularly adverse GWP yield. The LCA in question was implemented using commercial software.

In this context, the client, sensitive to ecological issues, requested an in-depth study on material selection. Specifically, various types of concrete with different binders and percentages of recycled aggregates were examined. An assessment was made in terms of embodied carbon, cost-benefit analysis, structural stiffness, and other technical aspects [8], considering traditional binders with low clinker content, such as CEM II/B, CEM III, and more innovative ones like Super-sulfated Cement (SCC) [9].

Following the initial applications of Life Cycle Assessment for projects in the design phase, we initiated a retrospective analysis of some projects designed and already implemented in past years. In particular, we questioned the positioning of high-rise buildings compared to other building typologies in terms of embodied carbon.

Using available documentation such as the as-built project, bill of quantities, and the testing dossier for structures and foundations, we estimated CO<sub>2</sub> emissions in phases A1-A3 with a certain degree of approximation. Data related to "Torre Generali," the iconic Milanese skyscraper designed by Zaha Hadid, nearly 200 meters tall, whose structures were designed using Algorithms-Aided Design (AAD) [10] processes that strongly influenced the LCA performance, were examined. A similar approach was employed for the review of the project for the "Torre PWC" designed by Libeskind, with its 175 meters, characterized by its concave shape and the presence of a large steel volume at the top called the crown.

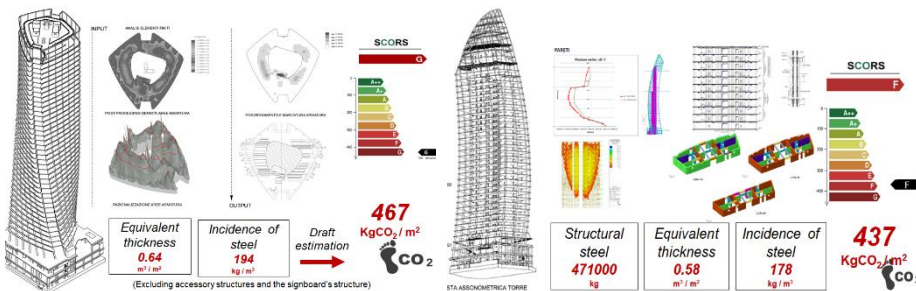


Fig. 9 e 10 Extract from the report on the LCA of Torre Generali and Torre PWC

Taking into account the particular features of these two buildings, along with analyses conducted on other examined projects such as "Torre Malta" and "Tour Pictet," we have gained insights into the environmental impact of tall buildings in terms of CO<sub>2</sub>eq/m<sup>2</sup>.

## 5 Conclusions

We have established a small internal data library, collecting the LCA outcomes of various projects, benchmarks and baselines from different sources, EPDs of materials, and data on energy consumption of construction machinery; assessing the overall environmental impact of our actions. Therefore, we require a broader comparison with professionals and companies who have undertaken a similar path.

Below, we provide an illustrative table summarizing the outcomes of some analyses, the GWP value accompanied by a brief commentary on the distinctive characteristics of the analyzed building.

Table 1 Global warming potential (GWP) Index of selected case studies

Project examined	GWP [kgCO <sub>2eq</sub> /m <sup>2</sup> ]	Comment
Pictet Tower	575	Unfavorable geology
Hadid Tower	467	Structural torsion
Libeskind Tower	437	Structural curvature
Malta Tower	360	Favorable geology and simple geometry
BNL Headquarters	493	Horizontal skyscraper with large cantilevered prow
Mind Westgate	277	Carbon sequestration from wood

Following an essential step, we compared the obtained results with public baselines and benchmarks to assess the positioning of the case studies and improvement margins. Currently, statistically consistent values for such comparisons do not yet exist. However, a good usable source is the EC3 Building Transparency portal by the CLF [11]: a continuously evolving data collection platform where the results of our LCA analyses can be published once completed.

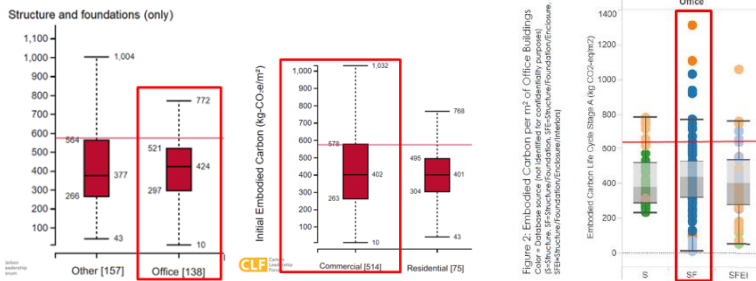


Fig. 11 Extract from an LCA report, identification of baselines and project positioning.

We have found that tall buildings, despite appearances, are not "eco-monsters" in terms of GWP when compared to other building types; on the contrary, they exhibit values entirely comparable to horizontally extended buildings. Despite their specialized nature and sometimes dramatic geometries, they represent a sustainable alternative even from the perspective of embodied carbon.

Multiple aspects have emerged from the experiences described above: specific to individual projects and of a general nature. In accordance with guidelines, we use to prepare a report attached to the calculation report that provides an overview of the environmental footprint of the work. These reports represent a milestone from which to improve LCA in subsequent project phases and are a crucial decision-making and awareness-raising tool for clients. While the general aspects, gradually acquired from various experiences, enrich the know-how of designers and managers.

We know we can get involved on the intrinsic characteristics of structures: optimizing geometries, exploiting all static resources, calibrating performance, selecting materials, even if this entails an increase in design costs. And we hope, in the long term, to be able to get involved on the external characteristics of projects through the promotion of a more modern culture of construction. Indeed,

the boundary conditions on which designers cannot directly act are fundamental. These include urban planning, where geology has a very significant impact on structures and foundations, and contractual and regulatory aspects.

On these latter aspects, what has been observed in various discussion tables and workshops is indicative: the construction sector struggles to innovate environmentally, requiring enlightened action from clients and even more so from legislators. What was previously highlighted requires overcoming the general settings of technical standards for construction.

More flexible regulations are needed, along with a general reduction in safety margins and required performance [12], often distant from real needs, in the face of greater demand for skills and attention from designers.

The lawmaker is called upon to introduce environmental specifications with defined numerical thresholds, as measurable through LCA tools, for example, in terms of available embodied carbon for a work. There is a need for modern technical standards to begin treating CO<sub>2</sub> as a finite resource, following virtuous examples such as Canada or Denmark, which with the introduction of new BR [13] integrate specific limits on pollutant factors into their technical standards.

Finally, given the lack of reliable data and baselines, it would be necessary to sensitize Italian publishers so that specialized publications can bridge the cultural gap. Concepts of measuring the environmental impact of our activity should be included in technical manuals and material price lists as well.

## 6 Future prospects and call for collaboration

Part of the work necessary to improve design practices in ecological terms has been highlighted. Utilizing LCA represents one of the steps to be taken, but it is essential to first build a cultural, informational, and regulatory foundation.

Looking at successful international examples, it becomes clear how important it is to adopt a proactive and collaborative approach. As professionals in Italy, we must aspire to be pioneers of modernization and influence the sector, particularly the legislator, guiding them towards structured, effective, and suitable solutions, rather than passively enduring initiatives due to a lack of preparation.

Through this ACI Italy Chapter publication, we encourage the sharing of data in every form and the initiation of awareness-raising initiatives among all stakeholders, including builders, regulators, and publishers. It is necessary to create a framework to carry out our work in a fully ethical manner, also towards the environment.

## Acknowledgements

Sincere gratitude is extended to all colleagues at Redesco Progetti, whose dedicated efforts in data collection and discussion are crucial for advancing the company's mission. Thanks to Engineer Gian Carlo Giuliani for his vision and initiative, both in this effort and in other capacities, hoping to continue along the path he has set forth.

## References

- [1] Associazione nazionale costruttori edili, ANCE. "Osservatorio" anni 2023-2024 <https://ance.it/>.
- [2] The Paris Agreement 2015. Text presented by United Nations Framework Convention on Climate Change.
- [3] Giuliani, Gian Carlo. 2023. "Impalcati a piastra". Internal report of Redesco Progetti.
- [4] Nervi, Pier Luigi. 1945. *Scienza o arte del costruire? Caratteristiche e possibilità del cemento armato*. Rome: Edizioni delle Bussola.
- [5] Gibbons, O.P., and Orr J.J. 2020. "How to calculate embodied carbon." The institution of Structural Engineers, London.
- [6] LETI. 2020. "Embodied carbon primer." First edition Jan 2020.
- [7] Master plan "Milan Innovation District." Info accessed by <https://www.mindmilano.it/>.
- [8] Coppola, Luigi, and Coffetti, Denny. 2021. "Il futuro del calcestruzzo. Molteplici strategie con un obiettivo comune: la sostenibilità." University of Bergamo.
- [9] Qingyong, and Zhuqing. "Research status of super sulfate cement." Nanjing Tech University.
- [10] Tedeschi, Arturo. 2014. *Algorithms aided design*. Potenza: Le Penseur
- [11] CLF Building transparency EC3 tool. Accessed by <https://carbonleadershipforum.org/>.
- [12] Solari, Giovanni. 2019 "L'ingegneria del vento". TEDxGenova
- [13] Danish Ministry of Transport, Building and Housing. "Bygningsreglementet."

# Comprehensive environmental comparison of different structural systems for multistorey buildings in Italian and French contexts

Laura Corti<sup>1</sup>, Manuel Manthey<sup>2</sup>, Pierre Navaro-Auburtin<sup>2,3,4</sup> and Giovanni Muciaccia<sup>1</sup>

<sup>1</sup>*Politecnico di Milano, piazza Leonardo da Vinci 32, Milano (20133), Italy*

<sup>2</sup>*CSTB (Centre Scientifique et Technique du Bâtiment), 84 Av. Jean Jaurès, F-77477 Champs-sur-Marne, France*

<sup>3</sup>*Laboratoire Navier, UMR 8205, ENPC, IFSTTAR, CNRS, 6-8 Av. B. Pascal, F-77455 MLV Cedex 2, France*

<sup>4</sup>*AREP, 16 Av. d'Ivry, F-75013 Paris Cedex 13, France*

## Abstract

Considering the path of sustainable development, it is necessary to make a step towards integration of multi-criteria design rules with assessment of environmental impact. This achievement is attainable through consideration of the whole building, with a broad perspective that aims at exploring critical points. One of the discussion topics is the utilization of bio-based materials, such as timber, which along with several environmental benefits, intrinsically carries some weaknesses that call out the necessity of combination with other materials. Starting from a benchmark of a reinforced concrete building, structural components are redesigned on an iso-performance basis, accounting for three alternatives: using only timber, a hybrid timber-steel solution and a hybrid timber-steel-reinforced concrete solution. According to the obtained results, the feasibility of the studied buildings considering the known established conditions (e.g., location, specific national regulations, etc.) is assessed. This is conducted with a constant monitoring of the environmental impact through cradle-to-cradle Life Cycle Analysis (LCA). The first focus is the assessment of uncertainties linked to the LCA, since the scenario adopted for the End-of-Life stage and for the manufacturing procedures drives the total environmental impact. The second target is establishing, according to external normalisation approach, relevance of other pollutants apart from carbon dioxide. The paper provides a comprehensive perspective concerning design of new multistorey buildings, where the potential benefits of composite solutions, both at level of single members and of the whole buildings, are fully exploited by assessing both structural and environmental performances at once.

## 1 Introduction

The issue of climate change is now very well-known to everyone, and it is widely acknowledged the role of human being in exponentially accelerating this process: this fact did come to the attention in the last years, since COP conferences became popular even in non-scientific contexts. Tracing the path of climate change negotiations, the first international meeting dates back to 1972, when the United Nations Conference on the Human Environment took place in Stockholm; this was the kick-off point that led first to make the scientific population aware of modifications on the Earth's surface, and then, with some delays, the government started to develop policies to limit greenhouse gases emissions, up to the newest aims of carbon neutral society [1]. Focusing on the European context, the negotiations speeded up in the last years: starting from aim of cutting at least 40% greenhouse gases (GHG) emissions by 2030 (with reference to 1990 values), established according to Paris Agreement [2], in 2021 the goal was improved to a reduction of 55% within 2030, in order to reach carbon neutrality before 2050 [1].

As one of the largest CO<sub>2</sub> emitters, the building sector carries out a key role in driving new policies, practical actions, and innovative solutions in order to counteract climate change and its harmful consequences. This sector is one of the most promising ones in guarantying remarkable lowering in CO<sub>2</sub> emissions, so that it is necessary to continuously update methodologies, on the one hand with strict regulations and on the other hand through constant scientific research. Considering European countries, they are welcome to develop regulations tailored on regional needs and specific aims: the framework remains the European guidelines, but even more ambitious goals can be targeted. An illustrative set of

two virtuous examples addressing regulations for building materials, waste processing and environmental impact of new and existing buildings is collected and hereby listed:

- In Italy according to the last update of Piano Nazionale Integrato per l'Energia e il Clima (PNIEC – National Integrated Plan for Energy and Climate) [3], the energy efficiency of buildings is targeted to reach every two-year period higher savings. The financial investments are planned to be 70% aimed for improving energy efficiency of existing building and 30% to build high energy efficiency buildings with low carbon footprint. Concerning building materials, some guidelines were established according to a decree on minimum environmental criteria for construction projects [4], requiring a minimum value of recycled materials for concrete (5%) and steel (the percentage varies according to the manufacturing procedures and the use). Considering e.g., an alloy steel for structural use manufactured in an electric arc furnace, the minimum quantity recycled is 75% and certifications of sustainable forest source (e.g., Forest Stewardship Council® or Programme for Endorsement of Forest Certification schemes) for timber products.
- In France the Stratégie Nationale Bas-Carbone (SNBC) [5] is specifically tailored for the building sector with the RE 2020 Environmental Regulations [6]. In this case, a specific focus is devoted to dynamic consideration of climate change effects: the increase in the number and intensity of heatwaves is taken into account, and the additional energy consumption to guarantee summer thermal comfort is calculated. Moreover, considering new energy efficient buildings, emissions related to construction and demolition stages embrace 60% to 90% of their whole life impact. Thus, the regulations enforce decreasing maximum thresholds for GHG emissions; considering e.g., residential buildings GHG emissions from energy consumption were 14 kg CO<sub>2</sub>/m<sup>2</sup>/year, they must be reduced to 6.5 kg CO<sub>2</sub>/m<sup>2</sup>/year by 2025. On the other hand, the use of wood and bio-based materials is strongly encouraged, and it is foreseen to be a common choice by 2030: this expectation is motivated by challenging targets established by national regulations.

Considering both regulations at the European and at the national levels highlights the importance of always considering the specific conditions that shape a regional framework: common guidelines are the usual way to set and to reach mutual objectives, but this cannot be pursued disregarding necessities, peculiarities, local conditions, etc.

Considering new buildings, choice of the structural system is a major driving parameter that affects the whole design process and consequently environmental impact, costs, and easiness in requirements fulfilment. One of the increasingly widespread solution is the use of engineered timber products (ETP) for structural elements [7], often combined with other traditional materials, as reinforced concrete, and steel, in order to arise hybrid solutions [8]. Therefore, timber used as a structural and engineered material should be properly investigated, to reach a knowledge comparable to other more widespread materials. It is essential to assess timber environmental impact according to Life-Cycle Assessment (LCA) analysis, focusing on different End-of-Life (EOL) stage options (Hart & Pomponi, 2020); traditionally, timber can be reused, recycled, incinerated (with energy recovery) or landfilled, but it is practically unrealistic to foresee 100% EOL scenario (e.g., 100% reuse scenario), so that mixed scenarios became of primary importance. In this context it is worth mentioning the France case study [9], since an established mixed scenarios is available for timber EOL stage, according to collected data on nowadays practices; timber members are hereby recycled (57%), incinerated with energy recovery (26%) and landfilled (17%).

This research focuses on a holistic comparison carried out on two equivalent multistorey buildings with four different structural systems located in two European countries (Italy and France), in order to evaluate the effects of site specific requirements on structural members design, environmental impact according to LCA analysis, and different seismic behaviours. Investigated structural systems are:

1. Full reinforced concrete solution (RC);
2. Full timber solution (T);
3. Hybrid timber-steel solution (T-S);
4. Hybrid timber-steel-reinforced concrete solution (T-S-RC).

The novelty introduced within this research is focused on two tailored scenarios for every considered material, since standard and traditional solutions are compared with sustainable and environmentally optimised options.




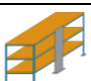
Concerning Italian context, a special attention is devoted to design the building in Ductility Class High (DCH, according to Eurocode 8) [10], while for this French case study no particular concern is required for seismic design, so that DCL (Ductility Class Low) is applied for design. Considering that Italian case study is designed in DCH, thicknesses of shear walls are dominated by seismic requirements, while for French one shear walls design is driven by fire regulations [11]. Moreover, in timber and hybrid Italian solutions slabs are fully made of timber, while in the French ones they are characterised by timber-concrete composite solutions, in order to maintain limited thickness and optimise acoustic insulation. These structural differences should be considered when carrying out environmental comparison, as an acknowledgement of the fact that decontextualizing building design from its environment is meaningless.

The paper is organised as follows: methodology, hypotheses and relevant differences between Italian and French buildings are addressed in section 2, obtained results are outlined in section 3, discussion and comparisons are presented in section 4, and conclusions with foreseen future development are provided in section 5.

## 2 Method

The investigation presented in this paper firstly assesses the feasibility of different structural systems, according to site-specific requirements and considered regulations. Characteristics of each solution are listed in Table 1.

Table 1. Structural systems characteristics of different investigated solutions for Italian (IT) and French (FR) case studies. GLT=glued-laminated timber; CLT=cross-laminated timber.

Building structural system	Beams	Columns	Slabs	Walls	Foundations
RC 	Reinforced concrete	Reinforced concrete	Reinforced concrete	Reinforced concrete	Reinforced concrete
T 	GLT	GLT	CLT	CLT	Reinforced concrete
T-S 	Steel	Steel	CLT	CLT	Reinforced concrete
T-S-RC 	Steel	Steel	CLT	Reinforced concrete	Reinforced concrete

RC solution is considered since it is the most widespread structural systems in Italy and France, while T solution is studied in order to provide a low-carbon emission target for new buildings. On the other hand, T-S solution is basically equivalent to solution 2, where beams and columns are optimised with steel sections. Eventually, T-S-RC solution is provided with RC shear walls, to make it easily suitable for regions characterised by medium and high seismicity.

Thereafter, in order to provide a comprehensive environmental assessment, two alternatives – “traditional” and “low-carbon” – for each considered material (timber, steel, and concrete) are presented. Engineered timber products (e.g., CLT and GLT) are already low-carbon impacts materials, so the focus is on the End-of-Life scenario; on the other hand, steel and concrete carbon emissions are mainly detected in the manufacturing phases, so that the focus is on LCA stage A. Description of each materials environmental alternative is presented in Table 2.

Table 2. Structural materials environmental assessment.

Material	Traditional solution (1)	Low-carbon solution (2)
Timber (X)	FCBA scenario is adopted for timber EOL [9]. Recycling (57%), incineration with energy recovery (25%), landfilling (17%)	“High-reuse prospective scenario” is developed, starting from FCBA one. Reuse (40%), recycling (24%), incineration with energy recovery (24%), landfilling (10%)
Steel (Y)	Steel manufacturing is processed in blast furnace, data from AIE4B software [12]	Steel manufacturing is processed in electric arc furnace supplied by 100% renewable energy, data averaged from selected European EPD [13], [14], [15], [16]
Concrete (Z)	Concrete is produced with traditionally manufactured cement (with high-clinker content), data from AIE4B software [12]	Concrete is produced with cement characterised by low-clinker content, data averaged from selected European EPD [17], [18], [19]

According to each material’s scenario, a set of scenarios for every building is hereby assessed, considering that every building structural system is followed by a triplet in the form X(=timber).Y(=steel).Z(=concrete), where each variable can assume one of these three values:

- 1, the material is considered according to its traditional solution
- 2, the material is considered according to its low-carbon solution
- 0, the material is not present (e.g., X=0 for RC building)

LCA analysis is carried out considering stages A to D (“cradle-to-cradle”) in terms of different parameters, in order to provide a comprehensive overview of the environmental impact of the structural part of a building. Choice of the parameters was motivated by the necessity to investigate other environmental fields apart from climate change and the listed parameters are the ones available for every material according to the involved sources and software:

- Global Warming Potential (GWP), measured in kg CO<sub>2</sub> eq.;
- Acidification Potential (AP), measured in kg SO<sub>2</sub> eq.;
- Ozone Depletion Potential (ODP), measured in kg CFC-11 eq.;
- Fossil Fuel Consumption (FFC), measured in MJ.

To improve interpretation of the LCA analysis results, the building impact is compared with the impact of a person during a European average lifespan, according to external normalisation approach [20] as listed in Table 3.

Table 3. Environmental impact of a person during the whole lifespan (lifespan assumed as a European average value).

LCA parameter	Impact per capita (average European lifespan)	Geographical and temporal accuracy
GWP (kg CO <sub>2</sub> eq.)	44.000 [21]	European Union (EU27), 2020 data
AP (kg SO <sub>2</sub> eq.)	3.390 [22]	Worldwide, 2010 data
ODP (kg CFC-11 eq.)	4.84 [22]	Worldwide, 2010 data
FFC (MJ)	5.200.000 [22]	Worldwide, 2010 data

## 2.1 Italian building design

Design of Italian building is developed starting from reinforced concrete (RC) solution and subsequently assessing the alternatives. It is a residential building located in Milan and characterised by 8 storeys with interstorey height of 3.35 m; the structural plan is approximately 64x14 m and regularity in plan and elevation is guaranteed. The building is designed according to Eurocode 8 DCH.

## French building design

Design of French building is made using a tool developed for study [22]. Starting from the drawing of a building geometry, spans and loads are deduced for each structural element. The dimensions of each structural element are then deduced from a pre-established database of pre-calculated structural elements (according to Eurocodes and to French Regulations). The geometry of the building was chosen similar to the Italian residential building mentioned above.

## 3 Results

Results are presented in terms of structural masses and LCA parameters defined in section 2, considering each structural element (beams, columns, slabs, shear walls, and foundations) impact.

### 3.1 Structural masses

According to results presented in Figure 1, the major share of masses comes from the slab for RC solutions, since in Italian and French buildings they represent respectively 50% and 56% of the total masses. On the other hand, in case CLT slabs are used, the total mass building reduction is significant, given that in Italian and in French buildings the slabs masses respectively shift from 3.880 and 4.170 tons to 833 and 1.486 tons.

Considering different structural alternatives, the noticeable gap between RC and other solutions acknowledges that, according to structural masses perspectives, focusing on slabs is already sufficient to emphasise a consistent mass reduction. On the other hand, in T, T-S and T-S-RC solutions the percentage mass share of other structural elements becomes more important, leading to a major level of attention in the environmental analysis; considering T and T-S solutions, the foundations account approximately for 35% of the total masses, since they are always made with reinforced concrete. The same rationale is valid for RC shear walls in T-S-RC building, which mass share accounts approximately for 25%.

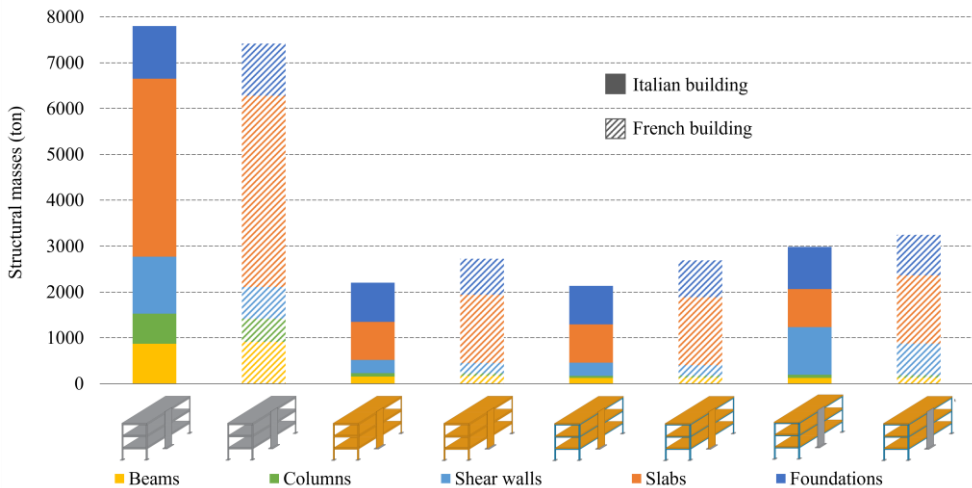


Figure 1. Masses of structural elements for studied structural systems in Italian and French buildings.

### 3.2 LCA analysis

The environmental analysis focuses firstly on GWP, and successively comparisons with other parameters impact are carried out. GWP impact of each case study is presented in Figure 2; considering RC-0.1.1 cases the slabs impact is approximately  $1\text{E}06$  kg CO<sub>2</sub> eq., while their contribution in Italian and French timber buildings (T-2.2.2) respectively decrease up to  $5.5\text{E}04$  and  $9.2\text{E}04$  kg CO<sub>2</sub> eq., driving the overall environmental impact. It is also worth comparing results of the same structural systems characterised by materials with different environmental impacts, according to assessment outlined in Table 2; 0.2.2 RC alternative is characterised by 65% GWP impact reduction with respect to 0.1.1, with a decrease in the range of one order of magnitude. On the other hand, also in the other structural systems



the use of low-carbon building material alternatives results in significant reduction in terms of kg CO<sub>2</sub> eq., but GWP order of magnitude remains the same since it is already low due to the presence of timber.

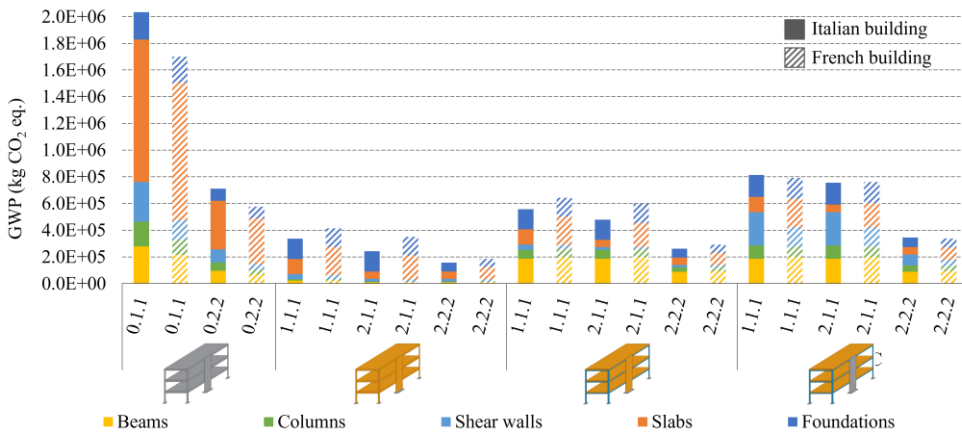


Figure 2. Percentage environmental impact, in terms of GWP, clustered by structural elements.

Considering that LCA analysis aims at providing a comprehensive overview of the environmental impact of a product, buildings impact according to a wider range of parameters is calculated, with reference to impact per capita, as shown in Table 4.

Table 4. LCA analysis results of buildings’ structural systems with reference to equivalent people impact during an entire lifespan.

Structural system and scenario	GWP impact	AP impact	ODP impact	FFC impact
RC – IT (0.1.1)	5 person icons	2 person icons		2 person icons
RC – FR (0.1.1)	5 person icons	2 person icons		2 person icons
T – IT (2.2.2)	1 person icon	1 person icon		1 person icon
T – FR (2.2.2)	1 person icon	1 person icon		1 person icon

According to results presented in Table 4, it is possible to cluster LCA parameters in two classes of importance, regarding relevance in terms of harmfulness and improvements achieved moving from reinforced concrete to timber buildings:

- Class 1 includes GWP, AP, and FFC. All parameters highlight a reduction shifting from T to RC building, where impact of the studied full timber solution is always lower than 1 person;
- Class 2 includes ODP. In this case the impact is just minimally affected by the structural system, and it is always extremely low.

#### 4 Discussion

The results carried out in the context of this analysis confirm the correctness of the prioritization methodology adopted, as slabs optimisation is the main reason behind GWP decrease. Slabs optimisation is intended in a wide context, since different solutions are considered, starting from use of concrete with low clinker cement, up to material substitution in the case of full CLT slabs. Another observation noticeable from the results is the broad range of advantages derived from slabs masses reduction when shifting from RC building to other solutions. The first and most evident result is cross section reductions in both vertical and horizontal elements, consequently followed by lighter foundations. Timber material offers the possibility of high level of prefabrication with better control of the whole manufacturing

process. This allows reduced construction times, higher construction quality. Moreover, waste and materials consumption are reduced, leading to economical and environmental benefits.

This investigation aims at being holistic, and to develop comparative and comprehensive analysis. Comparability is guaranteed by the presence of buildings in two different European countries, both assessed with different structural systems and studied with several material scenarios. On the other hand, comprehensiveness is ensured by considering other parameters for LCA analysis apart from GWP: this way the environmental impact of a building is evaluated not just in terms of climate change, but also considering indicators related to ecosystem quality (AP and ODP), human health (ODP), and resources depletion (FFC).

## 5 Conclusions

The initial aim of this investigation – comparing two equivalent residential buildings in the European context – revealed a much wider variety of topics that were investigated, starting from concept of equivalent buildings, which should be tailored, case by case, to the geographical location, building site, national regulations, etc. Moreover, the importance of considering more than a single scenario for LCA analysis is highlighted by significant gaps in the results, comparing both traditional and low-carbon solutions and reinforced concrete with timber ones; this conclusion arises from the fact that a product environmental impact is the result of a process where reusing and recycling practices establish key points.

On the other hand, it is worth considering that availability of low-carbon materials (e.g., concrete produced with low-clinker content cement) may not be homogeneous, so the prioritization of elements environmental impact is once again a key point. Another issue is linked with costs, as engineered timber products are, for now, more expensive than concrete, so considering barely the economic perspective timber and low-carbon reinforced concrete buildings results unfavourable with respect to traditional reinforced concrete one; on the other hand, it is necessary to consider also other parameters that support the benefits of such alternative solutions, not just from environmental outlook. Considering e.g., T-S-RC building with respect to RC one, it results in a total mass much lighter due to timber slabs and steel beams and columns, but lateral stiffness in case of strong lateral loading – e.g., earthquakes – is still ensured; on the other hand, presence of CLT shear walls may result in insufficient lateral stiffness and consequent excessive lateral drifts with extended and expensive damages.

It is worth mentioning that optimisation of carbon impact is not a fixed and permanent path, but it should be shaped as a function of building characteristics and site features; methodology standardisation is a desirable target, carried out with proper consideration of such characteristics that make each building unique and which lead to proper optimisation of environmental impact.

## Acknowledgements

Authors wish to acknowledge Nicolas Pinoteau and Omar Al-Mansouri from CSTB for the invaluable organisational support; moreover, authors thank François Consigny and Manuel Bazzana from CSTB for their precious advices for the environmental analysis. Authors are also grateful to Giulia Cavenago from Polimi for her essential support in the comprehension of LCA methodological issues.

## References

- [1] Fetting, Constanze. 2020. *The European Green Deal*. Wien: ESDN report.
- [2] United Nations Framework Convention on Climate Change. 2015. *Paris agreement*. Paris: HeinOnline.
- [3] Ministero dell'Ambiente e della Sicurezza Energetica. 2023. *Piano Nazionale Integrato per l'Energia e il Clima*.
- [4] Ministero della transizione ecologica. 2022. Decreto 23 giugno 2022, in G.U. n. 183 del 6 agosto 2022. *Criteri ambientali minimi per l'affidamento del servizio di progettazione di interventi edilizi, per l'affidamento dei lavori per interventi edilizi e per l'affidamento congiunto di progettazione e lavori per interventi edilizi*.
- [5] Ministère de la Transition Écologique. 2020. *Stratégie Nationale Bas-Carbone (SNBC)*.
- [6] Ministère de la Transition Écologique et de la Cohésion des Territoires. 2023. *Réglementation environnementale RE2020*.
- [7] Yadav, Ranjana, and Kumar, Jitendra. 2021. "Engineered Wood Products as a Sustainable Construction Material: A Review." London: IntechOpen. doi: 10.5772/intechopen.99597.

- [8] D'Amico, Bernardino, Pomponi, Francesco, and Hart, Jim. 2021. "Global potential for material substitution in building construction: The case of cross laminated timber." *Journal of Cleaner Production* 279. doi: 10.1016/j.jclepro.2020.123487.
- [9] FCBA. 2022. GDBAT : Gestion des déchets de produits de construction bois en fin de vie, Phase 2 : Modélisation ACV de la gestion des déchets bois de classes BR1 et BR2
- [10] European Committee for Standardization. 2005. *Eurocode 8: Design of structures for earthquake resistance. Part 1-1: General rules, seismic actions and rules for buildings*. Brussels.
- [11] Ministère de l'intérieur et de la décentralisation et le ministre de l'urbanisme, du logement et des transports. 2022. *French fire regulation for residential building « Arrêté du 31 janvier 1986 Modifié relatif à la protection contre l'incendie des bâtiments d'habitation »*
- [12] ASMI. *Impact Estimator for Buildings v.5.5.01*. Athena Sustainable Material Institute: Ottawa, ON, Canada. Accessed April 2, 2024. <https://calculatelca.com/software/impact-estimator/>.
- [13] ArcelorMittal Europe. 2021. *EPD in accordance with ISO 14025 and EN 15804+A1 - XCarb™ Recycled and renewably produced Reinforcing steel in bars and coils*. Institut Bauen und Umwelt e.V. (IBU). Accessed April 2, 2024. <https://europe.arcelormittal.com/sustainability/xcarb/RRP/recycled-and-renewably-produced-flat-long-epd#long>.
- [14] ArcelorMittal Europe. 2021. *EPD in accordance with ISO 14025 and EN 15804+A1 - XCarb™ Recycled and renewably produced Structural steel sections and merchant bars*. Institut Bauen und Umwelt e.V. (IBU). Accessed April 2, 2024. <https://europe.arcelormittal.com/sustainability/xcarb/RRP/recycled-and-renewably-produced-flat-long-epd#long>.
- [15] Stahlwerk Thüringen GmbH. 2022. *EPD in accordance with ISO 14025 and EN 15804+A1 – Structural Steel: Sections*. Stahlwerk Thüringen GmbH. Institut Bauen und Umwelt e.V. (IBU). Accessed April 2, 2024. [https://www.stahlwerk-thueringen.de/files/17EA0F6B493/SWT\\_Green\\_Steel\\_EPDPDF?randID=18E9E5A667E](https://www.stahlwerk-thueringen.de/files/17EA0F6B493/SWT_Green_Steel_EPDPDF?randID=18E9E5A667E)
- [16] Metalúrgica Galaica S.A. 2023. EPD in accordance with ISO 14025 and EN 15804+A2 - Hot-rolled ribbed steel proceeding from electric arc furnace. Accessed April 2, 2024. [https://www.en.aenor.com/Productos\\_DAP\\_pdf/MEGASA\\_001-007.pdf](https://www.en.aenor.com/Productos_DAP_pdf/MEGASA_001-007.pdf)
- [17] Hoffmann Green Cement Technologies. 2020. *Fiche de déclaration environnementale et sanitaire du produit en conformité avec les normes NF EN ISO 14025, NF EN 15804+A1 et son complément national NF EN 15804/CN - Plancher en béton non ferrailé d'épaisseur 20 cm, C35/45 H-UKR XC1 S5*. Programme FDES-INIES. Accessed April 2, 2024. <https://www.base-inies.fr/iniesV4/dist/infos-produit>
- [18] Lafarge France. 2023. *Fiche de déclaration environnementale et sanitaire du produit en conformité avec les normes NF EN ISO 14025, NF EN 15804+A1 et son complément national NF EN 15804/CN, et les Règles de Catégorie de Produit béton EN 16757 - ECOPact A C25/30 XC1 Dalle plein en béton d'épaisseur 0.23 m, C25/30 XC1 CEM III/B*. Programme FDES-INIES. Accessed April 2, 2024. <https://www.lafarge.fr/fdes>
- [19] Syndicat National du Béton prêt à l'Emploi. 2022. *Fiche de déclaration environnementale et sanitaire du produit en conformité avec les normes NF EN 15804+A1 et son complément national NF EN 15804/CN, et les Règles de Catégorie de Produit béton EN 16757 - Béton Impact réduit Dalle plein en béton d'épaisseur 0.20 m, C25/30 XC1 CEM III/A*. Programme FDES-INIES. Accessed April 2, 2024.
- [20] Pizzol, Massimo, Laurent, Alexis, Sala, Serenella, Weidema, Bo, Verones, Francesca, Koffler, Christoph. 2017. "Normalisation and weighting in life cycle assessment: quo vadis?" *The International Journal of Life Cycle Assessment* 22. doi: 10.1007/s11367-016-1199-1
- [21] Climate Watch. 2022. Historical GHG emissions. Accessed April 5, 2024. [www.climate-watchdata.org](http://www.climate-watchdata.org)
- [22] Andreasi Bassi, Susanna, Biganzoli, Fabrizio, Ferrara, Nicola, Amadei, Andrea, Valente, Antonio, Sala, Serenella, Ardente, Fulvio. 2023. "Updated characterisation and normalisation factors for the Environmental Footprint 3.1 method." European Commission, Joint Research Centre. doi: doi.org/10.2760/798894
- [23] Navaro Auburtin, Pierre, Baverel, Olivier, Saadé, Myriam, Manthey, Manuel, Louërat, Mathilde, Martin, Jean-Luc. 2023. "Environmental impacts of early stage structure choices using Life Cycle Assessment." *Academic Journal of Civil Engineering* 41. doi: 10.26168/ajce.41.1.17.

# Design and feasibility of sustainable solution for the Genoa sub-port tunnel project

Simone Spagnuolo<sup>2</sup>, Francesca Magnelli<sup>1</sup>, Matteo Pierani<sup>1</sup>, Andrea Magliocchetti<sup>1</sup>, Alberto Meda<sup>2</sup>

<sup>1</sup>*Tecne Gruppo Autostrade per l'Italia S.p.A.,  
Via Bergamini 50, 00159 Rome, Italy*

<sup>2</sup>*University of Rome Tor Vergata,  
Tunnelling Engineering Research Centre (TERC)  
Department of Civil Engineering and Computer Science Engineering  
Via del Politecnico 1, 00133 Rome, Italy*

## Abstract

The sub-port tunnel project forms an integral component of Genoa's urban road infrastructure, traversing the basin of the old port as an alternative to the existing causeway. Its primary objective is to enhance connectivity with the port area, establishing a direct link between the city's western and eastern sectors. The project aims to bolster the efficiency of rapid road penetration and transit through the city center, particularly by circumventing heavy vehicle traffic. Upon implementation, the tunnel is anticipated to contribute to the revitalization of the city's waterfront, reducing travel times, and delivering environmental benefits to the populace.

The undertaken activities have focused on assessing the feasibility of substituting a portion of energy intensive ordinary Portland cement with low carbon concrete, employing a calcium sulfoaluminate binder for fabricating precast concrete tunnel lining segments. Additionally, the conventional steel reinforcement has been replaced with a hybrid solution comprising glass fiber reinforced polymer (GFRP) bars in combination with fiber reinforced concrete (FRC). Engineered to withstand marine environmental conditions and unaffected by corrosion, this solution should ensure longevity without necessitating subsequent maintenance or repair interventions. Finally, to evaluate its cost-effectiveness and sustainability, comprehensive data on the utilized raw materials have been collected for Life Cycle Assessment (LCA) analysis, examining the environmental implications associated with the production of the new segments.

## 1 Introduction

This study is part of the broader project for the Genoa sub-port tunnel, as reported in Fig 1. The main work consists of two tunnels, 15 m diameter each, with a length of approximately 3400 m, excavated with Tunnel Boring Machine, which underpasses the port area of Genoa.

In the first length of 650 m, the tunnel underpass the west harbour area with increasing coverage up to 30 m, then for 400 m the tunnel goes under the seabed inside the harbour basin, with decreasing coverage until a minimum of 13 m and hydraulic head around 33 m. After that, the tunnel underpass the harbour east area for 950 m with coverage around 25-26 m and then the last length until the entrance of the tunnel Levante side along Viale Brigade Partigiane with significative coverage, from a maximum of 73 m to a minimum of 16 m.

Specifically, the study aims to analyze the environmental impacts associated with two construction methods for the construction of the precast concrete tunnel lining, with 15.4 m external diameter and thickness of 0.55 m. Applying the Life Cycle Assessment (LCA) methodology, the carbon footprint (CFP) of two design solutions will be estimated. The two types of lining guarantee the same structural performance by using different materials: a traditional reinforced segmental lining (classic solution)

and a new proposed hybrid solution consists of fiber-reinforced sulfoaluminated concrete segmental lining with glass fiber reinforced polymer (GFRP) bars (innovative solution).

In addition, qualitative considerations about road traffic and chemical resistance in marine environments are taken into account in order to evaluate sustainability beyond environmental boundaries.



Fig. 1 Genoa sub-port tunnel chorography.

## 2 Sub-port tunnel

The construction project is 3.4 km long work with the aim of enhancing the road connections between the west (Ponente) and the east (Levante) of the city, thus pursuing urban regeneration and enhancing the cultural heritage. Excavation is carried out by a 16 m diameter Hydrosshield Tunnel Boring Machine (TBM). The tunnel is supported by a reinforced concrete ring formed by nine modular units (segment). The impacts, in terms of climate-altering emissions, have been considered only for the segment constituting the tunnel support ring.

### 2.1 Comparing design solutions

The safety-check procedure based on the interaction diagrams is clarified through an example of practical application. Furthermore, a comparison with a tunnel segment with traditional steel reinforcement is developed to show the potential of the proposed hybrid solution.

The reference segment (classic solution) is reinforced with a traditional steel cage made of 15  $\varnothing 14$  mm longitudinal bars placed at the intrados and extrados surfaces.  $\varnothing 8$  mm stirrups, distributed along the segment, are used as transversal reinforcement. The total amount of steel is 476 kg/segment (incidence equal to 93 kg/m<sup>3</sup>). Table 1 shows the technical specifications of the materials used to design the traditional precast concrete segments.

The new hybrid solution is designed according to CNT-DT203/2006 and the guidelines of the Higher Council of Public Works within the Italian Ministry of Infrastructure and Transport (MIT), for the use of GFRP and FRC, respectively. The innovative solution is designed to provide the comparable design capacity of the reference one. This precast concrete segment is reinforced with 8  $\varnothing 13$  longitudinal GFRP closed-ring bars plus an uniform distribution of steel fibres along the segment.

The total amount of GFRP is 102 kg/segment (incidence equal to 20 kg/m<sup>3</sup>). Moreover, the total amount of steel fibres is 205 kg/segment (incidence equal to 40 kg/m<sup>3</sup>). Table 2 shows the technical specifications of the materials used to design the innovative precast concrete segments.

The design bending moment-axial force interaction diagrams, for both segments (traditional and innovative), are compared in Fig.2 showing the comparable structural capacity.

In addition to the differences summarized in Tables 1 and 2, further point of divergence between the two solutions concerns the maturation of the precast concrete segments. According to the traditional solution, in fact, the concrete needs a specific steam curing, in a pre-treatment plant, to reach a required compressive strength before its demoulding from the formwork. Conversely, for the innovative solution for which the concrete is based on calcium sulfoaluminated binder, the segment can be manufactured directly on site, without the need for a dedicated curing plant [1].

Table 1 Materials' technical specifications of traditional solution.

Traditional concrete	
Compressive strength class	C40/50
Compressive strength at 28 days	$f_{cd} = 0.85f_{ck}/1.5 = 22.7 \text{ MPa}$
Young Modulus at 28 days	$E_{cm} = 22000(f_{cm}/10)^{0.3} \text{ MPa} = 35 \text{ GPa}$
Maximum operation compressive strength	cfr. § 4.1.2.2.5 DM 17/01/18
Exposure classes	XS2 (UNI EN 206-1)
Nominal concrete cover	50 mm
Reinforcing steel bars 15Ø14	
Type	B 450 C
Design tensile strength	$f_{yd} = f_{yk}/\gamma_s = 450/1.15 = 391 \text{ MPa}$
Young modulus	$E_s = 200 \text{ GPa}$

Table 2 Materials' technical specifications of innovative solution.

Fiber-reinforced concrete (FRC)	
Compressive strength class	C45/55 – 4c
Compressive strength at 28 days	$f_{cd} = 0.85f_{ck}/1.5 = 25.5 \text{ MPa}$
Young Modulus at 28 days	$E_{cm} = 22000(f_{cm}/10)^{0.3} \text{ MPa} = 36 \text{ GPa}$
Tensile strength	$f_{R3k} = 3.6 \text{ MPa}$
Design tensile strength	$f_{t,d} = (f_{R3k}/3)/1.5 = 0.8 \text{ MPa}$
Nominal concrete cover	40 mm
Reinforcing GFRP bars 8 Ø13	
Characteristic tensile strength	$f_{fk} = 760 \text{ MPa}$
Design tensile strength	$f_{fd} = 0.7f_{fk}/\gamma_f = 532/1.5 = 355 \text{ MPa}$
Young Modulus	$E_f = 46 \text{ GPa}$

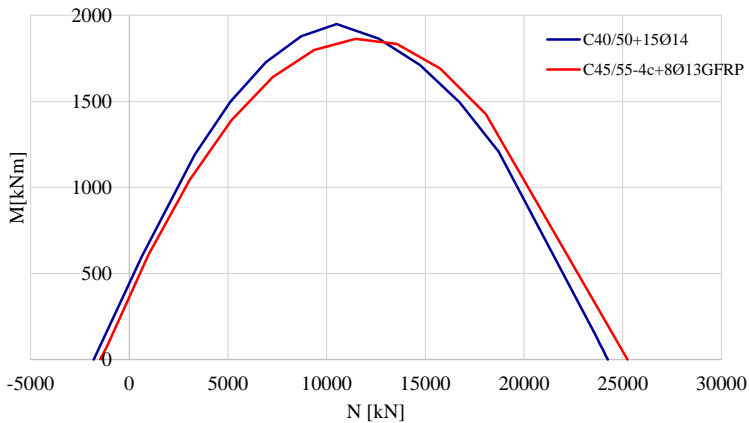


Fig. 2 Bending moment-axial force interaction diagrams at Ultimate Limit State (ULS): traditional versus innovative solution.

### 3 Life-Cycle assessment (LCA)

The determination of the carbon footprint (CFP) is based on principles, requirements and guidelines identified in international standards on Life Cycle Assessment. Carrying out the CFP is equivalent to implementing an LCA that expresses the results in terms of climate-changing emissions quantified in kg of carbon dioxide equivalent (kg CO<sub>2eq</sub>) [2].

Based on the current ISO standards [3-4], an LCA study consists of the following steps.

- Goal and scope definition: preliminary phase in which the purpose of the study, the functional unit, the boundaries of the system studied, and the assumptions are defined;
- Inventory analysis: quantification of incoming and outgoing flows for all analyzed processes;
- Impact assessment: aggregation of inventory results, with scientific modelling, into potential environmental impacts;
- Interpretation: analysis of results.

The four steps of a life cycle assessment are interrelated, making the entire process iterative, as shown in Fig. 3. In fact, each step is based on the results obtained in the previous step. This promotes the completeness and consistency of the study, and any changes made at previous steps are carried over to subsequent levels of the analysis.

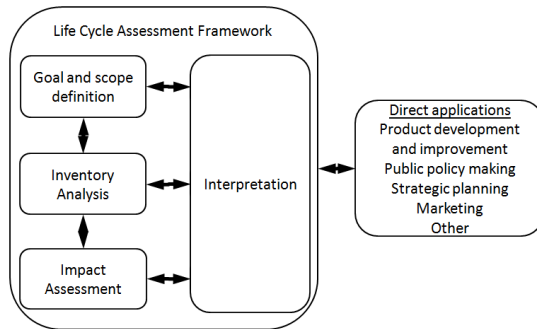


Fig. 3 LCA framework – ISO 14040/14044.

#### 3.1 Goal and scope definition

This study analyses the environmental implications of the production and transport to the construction site of reinforced concrete segments used in the realization of the Genoa Subport Tunnel. Two different reinforced concrete solutions constituting the segment were investigated.

- Traditional solution: concrete mix based on 100% CEM II-AL 42.5, reinforced with 93 kg/m<sup>3</sup> of steel bars;
- Innovative solution: concrete mix based on ternary binder (60% CEM II-AL 42.5 and 40% calcium sulphoaluminate/anhydride binder. From now called CSA), reinforced with hybrid combination of 40 kg/m<sup>3</sup> steel fibers and 20 kg/m<sup>3</sup> GFRP bars.

#### 3.2 Functional unit

The functional unit is the segment that represents the modular unit of a lining ring of the Genoa subport tunnel. It was assumed that the different solutions guarantee the comparable structural performance. The tunnel lining consists of external diameter of 15.4m, internal diameter of 14.3m, resulting in 0.55m of thickness. Each lining ring consists of 9 segments (12.8 ton/each) with a depth of 1.8m. The single segment volume is 5.13 m<sup>3</sup>, resulting in 46.2 cubic metre of whole lining ring.

#### 3.3 System boundaries

In the following study, the system boundaries consist of the production and transportation of a precast concrete segment from the manufacturing plant to the construction site in Genoa.

The decision not to consider the installation, maintenance and disposal phases of the segments was taken, at this time, to give more attention to the production phase in order to compare the environmental

sustainability of the construction materials. Specifically, the processes of concrete production, reinforcement production (including steel bars, steel fibers and GFRP bars), curing of the traditional precast concrete segment, transport of the concrete and the reinforcements from the production plant to the construction site are included. Fig. 4 summarizes the boundaries of the system.

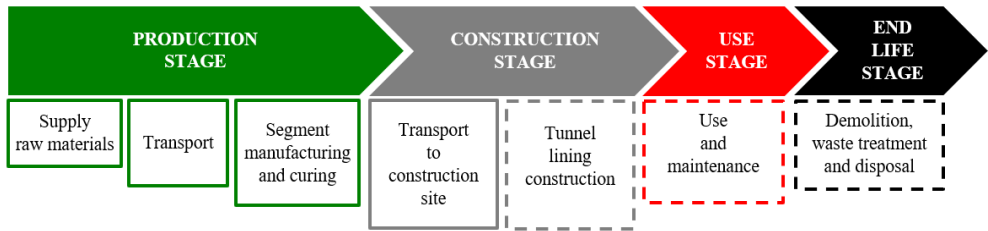


Fig. 4 System boundaries. The phases considered are represented in a box with a continuous line.

### 3.4 Inventory analysis

In this step of the LCA, all input and output material and energy flows are considered, related to the functional unit, for each life cycle phase studied. The sum of the climate-changing emissions of each process within the system boundaries constitutes the overall CFP of the production and transport of the segment. The sources of the material information can be summarized as information provided by the manufacturer, information provided through environmental product certification (EPD) and information taken from databases.

- Traditional concrete and CSA-based concrete: the specific production plant directly provided the emissions per cubic metre of the two types of concrete, without allocating the impact between the different concrete constituent materials. Assuming concretes are produced at the same production site, all variables associated with different production plants, e.g. the fuels used, the geographical production context or the raw material procurement method, have been eliminated;
- Steel fibers: as in the case of concrete, to model the impact of steel fibers, the CFP per 1 kg of material provided directly by the manufacturer through environmental product certification (EPD) was used [5];
- Steel bars: the steel bars impact was quantified using the emissions associated with 1 kg of a generic steel in the ecoinvent v3.6 database [6]. This database shows the raw materials and energy consumption required to make one unit of material. In the case of steel, its composition was modified to conform to a reinforcing steel produced in Italy by means of an electric furnace with a scrap steel percentage of 75%, as imposed by the Minimum Environmental Criteria (CAM) for construction [7] which, although not directly applicable to infrastructures, were taken as a reference to model the steel used in the traditional solution;
- GFRP bars: the impact of GFRP in terms of climate-changing emissions was derived from EPDs [8];
- Energy consumption for the curing in traditional solution: the amounts of electricity and LPG required for curing 1 cubic metre of a segment lining were estimated from similar projects. Information about CFP associated with these two energy sources come from the ecoinvent database. As in the case of steel, the generic electricity and LPG in the database were adapted to the Italian market;
- Transports: the climate-changing emissions associated with the transport of materials depend on the means of transport, the distance and the quantity of material transported. The ecoinvent database offers a wide variety of selectable means of transport but, in order to focus mainly on the impact of construction elements, a common means of transport was selected for all materials transported from the different production facilities to the construction site. The database expresses the CFP of the means of transport in terms of  $\text{kg} \times \text{km}$  because the emissions of a vehicle increase as the load transported increases. 60 km from the precast plant to the construction site and 180 km from the production plant of both reinforcements to the construction site were considered. The distance to the construction site of the two reinforcements is assumed to be



equal in order to limit the comparison only to the production phase, eliminating the 'distance' variable. The impact of concrete transport is quantified not in terms of distance but in terms of the fuel consumed by the concrete mixer on the way to the construction site. The quantity of fuel is estimated from similar construction sites.

Table 3 summarizes the origin of the different materials collected. The last column provides additional information about the production plant, EPD or the original ecoinvent process string.

### 3.5 Impact Assessment

Following [2], the determination of the CFP was carried out considering the impact on climate change (Global Warming Potential - GWP). Specifically, the impact is expressed as kilograms of carbon dioxide equivalent (kg CO<sub>2eq</sub>) emitted. CO<sub>2eq</sub> is calculated by multiplying the emissions of each greenhouse gas, emitted during the life cycle phases considered, by its equivalence factor. GHG equivalence factors, developed by [9], express the contribution of a given greenhouse gas to global warming compared to carbon dioxide, whose equivalence factor is equal to 1.

The emissions associated with the manufacture and transport to the construction site of a segment lining are the sum of the greenhouse gases associated with the materials collected during the inventory.

The application of the equivalence factors, in the case of data from ecoinvent, and the sum of the CO<sub>2eq</sub> of each material was carried out using the LCA software SimaPro 9.5 [10]. This software quantifies the environmental impact by applying the calculation method "EN 15804+A2 Method v1.00", which considers all greenhouse gases in the IPCC AR 5 report [11].

Global warming is also the most closely monitored environmental issue by national and international policies, other than the most communicative environmental aspect.

Table 3 Summary of the materials analyzed.

Material	Source	Specifications
Traditional concrete	Production plant	Concrete production plant
Innovative concrete	Production plant	Concrete production plant
Steel fibers	EPD	Reference [5]
Reinforcing steel	Ecoinvent database	Steel, low-alloyed {RER}  steel production, electric, low-alloyed   Cut-off, U
GFRP bars	EPD	Reference [8]
Electricity	Ecoinvent database	Electricity, medium voltage {IT}  market for   Cut-off, U
LPG	Ecoinvent database	Liquefied petroleum gas {Europe without Switzerland}  market for liquefied petroleum gas   Cut-off, U
Diesel	Ecoinvent database	Diesel, burned in building machine {GLO}  processing   Cut-off, U
Compressed air	Ecoinvent database	Compressed air, 1000 kPa gauge {RER}  market for compressed air, 1000 kPa gauge   Cut-off, U
Mean of transport	Ecoinvent database	Transport, freight, lorry >32 metric ton, EURO6 {RER}  transport, freight, lorry >32 metric ton, EURO6   Cut-off, U

### 3.6 Interpretation

Carbon Footprint of two lining solutions is shown in Table 4.

The precast segment based on innovative solution shows a reduction in CO<sub>2eq</sub> impact of 7% compared to the traditional one.

Table 4 GWP comparison of traditional and innovative solution. EN 15804+A2 Method.

Traditional solution	GWP (kg CO <sub>2eq</sub> )	Innovative solution	GWP (kg CO <sub>2eq</sub> )
Steel rebars	5.20E+02	GFRP rebars	3.43E+02
Traditional concrete	1.60E+03	Innovative concrete	1.56E+03
Energy for concrete curing	7.86E+01	Steel fibers	1.80E+02
Transports	1.12E+02	Transports	5.51E+01
Total	2.31E+03	Total	2.14E+03

Fig. 5 expresses the percentage contribution of the constituent elements to the precast concrete segment lining. In both cases, more than 70% of the impact can be attributed to the production of concrete, the main material towards which technological improvement strategies must be directed in order to limit environmental output. GFRP is less impactful than reinforcement steel.

It is crucial to stress that the steel used in this study represents an average Italian steel produced in an electric arc furnace converter and made by at least 75% of iron scrap, whose percentage is higher than European scenario, where reinforcing steel comes mainly from primary steel processed in a blast furnace converter. Due to the different production technology and content of iron scrap, a precast concrete segment made by an average European reinforcing steel would have higher CFP than the traditional solution present in this study.

Finally, transportation has a greater impact in the traditional solution due to the presence of a maturation plant which increases transportation times. However, in both classic and innovative solutions, less than 5% of project GWP depends on transport.

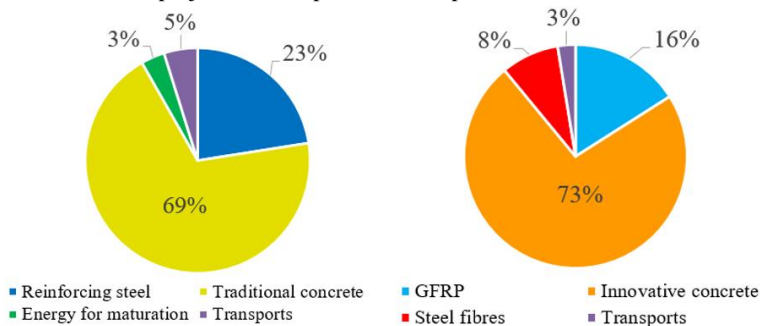


Fig. 5 Percentage contribution to GWP of segments: (left) Traditional; (right) Innovative

#### 4 Construction site area and logistics

Environmental impact associated with materials is not the only element to be analyzed, as the choice of construction type can significantly affect logistics and site construction.

As reported in previous paragraphs, the precast of traditional reinforced concrete segments requires the prefabrication plant with curing system. Generally, large spaces and dedicated areas are required for the installation of these prefabrication plants and the segments lining storage. These areas are not always available near the construction site. Specifically, the construction of the sub-port tunnel concerns the port area of the city of Genoa, closely interconnected with the city center, where there are no available areas to dedicate to a prefabrication plant.

Assuming that the prefabrication plant can be built around Novi Ligure, due to the industrial and manufacturing vocation of the area, transport and supply phase of the segments will have to be implemented at the tunnel entrance area, which will inevitably involve the city of Genoa's road system, with the consequent increase in traffic and road congestion.

The production of the segments by means of innovative solution, consists of concrete based on CSA binder (which do not require steam curing) and FRC/GFRP hybrid reinforcement, allows to eliminate the need to set-up large prefabrication plants. More specifically, for the traditional segments, the storage of a monthly production is needed, while for the innovative one, just the storage of a daily production

is required [1]. This would allow the prefabrication of the segments within the construction-site areas. In this configuration, there would be a significant environmental benefit. As a matter of fact, the avoidance of traffic congestion and the reduction of congestion induced by the construction-site guarantees an avoided impact and therefore a reduction in overall emissions.

Environmental benefits that would come from avoided traffic and road congestion are difficult to quantify but it's anyway a plus point to the innovative solutions. Another aspect not considered in this study that must be considered is the maintenance of the tunnel. For a structure in a marine environment, the assessment of the greater corrosion resistance of GFRP reinforcements compared to the traditional steel ones may become decisive. The greater the durability of the tunnel, the less repair and maintenance actions will be necessary, resulting in an extension of its service life, which constitutes a further environmental advantage.

## 5 Conclusions

In this study two different technologies for the construction of the prefabricated lining planned for the future Genoa Subport Tunnel are analyzed from environmental impacts point of view. The assessment was carried out by calculating the carbon footprint (CFP) associated with the manufacturing of traditional precast concrete segments and the proposed fibre-reinforced sulphoaluminate concrete segments with glass fiber reinforced polymer (GFRP) bars. The analysis showed that the innovative solution leads to a reduction in emissions compared to the classic one. The innovative solution also guarantees a parallel environmental advantage, as it speeds up the entire segment curing process and requires less areas for the prefabrication and temporary storage of the segments. This implicates easier management of logistics during the construction phase of the entire project and the consequent lower burden on the road network in the areas affected by the construction sites.

The increase in traffic and congestion caused by the need to use a prefabrication plant, although not quantified through LCA analysis in this study, is an actual problem that contributes to making the traditional solution less efficient.

Finally, the study shows that the carbon footprint of a reinforced concrete structure is closely dependent on the characteristics of the concrete and that GFRP can be an alternative to steel, especially in aggressive chemical environments, mitigating maintenance impact. In addition, it is highlighted that the prefabrication plant generates environmental and logistical negative output.

## References

- [1] Spagnuolo, Simone, and Meda, Alberto. 2024. "Precast CSA-based concrete tunnel lining segments reinforced with GFRP bars: Challenges and opportunities." *Construction and Building Materials* 425 (2024) 136007. Available online April 3, 2024. doi: 10.1016/j.conbuildmat.2024.136007.
- [2] UNI EN ISO 14067:2018. 2018. Greenhouse gases - Carbon footprint of products - Requirements and guidelines for quantification. <https://store.uni.com/>.
- [3] UNI EN ISO 14040:2021. 2021. Environmental management - Life cycle assessment - Principles and framework. <https://store.uni.com/>.
- [4] [3] UNI EN ISO 14044:2021. 2021 Environmental management - Life cycle assessment - Requirements and guidelines. <https://store.uni.com/>.
- [5] Dramix®, Steel fibres for Concrete Reinforcement EPD. Program Operator: Instytut Techniki Budowlanej (ITB).
- [6] [www.ecoinvent.org](http://www.ecoinvent.org).
- [7] DM 23.06.2022. "Criteri ambientali minimi per l'affidamento del servizio di progettazione di interventi edilizi, per l'affidamento dei lavori per interventi edilizi e per l'affidamento congiunto di progettazione e lavori per interventi edilizi".
- [8] ATP Srl, Straight bars and shaped stirrups in Glass Fiber Reinforced Polymer EPD. Program operator: EPD international AB.
- [9] Intergovernmental Panel on Climate Change (IPCC). <http://www.ipcc.ch/>.
- [10] Prè Consultants. Software SimaPro versione 9.5.
- [11] Climate Change 2013. The Physical Science Basis. Working Group I contribution to the Fifth Assessment Report of the IPCC.

# **Aging and deterioration of Concrete Structures**



# The effect of degradation on the structural response of a reinforced concrete arch bridge

Paolo Andrea Miglietta<sup>1</sup>, Gianni Blasi<sup>1</sup>, Daniele Perrone<sup>1</sup>, Francesco Micelli<sup>1</sup>,  
Maria Antonietta Aiello<sup>1</sup>

<sup>1</sup>*Department of Engineering for Innovation,  
University of Salento,  
Via per Monteroni, Lecce (73100), Italy*

## Abstract

In recent years, several bridge collapses have occurred worldwide, resulting in human life and economic direct and non-direct losses. Such events are likely related to the age of bridges, which is approaching their lifespan in most of the cases. Furthermore, older bridges were designed according to outdated standards and built by using outdated materials and technologies, and consequently, require major retrofitting. Since infrastructures play a fundamental role in the road network, stakeholders and governance are committed to improve their performance with urgency. Structural safety assessment is fundamental to properly plan and identify maintenance interventions, also accounting for the effects of degradation phenomena. In fact, steel reinforcement corrosion, concrete cracking, creep and shrinkage severely affect expected lifespan of a structural system exposed to external environment and fatigue loads. In this paper, a review of the degradation models available in the literature is provided, discussing the influence of the main parameters on each degradation phenomenon. Subsequently, a numerical model of a case study Maillart's bridge located in southern Italy is developed, implementing degradation effects to assess their influence on the structural performance. Since the bridge is located nearby the coast, both carbonation and chloride-induced corrosion of reinforcement were considered, as well as long-term physical effects on concrete mechanical behaviour. The results showed that material degradation may influence both local and global response of the structure and that predicting bridge behaviour evolution over time can be useful for its life cycle management.

## 1 Introduction

Recent bridge collapses have focused the attention of stakeholders on the health of infrastructures and on their need for maintenance. In Italy, many infrastructural assets (e.g. bridges, tunnels) were built over than fifty years ago, according to outdated standards and materials. Consequently, they are approaching their lifespan end or require retrofitting [1]. Despite their age or health, existing infrastructures still play a strategic role in the road network and their functionality loss could have a major impact on the economy, sustainability and logistics, especially in the event of seismic emergencies.

Several studies carried out in the last decades [2]-[5] have shown that building materials are affected by degradation processes, resulting in a reduction of the load-bearing capacity and ductility of the entire structure. Since the seismic behaviour is strongly dependent on the latter, life prediction, performance monitoring and bridge maintenance have become essential to avoid brittle failures and sudden collapses.

Steel rebars and tendons corrosion represents one of the main causes of deterioration of RC structures [6]. Corrosion may occur in general or localized form; the former is related to carbonation and results in a uniform reduction of reinforcement cross-section along its length, while localized corrosion is caused by chloride penetration and induces pits and notches. In addition, localized corrosion may be accelerated by freeze-thaw cycles and de-icing if joints are not maintained or inadequate. A large number of literature studies was addressed at modelling the phenomenon of corrosion and its consequences in RC structures. Particularly, degradation models [7], functionality curves [8], [9] and time-dependent N-M interaction curves for piers [10] were developed. The outcome of such studies provided useful tools for maintenance planning and showed a high correlation between structural safety index and corrosion rate.

In this work, the influence of degradation phenomena on the global structural response and the load-bearing capacity of a Maillart arch bridge was evaluated. Non-linear pushdown analyses were per-

formed on the structural system, accounting for the effect of the evolution over time of several degradation phenomena. Particularly, reinforcement corrosion and concrete degradation due to cracking within the cover depth due to carbonation were considered, alongside concrete creep. The performance of the structure was computed at different time intervals starting from the construction year, in order to compute functionality curves.

## 2 Degradation models considered

The structural response of reinforced concrete (RC) structures is deeply influenced by degradation phenomena affecting the mechanical properties of both steel and concrete. The hydration products of cement induce a high alkaline environment in concrete. Therefore, for PH higher than a specific threshold (generally around 11.5), steel reinforcements are surrounded by an iron oxide film that provide protection from corrosion. When carbon dioxide and moisture penetrate within concrete pores, the carbonation reaction occurs, neutralizing the alkalinity of the concrete. Although the mechanical properties of concrete are not directly affected by carbonation products, as carbonation reaches the concrete-reinforcement interface, the protective film is destroyed, leading to corrosion. Consequently, reduction in rebars-cross sectional area and mechanical properties decay occurs. Additionally, the production of expansive products induces tensile stress on concrete surrounding the reinforcement, leading to progressive increase of cracking up to cover spalling [6].

Carbonation penetration can be evaluated with equation (1):

$$s = K\sqrt{t} \quad (1)$$

where  $s$  is the carbonation depth in millimetres,  $t$  the time in years and  $K$  the carbonation rate in  $\text{mm/year}^{0.5}$ , which ranges between 2 for well compacted concrete and 15 for poor quality concrete. In this study  $K=7$  was assumed. Substituting the concrete cover thickness in equation (1), the corrosion initiation time can be estimated.

Once carbonation-induced corrosion was triggered, the reduction in cross-section diameter may be assessed through the corrosion rate  $v_{\text{corr}}$ . Since the chemical corrosion reaction requires water and oxygen, the corrosion rate is highly dependent on the water content within concrete pores. In fact, the corrosion rate is lower than  $1 \mu\text{m/year}$  and, consequently, can be neglected if concrete pores are dry or saturated. On the other hand, if the relative humidity (RH) is between 90% and 100%, corrosion rate may increase up to  $100 \mu\text{m/year}$ . Since the RH of the case study bridge environment is approximately 80%,  $v_{\text{corr}} = 15 \mu\text{m/year}$  was assumed [6].

As said before, both the properties of reinforcing steel and concrete are affected by corrosion of the reinforcement. A significant reduction of tensile strength, yielding strength and ductility is observed for rebars, while cracking due to expansive products of corrosion cause concrete compressive strength decay. The relationships proposed by Imperatore et al. [11] was employed herein to account for rebars properties decay, as shown in eq. (2)-(4).

$$f_{y,\text{corr}} = (1 - 0.0143453 \cdot M_{\text{loss}} [\%]) \cdot f_y \quad (2)$$

$$f_{t,\text{corr}} = (1 - 0.0125301 \cdot M_{\text{loss}} [\%]) \cdot f_t \quad (3)$$

$$\varepsilon_{u,\text{corr}} = e^{-0.0546993 \cdot M_{\text{loss}} [\%]} \cdot \varepsilon_u \quad (4)$$

where  $f_y$ ,  $f_t$  and  $\varepsilon_u$  are the uncorroded yield strength, the uncorroded tensile strength and the uncorroded ultimate strain respectively; while  $f_{y,\text{corr}}$  is the corroded yield strength,  $f_{t,\text{corr}}$  is the corroded tensile strength and  $\varepsilon_{u,\text{corr}}$  is the corroded ultimate strain; which are evaluated as a function of the percentage of mass loss  $M_{\text{loss}}$ . It is noteworthy that tensile strain, which decays according to an exponential law, is the most affected parameter in case of corrosion and can induce a wide reduction in local and global ductility.

The concrete compressive strength decrease is computed with the equation (5), proposed by Vecchio and Collins and modified by Coronelli and Gambarova [12]:

$$f_c^* = \frac{f_c}{1 + K \frac{2\pi X n_{\text{bars}}}{b \varepsilon_{c2}}} \quad (5)$$

Where  $f_c^*$  is the corroded compressive strength,  $f_c$  the uncorroded compressive strength,  $K$  a constant equal to 0.1 for medium rebar,  $X$  the corrosion penetration in mm,  $b$  the width of the cross-section in mm,  $n_{bars}$  the number of steel reinforcement in the compressive zone and  $\epsilon_{c2}$  the strain at the peak.

Lastly, creep effect should be considered when analysing long-term evolution of structural performance, particularly in case of bridges subjected to high static and dynamic loads, which lead to progressive increase of strain. Creep is evaluated through the relationship proposed by Model Code [13], as shown in eq (6):

$$E_c(t) = \frac{E_{ci}}{\varphi(t, t_0)} \quad (6)$$

where  $E_{ci}$  is the modulus of elasticity at 28 days and  $\varphi(t, t_0)$  is the creep coefficient, depending on the geometry of the cross-section of the considered element, the RH and the mean compressive strength of the concrete ( $f_{cm}$ ). Further details on  $\varphi$  evaluation may be found in [13].

### 3 Description of the case study bridge

The bridge analysed in this study is located in the south-east coast of Salento (Apulia, Italy) and was built in 1967. The original structure consists of a thin RC arch connected to the upper deck through vertical trusses, as depicted in Fig. 1 (left). The arch span and depth are equal to 44 m and 7 m, respectively, while its thickness varies from 250 to 300 mm. Such thickness value was designed in order to avoid buckling phenomena and reduce as much as possible the self-weight of the vault. The upper deck is 7 m wide and consists of a thin slab supported by four longitudinal beams with cross-section equal to 250x1000 mm. Each vertical truss connecting the arch to the deck is characterized by either a set of four columns (at the ends) or a thin wall (in the mid-span). Spandrel beams are used at the ends of the trusses for the connection to the arch and the deck [14].

The high flexural stiffness of the deck leads to negligible bending moment in the vertical elements. As a result, the arch behaves as a fully compressed element under dead loads. The foundation elements of the arch are plinths. The deck is constrained at the abutments on one side by a hinge and on the other by a roller, to allow for longitudinal displacements caused by thermal loads. Two access girders, 6.15 m and 9.75 m long respectively, connect the bridge to the abutments and are constrained to the main structure with half-joints.

The characteristic compressive strength of concrete,  $f_c$ , is equal to 25 MPa for foundation elements and 30 MPa for both the arch, columns and girders 30 MPa. Smooth steel rebars were used for concrete reinforcement, having yielding strength  $f_y=310$  MPa, tensile strength  $f_t=600$  MPa and ultimate strain  $\epsilon_{u}=10\%$  (Aq60 grade). All structural elements have a concrete cover equal to 25 mm.

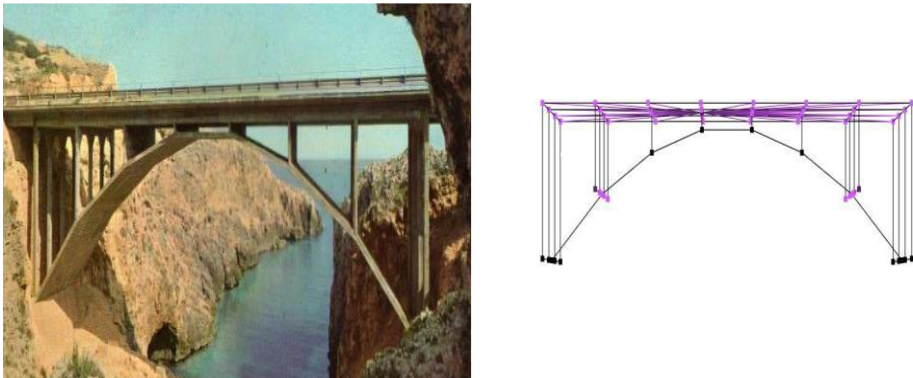


Fig. 1 The “Ciolo” Bridge in 1967 (left) and the numerical model of the “Ciolo” bridge (right).

#### 3.1 Description of the numerical model

The finite element model of the case study bridge was realized in STKO [15]. The structural elements were modelled using beam elements, except for the upper slab, which was simulated including rigid



diaphragm constraints for the deck beam, as shown in Fig. 1 (right). For the sake of simplicity, the geometric details of structural elements, such as rings and countersinks, were neglected in this study. Pinned restraints ( $U_x$ ,  $U_y$  and  $U_z$ ) were included at both ends of the arch and of the slab to simulate boundary conditions furthermore, access ramps were neglected in this study. Additionally, spandrel beams were assumed as rigid elements, by setting equalDOF constraints at all their nodes.

The mechanical behaviour of the arch, the struts and the deck beams was simulated through a smeared plasticity approach, adopting fiber-based non-linear beam elements. The stress-strain relationship of materials characterizing fiber sections was defined using Concrete02 and hysteretic mechanical model for concrete and steel rebars, respectively. Referring to spandrel beams, elastic beam elements were used.

### 3.2 Modelling of degradation phenomena

According to Tuuti's model [16], the service life of the structure exposed to corrosion can be divided into two periods: the trigger period and the propagation period, as shown in Fig. 2 (left). During the trigger stage, corrosion penetration is zero and only concrete creep occurs. In the propagation stage corrosion takes place, resulting in loss of the reinforcement cross sectional area and in the decay of the mechanical properties of steel, as shown in Fig. 3 (left and right). For the considered elements, the corrosion initiation time,  $t_{corr}$ , was computed by substituting the depth of concrete cover in (1). Since all elements had the same concrete cover depth, the resulting value of  $t_{corr}$  was equal to 12 years.

In order to account for concrete creep, a time-dependant reduction factor for Young's modulus was used, as shown in equation (6). The evolution of the elastic modulus is depicted in Fig. 2 (right).

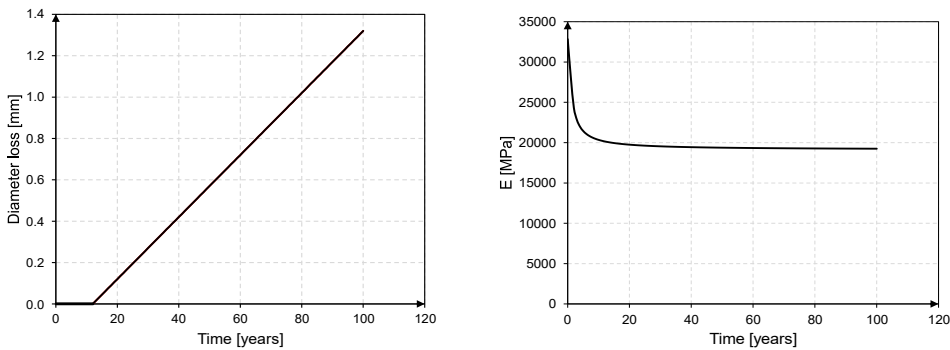


Fig. 2 Trigger period and propagation period for the “Ciolo” bridge (left). Decay of elastic modulus due to creep (right).

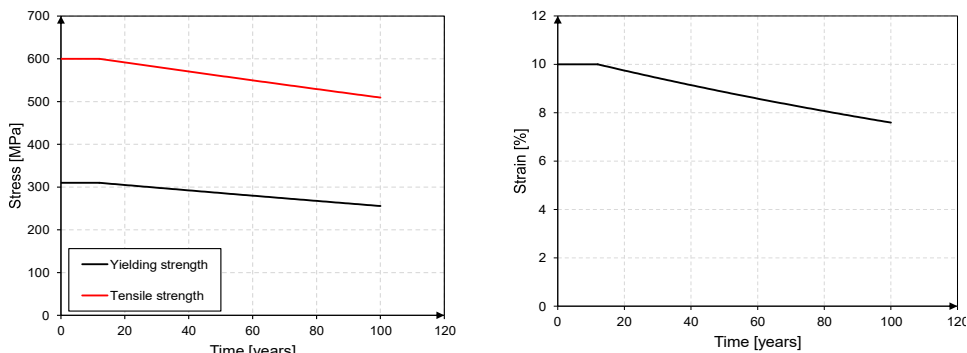


Fig. 3 Decay of yielding strength and tensile strength of the steel (left). Decay of ultimate strain of the steel (right).

As said before, concrete region surrounding reinforcement bars is affected by corrosion. To account for this aspect, the cross-sections of elements were divided into two regions: an inner core and a degraded region, including the concrete cover and an inner layer with depth equal to twice as the rebar diameter, as suggested by [10]. An example of such partition is depicted in Fig. 4 (left), where the green layer represents the degraded region and the grey area is the un-degraded inner core. Recent studies showed that the degraded area of the concrete should be defined through a circle having centre corresponding to the reinforcement rebar axis and with diameter equal to the depth of the cover [17], however, a more conservative and simplified approach was adopted in this study. The adopted approach allowed modifying the mechanical behaviour of the outer region of concrete cross-section depending on the corrosion penetration, as shown in Fig. 4 (right). On the contrary, the mechanical behaviour of the inner core was kept constant.

In summary, only the elastic modulus of concrete was reduced over time until the time of corrosion initiation, whereas both mechanical properties of steel and concrete in the outer region were reduced during the propagation period.

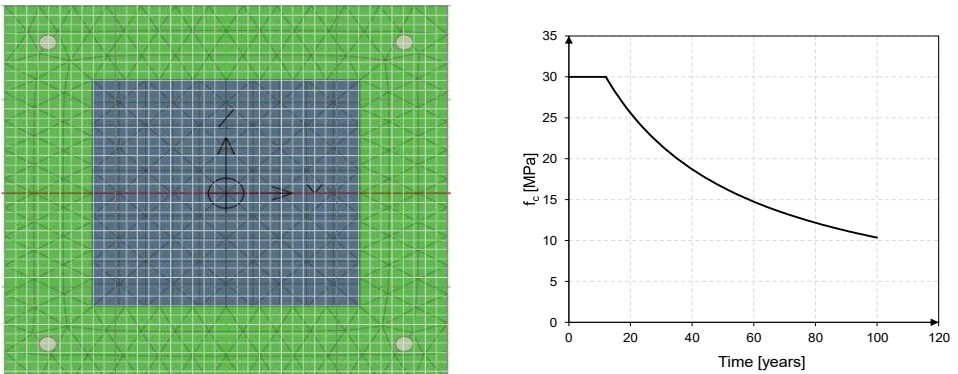


Fig. 4 Cracked region (green) and inner core (grey) for the cross-section of a square column (left) and decay of concrete compressive strength (right).

## 4 Numerical analysis of the bridge

With the aim to evaluate the structural behaviour as a function of degradation phenomena, non-linear Push-down analyses were carried out on the bridge at different time periods starting from construction time.

Firstly, a gravity load analysis was performed considering both the structural and non-structural dead loads and a live load equal to  $8 \text{ kN/m}^2$ , as defined by the Italian building design code [18]. Since the upper slab was not explicitly modelled, its relative non-structural and live loads were applied to the longitudinal beams, according to the tributary length method. As a result, the sum of dead and live loads was equal of  $17.6 \text{ kN/m}$  and  $8.8 \text{ kN/m}$  for central and side beams, respectively. At the end of the gravity load analysis, the push-down analysis was carried out using a loading protocol with magnitude proportional to that of the sum of dead and live load. The push-down load value was increased up to structural collapse. Further details of the analysis performed are provided in the following.

### 4.1 Push-down analysis setting

The push-down analysis was performed in displacement control, by setting the control node at the top of the arch. The adoption of displacement-controlled protocol allowed to detect the post peak branch in the load-displacement curve, in order to reliably assess the achievement of collapse. An example of the obtained pushdown curve is depicted in Fig. 5 (left). Because of the static scheme of the bridge analysed, the response is nearly elastic up to structural failure. In the initial stage, only minor cracking was obtained, while structural collapse occurs because of the failure of the longitudinal beams in correspondence to the connection to central walls. Such failure mode causes a noticeable load drop in the curve.

Since the main purpose of this study is to assess the influence of the degradation phenomena on the load-bearing capacity, the post-peak branch was not included in the curves discussed in the following.

As previously stated, several pushdown analyses were carried out to account for the evolution over time of degradation phenomena. Since the major decay of the elastic modulus occurs in the first years, analyses were carried out every year until the fifth year in order to detect its influence on the structural response. After this threshold, time-steps were set every five years. From year 15 to year 24, analyses were carried out every 3 years to detect the effect of the corrosion phenomenon on the load-bearing capacity. The push-down analyses were carried out up to the 24th year, since strengthening interventions were carried out on the bridge in 1992 and then the structural behaviour was modified.

The outcomes summarized in Fig. 5 (right), show that up to corrosion initiation time (grey curves) the load-bearing capacity of the bridge is almost constant however, the stiffness sharply decreases due to creep. When corrosion takes place (red curves), both load-bearing capacity and ultimate displacement decrease, due to loss of performance of the mechanical properties of materials.

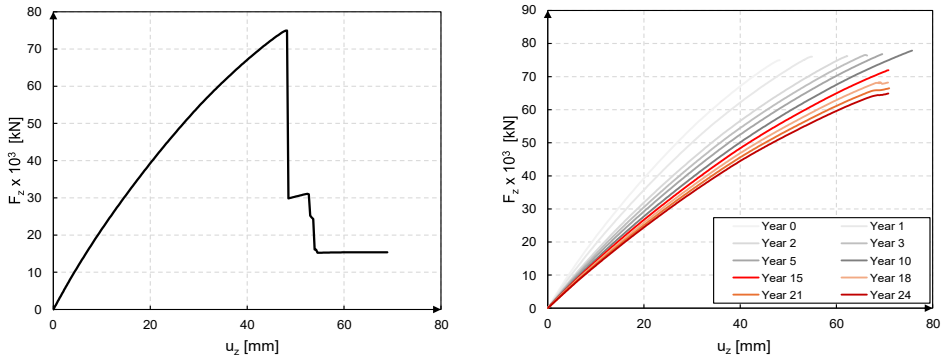


Fig. 5 Pushdown curve of the “Ciolo” Bridge in the undamaged state (left) and as a function of degradation phenomena (right).

The results obtained from the pushdown analyses were used to define the functionality curve of the case study bridge, which shows the evolution of the load-bearing capacity over time (Fig. 6). This curve may be useful to predict the performance of the bridge over time and to identify the time for required retrofit intervention, based on lower bounds of the performance level. It is worth mentioning that functionality curve was computed up to 24 years after construction (i.e. 1992), because major strengthening interventions were carried out between 1992 and 1994. The presence of such interventions leads to a “jump” in the curve in correspondence to the retrofit year and was neglected in this study. Future works will be addressed at computing functionality curve evolution after retrofit time.

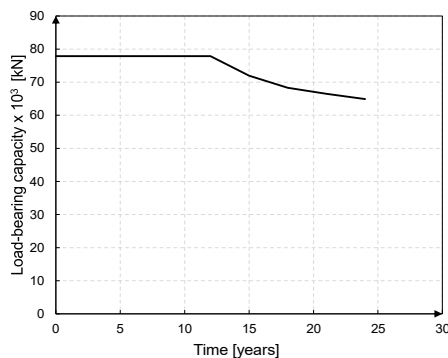


Fig. 6 Functionality curve of the “Ciolo” Bridge.

## 5 Conclusions

In this study, a simplified model with embedded damage of a RC arch bridge located nearby the coast was developed, aiming to define the structure functionality curve. The outcomes confirmed that the reinforcement corrosion is the main cause of degradation in RC structures, and it is closely related to construction details and quality of materials, such as cover depth and concrete porosity. Particularly, no losses in load-bearing capacity were detected in the functionality curve up to the triggering time. In fact, the only mechanical property decay within the triggering period is related to creep, which only affects global stiffness. After corrosion initiation time, load bearing capacity is related to cross-sectional area reduction of reinforcing rebars.

The functionality curve developed may be a useful tool for stakeholders to monitor the structural performance, prioritize retrofitting and define the maintenance strategies. Several aspects of this complex and innovative topic, such as the influence of degradation processes on the seismic response and influence of strengthening interventions on functionality curves, are demanded to future works.

## Acknowledgements

This work is part of the research activity developed by the authors within the framework of the “PNRR”: SPOKE 7 “CCAM, Connected Networks and Smart Infrastructure” - WP4.

## References

- [1] Calvi, Gian Michele, Moratti, Matteo, O'Reilly, Gerard J., Scattarreggia, Nicola, Monteiro, Ricardo, Malomo, Daniele, Calvi, Paolo M., and Rui Pinho. 2018. “Once upon a Time in Italy: The Tale of the Morandi Bridge.” *Structural Engineering International*, 29:198–217.
- [2] Andrade, Carmen. 2019. “Propagation of reinforcement corrosion: principles, testing and modelling.” *Materials and Structures* 52.
- [3] Pedrosa, Filipe and Carmen Andrade. 2017. “Corrosion induced cracking: Effect of different corrosion rates on crack width evolution.” *Construction and Building Material* 133:525-33.
- [4] Andrade, Carmen and Nuria Rebolledo. 2018. “Generic modelling of propagation of reinforced concrete damage.” Paper presented at the High Tech Concrete: Where Technology and Engineering Meet, Maastricht, The Netherlands, June 12-14.
- [5] Vecchio, Frank J, and Michael P. Collins. 1986. “The Modified Compression-Field Theory for Reinforced Concrete Elements Subjected to Shear.” *Journal Proceedings* 83:219-31.
- [6] Pedferri, Pietro and Luca Bertolini. 2000. *La durabilità del calcestruzzo armato*. McGraw-Hill Education.
- [7] Liu, Jinhong, Xiaoyong, Luo, and Chen Qi. 2023. “Degradation of Steel Rebar Tensile Properties Affected by Longitudinal Non-Uniform Corrosion.” *Materials* 2023 16.
- [8] Domaneschi, Marco, De Gaetano, Antonino, Casas, Joan R., and Gian Paolo Cimellaro. 2020. “Deteriorated seismic capacity assessment of reinforced concrete bridge piers in corrosive environment.” *Structural Concrete* 21:1823–38.
- [9] Loreto, Giovanni, Di Benedetti, Matteo, and Antonio Nanni. 2011. “Evaluation of corrosion effect in reinforced concrete by chloride exposure.” Paper presented at the SPIE Smart Structures and Materials + Nondestructive Evaluation and Health Monitoring, San Diego, United States, March 6
- [10] Di Sarno, Luigi and Francesco Pugliese. 2019. “Critical review of models for the assessment of the degradation of reinforced concrete structures exposed to corrosion.” Paper presented at the Earthquake Risk And Engineering Towards A Resilient World Conference, Greenwich, London, September 9-10.
- [11] Imperatore, Stefania, Rinaldi, Zila, and Carlo Drago. 2017. “Degradation relationships for the mechanical properties of corroded steel rebars” *Construction and Building Materials* 148:219–30.
- [12] Coronelli, Dario and Pietro Gambarova. 2004. “Structural Assessment of Corroded Reinforced Concrete Beams: Modeling Guidelines.” *Journal of Structural Engineering* 130.
- [13] CEB-FIP model code for concrete structures 2010. International Federation for Structural Concrete.

- [14] Micelli, Francesco, Perrone, Daniele, and Maria A. Aiello 2023. “Correspondence Influence of strengthening interventions on the structural performance of a Maillart-type arch bridge: the case of ‘Ciolo Bridge’ in the South of Italy.” *Eurostruct* 6:89-98
- [15] Petracca, Massimo et al. 2017. STKO user manual. ASDEA Software Technology Pescara, Italy, 2017.
- [16] Tuutti, Kyosti. 1982. “Corrosion of steel in concrete.” PhD thesis, Swedish cement and concrete research institute, Lund University, Stockholm.
- [17] Felitti, Matteo, Oliveto, Francesco, Pelle, Danilo, and Filippo Valvona. 2023. Valutazione di ponti e viadotti esistenti soggetti a rischi strutturale in condizioni statiche, sismiche e di degrado. Maggioli Editore.
- [18] D.M. 17/01/2018. “Norme tecniche per le costruzioni.” Italian Ministry of Infrastructure.

# On field evaluation and durability of protective silane-based treatments for concrete structures

Denny Coffetti<sup>1</sup>, Simone Rapelli<sup>1</sup>, Andrea Nicoletti<sup>2</sup>, Luigi Coppola<sup>1</sup>

<sup>1</sup> *Department of Engineering and Applied Sciences,  
University of Bergamo,  
via Marconi, 5 - 24044 Dalmine (BG), Italy*

<sup>2</sup> *Sika Italia Spa  
Via Luigi Einaudi, 6 – 20068 Peschiera Borromeo (MI), Italy*

## Abstract

Concrete-based tunnels for high-speed railways should exhibit remarkable durability, ensuring extended service life. The use of protective coatings and migrant corrosion inhibitors offers a viable solution to enhance the longevity of existing tunnels designed with ordinary service life or reduced concrete covers. The purpose of this work is to evaluate the effectiveness of a silane-based treatment (SBT) applied on the surface of the concrete of existing Italian high-speed railways tunnels. The effect of the surface treatment has been evaluated through accelerated carbonation test while the carbonation depth at the end of the service life of tunnels was assessed using the Fick's law. Experimental results evidenced that the use of SBT allows to strongly reduce the risk of carbonation of concrete cover at the end of the service life both on areas exposed to wet-and-dry cycles and on regions with dry atmosphere.

## 1 Introduction

The European railway network stands as a crucial asset for ensuring sustainable mobility for both people and goods. Recent statistics reveal that Europe boasts an extensive railway network spanning more than 200,000 kilometers, capable of efficiently transporting significant quantities of cargo and passengers. Notably, within the EU-27, freight transport accounts for more than 400 billion tonne-kilometers (tkm) annually, while passenger transport exceeds 420 billion passenger-kilometers (pkm). In this landscape, high-speed railway plays a pivotal role in enhancing transport speed and competing with air travel.

The most recent data from the European Union's report indicates that there are currently 11,527 kilometers of active high-speed railways (HSR) lines, with an additional 2,000 kilometers under construction. Italy takes a prominent position in this context, with nearly 1,000 kilometers of high-speed rail already in use and over 300 kilometers (Genoa-Milan, Naples-Bari, Brescia-Verona-Padua) under construction. This constitutes roughly 16% of the total investments in high-speed rail infrastructure within the EU-27.

Given the strategic importance of this transportation system, it is imperative that the infrastructure supporting high-speed rail exhibits exceptional qualities. The infrastructures supporting HSR ought to demonstrate exceptional durability, guaranteeing prolonged service life. Through meticulous design, robust construction methods, and proper choice of materials, these infrastructures can withstand harsh environmental conditions, heavy traffic loads, and dynamic forces [1]. Extensive research and real-world observations have demonstrated service life expectancy exceeding 75-100 years, making them reliable and sustainable solutions for efficient and safe high-speed rail networks [2-5]. Concrete-based tunnels, among the various infrastructures that compose railway lines, are of paramount strategic significance, requiring constant assurance of optimal efficiency and functionality in the long run. With this aim, the use of protective coatings and migrant corrosion inhibitors offers a viable solution to enhance the longevity of existing tunnels designed with ordinary service life or reduced concrete covers [6]. These measures effectively mitigate the detrimental effects of moisture and water, aggressive chemicals, and carbonation-induced corrosion of steel reinforcement on the tunnel's structural integrity. In this way, the maintenance requirements can be minimized, thereby optimizing the overall lifecycle cost of the infrastructure.

The objective of this study is to assess the efficacy of a silane-based treatment (SBT) in reducing the carbonation rate of concrete when applied to the internal surfaces of three different existing Italian HSR tunnels. Furthermore, Fick's law-based analysis was employed to evaluate the carbonation depth of the concrete cover at the end of the service life of tunnels. This analysis considered the carbonation rate of silane-based treated concrete at various dosages and the average thickness of the concrete cover, which was determined through non-destructive testing methods.

## 2 Main characteristics of tunnels' concrete

Five different test regions of about 12 m<sup>2</sup> were selected in three different concrete-based tunnels along an HSR in northern Italy built from 6 to 10 years ago as reported in Table 1. Fifteen concrete cores, three for each test region, with diameter (d) of 100 mm and height (h) up to 400 mm were extracted from the vaults by means of a water-cooled diamond-tipped core barrel. All the cylindrical samples were sectioned and rectified in order to obtain, for each sample, four specimens with h/d = 1 and perfectly regular surface for concrete characterization in terms of specific mass [7], water absorption [8], ultrasonic pulse velocity and dynamic modulus elasticity estimation [9], compressive strength [10] and natural carbonation depth with phenolphthalein.

Table 1 General characteristics of tunnels

Tunnel	Length [m]	Test region code	Date of construction	Age [years]	Design compressive strength class
A	1435	A	02/2015	7.2	C 25/30
B	1500	B	03/2013	9.1	C 28/35
C	2860	C1	07/2015	6.8	C 28/35
		C2	03/2013	9.1	C 28/35
		C3	07/2012	9.8	C 28/35

The experimental tests carried out on concrete cores have revealed outstanding material quality. The results presented in Table 2 demonstrate a notably high specific mass of dry concrete, averaging between 2365 and 2430 kg/m<sup>3</sup>, along with low water absorption of about 0.5% - 0.8%. Moreover, the concrete exhibits high compressive strength ( $R_{cm}$ ) compared to the designed values, with average values approximately ranging from 48 to 60 MPa, and a pulse velocity near 5 km/s. These values enable the estimation of the dynamic modulus of elasticity within the range of 48 - 54 GPa using the relationship (1)

$$E_d = v^2 \rho \frac{(1 + \gamma_d)(1 - 2\gamma_d)}{(1 - \gamma_d)} \quad (1)$$

with

- $E_d$ : dynamic modulus of elasticity
- $\gamma_d$ : Poisson modulus (assumed equal to 0.25)
- $\rho$ : specific mass (kg/m<sup>3</sup>)

Through the analysis of natural carbonation measurements and taking into account the age of the tunnels, it is possible to estimate the concrete's natural CO<sub>2</sub> diffusion coefficient ( $K_{CO_2-n}$ ) using the relationship (2)

$$x_{CO_2} = K_{CO_2-n} \cdot \sqrt{t} \quad (2)$$

with

- $x_{CO_2}$ : depth of initial carbonation [mm]
- $t$ : age of tunnels [years]

Table 2 Main properties of concrete

Test region	Specific mass [kg/m <sup>3</sup> ]	Water absorption [%]	R <sub>cm</sub> [MPa]	Pulse velocity [km/s]	E <sub>d</sub> [GPa]
A	2400 ± 30	0.8 ± 0.1	55.1 ± 3.8	4.93 ± 0.09	48.7 ± 1.9
B	2365 ± 39	0.5 ± 0.1	59.7 ± 4.5	4.98 ± 0.12	48.9 ± 2.5
C1	2410 ± 13	0.7 ± 0.1	47.9 ± 4.0	5.18 ± 0.10	54.0 ± 2.1
C2	2380 ± 42	0.5 ± 0.1	60.3 ± 4.9	5.12 ± 0.15	52.0 ± 3.2
C3	2430 ± 28	0.5 ± 0.1	57.3 ± 3.5	5.01 ± 0.12	50.8 ± 2.4

The findings presented in Table 3 reveal considerable variations in initial carbonation depths of samples. Specimens from test regions B and C2 show depths around 5 mm, while concretes in C1 and C3 exhibit carbonation depths of approximately 10 mm. On the other hand, cores from A evidence depths up to 15 mm. Consequently, the CO<sub>2</sub> diffusion coefficients (K<sub>CO<sub>2</sub>-n</sub>) range from 1.8-1.9 mm/ $\sqrt{\text{years}}$  for B and C2, 3.4-3.9 mm/ $\sqrt{\text{years}}$  for C1 and C3, and 5.4 mm/ $\sqrt{\text{years}}$  for A. The variations in carbonation rate, despite the similar compressive strength of the concrete, can be attributed to different microclimatic conditions within the tunnels. These conditions exert a significant influence on the rate of carbonation across different test fields, regardless of the porosity and quality of the cementitious matrix.

Table 3 Carbonation depth and carbonation rate of concrete in different test regions

Test region	Carb. depth [mm]	Carb. rate [mm/ $\sqrt{\text{year}}$ ]
A	14.6 ± 1.4	5.44 ± 0.52
B	5.5 ± 1.0	1.82 ± 0.33
C1	10.2 ± 2.8	3.92 ± 1.07
C2	5.8 ± 2.0	1.93 ± 0.66
C3	10.6 ± 3.6	3.39 ± 1.15

### 3 Protective treatment efficiency

This study employs a commercial SBT which is applied to the surface of hardened concrete. Its purpose is to hinder the penetration of chlorides into the concrete's structure and thus to delay the initiation of corrosion in carbon steel rebars. The authors' prior research [11] demonstrated significant effectiveness of this product on several concretes manufactured by using different types of cement, cement-to-water ratios, and cement factors. The result was a notable reduction (up to 60% with respect to untreated concrete) in the chloride diffusion coefficient (D<sub>nssn</sub>) as measured through rapid chloride tests. Furthermore, tests involving natural chloride diffusion indicated a substantial drop in the apparent diffusion coefficient (D<sub>app</sub>), reaching around 75% reduction when compared to untreated surfaces. The mechanism of action of this SBT (the main properties are reported in Table 4) in slowing down the chloride penetration inside the cement matrix is basically related to the increase of concrete electrical resistivity due to hydrophobic impregnation.

In this study, the various test areas were divided into three smaller subregions, namely D0, D1, and D2, each spanning an area of 4 m<sup>2</sup>. The D0 subregion served as the reference group with no treatments applied. The D1 subregion underwent treatment with SBT at a dosage of 0.6 l/m<sup>2</sup>, while the D2 subregion received a higher dosage of 1.0 l/m<sup>2</sup>. Application of the SBT was accomplished using a brush, and the subsequent drying period was maintained for 14 days.

The effectiveness of SBT in reducing concrete cover carbonation was assessed through accelerated carbonation tests. For this purpose, six concrete cores were utilized for each subregion (in total, 90 samples). These cores were subjected to an artificial environment with a CO<sub>2</sub> concentration of 3.0 ± 0.5%, a temperature maintained at 20 ± 2°C, and a relative humidity of 57 ± 3% over a 120-day period.



Throughout this duration, the depth of carbonation was periodically measured using phenolphthalein-based solution.

Table 4 Properties of the commercial SBT

Property	Value
Physic form	Straw yellow liquid
Viscosity	$0.95 \pm 0.05$ mPa·s
Dry residue	$7 \pm 0.3$ %
pH	$6.5 \pm 0.2$
Density	$0.88 \pm 0.05$ kg/dm <sup>3</sup>

The outcomes, presented in Table 5 and Figure 1, enabled the determination of the accelerated CO<sub>2</sub> diffusion coefficient ( $K_{CO_2-a}$ ) for each test region and SBT dosage. This determination was carried out in accordance with the EN 12390-12 [12] standard, utilizing the formula (3) as follows:

$$x_{CO_2} = a + K_{CO_2-a} \cdot \sqrt{t} \quad (3)$$

with

- $x_{CO_2}$ : average carbonation depth at age  $t$  [mm]
- $a$ : intercept, depending on the initial carbonation of samples [mm]
- $t$ : age of exposure [days]

Table 5 Average carbonation depth of samples during accelerated tests and  $K_{CO_2-a}$  coefficient estimation

Test region	Dosage	Average carbonation depth [mm]						$K_{CO_2-a}$ [mm/ $\sqrt{\text{days}}$ ]	$\eta$
		7 d	28 d	60 d	70 d	90 d	120 d		
A	D0	13.0	19.0	24.0	27.0	31.0	33.0	2.04	-
	D1	15.0	17.5	21.0	23.0	25.0	27.0	1.24	1.65
	D2	16.0	17.5	19.0	22.0	25.0	26.0	1.03	1.98
B	D0	8.0	10.5	14.0	16.0	18.0	21.0	1.51	-
	D1	6.0	8.0	10.5	11.0	12.0	13.0	0.78	1.94
	D2	7.0	8.0	9.0	10.5	11.0	11.0	0.49	3.08
C1	D0	14.0	18.5	21.0	22.0	25.0	28.0	1.44	-
	D1	11.0	12.5	14.0	15.0	16.0	18.0	0.77	1.87
	D2	9.0	10.5	11.0	12.0	14.0	15.0	0.69	2.09
C2	D0	11.0	16.5	18.0	22.0	23.0	29.0	1.79	-
	D1	7.0	9.0	10.0	11.0	12.0	15.0	0.75	2.39
	D2	9.0	10.5	12.0	13.0	13.5	15.0	0.64	2.80
C3	D0	15.0	19.5	22.0	25.0	26.0	30.0	1.46	-
	D1	9.0	12.5	15.0	17.0	17.5	19.0	1.08	1.35
	D2	10.0	12.5	14.0	15.0	16.0	18.0	0.92	1.59

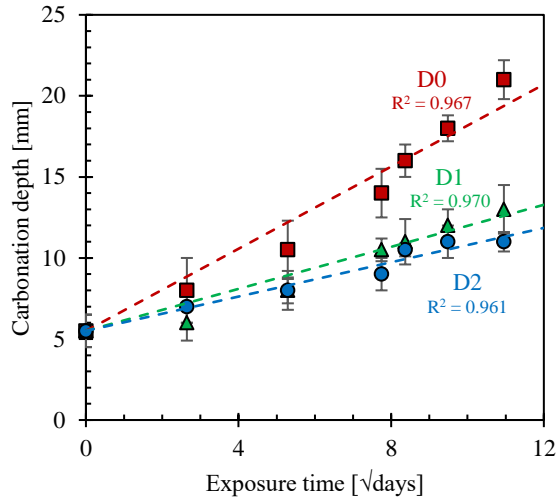


Fig. 1 Accelerated carbonation depth as a function of square root of time of concrete cores from test region B. The same procedure was adopted for all the test regions

The results have demonstrated a substantial decrease in the  $K_{CO_2-a}$  coefficient across all subregions when the SBT is used, underscoring the potential of SBT application to curtail the carbonation rate of concrete. This, in turn, enhances the overall service life of concrete structures. The efficiency of the treatment can be appraised also using the  $\eta$  coefficient, calculated by dividing the  $K_{CO_2-a}$  coefficient of untreated concrete by that of the treated concrete. By employing a dosage of  $0.6 \text{ l/m}^2$  (D1), the  $\eta$  coefficient ranges between 1.35 and 2.39. This range signifies a reduction in  $K_{CO_2-a}$  varying from 26% to 58% when compared to untreated concrete. As expected, a higher dosage of SBT leads to a greater reduction in carbonation of the concrete cover, spanning from 37% to 68%.

Considering the coefficients derived from the accelerated carbonation tests (Table 5), it becomes feasible to project the carbonation depth at the end of tunnel service life, fixed at 75 years [13]. Simultaneously, this approach facilitates the determination of a minimum concrete cover essential to ensure that carbonation does not approach the carbon steel rebars during the structure's operational lifetime. To achieve this, the equation (4) can be employed:

$$x_{\min} = \frac{a + K_{CO_2-n} \cdot \sqrt{t}}{\eta} \quad (4)$$

with

- $x_{\min}$ : minimum concrete cover for durability [mm]
- $a$ : intercept, depending on the current carbonation of concrete [mm]
- $t$ : remaining service life of tunnels [years]
- $\eta$ : coefficient of efficiency of SBT

The information presented in Table 6 reveals a variable scenario. Within test regions A, C1, and C3, a concrete cover measuring 59.4 mm, 42.5 mm, and 38.0 mm respectively, is imperative if no superficial treatment is applied. This thickness is fundamental to prevent steel rebars from becoming enveloped by carbonated concrete during the service life of tunnels, exposing them to the risk of corrosion of reinforcements. Conversely, other test regions (B and C2) necessitate comparatively thinner concrete covers, approximately 20-21 mm, owing to the relatively lower carbonation rate of concrete in those zones.

The SBT application determines a substantial reduction in concrete cover thickness, not solely in the more problematic sections, but also in regions B and C2 where carbonation, even without the SBT,

is constrained. Employing SBT at the D2 dosage level (1.0 l/m<sup>2</sup>) can facilitate a reduction of up to 50% in the minimum thickness of concrete cover to guarantee a proper durability of HSR tunnels.

Table 6 Minimum concrete cover thickness for durability and probability of full carbonation of concrete cover at the end of service life of tunnels

Minimum concrete cover [mm] <i>Probability of full carbonation of concrete cover</i>	Test region				
	A	B	C1	C2	C3
D0 – no treatment	59.4 <i>21.1%</i>	20.3 <i>0.8%</i>	42.5 <i>26.4%</i>	21.5 <i>2.0%</i>	38.0 <i>23.7%</i>
D1 – 0.6 l/m <sup>2</sup>	41.9 <i>5.5%</i>	13.1 <i>0.2%</i>	27.5 <i>10.4%</i>	12.4 <i>0.5%</i>	30.8 <i>13.8%</i>
D2 – 1.0 l/m <sup>2</sup>	37.3 <i>3.6%</i>	10.3 <i>0.1%</i>	25.6 <i>9.1%</i>	11.4 <i>0.4%</i>	27.9 <i>10.9%</i>

A more refined solution for studying the effectiveness of the SBT involves the determination of the probability of complete carbonation of the concrete cover at the end of the service life of tunnels, given the statistical distribution of the concrete cover in the different test fields and the predicted carbonation depth at the 75<sup>th</sup> year of the structure's life. This serves as an indicator of potential corrosive attack on the carbon steel reinforcements.

Based on the results of tests conducted with ground-penetrating radar employing an 8x8 cm grid (involving approximately 2,000 measurements for each test region), it was possible to determine the distribution of the concrete cover around the selected test field. This analysis allowed the identification of the concrete cover thickness distribution in the investigated section for all the test fields, which can be approximated by a normal distribution with mean  $\mu$  and variance. Similarly, starting from the measurements of the  $K_{CO_2-natural}$  coefficients (for which the mean and variance can be easily calculated) and the efficiency parameters  $\eta$ , it is possible to build the normal distribution of the carbonation depth at the 75<sup>th</sup> year. The probability of complete carbonation of the concrete cover at the end of the service life of the works (75 years) is then identified by the area under the two curves, the normal distribution of the concrete cover and that of the carbonation depth.

The results reported in Table 6 confirm the effectiveness of the SBT in reducing the probability of concrete cover carbonation in all test fields, regardless of the expected carbonation depth. In particular, tunnels B and C2 show an extremely limited probability of concrete cover carbonation in the absence of protective treatment, respectively equal to 0.8% and 2.0%; the application of SBT makes this probability engineeringly negligible (< 0.5%). For the other three test fields, however, it is possible to estimate, in the absence of protective treatments, a probability of concrete cover carbonation exceeding 21-26%; this risk can be significantly mitigated by applying the SBT at dosage D2, thereby limiting the probability of total concrete cover carbonation to about 9-11% (C1 and C3) or even to 3.6% (A).

#### 4 Durability of silane-based treatment

Currently, investigations are being conducted into the durability of SBT exposed to UV light, thunder-shower cycling or combination of them. The efficiency of the protective treatment is under evaluation by comparing the contact angle, colour variations and carbonation resistance of concrete protected with SBT before and after ageing. Preliminary results seem to evidence a prolonged service life of the superficial treatment under aggressive environments.

#### 5 Conclusions

Upon the conclusion of the experimental campaign conducted across three distinct Italian HSR tunnels, several conclusions can be drawn:

- The quality of concrete across all test regions is excellent, exceeding the standards set by designers. However, the carbonation depths after 6-10 years exhibit variability among the test regions, attributed to microclimatic disparities.

- The application of SBT has exhibited a pronounced capacity to reduce the accelerated carbonation rate of concrete. The efficiency of the SBT varies across the diverse test regions, ranging from approximately 30% to 60% in terms of  $K_{CO_2-a}$  reduction in comparison with the untreated material.
- The findings of this research are fundamental to ensure the requisite durability of the tunnels in case of limited concrete cover thickness. In this case, it is essential the assessment of concrete cover within the test regions in order to estimate the probability of carbonation of concrete around the carbon steel reinforcements, both with and without superficial treatment.

## References

- [1] H.S. Deng, H.L. Fu, W. Chen, Y.B. Zhao, H.D. Yi, Study on deterioration, cracking mechanism and treatment measures of plain concrete lining with cold joints in high-speed railroad tunnel, *Case Studies in Construction Materials*. 18 (2023) e01895. <https://doi.org/10.1016/j.cscm.2023.e01895>.
- [2] A. Kortazar, G. Bueno, D. Hoyos, Environmental balance of the high speed rail network in Spain: A Life Cycle Assessment approach, *Research in Transportation Economics*. 90 (2021) 101035. <https://doi.org/10.1016/j.retrec.2021.101035>.
- [3] G. Bueno, D. Hoyos, I. Capellán-Pérez, Evaluating the environmental performance of the high speed rail project in the Basque Country, Spain, *Research in Transportation Economics*. 62 (2017) 44–56. <https://doi.org/10.1016/j.retrec.2017.02.004>.
- [4] Y. Yue, T. Wang, S. Liang, J. Yang, P. Hou, S. Qu, J. Zhou, X. Jia, H. Wang, M. Xu, Life cycle assessment of High Speed Rail in China, *Transportation Research Part D: Transport and Environment*. 41 (2015) 367–376. <https://doi.org/10.1016/j.trd.2015.10.005>.
- [5] H. Jones, F. Moura, T. Domingos, Life cycle assessment of high-speed rail: a case study in Portugal, *International Journal of Life Cycle Assessment*. 22 (2017) 410–422. <https://doi.org/10.1007/s11367-016-1177-7>.
- [6] D. Coffetti, E. Crotti, G. Gazzaniga, R. Gottardo, T. Pastore, L. Coppola, Protection of Concrete Structures: Performance Analysis of Different Commercial Products and Systems, *Materials*. 14 (2021). <https://doi.org/10.3390/ma14133719>.
- [7] EN 12390-7 - Testing hardened concrete. Density of hardened concrete, (2019).
- [8] UNI 7699:2018 “Prova sul calcestruzzo indurito - Determinazione dell’assorbimento di acqua alla pressione atmosferica,” (2019).
- [9] EN 12504-4 - Testing concrete in structures. Determination of ultrasonic pulse velocity, (2021).
- [10] EN 12504-1 - Testing concrete in structures. Cored specimens - Taking, examining and testing in compression, (2019).
- [11] L. Coppola, D. Coffetti, E. Crotti, G. Gazzaniga, T. Pastore, Chloride diffusion in concrete protected with a silane-based corrosion inhibitor, *Materials*. 13 (2020). <https://doi.org/10.3390/MA13082001>.
- [12] EN 12390-12 - Testing hardened concrete. Determination of the carbonation resistance of concrete - Accelerated carbonation method, (2020).
- [13] A. Neville, *Properties of Concrete*, 2011.



# **Structural health monitoring**



# Manini Connect: integrated continuous monitoring of precast structures subject to multiple hazards

Manuel Boccolini<sup>1</sup>, Leonardo Casali<sup>1</sup>, Salvatore Romano<sup>1</sup>, Giuseppe Paci<sup>1</sup>, Arianna Peppoloni<sup>1</sup>, Bruno Dal Lago<sup>2</sup>

<sup>1</sup>Manini Prefabbricati S.p.A., Via San Bernardino da Siena 33, 06081 S. Maria degli Angeli (PG), Italy

<sup>2</sup>Università degli Studi dell'Insubria, Department of Theoretical and Applied Sciences, Via Dunant 3, 21100 Varese, Italy

## Abstract

In the context of a rapid climate change, constructions are continuously subjected to numerous critical events caused by both natural and anthropic hazards. Nevertheless, the absence of a praxis towards the installation and the management of sensors dedicated to the performance of the whole building, makes the post-event field surveys and damage mapping extremely difficult. Manini Connect is an innovative patented system providing a response to this issue through integrated monitoring of precast structures, and through a set of interconnected sensors, the system monitors the static and dynamic behavior of the structures during critical events (earthquakes, strong winds, heavy rainfalls, collisions, blasts, etc.) and thermo-hygrometric parameters inside/outside the building. Moreover, it can be coupled with sensors devoted to the monitoring of the air quality inside the building, the local production of energy from renewable sources, and the consumptions in terms of electricity, water, gas, waste, etc. Taking advantage of the production of precast structures in offsite permanent plants, some sensors and utilities are cast within the columns during their production, whilst other typologies are collected into an external box installed on the roof throughout the building construction process. The system sends the data in real-time to the internal control center of Manini Prefabbricati SpA and, after the occurrence of an exceptional event is revealed by the overcoming of predetermined thresholds of demand parameters, the system sends alerts for check. The user has constant access to the data through a dedicated platform. This allows to set predictive retrofit/maintenance works in response to anomalies or damages detected by the system, as a function of the parameters archived from the structural design of each specific building.

## 1 Introduction

The integration of infrastructure monitoring (e.g., bridges, dams) has been rising in response to recent tragic collapses. This approach involves continuous performance checks during operation and in the event of exceptional natural or human-induced actions (such as earthquakes, heavy rainfall, collisions, etc.).

Despite advancements in devices, software and hardware for data acquisition, processing, and display, monitoring techniques focused on overall building behavior remain uncommon. This scarcity complicates post-event field surveys, damage mapping, and retrofit intervention timescales, negatively impacting the resilience of built heritage.

However, the development of integrated monitoring systems, capable of detecting multiple parameters, is gaining interest due to the increased attention to environmental sustainability policies and the involvement of international certification bodies (e.g., USGBC, BRE, IWBI). These systems encompass energy surveys for consumption control and optimization, environmental measurements for occupant health monitoring, and engineering parameters assessing structural durability, robustness, and resilience.

Manini Prefabbricati SpA, among the leading EU companies in the precast construction sector, patented the "Manini Connect" system in 2017, consisting in an integrated and scalable monitoring system designed and developed following the guidelines of Industry 4.0 and the Internet of Things [1]. The rationale is to offer a new after-sales service of continuous active control of the building, monitoring specific performances both during operation and in case of exceptional events.



The development team has continuously worked over the last years to make the Manini Connect system increasingly efficient, optimizing and integrating new related functionalities, including the urgent need to implement environmentally sustainable development policies. Currently, the system includes integrated continuous monitoring of structures, energy, and environment, performed via real-time continuous acquisition.

Up to now, the system has been deployed in numerous building structures, predominantly in industrial and commercial settings.

This paper offers a concise technical overview of the Manini Connect system, outlining its functionality and detailing selected real applications.



Fig. 1 Sensors and pipes installed over the reinforcement cage of a smart column at one of the Manini production plants

## 2 Structural Monitoring

Structural monitoring is conducted using different sensors, the physical supports of which are embedded, along with wiring conduits, inside the structural elements during the concrete casting phase. This ensures that the system is perfectly coupled with the element, and the columns containing it are referred to as "smart columns" (Fig. 1).

Additionally, an external environmental station is typically installed over the roof (Fig. 2). Its dimensions allow to easily position it even in curved roofs such as those employing the Ondal system with wing-shaped roof elements [2]. The station contains, in addition to another series of sensors, a Programmable Logic Controller (PLC), enabling data transmission to a dedicated platform constantly monitored by the Control Center at Manini Prefabbricati S.p.A. An early warning alert activates upon exceeding one of the thresholds set for each recorded parameter.

### 2.1 Integrated Sensor System

Each smart column features a minimum of three compartments designated to accommodate sensors, positioned as follows:

- an accelerometer positioned in the bottom box of the column to monitor accelerations generated by exceptional events such as earthquakes [3], [4], or impacts/blasts (input towards the structure);
- an accelerometer positioned in the top box of the column and eventually in the intermediate box(es) to measure accelerations near the floor resulting, for example, from oscillations caused by a seismic event, or wind-induced vortex shedding, or mechanical vibrations induced by machines installed over the floor, or human-induced vibrations over slender slabs [5];
- an inclinometer positioned in the top box of the column to measure residual inclinations resulting, for example, from seismic events or subsidence;
- a temperature sensor to monitor thermal drifts and an environmental sensor for monitoring CO<sub>2</sub>, relative humidity, and internal temperature, both positioned in the bottom box, aimed at monitoring the internal air quality, as well as local fire development [6];
- a flow meter positioned inside the internal rainwater downpipes of the smart column to verify proper drainage, detecting any possible obstruction of the conduct, positioned in the intermediate box.

On the roof, an environmental weather station is installed housing:

- an anemometer for monitoring the wind speed acting at the level of the roof;

- a rain gauge for monitoring the amount of rainfall on the roof;
- a temperature sensor for monitoring external climatic conditions;
- a webcam for monitoring the roof;
- a PLC for sensor management.

Moreover, additional sensors may be plugged to monitor the performance of specific dampers installed for the mitigation of earthquake-induced motions [7], [8], or wind-induced vortex shedding [9] or pressure sensors may be incorporated into the roof station to monitor the pressure induced by snow accumulation [10].

Structural monitoring addresses both static and dynamic responses. Accelerometric sensors transmit 100 data points per second, while all other sensors transmit data every 10 minutes. The system, comprised of sensors and a PLC, is developed to send recorded data to the cloud platform, where it is processed using dedicated algorithms and then displayed on a web portal accessible by both the building's client (client area) and the Control Room at Manini Prefabbricati (administrator area), with the workflow described in Fig. 3.

The set of parameters monitoring internal and external climatic conditions of the building provides information on the efficiency of energy systems. The environmental sensor detects abnormal CO<sub>2</sub> levels, which can be harmful to human health, and thermo-hygro-metric conditions indicated by relative humidity. The monitoring service provided with Manini Connect notifies the user of threshold-exceeding values in real-time, aiming to avoid prolonged exposure, especially during certain production activities characterized by higher pollutant emissions.

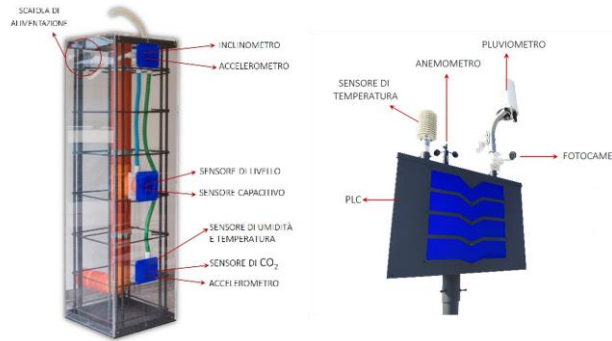


Fig. 2 Sensor disposition on smart columns and roof environmental weather station

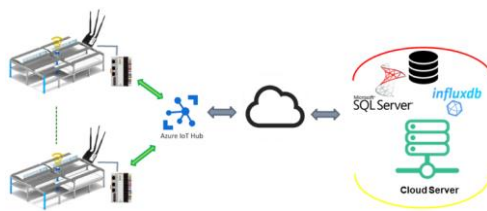


Fig. 3 Manini Connect system workflow

## 2.2 Platform and Data Visualization

The platform allows for the visualization of incoming alerts, sensor readings, and frames captured by the roof-mounted webcam during each threshold-exceeding event. Through this tool, Control Room technicians can analyze the correspondence between alerts and measured data and provide early warning service to the client, offering information regarding any detected issues if necessary. Data communication from the site to the centralized cloud infrastructure is based on M2M protocol using MQTT (Message Queuing Telemetry Transport), implementing TLS 1.3 security algorithms.

Each client, through their dedicated area, can view collected data presented in graphs depicting the current state of the monitored structure, updated in real-time. If needed, data collected for each sensor

can be viewed within a specific time window. Similarly, users can view sequential photos of the roof by setting a reference time period. An example of the software interface is shown in Fig. 4.

Timestamp	Impianto	Controllore	Sensore	Valore	Severità	Utente	Ack	Note
30/01/2024 08:36:54		CX-427D7F	temperatura_2	4.98	ALLARME	ADMIN MANINI	<input checked="" type="checkbox"/>	Check ok
25/01/2024 13:14:45		CX-537F24	anemometro_0	22.0	ALLARME	ADMIN MANINI	<input checked="" type="checkbox"/>	Check ok
24/01/2024 12:59:12		CX-915D4E	co2_1	1250	ALLARME	ADMIN MANINI	<input checked="" type="checkbox"/>	Check ok
22/01/2024 08:41:48		CX-6D089B	capacitivo_1 capacitivo_2 capacitivo_3	0 0 0	ALLARME	ADMIN MANINI	<input checked="" type="checkbox"/>	Check ok

Fig. 4 Manini Connect software interface

### 2.3 Control Room

Upon the transmission of alerts, these are received on the platform and examined in real-time by the Control Room at Manini Prefabbricati S.p.A. (Fig. 5), which continuously monitors the supervised buildings.

The early warning service alerts the user of the occurrence of specific events and how the structure responded to the specific events. A threshold is set for each sensor at which the system forwards alarms; these are set in accordance with design criteria and user needs.

The monitoring service also includes the sending of bi-monthly and annual reports, detailing the trends of all monitored parameters and highlighting values outside normal conditions. Annual reports provide a broader view of how the structure responded to critical events over the last five years, documenting all threshold exceedances and identifying possible issues. This allows for the organization of predictive maintenance in response to real problems.

Annually, a meeting is scheduled to identify maintenance activities carried out and assess the building status based on the events it has experienced; in the case of particularly critical events, the organization of specific maintenance activities will be prompted in line with the building's user manual and maintenance guidelines.

The collection of reports, notifications, and minutes provided following maintenance activities allows for the updating of the "building logbook," which tracks events affecting the structure over the years, serving as a useful tool for positioning the property in the market in the event of sale.



Fig. 5 Control Room

### 2.4 Algorithm for the derivation/integration of data in the time domain

Dynamic monitoring involves a special processing that allows, through double integration algorithms, to calculate the displacement experienced in the roof following a major seismic event after the acceleration time history has been recorded. This procedure provides useful information regarding the state of the structure following a seismic event, and to this parameter specific survey actions may be associated.

Data from the base of the smart columns allow the intensity of the event to be placed within the scale of thresholds provided by the standard, while the accelerations received at the intermediate and roof levels are doubly integrated into displacement in the time domain by the algorithms. This allows a

direct comparison with the calculation model and the design limit state values provided by the standard. The inclinometer allows the residual rotations of the column head to be recorded at the end of the seismic event.

A further activity potentially conducted in case of occurrence of strong motions or windstorms with significant vortex shedding is to compare the result obtained in real-time by the algorithm with that deduced from the FEM analysis, to which the signals recorded by the accelerometers installed at the base of the columns are set as input.

### 3 Applications

#### 3.1 Seismic event

A case study is presented involving a monitored building that experienced a seismic event. On March 9, 2023, the Manini Connect system detected accelerations caused by a 4.3 magnitude earthquake occurred in the Umbria region, with the epicenter in Umbertide (PG) at a depth of 10 km below the surface (further information available at <https://earthquake.usgs.gov/earthquakes/eventpage/us7000jiiim/execute>). The smart columns of the monitored building are situated at the two opposite corners, as depicted in Fig. 5.

Once the alert was received in real-time, the team of technicians analyzed the data recorded by the sensors and the curves calculated by the algorithm, through the analysis of accelerometric responses and their spectra (as in Fig. 6 and Fig. 7), immediately obtaining the maximum acceleration recorded by the accelerometers installed at base and top of the smart column. Filtering procedures and double integration of the recorded signals derive the maximum displacement experiences by the smart column at its top. This allowed for the preparation of a technical report containing the accelerogram and related analyses, which was sent to the client within a few hours from occurrence of the event. In this specific case, the results showed levels of accelerations and displacements above the alarm activation threshold which, as shown in Fig. 6 with reference to the base accelerometer, were indeed clearly above the noise range. Nevertheless, the data resulted not exceeding the Damage Limit State adopted in the design procedure. This allowed the manager of the building to safely conduct normal activities after a quick visual survey, without having to carry out inspections or specific surveys which, anyhow, are always subject to the inspector subjectivity.

The service provided by Manini Connect serves as a support tool, allowing those conducting inspections to compare the data recorded by the sensors (accelerometers and inclinometers) and processed by the software with visual analysis of the structure, which may not always be sufficient in these situations. This enables the scheduling of inspections, maintenance, or necessary interventions for the retrofit of the structure, thereby preventing further damage and safeguarding the lives of living/working occupants.

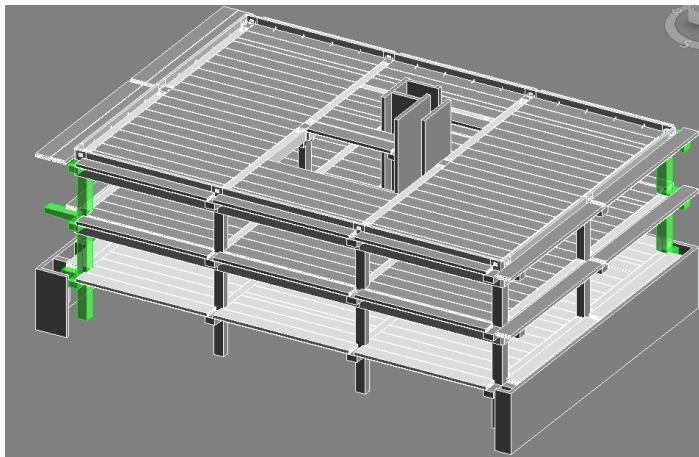


Fig. 5 The most stressed columns are at the opposite corners of the building (highlighted in green)

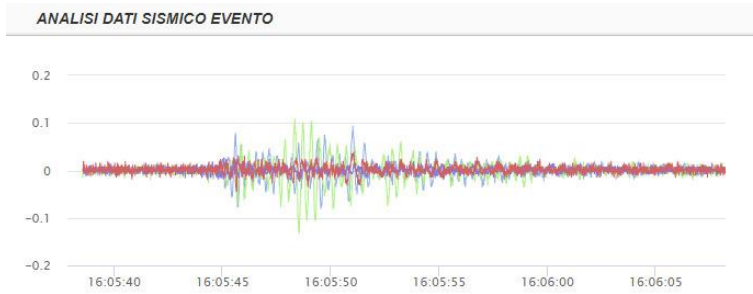


Fig. 6 Accelerogram components recorded at the base of the smart column as displayed in the software: vertical in red, horizontal along SN in green, and horizontal along EW in blue. Unit: [g]

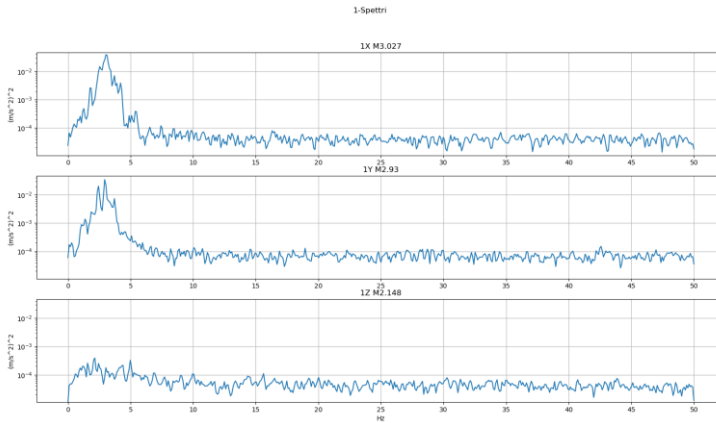


Fig. 7 Acceleration spectra associated to the x (at the top), y (at the center) and z (at the bottom) component axes

### 3.2 Wind velocity

The wind velocity is monitored by the anemometer. The record of a full year is shown in Fig. 8, demonstrating for a typical random year that the site experienced strong winds for few days along the year, however with peak velocities of about 20 m/s, below the characteristic value employed for SLS design.

### 3.3 Rainfall

The measurements of the pluviometer allow to detect events with rainfall flow larger than design one with which the drainage system was proportioned. In the example shown in Fig. 9, this flow was attained in two events in one year.



Fig. 8 Wind velocity time history over a time span of one year. Unit: [m/s]

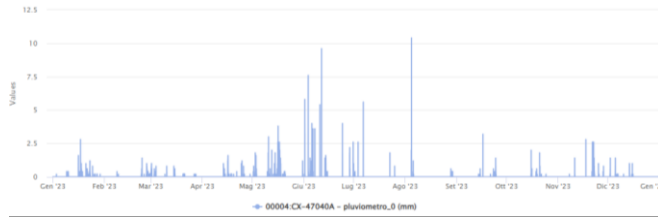


Fig. 9 Rainfall flow time history over a time span of one year. Unit: [mm/h]

### 3.4 Energy production

Manini Prefabbricati also provides a service integrated with the other functions concerning the sale, installation, and maintenance of photovoltaic systems installed on the building roof. The management of the system has been integrated into the Manini Connect system, allowing for the monitoring of various parameters and receiving real-time alerts in case of operational anomalies or interruptions of the system. This enables the monitoring of panel activity and the scheduling of routine and extraordinary maintenance interventions.

Throughout the year, the system automatically generates reports on the efficiency of the system, providing data and information on the energy actually produced and expected, the energy absorbed, and any energy stored or sold.

All customers can access the data through the dedicated web portal's reserved area, designed entirely by Manini with the assistance of APIs (Application Programming Interfaces) provided by the system suppliers.

## 4 Energy management and air quality

Manini Prefabbricati also provides an integrated service for the sale, installation, and maintenance of Building Energy Management Systems (BEMS) for the monitoring and management of those parameters that mostly define the sustainability of a living/working site: environmental parameters (particularly CO<sub>2</sub> and TVOC), energy consumption from traditional utilities (water, electricity, gas, etc.), and recycled waste.

This type of monitoring is specifically aimed at clients who have the intention to implement green strategies and monitor their efficiency, which can be used to certify their building with bodies prepared to recognize environmental sustainability policies.

The service includes the semi-automatic compilation of personalized reports on the efficiency of the system, providing data and information that attest to the successful implementation of sustainable strategies by the user.

## 5 Conclusion

The Manini Connect monitoring system offers an advanced solution for interpreting building structural behavior, facilitating intelligent and predictive maintenance management through integrated monitoring. This approach optimizes interventions and ensures prolonged functionality. Its widespread adoption is characterized by cost-effective installation and substantial reductions in insurance premiums, promoting an eco-sustainable vision within the construction sector. The system's industrialization yields financial benefits, including annual reductions in all-risk insurance premiums for equipped buildings. Its adaptable and modular architecture enables broad application, potentially extending to sectors like preserving artistic and architectural heritage and managing large public works projects.

Future development may involve integrating with Italy's national network of accelerometers and the Department of Civil Protection, providing additional valuable insights into local event demand and building response patterns.

## References

- [1] Coviello, G., Zichi A., Bellini, S., 2020. „BIM and BMS for the management of the building: the Manini Connect case for Digital Twin services.“ Politecnico di Milano, European Master in Building Information Modeling BIM A+.
- [2] Dal Lago, B., 2017. *Experimental and numerical assessment of the service behaviour of an innovative long-span precast roof element*. *International Journal of Concrete Structures and Materials* 11(2), 261–273
- [3] Dal Lago, B., 2021. *Vulnerability assessment of precast industrial facilities*. *Seismic Vulnerability Assessment of Civil Engineering Structures at Multiple Scales: From Single Buildings to Large-Scale Assessment*, T.M. Ferreira and H. Rodrigues (ed.), Elsevier, 205–228.
- [4] Bosio, M., Di Salvatore, C., Bellotti, D., Capacci, L., Belleri, A., Piccolo, V., Cavalieri, F., Dal Lago, B., Riva, P., Magliulo, G., Nascimbene, R., Biondini, F., 2023. *Modelling and seismic response analysis of non-residential single-storey existing precast buildings in Italy*. *Journal of Earthquake Engineering* 27(4), 1047–1068.
- [5] Dal Lago, B., Martinelli, L., Foti, F., 2022. *Slender precast voided slabs under walking-induced vibration*. *Structural Concrete* 23(6), 3416–3443.
- [6] Dal Lago, B., Tucci, P., 2023. *Causes of local collapse of a precast concrete industrial roof after a fire event*. *Computers & Concrete* 31(5), 371–384.
- [7] Casali, L., Dal Lago, B., Fulco, A., Mezzi, M., 2023. „Environmental impact reduction of precast multi-storey buildings by crescent-moon seismic dampers hidden in beam-column joints. Proceedings of Life-Cycle of Structures and Infrastructure Systems“ – IALCCE2023 – 8th International Symposium on Life-Cycle Civil Engineering, Biondini F., Frangopol, D.M. (Eds), Milan, Italy, 2nd-6th July, 2523–2530.
- [8] Fulco, A., Casali, L., Dal Lago, B., Comodini, F., Mezzi, M., 2024. “Energy dissipation systems to optimize the seismic performance of precast residential buildings.” Proceedings of 18th World Conference of Earthquake Engineering (18WCEE), Milan, Italy, 30th June-05th July, in print.
- [9] Foti, F., Dal Lago, B., 2021. “Mitigation of wind-induced vibrations in high-rise dry-assembled precast concrete residential tower buildings.” 10th UBT International Conference on Civil Engineering, Infrastructure and Environment, Pristina, Kosovo, 29th-30th October, Paper No. 301.
- [10] Dal Lago, B., Dal Lago, A., Marchetti, U., Basso, A., 2021. „Behaviour and overstrength of a precast concrete roof with prestressed elements subjected to snow loading“. Italian Concrete Days 2020 (ICD2020), Napoli, Italy, 10th-12th June.

# Reinforced concrete bridge serviceability displacement estimation for DInSAR data interpretation

A. Sandoli<sup>1,2</sup>, S. Scoccola<sup>1</sup>, C. Rainieri<sup>3</sup> and G. Fabbrocino<sup>1,2</sup>

<sup>1</sup>*Department of Biosciences and Territory, University of Molise, Via Francesco De Sanctis n. 1, Campobasso (CB) 86100, Italy*

<sup>2</sup>*Construction Technologies Institute-National Research Council, Via Carducci n. 2, L'Aquila (AQ) 67100, Italy*

<sup>3</sup>*Construction Technologies Institute-National Research Council, Corso N. Protopisani n. 17, Napoli (NA) 80146, Italy*

## Abstract

Structural health monitoring of existing bridges is gaining attention of the technical community for an informed management of the structural safety under service conditions. In this context - complementary to the traditional installation of sensors - the satellite interferometry is exhibiting a large potential in monitoring the displacements of the existing bridges network. To date, the scientific literature highlights that this technique is still critical in evaluating the deformations of the structures induced by thermal variations, being it difficult to establish when the displacement field is due to physiological temperature gradients or to structural defects. The present paper deals with an estimation of the displacements induced by thermal effects (in combination with traffic loads) in existing reinforced concrete bridges by means of simplified approaches in order to support satellite (or instrumental) data interpretation and expand capabilities of existing remote sensing-based monitoring techniques. Analytical formulations and numerical procedures to estimate the displacements of the structural members associated with uniform and linear thermal load distributions are proposed. As outcomes, diagrams and schedules including displacements associated with the considered variables have been generated: they allow to quantify the displacements due to thermal effects for all the considered cases, also representing a baseline to help the processing of the displacement detected through monitoring systems (instrumental- or satellite-based).

## 1 Introduction

Knowledge of the displacement fields of existing bridges under serviceability conditions plays a crucial role for an effective management of road transportation networks [1]. These effects can be taken in due consideration for assessment and diagnostic purposes of bridges, especially when characterized by large spans.

Complementary to the traditional Structural Health Monitoring (SHM) techniques, the satellite interferometry is an interesting emerging technology used to detect the displacement fields of structures and infrastructures, with the advantage of covering long time intervals and of operating remotely [2]. To date, the potentialities offered by the satellite data in SHM, and the development of methodologies and technologies devoted to data post-processing aimed at detecting the bridge displacements are investigated in the literature [3, 4]. For instance, the assessment of possible pre-failure bridge deformations or anomalies based on SAR (Synthetic Aperture Radar) observations with application to the Morandi bridge in Italy (collapsed in 2018) was investigated by Milillo et al. [5]. Post-processing procedures of the satellite Measurement Points (MPs) based on two- or three-dimensional clustering are described in [6] and [7], respectively. Ponzo et al. [8], instead, used the Differential Synthetic Aperture Radar interferometry (DInSAR) technique for monitoring the service displacements of the Trovajoli bridge in Rome (Italy). In this regard, other interesting works dealing with the monitoring of bridges through satellite data are available in [9, 10].



Satellite interferometry provides the displacement time-series of the investigated bridge, including all the potential effects influencing their dynamic behaviour under service conditions, such as traffic, temperature, landslides, subsidence or other effects. On the other hand, for a comprehensive analysis of the service behaviour of the bridges, the computation and differentiation of the displacement components appears fundamental [11]. Among these, the evaluation of the displacements induced by daily seasonal temperature variations, which are often comparable with the displacements induced under dead and live loads, is a challenging task [12]. To this scope, theoretical, experimental and numerical complex models have been developed to study the temperature distribution and their effect in bridge structures. Recently, Zhu and Meng [12] developed a three-dimensional sunlight-sheltering algorithm to predict temperature fields with an application to cable-stayed bridge, while Larson and Thelandersson [13] proposed a finite element model to predict positive and negative gradient variations in reinforced concrete structures based on climate data coming from meteorological stations. Lee and Kalkan [14] studied the transverse temperature distribution in the cross-section of prestressed concrete girder.

Nevertheless, in the framework of large-scale remote assessment of bridges based on satellite interferometry, comprehensive approaches devoted to extrapolating the service displacements related to seasonal temperature variations and the evaluation of their effect on the overall displacements of the structures needs to be developed. This paper presents an estimation of the displacements induced by thermal effects in existing reinforced concrete bridges by means of simplified approaches with the aim of supporting the satellite (or instrumental) measures interpretation and of expanding capabilities of existing remote sensing-based monitoring techniques.

A comparative analysis between the time-series processed by Small BASeline Subset - Differential Synthetic Aperture Radar Interferometry (SBAS-DInSAR) technique [15] and the displacement estimations due to serviceability loads (temperature variations and vehicles) made on simplified mechanical models was conducted. Results are discussed with reference to the explanatory case study of the Tor di Quinto (TdQ) reinforced concrete bridge located in the Rome metropolitan area.

## 2 Materials

The issue of the assessment of serviceability displacements of reinforced concrete bridges induced by serviceability loads, i.e. service traffic and thermal variations, is a critical task for planning maintenance and management protocols. Recent literature studies demonstrated the potentialities offered by satellite-based SHM of bridges. Despite this, some issues still affect the displacement assessment, especially when correlation with displacement field induced by thermal loads in combination with those related to traffic are sought.

In this perspective, the interpretation of the interferometric data requires the support of analytical solutions aimed at detecting the displacement generated by temperature gradients. Thus, qualitative and quantitative displacement components induced by temperature can be assessed, providing a comprehensive SHM of the investigated bridge.

Different structural members of the bridge can be affected by temperature loadings, which can be simulated by means of a uniform or variable component assumed to be linearly distributed over the thickness of the elements. Since the reinforced concrete bridges consist of different structural types, the primary effects of uniform temperature variations are related to: *i*) height variation of the bridge piles, *ii*) elongation of the bridge decks, *iii*) variations of the arch rise. Analytical and numerical solutions for assessing the displacement fields in reinforced concrete members, related to both uniform and linear thermal effects, have been recently proposed [7]. The research has been conducted with a parametric approach, i.e. by considering as variables the rise-to-span ratios of arch bridges, transversal cross-section-to-span ratios of beams and pile-to-height of cross section ratios of piles to calculate the displacements. Moreover, [7] also points out, as main issue, the importance of the wavelength amplitude of the radar sensor in comparison with the magnitude of the displacements associated to temperature gradients: when the displacements due to thermal loads (or whatever other type of displacement) overcome the wavelength of the satellite operating in a given band, such displacement cannot be read by the satellite [16]. Typically, the fraction of displacement observable by the satellite is  $\lambda/4$  (where  $\lambda$  is the wavelength) [17].

In this perspective - and as research advancement of the present paper - the Figs. 1 and 2 report the maximum values of span and pile length (i.e., limit lengths) for which the displacement induced by temperature variations are compatible with the wavelength of the satellite operating in band X (i.e.,

$\lambda/4= 0.775$  cm) as a function of the temperature load (linear or constant).The formulas for calculating the maximum (o limit) span of beam and pile height when loaded by linear temperature gradients are reported in the following, respectively:

$$L_{lim} = \sqrt{\frac{8k}{\alpha \beta_{linear}}} \tag{1}$$

$$H_{lim} = \sqrt{\frac{2k}{\alpha \beta_{linear}}} \tag{2}$$

While, the limit height of the piles loaded by uniform temperature distribution is given by:

$$H_{lim} = \frac{k}{\alpha \Delta T} \tag{3}$$

where  $\beta_{linear} = \Delta T/H$ ,  $k$  is the maximum wavelength of the satellite (that in band X is  $k=0.25 \times 3.1$  cm =0.775 cm), and  $\alpha$  is the linear thermal coefficient of material. Note that for the cases of piles, uniform variation of temperature has been reasonably considered ranging between  $-30^{\circ}\text{C}$  and  $+30^{\circ}\text{C}$ , while the linear one ranged between  $-15^{\circ}\text{C}$  and  $+15^{\circ}\text{C}$  [18].

The diagrams reported in the Figs.1 and 2 - in combination with analytical and numerical solutions devoted to estimating thermal displacements of reinforced concrete bridge members reported in [7] - allow to compute, in a simplified way, the limit beam span and pile length compatible with the satellite data and to quantify if thermal oscillations are or not of major interest for post-processing satellite data. In this perspective, the possible use of the data reported below is twofold: a) an assessment of the expected performance of the standard radar data processing, as a function of the type of structure and the environmental conditions in terms of daily temperature at the site of interest; b) a guide and an easy to manage reference for specialists involved in the optimization and refinement of the SAR data processing to include thermal deformations.

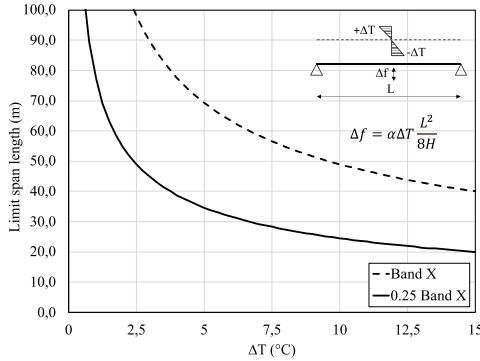


Fig. 1 Limit span length for beam subjected to linear temperature loads.

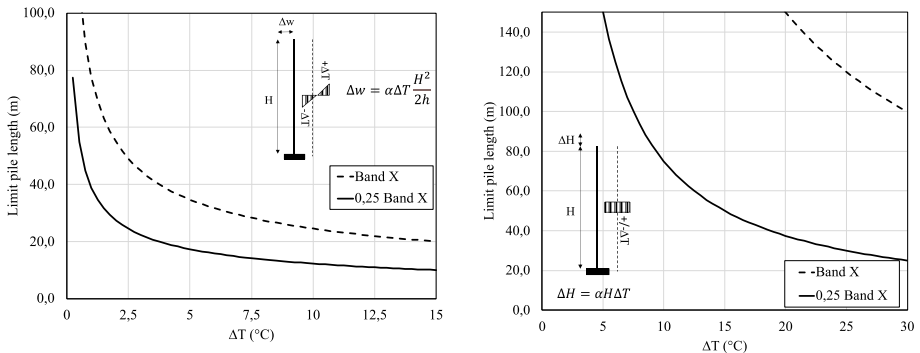


Fig. 2 Limit height for pile subjected to linear (left) and uniform (right) temperature loads.

### 3 Methods

#### 3.1 Tor di quinto bridge

In the present research, the Tor di Quinto (TdQ) bridge located over the Tiber river of the city of Rome (Italy) has been considered as an explanatory case study (Fig. 3). The structural-typological characteristics and the geometrical data of the bridge have been detected remotely through the crowd-sourcing paradigm [7]. Web-mapping platforms, i.e. Google Maps and Google Earth, have been used to perform virtual street tours around the bridge, definition of the most relevant structural and functional features and thus estimating the dimensions of spans, beams and deck. The bridge is made of reinforced concrete and was erected in the 1960s. It consists of multiple spans (seven) with different length and the total length of the bridge is about 275 m. In the zone of the bridge crossing the lateral side of the river the beams, with rectangular cross-section, are simply supported by the vertical piers and by Gerber saddles, alternatively, whereas in the zone crossing the river, the beam consists of a single span element with variable hollow cross-section. At the top of the beam system, a 50 cm thick reinforced concrete deck is present. Fig. 3 highlights the span considered as explanatory case study in this paper, while Fig. 4 reports some details of the span itself: it consists of parallel reinforced concrete beams with rectangular cross-section (dimensions 20 x 150 cm) simply supported to abutment on one side and, on the other one, to Gerber saddle.



Fig. 3 General view of TdQ bridge (<https://maps.app.goo.gl/95aAR73H6JM6wCvFA>); the selected simply supported span is shaded in yellow.



Fig. 4 Details of investigated span (adapted from <https://maps.app.goo.gl/BYHCM9kHMvgMR-BiU8>); span length on the left (View #1), cross-section height of the beam on the right (View #2).

#### 3.2 DInSAR data

The dataset used for estimating the displacement of the TdQ bridge was provided by IREA-CNR Institute in the context of the research project Reluis WP6 issued by the Italian National Department of Civil Protection. Both ascending and descending orbits were made available for the entire metropolitan area

of Rome and for a time interval covering about ten years (2011-2019). The dataset has been processed using COSMO-SkyMed Stripmap HIMAHE according to Small Baseline Subset (SBAS) algorithm characterized by a spatial resolution of about 3 m in azimuth as well as range directions.

The raw data provided by CNR-IREA have been post-processed according to the DInSAR data processing workflow proposed in [7] to obtain displacement time-series of the bridge. In such a procedure, a Matlab script was developed to read, reorder and feed both ascending and descending orbits of the dataset. DInSAR data are uploaded over a Geographic Information System (GIS) to visualize the MPs over the earth surface. According to the clustering procedure presented in [7], both 2D and 3D displacement maps of the different MPs can be represented, allowing to assess and localize deformation phenomena of the investigated structure. Moreover, the procedure performs the spatial and temporal resampling of the MPs necessary to obtain a set of spatially referenced MPs: in such a way the information concerning the displacement velocities along the Line of Sight (LOS) are available, both for ascending and descending orbits. Thus, MPs are georeferenced and clustered into spatial referenced grids including the MPs defining the volume of the investigated object (or area). Each sub-grid contains a given number of MPs, depending on the dimensions chosen for the sub-grids. For each sub-grid the displacement time-series are described through the definition of an average MP representative of the entire cluster of ascending and descending MPs included in the sub-grids [7]. In Fig. 5 the MPs distribution is shown for the TdQ bridge in GIS environment and, both for ascending (ASC) and descending (DSC) orbits, the relative displacement velocities expressed in centimetres per year. As it can be noted, for the selected span - and for the entire bridge also - the displacement velocities are very reduced (in the order of 0.05-0.02 cm/year) and then out of the typical range of differential settlements or that associated to low landslides under serviceability condition [19].

In Fig. 6, the 3D-cluster containing the MPs of the ascending and descending orbits of the selected span is shown. In the same figure, the cell at the middle of the span is also highlighted, from which time series displacement are extrapolated and discussed in the following Section.

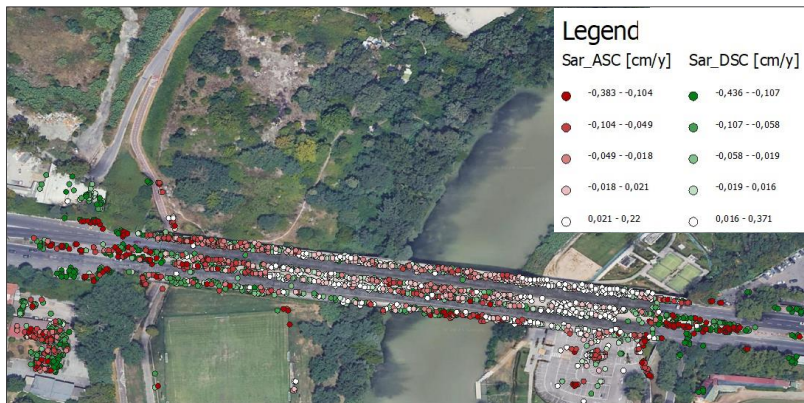


Fig. 5 Ascending and descending MPs for the TdQ bridge.

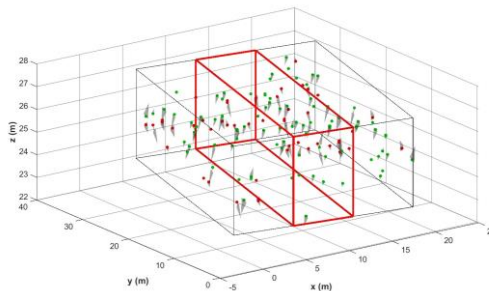


Fig 6 Clustering of the selected span with ascending (red) and descending (green) points.

### 3.3 Girder displacements under serviceability loads

Estimation of the girder displacements under serviceability loads is reported in the following with reference to effects of thermal and vehicle loads, separately. Simplified calculations are performed accounting for linear temperature gradients on the cross-sections first, then assuming static loading conditions corresponding to different traffic jam scenarios. To this scope, the mid-span displacements have been calculated with reference to the selected span shown in Fig. 3.

Fig. 7 reports the synchronized time-series obtained through the post-processing procedure discussed in the Section 3.2 [7], including the limit displacement values associated with the maximum displacement observable from the satellite in band X. The time-series is relative to the average MP of the cluster located at mid-span of the selected span of the TdQ bridge (Fig. 6).

For comparison purposes, over the same diagram of Fig. 7 the vertical displacements at mid-span due to linear temperature variations are reported. The latter have been calculated according to [7] assuming temperature gradients  $\Delta T$  equal to 2°C, 4°C, and 6°C, which are representative for typical serviceability conditions, whose values are also suggested in [12] and [13].

For a more comprehensive assessment of the beam displacement under service conditions, the static vertical displacements associated to service traffic loads have been also computed and compared in Fig. 7. The mid-span traffic vertical displacements are those resulting from the two loading conditions provided by the Italian Guidelines [20], which enables to assess the transit conditions of existing bridges. The Guidelines provide three traffic jam conditions named with Light (L), Medium (M) and Heavy (H). The combination L considers a load distribution associated with the presence of a vehicle having a weight equal to 75 kN placed in the middle of the span and 4.2 kN/m<sup>2</sup> of distributed load after and before of the vehicle. The combination M considers a load distribution associated with the presence of a vehicle having weight equal to 26 tons placed in the middle of the span and 7.5 kN/m<sup>2</sup> of distributed load after and before of the vehicle.

The combination H considers a load distribution associated to the presence of a vehicle having weight equal to 440 kN placed in the middle of the span and 9.0 kN/m<sup>2</sup> of distributed load after and before of the vehicle. In this paper, to simulate service traffic, the conditions L, M and H have been combined by varying the load distribution over the two lanes constituting the span of the bridge as follows: *a*) LL, light loads equal to 440 kN uniformly distributed on both lanes of the bridge; *b*) LM, light (7.5 tons) and medium (260 kN) loads alternates along the two lanes; *c*) LH, light (75 kN) and heavy (440 kN) loads alternates along the tow lines. For such load combinations, the maximum (static) mid-span deflection ( $f$ ) has been calculated by considering the tension stiffening effect of the concrete, as suggested by the Italian Building Code for Construction [21]:

$$f = \xi f_1 + (1 - \xi) f_2 \quad (4)$$

where  $\xi = (1 - c\beta^2)$ ,  $\beta = M_{cr}/M$  ( $M_{cr}$  is the first cracking bending moment of the cross-section and  $M$  is the acting moment at mid-span due to uniform loads),  $f_1$  is the mid-span deflection associated with uncracked cross-section,  $f_2$  the mid-span displacement associated with cracked cross-section and  $c = 1.0$  or 0.5 in the case of short-or long-term loads, respectively.

Fig. 7 highlights that the mid-span time-series displacements provided by the satellite interferometry are lower than those associated with static deflections due to temperature gradients, thus the latter do not have any effect on the displacement of the bridge detected by the satellite. As far as the influence of traffic is concerned, Fig. 7 shows that it also seems to have an influence on the time-series displacements: the combinations LM and LH provide static displacements out of the wavelength signal of the satellite, while the combination LL (which potentially can be read from the signal) gives mid-span deflections higher than those of the time-series. Moreover, as discussed in the previous section, Fig. 5 shows that the displacement velocities affecting the bridge are not representative of settlements or displacements at foundational level.

These considerations confirm that the displacements detected by satellite interferometry can be addressed as noise polluted measures and are not representative of any significant structural for the considered case study. Furthermore, it is worth noting that despite the magnitude of the serviceability vertical displacements of the girder, the presence of measurements along the most reflective lines of the

girder (i.e. protective railings) is observed, highlighting in the present case the role of the reflective capabilities of non-structural components combined with the poor performance of the road surface.

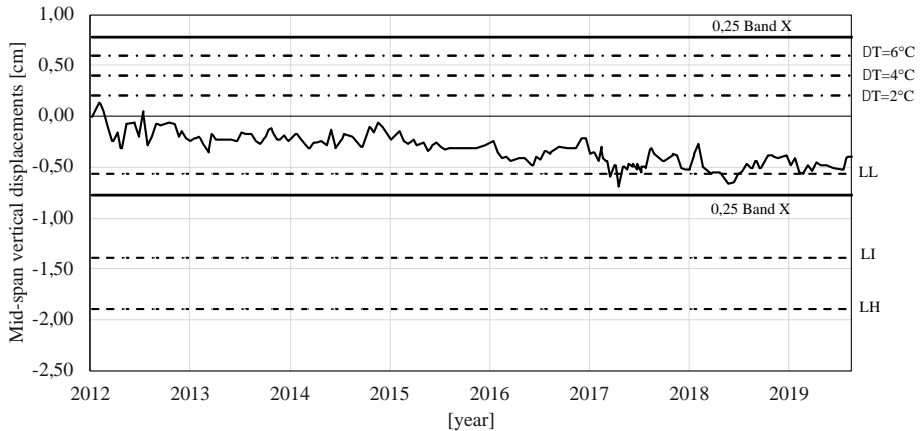


Fig. 7 Mid-span vertical DInSAR time-series displacement versus thermal and traffic loads estimates.

#### 4 Concluding remarks

The present paper presents preliminary research outcomes about a more comprehensive study devoted to estimate the serviceability displacements in existing reinforced concrete bridges monitored through satellite interferometry. The aim is supporting the interpretation of satellite data and expanding the capabilities of existing remote sensing-based monitoring techniques. In this perspective, diagrams providing the limit length of span and piles for which the displacements induced by temperature variations are compatible with the wavelength of the satellite operating in Band X (i.e.,  $\lambda/4 = 0.775$  cm) as a function of the temperature loads are provided.

As an explanatory case study, the Tor di Quinto bridge (Rome, Italy) was considered, for which a long term DInSAR monitoring between 2011 and 2019 is available. A comparison between displacements associated with both thermal effects and from traffic with those estimated through DInSAR technology was performed. The research outcomes showed the potentialities offered by simplified procedures in supporting the interpretation and validation phases of structural health satellite-based monitoring. Despite any conclusive consideration can be made from this single case study, the results pointed out how the displacement estimates provided by the satellite can be often related to noise pollution rather than real displacement of the bridge associated with service vibrations; as result, a careful analysis from the a structural engineering perspective of the SBAS-DiNSAR measurements is recommended for a rational and informed interpretation whenever single structures are of interest. In such a context, simplified methodologies and tools able to deliver reliable estimates of the expected deformations under serviceability loads appear to be crucial for a rational and informed large scale remote-sensing monitoring of bridges.

#### Acknowledgments

This study is partially funded by the Superior Council of Public Works and RELUIS in the framework of the WP3 – Task 3.2 – and WP5 Special Projects – Task 5.6. – of the research aimed at assessing and validating the National Guidelines for the mitigation of the risk of bridges and transportation networks. Part of the research activities were also developed by the third author in the framework of the PNRR Program, National Center for Sustainable Mobility, SPOKE 7 “CCAM, Connected Networks and Smart Infrastructure” - WP4.

#### References

- [1] Rainieri C, Notarangelo M, Fabbrocino G. 2020. “Experiences of Dynamic Identification and Monitoring of Bridges in Serviceability Conditions and after Hazardous Events.” *Infrastructures* 5(10), 86.

- [2] Talledo DA, Miano A, Bonano M, Di Carlo F, Lanari R, Manunta M, Meda A, Mele A, Prota A, Saetta A, Stella A. 2022. "Satellite radar interferometry: Potential and limitations for structural assessment and monitoring". *Journal of Building Engineering* 46: 103756.
- [3] Nettis A, Massimi V, Nutricato R, Nitti DO, Samarelli S, Uva G. 2023. "Satellite-based interferometry for monitoring structural deformations of bridge portfolios." *Automation in Construction*, 147: 104707.
- [4] Hoppe E, Novali F, Rucci A, Fumagalli A, Del Conte S, Falorni G, Toro N. 2019. "Deformation monitoring of posttensioned bridges using high-resolution satellite remote sensing." *Journal of Bridge Engineering* 24(12), 04019115.
- [5] Milillo P, Giardina G, Perissin D, Milillo G, Coletta A, Terranova C. 2019. "Pre-collapse space geodetic observations of critical infrastructures: the Morandi bridge, Genoa, Italy." *Remote Sensing* 11, 1403.
- [6] Giordano PF, Turksezer ZI, Previtali M, Limongelli MP. 2022. "Damage detection on a historic iron bridge using satellite DInSAR data." *Structural Health Monitoring* 21(5):2291-2311.
- [7] Sandoli A, Petracca E, Rainieri C, Fabbrocino G. 2024. "Operation of interferometric SBAS-DInSAR data for remote structural monitoring of existing bridges." *Journal of Bridge Engineering*, accepted for publication.
- [8] Ponzo CF, Iacovino C, Ditommaso R, Bonano M, Lanari R, Soldovieri F, Cuomo V, Bozzano F, Ciampi P, Rompato M. 2021. "Transport Infrastructures SHM using integrated SAR data and on-site vibrational acquisitions: "Ponte della Musica-Armando Trovajoli" case study." *Applied Sciences*, 11, 6504.
- [9] Cusson D, Rossi C, Ozkan IF. 2021. "Early warning system for the detection of unexpected bridge displacements from radar satellite data." *Journal of Civil Structural Health Monitoring* 11: 189-204.
- [10] Farneti E, Cavalagli N, Costantini M, Trillo F, Minati F, Venanzi I, Ubertaini F. 2023. "A method for structural monitoring of multispan bridges using satellite InSAR data with uncertainty quantification and its pre-collapse application to the Albiano-Magra Bridge in Italy." *Structural Health Monitoring* 22:353-371.
- [11] Ponzo FC, Auletta G, Ielpo P, Ditommaso R. 2024. "DInSAR-SBAS satellite monitoring of infrastructures: how temperature affects the "Ponte della Musica" case study". *Journal of Civil Structural Health Monitoring* 14(3), 754-761.
- [12] Zhu J and Meng Q. 2017. "Effective and Fine Analysis for Temperature Effect of Bridges in Natural Environments." *Journal of Bridge Engineering* 22, 6.
- [13] Larson O, Thelandersson S. 2011. "Estimating extreme values of thermal gradients in concrete structures." *Materials and Structures* 44: 1491-1500.
- [14] Lee JH and Kalkan I. 2012. "Analysis of Thermal Environmental Effects on Precast, Prestressed Concrete Bridge Girders: Temperature Differentials and Thermal Deformations." *Advances in Structural Engineering* 15, 3.
- [15] Lanari R, Bernardino P, Bonano M, Casu F, Manconi A, Manunta M, Manzo M, Pepe A. 2010. Surface displacement associated with the L'Aquila 2009 Mw 6.3 earthquake (central Italy): New evidence from SBAS-DInSAR time series analysis. *Geoph. Research Letter* 37, 20.
- [16] Guidelines for the use of interferometric satellite data aimed at interpretation of the structural behaviour of the constructions. ReLUIS Consortium. Rome, Italy (in Italian).
- [17] Crosetto M, Monserrat O, Cuevas-Gonzalez M, Devanthery N, Crippa B. 2015. "Persistent Scatterer Interferometry: a review". *ISPR J. of Photogrammetry and Remote Sensing*, 115, 78-89.
- [18] EN 1991-1-1. Eurocode 1: Actions on structures – part 1-5: General actions: Thermal actions.
- [19] Cestelli Guidi C. 1991. *Geotecnica e Tecnica delle Fondazioni*. Hoepli editor. Milan, Italy.
- [20] Italian guidelines for the classification and management of the risk, safety assessment and monitoring of existing bridges. Ministry of Infrastructures and Sustainable Mobility. Rome 2022.
- [21] Italian Building Code for Construction. Ministry of Infrastructures and Transports 14/01/2018. Rome.

# Automatic crack pattern detection and assessment of corroded reinforced concrete structures

Stefania Imperatore<sup>1</sup>, Cristina Martellini<sup>2</sup>, Cristina Monteleone<sup>3</sup>, Tiziano Pagliaroli<sup>4</sup>, Fabrizio Patanè<sup>5</sup>, Annalaura Casanova Municchia<sup>6</sup>

<sup>1</sup> *Researcher at Niccolò Cusano University, Department of Engineering, Via don Carlo Gnocchi 3, 00166 Rome, Italy, stefania.imperatore@unicusano.it*

<sup>2</sup> *Research Fellow at Niccolò Cusano University, Department of Engineering, Via don Carlo Gnocchi 3, 00166 Rome, Italy, cristina.martellini@unicusano.it*

<sup>3</sup> *PhD Student at Niccolò Cusano University, Department of Engineering, Via don Carlo Gnocchi 3, 00166 Rome, Italy, cristina.monteleone@unicusano.it*

<sup>4</sup> *Associate Professor at Niccolò Cusano University, Department of Engineering, Via don Carlo Gnocchi 3, 00166 Rome, Italy, tiziano.pagliaroli@unicusano.it*

<sup>5</sup> *Full Professor at Niccolò Cusano University, Department of Engineering, Via don Carlo Gnocchi 3, 00166 Rome, Italy, fabrizio.patane@unicusano.it*

<sup>6</sup> *Researcher at CNR-ISPC, National Research Council of Italy - Institute of Heritage Science, Area della Ricerca di Roma 1, Montelibretti, Italy, annalaura.casanovamunicchia@cnr.it*

## Abstract

The present work illustrated the potential of an innovative smart sensor for the structural health monitoring of existing reinforced concrete infrastructures. The employed technology has been initially conceived to evaluate the occurrence of damage on cultural heritage through a non-contact approach. The measurements performed on artificially corroded specimens validate the already assessed methodology to automatically identify and quantify the crack patterns of structural elements prone to corrosion degradation. Moreover, with the main aim of developing an innovative tool to assist in identifying the deterioration level, as well as the maintenance time and the residual service life, the feasibility of existing literature models has been finally explored to estimate the corrosion level from the crack width.

## 1 Introduction

Ageing of existing reinforced concrete structures combined with harsh environmental conditions frequently cause the steel reinforcement corrosion. The main manifestation of the corrosion degradation is the crack pattern, since the expansive force exerted by the corrosion products around the bar causes fractures in the concrete cover. Depending on both the concrete strength and cover depth, the corrosion level causing a certain crack width obviously changes. Anyway, it is currently well-established that corrosion cracks with thicknesses of a few millimeters can be a clear indicator of structural problems, since they can be associated with a non-negligible corrosion attack, where the bond strength is significantly reduced, and strength and ductility of the steel reinforcements begin to be compromised. Therefore, the extent and width of the crack pattern on corroded reinforced concrete structures allow assessing both the damage level and the structural vulnerability.

Among the several non-destructive test methods (NDT) recently developed, the crack detection techniques based on Machine Learning (ML) and Deep Learning (DL) seem to be particularly challenging for a preliminary screening of potential structural issues in the targeted site, which can be conducted remotely with the assistance of mobile cameras and drones. On the other hand, ML and DL are applications of Artificial Intelligence (AI), and Unmanned Aerial Vehicles (UAVs) frequently utilize the benefits from AI and are equipped with on-board processing capabilities. Therefore, a new technological equipment capable to identify, quantify, and record over time the crack pattern of a deteriorated



reinforced concrete structure seems to be extremely promising. The use of Deep learning algorithms has garnered significant interest recently for visual defect inspection automatization on reinforced concrete structures [1]-[4]. Moreover, the combination of UAVs with Deep Learning methods (like Yolo and Faster R-CNN) for crack detection is beginning to be an effectively explored, even in the Structural Engineering field [5]-[10]. By associating these new technologies with the capability of performing non-contact measurements to obtain information like length, depth, and width of cracks [11]-[13], overcoming risks, costs, and criticality related to the human-based bridge inspection. The result could be employed to estimate the corrosion level through statistical formulations [14].

This paper describes a software platform able to govern a sensor for the defect inspections on corroded reinforced concrete structures. The technology has been initially designed and developed for assessing the damage occurrence on artistic assets, likes marbles and frescoes, through non-contact measurements [15]. The sensor, called *ATTENTO*, can catch photographic, thermographic, and stereographic images, and identify the focal distance estimating the image size in metric units. Through a self-developed software governing the sensor, the captured images are divided into ROIs, and the portions damaged by cracks are identified by means of machine learning techniques. Moreover, point-by-point measures of crack width can be performed thanks to computational approaches of edge detection and skeletonization algorithms. The core of the research is to assess the proof-of-concept of a sensor adaptable for drones, which can accelerate the inspection processes with improved objectivity and accuracy, providing a better reference for follow-up decisions on existing reinforced concrete infrastructures and avoiding uncomfortable and unsafe exposition of the operator to dangerous environments.

## 2 Development of a software platform for the crack detection based on a Convolutional Neural Network approach.

The first step in defining an automated process for identifying a structural damage, whether it is on a cultural heritage asset or on an existing reinforced concrete infrastructure, involves developing an intelligent system capable of researching and automatically detecting cracks on surfaces. The methodology described in the following has been implemented to assess the damage occurring on a cultural heritage asset [15]. In this preliminary work its adaptability in identifying crack patterns due to the corrosion of reinforced concrete structures has been verified.

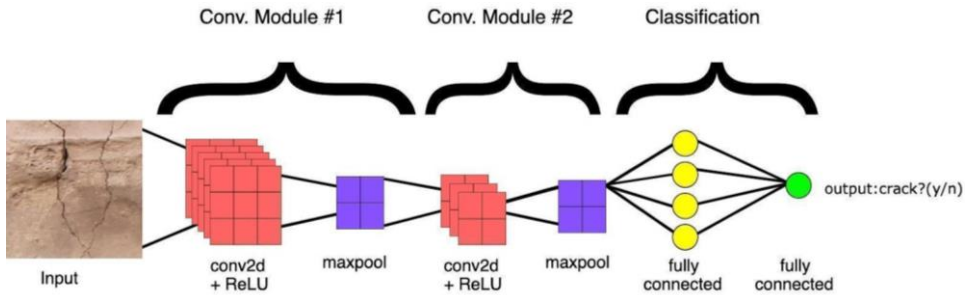


Fig. 1 The adopted CNN, containing two convolution modules (convolution + TeLU + pooling) for extracting features and two fully connected layers for the classification.

The optimal methodology to reach this goal led to the choice of a Convolutional Neural Network (CNN) including 19 layers, 16 convolutional layers and 3 fully connected layers. The algorithm was implemented using Python 3.6.8, employing the Keras-TenforFlow and Segmentation Model libraries. Fig. 1 shows the end-to-end structure of the adopted convolutional neural network. The CNN is provided with raw pixel data of the image as input. The convolution part extracts elements of the input matrix and applies filters to calculate new features, producing another output matrix. For each pair of filters, the CNN carries out an element-wise multiplication of matrixes and all the resulting elements are employed to obtain a single value. The neural network is trained before its application in order to “learn” which features of the raw image have to be extracted. In this way, the implemented CNN progressively collects and filters the most important data (textures, edges, shapes), deducing which object is repre-

sented with increasingly higher precision. To train the crack identifier, a dataset available in the scientific literature was employed as benchmark [16]-[17], consisting in RGB trichrome images on different surfaces, sized 256 x 256 pixels, for a total of 196.608 input parameters. The procedure adopted involved the following steps:

- Database Definition to draw in the network through a right number of input parameters.
- Identification of the damage classes (crack, no crack).
- Development of the algorithm in Python 3.0 and TensorFlow.

An example of images contained in the annotated database and related to a bridge deck surface are shown in Fig. 2. From the pool of 7744 images, the benchmark dataset was splitted in model training, validation, and testing sets. Specifically, the 60% was used to build the training set, the 15% for the validation set and the rest was employed as a test sample. Batches of tensor image data were moreover generated with real-time data augmentation using Keras-ImageDataGenerator to enhance the robustness of the neural network. The network was trained on the benchmark dataset for 100 epochs with a batch size of 32 and a learning rate of 0.0001, using the Adam optimizer. In the testing phase, a fixed threshold of 0.93 was set, just below the accuracy value, to extract images from the probability map.

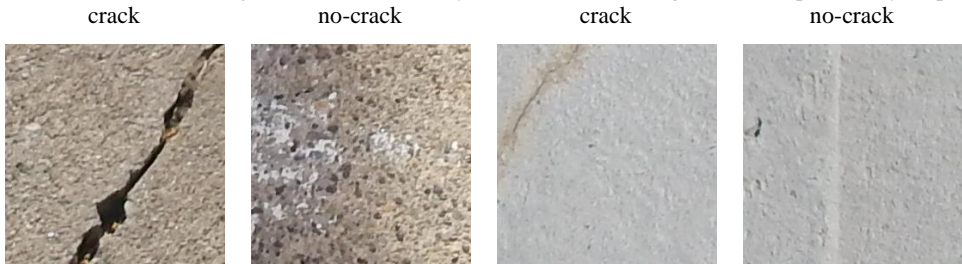


Fig. 2 Images used to build the dataset for AI-based crack detection.

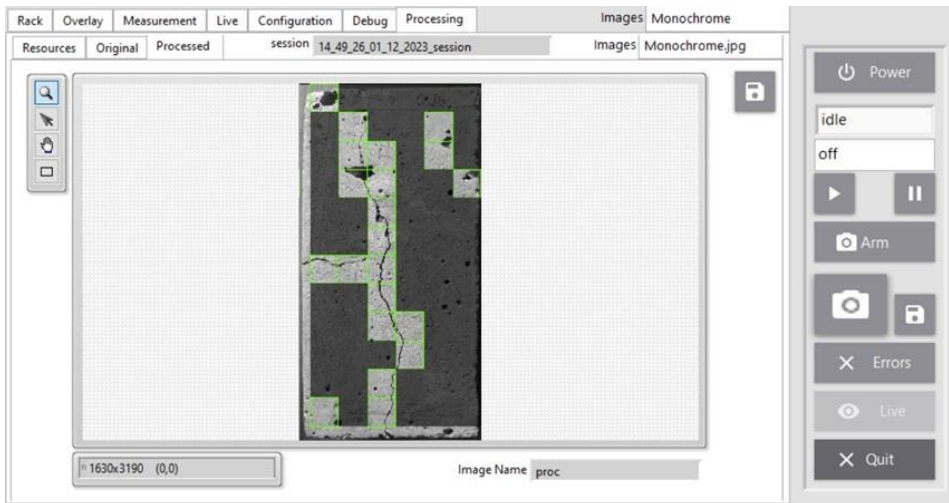


Fig. 3 Screen of the processed panel on the software platform for detecting and locating cracks.

To automatically identify the position of the cracks on the structure, an additional software has been developed. The main aim is to subdivide the original image, which is hypothesized to represent a portion of the structure under investigation, into 256x256 pixel ROIs, on which the proposed neural net-

work model automatically identifies any cracks. The cracked areas are highlighted to be easily detectable by the end-user, who can then examine them closely. Fig. 3 shows the software Processed Panel, in which the non-cracked areas overlaid in opaque while cracked areas are highlighted with colored borders remaining fully visible.

### 3 Crack quantification using image processing techniques and experimental validation.

The quantification of cracks' geometrical features is performed by means of a purposely developed software based on algorithms of skeletonization processing and edge detection. At the actual stage the software enables measurement of the crack width along its development in the selected ROIs.

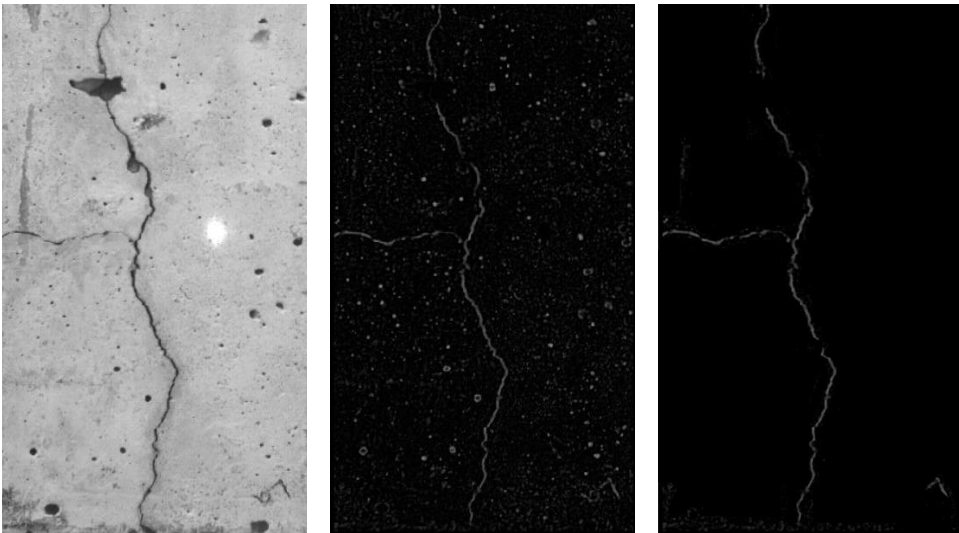


Fig. 4 Implementation of the denoising algorithm on a real crack: original image (left) and image skeletonization before (center) and after (right) the application of the particle filter

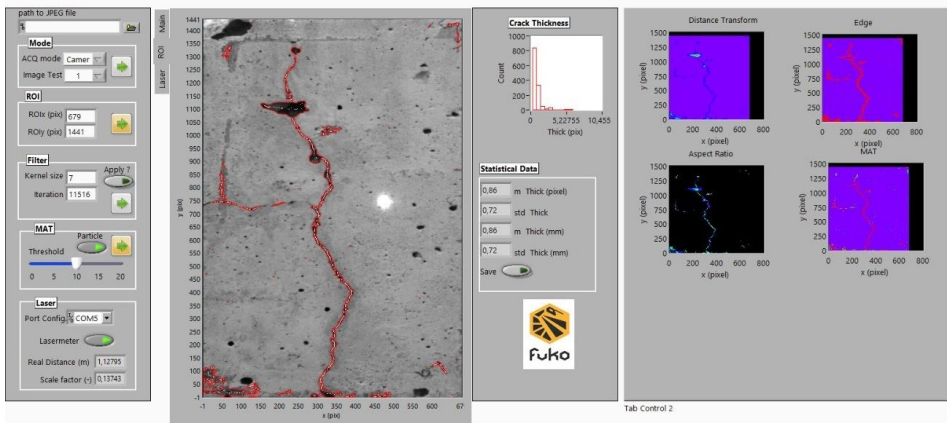


Fig. 5 Screen of the software platform for the crack width measurement.

Starting from the initial image (Fig. 4, left), a denoising algorithm is firstly applied in the pre-processing phase to minimize the background (Fig. 4, center). The “noise” removal is crucial for accurate measurement outcomes. The residual background, appearing as small particles, is finally removed

through outlier identification (Fig. 4, right). The edge detection procedure subsequently employed enable the measurement of the dimensions of the skeletonized crack. At this aim, the original image is correlated with the focal distance to facilitate the conversion from pixels to millimeters. To enhance the usability of the developed algorithm and make it user-friendly for operators involved in structural monitoring, the program has been equipped with a dedicated graphical user interface (Fig. 5). Among the displayed features, it is necessary to mention the processed image window to which edges and midline, as well as the statistical results (like thickness distribution, mean value, and standard deviation) are associated.

The adopted image processing analysis procedure has been validated by means of an experimental campaign on artificially corroded reinforced concrete specimens. A collection of 30 samples with different crack patterns and average crack widths was generated by means of a conventional electrolytic process (Fig. 6). In this way, the radial stress state mobilized by the expansive oxides allows small deformation gradients capable of overcoming the extremely low concrete tensile strength (on the order of 2 MPa). The duration of the electrolytic process influences width and extension of the crack pattern. In the present study, specimens with crack widths between 0.16 mm and 2.17 mm are examined.

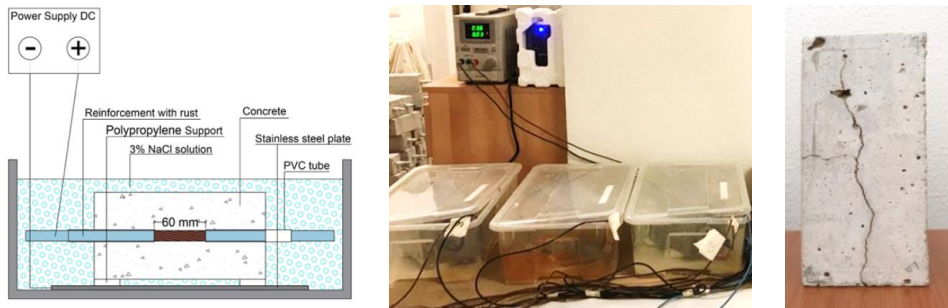


Fig. 6 Experimental campaign performed for the corrosion crack pattern realization.

After inducing the crack patterns, measurements have been carried out using three different techniques that with instrument contacting the surface under examination (Fig. 7). The first method involves the use of a traditional crack meter (Fig. 7, left). The second technique utilizes a digital microscope providing highly magnified images of the analyzed section. The measurements are thus conducted on the image using a specialized software that accurately correlates pixels to millimeters (Fig. 7, center). In Fig. 7 (right), measurements obtained with the two different approaches are compared. A total of 60 data points is measured. It is shown that the linear relationship between measurements taken with the digital microscope and the ones based on the traditional crack meter falls under the quadrant's bisector. Therefore, the traditional crack meter provides measurements lower than the actual values.

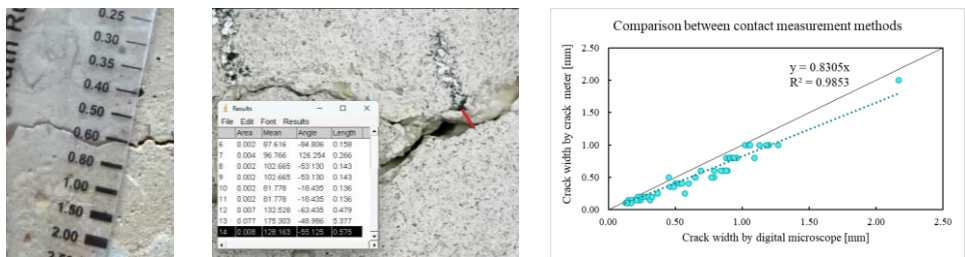


Fig. 7 Laboratory measurements of crack patterns. From the left: a measure performed with the crack meter; a measure taken with the digital microscope; the comparison of the measurements taken with the two contact techniques.

Lastly, a comparison between the traditional contact techniques and the non-contact measurement method described in this study was performed (Fig. 8). In the graphs the measurements taken with the crack meter (green dots), the digital microscope (orange dots) and the proposed non-contact technique

(blue dots) are represented. The estimated error of the traditional contact techniques is moreover shown as ellipses (green for the crack meter and orange for the digital microscope), which axes represent the measurement point position and the measurement error. Finally, the average crack width evaluated with the proposed non-contact technique is represented by a dashed blue line.

The analyzed cases proved the most challenging condition for the sensor validation, since the two selected samples featured an irregular surface, resulting in occasional false positives, coupled to extremely small cracks (tenths of millimeters). The application on the specimen 1a returns an average value of 1.01 mm, versus 0.69 mm and 0.85 mm taken with the traditional crack meter and the digital microscope, respectively. In this context it is worth noting that the non-contact measurement also accounts for the presence of the concrete porosity, not fully filtered yet by the implemented procedure. Concerning the application on the specimen 1b, the smaller dimension of the corrosion crack implies more scattered results. However, it is worth to note that the non-contact measurement method gives an average crack width of 0.58 mm, while the traditional contact measurements return average values of 0.47 mm and 0.64 mm for the traditional crack meter and the digital microscope, respectively.

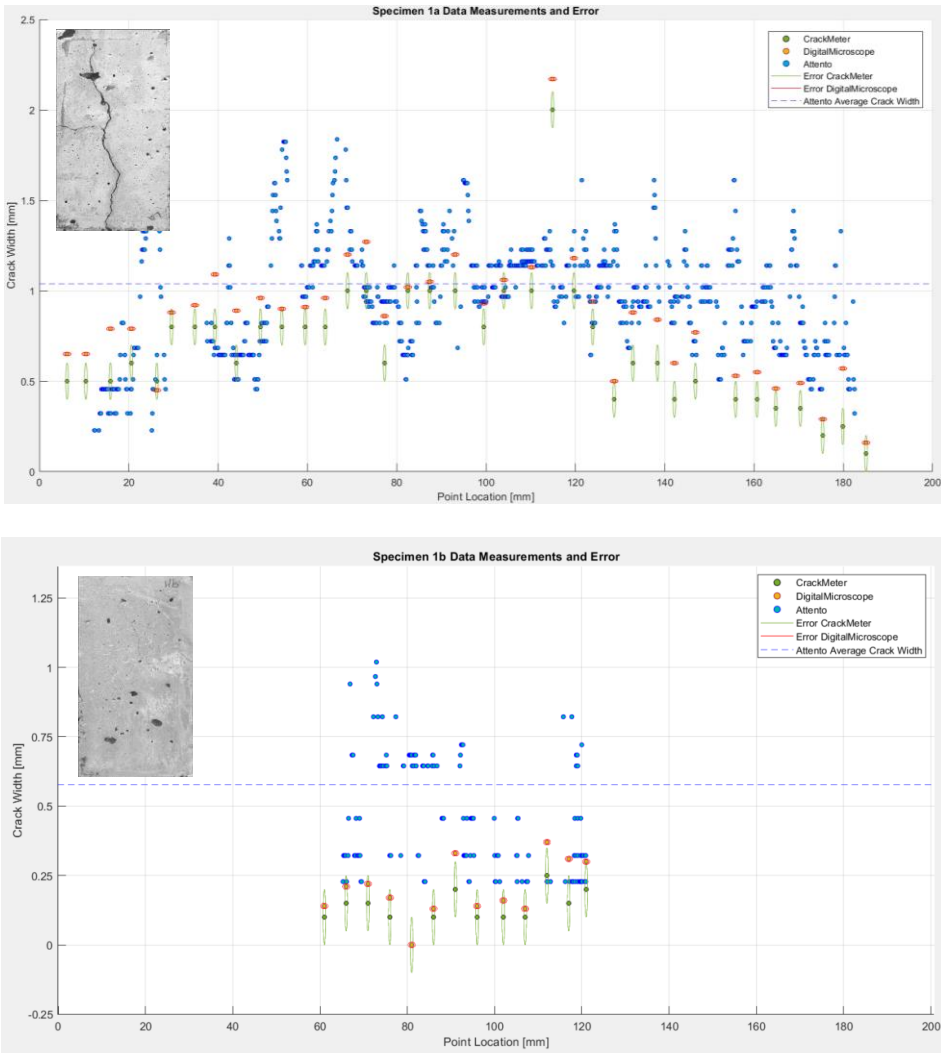


Fig. 8 Comparison of measurements performed according to the selected approaches. The x-axis indicates the location of the measurement point, the y-axis denotes the width of the cracks.



#### 4 Corrosion level estimation from the no-contact crack width measurements

The feasibility of the relationships available in the scientific literature in catching the corrosion level from the knowledge of the surface crack width is finally presented. At this aim it is worth noting that the existing formulations need of the knowledge of several parameters, like the concrete strength, the cover depth and the reinforcement nominal diameters. Such data cannot be assessed through non-contact approaches on existing reinforced concrete structures, neither by using proper innovative technologies applied to on drones. However, their knowledge can be initially deduced from the design documentation or from previously planned non-destructive investigation. In this context, the proposed approach, coupled with a sensor mounted on optimized AI-enabled drones, could help in streamline survey operations on existing civil infrastructures, performing cost-effective structural monitoring campaigns on a regular basis and automatically pinpoint structural deficiencies.

Due to the restricted space available, just some literature relationships [14],[18]-[21] are compared with the experimental data and represented in Fig. 9. It can be observed that the proposed methodology falls in the range of variability of some formulations currently available in the scientific literature, therefore can be effectively used in application on field.

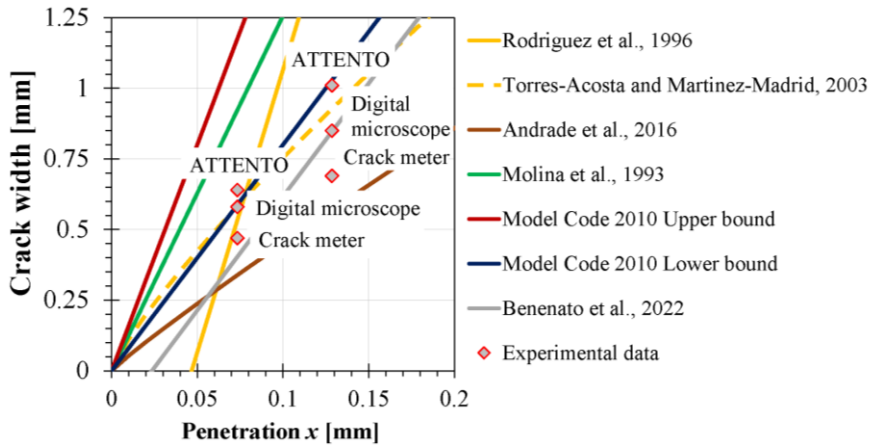


Fig. 9 Measurements performed according to the selected approaches (average values) and literature relationships relating the corrosion level and the surface crack width.

#### 5 Conclusions

This paper describes the application of an innovative methodology aimed at the automatic detection and quantification of crack patterns using a new non-contact measurement technology. Initially developed to identify and measure defects on marble surfaces or frescoes, the research has been extended with the main aim to detect crack patterns on concrete surfaces caused by rebar corrosion. The comparison with traditional measurement techniques is promising, suggesting that the new technology could be used for periodic and scheduled monitoring of civil infrastructures. Finally, the comparison with the results obtained from literature relationships relating the corrosion level and the crack width shows that any measurement error is within the uncertainty range of the predictive models.

#### Acknowledgment

The study was carried out within the project “ICARUS: multiscale Integrated approach for the deterioration assessment of Reinforced concrete structures” financially co-funded by MUR (Project code: 202259KCPF). The authors thank FUKO SRL for the support provided during the scientific activities.

#### References

- [1] Abubakr, M., Rady, M., Badran, K., Mahfouz, S. Y. 2024. “Application of deep learning in damage classification of reinforced concrete bridges”. *Ain Shams engineering journal*, 15(1), 102297.

- [2] Laxman, K. C., Tabassum, N., Ai, L., Cole, C., Ziehl, P. 2023. "Automated crack detection and crack depth prediction for reinforced concrete structures using deep learning". *Construction and Building Materials*, 370, 130709.
- [3] Golding, V. P., Gharineiat, Z., Munawar, H. S., Ullah, F. 2022. "Crack detection in concrete structures using deep learning". *Sustainability*, 14(13), 8117.
- [4] Yang, G., Liu, K., Zhang, J., Zhao, B., Zhao, Z., Chen, X., Chen, B. M. 2022. "Datasets and processing methods for boosting visual inspection of civil infrastructure: A comprehensive review and algorithm comparison for crack classification, segmentation, and detection". *Construction and Building Materials*, 356, 129226.
- [5] Munawar, H. S., Ullah, F., Heravi, A., Thaheem, M. J., Maqsoom, A. 2021. "Inspecting buildings using drones and computer vision: A machine learning approach to detect cracks and damages". *Drones*, 6(1), 5.
- [6] Zinno, R., Haghshenas, S. S., Guido, G., Rashvand, K., Vitale, A., Sarhadi, A. 2022. "The state of the art of artificial intelligence approaches and new technologies in structural health monitoring of bridges". *Applied Sciences*, 13(1), 97.
- [7] Cardellicchio, A., Ruggieri, S., Nettis, A., Renò, V., Uva, G. 2023. "Physical interpretation of machine learning-based recognition of defects for the risk management of existing bridge heritage". *Engineering Failure Analysis*, 149, 107237.
- [8] Liang, H., Lee, S. C., Bae, W., Kim, J., Seo, S. 2023. "Towards UAVs in construction: advancements, challenges, and future directions for monitoring and inspection". *Drones*, 7(3), 202.
- [9] Qiu, Q., Lau, D. 2023. "Real-time detection of cracks in tiled sidewalks using YOLO-based method applied to unmanned aerial vehicle (UAV) images". *Automation in Construction*, 147, 104745.
- [10] Li, R., Yu, J., Li, F., Yang, R., Wang, Y., Peng, Z. 2023. "Automatic bridge crack detection using Unmanned aerial vehicle and Faster R-CNN". *Construction and Building Materials*, 362, 129659.
- [11] Khan, M. A. M., Kee, S. H., Pathan, A. S. K., Nahid, A. A. 2023. "Image Processing Techniques for Concrete Crack Detection: A Scientometrics Literature Review". *Remote Sensing*, 15(9), 2400.
- [12] Tang, Y., Huang, Z., Chen, Z., Chen, M., Zhou, H., Zhang, H., Sun, J. 2023. "Novel visual crack width measurement based on backbone double-scale features for improved detection automation". *Engineering Structures*, 274, 115158.
- [13] Ding, W., Yang, H., Yu, K., Shu, J. 2023. "Crack detection and quantification for concrete structures using UAV and transformer". *Automation in Construction*, 152, 104929.
- [14] Benenato, A., Ferracuti, B., Imperatore, S., Lignola, G. P. 2022. "Corrosion level estimation by means of the surface crack width". *Construction and Building Materials*, 342, 128010.
- [15] Casanova Municchia, A., Martellini, C., Patanè, F., Pagliaroli, T., Imperatore, S. 2024. "Automatic damage detection in architectural heritage structures". In *18th World Conference on Earthquake Engineering*. WCEE2024.
- [16] Dorafshan, S., Thomas, R. J., Maguire, M. 2018. "SDNET2018: An annotated image dataset for non-contact concrete crack detection using deep convolutional neural networks". *Data in brief*, 21, 1664-1668.
- [17] Elhariri, E., El-Bendary, N., Taie, S. A. 2022. "Historical-crack18-19: A dataset of annotated images for non-invasive surface crack detection in historical buildings". *Data in Brief*, 41, 107865.
- [18] Rodriguez, J., Ortega, L. M., Casal, J., Diez, J. M. 2016. "Corrosion of reinforcement and service life of concrete structures". In *Durability of Building Materials & Components 7 vol. I* (pp. 117-126). Routledge.
- [19] Torres-Acosta, A. A., Martinez-Madrid, M. (2003). Residual life of corroding reinforced concrete structures in marine environment. *Journal of Materials in Civil Engineering*, 15(4), 344-353.
- [20] Andrade, C., Cesetti, A., Mancini, G., Tondolo, F. (2016). Estimating corrosion attack in reinforced concrete by means of crack opening. *Structural Concrete*, 17(4), 533-540.
- [21] Model Code 2010, fib Bulletin n°66, 2012.

# Integrated System for monitoring and management of Infrastructures

Antonino Fotia<sup>1</sup> and Raffaele Pucinotti<sup>1</sup>

<sup>1</sup>*DICEAM Civil, Environmental Energy and Material Engineering Department, Mediterranea University of Reggio Calabria, Via dell'Università 24, 89124, Reggio C. Italy*

## Abstract

The infrastructure landscape in Italy has faced interpretative complexity due to tragic events like collapses, prompting the Ministry of Infrastructure and Transport (MIT) to develop guidelines for monitoring and proactive measures. Similarly, ensuring the long-term sustainability of Italy's vast architectural and infrastructure heritage requires innovative monitoring approaches. Reinforced concrete constructions are particularly susceptible to mechanical and environmental deterioration over time, necessitating a more comprehensive review and monitoring strategy. In this paper an automated system for infrastructure analysis and monitoring is presented with the objective to overcome this complexity. The system integrates data from both aerial and on-site sensors into a Building Information Modeling (BIM) framework, providing a comprehensive view of infrastructure conditions. This makes easier interpretation and, enables stake-holders, to assess the exact state of structures and identify critical issues. The proposed solution advocates for a shift from traditional scheduled maintenance to predictive maintenance, leveraging continuous Geographic Information System (GIS)-based monitoring. By collecting real-time data on infrastructure conditions, this approach enables the prioritization of interventions, enhancing safety and optimizing resource allocation. The goal is to create a decision-support system that allows authorities to distribute economic resources based on a risk index. Therefore, this methodology not only improves the safety and sustainability of infrastructure but also addresses the limitations posed by limited funds. By transitioning to predictive maintenance based on acquired data rather than fixed deadlines, resources can be allocated more efficiently, reducing operating costs in the long run. Overall, the proposed system offers a comprehensive and proactive approach to infrastructure management, ensuring the safety and longevity of Italy's vital transportation networks and architectural heritage. The proposed solution is applied to some viaducts and bridges face security concerns due to degradation phenomena.

## 1 Introduction

The evolution of road infrastructure in Italy experienced a rapid acceleration in the post-war period with the construction of major roadways, which remain essential to the country's economy. These numerous and modern engineering works, indispensable for the mobility of people and goods in a geographically challenging territory like Italy, now have an average age exceeding 40 years. Additionally, the significant increase in traffic has resulted in the actual load exceeding the initially estimated design load, highlighting the need for comprehensive monitoring and maintenance strategies to ensure their longevity and safety. [1, 2, 3]

This necessity led to the drafting of the "guidelines for the classification and management of risk, safety assessment, and monitoring of bridges" by the Ministry of Infrastructure and Sustainable Mobility. These guidelines provide a framework for systematically evaluating and addressing the structural integrity and safety of Italy's extensive network of bridges and viaducts. [4,5]

The aim of this research is to propose an advanced automated system for the analysis and monitoring of infrastructure, adhering to the ministerial guidelines.[6-7] This innovative system interconnects the processes of data acquisition, integration, and processing from both aerial and on-site sensors, thereby offering precise and predictive responses regarding action priorities. The integration of such a system into existing monitoring methodologies can significantly enhance their effectiveness and efficiency.

The database obtained from the detailed analysis of each infrastructure component is implemented into a Building Information Modeling (BIM) model. This sophisticated modelling allows end users to interface with a scalable, easy-to-interpret digital replica of the infrastructure. The BIM model accurately depicts the current state of the structure and highlights the distribution of critical issues, thus



facilitating comprehensive network integration and the strategic planning of maintenance and intervention activities across the entire road network [8,9,10,11].

Subsequently, the analysis results are incorporated into a Geographic Information System (GIS) environment, which enables the examination of the entire set of viaducts. This system evaluates the conditions of structural elements such as pillars, decks, and parapets through various degradation indicators including cracks, corrosion, and other forms of deterioration. These indicators are meticulously detected and classified based on their severity and frequency, using a standardized scale from 1 to 5. This process generates a degradation index for each viaduct element, providing a clear representation of the level of criticality and the urgency for intervention [20, 21, 22, 23].

The final output is a thematic map of the viaduct, which visually identifies the most degraded and the best-preserved areas. This map serves as a crucial tool for planning maintenance and restoration activities, ensuring resources are allocated effectively. This method not only offers detailed and up-to-date information on the conditions of viaducts without requiring invasive or costly interventions but is also easily replicable and scalable. This flexibility allows the method to be applied to various types of infrastructure, thereby enhancing the overall resilience and reliability of the country's transport network.

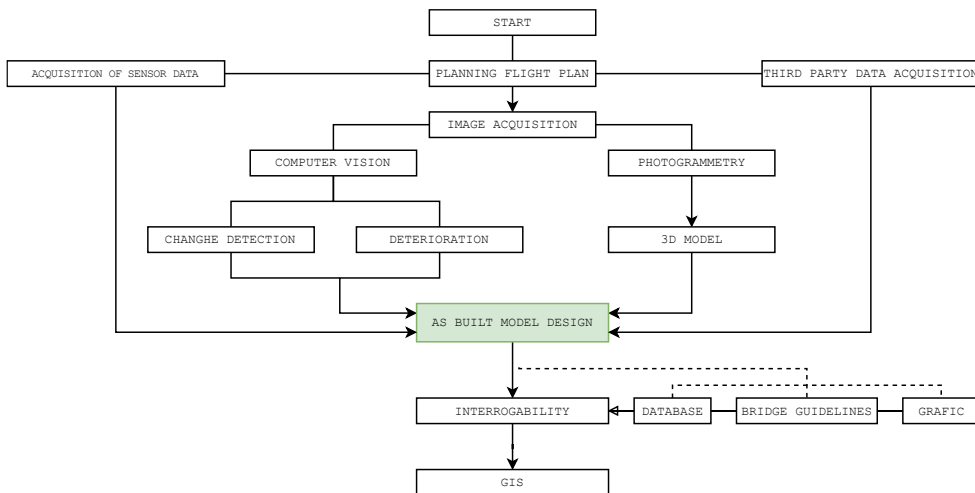


Fig. 1 Flowchart to determine the as-built model to integrate into GIS environment.

## 2 Case Study

In accordance with Level 1 of the multilayered approach prescribed by the "Ministerial Guidelines," the classification, risk management, safety assessment, and monitoring of existing bridges begin with visual inspections of the structures.

The inspection analysis was carried out on several viaducts and bridges in the province of Reggio Calabria. These infrastructures are located in diverse urban settings, and given the insufficient maintenance activities, some of them exhibit significant signs of advanced deterioration, which could potentially compromise the safety of users.

The acquisition plan was meticulously designed using Drone Harmony, taking into account previously addressed interference. The precise definition of these processes allows the software to autonomously develop the flight mission based on the user-defined parameters. In the initial phase, a strip mapping of the target object was performed, employing nadiral angle capture points, which can be dynamically adjusted to meet required overlap values (Fig. 2).



Fig. 2 Bridge subject to inspection (left). Automated flight plan (right)

### 2.1 3D Modelling and database implementation

For the construction of the BIM model in the Archicad environment, the point cloud generated through Agisoft Metashape served as a guideline (Fig. 3a). In compliance with prevailing regulations and the Work Breakdown Structure (WBS) classification standard, each component of the structure is uniquely positioned and labeled. This approach facilitates the precise analysis and identification of any defects associated with each component (Fig. 3b).



Fig. 3 BIM model superimposed by point cloud (left) WBS classification on BIM model (right)

Table 1 example of database CSV to import in BIM environment.

	A	B	C	D	E
2		WBS Code	PLOT	Opera	Elemet
3	1238DD82-20	00.PT.01.IP.01.ST.00	00	PT.01	ST
4	640650F8-E7	00.PT.01.IP.01.ST.01	00	PT.01	ST
5	0A91D892-CS	00.PT.01.IP.01.ST.02	00	PT.01	ST
6	78D02A55-43	00.PT.01.IP.01.TV.00	00	PT.01	TV
	F	G	H	I	
DEFECT		CdA Structural and Foundational	CdA Seismic	CdA Total	
MEDIUM		MEDIUM-LOW	MEDIUM	HIGH	
LOW		LOW	MEDIUM	HIGH	
LOW		LOW	MEDIUM	HIGH	
MEDIUM-HIGH		MEDIUM	MEDIUM	HIGH	

In the context of each frame, various masks were meticulously applied to the individual components of our infrastructure. This process facilitated the precise identification and individual analysis of each element by detecting homologous points within the point cloud and frames. As a result, multiple frames are associated with each element, ensuring a more detailed and comprehensive view.

The level of deterioration is determined automatically through advanced soft computing algorithms and subsequently converted into CSV format based on the defect reports issued by the Ministry. The estimation of the extent of degradation relies on a surface ratio between the pixels affected by the dete-

rioration and the total area of the element, reconstructed from the aggregation of masks for each individual component. This method ensures a precise and quantifiable assessment of the degradation present in each structural element.

The proposed system is capable of assigning a defect class to each parametrically modelled element, and consequently, determining the attention class of the entire bridge. The UAV photogrammetric acquisition plan enabled the execution of these processes with minimal cost and risk exposure while providing detailed and accurate information on the anomalies of the bridge. The data obtained, analysed through computer vision techniques, is automatically integrated into a CSV file within the BIM model. This integration allows for the creation of a dynamic database reflecting the health status of the bridge, also providing essential data for the structural survey.

The interaction between intrinsic and extrinsic elements of the structure assigns a priority estimate for intervention that transcends merely identifying the structural defect. This comprehensive approach considers various factors, including the severity and frequency of defects, to prioritize maintenance and repair actions effectively.

The visualizations extracted from the BIM model, resulting from the imposition of specific parameters and conditions, provide the operator with easily interpretable documentation, both graphical and textual. This documentation is invaluable for analysing the conservation status of the infrastructure. The graphical representations and detailed textual reports ensure that the condition of the infrastructure is communicated clearly, facilitating informed decision-making regarding maintenance and repairs (Fig. 4 - Table 1).

This integrated system not only enhances the precision and efficiency of infrastructure monitoring but also ensures that interventions are prioritized based on a comprehensive understanding of the structure's condition, ultimately contributing to the long-term safety and resilience of the infrastructure [17].



Fig. 4 Model classified according to the level of defectiveness

## 2.2 Attention class by new parameters

In the GIS environment, a comprehensive database was developed by integrating additional parameters beyond those specified in the "Guidelines for the Classification and Management of Risks, Safety Assessment, and Monitoring of Existing Bridges"[16]. The proposed methodology aims to enhance the prioritization of intervention for each structure, taking into account various factors, thus enabling the managing entity to establish intervention priorities objectively, based also on the available financial resources.

While the "Guidelines" introduce parameters capable of determining significant risks (such as structural and foundational, seismic, landslide, and hydrogeological risks) and evaluate these separately in terms of hazard, vulnerability, and exposure before integrating them into an overall attention class, the inclusion of additional parameters in the database is intended to support the managing entity in objectively identifying the priority of intervention among different alternatives. This approach helps to avoid subjective decisions regarding which interventions to prioritize and directs the allocation of available financial resources more effectively.

These new parameters pertain to external conditions of the examined structure that are not defined in the "Ministerial Guidelines"[16] but impact the prioritization of interventions. Specifically, criteria related to the proximity of residential areas, the presence of elements of interest such as buildings with public and collective functions, equipped green areas, parking lots, public transport stops, and construction sites, among others.

The final analysis of the database follows the guidelines, which define five classes of attention:

- High Class: bridges at high risk of collapse or irreversible damage in exceptional events, requiring urgent adaptation or replacement;
- Medium-High Class: bridges at high risk of collapse or irreversible damage in exceptional events, requiring adaptation or replacement in the short term;
- Medium Class: bridges with moderate risk of collapse or irreversible damage in exceptional events, requiring adaptation or replacement in the medium term;
- Medium-Low Class: bridges with low risk of collapse or irreversible damage in exceptional events, requiring adaptation or replacement in the long term;
- Low Class: bridges with negligible risk of collapse or irreversible damage in exceptional events, not requiring extraordinary interventions.

The tables below present the parameters outlined by the Ministerial Guidelines (Table 2), along with the parameters selected by the authors (Table 3), in order to refine the prioritization of intervention for a given infrastructure asset within a specific class of attention, considering the economic resources available to the managing entity, thus enabling a more efficient distribution of resources.

Table 2 Table showing the parameters set out in the "Ministerial Guidelines".

STRUCTURAL AND FOUNDATIONAL ATTENTION CLASS		
ETE	Extent of heavy transport loads	STRUCTURAL AND FOUNDATIONAL RISK
TGE	frequency of transit commercial vehicles	
DIF	level of defectivity	VULNERABILITY STRUCTURAL FOUNDATION RISK
RED	rapid evolution of degradation	
NP	design standards	
STAT	Static light scheme, materials, and number of spans	
TGMLMC	TGM level and mean span light	
AS	road alternatives	STRUCTURAL FOUNDATION RISK EXPOSURE
TES	types of entity overrun	
SEISMIC RISK ATTENTION CLASS		
AgTi	Ground peak acceleration and topographic category	SEISMIC HAZARD
CS	Subsoil category	
STAT	Static light scheme, materials and number of spans	VULNERABILITY SEISMIC RISK
DIF	level of defectivity	
CPR	design criteria	
ESF	structural and foundation risk exposure	
SO	Strategy of the work	EXPOSURE TO SEISMIC RISK
LANDSLIDE HAZARD ATTENTION CLASS		
IV	slope instability (Magnitude, Speed, State of activity)	SUSCEPTIBILITY TO LANDSLIDES
AV	model uncertainty	
MM	mitigation measures	
TFS	bridge type/strength and type of foundation	VULNERABILITY LANDSLIDE RISK
EI	interference extension	
ESF	structural and foundation risk exposure	LANDSLIDE RISK EXPOSURE
SO	strategy of the work	
HYDRAULIC RISK ATTENTION CLASS		
PEL	Danger from localized erosion	DANGER/SUSPECTIBILITY HYDRAULIC RISK
PEG	Danger from generalized erosion	
REN	resilience to the natural event	VULNERABILITY HYDRAULIC RISK
TMF	typological, magnitude and frequency event	
TEOM	type and efficiency mitigation works	
DP	potential damage	
TES	type of entity overrun	EXPOSURE TO HYDRAULIC HAZARDS
SO	strategic importance of the work	
ED	extent of damage	

Table 3 Parameters set out by authors.

SURROUNDING ENVIRONMENTAL PARAMETERS		RISKS FROM CONTEXT VARIABLES
CA	Presence of built-up areas	
PC	Presence of construction sites	
TU	Type of use	
VA	Presence of equipped green areas	
AP	Presence of pedestrian areas	
EP	Presence of public buildings	
PI	Presence of infrastructure	
FTP	Presence of public transport stops	
P	Presence of car parks	

The construction of a GIS system was carried out, through the georeferencing of the orthophotos, the vector file representing the elements and their degradation (reported in the database as characteristics) and the association of the data extracted from the photographic survey within the database, as reported, thus proceeding with the dynamic calculation of the Risk Class for each category and the dynamic calculation of the Overall Risk Class (pag.6, Figure 5).

18	TSF	Testo (stringa)	String	12	0	
19	PSF	Testo (stringa)	string	0	0	IF ( "ETE" IS 'CLASSE A' AND "TGE" IS 'BASSA', 'MEDIO-ALTA', IF ( "ETE" IS 'CLASSE A' AND
20	VSF	Testo (stringa)	string	0	0	IF ( "DIF" IS 'BASSA' AND "RED" <= 1945 AND "NP" IS 'CLASSE A' AND "STAT" IS 'ALTA', ME
21	ESF	Testo (stringa)	string	0	0	IF ( "LUMIN" IS 'BASSA' AND "AS" IS 'SI' AND "TES" IS 'BASSA', 'BASSA',
22	CdACSF	Testo (stringa)	string	0	0	IF ( "TGMUM" IS 'BASSA' AND "AS" IS 'SI' AND "TES" IS 'ALTA', 'MEDIO-BASSA',
23	PS	Testo (stringa)	string	0	0	IF ( "PSP" IS 'BASSA' AND "VSP" IS 'BASSA' AND "ESP" IS 'MEDIO-BASSA', 'BASSA',

Fig. 5 Example of setting authors parameter in GIS implementation.

Subsequently, the attention class of surrounding environmental factors and the final attention class were derived. The final result is visualized through a thematic map that highlights the three works considered, each colored according to the priority of intervention. (see Figure 6).

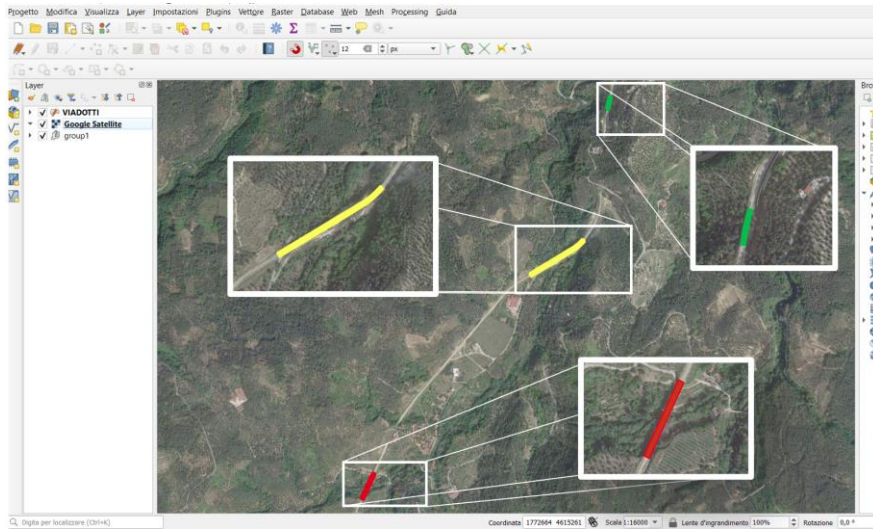


Fig. 6 Example of three viaducts examined, in the three different colors

Figure 6 shows three viaducts examined according to the priority of intervention. The colors indicate different levels of criticality, in particular red represents high criticalities, orange represents medium-high criticalities, yellow represents medium criticalities, green represents medium-low criticalities and light green represents low criticalities.

### 3 Conclusion

In the Italian context, the management of infrastructure has emerged as a strategic imperative, driven by the intricate nature of the national terrain and the need to develop robust frameworks for the oversight and administration of these essential networks.

Addressing such complexities necessitates the pursuit of pioneering methodologies. The proposed methodology involved the creation of a dynamic database capable of real-time updates, facilitated by the integration of custom fields within the BIM (Building Information Modelling) model. Through this approach, each component of the infrastructure was precisely classified based on its characteristics and purpose, allowing for comprehensive cataloguing within the system. In a broader perspective, this method extended its application to entire infrastructure networks, interfacing with Geographic Information Systems (GIS) to enhance the understanding of the environmental context. As a result, the system allows for a sophisticated assessment of priority factors, enabling more precise and effective allocation strategies. The integration of traditional methods with multicriteria analysis allowed for an accurate and thorough assessment of the conservation state and safety of the examined infrastructures. This analysis considered various parameters (those specified in the "ministerial guidelines" and those related to the surrounding environment), enabling the establishment of an objective intervention priority order that also accounts for the economic resources available to the managing entity. The primary objective of this research is to propose a robust and adaptable methodology to support the decision-making processes of the managing entity regarding interventions and the investment of available economic resources. Its implementation could significantly enhance the efficiency and effectiveness of infrastructure management strategies, ensuring optimal use of available resources and promoting the long-term safety of the analysed structures. Furthermore, by integrating the GIS system with the BIM system, operators have the ability to visualize, with a simple click, the 3D model of each constituent element of the infrastructure and gain insights into the condition of each element. This capability represents a significant advancement in the management and monitoring of infrastructure, providing detailed and accessible information to support informed decision-making.

### References

- [1] L. de Rosa. 2017. Applicazione GIS/VGI per la gestione ed il controllo del territorio. *ASITA2017*, pp. 407-414.
- [2] M. Di Prisco. 2019 Critical infrastructures in Italy: State of the art, case studies, rational approaches to select the intervention priorities. *International Federation for Structural Concrete*, 49-58.
- [3] P. Clemente. 2020, Monitoring and evaluation of bridges: lessons from the Polcevera Viaduct collapse in Italy, *Journal of Civil Structural Health Monitoring*.
- [4] M. Morgese, F. Ansari, M. Domaneschi, G. Cimellaro. 2020. Post-collapse analysis of Morandi's Polcevera viaduct in Genoa Italy. *Journal of Civil Structural Health Monitoring*.
- [5] E. Farneti, N. Cavalagli, I. Venanzi, M. Costantini, F. Trillo, F. Minati, F. Ubertini. 2022. On the Use of SAR Data for Structural Monitoring of Bridges: The Case of Albiano-Magra Bridge in Italy. *1st Conference of the European Association on Quality Control of Bridges and Structures*, pp.518-526.
- [6] A. Comi, S. Mazzaferro, A. Fotia. 2024. Innovative techniques for analysis, monitoring and priorities infrastructure interventions through the application of GIS systems. NMP 2024 (in press)
- [7] S. Mazzaferro, A. Comi, A. Fotia. 2024. From UAVs to as-built BIM models: automation in infrastructure management and monitoring processes NMP 2024 (in press)
- [8] D. Agdas, J. A. Rice, J. R. Martinez and I. R. Lasa. 2016. "Comparison of Visual Inspection and Structural-Health Monitoring As Bridge Condition Assessment Methods," *Journal of Performance of Constructed Facilities*, vol. 30.
- [9] H.-J. Jung, 2019. " Bridge Inspection and condition assessment using Unmanned Aerial Vehicles (UAVs): Major challenges and solutions from a practical perspective," *Smart Structures and Systems, An International Journal*, vol. 24.

- [10] K. H. Sato, F. Daiki and Kazuya, 2019. "Autonomous Adaptive Flight Control of a UAV for Practical Bridge Inspection Using Multiple-Camera Image Coupling Method," *Journal of Robotics and Mechatronics*, vol. 31.
- [11] F. S. Billie, H. Vedhus and N. Yasutaka, 2019. "Advances in Computer Vision-Based Civil Infrastructure Inspection and Monitoring," *Engineering*, vol. 5, pp. 199-222.
- [12] G. Buratti, S. Celati, A. Cosentino, D. Gaudio, I. Mazzatura, F. Morelli e W. Salvatore. . 2022. The New Guidelines of Italian Ministry of Infrastructures for the Structural Risk Classification of Existing Bridges: Genesis, Examples of Application and Practical Considerations. *Springer International Publishing*, 835-844.
- [13] R. Fedele, F. Praticò, G. Cogliandro e F. Laganà. 2022. Evaluation of the Structural Health Conditions of Smart Roads Using Different Feature-Based Methods. *INTERNATIONAL SYMPOSIUM: New Metropolitan Perspectives*, pp. 334-345.
- [14] Ceballos, M. T. Lamata e D. Pelta. 2016. A comparative analysis of multi-criteria decision-making methods. *Progress in Artificial Intelligence*.
- [15] H. ElSawah, I. Braky, O. Moselhi. 2016. Decision Support Model for Integrated Risk Assessment and Prioritization of Intervention Plans of Municipal Infrastructure. *Journal of Pipeline Systems Engineering and Practice*.
- [16] Ministero delle Infrastrutture e dei Trasporti, Consiglio Superiore dei Lavori Pubblici. 2020. linee guida sulla Classificazione e Gestione del Rischio e la Valutazione della Sicurezza ed il Monitoraggio dei Ponti Esistenti, Allegate al parere del Consiglio Superiore dei Lavori Pubblici n.88/2019, espresso in modalità "agile" a distanza dall'Assemblea Generale in data 17.04.2020.
- [17] Fotia, A., Alvaro, M.R., Oliveto, F., Pucinotti, R.. 2022. Safety Management of Existing Bridges: A Case Study. In: Calabrò, F., Della Spina, L., Piñeira Mantiñán, M.J. (eds) *New Metropolitan Perspectives*. NMP 2022. Lecture Notes in Networks and Systems, vol 482. Springer, Cham, pp.2268-2277. [https://doi.org/10.1007/978-3-031-06825-6\\_218](https://doi.org/10.1007/978-3-031-06825-6_218).

# Evaluation of Bridge Deflections by means of Clinometers based on Micro-Electro-Mechanical Systems (MEMS).

Francesco Filippo Bico, Fabio Di Carlo and Alberto Meda

*Department of Civil Engineering and Computer Science Engineering  
University of Rome „Tor Vergata“  
Via Del Politecnico 1, Rome 00133, Italy*

## Abstract

This paper introduces a method for measuring bridge deflection using data acquired from Micro Electro-Mechanical Systems (MEMS) sensors. The study demonstrates that it is possible to reconstruct the deflected configuration of a bridge directly from the deflection curves obtained by means of clinometers. This research takes advantage also of the many data obtained from the tests performed at the University of Roma “Tor Vergata” on full-scale reinforced concrete beams that simulate bridge girders. A data processing method utilizing polynomial functions was employed to reconstruct the actual displacements of the structures. Unlike other deflection measurement methods, this new approach based on MEMS sensor data does not require fixed observation points, as the clinometers are installed directly on the structure. The aim is to develop an artificial intelligence algorithm that can monitor bridge deflection in real time and predict its future behavior based on data from the sensors.

## 1 INTRODUCTION

Structural monitoring has become a crucial aspect of preserving existing infrastructure over the past few decades. Many buildings, bridges, and viaducts are nearing the end of their service lives, raising the interest in the assessment of their current health to prevent decommissioning or catastrophic collapse. Numerous incidents highlight how neglected maintenance and lack of monitoring may lead to disastrous outcomes, including loss of life.

Recently, there has been significant interest in evaluating operational conditions and actively monitoring strategic structures like bridges and viaducts, which are vital to societal development. With much of the existing road infrastructure nearing the end of their lifespan, active monitoring processes are becoming of primary interest.

Given that these strategic structures can collapse without clear warning signs, implementing a continuous monitoring system is crucial. Today, this is possible using MEMS (Micro Electro-Mechanical Systems) sensors, which are both low-cost and easy to install on existing structures. The major advantage of MEMS sensors is that they do not require a fixed reference point, making them ideal for monitoring the dynamic deflection of bridges and viaducts.

*Burdet et al. [1]* propose the idea of using clinometric sensors to reconstruct a vertical deformation for a viaduct using polynomial functions. Subsequently *Hou et al. [2]* propose an analytical calculation method, defining the boundary conditions for the problem and a set of orthogonal polynomials for the deformation reconstruction; in their article they show some experimental results extracted from static and dynamic tests carried out on both simple and continuous beams. *He et al. [3]* define a clear calculation method for the reconstruction of deflection curves and for optimizing the positioning of sensors on a bridge span. The topic of optimization is explored by *Sousa et al. [4]* who, studying two existing continuous beam bridges, perform a parametric analysis to determine the optimal sensor’s location.

This article presents an experimental study on the reliability of such MEMS sensors installed on structural longitudinal elements; the calculation methods extracted from the aforementioned studies are used and integrated with different analytical approaches. These curves are then compared to the displacement results obtained with traditional measuring sensors (potentiometers) to assess the accuracy of the method.

The tests presented in this paper were carried out within a comprehensive national project (PRIN = Research Project of National Relevance) aimed at evaluating the flexural response of corroded reinforced concrete (RC) beams [5][6] and prestressed concrete (PC) beams [7], planned and conducted at



the Laboratory of the University of Rome “Tor Vergata”. The research program is based on a set of twelve RC and twelve PC beams: one of each type was left uncorroded for reference, while the others have been subjected to different levels of artificial corrosion process of longitudinal reinforcements and to four-point bending tests. Among the objectives of this research project there is the quantification of the corrosion level of the steel bars that may significantly affect the structural bearing capacity.

## 2 EXPERIMENTAL CAMPAIGN

As mentioned before, the outcomes presented in this paper are part of a large research project aimed at evaluating the effect of corrosion degradation of reinforcement present in longitudinal structural elements like bridge girders. Some of the experimental results are presented and commented below. In particular, the results obtained on a corroded RC beam and on a non-corroded PC beam are reported.

### 2.1 Geometry and Materials of the specimens

#### 2.1.1 Reinforced Concrete Beams

RC beams were characterized by a  $200 \times 300$  mm rectangular cross section and a total length of 3700 mm. As shown in Fig. 1, the longitudinal reinforcements were made of four  $\text{Ø}20$  mm ordinary rebars, two placed at the bottom of the section and two at the top.  $\text{Ø}8$  mm bars were adopted for the stirrups, with a spacing of 100 mm and 200 mm in the outer (1450 mm) and inner (800 mm) zones of the beams, respectively. The concrete cover is equal to 20 mm.

The mean compressive strength of concrete, measured on 100 mm side cubes, was close to 57 MPa, while Italian B450C rebars were used, characterized by yielding and ultimate strengths equal to 510 MPa and 630 MPa, respectively.

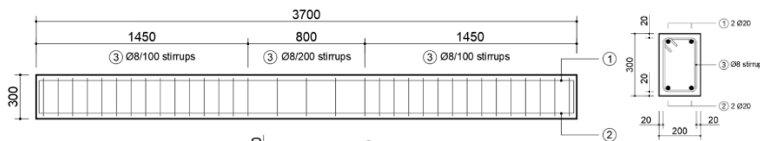


Fig. 1 RC specimen

#### 2.1.2 Prestressed Concrete Beams

Fig. 2 shows the PC specimens. The main geometry is identical with respect to the RC beams, except the longitudinal reinforcements: these are made of three  $\frac{1}{2}$ -inch seven wires strands, two placed at the bottom of the section and one at the top, and four  $\text{Ø}10$  mm ordinary rebars. The material of the concrete and the rebars is the same of the RC beams, while the initial wire prestressing stress is equal to 1300 MPa, corresponding to about 70% of the ultimate strength equal to 1860 MPa.

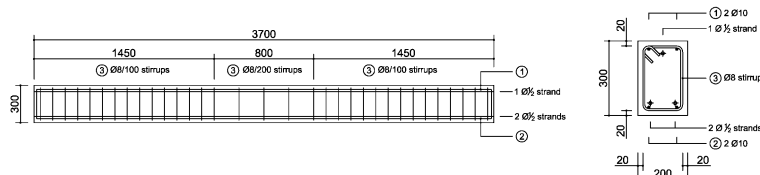


Fig. 2 PC specimen

#### 2.1.3 Tilt clinometers

In this study, a series of clinometer that uses an accelerometer based on MEMS technology is installed on the test specimens. The MEMS accelerometer – being also sensitive to gravity – can measure the change in acceleration with respect to gravity. In this case, a certain angle is generated between the static acceleration and the acceleration due to gravity. This angle corresponds to the slope of the sensor and is called ‘tilt’.



Fig. 3 Clinometer working principle [8] (left), MEMS detail (center) and sensors used in the tests (right)

The previous Fig. 3 shows the acceleration along the x-axis ( $a_x$ ) and the acceleration due to gravity ( $g$ ) generated by changes in the location of the sensors. The relationship between  $a_x$  and  $g$  is expressed in the following equations, where  $\alpha$  denotes the slope of the sensor:

$$a_x = g \cdot \sin(\alpha) \quad (1)$$

$$\alpha = \sin^{-1}(a_x / g) \quad (2)$$

### 3 TEST SET-UP

#### 3.1 Pre-Corroded symmetrically-loaded beam subjected to 4-point bending

The test was conducted on a reinforced concrete beam initially subjected to an artificial electrolytic corrosion process modulated according to Faraday's law and subsequently brought to the collapse situation through a four-point bending test. Fig. 4 and Fig. 5 show the configuration of the test performed. The span of the beam during the test was equal to 2700 mm. The force was applied through a centered load cell which, thanks to a system of steel beams, distributed the load simultaneously across two load points. Three potentiometers placed at half of the height of the cross section measured the vertical displacements at the midspan (P1) and under the two-point loads (P2 and P3). Furthermore, five 2-axes MEMS clinometer (T1 to T5) are placed symmetrically on the extrados of the beam to measure the tilting of the five monitored cross-sections during the entire test period.

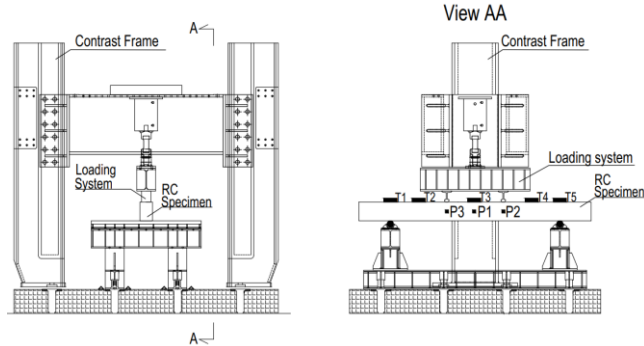


Fig. 4 Experimental test scheme



Fig. 5 Laboratory setup: longitudinal (left) and frontal (right) view

### 3.2 Uncorroded asymmetrically-loaded beam subjected to 4 point bending

The test was carried out on a prestressed concrete beam not subjected to degradation phenomena. In this case the purpose was to study the effect of an asymmetric load on the structure, with the aim of simulating a typical traveling load on a bridge deck. The experimental test-set is shown in Fig. 6 and Fig. 7. The span of the beam during the test was equal to 3000 mm. The load was applied through two mutually independent load jacks. Initially, only jack F2 was operated, ranging from 0 to 35 kN through 8 load steps; subsequently, while maintaining the load of F2 constant, the load of F1 was increased until it also reached 35 kN. The maximum load, distributed between the two load points, was 70 kN, calculated to prevent cracking phenomena in the structural element and thus ensure elastic conditions. Five potentiometers placed at the bottom of the beam measured the vertical displacements at the midspan (P3), under the two-point loads (P2 and P4) and at the same abscissa as the clinometers adjacent to the load points (P1 and P5). The MEMS clinometers (T1 to T5) are placed symmetrically on the extrados of the beam to measure the tilting of the five monitored cross-sections during the entire test period.

This type of test differs from the other presented because the load is applied asymmetrically and because the structural element does not collapse but, remaining within the elastic range, returns to its original state without showing appreciable deformations. The interest of this experimentation was to ascertain if the clinometers could record infinitesimal rotations capable of reconstructing a congruent deformation of the beam.

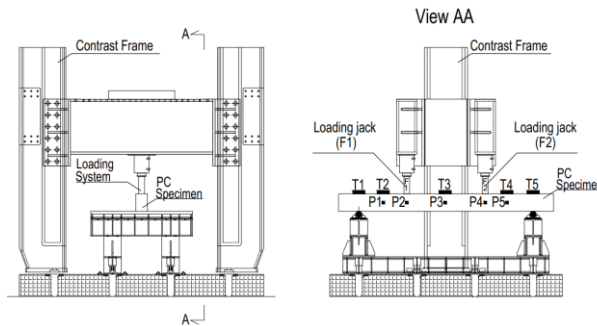


Fig. 6 Experimental test scheme



Load Steps		
N. Step	F1 [kN]	F2[kN]
1	0	0
2	0	5
3	0	10
4	0	15
5	0	20
6	0	25
7	0	30
8	0	35
9	9	35
10	18	35
11	26	35
12	35	35

Fig. 7 Laboratory setup (left) and load steps (right)

## 4 ANALYTICAL METHODS FOR DISPLACEMENT CURVE CONSTRUCTION

Sousa *et al.*[4] in their article state that for the study of a generic bridge span  $j$ , if  $n+1$  boundary constraints are known, a  $n$  degree polynomial function  $P_j^n(x)$  can be fitted to obtain the vertical displacement  $\delta_j(x)$ :

$$\delta_j(x) \cong P_j(x_k) = \sum_{p=1}^n c_{j,p} x_k^p \quad (3)$$

The polynomial coefficients  $c_{j,p}$  are the unknowns, which are calculated considering the boundary conditions. A system of linear equations can be set as expressed in matrix notation by:

$$[A]_j \cdot \{c\}_j = \{b\}_j \tag{4}$$

The matrix  $[A]$  depends on the span geometry, on the location of the instrumented cross sections  $x_j$  and on the span length  $L$ . The vector  $\{c\}_j$  contains the problem unknowns (the polynomial coefficients) and the vector  $\{b\}_j$  the boundary constraints. The problem solution is given by:

$$\{c\}_j = [A]_j^{-1} \cdot \{b\}_j \tag{5}$$

under the hypothesis that the matrix  $[A]$  is not singular.

So, if are known the coordinates of the instrumented cross sections, and the values of tilt sensors installed on, the resolving equations can be written as:

$$\delta : P_j(x_k) = \sum_{p=0}^n c_{j,p} x_k^p \quad k = 1, 2, \dots, n \tag{6}$$

$$\theta : P_j(x_k) = \sum_{p=1}^n p c_{j,p} x_k^{p-1} \quad k = 1, 2, \dots, n \tag{7}$$

In particular, the test configurations of the specimens reported in this paper generate 7 boundary conditions: 2 on displacements and 5 on rotations.

According to *Hou et al*[2], *Lan et al*[9], the deflection of a bridge span based on the angular records is calculated assuming that  $n$  clinometer are installed along a line palalleling the span axis; defining the total measuring time as  $T$ , and the length of the bridge span as  $L$ , angular time histories  $\Theta_i(t)$  ( $i=1, 2, \dots, n$   $0 \leq t \leq T$ ) at  $n$  controlling positions can be acquired based on the real time outputs of  $n$  clinometers. The deflection time history  $y(x,t)$  ( $0 \leq x \leq L$ ,  $0 \leq t \leq T$ ) at  $x$  is known if  $y(x,t_0)$  at any time  $t_0$  ( $0 \leq t_0 \leq T$ ) is calculated.

Defining the  $n$  angular values of the span at  $t_0$  as  $\theta_i(t_0)$  ( $i=1, 2, \dots, n$ ), the deflection curve  $y(x,t_0)$  of the span can be calculated as:

$$y(x, t_0) = A(x) \sum_{j=1}^{n-1} X_j(t_0) g_j(x) \tag{8}$$

Where  $g_j(x)$  is an appropriately selected function group (simplest function group is  $n-1$  order power series) and  $X_j(t_0)$  is an undetermined coefficient, which only depends on time  $t_0$ .  $A(x)$  is a chosen function such as to make the deflection curve satisfy boundary conditions at the supports. For example, when neglecting the supports settlement,  $A(x)$  can be selected as:

$$A(x) = x(x - L) \tag{9}$$

According to the  $n$  angular values at  $t_0$ , can be obtained that:

$$[A'(x) \sum_{j=1}^{n-1} X_j(t_0) g_j(x) + A(x) \sum_{j=1}^{n-1} X_j(t_0) g_j'(x)]_{x=x_i} = \theta_i(t_0) \quad (i = 1, 2, \dots, n) \tag{10}$$

Where  $x_i$  = coordinate of the  $i$ -th clinometer,  $A'(x)$  and  $g_j'(x)$  = first derivative of functions  $A(x)$  and  $g_j(x)$ . It is convenient to resolve the unknown coefficient  $X_j(t_0)$  through the least – square method: in this way the deflection curve  $y(x,t_0)$  can be determined and, subsequently, the whole deflection time history  $y(x,t)$  is calculated.

Based on their experiments, *He et al.*[3] state that the method using five clinometers that are placed evenly across the bridge beam provides a good measure of dynamic deflection. As a matter of fact, a cubic polynomial needs to determine four unknown coefficients that can fit the deflection curve better, which requires at least five clinometers. From this, it is clear that 5 clinometers are the best choice on testing deflections of simply or continuous supported bridges.

In the present paper, three additional families of orthogonal polynomials were proposed, in addition to the one reported in [2], for the analytical construction of displacement curves.

The following Table 1 shows the sets of orthogonal polynomials chosen up to the polynomial degree of interest.

Table 1 Families of orthogonal polynomials used in analytical methods

Function	Hou et al.[2]	Hermite polynomials	Chebyshev kind I polynomials	Chebyshev kind II polynomials
$g_1(x)$	1	1	1	1
$g_2(x)$	x	x	x	2x
$g_3(x)$	$x^2$	$x^2-1$	$2x^2-1$	$4x^2-1$
$g_4(x)$	$x^3$	$x^3-3x$	$4x^3-3x$	$8x^3-4x$

These polynomial families were instrumental in improving the analytical modelling of the displacement curves and provided new information on the structural behavior.

## 5 RESULTS

In the tests described in this article, two different types of sensors were used: traditional sensors (potentiometers) that require a rigid reference point to measure deflection, and innovative MEMS sensors capable of acquiring data on specimen inclinations. The sensors of two different types operated independently and their collected data – once acquired and processed – allowed for a comparison of the results obtained in terms of displacements. In Fig. 8 is reported a flowchart explaining the work behind the results that will be presented in this chapter.

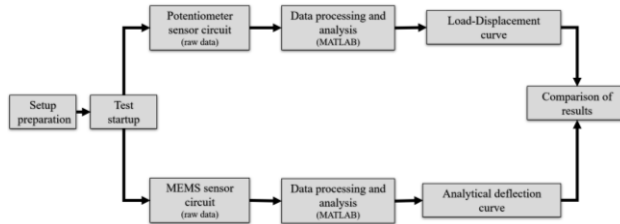


Fig. 8 Work flowchart for comparison of results

### 5.1 Uncorroded asymmetrically-loaded beam subjected to 4 point bending

The graphs in Fig. 9 show the key results of the test. As can be observed, during the initial phases of the test where the beam is loaded only through the loading point F2, the absolute rotation values recorded by sensors T4 and T5, closest to F2, are larger compared to that recorded by the opposite sensors T1 and T2. This phenomenon is in accordance with the initial asymmetric loading configuration. Subsequently, when the loading configuration becomes symmetric, the rotation values recorded by T1, T2, and T4, T5 become almost identical in magnitude. The inclination value of the central sensor T3 remains close to zero during the entire test.

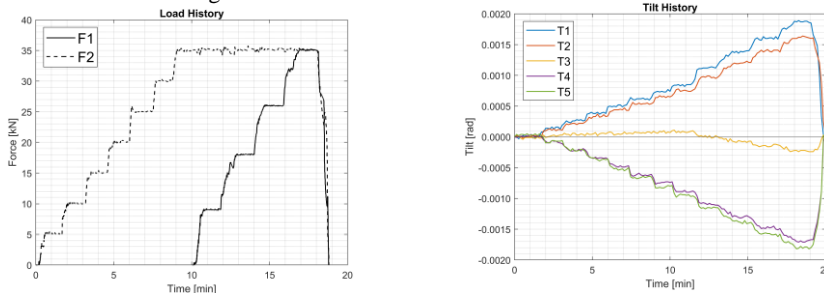


Fig. 9 Test load history (left) and trend of the beam tilting with time (right)

In Fig. 10 are reported the deflection curves representing the maximum asymmetric loading condition (left) and the final symmetric loading condition (right). While the 'Experimental' curve was obtained from the deflection values recorded by the five fixed potentiometers (P1 to P5 of Fig. 6-right)

installed on the specimen, the other curves were analytically calculated from the rotation values recorded by the MEMS sensors adopting the calculation methods described in Chapter 4 and the orthogonal polynomials families indicated in Table 1.

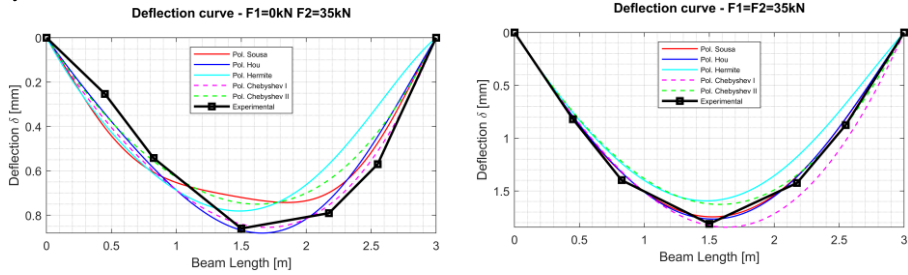


Fig. 10 Deflection curves: asymmetric load condition (left) and final symmetric load condition (right). Experimental – Analytical comparison

## 5.2 Pre-Corroded symmetrically-loaded beam subjected to 4-point bending

The graphs reported in Fig. 11 show the main results of the test. The load was applied incrementally with time intervals during which it was kept constant. This condition is clearly visible in the graph of Fig. 11-right: the tilt values recorded by the MEMS sensors (T1 to T5 of Fig. 4-right), show intervals where the angles increase and others in which they remain constant.

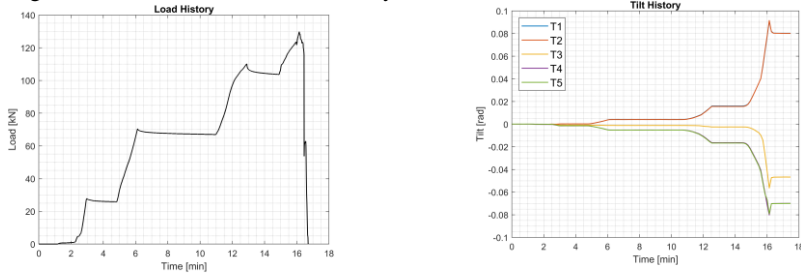


Fig. 11 Test load history (left) and trend of the beam tilting with time (right)

Starting from the data collected by the MEMS sensors and potentiometers, the load-displacement curve of the midspan section of the beam was studied until the collapse of the specimen. Fig. 12 shows the results of the comparison. The curve ‘Experimental’ was obtained directly from the potentiometer positioned at point P1 of Fig. 4-right, while the other curves were derived from clinometric data using the calculation methods described in Chapter 4 (‘Pol.Sousa’ from [4], ‘Pol.Hou’, ‘Pol.Hermite’, ‘Pol.ChebI’ and ‘Pol.ChebII’ derived from their respective orthogonal polynomials families indicated in Table 1). It is observed how the analytical methods can reconstruct with good approximation the displacement recorded directly by the potentiometer.

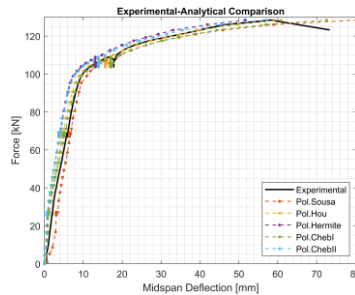


Fig. 12 Load-Displacement curve for the midspan section. Experimental – Analytical comparison

## 6 CONCLUSIONS

This paper provides some detailed information on a method aimed at reconstructing the displacements of longitudinal structural elements using raw data from MEMS clinometric sensors. To validate the method, the paper presents experiments conducted as part of a comprehensive survey under an Italian PRIN project. These experiments, focused on evaluating the flexural response of reinforced concrete (RC) and prestressed concrete (PC) beams, were carried out at the Laboratory of the University of Rome "Tor Vergata". The methods demonstrate their capability to accurately calculate the displacements of structural elements, regardless of degradation, under both symmetrical and asymmetrical loading conditions. Validation was achieved by comparing the proposed methods with traditional displacement sensors like potentiometers. The findings suggest that low-cost MEMS sensors are a viable alternative to traditional monitoring systems, particularly because they do not require fixed observation points, making them easy to install on structures such as bridges over rivers, railways, and highways.

Given the granted reliability of the proposed approach, this research project aims to develop optimized calculation algorithms that can use sensor data to reconstruct structural displacements and autonomously assess safety levels, ultimately enabling a continuous monitoring system.

### Acknowledgements

The research presented in this paper is supported by the PRIN 2017 grant, from the Italian Ministry of University and Research, within the project "Life-long optimized structural assessment and proactive maintenance with pervasive sensing techniques".

### References

- [1] Burdet, Olivier & Zanella, Jean-Luc. (2000). "Automatic Monitoring of Bridges using Electronic Clinometer". IABSE Congress Report. 16. 10.2749/222137900796314284.
- [2] Hou, Xingmin & Yang, Xueshan & Huang, Qiao. (2005). "Using Inclinometers to Measure Bridge Deflection.". *Journal of Bridge Engineering - J BRIDGE ENG.* 10. 10.1061/(ASCE)1084-0702(2005)10:5(564).
- [3] He, Xianlong & Yang, Xueshan & Zhao, Lizhen. (2014). "New Method for High-Speed Railway Bridge Dynamic Deflection Measurement". *Journal of Bridge Engineering.* 19. 05014004. 10.1061/(ASCE)BE.1943-5592.0000612.
- [4] Sousa, Helder & Cavadas, Filipe & Henriques, António Abel & Bento, João & Figueiras, Joaquim. (2013). "Bridge deflection evaluation using strain and rotation measurements." *Smart Structures and Systems.* 10.12989/sss.2013.11.4.365.
- [5] Di Carlo, Fabio & Meda, Alberto & Rinaldi, Zila. (2023). "Structural performance of corroded R.C. beams". *Engineering Structures.* 274. 115117. 10.1016/j.engstruct.2022.115117.
- [6] Di Carlo, Fabio & Isabella, Paolo & Bico, Francesco Filippo & Meda, Alberto & Rinaldi, Zila (2024). "Experimental behavior of a RC beam under simultaneous accelerated artificial corrosion and sustained loads". Accepted in ICC Conference, Italy
- [7] Bico, Francesco Filippo & Bartoli, Manuel & Di Carlo, Fabio & Meda, Alberto & Molaioni, Filippo & Rinaldi, Zila (2023). "Structural behavior of PC beams under simultaneous corrosion and sustained loads." *Life-Cycle of Structures and Infrastructure Systems* (pp. 2941-2948). CRC Press.
- [8] Ha, Dae & Park, Hyo & Choi, Se Woon & Kim, Yousok. (2013). "A Wireless MEMS-Based Clinometer Sensor Node for Structural Health Monitoring". *Sensors (Basel, Switzerland).* 13. 16090-104. 10.3390/s131216090.
- [9] Lan, Riqing & Wang, Yushi & Chi, Qinglei. (2019). "Reconstitution of Static Deflections of Suspension Bridge Based on Clinometer Data". *IOP Conference Series: Earth and Environmental Science.* 304. 032081. 10.1088/1755-1315/304/3/032081.

# Structural Assessment and Maintenance Optimization via Satellite Radar Imagery and Data Integration

Teresa Celozzi<sup>1</sup>, Fabio Di Carlo<sup>1</sup> and Alberto Meda<sup>1</sup>

<sup>1</sup>*Department of Civil Engineering and Computer Science Engineering,  
University of Rome Tor Vergata,  
Via del Politecnico, 1, Rome (00133), Italy*

## Abstract

Structural Health Monitoring (SHM) plays a pivotal role in ensuring bridge safety, necessitating sophisticated methods for continuous evaluation. This is particularly significant in Italy, where many infrastructures have reached or exceeded their designed operational lifespan. This research examines the effectiveness of Multi-Temporal Differential Interferometry Synthetic Aperture Radar (MT-DInSAR) using COSMO-SkyMed (CSK) data for the surveillance of bridges, focusing on a specific case study. MT-DInSAR employs satellite data to detect ground movements, enabling continuous and non-invasive monitoring of structural deformations. Various analytical techniques, such as nearest neighbors, grid-subsampling, and spatial interpolation, are utilized to assess displacements along different axes. The study highlights the impact of these methods on the evaluation of the structural behavior, underlining the necessity for robust monitoring strategies that are applicable to bridges of different designs and materials. By combining historical data with satellite-based analysis, this approach provides a comprehensive understanding of bridge conditions, which is crucial for maintenance and improvement efforts. The research demonstrates the potential of satellite-based monitoring to provide continuous and weather-independent oversight of critical infrastructure, addressing the urgent need for effective structural monitoring.

## 1 Introduction

A prominent discussion in the field of structural engineering in Italy revolves around the need to preserve existing infrastructure. It is widely recognized that many reinforced concrete structures in Italy have exceeded or are nearing the end of their service lives. This scenario requires continuous monitoring to ensure the safety and stability of these structures [1]–[2].

Among the innovative technologies in this domain, satellite radar remote sensing systems have become particularly important. They enable the study of objects from considerable distances by leveraging the interaction between the electromagnetic waves emitted by a sensor and the Earth's surface [3]. These systems can acquire numerous images of the same area over several years, allowing for the reconstruction of the temporal evolution of phenomena in the case of a catastrophic event by analyzing the recorded deformations.

Within the spectrum of satellite sensors, the Synthetic Aperture Radar (SAR) is crucial. As an active sensor operating in the microwave range (with wavelengths from 1 cm to 1 m), SAR's key advantage is its ability to function regardless of external light sources and weather conditions. In structural monitoring, Multi-Temporal Differential SAR Interferometry (MT-DInSAR) techniques are particularly noteworthy [4]. This technique is widely utilized to detect deformations caused by slow-evolving phenomena such as thermal variations, landslides, and subsidence. Its accuracy and ability to continuously detect changes in the Earth's surface over time make it an essential tool for mitigating and preventing risks associated with such phenomena.

## 2 Case Study and Satellite Data

This study describes the results of data processing in the case study of the “Mezzocammino” Bridge in Rome using different resampling techniques. The “Mezzocammino” Bridge is a significant infrastructure spanning the Tiber River, linking the areas of Mezzocammino and Spinaceto. Its origins trace back to 1937, when plans were developed to address the recurrent floods, including the arrangement of the river and the construction of an aerodrome in Rome. Initially, the project included a movable barrier with a navigation lock at Mezzocammino. However, following a devastating flood in December of the



same year, the project was revised to focus solely on the construction of a new bridge connecting the aerodrome to the existing road network. The construction of the “Mezzocammino” Bridge subsequently became part of the urban plan for the E42, a universal exhibition intended to commemorate the 20th anniversary of fascism [5]. Currently, the “Mezzocammino” Bridge connects Via Appia and Via Aurelia. It is an integral part of the Grande Raccordo Anulare (GRA) and has been classified as a national monument since 2003, serving as the access ramp to the GRA from Via del Mare.



Fig. 1 “Mezzocammino” Bridge, image acquired by drone, 2023 (Anas S.p.A.)

In this research project, the processed data coming from the COSMO-SkyMed (CSK) constellation. The CSK system consists of four medium-sized satellites in low Earth orbit, each equipped with a high-resolution multimodal Synthetic Aperture Radar (SAR) operating in the X-band, with a wavelength of 3.12 cm. CSK offers various acquisition modes, with the STRIPMAP-HIMAGE mode being particularly relevant for satellite interferometry. In this mode, the revisit time is 16 days per satellite, with a resolution of 3 x 3 meters in the azimuth and range directions and a swath of approximately 40 x 40 kilometers. This configuration allows the satellite to capture the same geographic area in both ascending geometry, with a viewing angle of 34.6°, and descending geometry, with a viewing angle of 26.8°. The data utilized in this study pertain to displacement measurements recorded from March 2011 to March 2019. Full-resolution multi-temporal interferometric processing provides valuable results, including comprehensive maps of average displacement velocity and time series of displacement for all coherent points in the scene, referred to as Persistent Scatterers (PS), relevant to the analyzed temporal interval [6]. Specifically, the PS, as illustrated in Fig. 2, are concentrated near buildings and infrastructure, forming high-density zones. Conversely, areas on the map lacking measurement points are generally identified as green areas and undeveloped zones. For each PS are typically provided: an identification code (ID), geographic coordinates (latitude and longitude), elevation relative to a global reference system, direction cosine values of the line of sight (LOS) along the East-West, North-South, and vertical directions, a coherence value indicating the reliability of the displacement information, the temporal series of displacements along the LOS and the average annual displacement velocity along the same direction.

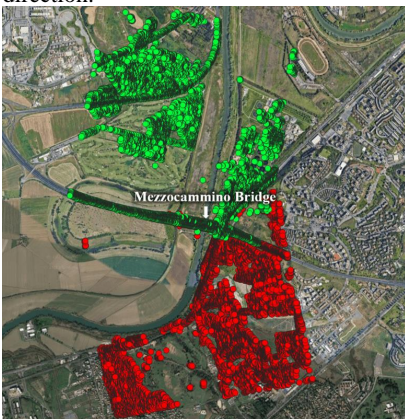


Fig. 2 Satellite data from the COSMO-SkyMed constellation pertaining to the ascending (red) and descending (green) orbits of the quadrant of interest where the structure under study is located.

### 3 Data Processing

To perform a detailed analysis of the “Mezzocammino” Bridge, the original datasets were segmented to create two new series focused solely on the structure of interest. It is important to note that the PSs in the ascending and descending datasets typically do not coincide and may exhibit significant variability in their spatial distribution. This variability is primarily due to the different satellite observation points along the two acquisition orbits and the varying viewing angles.

Fig. 3 and Fig. 4 depict the average displacement velocity values measured along the LOS direction of the satellites, expressed in mm/year, for the two datasets. According to the convention commonly used in the literature, positive velocity values indicate movement towards the satellite, while negative values indicate movement away from the satellite.



Fig. 3 Map of average displacement velocities along the LOS - ascending orbit



Fig. 4 Map of average displacement velocities along the LOS - descending orbit

From a preliminary qualitative analysis of the deformation velocities along the LOS, it is evident that there is a movement away from the satellite, with higher velocities observed at the lateral zones of the bridge, while the central part exhibits reduced velocities around an average of 0 mm/year.

As mentioned earlier, interferometric data are typically represented by points with significant coherence over the observation period, the PSs. However, it is important to note that it is uncommon for deformation measurements along the satellite's LOS, relative to the two acquisition orbits, to coincide exactly for the same points. Similarly, DInSAR measurements from the two orbits may not cover the same time interval. Therefore, to effectively combine the data from ascending and descending geometries, a spatial and temporal resampling process of the data series was necessary [7]–[8]. In this case, the analyses were conducted using only spatial resampling, utilizing the average velocity values obtained from the linear regression of the displacement time series.

However, before proceeding, the displacement time series were truncated to refer to the same period, aligning the initial and final acquisition times and were filtered based on their topographic values to limit the processing to points belonging to the bridge deck, which is at an altitude of 13 meters. Points with topographic values between 11 meters and 15 meters were included, as the elevation position value of the points, relative to the processing of a full spatial resolution CSK dataset with a mean look angle of approximately  $33^\circ$  for the SBAS-DInSAR technique, is associated with an error of  $\pm 2$  meters [9].

Data processing operations were conducted by subdividing the bridge into six reference zones. Fig. 5 illustrates this subdivision, highlighting the quadrants that underwent thorough analysis during the data processing phase.



Fig. 5 Bridge's subdivision into zones of interest

### 3.1 Spatial resampling

In the context of displacement evaluation, three different spatial resampling techniques are illustrated below. It is necessary to make assumptions because the PSs in the two orbits do not spatially coincide.

#### 3.1.1 Nearest neighbors

The initial spatial resampling technique employed involves identifying pairs of points from the two datasets that are sufficiently close to be considered representative of the same ground target. However, it is crucial to account for the intrinsic error associated with the system, which is related to the precision of the spatial positioning of the data. Within the six predefined zones, pairs of sufficiently close points were selected. The average LOS displacement velocity value was derived from the linear regression of the displacement series from both acquisition geometries. Fig. 6 shows the pair of points chosen in zone 1 with the relative displacement series.

The average LOS displacement velocities observed for each pair of points were combined with the direction cosines to evaluate the velocity in the two directions, vertical and E-W. The obtained values for the six quadrants of interest are reported in the final paragraph and compared with the other two applied techniques.

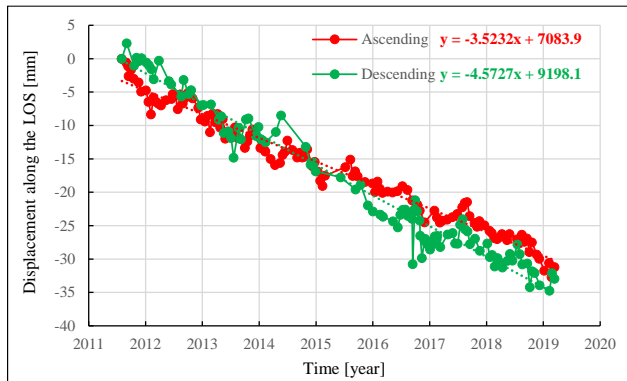


Fig. 6 Pair of points analyzed in Zone 1 of the bridge and related displacement series

#### 3.1.2 Grid-subsampling

The second technique employs resampling methods on a regular grid. The area of interest was subdivided into square cells measuring 5 x 5 meters, onto which resampling was applied. The grid size was selected based on the dimensions of the bridge to ensure comprehensive coverage of the entire area. Once the grid was established, the average velocity of the points within each cell was calculated, and this value was assigned to the corresponding quadrant. The annual average displacement velocity was determined as the slope of the linear regression line fitted to the displacement function. Fig. 7 and Fig. 8 show all the quadrants with their respective average velocities, both for the ascending and descending orbits.



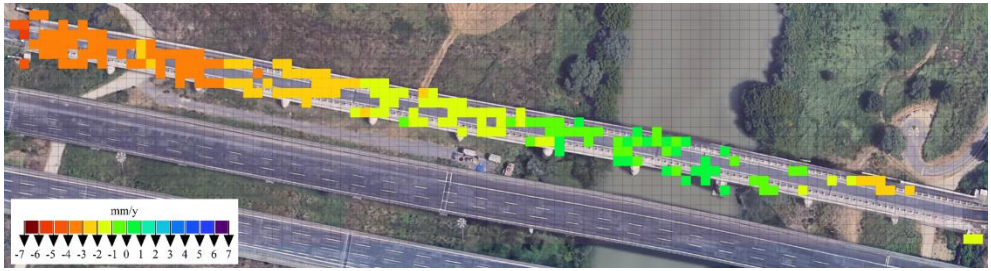


Fig. 7 Map of average displacement velocities along the LOS - ascending orbit (Grid-subsampling)

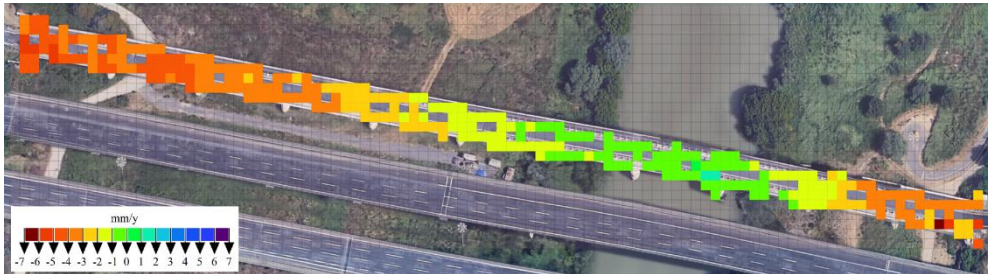


Fig. 8 Map of average displacement velocities along the LOS - descending orbit (Grid-subsampling)

Subsequently, quadrants containing points in both ascending and descending orbits were intersected. The average velocities from both orbits, measured along the LOS, were combined with the direction cosines. This step was performed to obtain the mean values of displacement velocity along the vertical and E-W directions. Fig. 9 and Fig. 10 depict the maps of average velocity along these two directions.



Fig. 9 Map of average displacement velocities in the vertical direction (Grid-subsampling)



Fig. 10 Map of average displacement velocities in the horizontal direction (Grid-subsampling)

It is important to note that by considering only the quadrants containing information for both ascending and descending orbits a large part of the potential information is lost. In the final paragraph, the average velocity and displacement values along the two directions are reported for the six quadrants of interest and compared with the other two applied techniques.

### 3.1.3 Interpolation

The third technique involves the application of spatial interpolation methods, specifically the Inverse Distance Weighted (IDW) method was chosen. The weights assigned to points are inversely proportional to their distance from the prediction point and typically raised to a power, often fixed at 2, as in the present study. Predicted values cannot exceed the maximum or minimum measured value.

IDW interpolation was performed for both ascending (Fig. 11) and descending (Fig. 12) series.

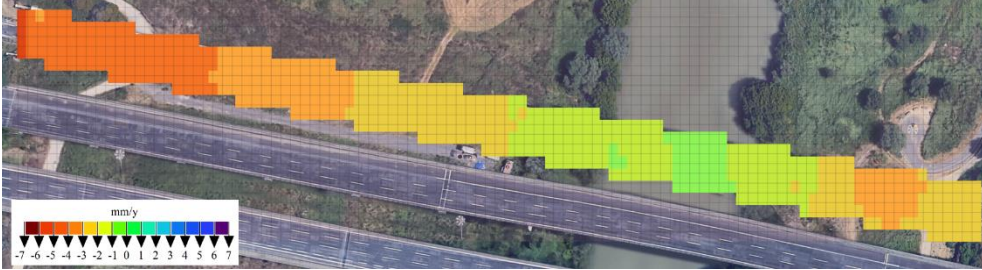


Fig. 11 Map of average displacement velocities along the LOS - ascending orbit (Interpolation)

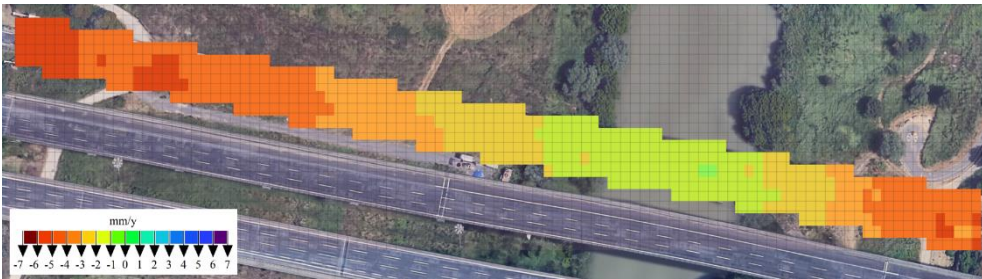


Fig. 12 Map of average displacement velocities along the LOS - descending orbit (Interpolation)

Then the average velocity values along the LOS of the two orbits were combined with the direction cosines to obtain the average velocity values along the vertical (Fig. 13) and E-W (Fig. 14) directions.

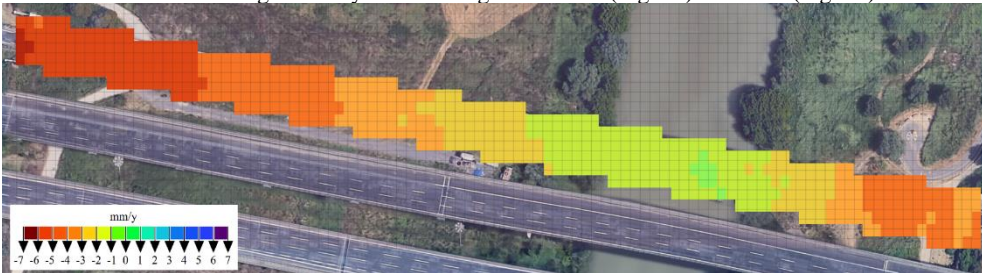


Fig. 13 Map of average displacement velocities in the vertical direction (Interpolation)



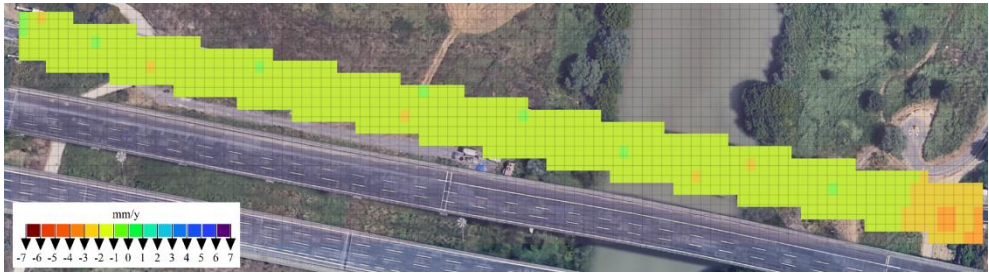


Fig. 14 Map of average displacement velocities in the horizontal direction (Interpolation)

In the final paragraph, the average velocity and displacement values along the two directions are reported for the six quadrants of interest and compared with the other two applied techniques.

#### 4 Conclusions

The analysis conducted indicates that the average displacement velocities observed during the acquisition period are predominantly vertical. This is supported by the fact that the average displacement velocities measured along the line of sight exhibit the same sign in both ascending and descending acquisition geometries. Table 1 shows the values of the velocity components in the vertical and horizontal directions, calculated using the three different techniques.

Table 1 Comparison of mean velocity values in the vertical and horizontal directions for the six zones

	Zone 1	Zone 2	Zone 3	Zone 4	Zone 5	Zone 6
<b>Nearest neighbors</b>						
<b>V<sub>U</sub> [mm/year]</b>	-5.712	-4.219	-2.908	-0.696	-0.950	-4.318
<b>V<sub>E-W</sub> [mm/ year]</b>	-2.259	-1.045	-1.333	-0.424	-0.637	-1.512
<b>Grid-subsumpling</b>						
<b>V<sub>U</sub> [mm/ year]</b>	-4.920	-3.527	-2.527	-0.652	-0.914	-3.593
<b>V<sub>E-W</sub> [mm/ year]</b>	-1.058	0.010	-0.429	-0.210	-0.836	-0.337
<b>Interpolation</b>						
<b>V<sub>U</sub> [mm/ year]</b>	-4.686	-3.470	-2.369	-0.665	-1.198	-3.493
<b>V<sub>E-W</sub> [mm/ year]</b>	-0.713	-0.113	-0.362	-0.305	-0.578	-0.481

The comparison of results shows that the outcomes do not differ substantially from one another. The nearest neighbors method, which combines velocity values from proximate and representative ground points, provides a more precise evaluation of local phenomena. However, satellite data may not capture every point within the scene. Consequently, grid and interpolation methods, which incorporate points within defined areas, may lack precision but offer more widely distributed information. The distribution of points within the studied areas may be non-uniform and occasionally data-sparse, which can impact the accuracy of these two methods. Finally, Table 2 shows the displacement values, both in the vertical and horizontal directions, obtained by multiplying the mean velocity values, previously shown, by the acquisition period (2011-2019).

Table 2 Comparison of displacement values in the vertical and horizontal directions for the six zones

	Zone 1	Zone 2	Zone 3	Zone 4	Zone 5	Zone 6
	<b>Nearest neighbors</b>					
$\delta_U$ [cm]	-4.350	-3.213	-2.215	-0.530	-0.723	-3.288
$\delta_{E-W}$ [cm]	-1.720	-0.796	-1.015	-0.322	-0.485	-1.151
	<b>Grid-subsampling</b>					
$\delta_U$ [cm]	-3.747	-2.686	-1.925	-0.497	-0.696	-2.737
$\delta_{E-W}$ [cm]	-0.806	0.008	-0.326	-0.160	-0.637	-0.257
	<b>Interpolation</b>					
$\delta_U$ [cm]	-3.569	-2.643	-1.804	-0.506	-0.912	-2.660
$\delta_{E-W}$ [cm]	-0.543	-0.086	-0.276	-0.232	-0.440	-0.366

It is important to emphasize that displacement analysis is only one of the many factors that must be considered in the safety assessment of a bridge. To achieve a comprehensive evaluation of the structural condition of a bridge, it is essential to integrate various parameters, including materials' degradation, load conditions and environmental conditions. Therefore, displacement analysis must be coupled with other monitoring technologies to provide a complete and accurate assessment of structural health, enabling the optimization of intervention and maintenance strategies.

## References

- [1] Delo G., Civera M., Lenticchia E., Miraglia G., Surace C., Ceravolo R. 2022. "Interferometric Satellite Data in Structural Health Monitoring: An Application to the Effects of the Construction of a Subway Line in the Urban Area of Rome" *Applied Sciences* 12(3): 1658.
- [2] Giordano P. F., Turksezer Z. I., Previtali M., Limongelli M. P. 2022. "Damage detection on a historic iron bridge using satellite DInSAR data" *Structural Health Monitoring* 21(5): 2291-2311.
- [3] Di Carlo F., Miano A., Giannetti I., Mele A., Bonano M., Lanari R., Meda A. e Prota A. 2021. "On the integration of multi temporal synthetic aperture radar interferometry products and historical surveys data for building s structural monitoring" *Journal of Civil Structural Health Monitoring*.
- [4] Lanari R., Mora O., Manunta M., Mallorquí J.J., Berardino P., Sansosti E. 2004. "A small baseline approach for investigating deformations on full resolution differential SAR interferograms" *IEEE Trans Geosci Remote Sens* 42(7):1377-1386.
- [5] Giannetti I., Mornati S. 2022. *Ponti Gerber in Italia. Indagini storiche per la salvaguardia*. Gangemi Editore.
- [6] Di Carlo F., Giannetti I., Romualdi A., Meda A., Rinaldi Z. 2022. "On the DInSAR technique for the structural monitoring of modern existing bridges" *Bridge Engineering*.
- [7] Miano A., Di Carlo F., Mele A., Bonano M., Prota A., Meda A. 2023. "Damage Assessment Through the Use of SBAS-DInSAR Data: An Application to the "Vittorino da Feltre" Masonry School Building in Rome" *International Journal of Architectural Heritage*.
- [8] Talledo D. A., Miano A., Bonano M., Di Carlo F., Lanari R., Manunta M., Meda A., Mele A., Prota A., Saetta A., Stella A. 2022. "Satellite radar interferometry: Potential and limitations for structural assessment and monitoring" *Journal of Building Engineering* 46:103756.
- [9] Miano A., Di Carlo F., Mele A., Giannetti I., Nappo N., Rompatò M., Striano P., Bonano M., Bozzano F., Lanari R., Mazzanti P., Meda A., Prota A., Mugnozza G. S. 2022. "GIS Integration of DInSAR Measurements, Geological Investigation and Historical Surveys for the Structural Monitoring of Buildings and Infrastructures: An Application to the Valco San Paolo Urban Area of Rome" *Infrastructures* 7(7):89.



TOR VERGATA  
UNIVERSITÀ DEGLI STUDI DI ROMA

